Institute of Nuclear Physics of the
Uzbekistan Academy of Sciences

THE XII INTERNATIONAL CONFERENCE

NUCLEAR SCIENCE AND ITS APPLICATION (ICNSA2026)



Dedicated to the 70th anniversary of the
Institute of Nuclear Physics of the Uzbekistan Academy of Sciences

BOOK OF ABSTRACTS

October 12-15, 2026
Ulugbek,Tashkent

RADIOPREPARAT

RT

XII XALQARO KONFERENSIYA
YADRO FANI VA UNING TATBIQI (ICNSA2026)

2026-yil 12–15-oktabr
Ulug‘bek, Toshkent

MA’RUZALAR TEZISLARI TO‘PLAMI

TASHKILOTCHI: O‘ZBEKISTON FANLAR AKADEMIYASINING YADRO FIZIKASI INSTITUTI

O‘ZBEKISTON FANLAR AKADEMIYASI YADRO FIZIKASI INSTITUTINING 70 YILLIGIGA BAG‘ISHLANGAN



THE XII INTERNATIONAL CONFERENCE
NUCLEAR SCIENCE AND ITS APPLICATION (ICNSA2026)

October 12-15, 2026
Ulugbek, Tashkent

BOOK OF ABSTRACTS

ORGANIZED by Institute of Nuclear Physics of Uzbekistan Academy of Sciences

Dedicated to the 70th anniversary of the Institute of Nuclear Physics of the Uzbekistan Academy of Sciences

Ulugbek, Tashkent – 2026

“YADRO FANI VA UNING TATBIQI” (ICNSA2026):
XII XALQARO KONFERENSIYA,
2026-yil 12–15-oktabr, Ulug‘bek, Toshkent
MA’RUZALAR TEZISLARI TO‘PLAMI
O‘zbekiston Fanlar akademiyasi Yadro fizikasi instituti, 2026, 366 bet.

THE XII INTERNATIONAL CONFERENCE
NUCLEAR SCIENCE AND ITS APPLICATION (ICNSA2026)
October 12-15, 2026, Ulugbek, Tashkent
BOOK OF ABSTRACTS
Institute of Nuclear Physics, Academy of Sciences of Uzbekistan, 2026, 366 pages.

© Institute of Nuclear Physics of Uzbekistan Academy of Sciences, 2026

INTERNATIONAL ADVISORY COMMITTEE

Ayupov Sh. (Uzbekistan)
Akhmedkhadjaev A. (Uzbekistan)
Bakhramov S. (Uzbekistan)
Belushkin A. (JINR)
Chizhik S. (Belarus)
Dong J. (China)
Garibov A. (Azerbaijan)
Gunter Meelis (Germany)
Jeenbaev N. (Kyrgyzstan)
Kadyrov A. (Australia)
Kalmykov S. (Russia)
Kulikov S. (JINR)
Konstantinov V. (Russia)
Kovalchuk M. (Russia)
Kozlenko D. (JINR)
Leo Sangik Wu (Korea)
Likhachev A. (Russia)
Logachev P. (Russia)
Lychagin E. (JINR)
Mimura Koichi (Japan)
Mirzaev S. (Uzbekistan)
Salikhbaev U. (Uzbekistan)
Nasirov A. (JINR)
Rosta L. (Hungary)
Sakhiyev S. (Kazakhstan)
Sanakulov K. (Uzbekistan)
Shvetsov V. (JINR)
Shevchenko V. (Russia)
Trubnikov G. (JINR)
Tuzov A. (Russia)

PROGRAM COMMITTEE

Chairman: Sadikov I.
Vice-Chairman: Tashmetov M.
Secretary: Fazilova Z.

Abdullaeva G.
Artemov S.
Ashurov M.
Baytelesov S.
Bozorov E.
Ganiev O.
Eshanqulov G.
Ibragimova E.
Igamov S.
Khaydarov R.
Khujaev S.
Kulabdullaev G.
Kuldjanov B.
Kungurov F.
Kurbanov B.
Kurbanov U.
Makhkamov Sh.
Malikov Sh.
Mukhtarov A.
Mussaeva M.
Nuritdinov I.
Olimov Kh.
Rakhimov A.
Tojiboev O.
Turakulov S.
Tursunov E.
Vasidov A.

ORGANIZING COMMITTEE

Chairman: Sadikov I.
Vice-Chairman: Tashmetov M.

Abdukayumov A.
Boltabaev A.
Boyboboeva S.
Bozarov O.
Ergashev F.
Esanov Z.
Fayzullaev R.
Ibraimov I.
Ismatov N.
Kerimova E.
Khamidova S.
Kurbanova Z.
Lutpullaev O.
Madaminov B.
Mirzaev B.
Rafikov A.
Sotvoldiev A.
Tadjibaev D.
Turdaliev K.
Umerov R.
Valieva L.
Yarmatov B.

SECRETARIAT OF CONFERENCE:

FAZILOVA Zekie, fazilovaz@mail.ru; tel: (+998)93-557-69-04
VALIEVA Leyla, leyla.valieva.00@bk.ru; tel: (+998)97-766-07-47

THE XII INTERNATIONAL CONFERENCE

NUCLEAR SCIENCE AND ITS APPLICATION (ICNSA2026)

is sponsored by the following organizations:

"RADIOPREPARAT" State Institution, Tashkent, Uzbekistan

"TEZLATGICH" Enterprise, Tashkent, Uzbekistan

Design department with experimental plant, Institute Nuclear Physics, Academy of Sciences, Tashkent, Uzbekistan

The organizers of the conference thank the sponsors of conference and authors of reports and all participants for their contribution to success of the conference

Уважаемые коллеги!

От имени Организационного комитета приветствуем участников XII Международной конференции «Ядерная наука и ее применение», проходящей 12–15 октября 2026 года в Ташкенте и посвященной 70-летию Института ядерной физики Академии наук Республики Узбекистан.

На протяжении семи десятилетий Институт ядерной физики вносит значительный вклад в развитие фундаментальной и прикладной науки, подготовку научных кадров и внедрение результатов научных исследований в различные отрасли экономики и социальной сферы. Юбилей Института – это не только повод подвести итоги многолетней научной деятельности, но и возможность определить новые направления исследований, обсудить перспективы развития ядерной науки и укрепить международные научные связи.

Наша конференция продолжает добрую традицию объединения ученых и специалистов для обсуждения актуальных проблем современной науки, обмена результатами исследований и опытом. Широкая география участников и разнообразие представленных научных направлений свидетельствуют о высоком интересе научного сообщества к развитию ядерной физики и технологий. Особую значимость придает конференции активное участие молодых ученых, которым предстоит определять будущее научных исследований и технологического прогресса.

В настоящем сборнике представлены тезисы докладов, отражающие современные достижения и перспективы развития теоретической и экспериментальной ядерной физики, радиационной физики конденсированных сред и нанофизики, применения ядерных технологий в медицине, экологии и промышленности, ядерной энергетики и перспективных ядерно-энергетических систем.

Уверены, что конференция станет эффективной площадкой для профессионального диалога, обмена новыми идеями, установления научных контактов и развития совместных исследовательских проектов. Надеемся, что представленные работы будут способствовать дальнейшему развитию научного сотрудничества и расширению практического применения достижений ядерной науки.

Желаем всем участникам плодотворной работы, интересных дискуссий, новых научных открытий и успешной реализации намеченных планов!

От имени Организационного комитета выражаем благодарность нашим постоянным спонсорам конференции:

Государственному учреждению «Радиопрепарат»,

ООО «Тезлатгич»,

Конструкторскому бюро с опытным заводом.

Организационный комитет
XII Международной конференции
«Ядерная наука и ее применение»

Dear Colleagues!

On behalf of the Organizing Committee, we are pleased to welcome you to the XII International Conference "Nuclear Science and its Application," taking place in Tashkent on October 12–15, 2026, and dedicated to the 70th anniversary of the Institute of Nuclear Physics of the Academy of Sciences of the Republic of Uzbekistan.

For seven decades, the Institute of Nuclear Physics has made a significant contribution to the advancement of fundamental and applied science, the training of scientific personnel, and the practical application of research findings across various sectors of the economy and society. The Institute's anniversary is not only an occasion to reflect on its longstanding scientific achievements but also an opportunity to identify new research directions, discuss prospects for the development of nuclear science, and strengthen international scientific cooperation.

Our conference continues the longstanding tradition of bringing together scientists and specialists to discuss current challenges in modern science, exchange research findings, and share professional experience. The broad geographical representation of participants and the diversity of scientific topics demonstrate the international research community's strong interest in the advancement of nuclear physics and technology. The active participation of young scientists is particularly important, as they will shape the future of scientific research and technological progress.

This collection presents abstracts reflecting current achievements and future prospects in theoretical and experimental nuclear physics, radiation physics of condensed matter and nanophysics, the application of nuclear technologies in medicine, ecology and industry, nuclear energy, and advanced nuclear energy systems.

We are confident that the conference will provide an effective platform for professional dialogue, the exchange of new ideas, the establishment of scientific contacts, and the development of collaborative research projects. We hope that the contributions presented here will foster further scientific cooperation and expand the practical application of advances in nuclear science.

We wish all participants a productive conference, stimulating discussions, new scientific discoveries, and every success in achieving their research goals!

On behalf of the Organizing Committee, we express our gratitude to our regular conference sponsors:

"Radiopreparat" State Institution,

"Tezlatgich" Enterprise,

Design Department with Experimental Plant.

Organizing Committee of the
XII International Conference
"Nuclear Science and its Application"

Plenary Reports	8
Section I: Theoretical and Experimental Nuclear Physics	34
Section II: Radiation Physics of Condensed Matter and Nanophysics	130
Section III: Application of Nuclear Technologies in Medicine, Ecology and Industry	230
Section IV: Nuclear Energy and Advanced Nuclear Power Systems	294
ALPHABETICAL INDEX	328
CONTACTS OF CONFERENCE PARTICIPANTS	337
CONTENTS	348

NUCLEAR SCIENCE AND ITS APPLICATION
XII INTERNATIONAL CONFERENCE
Ulugbek, Tashkent, 12-15 October 2026



Plenary Reports

NEUTRON RESEARCH OF FERROELECTRICS, FERROELASTICS, AND SUPERPROTONIC MATERIALS. A HISTORICAL OVERVIEW AND CURRENT DEVELOPMENTS

Belushkin A.V.
Joint Institute for Nuclear Research, Dubna, Russian Federation

One of the first objectives of the early research in the field of ferroelectrics and ferroelastics in Dubna was to establish general patterns of domain structure formation in these crystals and its modification under the influence of external fields. Macroscopic experimental methods used at that time to observe ferroelastic domains did not provide a complete picture of their configuration and did not allow for the in-situ tracing of domain rearrangement. X-ray diffraction provided information limited to the crystal's surface layer, whereas it was desirable to obtain information on domain rearrangement within the crystal's bulk, undistorted by surface effects. For these reasons, it was decided to utilize neutron diffraction, which was then being successfully developed at the Laboratory of Neutron Physics (LNP) of the Joint Institute for Nuclear Research (JINR) in Dubna, to address this problem.

The very first experiments, which examined the effect of an electrostatic field on domains in the ferroelectric KD_2PO_4, demonstrated the informative nature of this method, even in its simplest implementation. In subsequent years, neutron diffraction and inelastic scattering were used to study the structural features and phase transitions in several types of crystals with structures including hydrogen bonds, which exhibit proton conductivity. Cesium hydrosulfates and hydro(deutero)selenates were studied in particular detail. The paper [1], published based on the results of these experiments, summarizes a number of new, interesting and important results.

Today the work on the use of neutrons in the study of ferroelectrics and ferroelastics continues to be effectively developed. Thus, the microscopic mechanism of phase transitions leading to the appearance of ferroelectric properties in classical perovskite ferroelectrics was studied using new methods of neutron experiments and data processing [2, 3].

Relaxor ferroelectrics play a special role in the physics of ferroelectric materials today, attracting significant interest for practical applications. Like conventional ferroelectrics, relaxor ferroelectrics exhibit a permanent dipole moment in their domains. However, these domains are nanoscale, unlike those of conventional ferroelectrics. The mechanisms underlying the ferroelectric properties and the microscopic nature of the diffuse phase transition remain the subject of active research. Neutrons provide important experimental information to clarify the physical nature of relaxor ferroelectrics, see for example [4,5,6].

The development of the density functional method and the creation of accessible software products based on it for first-principles calculations of crystal dynamics make it possible today to compare theoretical predictions with the results of neutron spectroscopy and obtain information on microscopic atomic and molecular dynamics and make predictions about possible ways to improve the parameters of ferroelectric materials [7,8].

References:

1. A.M. Balagurov, A.V. Belushkin, A.I. Beskrovnyy, B.N. Savenko. Kristallografiya. 2023. T. 68, No. 5, pp.697–708.
2. S.N.Gvasaliya, B.Roessli, R.A.Cowley, S.G.Lushnikov, A.Choubey and P.Gunter, JETP Lett. 2004. 80. p.355-358.

3. A.V. Belushkin, D.P. Kozlenko, N.O.Golosova, P.Zetterstrom, B.N.Savenko. Physica B. 2006. v.385–386. p.85–87.
4. S.N.Gvasaliya, B. Roessli, R.A.Cowley, S.Kojima, S.G.Lushnikov. J. Phys.: Condens. Matter. 2007. V. 19. P. 016219-016233.
5. S.Vakhrushev, A.Ivanov, J.Kulda. Phys. Chem. Chem. Phys. 2005. v.7. issue 11. p.2340-2345.
6. T.J.Hitchings, H.M.Wickins, G. U. L. Peat, e.a. *J. Mater. Chem. C.* 2023. v.11. p.9695-9706.
7. Sanghamitra Mukhopadhyay. Front. Phys. 2022. v.10. p.834904-834906.
8. V.A.Abalmasov, A.S.Ivanov, R.A.Sadykov, A.V.Belushkin. Physical review B. 2025. v.112, p.214101-214112.

HIGH-ENERGY INDUSTRIAL ELECTRON ACCELERATORS ILU TYPE FOR MEDICAL DEVICE STERILIZATION AND FOOD IRRADIATION

Bryazgin A.
Budker Institute of Nuclear Physics, Novosibirsk, Russian Federation

Budker Institute of Nuclear Physics is constantly developing new industrial accelerators. This report is describing to a series of accelerators of the ILU type. These accelerators are successfully operating in the market for sterilization of disposable medical devices. Entering the promising food processing market requires increasing the power of accelerators and their efficiency to operate in the bremsstrahlung mode. A line of 3 accelerators with energies up to 5 MeV, up to 7.5 MeV and up to 10 MeV with an electron beam power of up to 100 kW has been developed. Ilu-14 manufactured for industrial enterprise in Vietnam and it is planned to produce an accelerator for Uzbekistan. New physical solutions for accelerators and features of the layout and conveyor systems for irradiation both in boxes and on pallets are described. Irradiation of large pallets with acceptable dose distribution requires the implementation of a mechanism for rotating the pallets under the bremsstrahlung X-ray beam.

PRODUCTION OF RADIOCHEMICALS FOR MEDICAL APPLICATION AT ROSATOMS’ SCIENTIFIC DIVISION

Tuzov A.A.
JSC State Scientific Center - Research Institute of Atomic Reactors, Dimitrovgrad, Russian Federation

Russia’s nuclear industry produces even today the world's widest range of radioactive and stable medical isotopes that are used to annually diagnose and treat over 2.5 million people worldwide. For over 50 years, Rosatom’s companies have been producing radionuclides and ionizing radiation sources. The unique reactors and technologies of the Rosatom’s Scientific Division being a base for such production, allow for a wide range of radionuclides with high specific activity to be accumulated. The availability of these reactors provides for irradiation of starting

materials in various spectra (thermal, resonance, and fast) over a wide range of neutron fluxes (from 10^{13} to $2 \cdot 10^{15}$ $cm^{-2}s^{-1}$). The SM-3 is one of the reactors to accumulate radionuclides. Following its refurbishment in 2019–2020, its operating license was extended till 2034. The refurbishment resulted in the modernized highest-flux irradiation position of the reactor that is the central neutron trap thus increasing the useful volume more than twofold (the number of irradiation cells increased from 27 to 57).

Radiochemical facilities, which include hot cells, radiation-shielded chambers, and boxes, are used for processing of irradiated targets, including the extraction, deep purification, and characterization of isolated radiochemicals. Great attention is paid to quality control of the finished products. The developed and metrologically certified analytical methods for radiochemical analysis allow for determining the activity of both the main component and trace amounts of radioactive impurities, down to the levels of $10^{-3} \div 10^{-4}$% and, in certain cases, down to $10^{-5} \div 10^{-7}$% of the target radionuclide activity. These methods also include the use of radiochemical extraction techniques for impurity elements.

Nowadays, the companies of the Rosatom's Scientific Division produce radiochemicals ^{89}Sr, ^{99}Mo, ^{106}Ru, ^{125}I, ^{131}I, ^{131}Cs, ^{177}Lu, ^{188}W, ^{153}Gd on a regular basis.

A technology has been developed to produce ^{161}Tb and ^{14}C. There is also experience in producing ophthalmic applicators ^{90}Sr and ^{106}Ru, and radiochemicals ^{32}P, ^{33}P, ^{90}Y, ^{119m}Sn, ^{113}Sn, and ^{153}Sm.

Currently, the most promising avenue for radionuclide production is the development of medical alpha emitters. New facilities have been commissioned and regular production of radiochemicals ^{223}Ra, ^{227}Th, and ^{225}Ac have been started. These are produced using the radionuclide generator method from long-lived parent isotopes such as ^{227}Ac and ^{229}Th. A facility has been set up to produce ^{228}Th, which is used as raw material for producing radiochemicals ^{224}Ra and ^{212}Pb. Currently, a new line is under construction at one of the sites of Rosatom's Scientific Division to scale up the production capacity of medical alpha emitters.

MEASUREMENT OF $^{19}F(p, \alpha\gamma)^{16}O$ REACTION REOPENS THE FLUORINE CONUNDRUMS IN STARS

La Cognata M.

Laboratori Nazionali del Sud, Istituto Nazionale di Fisica Nucleare, Catania, Italy

The amount of fluorine in stars is a crucial indicator of the internal physical conditions and of the processes taking place within them, such as extra mixing in asymptotic giant branch stars. Also, it is a branching point in proton induced nucleosynthesis, since its proton radiative capture may lead to the synthesis of heavier nuclei (such as Ca in early stars). Recent extrapolated findings on the $^{19}F(p,\alpha\gamma)^{16}O$ and $^{19}F(p,\gamma)^{20}Ne$ fluorine-destruction channels by the JUNA collaboration [1] indicated a rise in the astrophysical factor by several orders of magnitude below about 100 keV, significantly affecting our comprehension of stellar evolution and nucleosynthesis. Utilizing the Trojan Horse Method (THM), we have indirectly measured the $^{19}F(p,\alpha\gamma)^{16}O$ cross section, fully covering astrophysical energies without requiring extrapolations (and with no electron screening enhancement). The strength of the 11-keV resonance was determined, revealing a considerable decrease in the reaction rate compared to earlier studies (see Fig.1). The THM results on the αγ

channel were also used to rescale the $^{19}F(p,\gamma)^{20}Ne$ astrophysical factor, with similar conclusions. Our analysis of its astrophysical significance suggests that this measurement challenges existing models of fluorine and heavier element abundances, reopening unresolved questions in the field, in particular in the case of early stars. Results are discussed in detail in Ref.[2].

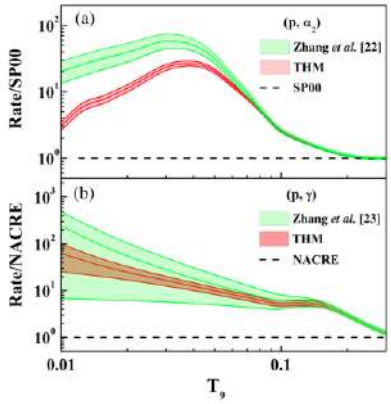

Figure 1. THM reaction rates and comparison with the literature. (a) Ratio of the JUNA rate [1] and the one in K. Spyrou et al., Eur. Phys. J. A 7, 79 (2000) (SP00) used as reference value (green band), compared with the one based on the THM astrophysical factor, also divided by SP00 (red band). The bands highlight the uncertainty range. The temperature is expressed in billion kelvin (T_9=T/10^9 K). (b) Same as panel (a), where the rate from Ref.[1] (green band) and the THM rate (red band) are divided to the NACRE one (C. Angulo et al., Nucl. Phys. A656, 3 (1999)).

References:

1. L.Y. Zhang et al., Phys. Rev. Lett. 127, 152702 (2021); Phys. Rev. C 106, 055803 (2022); Nature (London) 610, 656 (2022).
2. X.D. Su et al., Phys. Rev. Lett. 135, 182701 (2025).

RADIATION-HETEROGENEOUS PROCESSES OF WATER DECOMPOSITION ON THE SURFACE OF METALLIC AND NANO-ALUMINUM

Agayev T.N.
Institute of Physics Public Legal Entity, Baku, Azerbaijan

The kinetics of radiation, radiation-thermal, and thermal metal oxidation and H_2 accumulation during the interaction of aluminum with water at temperatures ranging from 300 to 973 K were studied. It was found that radiation-induced processes during aluminum contact with water accelerate water radiolysis. With increasing temperature, the rates of surface aluminum oxidation and H_2 accumulation increase at $T \geq 973$ K, at which point the oxidation process is destructive. Furthermore, the kinetics of molecular hydrogen accumulation during catalytic and radiation-catalytic decomposition of water on the surface of nano-aluminum at various temperatures was studied. Kinetic parameters were determined, and mechanisms for the processes were proposed.

Aluminum and its alloys are widely used materials in nuclear reactors and their auxiliary components. Aluminum is one of the most common and therefore readily available elements. It was the first metal to be used in aviation as a structural material. Aluminum production and the number of alloys used have grown along with the development of aviation. In the nuclear energy industry, aluminum and aluminum alloys are used in the construction of nuclear reactors. To understand the patterns and mechanical processes occurring under normal and emergency conditions in nuclear reactors, it is of great interest to study the radiation and radiation-thermal processes occurring when these materials come into contact with the coolant—water. The literature contains information on the patterns of processes occurring when aluminum and aluminum materials come into contact with

water [1-4]. Therefore, the actual course of processes in normal and emergency conditions of nuclear reactors is currently difficult to understand. Nanoaluminum (aluminum nanopowder, Al) and its oxides are used in nuclear power to improve the efficiency, safety, and durability of materials. Key applications include the creation of dispersion-strengthened structural steels, improved nuclear fuel properties, and the development of energy-storage compounds and functional coatings. The addition of nanostructured materials improves the thermal conductivity and stability of fuel assemblies (FEAs). Furthermore, aluminum nanopowders are used in special energy-intensive materials [5-8].

Recently, aluminum nanopowder has been studied as a component for generating hydrogen by reaction with water, which holds promise for safe emergency power supply systems. The use of aluminum-based nanostructured materials helps extend the service life of reactor vessels and internals by reducing radiation embrittlement. In this work, in order to identify the patterns of radiation and radiation-thermal processes during contact of aluminum materials of nuclear reactors with water coolant, the kinetics of H_2 accumulation and oxidation of aluminum by water under the influence of γ-radiation at different temperatures was studied [9-11].

The studies were conducted under static conditions in 1 cm³ quartz ampoules. The sample used was AD-OO aluminum in the form of a thin ribbon. To eliminate the contribution of organic contaminants on the surface to the H_2 accumulation process, the samples were pre-cleaned with solvents (ethyl alcohol, acetone) and then rinsed with distilled water. This process was repeated three times. The samples in the ampoules were subjected to thermal vacuum treatment, first at T = 373 K and then at 573 K at a pressure of 10^{-2} Pa. Bide-distilled water, deaerated five times, was used for the study. The required amount of water was added to the ampoules and sealed using a vacuum adsorption unit. The accuracy of recording the amount of water added under the experimental conditions was < 5%. The temperature during the experiments was maintained with an accuracy of + 1°C. The objects of study were samples of nano-powder of metallic aluminum with a purity of 99.9%, particle size d = 40 ÷ 90 nm, manufactured by Skyspring Nanomaterials, INC., USA. The amount of nano-aluminum in the ampoules was approximately 3 x 10^{-2} g. Bidistilled water was used for the studies. Water was introduced into the ampoules by two methods. In the first case, water from the vapor state (H_2O_v) was adsorbed onto the surface of nano-Al at T = 77 K. The amount of water introduced into the ampoules corresponded to the density of water vapor in the ampoules, at ρ = 5 mg/cm^3. In the studied temperature ranges, equilibrium occurs between the amount of water in the vapor and adsorbed states. In the second case, water from the calibration volume was introduced into the ampoules until the nano-Al sample was completely covered with liquid water. The ampoules containing the samples were then cooled to 77 K and sealed.
Irradiation was performed with ^{60}Co γ rays using an isotopic source. The absorbed dose rate was determined using ferrosulfate, cyclohexane, and methane dosimeters [1-3].

The gaseous reaction products were transferred to special graduated volumes and analyzed by gas chromatography (Agilent 7890). Metal oxidation was studied gravimetrically based on the weight gain of the samples after the process. The contact surface area of the samples was determined based on their geometric dimensions with an accuracy of ~10%.

Thus, the kinetics of molecular hydrogen accumulation during γ-radiolysis of water on the surface of metallic and nano-Al was studied. It [1] found that the radiation-chemical yield of molecular hydrogen for Al + water and nano-Al + water is higher ($G(H_2)$ = 0.58 and $G(H_2)$ = 1.17 molecules/100 eV, respectively) than for the radiolysis of pure water ($G(H_2)$=0.45 molecules/100 eV). Furthermore, the kinetics of molecular hydrogen accumulation during radiation-induced, radiation-catalytic, and catalytic processes in contact between nano-Al and water was studied. It has been shown that the formation of surface-active sites and secondary electrons in the presence of nano-AI increases the rate of molecular hydrogen accumulation during catalytic and radiation-

catalytic processes in the nano-AI + H_2O system. It has been established that, starting at T≥373 K, surface-active sites for water decomposition accumulate in nano-AI during catalytic and radiation-catalytic processes [30-32].

The rate of heterogeneous catalytic processes at a stable concentration of active sites on the catalyst surface depends on the contact area of the surface with the substances undergoing transformation. It has been established that energy transfer processes between the phases of heterogeneous systems make the main contribution to radiation-catalytic water decomposition processes in the presence of nanosized catalyst samples. In radiation-catalytic processes in catalyst + water systems, the majority of the electron density is concentrated in the oxide phase, and therefore the decomposition of water molecules occurs as a result of energy transfer from the catalyst to the water. The transfer of ionizing radiation energy from oxides to water molecules occurs at the catalyst + water phase boundary. Therefore, the efficiency of energy transfer in radiation-catalytic processes increases with increasing contact area and decreasing catalyst particle size. Radiation-chemical yields of molecular hydrogen increase with decreasing catalyst particle size.

References:

1. I.Ali, G.Imanova, T.Agayev et al. A comparison of hydrogen production by water splittingon the surface of α-, δ- and γ-Al_2O_3 // ChemistrySelect, 2022, 7(34); https://doi.org/10.1002/slct.202202618
2. T.N.Agayev, S.Z.Melikova, Z.A.Mansimov, M.M.Tagiyev. Study of the influence of aluminum content on the radiation-catalytic activity of aluminosilicate in the process of water decomposition // Protection of Metals and Physical Chemistry of Surfaces, 2022, 58(4), p.677-679; https://doi.org/10.1134/S2070205122040037
3. T.N.Agayev, S.Z.Melikova, H.F.Hadzhiyeva. Radiation-termocatalytic processes for hydrogen production from water // Problems of Atomic Sciences and Technologies, 2019, 2(120), p.50-54.

ELECTROCHEMICAL SYNTHESIS OF CARBON NANOSTRUCTURES AND THEIR APPLICATION FOR HEAVY-METAL REMOVAL FROM WATER

Khaydarov R.R., Gapurova O.U., Naumovskiy V.B., Galiulin I.G.
Institute of Nuclear Physics, Uzbekistan Academy of Sciences, Tashkent, Uzbekistan

The sorption behaviour of carbon nanomaterials is governed less by the carbon skeleton than by the oxygen-containing groups on its surface: carboxyl and carbonyl groups bind metal ions and keep the particles dispersed, so that the sorption capacity is largely set by their surface density. In the conventional preparation sequence these groups are introduced last. CVD, arc discharge and laser ablation give a hydrophobic product at considerable energy cost, and the material is then oxidised in concentrated H_2SO_4/HNO_3 mixtures to obtain the required surface chemistry, which consumes reagents and produces acidic waste.

In anodic oxidation of graphite the two stages are combined: the electrode reaction that exfoliates the graphite also oxidises the detached fragments while they are still held at the anode, so that the particles enter the solution already functionalised. Electrochemical exfoliation is a known route to oxidised carbon nanoparticles. The protocol reported here operates in pure deionised water with a small addition of H_2O_2 instead of an acid or salt electrolyte, uses cyclic reversal of the electrode polarity, and maintains the current density by means of an active current limiter. Under these conditions the particle size is set by the current density alone, and carboxyl-terminated

particles are obtained directly as a stable aqueous colloid, without post-synthesis acid oxidation, surfactants or organic solvents.

The cell contained high-density graphite electrodes (65×30×15 mm) in deionised water at a gap of 10–12 mm, with 0.1–0.5 % H_2O_2 added at the start to accelerate the initial oxidation. After anode activation (30–50 h at 60–100 V, or 5–7 h for a re-used electrode) the process runs as repeating cycles of 10 min electrolysis and 20 s stirring with the voltage switched off or the polarity reversed, a current limiter holding the current density at 2.5–5.0 mA/cm^2. Particle size was taken from TEM, with DLS used for the coarser fractions; surface chemistry from FTIR and from titration of the total surface acidity with 0.1 N NaOH; structure from XRD.

Water oxidation at the anode generates •OH and •O radicals that attack edge and defect sites, while the evolved oxygen intercalates between the graphene layers, widens the interlayer spacing and exfoliates the graphite. The detached fragments carry a negative charge and remain held at the anode until the field is removed or reversed, when stirring releases them into the bulk electrolyte.

The particle size is controlled primarily by the current density. The mean diameter rises from 1.2–1.6 nm at 2 mA/cm^2 to 100–370 nm at 12 mA/cm^2. Above 8–10 mA/cm^2 oxygen forms faster than it diffuses out, and the internal pressure destroys the electrode surface, so the colloid sediments within 2–3 weeks. The yield of exchangeable protons peaks at ≤ 8 mA/cm^2 (7.0 ± 0.3 mmol/g), which fixes the optimum at 2.5–5 mA/cm^2 for 10 min.

Four morphologies are obtained depending on the regime (Fig. 1): fibrous aggregates, globular networks, tubular or scrolled fragments, and quasi-spherical particles. XRD shows only broad features, i.e. no long-range graphitic order. In FTIR the band at 1727 cm^{-1} (>C=O) is diagnostic of surface carbonyl and carboxyl groups, and titration gives a total surface acidity up to 7.4 mmol/g. These groups make the particles hydrophilic and negatively charged: the colloid has pH 2.8–3.4 and 145–400 mg/L, and shows no sedimentation for at least 300 days, over which the mean size drifts from 19 ± 7 to 52 ± 25 nm through slow aggregation.

The carboxylated nanocarbon sorbs metal ions directly, with removal above 99 % at pH 7.1 for Cr(III), Co(II), Ni(II), Cu(II), Zn(II), Sr(II), Cd(II) and Sb(III), the distribution coefficients spanning two orders of magnitude in the order Zn > Sr > Cu > Ni > Cd. The pH dependence shows that the uptake is due to sorption and not to hydroxide precipitation: Cu(II) plateaus already at pH 3, well below the onset of $Cu(OH)_2$ formation, while Zn(II), Ni(II), Cd(II), Co(II) and Sr(II) do not hydrolyse under these conditions. Cs(I) is essentially not retained (60 %) and passes through, separating from the other ions studied.

The practical obstacle to any nanosized sorbent is recovering it from the treated water. We address this by conjugating the particles with polyethyleneimine (PEI): the positively charged Me–PEI complex attaches to the carboxylated nanocarbon through hydrogen bonding and electrostatic attraction, and the composite coagulates and settles. The coagulation point is governed by the ratio C_{PEI}/C_{NC}, independent of PEI concentration over 2×10^{-4}–0.1 % but shifting with particle size, smaller particles requiring proportionally less nanocarbon per unit of polymer. The coagulation time can be set from about 1 s to 10^3 min, so that sorption and separation may be carried out at different times.

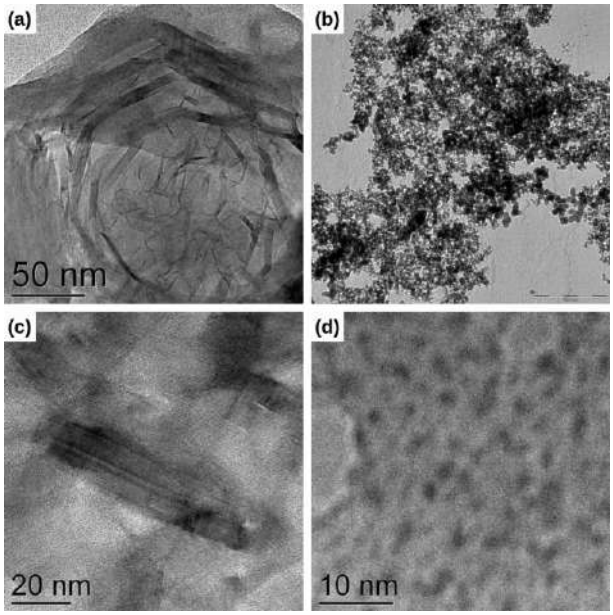

Figure 1. TEM images of the electrochemically synthesised carbon nanostructures: fibrous (a), globular (b), tubular/scrolled (c), quasi-spherical particles (d)

The composite takes up 4.0–5.7 mmol/g at pH 6 after 5 min of contact under the batch conditions used, removing ~99 % of Zn(II), Cd(II), Cu(II) and Ni(II); Hg(II) reaches a similar level but binds an order of magnitude more weakly. The pH dependence separates the two classes of contaminant: divalent cations plateau above pH 4–5, whereas Cr(VI), present as anionic chromate, peaks at pH 2–3 and is poorly held at pH 6. Cationic and anionic species can therefore be removed sequentially on the same sorbent by adjusting pH alone.

The proposed route gives carboxyl-terminated carbon nanostructures directly as a stable aqueous colloid, the size and morphology being set by the current density, and requires no post-synthesis acid treatment. Conjugation with PEI provides controllable coagulation, which solves the problem of separating the sorbent from the treated water

The method and the device are protected by patent Uz IAP 06885.

THE EXPERIMENTAL INFRASTRUCTURE OF THE LABORATORY OF NEUTRON PHYSICS FOR RESEARCH

Lychagin E.V.
Joint Institute for Nuclear Research, Dubna, Russian Federation

The Frank Laboratory of Neutron Physics (FLNP) of the Joint Institute for Nuclear Research (JINR) is one of the leading centers for neutron physics in the member states of JINR. The scientists at the FLNP conduct research in the fields of condensed matter physics and the field of nuclear reactions with neutrons, as well as for solving a wide range of applied problems using nuclear physics techniques. The basic facility of the laboratory is the unique periodic pulsed reactor IBR-2. Most modern research methods using neutron scattering are realized at neutron beams of the reactor, as well as neutron activation analysis and studies of the radiation effects from neutrons and gamma rays. FLNP has accumulated a significant amount of state-of-the-art laboratory equipment. It allows

supplementing information to neutron research about studied samples using various physical methods. This enables comprehensive information about the objects under study to be obtained. The available instruments make it possible to implement an extensive scientific research program in various fields of science: fundamental solid-state physics, materials science, biology, pharmacology, ecology, etc.

The User Program implemented at the laboratory provides a unique opportunity for scientists from around the world to get access to the research infrastructure of the IBR-2 reactor.
The report will provide information about the experimental infrastructure available at the FLNP, including examples of the research, and information on how to access the infrastructure through the User Program.

SYNERGISM OF IONIZATION AND SHOCK WAVE EFFECTS IN COMPLEX MEDIA UNDER INTENSE RADIATION EXPOSURE

Oksengendler B.L.[1], Suleymanov S.Kh.[1], Ashurov M.Kh.[2], Turaeva N.N.[1], Akhmatova G.Y.[1], Ibrokhimov R.R.[1]

[1]Institute of Materials Science, Uzbekistan Academy of Sciences, Tashkent, Uzbekistan
[2]Institute of Nuclear Physics, Uzbekistan Academy of Sciences, Tashkent, Uzbekistan

Modern radiation physics and the associated radiation technologies are characterized by what is commonly referred to as complexity: the complexity of irradiation processes, characterized by increased intensity; the multifactorial nature of radiation effects; the complexity of irradiated objects, characterized by a wide variety of structural features; and the openness of radiation-induced processes, with their inherent nonequilibrium and nonlinear behavior. All these factors have led to the development of a powerful methodological approach—complexity, supported by an advanced methodological framework (Fig. 1).

It is particularly important that each of these paradigms is implemented through specific physical and mathematical models that take into account both the properties of new materials and the characteristics of modern radiation, as well as the capabilities of the Complexity methodology.

Within this framework, it is important to note that each of the five paradigms is represented by its own set of models. In recent years, particular attention has been devoted to the concept of synergetics [1–3]. One of the models implementing this concept is the “fracton medium,” which combines several characteristic dimensions and nanoscale features, as well as the fractality of chain elements. This model is important in many situations: under Big Solar Furnace (BSF) conditions, under intense ion and electron irradiation, as well as under laser and synchrotron irradiation, when the quasi-one-dimensional atomic chain becomes the “weak link.”

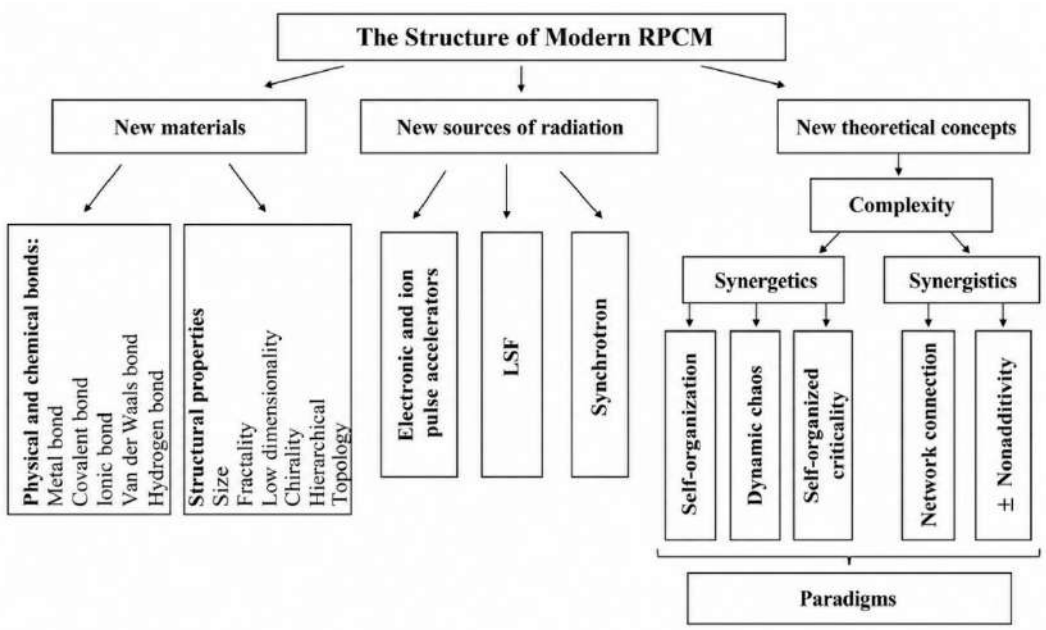

Figure 1. Extended scheme of radiation physics of condensed complex systems (RPCMS) [1–5].

The synergistic process under consideration in an atomic chain—Auger ionization → defect formation → shock wave → annealing of metastable states—can occur following a single K-shell ionization event with a subsequent Auger cascade. It can also occur after n>K ionization events only when these events take place in pairs at a small separation a. However, paired ionization is an unlikely process under ordinary conditions and can occur with an appreciable probability only under conditions of strong ionization correlation, i.e., in situations of pronounced nonequilibrium that establishes a quasi-coherence of synergistic processes [6]. In the latter case, the cross section for paired ionization is given by [5]:

$$\sigma_d \cong 2Z_A \left[\sigma_A^{i>K} g_{cor}^{(i=K+1)}(a)\alpha_A\left(Z_A^{(i>K)}\right)exp\left(-\frac{\tau_+}{\tau_e^{i>K}}\right)\gamma\right] \quad (1)$$

Here, γ is the energy required for ionization and sufficient to ionize $i = K + 1$ and the subsequent electron shell, which is important for the BSF; $\tau_\times \cong 10^{-14}s$, where $\tau_\times$ is the filling time of the Auger charge, and $g(a) = const\, J_S/a$ where J_S – is the amplitude of the nonequilibrium parameter [6] and a is the interatomic distance. Further, since the velocity of the molecular fragments is higher than the speed of sound ($V_\times > V_s$), a shock wave with spherical symmetry is generated in the region of the resulting defect. The pressure at the shock-wave front at a distance R follows the dependence $P \cong E_{SW}^0/R^3$, where

$$E_{SW}^0 \cong \left(Z_A^{i>K}\right)^2 e^2/a. \quad (2)$$

Then, the condition $P(R)\Omega_0 \leq \tilde{Q}$ defines a volume $(R^\times)^3$ that clears the medium of metastable states characterized by the volume Ω_0 and the metastability energy $\tilde{Q}$. This makes it possible to write the probability of eliminating metastability by a single Auger charge, $2Z_A$, as

$$W \cong \int_a^{R^+} f(R)dR, \quad (3)$$

where $f(R)$ is the probability of the nearest neighbor occurring between the Auger charge and the metastable state.An estimate of the parameters of the BSF and known synchrotrons shows that the above considerations are fully consistent with the actual situation. Therefore, in addition to the four factors of radiation exposure in the BSF, a fifth factor—shock waves—should also be included.

References:
1. Oksengendler B., Ashurov M., Suleymanov S., et al. Synergism in radiation effects in condensed matter. Fundamental and application aspects // arXiv. – 2026. – arXiv:2602.14085.
2. Oksengendler B.L., Maksimov S.E., Suleymanov S.Kh., et al. Aspects of modern concepts of charged particle interaction with complex media // Poverkhnost (Surface). – 2026. – № 6. – P. 68–77.
3. Zatsepin A.F., Oksengendler B.L, Suleymanov S. Kh., et al. Radiation effects in complex objects and complexity: genesis, structure, achievements, and prospects // Int. Conf. "Scientific research of the SCO countries". – Beijing, 2026. – P. 9–17.
4. B.L.Oksengendler, F. A. Iskandarova, S. Suleimanov et al. Interaction of Radiation with Hierarchical Structures // J. Surf. Investig. – 2023. – V. 17, № 1. – P. 31–42.
5. B.L.Oksengendler A.Kh.Ashirmetov, N.N.Turaeva et al. The Features of Auger Destruction in Quasi-One-Dimensional Objects // Nucl. Instrum. Methods Phys. Res. B. – 2022. – V. 512. – P. 66–75.

Nicolis G., Prigogine I. Exploring Complexity: An Introduction. – Moscow: URSS, 2025. – 352 p.

BEYOND THE HEADLINE EFFICIENCY NUMBER: A METROLOGY-DRIVEN BENCHMARK OF 2026 BETAVOLTAIC CONVERTERS FROM PEROVSKITE TO SiC

Dolgopolov M.V.[1,2]
[1]*Samara State Technical University, Samara, Russian Federation*
[2]*BetaVoltaics LLC, Samara, Russian Federation*

Betavoltaic energy conversion has entered a period of rapid, geographically diverse progress: 2025–2026 alone brought a record 10.79% energy-conversion efficiency (ECE) in a ^{14}C-perovskite cell (Republic of Korea) [1], systematic TCAD trap-engineering of 4H-SiC p–i–n structures under a Ni-63-representative electron-beam spectrum, with measured mesh-pattern power-density gains (Republic of Korea) [2,3], tritium-storage-film optimisation for SiC PIN converters [4], measured SiC fabrication-process optimisation (ECE 2.43–2.63%, <3% drift after 5-yr-equiv. aging) [5], and a record-adjacent 11.72% ECE Ce-mediated TiO2 β-electrochemical generator [6] (all China). A comprehensive numerical survey of six semiconductors (Ga_2O_3, GaAs, GaN, GaP, Si, SiC) with a ^{14}C source reports a maximum 7.20% ECE and 20.97 μW/cm² for the Ga_2O_3 p–n junction, identifying wide-bandgap oxides as a competitive betavoltaic absorber class [7], a Monte Carlo/analytical study trading efficiency for power density in multi-stage SiC + 3H/90Sr structures (Iran) [8], our own metrology-resolved 3C-SiC/Si comparison with lattice-integrated ^{14}C (Russia) [9,10], an indirect-conversion route (scintillator waveguide) reaching a record 2.96% ECE for ^{90}Sr radio-photovoltaic cells, whose accelerated-aging data directly evidence the high-energy-β displacement damage discussed below [11], and a directly measured demonstration that adding an epitaxial SiC layer raises efficiency 8.6× for ^{63}Ni but 63× for ^{90}Sr/^{90}Y on the same device — yet absolute efficiency remains 22× higher for ^{63}Ni, confirming that isotope/depletion-width matching, not β-energy alone, sets performance [12]. Table 1 places these results side by side, method explicitly labelled (TCAD-only, e-beam proxy, or true-isotope), since pooling them uncritically is itself a common source of misleading comparison. Concurrently, a surface-potential model for GaN betavoltaic cells has been developed, showing that collection efficiency is critically limited by

surface Fermi-level pinning — a direct analogue of the interface-state limitation we resolve here for SiC/Si [13].

Table 1. Cross-regional 2025–2026 benchmark (method explicitly labelled)

Group / Year	Isotope / proxy	Material	Method	V_{OC}	J_{SC}/I_{SC}	Pmax / ECE
S. Korea (2025-26) [2,3]	e-beam proxy, 17 keV ≈ Ni-63 mean	4H-SiC mesh/planar p–i–n	TCAD + meas.	2.21→2.47 V (sim)	1.34 μA/cm² (sim)	2.60→3.08 μW/cm² (sim); +65/+4.6/+4.3% meas. gain vs planar (5/17/25 keV); traps cut Voc 2.47→2.07V
entX/Adelaide U., Australia (2026) [12]	63Ni and 90Sr/90Y (real, both)	4H-SiC Schottky, epi vs non-epi	Measured, Keithley 2450	0.35 V (63Ni)/0.37 V (90Sr)	0.045-0.054 μA/cm²	ECE: 4.09% (63Ni) vs 0.19% (90Sr) on same epi device; epi layer gives 8.6×/63× gain resp.
DGIST, S. Korea (2026) [1]	14C (real)	FAPbI3 perovskite+14C NPs	Measured	76.9 mV	10.60 nA/cm²	ECE=10.79% (record); ≈10% /15 h
Xiamen U./CIAE, China (2025) [11]	90Sr (real), indirect: scint.+PV	GAGG:Ce/AlGaInP	Measured	1.16-2.14 V	60.3 uA-2.23 mA	ECE=2.96% (RPVC record); Pmax=48.9uW-3.17mW; RL loss 13.8% at 50-yr-eq. e-beam dose (vs 3.3% gamma)
China (2026) [4]	Tritium films (MgT2, Mg2YT7, TiT2)	SiC PIN	Simulation	—	—	0.310/0.233/0.196 μW/cm²
China (2026) [5]	63Ni (real)	SiC (surface-passivated)	Measured	—	≈18 nA/cm²	≈20 nW/cm²; ECE 2.43–2.63%; FF>0.8; <3% drift/5-yr-eq. aging
China (2026) [6]	63Ni (real)	Ce/CeO2-TiO2 nanorods (β-electrochem.)	Measured	0.33 V	1.32 μA/cm²	ECE=11.72% (source-power-normalised)
Iran (2026) [8]	3H + 90Sr aux. sources	SiC, 1- and 10-stage	Monte Carlo + analytical	2.09→2.21 V (1-stage→10-stage)	72→5730 nA/cm²	ECE 13.9%→0.8% (1-stage); 3.43% (10-stage)
This work, Russia (2026) [9,10]	14C (real, lattice-integrated)	3C-SiC/Si, anisotypic (n-SiC/p-Si)	Meas., 4-wire Kelvin	≈ 1.2 V	up to 900 nA/cm²	25× stored energy vs. isotypic (0.1 F cap., 30 min)

For the 3C-SiC/Si interface itself, in situ KPFM/STS mapping (30 nm resolution) resolves $Dit(x)=D0\cdot\exp(-x/\lambda)+Dbulk$ with $D0=(5.67\pm0.20)\times10^{12}$, $\lambda=40\pm5$nm, $Dbulk=(1.0\pm0.2)\times10^{11}$ $cm^{-2}eV^{-1}$, and a fivefold Dit excess in dislocation-rich regions relative to smooth terraces. Minority-carrier injection shows a threshold delay $ta=2.3\pm0.5$s and stretched-exponential relaxation $\Delta\Phi(t)=\Delta\Phi0\cdot\exp[-(t/\tau)^{\beta}]$, $\tau = 35\pm2$ s, $\beta = 0.65\pm0.05$ (canonical parameters from the full dataset of [10]; single-scan fits in that work yield slightly different values, as discussed therein) — a directly measured, structural counterpart to the electrical figures of merit in Table 1 [10]. The characterisation toolbox enabling this interface sensitivity is summarised in Table 2.

Table 2. Characterisation toolbox for interface-limited betavoltaic converters

Method	Probed quantity	Spatial res.	Key value for betavoltaics
Raman	Phonon modes, strain, polytype, isotopic shift (12C/14C) [14]	~1 μm	Polytype ID; residual stress; isotope engineering diagnostic
XRD (HRXRD)	Crystal structure, coherence length, mosaicity	mm / arcsec	Substrate-resistivity dependence of epitaxial quality
PL	Band-edge & deep-level recombination	~1–10 μm	Stacking faults, impurity–defect complexes (2.2 eV band)
AFM/KPFM/STS	Topography, contact potential difference Φ(x,y), local dI/dV	30 nm	Local work function; barrier inhomogeneity vs. dislocations; energy-resolved Dit(E,x)

A minimal 5-parameter measurement-protocol template (V_{OC}, I_{SC}/J_{SC}, Pmax/FF, Dit(x,E), stored energy) — each recorded for both two-wire and four-wire protocols with a Type A/B uncertainty — is recommended as the reporting baseline for any new betavoltaic device.

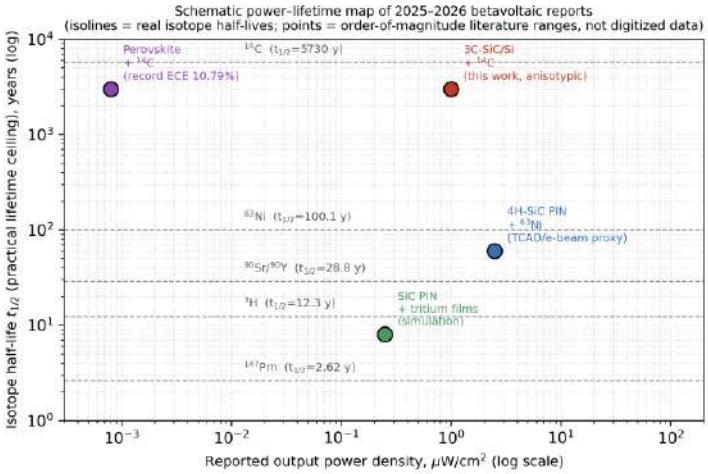

Figure 1. Schematic power–lifetime map: isolines are real isotope half-lives; points mark order-of-magnitude ranges for the classes in Table 1 (not digitised data). Such Ragone-style efficiency–power–lifetime plots, as also proposed for hybrid PV/BV–ZIB architectures in [12], are most informative once every axis uses measured, not projected, values.

Conclusions. (i) 2025–2026 results span TCAD-only, e-beam-proxy, and true-isotope measurements that are not interchangeable; explicit method labelling (Table 1) should be mandatory. (ii) Four-wire Kelvin sensing, a specified output-off state, and full I–V/P–V curves — not isolated V_{OC}/I_{SC} — are the emerging minimum bar. (iii) Interface-state density Dit(x,E), resolved here by KPFM/STS to 30 nm, sets the practically achievable low-bias performance and must be addressed before the band-diagram efficiency ceiling can be approached. (iv) The regional picture is complementary: growth/interface metrology (Russia), TCAD-guided optimisation and record absorbers (East Asia), isotope-source and oxide-electrochemical materials (China), multi-stage design (Iran), and indirect scintillator-based conversion (Xiamen/CIAE) together define the state of the art.

References

1. H.S.Kim et al., Carbon-14 perovskite betavoltaics reach record 10.79% efficiency, Carbon Energy 8(5), e70149 (2026).
2. K.M.Kim et al., Mesh-patterned 4H-SiC betavoltaic cells for enhanced power density, Sci. Rep. 16, 11906 (2026).
3. K.Kim et al., Structural optimization and trap effects in 4H-SiC betavoltaic cells, Nanomaterials 15(21), 1625 (2025).
4. J.Liu, G.Yang, L.Lv et al., Metal tritide films for PIN SiC betavoltaics (simulation), Phys. Scr. 101, 335915 (2026).
5. J.Zhang et al., Impact of fabrication processes on betavoltaic battery performance, J. Energy Storage 152(C), 120816 (2026).
6. Y.Li et al., Ce-mediated TiO2 nanorod arrays for β-electrochemical power generators, Electrochim. Acta 577, 149767 (2026).
7. N.Mohammadi, Comprehensive study on p-n junction and Schottky barrier betavoltaic battery with 14C beta-emitting source, Nucl. Technol. 212(4), 1035–1049 (2026).
8. H.Fathi et al., Performance metrics in high-volumetric-utilization betavoltaic convertors, Results Phys. 82, 108599 (2026).
9. M.V.Dolgopolov, A.S. Chipura, Heterojunction betavoltaic Si¹⁴C-Si converter, J. Power Sources 613, 234896 (2024).

10. M.V.Dolgopolov et al., SCR activation dynamics in SiC/Si by KPFM/STS, Phys. Part. Nucl. Lett. 23(2), 240–250 (2026).
11. T.Jiang et al., High-efficiency 90Sr radio-photovoltaic cells via waveguide light concentration, Light Sci. Appl. 14, 214 (2025).
12. C.A.G. Kalnins et al., Epitaxial layer to boost betavoltaic performance in SiC Schottky diodes, Appl. Phys. Lett. 128, 263901 (2026).
13. M.L.Hendrix, K. Cinfwat, M.G. Spencer, Modeling the effects of surface potential on gallium nitride betavoltaic cell collection efficiency, Appl. Phys. A 132(8), (2026).
14. M.V. Dolgopolov, A.S. Chipura, Negative isotopic shift of LO phonon in 3C-SiC, JETP Lett. 122, 500–506 (2025).
15. A.S.Chipura, M.V. Dolgopolov et al., Hybrid PV/betavoltaic-Zn-ion batteries, Mater. Sci. Semicond. Process. 204, 110289 (2026).
16. V.I.Chepurnov, M.V. Dolgopolov et al., Optimisation of beta-converter using Monte-Carlo method, Tashkent (2019).
17. B.Chen, H.San, A.S. Chipura, M.V. Dolgopolov et al., Betavoltaic power: global trends and Asian perspectives, Tashkent (2025).

DSTAR: A MODULAR 4π MUON DETECTOR COSMIC RAY MEASUREMENTS

Dovbnenko M., Fateev S., Kuznetsov A., Shirchenko M.
Joint Institute for Nuclear Research, Dubna, Russian Federation

Low-background experiments are strongly affected by the cosmic-ray muon background, which is commonly characterized in terms of meters of water equivalent (m.w.e.). However, direct measurements of the effective overburden in natural environments, in particular in water, remain limited and are often restricted in angular coverage.

We present the DSTAR, a compact modular 4π muon detector, composed of paired scintillator–SiPM modules with dedicated DAQ and slow control and arranged in reconfigurable three-dimensional geometries. In its full configuration, the detector forms a near-spherical modular geometry providing a full solid-angle (4π) coverage. The detector architecture is easily scalable. The DSTAR is portable, enabling rapid deployment and long-term autonomous field operation in different natural and experimental environments.

A 14-module prototype has been operating at the Kalinin Nuclear Power Plant since October 2025, providing a continuous muon background monitoring for background rejection in a neutrino experiment and demonstrating a stable performance. On the basis of the results obtained by the prototype, the system has been scaled up to a 64-module configuration. The full-scale detector is prepared for underwater deployment in Lake Onega for direct measurements of the effective water equivalent at the depths up to 30 m. The modular design provides a flexible platform for evaluating ambient conditions in future low-background experiments and, in the longer term, for near-surface muon radiography and tomography.

DISTINCTIVE DOPING- AND TEMPERATURE-DEPENDENT METALLIC CONDUCTIVITY IN MODERATELY DOPED Y-BASED CUPRATE SUPERCONDUCTORS

Dzhumanov S.[1], Kurbanov U.T.[1,2], Djumanov Sh.S.[2]
[1]*Institute of Nuclear Physics, Uzbekistan Academy of Sciences, Tashkent, Uzbekistan*
[2]*Tashkent State Technical University named after Islam Karimov, Tashkent, Uzbekistan*

The origin of a pseudogap emerging above the superconducting transiton temperature T_c and the mechanisms underlying charge transports in the normal state of high-T_c cuprate superconductors have been subject of prolonged debates and continuing intensive investigations [1-6]. These high-T_c superconductors are doped polar materials and have many distinctive electronic properties that distinguish them from conventional metals and superconductors. The Landau Fermi-liquid theory and the Bardeen-Cooper-Schriffer (BCS) theory of superconductivity have been quite successful in describing the normal-state charge transport properties and the superconducting properties of ordinay metals, but these theories have proven inadequate for moderately doped high-T_c cuprates, which are unusual metals above T_c and unconventional superconductors below T_c [5, 7, 8]. One of the most striking features of the doped cuprate superconductors is the appearance of a small pseudogap and a large pseudogap in the excitation spectrum of moderately doped high-T_c cuprates (i.e. underdoped, optimally doped and slightly overdoped cuprate materials) below characteristic temperatures T^* [1, 2, 8] and T_p [8, 9]. The pseudogap features observed in these materials by different experimental techniques [8, 10] are manifested in their electronic properties, in particular, in their normal-state charge transport properties. Therefore, understanding the peculiar charge transport properties of moderately doped cuprates can provide important clues for determining the nature of the pseudogap state and for unveiling the underlying mechanism of high- T_c superconductivity. One of the puzzling transport properties of moderately doped cuprates is the remarkable temperature dependence of their resistivity in thin CuO_2 layers of finite thickness, which is called as the in-plane resistivity $\rho_{ab}(T)$. Most mysterious anomalies in $\rho_{ab}(T)$, distinctly different downward or upward deviations from the *T*-linear law, were observed experimentally in various underdoped and optimally doped cuprate materials below T^*. Such anomalies in $\rho_{ab}(T)$ are believed to be intimately related to the opening of a pseudogap in these materials at a certain characteristic temperature T^* which systematically shifts to lower temperatures with increasing doping x and finally merges with T_c in slightly overdoped cuprates, as observed in various experiments [11,12]. The opening temperature T^* of the pseudogap in high-T_c cuprates at different doping levels can be defined accurately [13] as a deviation point from the *T*-linear behavior in $\rho_{ab}(T)$.

Thus, the properties of the pseudogap state and the microscopic mechanisms underlying the distinctive metallic conductivity in underdoped to overdoped cuprates have not yet been fully understood or systematically studied within a comprehensive theoretical framework. In order to gain deeper insight into the anomalous normal-state properties of high-T_c cuprates, it is essential to obtain detailed information on the systematic evolution of the pseudogap state and the distinctive metallic conductivity as a function of both doping *x* and temperature *T*.

In this work, we address the above unresolved issues of the pseudogap and distinctive charge transport phenomena in the normal state of moderately doped cuprate superconductors that are not encountered in conventional metallic superconductors. We investigate the systematic evolution of the pseudogap temperature T^* and anomalous metallic conductivity with doping *x* and temperature *T*

in yttrium-based (Y-based) cuprate superconductors. We consider the conductivity mechanisms of polaronic carriers scattered by lattice vibrations above T^* as well as two other types of charge carriers (excited polaronic components of bosonic Cooper pairs and bosonic Cooper pairs themselves) scattered by acoustic and optical phonons below T^* in moderately doped cuprates. We give a special emphasis to the quantitative comparison of the numerical results obtained for the doping- and temperature-dependent inplane resistivity $\rho_{ab}(x,T)$ with the experimental data from previous reports for different Y-based cuprate superconductors. We show that the opening temperature T^* of the BCS-like pseudogap in these materials corresponds to the inflection point in the $\rho_{ab}(T)$ curve, marking the cessation of the T-linear resistivity and the onset of a systematic deviation from this behavior in $\rho_{ab}(x,T)$.

The work is financed by the state budget of the Republic of Uzbekistan.

References:

1. S.Dzhumanov and P.K.Khabibullaev, Pramana J. Phys. 385, 45 (1995).
2. V.J.Emery and S.A. Kivelson, Nature 374, 434 (1995).
3. P.W.Anderson, The Theory of Superconductivity in the High-T_c Cuprates, Princeton University Press, Princeton, (1997).
4. B.P.Stojkovic and D. Pines, Phys. Rev. B 55, 8576 (1997).
5. A.L.Solovjov, E.V. Petrenko, L.V. Omelchenko, R.V. Vovk, I.L. Goulatis, and A. Chroneos, Sci. Rep. 9, 9274 (2019).
6. Z.-J.Lang, A. Hegg, Y. Yildirim, S. Jiang, L. Zou, X. Vue, T. Zeng, J. Hou, and W. Ku, Physica C 634, 1354723 (2025)
7. P.Phillips, Rev. Mod. Phys. 82, 1719 (2010).
8. M.Imada, A.Fujimori, and Y.Tokura, Rev. Mod. Phys. 70, 1039 (1978).
9. S. Dzhumanov, Solid State Commun. 115, 155 (2000).
10. A.L.Solovjov, and V.M.Dmitriev, Low Temp. Phys. 32, 99 (2006) [Fiz.Nizk.Temp. 32, 139 (2006)].
11. M. Eschring, Adv. Phys. 55, 47 (2006).
12. Y.Noat, A.Mauger, M.Nohara, H.Eisaki, S.Ishida, and W.Sacks, Solid State Commun. 348-349, 114689 (2022).
13. Y.Ando, S.Komiya, K.Segawa, S.Ono, and Y.Kurita, Phys. Rev. Lett. 93, 267001 (2004).

COLLISIONAL BREAKUP IN A COULOMB FEW-BODY SYSTEM WITH TWO ATTRACTIVE CENTERS

Kadyrov A.S.
Curtin University, Perth, Australia

We review recent progress in modelling ion-induced ionization of H and He using the heavy-particle convergent close-coupling method. Emphasis is placed on various differential cross sections. Comparisons with available experimental data are discussed, demonstrating the accuracy and predictive capability of the approach.

The close-coupling formalism provides a powerful framework for modelling ion–atom collisions. In particular, the wave-packet convergent close-coupling (WP-CCC) method [1] can give accurate descriptions of all single-electron processes in intermediate-energy ion–atom collisions. The approach has been applied to modelling charge transfer, target excitation, and ionisation in

proton collisions with H [2] and He [3]. It has been generalised to ion collisions with multielectron targets using an effective single-electron method that accounts for contributions from all atomic shells. This provides a superior alternative to commonly used independent-event models, which become impractical when more than two shells are involved. The approach can also model collisions involving both fully stripped and dressed highly charged ions. Overall, where experimental data are available, the results are in good agreement, demonstrating the robustness and reliability of the approach for modelling various ion–atom collisions.

The two-centre four-body WP-CCC method has been employed to calculate the singly and doubly differential cross sections for ionization in p–He collisions. The results show excellent agreement with experimental measurements. In particular, we investigated ionisation dynamics in intermediate-energy collisions [4]. By analyzing the energy and angular distributions of electrons ejected in p–He collisions at 52 and 103 keV, we found no evidence for a saddle-point mechanism when electrons are emitted with velocities equal to one half of the projectile velocity, contrary to earlier predictions. Instead, our results indicate that ionization is dominated by direct ionization and electron capture to the continuum. Further support for these conclusions come from calculations of ionization in He2+–He collisions [5].

For fully differential cross sections of ionization in p–He collisions, theory and experiment agree very well at high energies. However, significant discrepancies persist in the intermediate-energy regime [6], suggesting that resolving the p–He differential ionization problem requires both additional experimental measurements and further theoretical developments. We have also presented a kinematically complete experimental and theoretical investigation of single ionization of He [7]. The WP-CCC method was used to calculate the momentum distributions of emitted electrons, and excellent agreement was obtained between the experimental and theoretical results in both scattering and perpendicular planes.

Recently, we have developed a single-centre Coulomb–Sturmian convergent close-coupling (CS-CCC) approach to ion–atom collisions [8]. The approach gives integrated cross sections for all target states, including highly excited Rydberg states. Moreover, it provides the energy-differential ionization cross section at, and arbitrarily close to, the ionisation threshold. The CS-CCC approach is capable of accurately solving single-centre three-body Coulomb problems, such as intermediate-energy p−H scattering, yielding benchmark results [9].

References:

1. I.B. Abdurakhmanov, A. S. Kadyrov, and I. Bray 2016 Phys. Rev. A 94 022703.
2. I.B. Abdurakhmanov, J. J. Bailey, A. S. Kadyrov, and I. Bray 2018 Phys. Rev. A 97 032707.
3. Sh.U. Alladustov, I. B. Abdurakhmanov, A. S. Kadyrov, and I. Bray, and K. Bartschat 2019 Phys. Rev. A 99 052706.
4. K.H. Spicer, C. T. Plowman, N. W. Antonio, M. S. Schöffler, M. Schulz, and A. S. Kadyrov 2024 Phys. Rev. A 109 062805.
5. Sh.U. Alladustov, K. H. Spicer, N. W. Antonio, A. M. Kotian, and A. S. Kadyrov 2025 Phys. Rev. A 112 012804.
6. K.H. Spicer, N. W. Antonio, M. S. Schöffler, M. Schulz, and A. S. Kadyrov 2025 Phys. Rev. A 112 032806.
7. K.H.Spicer, L.Ph. H. Schmidt, C. T. Plowman, N. W. Antonio, Sh. U. Alladustov, I. B. Abdurakhmanov, I. Bray, M. S. Schöffler, R. Dörner, and A. S. Kadyrov 2026 Phys. Rev. A 113 012816.
8. N.W.Antonio and A. S. Kadyrov 2025 Phys. Rev. A 111 052806.
9. N.W.Antonio, I. Bray, and A. S. Kadyrov 2024 Phys. Rev. A 110 032810.

ENTRALITY DEPENDENCIES OF TRANSVERSE MOMENTUM DISTRIBUTIONS OF IDENTIFIED LIGHT-FLAVOR HADRONS IN p+Pb COLLISIONS AT $\sqrt{s_{nn}}$ = 5.02 TeV AT THE LHC WITHIN A TWO-COMPONENT MODEL

Olimov Kh.K.[1,2], Fedosimova A.[3,4], Liu Fu-Hu[5], Musaev K.A.[1], Lebedev I.A.[3], Tokhirov A.[1], Ibraimova S.[3], Bondar E.[3]

[1]*Physical-Technical Institute, Uzbekistan Academy of Sciences, Tashkent, Uzbekistan*
[2]*National University of Science and Technology MISIS, Almalyk, Uzbekistan*
[3]*Institute of Physics and Technology, Satbayev University, Almaty, Kazakhstan*
[4]*Institute of Nuclear Physics, Almaty, Kazakhstan*
[5]*Institute of Theoretical Physics, Shanxi University, Taiyuan, China*

High-energy Xe+Xe and Pb+Pb collisions at the LHC (Large Hadron Collider, Switzerland) are primarily aimed to produce QGP (Quark-Gluon Plasma) - very dense state of nearly free quarks and gluons - and studying its various properties and evolution, as well as understanding the strong interaction at extreme matter densities. Our Universe is believed to be in QGP state a few microseconds after the so-called Big Bang, which is assumed to be a starting moment of Universe creation. Production of QGP was firmly established in high-energy Au+Au and Pb+Pb collisions at the RHIC (Relativistic Heavy-Ion Collider, USA) and LHC/CERN experiments. QGP with very short lifetime of the order of 10^{-23} seconds behaves as nearly perfect quark-gluon liquid with very small viscosity. Produced QGP decays very quickly into large number of particles during hadronization stage. Afterwards, very dense and hot system of produced hadrons, called fireball, expands and cools down very swiftly, going through the chemical and kinetic freeze-out stages. At the chemical freeze-out, the particles of a fireball stop interacting inelastically, which fixes the numbers of produced hadron species. The temperature of the system ($T_{\rm ch}$) and chemical potential (μ) at the chemical freeze-out stage are extracted from yield ratios of various particle species using thermal or statistical hadronization models. At the kinetic freeze-out, the particles of the fireball stop interacting elastically, and the momenta and energies of the final particles do not change anymore until they reach detectors. Therefore, it is important to analyze the transverse momentum (p_T) distributions of the final particles with the help of various thermodynamic and phenomenological models to extract the thermodynamic and hydrodynamic parameters of the fireball at the moment of kinetic freeze-out.

We analyze [1] the centrality ($\langle N_{part}\rangle$) dependencies of midrapidity transverse momentum (p_T) spectra for identified light-flavor hadrons (charged pions and kaons, protons and antiprotons) in asymmetric p+Pb collisions at $\sqrt{s_{nn}}$ = 5.02 TeV at the LHC. Using the new two-component Tsallis-Hagedorn Model with Transverse Flow (THMTF), we describe [1] the ALICE experimental data up to p_T = 20 GeV/c across seven multiplicity classes. To reveal potential system-size dependencies, these results [1] are systematically compared with symmetric Pb+Pb collisions at $\sqrt{s_{nn}}$ = 2.76 and 5.02 TeV. It is estimated that collective radial flow emerges at $\langle N_{part}\rangle \approx 4.0 \pm 0.5$ [1] along with simultaneous transitioning of kinetic freeze-out temperature (T_0) to a nearly plateau region in p+Pb collisions. The kinetic freeze-out temperature (T_0) appears to demonstrate distinct centrality dependencies in small and large collision systems before reaching a stable plateau. In p+Pb collisions, T_0 initially rises up to its threshold value before stabilizing, suggesting that high energy densities in central p+Pb events might cause the compact system to decouple rapidly before undergoing significant expansion. Conversely, in Pb+Pb collisions, T_0 steadily decreases up to a

larger threshold $\langle N_{part} \rangle$ value before reaching a plateau. This initial downward trend of T_0 in Pb+Pb collisions is consistent with the larger volume of heavy-ion fireballs, which may undergo more prolonged hydrodynamic expansion and extensive cooling before reaching the low-density decoupling limit. In both p+Pb and Pb+Pb collision environments, central collisions point toward enhanced thermalization, as deduced from decreasing-with-centrality trend of non-extensivity parameter q. Parameter q hierarchy (q (mesons) > q (baryons)) suggests that baryons may form predominantly in the highly thermalized core. In both p+Pb and Pb+Pb systems, the momentum scale parameter (P_0) rises steadily with centrality and correlates strongly positively with the average flow velocity ($\langle \beta_T \rangle$), suggesting that larger pressure gradients may simultaneously drive collective flow and high-p_T particle production. However, at high p_T, the power-index n points to potentially different dynamics between the two systems. While large-scale Pb+Pb collisions exhibit spectral flattening likely related to strong hydrodynamic pressure, the p+Pb system shows a stable n for mesons (consistent with vacuum-like jet fragmentation), but a rising-with-centrality trend of n for protons and antiprotons. This rise of power-index n may indicate intermediate-p_T baryon enhancement via parton recombination/coalescence. These different physical trends are supported [1] by Pearson correlation analyses of extracted model parameters in p+Pb and Pb+Pb collision systems. The results of present work establish critical benchmarks for theoretical models describing the transition from microscopic interactions to collective behavior in high-energy collisions.

References:

1. Khusniddin K. Olimov *et al*., Centrality Evolution of Transverse Momentum Spectra of Identified Light-Flavor Hadrons in p+Pb Collisions at $\sqrt{s_{nn}}$ = 5.02 TeV at the LHC Within a Two-Component Model, Preprints 2026071769 (2026). https://doi.org/10.20944/preprints202607.1769.v1

THE EFFECT OF THE ENTRANCE CHANNELS ON THE DYNAMICS OF THE COMPETITION OF PROCESSES OF NUCLEAR REACTIONS IN HEAVY-ION COLLISIONS.

Nasirov A.K.[1,2], Kayumov B.M.[2,3], Yuldasheva G.A.[2], Ganiev O.K.[2,4], Khusanov E.D.[4]

[1]*Joint Institute for Nuclear Physics, Dubna, Russian Federation*

[2]*Institute of Nuclear Physics, Uzbekistan Academy of Sciences, Tashkent, Uzbekistan.*

[3]*New Uzbekistan University, Tashkent, Uzbekistan*

[4]*National University of Uzbekistan, Tashkent, Uzbekistan.*

Theoretical and experimental studies of the formation mechanisms of the heavy-ion reaction products are of interest for selecting the colliding ion pairs for the synthesis of new superheavy ions and for the development of advanced theoretical methods. To reach as possible the largest values of the evaporation residues (ER) cross section is a main goal of the experiments. Recently, several attempts have been made to synthesize the elements 119 and 120 in fusion reactions, including: ^{50}Ti+^{249}Bk [1], ^{50}Ti+^{249}Cf [1], ^{51}V+^{248}Cm [2], and ^{54}Cr+^{248}Cm [3]. But no events were observed. The experiments were carried out during several months. The probability of the formation of the compound nucleus is determined by the cross section of the fusion-fission products. These experiments are performed during much shorter time. Therefore, the results of the excitation function of the fusion-fission processes are important to study fusion mechanisms. The estimation of the fusion probabilities from analysis of experimental data can contain ambiguities due to the overlapping mass distributions of fusion-fission and quasi-fission products, which are products of

competing reaction channels. Experimentally, this manifests itself as mixing of binary products formed in different channels in the same detector.

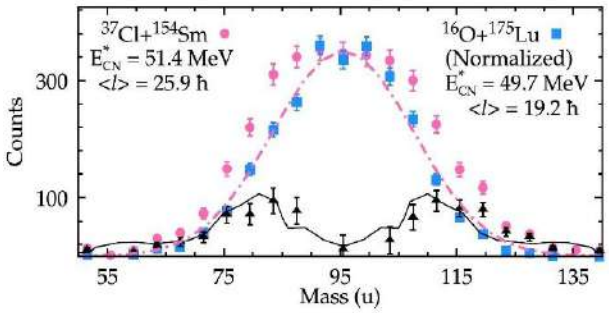

Figure 1. Description of the experimental values of the quasifission yields (triangles) are presented as a difference between measured yields of the binary fusion-fission products in the ^{37}Cl+^{154}Sm (circles) and ^{16}O+^{175}Lu (squares) reactions by the DNS model (solid curve) [4].

In this work we have demonstrated that theoretical methods based on the dinuclear system (DNS) concept allow us to estimate the contributions of quasi-fission products with mass numbers matching those of the asymmetric [4] and symmetric [5] fission products of a compound nucleus. The advantage of the computational method under discussion is that it allows us to establish the dependence of the mass distribution of quasi-fission products on the energy and orbital angular momentum of the ion collision, as well as on the orientation angles of the axial symmetry of the nuclei relative to the beam. We will prove that successful description of the experimental data is the way to extract interesting information about dependence competition of processes. The authors of Ref. [4] estimated the contribution of the quasifission products in the mass-asymmetric part of the fusion-fission products by extraction of the measured mass distribution (squares in Fig. 1) of the fission-like products of the ^{16}O+^{175}Lu reaction from the ones (circles in Fig. 1) of the ^{37}Cl+^{154}Sm reaction. Since the measured data of the former reaction is described well by the results GEF code [6] which is used to estimate the mass distribution of the fusion-fission products. The difference (up trianles) between yields of the fission-like products is described as a yield of the quasifission products by the DNS model (solid line) [4].

Theoretical calculations of the contribution of quasi-fission products to the mass distribution of binary products provided the first explanation for the nonlinearity in the half-width of the fusion-fission mass distribution observed in the ^{30}Si+^{197}Au (see Fig. 2) reaction at certain collision energies. This behavior of the quasi-fission product mass distribution explains the appearance of its contribution in the mass-asymmetric part of the mass distribution of the fusion-products as a function of energy in some reactions [5].

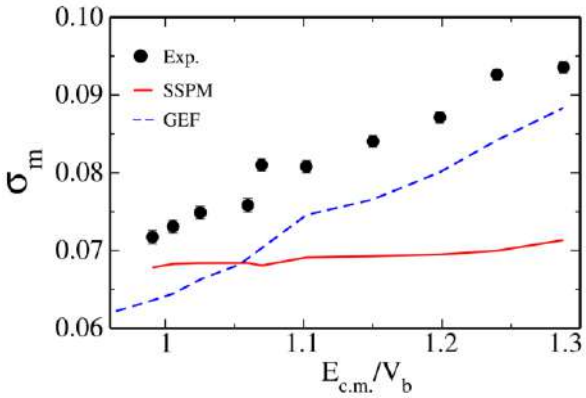

Figure 2. The measured values of the standard deviation (σ_m) plotted as a function of $E_{c.m.}/V_{b\ is}$ .is compared with the results of GEF code and scission point model calculations [5].

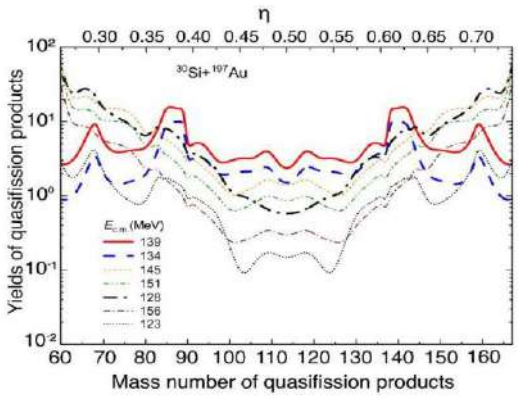

Figure 3. The mass distributions of the quasifission products for the ^{30}Si + ^{197}Au reaction as a function of $E_{c.m.}$ calculated using the DNS model [5].

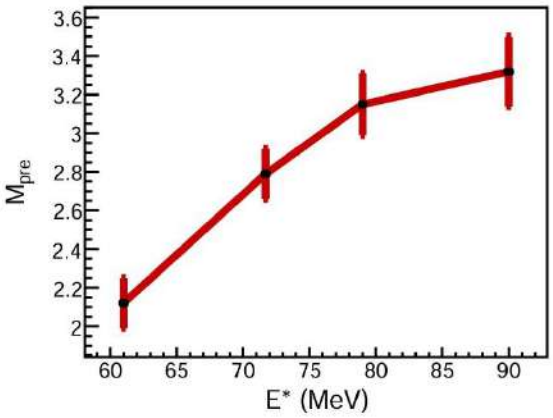

Figure 4. Excitation-energy dependence the pre-scission neutron multiplicity M_{pre} in the ^{28}Si + ^{176}Hf [7].

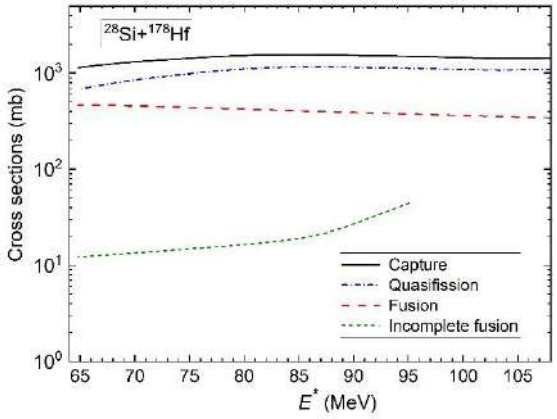

Figure 5. The calculated cross sections of the capture, quasifission, fusion and incomplete processes.

The deviation from the linearity of the pre-scission neutron multiplicity observed in the ^{28}Si + ^{176}Hf reaction at the excitation energy of compound nucleus E^*> 85 MeV is explained by the increase of the incomplete fusion contribution: kinetic energy of α-particle emitted in the incomplete fusion decreases the excitation energy of the conjugate nucleus, as a result its pre-scission neutron multiplicity decreases.

References:

1. J. Khuyagbaatar, *et al.*, Phys. Rev. C **102**, 064602 (2020).
2. M. Tanaka, et al., J. Phys. Soc. Jpn. 91, 084201 (2022).
3. S. Hofmann, *et al.*, Eur. Phys. J. A 52, 180 (2016).
4. Shilpi Gupta, *et al.*, Phys. Lett. B**803**, 135297 (2020).
5. B. Ashna, *et al.*, Phys. Rev. C**113**, 034606 (2026).
6. K.-H. Schmidt, et al., Nucl. Data Sheets 131, 107 (2016).
P. Dubey, et al., Phys. Rev. C 112: L011602 (2025)

SIBERIAN CIRCLE SOURCE OF PHOTONS (SKIF): PHYSICAL POSSIBILITIES AND TECHNICAL REQUIREMENTS

Churkin I.
Budker Institute of Nuclear Physics, Novosibirsk, Russian Federation

As part of the “Federal Scientific and Technical Program for the Development of Synchrotron and Neutron Research and Research Infrastructure until 2030 and Beyond”, Shared Research Center “Siberian Circular Photon Source” (SKIF) has been established in the science city of Koltsovo (Novosibirsk Region), featuring the 4+ generation synchrotron radiation source with an electron energy of 3 GeV, record-low emittance (less than 75 pm·rad), and a brightness around 10^{22} photons/s/mm²/mrad²/0.1% bandwidth.

The accelerator complex consists of: Linear Accelerator (200 MeV); Booster Synchrotron that accelerates electrons to 3 GeV at 1 Hz (circumference - 158.7 m); and Storage Ring (circumference – 476 m; 16 super-periods with straight sections).

In the first phase of the project, seven Synchrotron Radiation (SR) user stations have been launched: six stations utilize radiation from insertion devices (wigglers and undulators), while the seventh station uses radiation from a bending magnet. The facility’s maximum design capacity is 30 SR stations.

To achieve the design specifications of the electron beam and the generated synchrotron radiation, stringent requirements are imposed on the stability of the engineering support systems.

Vibration stability of support structures: better than 150 nm (for the booster synchrotron, LINAC); less than 30 nm in the 10-100 Hz frequency range and less than 50 nm at 10 Hz and below (for the Storage Ring tunnel and experimental hall). Temperature stability of deionized cooling water: ± 0.1°C (for the Storage Ring equipment); ± 1°C (for LINAC, booster synchrotron, and SR user station equipment). Air temperature stability in specialized equipment areas: ± 0.1°C (in the Storage Ring tunnel); ± 1°C (in the LINAC, booster tunnel, experimental hall).

Comprehensive optimization of the accelerator complex system, SR user station equipment, and supporting engineering systems is currently underway to achieve the design parameters of the electron beam in the Storage Ring and the synchrotron radiation at the SR stations.

ASSESSMENT OF THE POSSIBILITY OF PREDICTING THE AVERAGE INTEGRAL CLTE OF REACTOR MATERIALS UP TO 1800°C BASED ON DILATOMETRY DATA UP TO 1000°C

Kulsartov T.[1,2], Baklanova Yu.[2], Kenzhina I.[1], Zaurbekova Zh.[1,2]
[1]*Satbayev University, Almaty, Kazakhstan;*
[2]*Institute of Atomic Energy Branch of NNC RK, Kurchatov, Kazakhstan*

The coefficient of linear thermal expansion (CLTE) is one of the key thermophysical properties of materials used in nuclear and fusion reactors. Reliable data on thermal expansion are necessary for calculating thermal deformations, stresses, and clearances in structural components. However, the range of available dilatometric measurements is often limited to temperatures around 1000°C, while the operating or emergency temperatures of individual reactor materials can reach 1500–1800°C.

The aim of this study was to assess the feasibility of predicting the average integrated CLTE of reactor materials up to 1800°C based on experimental data obtained in the range from room temperature to 1000°C. The study was conducted for materials of various classes, including reactor-grade graphite, uranium dioxide, and refractory metals, particularly molybdenum. The selection of materials with different chemical bond types and temperature dependence patterns allowed for an assessment of the overall capabilities and limitations of the approach used.

The method was validated using experimental dependences of the relative elongation of materials over the entire temperature range. The initial curves were artificially limited to a temperature of 1000°C and then approximated using a linear relationship and polynomials of varying degrees. The resulting relationships were extrapolated to 1800°C.

The most consistent results were obtained using quadratic and cubic approximations of the relative elongation. In the absence of phase transformations, pronounced structural relaxation, and other

anomalous changes in the material, this approach allows for an acceptable estimate of the average integrated CLTE up to 1800°C. However, a single universal approximation relationship cannot be recommended for all the materials considered: the choice of model must take into account the physical properties of the material and the shape of the experimental curve.

OPTICAL AND LUMINESCENT DEVELOPMENT OF VACANCY DEFECTS IN ALKALI-HALIDE CRYSTALS (KBr, KCl)

Taiirov M.M.[1], Oskonbaev M.Ch.[2], Berdibaev A.K[1].Temirbaev M.M.[1]
[1]Kyrgyz National University named after J.Balasagyn, Bishkek, Kyrgyz Republic
[2]Osh State University, Osh, Kyrgyz Republic

The article examines the characteristics of the radiative decay of near-vacancy electronic excitations in potassium bromide and potassium chloride, and investigates the optical properties of divacancies and other vacancy-type defects.

In the long-wavelength absorption edge spectra of KBr crystals deformed at 300 K and measured at 77 K, weakly defined absorption bands appear with maxima at 6.1 and 6.35 eV; similarly, for deformed KCl crystals, absorption bands appear with maxima at 6.9 and 7.1 eV. The spectral characteristics of anion vacancies in KBr do not coincide with the emission and excitation spectra of the defects responsible for the absorption band with a maximum at 6.1 eV in deformed KBr. It should be noted that the migration energy of isolated anionic and cationic vacancies in KBr is 0.84–0.92 eV (Ch. Lushchik, A. Lushchik, 1989). This implies that isolated anionic and cationic vacancies are mobile and unstable defects at room temperature. Consequently, during the plastic deformation of the crystal at 300 K, isolated anionic and cationic vacancies do not "survive" in an isolated state.

The absorption band with a maximum at 6.35 eV in KBr may be associated with exciton absorption near divacancies or vacancy quartets. To elucidate the nature of the 6.35 eV absorption band in KBr, uniaxial compression of the crystals was performed at 520 K—a temperature at which vacancy quartets form and divacancies migrate to dislocations. Indeed, the absorption spectrum of KBr deformed at 520 K does not exhibit the 6.35 eV band; instead, the background level of the absorption spectrum rises, and a poorly defined band with a maximum at approximately 6.5 eV begins to emerge. This band may be associated with vacancy quartets that are thermally stable up to 520 K. It should be noted that a one-year dark storage period for a KBr crystal deformed at 300 K also resulted in the disappearance of the absorption band with a maximum at 6.35 eV. At low degrees of KBr deformation (up to 4%), a band with a maximum at 6.35 eV begins to emerge in the absorption spectrum, indicating the elementary nature of this band. At higher degrees of KBr deformation (>10%), a broad, non-elementary band with a maximum at ~6.65 eV additionally appears in the absorption spectrum. In our opinion, this broad band differs from the band with a maximum at 6.5 eV and is associated with larger vacancy clusters or dislocations.

Upon excitation of a deformed KBr crystal in the 6.35 eV region, a new emission band with a maximum at 2.75 eV is observed in the emission spectrum. This emission band differs from the crystal's exciton luminescence and α-luminescence. The maximum of the excitation spectrum for this new emission band lies in the 6.25–6.45 eV range for KBr. Heating the deformed KBr crystal to 540 K resulted in the disappearance of these emission and excitation bands, along with the corresponding absorption bands. Consequently, this emission band corresponds to the radiative

decay of excitons near deformation-induced divacancies. Thus, the formation of divacancies in KBr during uniaxial compression of the crystals has been demonstrated.

In a plastically deformed KBr crystal, VUV radiation generates not only exciton excitations at regular lattice sites (c^0), but also excitons localized near isolated anion vacancies (e_{α}^{0} $\boldsymbol{\alpha}$), divacancies (e_{b}^{0}), vacancy quartets ($e_{к}^{0}$), and dislocations (e_{d}^{0}). We have designated the divacancies, vacancy quartets, and dislocations as b-, k-, and d-centers, respectively, by analogy with α-centers. Using selective VUV excitation at 4.2 K, we isolated the excitation and emission spectra of excitons localized near the divacancies, vacancy quartets, and dislocations created in the crystals through preliminary plastic deformation.

A general pattern observed is that, in all the crystals we studied, the magnitude of the shift (Δ) of the absorption and excitation band maxima from the position e_{r}^{0} decreases in the sequence $e_{\alpha}^{0} .\rightarrow e_{b}^{0} \rightarrow e_{k}^{0} \rightarrow e_{d}^{0}$. The maximum shift value Δ in KBr, caused by the presence of an anion vacancy ($\Delta_{\alpha}=e_{r}^{0}- e_{\alpha}^{0}$), is Δ_{α}=0,66 eV; for divacancies, it is somewhat smaller: Δ_{b}= 0.46 eV; for vacancy quartets, it is even smaller: Δ_{k}= 0,31 eV; and for a dislocation, it is the smallest: Δ_{d}=0,16 eV. Similar results were obtained for the deformed KCl crystal.

It is reasonable to attribute this pattern to the magnitude of the vacancy defect's charge. Indeed, the optical transition in the c_{α}^{0} center occurs in the field of a point defect with an effective charge of +1. In the b-center, the charge of the anion vacancy is partially compensated by the charge of the cation vacancy, and the optical transition takes place in the field of a dipole. In the case of the k-center, the charge is compensated to an even greater extent, and the electric field surrounding the nearby halogen ions closely resembles that of the regular lattice.

With a further increase in the size of the vacancy defect—that is, the formation of a dislocation—the shift of the absorption and excitation bands associated with the dislocation should decrease further. For a surface, which can be viewed as the limiting case of a vacancy defect, the shift value was estimated by Sachs (1980) to be in the range of 0.1–0.15 eV; this may overlap with the case of the d-center, given that the shift for a dislocation is 0.16 eV.

An analysis of the emission spectra of α-, b-, k-, and d-centers in a KBr crystal can explain the mechanism of the radiative decay of electronic excitations in this crystal. The emission spectra of α-, b-, k-, and d-centers lie within the spectral range of the π-luminescence of the self-trapped exciton, which has the structure of ($X_2^- + e^-$) centers. We did not observe any luminescence analogous to the σ-luminescence of an exciton distorted by vacancy defects. A significant shift of the emission spectra of α-, b-, k-, and d-centers in KBr and KCl toward higher energies is observed in the sequence α → b → k → d, accompanied by a corresponding decrease in Stokes losses. This is quite natural, since the increase in the size of the vacancy defect (α → b → k → d) reduces the number of crystal vibrations with which the electronic excitation localized near the vacancy can interact during relaxation.

The values of Stokes losses for the KBr crystal are as follows: for e_{α}^{0} : S_R (α)=0,59: для e_{b}^{0}: S_r (b)=0,57; для e_{k}^{0}: S_R (k)=0,55; для e_{d}^{0}:S_R(d)=0,52.

In conclusion, we can state that in KBr and KCl, upon the optical creation of excitons localized near a single anion vacancy, a divacancy, a vacancy quartet, or a dislocation, the charge of the vacancy defect is the primary lattice-perturbing factor, while the size of the vacancy defect directly influences the process of radiative exciton decay.

ON TRAINING OF A STAFF FOR NUCLEAR POWER AT THE INTERNATIONAL SAKHAROV ENVIRONMENTAL INSTITUTE OF BELARUSIAN STATE UNIVERSITY

Kiyavitskaya H., Dashkevich T., Gusakova O., Germenchk M.
The International Sakharov Environmental Institute of Belarusian State University, Minsk, Belarusia

Due to the absence of domestic energy resources in the Republic of Belarus, the use of nuclear energy is of particular significance. Moreover, a large-scale project such as a nuclear power plant promotes technological advancement in industry and necessitates the training of specialists for various sectors of the national economy. On January 31, 2008, a decision was made to construct the first nuclear power plant in the Republic of Belarus. To support this initiative, a number of legislative acts concerning the peaceful use of nuclear energy were adopted, including the State Program for Personnel Training for the Nuclear Power Industry for 2009–2020. The continuation of these activities is being implemented through new state programs extending to 2030.

Personnel training for Belarus’s nuclear industry is a comprehensive system encompassing universities and colleges (over 13 educational institutions) that supplies the Belarusian NPP (Nuclear Power Plant) with qualified staff. The key educational institutions and this fields include the Belarusian State University (BSU), the International Sakharov Environmental Institute of Belarusian State University, Belarusian National Technical University (BNTU), and the Belarusian State University of Informatics and Radioelectronics.

At the International Sakharov Environmental Institute of Belarusian State University (ISEI BSU) the Department of Nuclear and Medical Technologies (formerly the Department of Nuclear and Radiation Safety) provides training for personnel for Belarus's nuclear industry. This includes advanced training and professional retraining in the safety of nuclear and radiation technologies, through first-level degree programs in “Nuclear and Radiation Safety” and “Medical Physics,” as well as second-level degree programs in the same specialties.

With technical support of the IAEA, the International Sakharov Environmental Institute of Belarusian State University (ISEI BSU) also conducts personnel retraining in the specialty “Radiation Protection and Safety of Ionizing Radiation Sources” (Code 1-33 01 71), conferring the qualification of “Radiation Safety Specialist”.

This paper outlines the key activities of the ISEI BSU in personnel training for the Belarusian NPP, other organizations utilizing ionizing radiation sources or operating nuclear research facilities, as well as for Belarusian state administrative bodies.

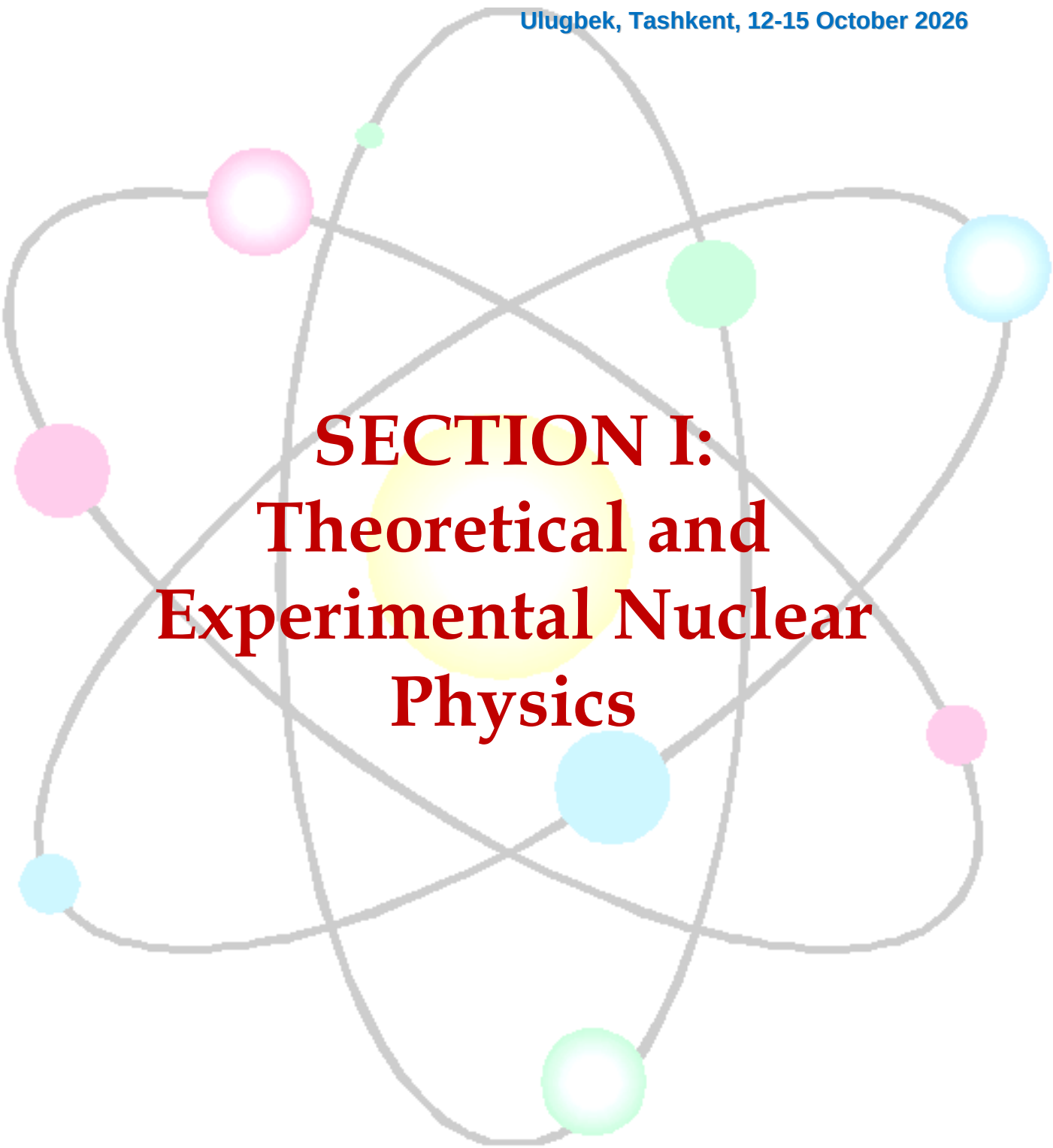

SECTION I: Theoretical and Experimental Nuclear Physics

^{21}Ne STRUCTURE IN THE ^{17}O (α,α) RESONANCE REACTION

Nauruzbayev D.K.[1,2], Nurmukhanbetova A.K.[1,2,3], Goldberg V.Z.[4], La Cognata M.[5], Di Pietro A.[5], Figuera P.[5], Cherubini S.[5], Gulino M.[5], Lamia L.[5], Pizzone R.G.[5], Spartà R.[5], Tumino A.[5]

[1]Nazarbayev University Research Administration, Astana, Kazakhstan
[2]School of Intelligent Systems, Astana IT University, Astana, Kazakhstan
[3]Energetic Cosmos Laboratory, Nazarbayev University, Astana, Kazakhstan
[4]Cyclotron Institute, Texas A&M University, College station, USA
[5]Istituto Nazionale di Fisica Nucleare, Catania, Italy

The excitation function for the ^{17}O+α elastic scattering was studied in the energy range from 1.5 to 5.3 MeV of c.m.s. [1] using the Thick Target Inverse Kinematics (TTIK) method at the DC-60 cyclotron in Astana [2]. We performed an R-matrix analysis of the resonant data [1] up to 4 MeV in the c.m.s, which demonstrated a well-developed α-cluster structure. At higher energies, groups of very strong peaks are observed. We then performed measurements of the ^{17}O (α,α) excitation functions at higher energies using the TTIK method at the INFN-LNS tandem [3]. The ^{17}O beam energy was ~3.5MeV/A and the intensity ~10 nA. This made it possible to measure excitation functions up to 9 MeV in the center-of-mass system. To detect light recoil nuclei from ^{17}O +α interaction, an array of single silicon detectors and a dE-E telescope of Si detectors were used in a large scattering chamber with a diameter of 200 cm. The telescope was needed to evaluate a possible contribution of protons to the charged particle spectra. These detectors covered an angular region from 0° up 30° degrees in the laboratory system with respect to the chamber center.

This research was funded by the Science Committee of the Ministry of Science and Higher Education of the Republic of Kazakhstan (Grant No. AP23489860).

References:

1. A.K.Nurmukhanbetova, et al, Evidence for α -cluster structure in 21Ne in the first measurement of resonant 17O+α elastic scattering. Phys. Rev. C 100, 062802(R) – Published 26 December 2019.
2. A.K.Nurmukhanbetova et al, Implementation of TTIK method and time of flight for resonance reaction studies at heavy ion accelerator DC-60. Nuclear Instruments and Methods in Physics Research Section A, November 2016.
3. D.K.Nauruzbayev et al, Strong resonances at high excitation energy in 17O+alpha resonance scattering. Physics of Atomic Nuclei. Volume 83, Issue 4, 1 July 2020, Pages 520-522.

NEUTRON INDUCED REACTIONS EXPLORED VIA THE TROJAN HORSE METHOD

Sergi M.L. on behalf of ASFIN collaboration
Dipartimento di Fisica e Astronomia, Università degli Studi di Catania, Catania, Italy
INFN, Laboratori Nazionali del Sud, Catania, Italy

Neutron induced reactions on stable or unstable nuclei play a significant role in the nucleosynthesis of the elements in the cosmos. Their interest ranges from the primordial processes occurred during the Big Bang Nucleosynthesis up to the "stellar cauldrons" where neutron capture

reactions build up heavy elements. In the last years, several efforts have been made to investigate the possibility of applying the Trojan Horse Method (THM) to neutron induced reactions mostly by using deuteron as "TH-nucleus".

My talk will be focused on describing the application of THM on the neutron induced reactions relevant for astrophysics. The results of some data analysis will be shown focusing on the advantages of the THM for these measurements. These applications open new frontiers in the application of the method (i.e. the study of ^{7}Be+d, ^{14}N+d or ^{11}C+alpha reactions) extending its range of applicability for contributing to astrophysically relevant problems.

SINGLE-PROTON TRANSFER IN THE REACTION ^{45}Sc(^{3}He,d)^{46}Ti AT 29 MeV

Sadykov B.M.[1], Zholdybayev T.K.[1], Duisebayev B.[1], Ussabayeva G.[1,2], Temirzhanov A.[1,3], Mendibayev K.O.[1,4], Issatayev T.[1,4], Urazbekov B.A.[5], Shneidman T.M.[4]

[1]Institute of Nuclear Physics, Almaty, Kazakhstan

[2]Abai Kazakh National Pedagogical University, Almaty, Kazakhstan

[3]Satbayev University (Kazakh National Research Technical University), Almaty, Kazakhstan

[4]Joint Institute for Nuclear Research, Dubna, Russian Federation

[5]L.N.Gumilyov Eurasian National University, Astana, Kazakhstan

The interplay between shell-model and cluster degrees of freedom remains one of the central open problems of nuclear structure for N ≈ Z nuclei in the sd–pf shell region. Around the doubly magic core ^{40}Ca, an α+^{40}Ca configuration is known to coexist with shell-model states in ^{44}Ti, generating strongly deformed and superdeformed rotational bands [1]. For the neutron-richer partner ^{46}Ti, angular-correlation measurements of the ^{42}Ca (^{7}Li, tα) ^{42}Ca reaction have revealed a dense spectrum of states above $E_x \approx 11$ MeV whose angular correlations are consistent with an $\alpha + ^{42}$Ca cluster interpretation [2]. A recent study of the ^{45}Sc (^{3}He, d) ^{46}Ti reaction at 29 MeV independently populated a series of previously unreported high-lying states up to $E_x \approx 17$ MeV, i.e. above the proton-separation energy, and their energies were compared with the lowest excitations of an $\alpha + ^{42}$Ca dinuclear-system (DNS) model [3, 4]. However, because these states lie above the particle-separation threshold, they are expected to carry a substantial admixture of multi-particle–multi-hole configurations, and the numerical agreement with the DNS energies alone does not establish their cluster character. Since (^{3}He, d) is nominally a single-proton transfer reaction, a quantitative assessment of this population mechanism requires an independent, reaction-model-based determination of the single-particle structure of the low-lying states of ^{46}Ti, which is the subject of the present work.

The single-proton transfer reaction ^{45}Sc (^{3}He, d) ^{46}Ti was investigated at an incident ^{3}He energy of 29 MeV on the U-120M cyclotron of the Nuclear Physics Institute of the Czech Academy of Sciences (Řež), using a self-supporting ^{45}Sc target of 1.8 μm thickness. Reaction products were identified with four ΔE–E semiconductor telescopes, and angular distributions of the outgoing deuterons populating the ground state and the excited states at 0.889 and 2.009 MeV of ^{46}Ti were measured over the laboratory angular range $\theta_{lab} = 5–45°$ and analyzed within the distorted-wave Born approximation (DWBA) using the DWBA module of the NRV code [5]. Optical-model parameters for the entrance and exit channels were adopted from the analysis of Ohmura et al. [6] and adjusted for the present beam energy.

The calculated angular distributions reproduce the main diffractive features of the experimental data (Fig. 1) and are consistent with a dominant $l_p = 3\,(1f_{7/2})$ proton transfer for the ground state (0^+) and the 0.89 MeV (2^+) and 2.01 MeV (4^+) states, in agreement with the classic (^{3}He, d) study of Ohmura et al. [6], confirming that these low-lying states of ^{46}Ti are populated predominantly through a direct one-proton transfer mechanism, with spectroscopic factors consistent with the low-lying single-particle structure expected for ^{46}Ti built on the ^{45}Sc core. This single-particle reference is a necessary starting point for interpreting the high-lying states of the same reaction above $E_x \approx 10$ MeV [3]. There, a possible $\alpha + {}^{42}$Ca cluster component was discussed on the basis of energy agreement with the DNS model [4]; however, since these states lie above the proton-separation threshold, an admixture with multi-particle–multi-hole configurations is expected, and the present analysis by itself does not establish a dominant cluster character for them. A more conclusive test would require measured angular distributions and extracted spectroscopic strengths for these high-lying states, analogous to those obtained here for the low-lying levels, to quantify the extent of single-particle versus cluster admixture as a function of excitation energy.

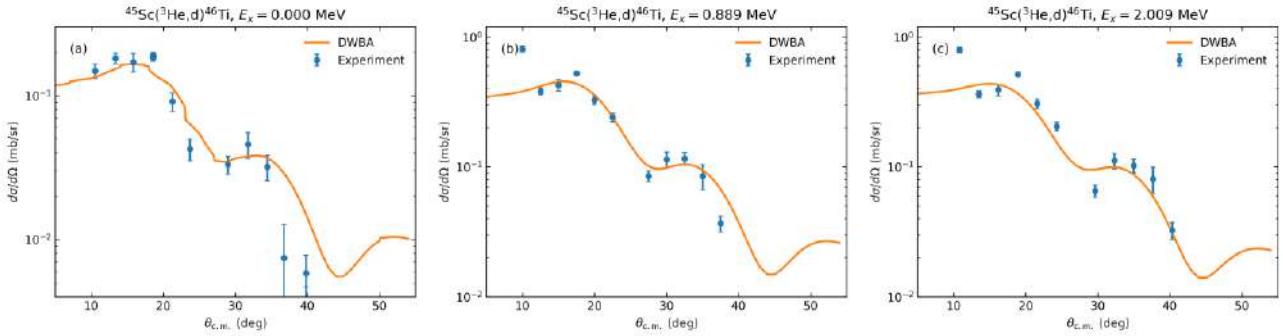

Figure 1. Experimental angular distributions for the reaction ^{45}Sc (^{3}He, d) ^{46}Ti at E_{lab} = 29 MeV. Symbols denote the experimental data and solid curves represent the DWBA calculations for the ground state and the excited states at E_x = 0.889 and 2.009 MeV.

Acknowledgements. This research is funded by the Science Committee of the Ministry of Science and Higher Education of the Republic of Kazakhstan (Grant No. AP26102053).

References:

1. M.Fukada, M.K. Takimoto, K. Ogino, S. Ohkubo, Phys. Rev. C 80, 064613 (2009).
2. T.Wada and H.Horiuchi, Phys. Rev. C 38, 2063 (1988); F. Michel, G. Reidemeister, S. Ohkubo, Phys. Rev. C 37, 292 (1988).
3. T.Issatayev, N.K. Skobelev, T.M. Shneidman, Yu.E. Penionzhkevich, V. Burjan, J. Mrazek, Phys. Part. Nucl. Lett. 20, 1106–1115 (2023).
4. T.M. Shneidman, G.G. Adamian, N.V. Antonenko, R.V. Jolos, S.-G. Zhou, Phys. Rev. C 92, 034302 (2015).
5. V.I. Zagrebaev, A.S. Denikin, A.V. Karpov, et al., NRV web knowledge base on low-energy nuclear physics, Nucl. Instrum. Methods Phys. Res. A 596, 67 (2008); http://nrv.jinr.ru
6. H. Ohmura, T. Ishimatsu, K. Yagi, H. Ejiri, Y. Nakajima, T. Tōhei, T. Nakagawa, J. Phys. Soc. Jpn. 25, 953 (1968).

CALCULATION OF THE ASTROPHYSICAL S-FACTOR AND REACTION RATE FOR THE $^{11}B(p,\gamma)^{12}C$ REACTION USING ANC INFORMATION FOR BOUND STATES

Igamov S.B.[1], Artemov S.V.[1], LaCognata M.[2], Rusek K.[3], Son I.Ya.[1], Tojiboev O.R.[1], Ergashev F.Kh.[1]

[1]*Institute of Nuclear Physics, Uzbekistan Academy of Sciences, Tashkent, Uzbekistan*
[2]*National Institute of Nuclear Physics, South National Laboratories, via S.Sofia Catania, Italy*
[3]*Heavy Ion Laboratory, University of Warsaw, Warszawa, Poland*

Within the framework of the modified **R-matrix** approach, an analysis of the available experimental data on the astrophysical **S-factor** for the **$^{11}B(p,\gamma)^{12}C$** reaction was performed over the energy range **E ≤ 2.5 MeV**. One of the principal advantages of this approach is the direct use of the **ANC** to constrain the direct radiative-capture contribution. This significantly simplifies the fitting procedure and improves the reliability of the determination of the resonance parameters. Despite the existing **1.6-fold uncertainty** in the squared ANC for the ground state of **^{12}C**, the corresponding uncertainty in the total astrophysical S-factor at zero energy, **S(0),** does not exceed **5%**. The sum of the zero-energy astrophysical S-factors calculated for radiative capture to the ground state (0^+) and the first excited state at 4.44 MeV (2^+) yields a total astrophysical S-factor of S(0)=3.38±0.37 keVb

It was shown that both the uncertainty associated with the adopted ANC value and the contributions of proton capture to the **12.71 MeV (1^+)** state and the subthreshold **15.11 MeV (1^+)** state contribute less than **1%** to the total astrophysical S-factor.

As a result of the present analysis, revised and more accurately constrained values of the radiative widths, $\Gamma_{J_i}^{(\gamma 0)}$ and $\Gamma_{J_i}^{(\gamma 1)}$, were obtained for the **16.10 MeV (2^+), 16.57 MeV (2^-), 17.23 MeV (1^-),** and **19.20 MeV (1^-)** states. In addition, the total width Γ_{J_i} of the **16.10 MeV (2^+)** resonance was refined. The use of these revised parameters made it possible to reproduce accurately the observed resonance peak heights in the available experimental data.

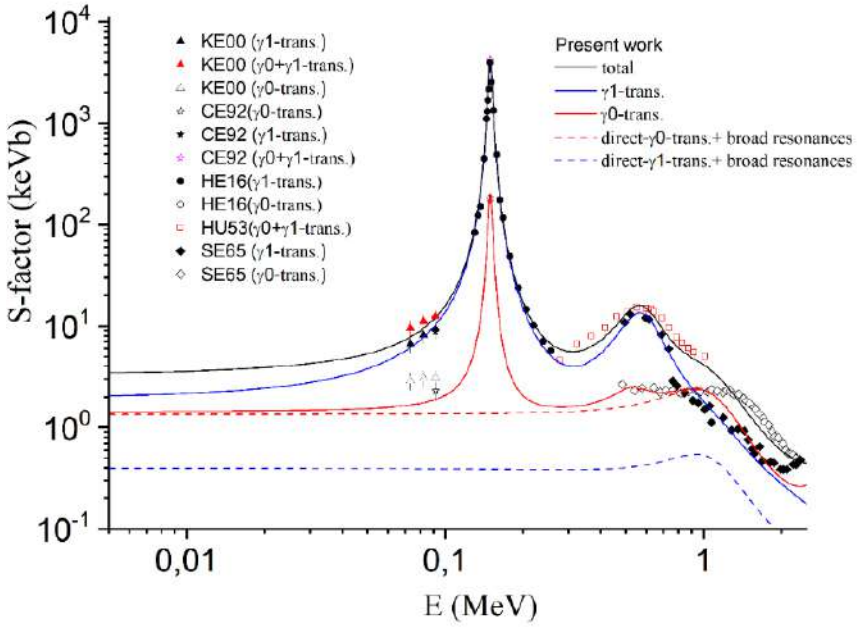

Figure 1. Astrophysical *S* - factors of γ_0-, γ_1- transitions and - total (γ_0 + γ_1) astrophysical S-factor in the $^{11}B(p,\gamma)^{12}C$ reaction.

Overall, a good description of the experimental data was achieved both within the resonance region and at non-resonant energies. The zero-energy astrophysical S-factor obtained in the present work is in excellent agreement with previously published values. However, the present model fails to reproduce the three experimental data points for radiative capture to the ground state reported in Ref. [1] in the energy region E_p < **100 keV**. Consequently, the corresponding experimental data for the total astrophysical S-factor from Ref. [1] are also described less satisfactorily. Resolving this discrepancy requires new high-precision experimental measurements aimed at determining more accurately the contribution of the **16.10 MeV (2^+)** resonance to radiative capture leading to the ground state.

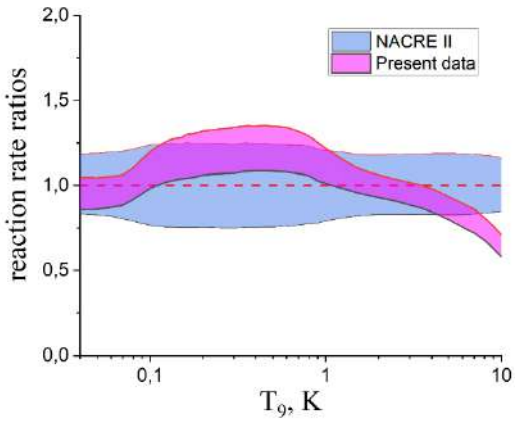

Figure 2. $^{11}B(p,\gamma)^{12}C$ reaction rates in units of the NACRE II (adopt) values.

The reaction rates calculated using the astrophysical S-factor obtained in the present work are in good agreement with the **NACRE II [6]** evaluation. The small discrepancy observed in the temperature region associated with the first resonance (E_r = **0.163 MeV**) is attributed to the fact that the line shape of this resonance, including both the resonance peak and its low- and high-energy tails, has not been constrained by available experimental data.

References:

1. J. H. Kelley, R.S. Canon, S.J. Gaff, R.M. Prior, B.J. Rice, E.C. Schreiber, M. Spraker, D.R. Tilley, E.A. Wulf, H.R. Weller, Phys. Pev. C 62 (2000) 025803
2. F.E. Cecil, et al., Nucl. Phys. A539 (1992) 75-96
3. J. J. He, B. L. Jia, S. W. Xu, S. Z. Chen, S. B. Ma, S. Q. Hou, J. Hu, L. Y. Zhang, and X. Q. Yu. Phys. Rev. C **93**, 055804 (2016); DOI: 10.1103/PhysRevC.93.055804
4. T. Huust and R.B., Phys. Rev 91 (1953) P. 599
5. R.E. Segel, S.S. Hanna, and R.G. Allas. Phys. Rev. **139**, B818 (1965)
6. Xu Y, Takashi K, Goriely S, Arnould M., M. Ohta H. Utsunomiya. Nuclear Physics A, Volume 918, p. 61 2013

THE ESTIMATION OF THE ASTROPHYSICAL $S_{17}(0)$-FACTOR OF THE $^{7}Be(p,\gamma)^{8}B$ DIRECT CAPTURE PROCESS WITHIN A THREE-BODY MODEL

Tursunov E.M.[1], Toshova D.S.[1], Turakulov S.A.[1,2]
[1]*Institute of Nuclear Physics, Uzbekistan Academy of Sciences, Tashkent, Uzbekistan*
[2]*Tashkent State Agrarian University, Tashkent, Uzbekistan*

The ground (2^+, 1) and first excited (1^+, 1) bound states of the mirror nuclei ^{8}B and ^{8}Li are studied within an α+^{3}He(^{3}H)+p(n) three-body potential cluster model, using the hyperspherical Lagrange-mesh method and realistic two-body α–N, α–^{3}He(^{3}H) and p(n)–^{3}He(^{3}H) interactions taken from the literature. The asymptotic normalization coefficients (ANCs) for the virtual decays ^{8}B→^{7}Be+p and ^{8}Li→^{7}Li+n are obtained self-consistently by matching the overlap integral of the three-body and two-body cluster wave functions to its Whittaker-function asymptotics. The three-body calculations reproduce the experimental ground-state (2^+) binding energies of ^{8}B and ^{8}Li (theoretical: −1.718 and −4.340 MeV, vs. experimental −1.724 and −4.499 MeV) without introducing any three-body force (Fig. 1). For the excited (1^+) states, a small 1.02 rescaling of the two-body potentials is needed to match the experimental values (−0.954 MeV for ^{8}B, −3.518 MeV for ^{8}Li). The convergence of these energies with respect to the maximal hypermomentum K_{max} is shown to saturate at K_{max} = 22 for the ground states, while the excited-state energies converge more slowly, requiring K_{max} =28 [1].

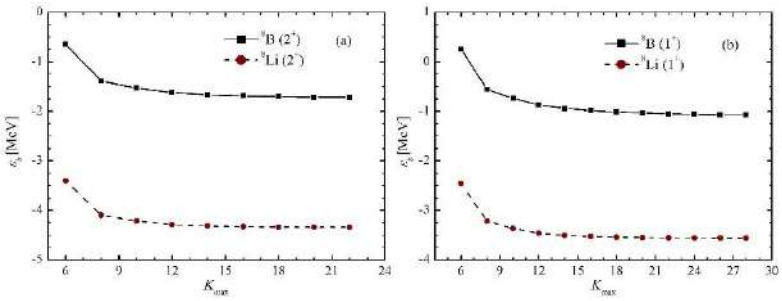

Figure 1. Convergence of the ground (2^+) (a) and firs exticed (1^+) (b) bound state energies of the ^{8}B, ^{8}Li nuclei with respect to K_{max}.

The root-mean-square matter radii, obtained from the three-body wave function together with experimental cluster charge radii, show smooth convergence with increasing K_{max} (Fig. 2). The calculated values are 2.76 fm for ^{8}B and 2.56 fm for ^{8}Li, which are in reasonable agreement with the experimental data of 2.58 ± 0.06 fm and 2.50 ± 0.06 fm, respectively [2].

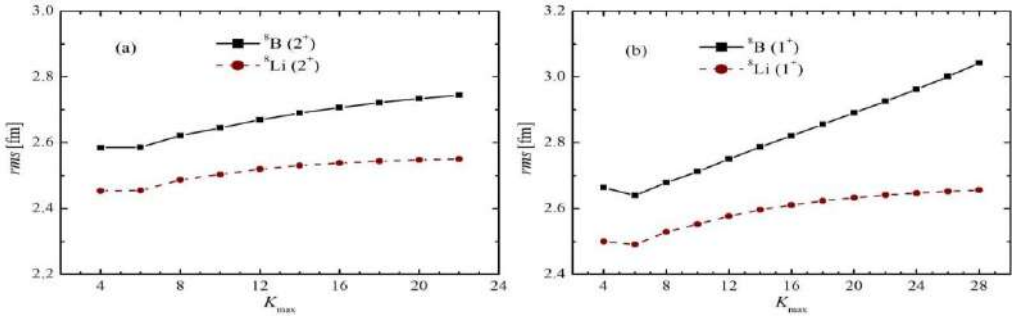

Figure 2. Convergence of the matter radii of the ^{8}B and ^{8}Li nuclei with respect to K_{max}

The α+^{3}He(^{3}H)+p(n) three-body cluster model, based on the hyperspherical Lagrange-mesh method and realistic two-body interactions, yields a consistent description of the structure of ^{8}B and

^{8}Li, with good convergence of binding energies (with K_{max} =22 for ground states, and K_{max} =28 for excited states) and matter radii. The ANCs were extracted self-consistently by matching the overlap integral of the three-body and two-body wave functions to its asymptotics expressed by the Whittaker function (Fig. 3). The obtained values are $\mathbf{C_{I=1}=0.211\ fm^{-1/2}}$ and $\mathbf{C_{I=2} = 0.739\ fm^{-1/2}}$ for the virtual decay $\mathbf{^{8}B \rightarrow {}^{7}Be + p}$, and $\mathbf{C_{I=1} =0.220\ fm^{-1/2}}$ and $\mathbf{C_{I=2} = 0.774\ fm^{-1/2}}$ for the mirror decay $\mathbf{^{8}Li \rightarrow {}^{7}Li + n}$. These numbers correspond to the squared ANC values $\mathbf{C^2(^{8}B) = 0.591\ fm^{-1}}$ and $\mathbf{C^2(^{8}Li) = 0.648\ fm^{-1}}$, yielding the ratio $\mathbf{C^2(^{8}B) / C^2(^{8}Li) = 0.912}$.

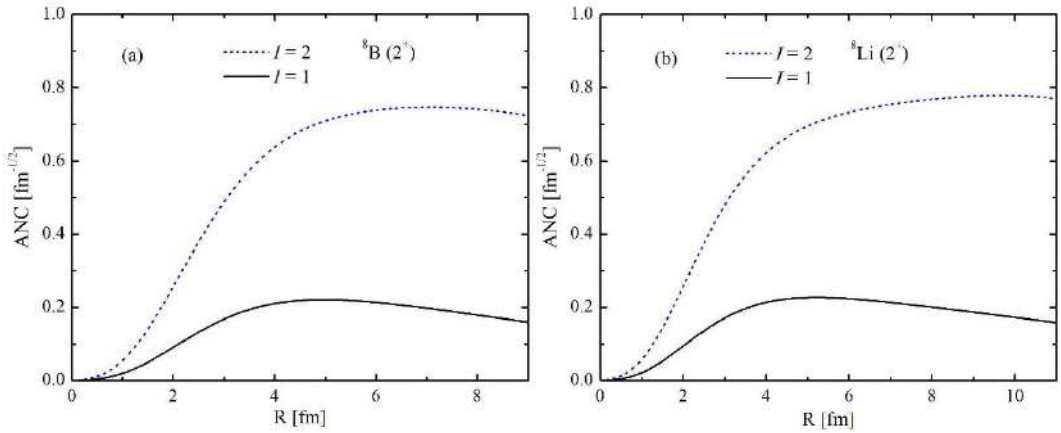

Figure 3. Calculated ANC values for the ground (2^{+}) states of the **^{8}B (a) and ^{8}Li (b) nuclei in dependence on the matching point of the overlap integral with its asymptotics.**

Based on above ANCs for the I=1 and I=2 spin channels, the zero-energy astrophysical factor for the ^{7}Be(p,γ)^{8}B reaction is found to be $S_{17}(0)$=22.492±0.014 eV·b, dominated by the spin-2 channel. This result is in good agreement with the Solar Fusion II [3] recommendation and with the value used in the successful BAR2M solar model [4], but overestimates recent Solar Fusion III recommended value [5]. This tension suggests that further experimental measurement of the ^{8}B solar neutrino flux is needed to resolve the discrepancy between the theory and current solar-fusion recommendations.

References:

1. L.V. Grigorenko, B.V. Danilin, V.D. Efros, N.B. Shul'gina, M.V. Zhukov, Phys. Rev. C 57, R2099 (1998)
2. D.R. Tilley, H.R. Weller, and G.M. Hale, Nucl.Phys. A 541, 1 (1992).
3. Solar Fusion II (E.G. Adelberger, et al.), Rev. Mod. Phys. 83, 195 (2011).
4. W. Yang and Z. Tian, The Astrophysical Journal, 970, 38 (2024).

Solar Fusion III (B. Acharya, et al.), Rev. Mod. Phys. 97, 035002 (2025).

NEW SPECTROSCOPIC INFORMATION FOR NUCLEOSYNTHESIS CALCULATIONS: ANCs OF ^{7}Li, ^{12}B, AND ^{12}C

Son I.Ya., Artemov S.V., Karakhodzhaev A., Tojiboev O.R., Ergashev F. Kh.
Institute of Nuclear Physics, Uzbekistan Academy of Sciences, Tashkent, Uzbekistan

Nucleosynthesis of the ^{12}C nucleus is one of the key processes in the evolution of the Universe, since it is with the formation of this nucleus that the carbon–nitrogen–oxygen (CNO) cycle of hydrogen burning in stars begins. The generally accepted scenario assumes that ^{12}C is produced in stellar nucleosynthesis via the triple-alpha process ($3\alpha \rightarrow ^{12}$C) through the Hoyle state [1] (E^{*}=7.654 MeV). However, in recent years, increasing attention has been paid to alternative mechanisms for the formation of ^{12}C, for example, through sequences of binary reactions involving stable and radioactive nuclei of lithium, beryllium, and boron [2], in particular via the ^{11}B$(p,\gamma)^{12}$C or ^{11}B$(n,\gamma)^{12}$B$(\beta^{-})^{12}$C reactions. These could significantly modify the existing understanding of primordial and stellar nucleosynthesis, especially at the early stages of stellar evolution and in environments with enhanced boron abundance.

A key challenge in calculating the reaction rates of these processes at stellar energies (tens to hundreds of keV) is the considerable uncertainty associated with extrapolating cross sections from the experimentally accessible energy range (MeV) down to astrophysical energies. Direct measurements at such low energies are extremely difficult due to the smallness of the cross sections and the effects of the Coulomb barrier. However, the spectroscopic characteristics of the single-particle states of the ^{12}C and ^{12}B nuclei, which are necessary for such calculations, remain ambiguous or partially unavailable to this day. The spread in literature values of spectroscopic factors for states in ^{12}C reaches 300% or more [3], making their use in astrophysical calculations unsatisfactory. In this context, the asymptotic normalization coefficient (ANC) method [4] plays a particularly important role, as it allows one to determine the contribution of direct radiative capture to the total reaction cross section. Within the ANC method, this contribution to the astrophysical S-factor of the radiative capture reaction A(p,γ)B at low energies is directly proportional to the square of the ANC for the B $\rightarrow$ p + A virtual decay, making accurate knowledge of the ANC critically important for reliable calculations. Unlike spectroscopic factors, ANC values depend significantly less on ambiguities in the model parameters of the binding potentials, which enables their successful use in calculating cross sections for deeply sub-barrier thermonuclear and nuclear astrophysical reactions.

In this work, we present new "experimental" values of the squared asymptotic normalization coefficients (ANCs) for the configurations ^{12}C $\rightarrow$ ^{11}B + p and ^{12}B $\rightarrow$ ^{11}B + n, obtained from the analysis of angular distributions of nucleon transfer reactions using the modified distorted-wave Born approximation (MDWBA). The analysis covers a set of reactions: ^{11}B$(^{3}$He,$d)^{12}$C (at incident energies of 22.3 and 32.5 MeV), ^{11}B$(d,n)^{12}$C, ^{11}B$(^{10}$B,^{9}Be$)^{12}$C (E_{10B}=41.3 MeV) for proton transfer, and ^{11}B$(d,p)^{12}$B (E_d =14.5 MeV) for neutron transfer. As a result of the performed analysis, the ANC values for the highly excited states of the ^{12}C nucleus at excitation energies of 10.84, 11.83, 13.35, and 14.08 MeV [5] have been determined for the first time. In addition, the values have been refined for the states involved in the ^{11}B$(p,\gamma)^{12}$C reaction, namely: the ground state (0^{+}), the first excited state (2^{+}), as well as the states at 9.64 MeV (3^{-}), 12.71 MeV (1^{+}), and 15.11 MeV (1^{+}). For the ^{12}B nucleus, the ANC values have been determined for the ground state (1^{+}) and the excited states at E^{*}=0.95 MeV (2^{+}), 1.67 MeV (2^{-}), 2.62 MeV (1^{-}), and 2.72 MeV (0^{+}).

Furthermore, this work presents new ANC values for the ^{7}Li nucleus [6], obtained from the analysis of the ^{7}Li$(d,^{3}$He$)^{6}$He reaction (at E_d = 14.5, 22, and 25 MeV) and the ^{7}Li$(d,t)^{6}$Li reaction (at E_d = 14.5 MeV).

The obtained "experimental" values of the squared ANCs can be directly used in *R*-matrix calculations to properly account for the contribution of direct radiative capture to the astrophysical *S*-factors of the ^{11}B(p,γ)^{12}C and ^{11}B(n,γ)^{12}B reactions. This makes it possible to significantly reduce the model dependence of the cross-section extrapolation into the stellar energy range and to enhance the accuracy of nucleosynthesis rate calculations.

References:

1. F.Hoyle. *Astrophys. J. Suppl. Ser. Sup* 1, 121 (1953).
2. T.Kajino. *Nucl. Phys. A* 588, 339 – 344 (1995) .
3. J.H.Kelley, J. E. Purcell and C. G. Sheu. *Nucl. Phys. A* 968 71 (2017).
4. A.M.Mukhamedzhanov and L. D. Blokhintsev *Eur. Phys. J. A* 58 29 (2022).
5. S.V.Artemov et al. *Ind. J. Phys.* 100 2479 (2026).
6. I.Ya.Son et al. *Phys. Scr.*, 100 (12) (2025).

STUDY OF THE ^{11}Be HALO NUCLEUS IN BREAKUP REACTIONS WITHIN A QUANTUM–QUASICLASSICAL APPROACH

Passiltay A., Valiolda D., Janseitov D., Melezhik V., Hamada Sh.
Al-Farabi Kazakh National University, Almaty, Kazakhstan

Exotic nuclei located far from the valley of stability often exhibit structural properties that differ significantly from those of stable nuclei. A characteristic example is the one-neutron halo nucleus ^{11}Be, which can be described to a good approximation as a ^{10}Be core and a weakly bound valence neutron. The neutron separation energy is about 0.5 MeV, and therefore the spatial distribution of the valence neutron extends far beyond the ^{10}Be core. This weak binding makes ^{11}Be especially sensitive to external Coulomb and nuclear fields and leads to a relatively high probability of breakup during collisions with target nuclei. For this reason, breakup reactions provide an effective tool for studying the structure of ^{11}Be, the properties of its bound and resonant states, and the reaction mechanisms characteristic of weakly bound nuclear systems.

In the present work, the breakup of ^{11}Be is investigated within a quantum–quasiclassical approach over a wide range of projectile energies from 5 to 70 MeV per nucleon. The projectile is treated as a two-body ^{10}Be+n system. The internal motion of the valence neutron is described quantum mechanically using the time-dependent Schrödinger equation, while the relative motion of the projectile and target nuclei is treated quasiclassically along a time-dependent trajectory. Such a description makes it possible to follow the quantum evolution of the weakly bound neutron during the collision without introducing a fully quantum-mechanical description of all degrees of freedom. The stationary neutron states are obtained by solving the Schrödinger equation for the ^{10}Be+n subsystem, while their evolution during the collision is calculated using a non-perturbative time-dependent method. A split-step propagation technique together with a discrete-variable representation is applied for the numerical evolution of the neutron wave function.

Two target nuclei with significantly different masses and charges are considered: ^{12}C and ^{208}Pb. The light ^{12}C target is useful for investigating breakup in which the nuclear interaction plays an important role, while the heavy ^{208}Pb target provides a strong Coulomb field and allows the Coulomb contribution to the breakup process to be studied. A comparison of these two systems makes it possible to understand how nuclear and Coulomb interactions influence the dissociation of the halo nucleus. The calculations are performed using both realistic projectile–target trajectories and the commonly used straight-line trajectory approximation. The comparison between these

descriptions becomes particularly important at low incident energies, where the projectile can be noticeably deflected by the target field.

The structure model of ^{11}Be includes the bound $1/2^+$ ground state and the low-lying $1/2^-$ excited bound state, as well as the $5/2^+$, $3/2^-$, and $3/2^+$ resonant states of the ^{10}Be+n continuum. The $5/2^+$ resonance appears at a relative energy of approximately 1.25 MeV, whereas the $3/2^-$ and $3/2^+$ resonances are located at approximately 2.79 and 3.37 MeV, respectively. These states are important for the analysis because the breakup process does not populate the continuum uniformly. Instead, the final neutron energy distribution contains structures associated with resonance formation and with the interaction between different transition pathways. The low-energy part of the breakup spectrum is also sensitive to the presence of the bound $1/2^-$ state. This indicates that breakup observables can provide information not only about continuum resonances but also about the bound-state structure of the halo nucleus.

For the ^{11}Be+^{12}C reaction, the influence of the projectile trajectory is found to be relatively small at intermediate and high incident energies. In the energy interval from approximately 10 to 67 MeV per nucleon, the difference between calculations using realistic and straight-line trajectories does not exceed about 2%. At the lower energy of 5 MeV per nucleon, however, the trajectory effect becomes more noticeable and reaches approximately 6–7% in the relative-energy interval from 0.3 to 1.1 MeV. The calculated breakup spectrum at this energy contains a pronounced structure near 1.25 MeV associated with the $5/2^+$ resonance, together with a broader enhancement in the low-energy region around 0.3 MeV. The latter is sensitive to the treatment of the $1/2^-$ bound state, demonstrating that a proper description of the low-lying structure of ^{11}Be is important for understanding the breakup mechanism.

For the heavy ^{208}Pb target, the effect of the realistic projectile trajectory becomes considerably stronger, particularly at low beam energy. At 5 MeV per nucleon, the difference between realistic-trajectory and straight-line calculations can exceed 20%. This behavior can be explained by the much stronger Coulomb deflection produced by the heavy target. Consequently, the straight-line approximation, which is often sufficiently accurate at high energies, may become inadequate for the description of low-energy collisions with heavy nuclei. As the projectile energy increases, the influence of trajectory curvature decreases and the results obtained with the two trajectory descriptions gradually become closer.

At higher energies, the calculated breakup observables for the ^{11}Be+^{12}C system are consistent with available experimental data, including measurements performed at 67 MeV per nucleon, as well as with previous non-perturbative time-dependent calculations. This agreement supports the applicability of the quantum–quasiclassical approach to the description of breakup reactions involving halo nuclei. At the same time, the low-energy calculations demonstrate that effects which may be neglected at intermediate and high energies, such as projectile deflection and the detailed contribution of low-lying bound and resonant states, become increasingly important when the collision energy decreases.

The obtained results show that the quantum–quasiclassical approach provides a useful framework for investigating the structure and reaction dynamics of weakly bound exotic nuclei over a broad range of collision energies. The method gives direct access to the time evolution of the halo neutron and makes it possible to investigate the relative roles of nuclear and Coulomb interactions, analyze the contribution of resonant states, and estimate the limits of commonly used trajectory approximations. The study of ^{11}Be breakup on light and heavy targets therefore provides valuable information about the structure of the one-neutron halo system and about the reaction mechanisms that should be taken into account in the analysis of low-energy collisions involving exotic nuclei.

INFLUENCEOF THE THREE-BODY COULOMB EFFECTS ON THE VALUES OF ASYMPTOTIC NORMALIZATION COEFFICIENTS FOR $^{12}C+p\rightarrow{}^{13}N$ AND ASTROPHYSICAL S FACTOR FOR THE $^{12}C(p,\gamma)^{13}N$ REACTION

Tursunmakhatov K.I.
Gulistan State University, Guliston, Uzbekistan

The differential cross sections (DCS) of the proton transfer reaction $^{12}C(^{7}Li,^{6}He)^{13}N$ were measured at the ^{7}Li energy of 44 MeV in Ref. [1] and 36 MeV in Ref. [2]. In the present work, the analysis of the experimental DCS of the $^{12}C(^{7}Li,^{6}He)^{13}N$ reaction from Refs. [1,2] have been performed within the framework of the Modified Distorted Wave Born Approximation (MDWBA) [3]. The results of calculations showed that this reaction is strongly peripheral. To determine the values of the asymptotic normalization coefficients (ANCs) for the $^{12}C+p\rightarrow{}^{13}N$ transition, the ANC value of 5.76±0.17 fm^{-1} for the $^{7}Li\rightarrow{}^{6}He+p$ transition recommended in Ref. [4], was used. The calculations of the single-particle transition differential cross sections were performed using the code LOLA [5]. New values of the ANC for the $^{12}C+p\rightarrow{}^{13}N$ configuration have been extracted from the experimental data in Refs. [1, 2] within MDWBA.

The contribution of the three-body Coulomb dynamics of the transfer mechanism to the partial wave amplitudes at $l \gg 1$ for the peripheral proton-transfer reaction $^{12}C(^{7}Li,^{6}He)^{13}N$ is estimated within the three-body approach combining the dispersion method and the DWBA approach [6]. For this reaction, the Coulomb renormalization factors are calculated, which arise as results of the correct description of the three-particle Coulomb dynamics of the proton transfer mechanism in the DWBA cross sections. New estimates are obtained for the values of the ANCs for the $^{12}C+p\rightarrow{}^{13}N$ configuration.

It is shown that the contribution of the three-body Coulomb dynamics of the proton-transfer mechanism [6] to the DWBA cross sections for the $^{12}C(^{7}Li,^{6}He)^{13}N$ reaction at energies 44 MeV and 36 MeV are verified as Δ = 4.8% and Δ = 4.7%, respectively. New estimates for the ANC values of the $p+^{12}C \rightarrow {}^{13}N$ transition have been obtained taking into account three body Coulomb effects.

The new value of the ANC recommended in this work was used to calculate the astrophysical S factor for the $^{12}C(p,\gamma)^{13}N$ reaction within the framework of modified R-matrix approach [7]. The χ^2 method was used for fitting to the experimental data from Ref. [8].

References:

1. Z. H. Li, J. Su, B. Guo, E. T. Li, Z. C. Li et al., Nucl. Phys. A 834, 661c (2010).
2. P. Schumacher, et al., Nucl. Phys. A 212, 573 (1973)
3. A.M.Mukhamedzhanov et al., Phys. Rev. C **56**, 3(1997)
4. K.I. Tursunmakhatov, et al., Int. J. Mod. Phys. E 32, 2350035 (2023)
5. R.M. Devries, Phys, Rev. C 8, 951 (1973)
6. Sh. S. Kajumov, A. M. Mukhamedzhanov, et al., Z. Phys. A336, 297 (1990).
7. K.I. Tursunmakhatov, S.B. Igamov, Mod. Phys. Lett. A 41, 2650099 (2026)

J. Skowronski, et al., Phys. Rev. C 107, L062801 (2023)

R-MATRIX ANALYSIS OF ^{22}NE STATES POPULATED IN ^{18}O(α,α) RESONANT ELASTIC SCATTERING

Serikbayeva G. E.[1], Nurmukhanbetova A.K.[2,3,4], Goldberg V.Z.[5], Nauruzbayev D.K.[2,4]

[1]*Department of Physics, School of Sciences and Humanities, Nazarbayev University, Astana, Kazakhstan*

[2]*Nazarbayev University Research Administration, Nazarbayev University, Astana, Kazakhstan*

[3]*Energetic Cosmos Laboratory, Nazarbayev University, Astana, Kazakhstan*

[4]*School of Intelligent Systems, Astana IT University, Astana, Kazakhstan*

[5]*Cyclotron Institute, Texas A&M University, College Station, Texas, USA*

Resonances in the ^{18}O + α interaction play an important role in the analysis of astrophysical processes and in understanding the evolution of α-cluster structures with the addition of neutrons to 4N nuclei. Although high-energy-resolution measurements of this system were previously reported, they have not been analyzed using R-matrix formalism.

In this work, we performed an R-matrix analysis of the resonant scattering data obtained in Ref. [1] and determined resonance parameters for 15 excited levels of ^{22}Ne in the excitation energy region of 11.7–12.5 MeV [2]. Unlike the neighboring nuclei ^{20}Ne, ^{21}Ne, and ^{19}F, no low-spin resonances with large α-particle reduced widths were identified in the investigated excitation region of ^{22}Ne. This behavior suggests that existing model calculations do not fully reproduce the observed trends in α-clustering for the ^{20}Ne-^{22}Ne isotopic chain.

Further measurements over a broader excitation energy range, together with analysis of higher-spin α-cluster states, are expected to provide additional insight into the development of α clustering in this region. This study represents the first step in a broader investigation of the ^{22}Ne level structure through resonant reaction analysis [2].

This research was funded by the Science Committee of the Ministry of Science and Higher Education of the Republic of Kazakhstan (Grant No. AP23489860).

References:

1. D. Powers, J. K. Bair, J. L. C. Ford, Jr., and H. B. Willard, "Elastic Scattering of Alpha Particles by ^{18}O", Phys. Rev. 134, B1237 (1964).
2. A.K. Nurmukhanbetova, V. Z. Goldberg, A. Volya, D. K. Nauruzbayev, G. E. Serikbayeva, and G. V. Rogachev, "R-matrix analysis of ^{22}Ne states populated in ^{18}Of_0(α,α) resonant elastic scattering," Phys. Rev. C 109, 024607 (2024).

ELASTIC AND INELASTIC SCATTERING OF α PARTICLES ON ^{25}Mg AT E_α = 29 MeV

Artemov S.V.[1], Tojiboev O.R.[1], Burtebayev N.[2], Nasurlla Maulen[2,3], Zholdybayev T.K.[2], Ikromkhonov E.Sh.[1], Ergashev F.Kh.[1], Karakhodzhaev A.A.[1], Igamov S.B.[1]

[1]*Institute of Nuclear Physics, Uzbekistan Academy of Sciences, Tashkent, Uzbekistan*

[2]*Institute of Nuclear Physics, Almaty, Kazakhstan*

[3]*Al-Farabi Kazakh National University, Almaty, Kazakhstan*

Various reaction channels may occur during the interaction of light particles with atomic nuclei, as governed by the conservation laws of energy and momentum. Each reaction channel corresponds to a specific final state of the system and leads to the formation of particular reaction products. In the interaction of α particles with the ^{25}Mg nucleus, the elastic scattering reaction ^{25}Mg(α,α)^{25}Mg and the inelastic scattering reaction ^{25}Mg(α,α′)^{25}Mg, accompanied by the excitation of nuclear energy levels, can take place. The investigation of these reaction channels provides important information on the nuclear structure of ^{25}Mg and the interaction mechanisms of α particles with medium-mass nuclei.

The differential cross sections (DCSs) for elastic and inelastic scattering of the α particles were measured at the external beam of the U-150M isochronous cyclotron at the Institute of Nuclear Physics, Republic of Kazakhstan (Almaty, Kazakhstan), using an α-particle beam with an energy of E_α=29 MeV (Fig. 1a). The reaction products were detected and identified using the well-established ΔE–E technique based on silicon semiconductor detector telescopes. The reaction chamber (Fig. 1b) was equipped with three remotely controlled detector-positioning systems, an automatic target-changing mechanism for solid targets, and the necessary auxiliary infrastructure for carrying out the measurements.

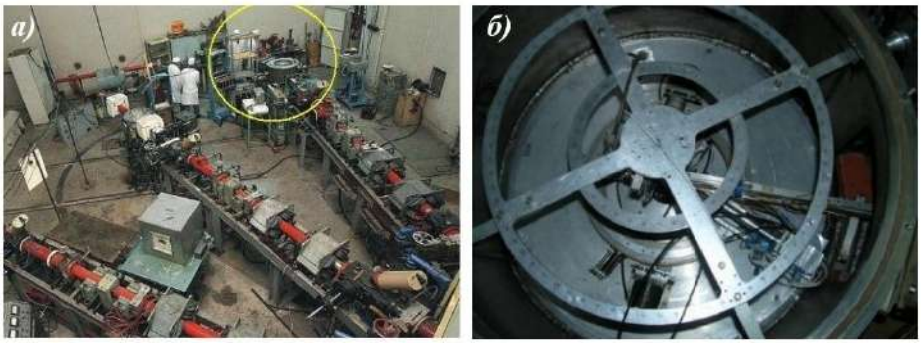

Figure 1. General view of the U-150M cyclotron experimental hall (a) and the reaction chamber equipped with the detector telescope positioning system (b).

The magnesium targets were prepared from metallic foils enriched to 97% in ^{25}Mg and manufactured at Oak Ridge National Laboratory (USA). The target thickness was 0.78 mg/cm². The experimental energy spectra were analyzed and the differential cross sections in the laboratory reference frame were extracted using the EDE_TOOLS software package, which provides comprehensive tools for spectrum analysis and data processing.

Analysis of the measured spectra yielded the angular distributions of the experimental DCSs for elastic and inelastic α-particle scattering on ^{25}Mg corresponding to the population of the ground state (E^*=0.0 MeV) and the excited states at E^*=1.61, 2.56, 3.41, and 3.91 MeV of the ^{25}Mg nucleus. The elastic-scattering differential cross sections were analyzed within the framework of the optical model by comparing the calculated and experimental angular distributions. Several global optical-

model potentials reported in the literature were tested, and those providing the best agreement with the experimental data were selected.

Figure 2 shows the experimental angular distribution of the differential cross section for elastic α + ^{25}Mg scattering at E_α=29 MeV together with the optical-model calculations.

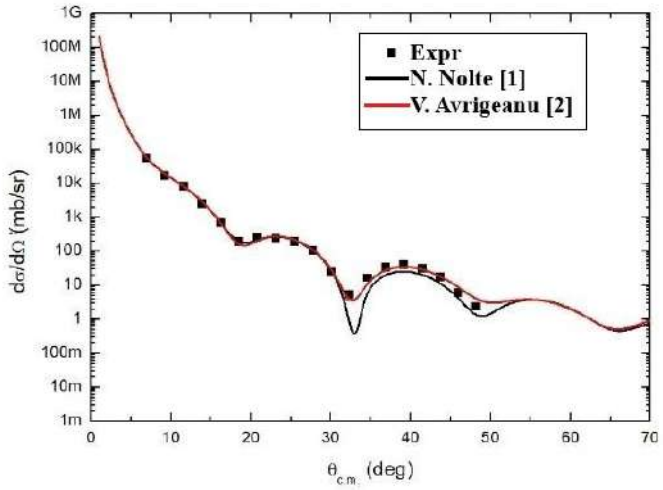

Figure 2. Experimental angular distribution of the differential cross section for elastic α+^{25}Mg scattering at E_α=29 MeV compared with optical-model calculations.

Overall, the calculated angular distributions are in good agreement with the experimental data. Among the considered optical-model parameter sets, the Avrigeanu potential [2] provides the best description of the experimental angular distribution over the entire measured angular range.

References:

1. M.Nolte, H.Machner, and J.Bojowald, Phys. Rev. C 36 (1987) 1312.
2. V.Avrigeanu, M.Avrigeanu, and P.E.Hodgson, Phys. Rev. C 49 (1994) 2136.

STUDY OF THE DECAY OF HIGH-SPIN ISOMERS OF HOLMIUM NUCLEI WITH A=156,158,160

Kalinnikov V.G., Stegailov V.I., Rozov S.V., Gons Z., Khushvaktov J.Kh., Kobets V.V., Solnyshkin A.A., Kartavenko V.G., Tyutyunnikov S.I., Shakun N.G.
Joint Institute for Nuclear Research, Dubna, Russian Federation

The report presents the experimental results of the study of the craspad of high-spin isomers of odd-odd holmium nuclei.

The research was carried out at the basic facilities of JINR: the DLNP Phasotron and the VBLHEP JINR Nuclotron. As a result of many years of research /1-8 / there were the decay schemes of ^{160,158,156} Ho were studied [1]. In holmium nuclei, the lifetimes of excited states were measured [2], the decay was studied, and the half-lives of high-spin isomers were measured [3]. On the basis of our [1,4] experimental data and on the basis of our calculations [5] made within the framework of quasi-partially, the phonon model (C.F.M.), the structure of low-lying states of odd-odd holmium nuclei of the transition region was established and the essence of the so-called

holonium was explained F- forbidden transitions. On the basis of our [1,4] experimental data and on the basis of our calculations [5] made within the framework of quasi-partially, the phonon model (C.F.M.), the structure of low-lying states of odd-odd holmium nuclei of the transition region was established and the essence of the so-called holonium was explained F-forbidden transitions. However, some facts reflecting the decay of holmium nuclei are not recognized, such as the decay of high-spin isomers into levels of daughter nuclei of dysprosium are insufficiently studied. The paper discusses the observed gamma transitions between the high-spin states of the rotational bands of the ground state of dysprosium daughter nuclei belonging to the decay of minute high-spin holmium isomers. Fig.1 shows the decay of a gamma transition of 857.6 keV and a period of five minutes in the core of ^{160}Dy, charging state (6+), the ground state band. We see similar five-minute decays up to the levels of the spin band (9+). Figure 3 shows the gamma spectrum of gamma lines coinciding with the "triplet" of lines in the nucleus of ^{160}Dy in the region of (297-298) keV obtained by irradiation of the ^{165}Ho targeat a 660 MeV proton beam.

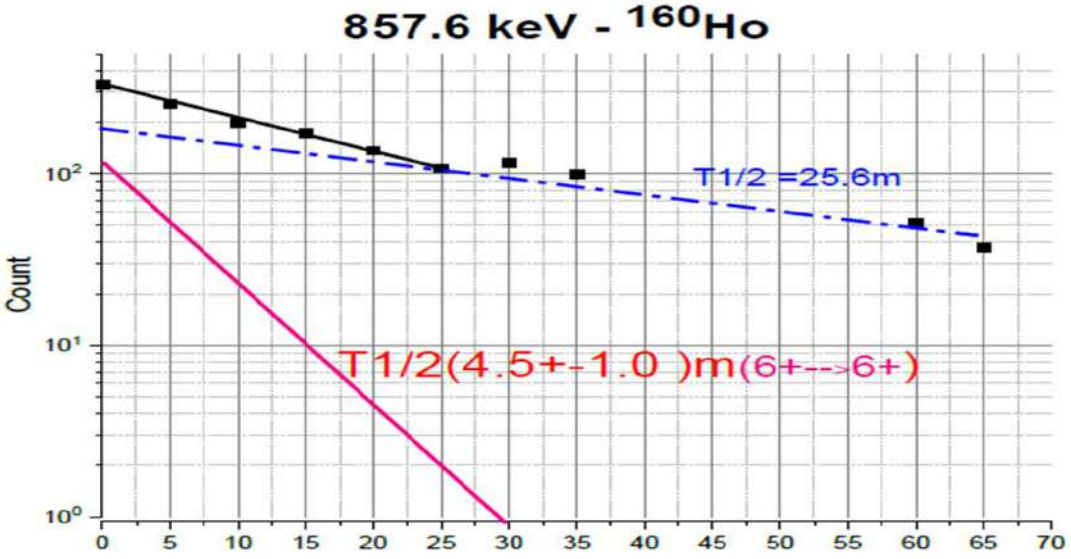

Figure1.

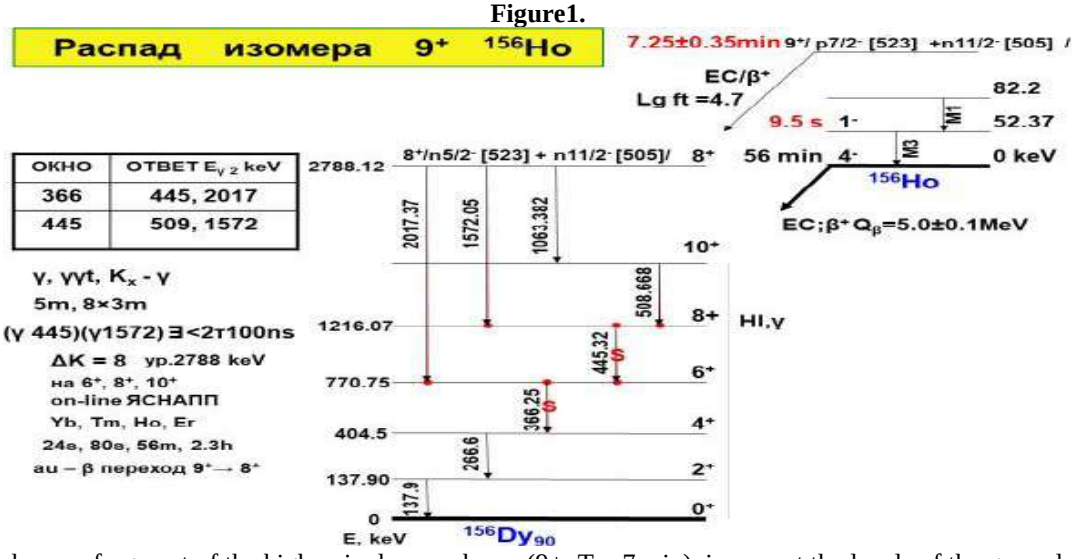

ОКНО	ОТВЕТ E_{γ} keV
366	445, 2017
445	509, 1572

γ, γγt, K_x - γ
5m, 8×3m
(γ 445)(γ1572) ∃<2τ100ns
ΔK = 8 γр.2788 keV
на 6+, 8+, 10+
on-line ЯСНАПП
Yb, Tm, Ho, Er
24s, 80s, 56m, 2.3h
au – β переход 9+→ 8+

Figure 2 shows a fragment of the high-spin decay scheme (9+, T = 7 min) isomer at the levels of the ground state band of the nucleus ^{156}Dy.

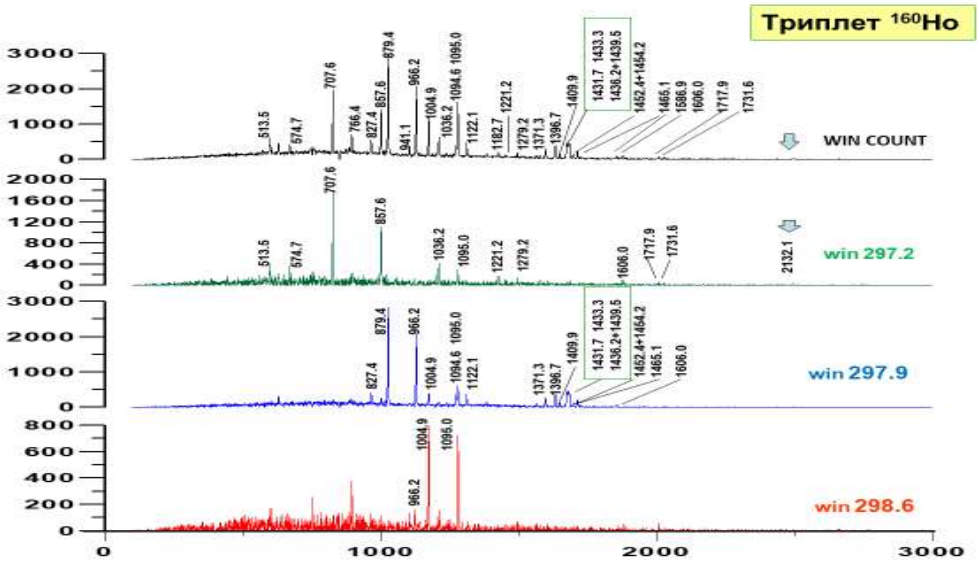

Figure 3 Gamma spectra coincidences with triplets in the (297.2, 297.9, 298.6) kev.

A similar pattern of minute change in the intensity of gamma transitions from time to spins (9+) is observed for gamma vibration and octupole-vibration bands in dysprosium nuclei during beta decay of ^{156,158,160}Ho nuclei into the levels of these bands.

References:

1. V.G.Kalinnikov, V.I.Stegailov, et al.//Thes.dokl. on nuclear physics. (Sarov, 2006), pp. 82-83.
2. V.G.Kalinnikov et al.//Thesis. dokl. on yad.phys. (St.-Petersburg, 2005), p.58.
3. V.I.Stegailov et al.//Theses. Doc. Mezhd.Conf. on Nuclear Physics. (St.-Petersburg,) p.72.
4. V.G. Kalinnikov and others. Thesis of the Inter. Conf. on nuclear physics. (Riga, 1987), p. 119.
5. A.V.Sushkov et al.//Thesis docl.mezhd.conf. on nuclear physics. (St.-Petersburg), p.59.
6. I. Adam et al. Izv. RAS, ser.phys.// vol.66, No.10 (2002), p.1384.
7. V.V. Pashkevich et al.// JINR Preprint, 4-83-535, Dubna, 1983.

V.G. Kalinnikov et al.//Thesis dokl.mezhd.conf. by yad.phys. (Cheboksary, 2009), see sb.

BETA DECAY HALF-LIFE OF ^{41}Sc

Irgaziev B.F., Khasanov J.A.
National University of Uzbekistan, Tashkent, Uzbekistan

The formula for calculating the half-life of beta decay using Fermi's Golden Rule, can be written in the following form:

$$T_{1/2} = \frac{k}{f_0 \left|\langle \varphi_f | \varphi_i \rangle\right|^2 (B_F + B_{GT})}, \quad (1)$$

where $k = \frac{2\pi^3 \hbar^7 \ln 2}{m_e c^4 G_V^2} = 6289\ s$. [1], f_0 is a phase-space function [2], B_F and B_{GT} are Fermi and Gamow-Teller reduced probabilities

$$B_F = g_V^2 = 1, \quad B_{GT} = q^2 g_A^2 \frac{3}{2j+1} M_{GT}^2, \quad (2)$$

and $\langle\varphi_f|\varphi_i\rangle$ is the overlap integral of the valence nucleon wave functions [3], [4], q is quenching coefficient, g_V is vector coupling constant, g_A is axial-vector coupling constant, M_{GT} is Gamow-Teller matrix element. We offer a simple empirical formula to calculate the quenching factor q:

$$q = q_\infty[1 + 0.32747\exp(-0.363\,A)]\,. \quad (3)$$

The overlap integral in Eq. (1) allows us to account for the modifications in Fermi and Gamow-Teller transitions caused by the proton-neutron mass difference and the Coulomb interaction between the proton and the core. If we don't account for any deformation and treat ^{41}Sc as a spherical nucleus, its theoretical and experimental half-lives are given in Table 1.

In the study of the β^+/EC process, we treated the exceedingly light electron neutrino as massless, which enables numerical estimations of the Fermi integral for the phase-space factor.

Table 1. Comparison of result by spherical case with experimental data.

	Our result	Experimental data [5]
$T_{1/2}$	500.02 ±0.64 ms	596.3±1.7 ms

However, according to Ref. [6], ^{41}Sc possesses an electric quadrupole moment, which in turn implies that it is not spherical but rather oblate ellipsoidal in shape. The corrections introduced to the nuclear and the Coulomb potentials based on this concept could explain the discrepancy between the theoretical results and the experimental data shown in Table 1.

The effect of nuclear-core deformation on the β^+/electron-capture decay of ^{41}Sc to ^{41}Ca is investigated within a single-particle model. The parent and daughter nuclei are described as a valence proton and a valence neutron, respectively, coupled to a ^{40}Ca core. The deformation is interpreted as the quadrupole polarization of the core induced by the valence nucleon. The proton and neutron wave functions are obtained by solving the coupled radial Schrödinger equations with a quadrupole-deformed Woods–Saxon potential. For the proton state, the Coulomb interaction of a deformed charge distribution is also included. The nuclear surface is parametrized as

$$R(\theta) = R_0\big(1 + \beta_2 Y_{20}(\theta)\big), \#(4)$$

where β_2 is the quadrupole-deformation parameter. Calculations are performed for the spherical limit and for different oblate and prolate deformations. Core deformation mixes the spherical components of the dominant $1f_{7/2}$ configuration and changes the radial overlap between the initial proton and the final neutron wave functions. Consequently, the Fermi and Gamow–Teller transition strengths, $B(F)$ and $B(GT)$, become deformation dependent. The corresponding (ft) value and beta-decay half-life are evaluated as functions of β_2. A comparison with the spherical calculation makes it possible to determine the contribution of core deformation to the beta-decay characteristics of ^{41}Sc.

References:

1. Particle Data Group and C. Patrignani and K. Agashe and G. Aielli and C. Amsler and M. Antonelli and Asner, D.M. and H. Baer and Sw Banerjee and Barnett, R. M. and T. Basaglia and Bauer, C.W. and Beatty, J.J. and Belousov, V.I. and J.Beri, «Review of particle physics,» *Chinese Physics C,* 2016.
2. P.Venkataramaiah and K. Gopala and A. Basavaraju and S. S. Suryanarayana and H. Sanjeeviah, «A simple relation for the Fermi function,» *Journal of Physics G: Nuclear Physics*, pp. 359-364, 1985.
3. B. F.Irgaziev and Jameel-Un Nabi and Abdul Kabir, «Analysis of β+ decay of 13N nucleus using a modified one-particle approach,» *Canadian Journal of Physics,* т. 99, pp. 176-184, 2021.
4. B.F.Irgaziev, Abdul Kabir, Jamel-Un Nabi, «Application of ANCs for calculation of β+ decay of 17F nucleus,» *Nuclear Physics A,* т. 1021, 2022.

5. C.D. Nesaraja, E.A. McCutchan, «Nuclear Data Sheets for A = 41,» *Nuclear Data Sheets,* т. 133, pp. 1-220, 2016.
6. T.Minamisono, K. Matsuta, K. Minamisono, et al., «“Quadrupole Moments of the 40Ca Core Plus One Nucleon Nuclei 41Sc and 41Ca,» *Zeitschrift für Naturforschung A,* т. 57, pp. 595-598, 2002.

FROM ORTHOGONALIZING PSEUDOPOTENTIAL TO THE FESHBACH–SCHUR PROJECTION

Nishonov M.M.
National University of Uzbekistan, Tashkent, Uzbekistan

The Pauli exclusion principle imposes an important structural constraint in cluster descriptions of light nuclei and is commonly taken into account using the Orthogonalizing Pseudopotential (OPP) approach. It is shown that the OPP may be interpreted as the singular $\lambda_0 \to \infty$ limit of the Feshbach–Schur projection, and that the Schur complement provides a natural operator-level framework for understanding this connection. In contrast to earlier approaches, the elimination is derived explicitly as a closed Schur-complement operator identity. When formulated in terms of operators and Green’s functions, the Feshbach–Schur projection eliminates Pauli-forbidden components algebraically and avoids the explicit introduction of large pseudopotential parameters. This reformulation clarifies the implementation of Pauli projection in cluster models and provides a convenient framework for few-body calculations.

Below we demonstrate explicitly how the OPP method may be interpreted as a singular $\lambda_0 \to \infty$ regularization of the Feshbach–Schur projection for a separable T–matrix. To this end, a two–body interaction is considered in the general separable form

$$V = \sum_{i,j=1}^{N_a} |\chi_i\rangle \ \lambda_{ij} \ \langle\chi_j| \,, \tag{1.1}$$

where $\{\chi_i\}$ are N_a linearly independent Pauli–allowed form factors and $\boldsymbol{\lambda}$ is an $N_a \times N_a$ coupling matrix.

The corresponding separable T–matrix for a general separable interaction (1.1) is

$$T(z) = \sum_{i,j} |\chi_i\rangle \ \tau_{ij}(z) \ \langle\chi_j| \,, \quad \text{with} \quad \boldsymbol{\tau}(z) = \left[\boldsymbol{\lambda}^{-1} - \boldsymbol{D}(z)\right]^{-1}, \tag{1.2}$$

and the form–factor propagators

$$D_{ij}(z) = \langle\chi_i| \, G_0(z) \, |\chi_j\rangle \,,$$

where $G_0(z) = (z - H_0)^{-1}$ is the free Green's function.

The orthogonalizing pseudopotential adds a repulsive separable term

$$V_{\mathrm{OPP}} = \lambda_0 \sum_{f=1}^{N_f} |\phi_f\rangle \, \langle\phi_f|$$

where λ_0 is the OPP strength parameter, with f labeling the Pauli–forbidden functions. The combined interaction is therefore

$$\widetilde{V} = V + V_{\mathrm{OPP}} = \sum_{i,j} |\chi_i\rangle \, \lambda_{ij} \, \langle\chi_j| + \lambda_0 \sum_{f} |\phi_f\rangle \, \langle\phi_f| \,.$$

The implementation of the Pauli exclusion principle is most transparent when the Hilbert space is decomposed explicitly into Pauli–allowed and Pauli–forbidden sectors. We therefore introduce the orthogonal decomposition

$$\mathcal{H} = \mathcal{H}_a \oplus \mathcal{H}_f,$$

where $\mathcal{H}_f$ is spanned by Pauli–forbidden states and $\mathcal{H}_a$ contains all Pauli–allowed states. This decomposition is not an approximation but an exact rewriting of the Hilbert space. It reflects the physical requirement that the total wave function must remain orthogonal to $\mathcal{H}_f$ at all energies, including in intermediate virtual processes.

To treat V and V_{OPP} on the same footing, the extended separable form-factor basis is introduced,

$$\boldsymbol{g} \equiv \{\chi_1, \ldots, \chi_{N_a}, \phi_1, \ldots, \phi_{N_f}\}.$$

The Pauli principle enters through the structure of the form factors $|g_i\rangle$, where the set $\{g_i\}$ is decomposed into Pauli–allowed (a) and Pauli–forbidden (f) components,

$$|g_i\rangle = \begin{cases} |\chi_a\rangle\,, & i \in \mathcal{H}_a, \\ |\phi_f\rangle\,, & i \in \mathcal{H}_f. \end{cases} \tag{1.3}$$

in which the total coupling matrix becomes block diagonal:

$$\widetilde{\boldsymbol{\lambda}} = \begin{pmatrix} \boldsymbol{\lambda} & 0 \\ 0 & \lambda_0 1_{N_f} \end{pmatrix}. \tag{1.4}$$

Including OPP, the separable T–matrix in Eq. (1.2) in the extended basis (1.3) with Eq. (1.4) becomes

$$T(z) = \sum_{\alpha,\beta} |g_\alpha\rangle\, \widetilde{\tau}_{\alpha\beta}(z)\, \langle g_\beta| \quad \text{with} \quad \widetilde{\boldsymbol{\tau}}(z) = \left[\widetilde{\boldsymbol{\lambda}}^{-1} - \widetilde{\mathcal{D}}(z)\right]^{-1}. \tag{1.5}$$

The corresponding matrix of form–factor propagator is

$$\widetilde{\mathcal{D}}_{\alpha\beta}(z) = \langle g_\alpha|\, G_0(z)\, |g_\beta\rangle\,.$$

Explicitly,

$$\left[\mathcal{D}_{aa}(z)\right]_{ij} = \langle \chi_i|\, G_0(z)\, |\chi_j\rangle\,, \quad \left[\mathcal{D}_{ff}(z)\right]_{fg} = \langle \phi_f|\, G_0(z)\, |\phi_g\rangle\,,$$

$$\left[\mathcal{D}_{af}(z)\right]_{if} = \langle \chi_i|\, G_0(z)\, |\phi_f\rangle\,, \quad \left[\mathcal{D}_{fa}(z)\right]_{fj} = \langle \phi_f|\, G_0(z)\, |\chi_j\rangle\,.$$

Thus the full $\widetilde{\mathcal{D}}(z)$ in the combined basis is

$$\widetilde{\mathcal{D}}(z) = \begin{pmatrix} \mathcal{D}_{aa}(z) & \mathcal{D}_{af}(z) \\ \mathcal{D}_{fa}(z) & \mathcal{D}_{ff}(z) \end{pmatrix}. \tag{1.6}$$

Because $\widetilde{\boldsymbol{\lambda}}$ in Eq. (1.4) is block diagonal, its inverse for finite λ_0 is

$$\widetilde{\boldsymbol{\lambda}}^{-1} = \begin{pmatrix} \boldsymbol{\lambda}^{-1} & 0 \\ 0 & \lambda_0^{-1} 1_{N_f} \end{pmatrix}. \tag{1.7}$$

The reduced propagator $\widetilde{\boldsymbol{\tau}}(z)$ in Eq. (1.5) with Eqs. (1.6) and (1.7) has the block structure

$$\left[\widetilde{\boldsymbol{\tau}}(z)\right]^{-1} = \begin{pmatrix} \boldsymbol{\lambda}^{-1} - \mathcal{D}_{aa}(z) & -\mathcal{D}_{af}(z) \\ -\mathcal{D}_{fa}(z) & \lambda_0^{-1} 1_{N_f} - \mathcal{D}_{ff}(z) \end{pmatrix}. \tag{1.8}$$

Applying the Schur–complement formula for a matrix,

$$M = \begin{pmatrix} A & B \\ C & D \end{pmatrix}, \qquad M_{aa}^{-1} = (A - B\, D^{-1}\, C)^{-1},$$

to the a–sector for finite λ_0 yields the effective reduced τ–matrix

$$\boldsymbol{\tau}^{(\lambda_0)}(z) = \left[\boldsymbol{\lambda}^{-1} - \mathcal{D}_{aa}(z) - \mathcal{D}_{af}(z)\left(\lambda_0^{-1} 1_{N_f} - \mathcal{D}_{ff}(z)\right)^{-1} \mathcal{D}_{fa}(z)\right]^{-1}. \tag{1.9}$$

Equation (1.9) represents the Pauli–allowed scattering operator for finite OPP strength. The fully projected Feshbach–Schur result is recovered only in the singular limit $\lambda_0 \to \infty$, yielding the effective τ–matrix in the Pauli–allowed (a) sector:

$$\boldsymbol{\tau}^{(\mathrm{eff})}(z) = \left[\boldsymbol{\lambda}^{-1} - \mathcal{D}_{aa}(z) + \mathcal{D}_{af}(z)\,\mathcal{D}_{ff}^{-1}(z)\,\mathcal{D}_{fa}(z)\right]^{-1}. \quad (1.10)$$

The expression (1.10) contains no reference to λ_0: the OPP strength has been eliminated analytically. The OPP term has been replaced by the exact Schur–complement subtraction

$$\Delta\mathcal{D}(z) = \mathcal{D}_{af}(z)\,\mathcal{D}_{ff}^{-1}(z)\,\mathcal{D}_{fa}(z),$$

which removes the propagation through Pauli–forbidden components at the operator level. The resulting expression (1.10) corresponds to the Feshbach–Schur projection (FSP), which projects the dynamics onto the Pauli–allowed subspace.

STUDY OF THE ^{11}C AND ^{11}B NUCLEAR STRUCTURES WITHIN THE THREE - CLUSTER MODELS $\alpha + \alpha + {}^3He$ AND $\alpha + \alpha + {}^3H$

Tursunov E.M., Khurramova S.N.
Institute of Nuclear Physics, Uzbekistan Academy of Sciences, Tashkent, Uzbekistan

In this work, the structure of the ^{11}C and ^{11}B nuclei was theoretically investigated within the framework of the three-cluster models α+α+^{3}He and α+α+^{3}H, respectively. The calculations were performed using a high - precision variational method based on a Gaussian basis. Realistic two-body interaction potentials were employed to describe the interactions between the clusters. The Orthogonalizing Pseudopotential (OPP) method was applied to remove the Pauli-forbidden states from the functional space of the three-body wave function [1]. The investigation of the cluster structure of ^{11}C and ^{11}B nuclei provides an opportunity to describe their ground and excited state energy spectra, electromagnetic properties, and spatial distributions of clusters [1,3]. In the present study, the energy spectra of these nuclei are studied within the α+α+^{3}He and α+α+^{3}H three-cluster models. The Hamiltonian of the three-cluster system can be written as:

$$\hat{H} = \hat{H}_0 + \hat{V}_{\alpha_1\alpha_2} + \hat{V}_{\alpha_1 c} + \hat{V}_{\alpha_2 c} + V_{3b}, \quad (1)$$

where c = ^{3}He or ^{3}H, and V_{3b} represents the three-body potential. To eliminate the Pauli-forbidden states from the functional space, the OPP method was used [1]. The corresponding pseudopotential reads

$$\hat{V}_i(r) = V_i(r) + V_C(r) + \sum_f \lambda_f\,\hat{\Gamma}_i^{(f)}, \quad (2)$$

where λ_f is the strength parameter of the projection operator. At sufficiently large values of λ_f, the solutions of the Schrödinger equation become free from the Pauli-forbidden components [1]. For the α+α subsystem, a realistic interaction potential BWF [1] was used. For α+^{3}He interaction we use a deep potential of Dubovichenko [3]. The three-body potential was chosen in the Gaussian form:

$$V_{3b}(\rho) = V_0 \exp(-\alpha\rho^2), \quad (3)$$

where α is a parameter that determines the range of the potential, and its value is usually chosen within the interval 0.01 – 0.1 fm^{-2}. In the present calculations, the value α = 0.1 fm^{-2} is adopted. The parameter ρ represents the hyperradius [4], which characterizes the geometrical size of the three-particle system and is defined through the Jacobi coordinates.

Table 1. The λ-dependence of the energy spectrum of the ^{11}C nucleus in the $3/2^-$ state within the OPP method.

λ (MeV) (^{11}C)	0	100	1000	10^4	10^5	10^6	10^7	10^8	$2*10^8$	$4*10^8$	V_0=-43 MeV α=0.1 fm^{-2}
E_1 (MeV)	-147.8	-16.4	-13.46	-12.74	-11.11	-9.96	-9.13	-8.66	-8.571	-8.489	-9.139
E_2 (MeV)	-107.1	-14.9	-11.74	-0.694	-0.146	-0.03	0.076	0.136	0.148	0.1597	0.089
E_3 (MeV)	-91.92	-14.3	-11.02	0.667	0.681	0.692	0.695	0.697	0.6989	0.7003	0.7003
E_4 (MeV)	-88.75	-2.31	-0.45	1.368	18.465	2.026	2.085	2.115	2.124	2.133	2.1292
Primes	0	1.086	0.198	0.565	0.635	0.415	0.286	0.141	0.1216	0.1151	0.1152

Table 2. The λ-dependence of the energy spectrum of the ^{11}B nucleus in the $3/2^-$ state within the OPP method

λ (MeV) (^{11}B)	0	100	1000	10^4	10^5	10^6	10^7	10^8	$2*10^8$	$4*10^8$	V_0=-24 MeV α=0.1 fm^{-2}
E_1 (MeV)	-152.4	-19.1	-16.1	-15.3	-13.56	-12.5	-11.6	-11.1	-10.9	-10.8	-11.13
E_2 (MeV)	-110.7	-17.6	-14.4	-2.66	-2.107	-1.99	-1.86	-1.79	-1.77	-1.76	-1.769
E_3 (MeV)	-95.92	-16.9	-13.9	-0.28	0.451	0.487	0.491	0.493	0.494	0.495	0.5025
E_4 (MeV)	-93.21	-4.42	-2.53	0.306	0.4757	0.705	1.023	1.161	1.181	1.197	1.101
Primes	0	1.109	0.216	0.586	0.6761	0.382	0.312	0.169	0.145	0.137	0.1531

Initially, the convergence of the energy spectrum in respect to the OPP parameter λ was investigated. In the calculations, the Pauli-forbidden states in the α+α (2 in S-wave and 1 in D-wave) and α+^{3}He (α+^{3}H) (2 in S-wave, 1 in $P_{3/2}$, and 1 in $P_{1/2}$ waves) subsystems were taken into account. With increasing λ, stabilization of the energy levels was observed. At the same time, the **Primes of forbidden states**, which characterize the residual projection of the forbidden states in the wave function, decreased. According to the calculations, the minimum value of this quantity was obtained at $\lambda=4\times10^8$ MeV, and no significant changes were observed for larger values of λ. Therefore, this value was adopted as the optimal parameter for further calculations. Tables 1 and 2 present the energy spectra of the ^{11}C and ^{11}B nuclei with the $J^\pi = 3/2^-$ state as a function of the OPP parameter λ. The results show that considering only two-body interactions is insufficient to reproduce the experimental ground-state energies. Keeping the optimal λ value fixed, the three-body potential V_{3b} was varied within the ranges from – 40 MeV to − 50 MeV and from -20 MeV to -30 MeV for the ^{11}C and ^{11}B spectrum, respectively. The best agreement with experimental data was obtained at V_{3b} = −43 MeV and -24 MeV, respectively. In particular, the calculated binding energy of the ^{11}C nucleus is − 9.139 MeV, which is in good agreement with the experimental value of − 9.131 MeV. For the ^{11}B nucleus, the calculated value approaches the experimental binding energy of −11.132 MeV with the same three-body potential, used for the ^{11}C nucleus.

The obtained results demonstrate that the α+α+^{3}He and α+α+^{3}H three-cluster models combined with the OPP method provide an effective approach for describing the energy structure of light nuclei.

References:
1. Buck B., Friedrich H., Wheatley C. Local potential models for the α–α interaction. Nucl. Phys. A, 275, 246-268 (1977).
2. Kukulin V.I., Krasnopolsky V.M., Horáček J. Theory of Resonances. Kluwer Academic Publishers, Dordrecht (1989).
3. Tursunov E.M., Turakulov S.A, Kadyrov A.S. Astrophysical ^{3}He(α,γ)^{7}Be and ^{3}H(α,γ)^{7}Li direct capture reactions in a potential-model approach Physical review c 97, 035802 (2018).
4. Tursunov E.M. Mazumdar I. Peculiarity of the $^{12}C(0^{+})$ and $^{12}C(2^{+})$ energy spectrum in a 3α model. PHAN, 85 (2022), 160.

ELASTIC SCATTERING AND BREAKUP IN THE e^{-} + d REACTION WITHIN THE THREE-BODY FADDEEV FORMALISM: A VERIFIABLE COMPUTATIONAL SCHEME

Pyak P.[1], Igamov S.[1], Khugaev A.[2]
Institute of Nuclear Physics, Uzbekistan Academy of Sciences, Tashkent, Uzbekistan
[2]New Uzbekistan University, Tashkent, Uzbekistan

Electron scattering off light nuclei has the distinctive feature that, in the one-photon-exchange Born approximation, the strong interaction is switched off at the electron vertex: the electron couples only to the electromagnetic current of the target, while the strong dynamics enters through the nuclear structure. This makes the e^{-}+p and e^{-}+d reactions a reference point for the subsequent separation of the strong-interaction contribution in the p+p, p+d and d+d reactions.

The physical content of few-nucleon electroweak reactions is the ultimate objective, for which a verified computational scheme is the necessary foundation. Such a scheme is constructed for the e^{-}+d reaction, in which every stage is equipped with checks against exactly solvable special and limiting cases. The two-body np interaction is described by a rank-1 and rank-2 separable Yamaguchi potentials [1, 2]: the t-matrix is obtained in closed form, while the Faddeev equations reduce to one-dimensional integral equations. Analytic expressions are derived for the basic integral

$$\int_0^\infty q^2 dq \;/\; [(q^2+A^2)(q^2+B^2)(q^2+C^2)] \;=\; \frac{\pi}{2(A+B)(B+C)(C+A)}$$

(q is the loop-momentum variable, A, B, C are positive parameters) for the scattering length a (α, β are the deuteron wave number and the form-factor parameter, both fixed by the potential)

$$a \;=\; \frac{2\cdot(\alpha+\beta)^2}{\alpha\cdot\beta\cdot(\alpha+2\beta)}$$

and for the effective range $r_e = 3/\beta - 4/(a\beta^2)$. The bound-state wave function of the Yamaguchi potential coincides identically with the Hulthén function $u(r) \propto e^{-\alpha r} - e^{-\beta r}$ which allows the numerical monopole form factor C_E(q) to be checked against the closed form (N is the wave-function normalization constant)

$$C_E(q) \;=\; N^2 \cdot \frac{2}{q}\left[arctan\,\frac{q}{4\alpha} \;-\; 2\,arctan\,\frac{q}{2(\alpha+\beta)} \;+\; arctan\,\frac{q}{4\beta}\right]$$

The three-body machinery is validated on the triton: the spin-isospin recoupling is computed via Wigner 6j symbols, and the resulting binding energy is 9.36 MeV against the experimental 8.48 MeV [3]. The 10% overbinding reflects the absence of tensor forces and short-range repulsion,

whereas the spread among parametrizations amounts to only 1.4% — an order of magnitude smaller than the deviation from experiment, indicating its physical rather than model origin.

Main results, bearing on the electromagnetic e^{-}+d baseline needed to isolate the strong-interaction contribution in p+p, p+d and d+d (see above). 1. The node of the deuteron charge form factor G_C is reproduced neither by rank 1 nor by rank 2 up to $Q^2 = 15.6$ GeV², whereas experimentally it appears at $Q^2 \approx 0.7$ GeV². Importantly, the repulsion in rank 2 was fitted to the scattering length and effective range, not to the node position. It follows that the node is not a consequence of low-energy NN dynamics and probes physics beyond the non-relativistic two-body picture: a hard core, relativistic effects, meson-exchange currents and isobar configurations. 2. The final-state interaction (FSI) in the d(e,e′)np breakup is not a correction but a requirement of internal consistency: as the momentum transfer $q \to 0$ the matrix element must vanish by orthogonality of the bound and continuum states. The impulse approximation violates this by six orders of magnitude, while the full calculation satisfies it (Fig. 1a). Near threshold an enhancement by a factor of 27 is obtained at an np relative energy ≈ 0.1 MeV due to the proximity of the deuteron pole in the $^3S_1$ channel; at higher energies it turns into suppression (Fig. 1b). Hence extracting the momentum distribution from breakup data is admissible only far from threshold. 3. In the inelastic calculation the node of G_C is masked by the quadrupole form factor G_Q, which exceeds the charge term at the node by a factor of about 1800, so that $A(Q^2)$ — the unpolarized elastic structure function combining the charge, quadrupole and magnetic form factors G_C, G_Q and G_M — decreases monotonically; separating G_C and G_Q therefore requires polarization observables, which defines the next stage of this work.

Thus a verified electromagnetic baseline for e^{-}+d is constructed, to be subtracted from p+p, p+d and d+d data in order to isolate the strong-interaction contribution; each transition between stages is confirmed by quantitative cross-checks down to machine precision. Further development implies the $^3S_1$–$^3D_1$ tensor coupling, the complete set of final-state partial waves, and meson-exchange currents.

Table 1. Checks against exactly solvable special and limiting cases
(k — np relative momentum; B_t — triton binding energy)

Check	Type	Result
Basic integral: analytic vs numerical	analytic benchmark	10^{-15}
Zero-range limit: $\beta \to \infty \Rightarrow a \to 1/\alpha$	limiting case	10^{-4}
Yamaguchi wave function = Hulthén function	analytic benchmark	machine precision
Monopole form factor = arctangent formula	analytic benchmark	10^{-12}
Thomas collapse: force range → 0 ⇒ B_t → ∞	limiting case	factor 18.5
Watson theorem: arg(M_FSI/M_PWIA) = δ(k)	general theorem	machine zero
Levinson theorem: δ(0) = π	general theorem	179.4° as k→0
Orthogonality $\langle \psi_k \vert \psi_d \rangle = 0$ at q→0	exact limit	suppression 10^6

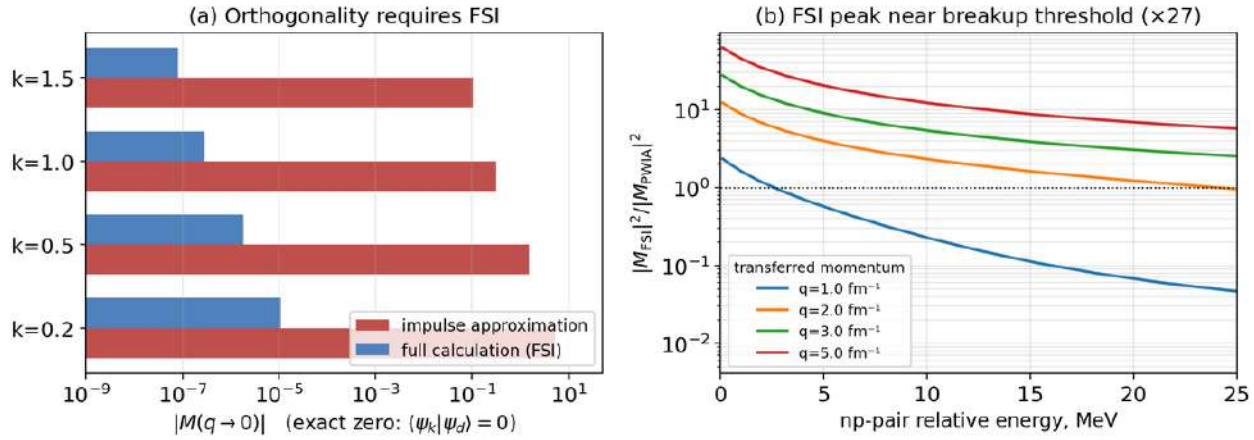

Figure 1. The d(e,e′)np breakup: (a) orthogonality requires FSI (log scale); (b) FSI enhancement near threshold.

References:

1. Yamaguchi Y. Two-Nucleon Problem When the Potential Is Nonlocal but Separable. I // Phys. Rev. — 1954. — Vol. 95. — P. 1628–1634.
2. Bondarenko S., Yurev S. Relativistic four-nucleon calculations with rank-one separable potential // Phys. Atom. Nucl. — 2025. — Vol. 88. — P. 768–772.
3. Egorov M.V. Binding energies of ^{3}H and ^{3}He nuclei in three-body Faddeev equations with direct integration // Phys. Atom. Nucl. — 2024. — Vol. 87. — P. 682–690.

COMPARATIVE ASSESSMENT OF GEANT4 CASCADE MODELS FOR THE PRODUCTION OF ^{11}C IN PROTON-INDUCED REACTIONS ON ^{16}O AT 15–200 MeV

Kayumova M.Sh., Tursunov E.M.
[1]Institute of Nuclear Physics, Uzbekistan Academy of Sciences, Tashkent, Uzbekistan

The production of positron-emitting radionuclides in proton-induced nuclear reactions is of considerable interest for proton therapy, where PET imaging is used for in vivo verification of the proton beam range. Among the radionuclides produced in oxygen-rich tissues, ^{11}C is one of the most important because its production cross section directly affects the accuracy of Monte Carlo simulations employed in treatment planning and dose verification [1,2]. Although Geant4 is widely used for simulating hadronic interactions in the proton therapy energy range, the predictive capability of its intranuclear cascade models strongly depends on the reaction channel and projectile energy [2,3]. Therefore, systematic validation of these models against reliable experimental data remains an important task.

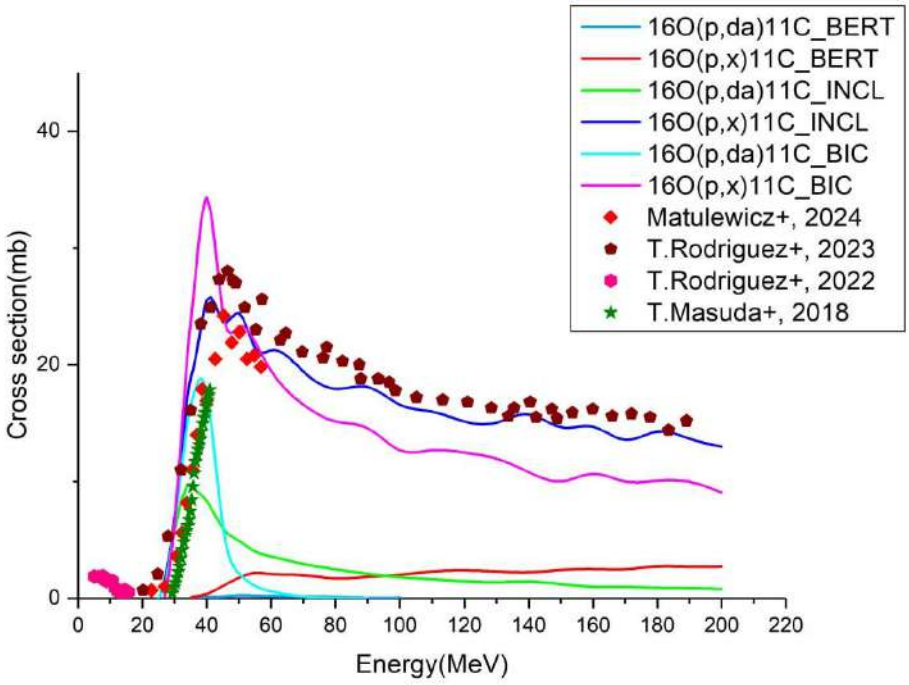

Figure 1. Comparison of the calculated excitation functions for the $^{16}O(p,x)^{11}C$ reaction obtained using the Bertini (BERT), Binary Cascade (BIC), and INCL++ models with experimental data from the EXFOR database.

In the present work, the $^{16}O(p,x)^{11}C$ reaction was simulated using the Geant4 Monte Carlo toolkit in the proton energy range from 15 to 200 MeV. Three intranuclear cascade models implemented in Geant4 were investigated: Bertini Cascade (BERT), Binary Cascade (BIC), and Liège Intranuclear Cascade (INCL++). The reaction cross sections were determined from the simulated reaction yields using

$$\sigma = \frac{Q \times M}{\rho \times d \times N_A \times N_p}$$

where Q is the number of reaction events, M is the molar mass of oxygen, ρ is the target density, d is the target thickness, N_A is Avogadro's constant, and N_p is the number of incident protons. The calculated excitation functions were compared with the experimental cross sections available in the EXFOR database [5], including recent measurements reported by Masuda et al. (2018), Rodríguez-González et al. (2022, 2023) [6], and Matulewicz et al. (2024) [7].

Figure 1 shows the comparison between the calculated excitation functions and the available experimental data. Significant differences are observed among the investigated Geant4 cascade models. The INCL++ model reproduces the experimental excitation function more accurately over a broad energy interval (approximately 40–200 MeV), providing the best overall agreement with the measurements. This behavior indicates that the description of the intranuclear cascade and subsequent cluster emission implemented in INCL++ [4] is more suitable for the inclusive production of ^{11}C from oxygen.

The Binary Cascade (BIC) model predicts the correct position of the reaction maximum but noticeably overestimates its magnitude in the vicinity of 40–45 MeV. At higher energies, the calculated cross section decreases more rapidly than the experimental trend. In contrast, the Bertini Cascade (BERT) model considerably underestimates the inclusive $^{16}O(p,x)^{11}C$ production cross section over most of the investigated energy range, although it reproduces the exclusive $^{16}O(p,d\alpha)^{11}C$ channel reasonably well. These differences demonstrate that the predictive capability of Geant4

depends strongly on the selected intranuclear cascade model and confirm the necessity of validation against modern experimental data before applying these models in proton therapy simulations.

The obtained results show that INCL++ provides the most reliable description of the $^{16}O(p,x)^{11}C$ reaction among the investigated Geant4 models. The present study also demonstrates the importance of recently published experimental measurements for improving and validating Monte Carlo nuclear reaction models used in medical physics applications.

References:

1. H. Paganetti, The Physics of Proton Therapy, CRC Press, 2012.
2. S. Agostinelli et al., Geant4—a simulation toolkit, Nucl. Instrum. Methods Phys. Res. A 506 (2003) 250–303.
3. J. Allison et al., Recent developments in Geant4, Nucl. Instrum. Methods Phys. Res. A 835 (2016) 186–225.
4. A.Boudard et al., New potentialities of the Liège intranuclear cascade model, Phys. Rev. C 87 (2013) 014606.
5. EXFOR Experimental Nuclear Reaction Data Library, IAEA Nuclear Data Section.
6. T. Rodríguez-González et al., Production of ^{11}C, ^{13}N and ^{15}O in proton-induced nuclear reactions up to 200 MeV, Nuclear Data Sheets 187 (2023) 579–596.

J. Matulewicz et al., Measurement of positron-emitting isotope production cross sections for proton interactions on oxygen, Eur. Phys. J. A 60 (2024) 203.

CALCULATION OF THE GNEIS NEUTRON SOURCE SPECTRA USING GEANT4 SOFTWARE PACKAGE

Tiagelskaia A.M., Olkhovich N.M., Vorobyev A.S.

Petersburg Nuclear Physics Institute named by B.P. Konstantinov of NRC «Kurchatov Institute»,

At the National Research Center "Kurchatov Institute" - PNPI, Gatchina, research is being conducted on the GNEIS neutron time-of-flight spectrometer to obtain new nuclear data. First of all neutron cross sections in a wide range of neutron energies from 0.1 eV to 500 MeV were measured. With the expansion of the range of tasks studied at the GNEIS installation, it became necessary to study the characteristics of the spectrometer more thoroughly.

In this work, using the Geant4 software package, a digital model of the GNEIS spectrometer, created on the basis of the SC-1000 accelerator, was compiled. Calculations of fluxes in the direction of “direct” and “reverse” geometry relative to the momentum of protons incident on a neutron-producing target were carried out, spectra in both directions were calculated and their comparison was carried out.

EXPERIMENTAL STUDIES OF RESONANT REACTIONS AT LOW ENERGIES

Nurmukhanbetova A.K.[1,2,3], Goldberg V.Z.[4], Nauruzbayev D.K.[1,3], Serikbayeva G.[5], Tenelbayev A.G.[5], Ilin K.P.[6], Rogachev G.V.[4]

[1]*Nazarbayev University Research Administration, Nazarbayev University, Astana, Kazakhstan*
[2]*Energetic Cosmos Laboratory, Nazarbayev University, Astana, Kazakhstan*
[3]*School of Intelligent Systems, Astana IT University, Astana, Kazakhstan*
[4]*Cyclotron Institute, Texas A&M University, College Station, Texas, USA*
[5]*Department of Physics, School of Sciences and Humanities, Nazarbayev University, Astana, Kazakhstan*
[6]*Simon Fraser University, Burnaby, Canada*

We will present a brief review of resonant reaction studies using the Thick Target Inverse Kinematics (TTIK) approach in combination with the time-of-flight method. These experiments were conducted at the Astana cyclotron, which provides heavy-ion beams ranging from Li to Xe with energies of 0.3–2.0 MeV per nucleon. The TTIK method offers the advantage of obtaining continuous energy excitation functions at angles close to 180 degrees in CM frame within a single run [1]. We studied the development of cluster structure in N≠Z nuclei as in well-known N=Z nuclei. The studies of the alpha cluster structure in N≠Z nuclei together with TTIK measurements at rare beams open new surprising possibilities of investigation of alpha cluster structure in mirror nuclei [2-9].

This research was funded by the Science Committee of the Ministry of Science and Higher Education of the Republic of Kazakhstan (Grant No. AP23489860).

References:

1. K.Artemov, O.P. et al, Sov. J. Nucl. Phys. 52, 408 (1990).
2. V.Z.Goldberg, et al., Phys.Rev. C 105, 014615 (2022).
3. Nurmukhanbetova A.K., et al., NIM on physics A. 2016 Vol.847. P.125-129
4. Nurmukhanbetova A.K., et al., Phys. Rev. C, Vol.100, P.062802 (2019).
5. Goldberg V. Z., et al., Phys. Rev. Research, Vol2, P.032036 (2020).
6. G.V.Rogachev, Ph.D. thesis, I.V. Kurchatov Institute of Atomic Energy, Moscow, 1999.
7. R.E.Azuma, et al., Phys. Rev. C 81, 045805 (2010).
8. A.Volya and Y.M.Tchuvil'sky, Phys. Rev. C91, 044319 (2015).
9. A.Volya, et al., Commun Phys 5, 322 (2022).

ISOSPIN SPLITTING OF GIANT DIPOLE RESONANCE IN MEDIUM AND HEAVY NUCLEI

Rasulova F.A.[1,2], Kuznetsov A.A.[3,4], Nesterenko V.O.[5], Khushvaktov J.H.[2,6], Alekseev S.I.[1], Fursova N.Yu.[3], Madumarov A.S.[1], Chuprakov I.[1,7], Aksenov N.V.[1]

[1]*Flerov Laboratory of Nuclear Reactions of Joint Institute for Nuclear Research, Dubna, Russian Federation*

[2]*Institute of Nuclear Physics of Uzbekistan Academy of Sciences, Tashkent, Uzbekistan*

[3]*Skobeltsyn Institute of Nuclear Physics of Lomonosov Moscow State University, Moscow, Russian Federation*

[4]*Lomonosov Moscow State University, Moscow, Russian Federation*

[5]*Bogoliubov Laboratory of Theoretical Physics of Joint Institute for Nuclear Research, Dubna, Russian Federation*

[6]*Dzhelepov Laboratory of Nuclear Problems of Joint Institute for Nuclear Research, Dubna, Russian Federation*

[7]*Institute of Nuclear Physics, Almaty, Kazakhstan*

In this study, experiments were conducted at bremsstrahlung endpoint energies of 10-23 MeV with a beam from the MT-25 microtron at the Laboratory of Nuclear Reactions at JINR using the γ-activation method. Electron energies ranged from 10-23 MeV with an energy step of 1 MeV. A tungsten radiator target was used to generate γ-radiation. The induced activity in irradiated targets from a natural mixture of Se [1], Mo [2], Cd [3], Te [3], Sm, Gd, Dy, Yb, Hf, and Pt [4] was measured using a high-purity germanium γ-detector, the experimental reaction yields were normalized to the reaction yield of ^{82}Se(γ,*n*)^{81}Se, ^{100}Mo(γ,*n*)^{99}Mo, ^{116}Cd(γ,*n*)^{115}Cd, ^{130}Te(γ,*n*)^{129}Te, ^{154}Sm(γ,*n*)^{153}Sm, ^{160}Gd(γ,*n*)^{159}Gd, ^{158}Dy(γ,*n*)^{157}Dy, ^{176}Yb(γ,*n*)^{175}Yb, ^{176}Hf(γ,*n*)^{175}Hf and ^{198}Pt(γ,*n*)^{197}Pt, respectively. As a result, experimental values of the relative yields of the reactions (γ,*n*) and (γ,*p*) forming the nuclei ^{73,75,81}Se, ^{91,99}Mo, ^{105,107,109,111m,115}Cd, ^{119,121,123m,125m,127,129}Te, ^{143,153}Sm, ^{151,153,159}Gd, ^{155,157}Dy, ^{167,169,175}Yb, ^{173,175,180m}Hf ^{189,191,193m,195m,197}Pt и ^{73,76,77,79}As, ^{91m,95,96,97}Nb, ^{105,111,112,113,115}Ag, ^{122,124,127,129}Sb, ^{143,148g,148m,149,151}Pm, ^{156,157,159}Eu, ^{160,161,162,163}Tb, ^{172,173,175}Tm, ^{176m,177,178,179}Lu, ^{194,195}Ir were obtained for the first time. The experimental values of relative yields were compared with theoretical results obtained using TALYS with standard parameters [5] and the combined photonucleon reaction model (CMPR) [6]. In the case of relative yields for photoproton reactions on heavy isotopes, the theoretical values calculated using the CMPR significantly exceed the TALYS results. The experimental results lie closer to the theoretical curve using the CMPR code. Taking into account isospin splitting in the CMPR allows one to describe experimental data on reactions with proton emission in the energy range from 12 to 23 MeV.

For a more thorough analysis of the obtained results, the ratios of the reaction yield (γ,*p*) to the reaction yield (γ,*n*) were calculated for the nuclei ^{74}Se (^{73}As/^{73}Se), ^{106}Cd (^{105}Ag/^{105}Cd), ^{116}Cd (^{115}Ag/^{115}Cd), ^{128}Te (^{127}Sb/^{127}Te), ^{176}Yb (^{175}Tm/^{175}Yb), и ^{130}Te (^{129}Sb/^{129}Te). In the case of ^{74}Se (^{73}As/^{73}Se) and ^{106}Cd (^{105}Ag/^{105}Cd) the CMPR cannot describe the experimental results. The reason for the observed discrepancy between theory and experiment can be explained by the fact that statistical models of photonuclear reactions do not take into account the individual structural features of the isotopes ^{74}Se and ^{106}Cd (these nuclei are also bypassed nuclei).

References:

1. F.A. Rasulova et. al., Photonuclear reactions on stable isotopes of selenium at bremsstrahlung end-point energies of 10−23 MeV Chinese Physics C, 2026, 50, 064003.

2. F.A. Rasulova et. al., Photonuclear reactions on stable isotopes of molybdenum at bremsstrahlung end-point energies of 10–23 MeV, Physical Review C, 2025, 111, 024604.
3. F.A. Rasulova et. al., Photonuclear reactions on stable isotopes of cadmium and tellurium at bremsstrahlung end-point energies of 10−23 MeV Chinese Physics C, 2024, 48, 024002.
4. F.A. Rasulova et. al., Photonuclear reactions on stable isotopes of platinum at bremsstrahlung end-point energies of 10–23 MeV, Physical Review C, 2025, 112, 054610.
5. A. Koning. TALYS-2.0: A Nuclear Reaction Program, User Manual, 2023.
6. B.S. Ishkhanov, V. N. Orlin, Physics of Atomic Nuclei, 78, 557-573, 2015.

THE METROLOGY OF HPGe DETECTORS: APPLICATION OF A NOVEL METHOD TO THE DECAY OF Bi-207

Jordanov D.[1], Nadjdjerdj L.[1], Inoyatov A.[2], Khushvaktov J.Kh.[2], Čebela M.[1], Rosić M.[1]
[1]*VINCA Institute of Nuclear Sciences-National Institute of the Republic of Serbia, Belgrade, Serbia*
[2]*Joint Institute for Nuclear Research, Dubna, Russian Federation*

Broad-energy germanium (BEGe) detectors enable simultaneous X-ray and gamma-ray spectroscopy; however, their use leads to complex true coincidence summing (TCS) effects, including X–X, X–γ, and γ–γ cascades. In this paper, we present a universal extension of the matrix formalism for calculating count rates. By exploiting the natural grouping of terms within the covariance matrix, we directly derive equations for count rates, thereby eliminating the need to work out decay pathways specific to individual cases. The formalism is further extended to account for metastable states by separating groups of prompt and delayed coincidences, thus generalizing the approach to arbitrary decay schemes.

The method was validated by application to the decay of the ^{207}Bi isotope, a radionuclide featuring metastable states. We determined the unknown source activity, as well as the full- energy peak detection efficiencies and total detection efficiencies for all emitted radiations (**Figure 1**). The results show excellent agreement with independent measurements performed using standard calibration sources (^{139}Ce, ^{133}Ba, ^{152}Eu) in identical geometry, confirming the reliability of the proposed approach and its potential for application in a broader metrological context, including cases where standard detector calibration is unavailable.

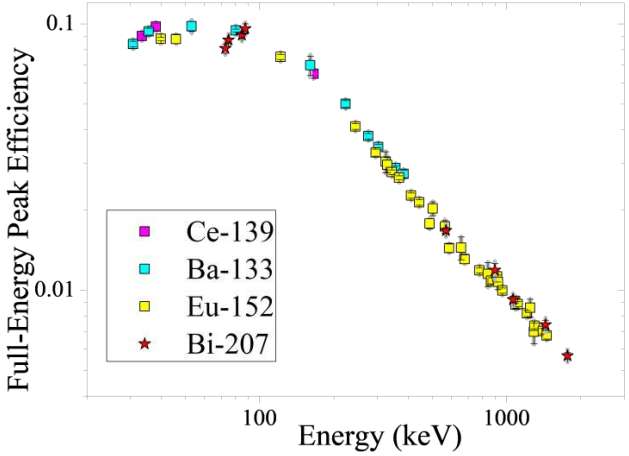

Figure 1. Full-energy peak detection efficiencies obtained from ^{207}Bi and from certified ^{139}Ce, ^{133}Ba, and ^{152}Eu sources measured in the same geometry. Thin bars represent statistical uncertainties, while wide gray bars represent total uncertainties.

SIMULATION OF THE PROCESS OF MEASURING THE FAST NEUTRON FLUX USING THE BICRON DETECTOR IN THE νGeN EXPERIMENT

Khushvaktov J.H.[1] for the νGeN collaboration
[1]*Joint Institute for Nuclear Research, Dubna, Russian Federation*

The ν**GeN experiment** is a particle physics facility at the Kalinin Nuclear Power Plant in Udomlya, Russia, designed to study rare neutrino interactions. Positioned just 11 meters from a 3.1 GW reactor core, it utilizes a highly sensitive, low-threshold germanium detector to fix interactions with an enormous antineutrino flux [1, 2].

Reactor-produced neutrons are one of the main source of background radiation in neutrino experiments; they can create significant, power-correlated backgrounds. In low-threshold HPGe detectors, reactorgenic and cosmogenic fast neutrons produce a nuclear recoil that is virtually indistinguishable from the expected signal from coherent elastic scattering of neutrinos by a nucleus. To evaluate and filter out these events, modern experiments use detailed Monte Carlo simulations using the Geant4 code, which allows modeling the absorbed neutron energy in the detectors.

The proton recoil energy in the Bicron detector (BC-501A) was determined using pulse shape discrimination analysis of the measured spectrum on the surface of the νGeN facility. Using simulation, the absorbed energy in the Bicron detector was calculated. Simulations were carried out for different shapes of the neutron spectrum, and the quenching factor was taken into account according to work [3]. By comparing the calculated energy absorbed in the detector with the measured proton recoil energy, the fluence of fast neutrons on the surface of the νGeN facility was preliminarily determined.

References:

1. Alekseev, et al., Physical Review D 106 (5), L051101 (2022)
2. V. Belov, et al., Chinese Physics C 49 053004 (2025)
N.V. Kornilov et al., Nuclear Instruments and Methods in Physics Research A 599 (2009) 226-233

CALCULATION OF THE EFFICIENCY OF THE FISCO MULTI-SECTION DETECTOR USING GEANT4 SOFTWARE PACKAGE

Olkhovich N.M., Tiagelskaia A.M., Vorobyev A.S.
Petersburg Nuclear Physics Institute named by B.P. Konstantinov of National Research Centre “Kurchatov Institute”, St.Petersburg, Russian Federation

The FISCO (FISsion COrrelation) installation is designed for multiparametric studies of the fission process of major and minor actinides, when the main characteristics of fission fragments and secondary radiation are simultaneously recorded for each specific act of fission. The installation has several detector systems, the main ones being a charged particle detector, a multi-section neutron and gamma quanta detector, and a neutron multiplicity detector. One of the most important indicators for detector systems is data on the effectiveness of the detectors included in the system and their effectiveness in this system.

This work shows the determination of efficiency characteristics for a multi-section detector using the GEANT4 software package.

MECHANISMS OF PROTON AND DEUTERON EMISSION FROM ^{59}Co AND ^{60}Ni INDUCED BY DEUTERONS AT MEDIUM ENERGIES

Temirzhanov A.[1,2], Zholdybayev T.[1], Sadykov B.[1,2], Ussabayeva G.[1,3], Duisebayev B.[1]
[1]*Institute of Nuclear Physics, Almaty, Kazakhstan*
[2]*Satbayev University, Almaty, Kazakhstan*
[3]*KazNPU named after Abay, Almaty, Kazakhstan*

Deuteron-initiated nuclear reactions play an important role in nuclear physics, fusion technologies, activation analysis, and the production of medical isotopes due to complex interaction mechanisms associated with the deuteron's weak binding energy. Since the deuteron consists of a proton and a neutron bound by an energy of only about 2.2 MeV, decay processes (breakup), nucleon transfer, and pre-equilibrium radiation significantly affect reaction cross sections even at relatively low incident particle energies. As a result, deuteron-initiated reactions differ significantly from those induced by protons and neutrons, especially at energies near and above the Coulomb barrier [1].

Nickel and cobalt isotopes are of significant interest in both fundamental and applied research, as they are widely used as structural materials in accelerators, fusion systems, and advanced energy technologies. Such research is particularly relevant in the context of developing materials and technologies for advanced energy systems, including fusion reactors and accelerator-controlled neutron sources. High-energy deuterons can significantly activate materials, alter their radiation properties, and generate complex secondary particle spectra. Therefore, a correct description of deuteron-initiated reactions is necessary for calculating the radiation hardness of materials, predicting induced activity, and developing new functional materials for energy applications [2, 3].

The study of emitted proton and deuteron spectra provides valuable information on the relative contributions of stripping, pickup, breakup, pre-equilibrium emission, and statistical evaporation mechanisms in modern nuclear reaction computational codes, such as TALYS and EMPIRE, that still face difficulties in describing cluster emission processes and breakup mechanisms for deuterons. Therefore, a systematic study of (d,xp) and (d,xd) reactions on ^{59}Co and ^{60}Ni nuclei in the energy range up to 100 MeV is of interest both for testing theoretical models and for developing computational methods for modeling nuclear processes in next-generation energy systems. Studying proton and deuteron radiation in (d,xp) and (d,xd) reactions provides information on compound nucleus decay mechanisms, direct reactions, nucleon transfer processes, and the contribution of breakup processes [4, 5].

The calculated results are used to examine the ability of the employed nuclear-reaction models to reproduce the main characteristics of proton and deuteron emission. The analysis also provides information on the sensitivity of the calculated spectra to the treatment of breakup and nucleon-transfer mechanisms. The results obtained contribute to improving the theoretical description of deuteron-induced reactions and to identifying reaction mechanisms that require further refinement in calculations for medium-mass nuclei.

Acknowledgements. The work was carried out within the framework of program-targeted funding of scientific and technical programs of the Science Committee of the Ministry of Science and Higher Education of the Republic of Kazakhstan, grant No. BR31716181.

References:
1. Voinov, A. V., et al. "Nuclear excitations at constant temperature."*Physical Review C—Nuclear Physics* 79.3 (2009): 031301.
2. Yiğit, M., E. Tel, and A. Kara. "Deuteron Induced (d, p) and (d, 2p) Nuclear Reactions up to 50 MeV."*Journal Of Fusion Energy* 32.3 (2013): 362-370.
3. Tuncel, Nina, et al. "Proton, neutron and deuteron induced nuclear reactions in medical application."*Journal of Radiation Research and Applied Sciences* 17.1 (2024): 100807.
4. Avrigeanu, M., and V. Avrigeanu. "Role of breakup and direct processes in deuteron-induced reactions at low energies." *Physical Review C* 92.2 (2015): 021601.
5. Ussabayeva, G., et al. "Emission of protons and deuterons from the interaction of 14.5 MeV deuterons with the 59Co nucleus." *Journal of Physics: Conference Series*. Vol. 3089. No. 1. IOP Publishing, 2025.

EXCITATION CROSS SECTION OF ISOMERIC STATES IN REACTIONS (γ,n) AND (n,2n) ON ^{197}Au NUCLEI

Palvanov S.R.[1], Inoyatov A.X.[2,3], Eshanqulov G.I.[1], Rustamova Kh.Z.[1], Axmedov S.E.[1], Tojiboev O.R.[3]

[1]National University of Uzbekistan, Tashkent, Uzbekistan
[2]Joint Institute for Nuclear Research, Dubna, Russian Federation
[3]Institute of Nuclear Physics, Uzbekistan Academy of Sciences, Tashkent, Uzbekistan

The study of isomeric ratios is one of the most actual issues that gives the possibility of obtaining useful information about the reaction mechanism, in particular, on the moment of inertia of the nucleus, the spin dependence of the level density, and the character of transitions between highly excited nuclear states. Moreover, it can also help get data from the isomeric ratios of the yields of nuclear reactions which are necessary for replenishing nuclear data in this area and to optimize experiments in analytical and numerical studies using methods of activation analysis [1,2].

In the present work, the isomeric ratios of the cross-sections for the (n,2n) reaction on ^{197}Au nuclei are studied using an induced activity method. The isomeric ratios of the reaction yields (γ, n) and (n,2n) on the ^{197}Au nucleus were also determined in the bremsstrahlung energy range of 22–25 MeV.

The studies were carried out on a neutron generator NG-150 of the Institute of Nuclear Physics of the Academy of Sciences of the Republic of Uzbekistan [3]. The neutron generator NG-150 realizes fluxes of fast neutrons with energies ~ 2.4 and 14 MeV from the reactions D + d → ^{3}He + n or T + d→ α + n using deuterium and tritium targets. In this case, the neutron fluxes are ~10^{8} and 10^{10} n/sec, respectively. The time of exposure to a neutron flux with the energy at 14 MeV is 40 min. The neutron flux is monitored using a natural isotopic aluminum plate, where it has been irradiated together with the targets. Samples weighing 0,5-1 g in the form of a disk 15 mm in diameter are used as targets.

Experiments on the (γ,n) reaction were carried out using the bremsstrahlung beam of the MT-25 microtron at the Nuclear Reactions Laboratory of the Joint Institute for Nuclear Research (Dubna, Russia). The average microtron current was ~3 μA.

The gamma activities of the samples were measured on an 8192-channel gamma spectrometer equipped with a HPGe pure germanium detector with an efficiency of 15%. The detector has an

energy resolution of 1.8 keV for the 1332 keV gamma line of the ^{60}Co radionuclide. The radionuclides ^{54}Mn, ^{57}Co, ^{60}Co, ^{109}Cd, ^{133}Ba, ^{137}Cs, ^{152}Eu, ^{210}Pb and ^{241}Am were used to calibrate the spectrometer for efficiency and energy. The population of the isomeric and ground levels was identified by γ-lines.

The absolute values of the excitation cross sections of the isomeric state were obtained from the experimental isomeric ratios of the reaction yields and the total cross section of the photoneutron reaction σ_{tot} [4]. The calculations of the cross section $\sigma(E_\gamma)$ from the yield curves were carried out using the Penfold-Liss method [3]. The cross section isomeric ratios at $E_\gamma=E_m$ are estimated. The spectrum of electron bremsstrahlung calculated using the GEANT4 [5] program. To evaluate and compare the experimental results, we calculated the reaction cross-section using the TALYS-1.6 [6] software package. TALYS is a program that allows calculations of the properties of nuclear reactions in a wide range of energies (1 keV – 200 MeV) and nuclei (A ≥ 12). TALYS combines many theoretical models for describing various processes (optical model, coupled channels method, Born approximation of distorted waves, etc.).

The isomeric cross-section ratios was determined in the case of the reaction (n, 2n). To obtain absolute values of cross sections for the ground and isomeric states, methods based on comparison of the yields of the reaction under study and the control reaction were used. The reaction ^{27}Al(n,α)^{24}Na ($T_{1/2}$ = 15 h, E_γ = 1368 keV) was used as a monitor reaction.

For comparison with the experiment, we calculated the isomeric ratios using the statistical model of the nucleus. The level density of the excited nucleus was estimated using the formula,

$$\rho(U,J)=\frac{2J+1}{24\sqrt{2}a^{1/4}U^{5/4}\sigma^3}\cdot\exp\left[2\sqrt{aU}-\frac{(J+1/2)^2}{2\sigma^2}\right],$$

where σ is the spin limitation parameter, *a* is the level density parameter, *U* is the excitation energy, which is understood as the effective energy. We managed to improve the quantitative agreement between the calculations and the experiment by fixing the spin limitation parameter σ.

The experimental results are discussed and compared with the results of other authors, as well as with the results of statistical modeling. The dependence of isomeric ratios on the mass number of the isotope was obtained. Theoretical values of the isomeric ratios have been calculated by using TALYS-1.6 code.

References:

1. Palvanov S.R. Physics of Atomic Nuclei, 2014. Vol. 77, No. 1. p. 35.
2. Mazur V.M. et al. Phys. Part. Nucl. Lett. 2008. Vol. 5, № 4. p. 374.
3. http://www.inp.uz
4. Varlamov A.V. et al. Atlas of GDR. INDS(NDS)-394. Vienna: IAEA, 1999.
5. Agostinelli S. et al. Nuclear Physics News. 2007.V. 17, No. 2. p.20.
6. Koning A.J. et al. TALYS: Comprehensive nuclear reaction modeling. Proc. of the Int. Conf. on Nuclear Data for Science and Technology. 2005. V.769. p. 1154.

RECONSTRUCTION AND COMPARISON OF NEUTRON-GAMMA SPECTRA AT THE COLLIMATOR EXIT OF THE VVR-SM REACTOR HORIZONTAL CHANNEL USING OPENMC AND GEANT4

Kulabdullaev G.A.[1], Abdullaeva G.A.[1], Kim A.A.[1], Nebesniy A.F.[1], Yuldashev D.O.[1,2]
[1]Institute of Nuclear Physics, Uzbekistan Academy of Sciences, Tashkent, Uzbekistan
[2]Bukhara State Medical Institute, Bukhara, Uzbekistan

The horizontal channel of the research reactor at the Institute of Nuclear Physics of the Academy of Sciences of the Republic of Uzbekistan was reconstructed using a system of collimators and filters to form a predominantly epithermal neutron flux. At the same time, in the radiation field at the exit of the collimator aperture, fast neutrons and gamma radiation are present along with thermal and epithermal neutrons. The neutron field of this channel of the WWR-SM reactor was previously characterized using the activation-foil method: based on the induced activity of the foils, the thermal- and epithermal-neutron fluxes, as well as the neutron flux at individual high-energy indicator points, were determined. However, the fast-neutron and gamma-ray spectra in this channel had not previously been measured directly.

In the present work, spectral measurements were performed using the SDMF-1608.PRO Mobile portable spectrometer-dosimeter. SDMF-type spectrometer-dosimeters are designed for the simultaneous measurement of the energy distributions of neutron and gamma fluxes. According to the technical data sheet of the SDMF-1608.PRO Mobile instrument used in this study, the total count rate of neutron and gamma pulses should not exceed 1.1×10^5 imp.$\cdot s^{-1}$. Therefore, the measurements were performed in three geometries of surrounding media that modified the radiation field in different ways.

For each experimental configuration, the response matrices were independently calculated in OpenMC and Geant4 codes using consistent geometry, material composition, and energy binning. The experimentally measured spectra were then used to solve the inverse problem of reconstructing the fast-neutron and gamma-ray spectra.

The experiment was carried out in three configurations: the detector was positioned in air at a distance of 270 cm from the collimator aperture, behind a 0.95 cm thick aluminum layer, and behind a 20 cm thick layer of borated paraffin. The measurement time in air and behind the borated paraffin was 600 s, whereas in the aluminum configuration it was 6 s because of the high pulse load. In the OpenMC and Geant4 models, the geometry, material composition, and 1023 energy intervals were matched. In each code, the neutron–neutron, gamma–gamma, and neutron–gamma response matrices were calculated independently. The solutions obtained for the three experimental configurations were combined to reconstruct a single spectrum at the collimator exit. The comparison was performed in terms of the integral flux, total particle emission rate in the computational model, position of the spectral maximum, mean energy, and integral contributions of the energy regions. Agreement in spectral shape was evaluated using the shape similarity coefficient K_f, defined as the scalar product of the normalized spectral vectors; a K_f value close to 1 indicates that the two spectra have practically identical shapes.

For the fast-neutron spectra, a value of (K_f = 0.9913) was obtained. The main spectral maximum was located at 5.867 MeV in OpenMC and 5.908 MeV in Geant4, while the mean energies were 5.813 and 5.794 MeV, respectively. The integral fluxes were (2.219 \times 10^4) and (3.645×10^4) $cm^{-2}\cdot s^{-1}$, whereas the total neutron emission rates in the computational models were (6.275×10^5) and (1.031×10^6) s^{-1}, respectively; the ratio of the Geant4 result to the OpenMC result was 1.642. For the gamma-ray spectra, (K_f = 0.9905); the peak energies were 0.267 and 0.279 MeV,

the integral fluxes were (5.239×10^3) and (1.272×10^4) $cm^{-2} \cdot s^{-1}$, and the total gamma-ray emission rates were (1.481×10^5) and (3.596×10^5) s^{-1}, respectively; the ratio of the results was 2.427. Thus, both codes reconstructed the energy-domain spectral shapes and the positions of the spectral maxima with close agreement; however, a systematic difference remained in the absolute normalization.

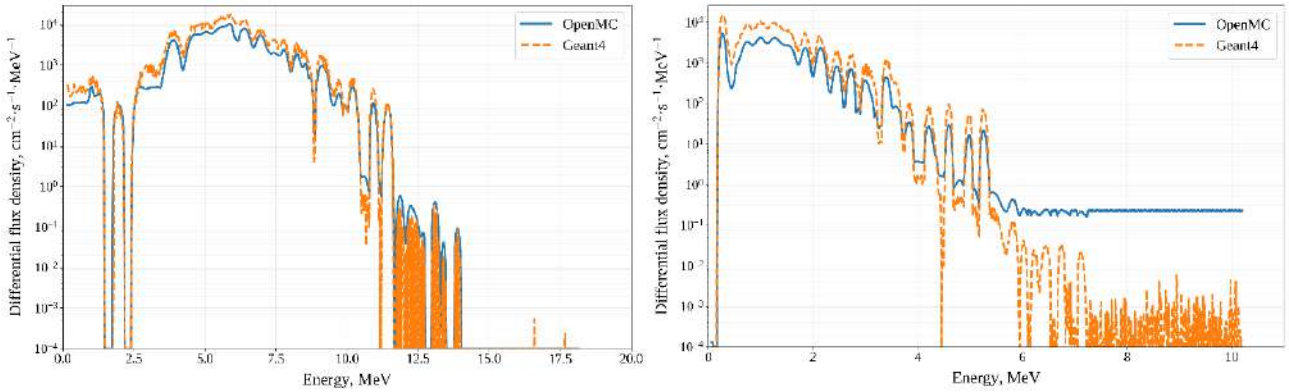

(*a*) (*b*)

Figure 1. Spectra reconstructed at the collimator exit: (a) fast-neutron spectrum; (b) gamma-ray spectrum, obtained using OpenMC and Geant4.

The close agreement in the positions of the spectral maxima, mean energies, and K_f coefficients obtained from the two independent reconstructions indicates the robustness of the main spectral features of the fast-neutron and gamma-radiation fields with respect to the choice of computational code. The differences in absolute fluxes and particle emission rates may be attributed to specific features of the physical models and nuclear-data processing implemented in OpenMC and Geant4, as well as to the normalization and conditioning of the response matrices and the sensitivity of the inverse solution to the regularization parameters. Since the true spectra at the collimator exit were not measured directly, the results are interpreted as a comparative verification of two independent computational models and an assessment of the stability of the inverse problem, rather than as evidence of the absolute superiority of one code over the other.

The independent response matrices generated in OpenMC and Geant4 codes provided closely consistent reconstructions of the spectral shapes and the positions of the energy maxima for the fast-neutron and gamma-ray spectra, while revealing systematic differences in the absolute fluxes and particle emission rates. This indicates the need for a separate assessment of model uncertainty in the reconstruction of spectra at the collimator exit.

COMPARISON OF NEUTRON–GAMMA SPECTRA CALCULATED USING OPENMC AND GEANT4 WITH EXPERIMENTAL SPECTRA IN DIFFERENT MEDIA

Kulabdullaev G.A.[1], Abdullaeva G.A.[1], Kim A.A.[1], Nebesniy A.F.[1], Yuldashev D.O.[1,2]
[1]*Institute of Nuclear Physics, Uzbekistan Academy of Sciences, Tashkent, Uzbekistan*
[2]*Bukhara State Medical Institute, Bukhara, Uzbekistan*

The horizontal channel of the WWR-SM reactor at the Institute of Nuclear Physics of the Academy of Sciences of the Republic of Uzbekistan is intended primarily for the formation of an epithermal neutron flux; together with the thermal and epithermal components, fast neutrons and

gamma rays also emerge from the collimator exit. Their spectra were measured using the SDMF-1608.PRO Mobile spectrometer-dosimeter in three different medium configurations. Instruments of the SDMF family enable simultaneous registration of the energy distributions of the neutron and gamma components; according to the technical data sheet of the instrument used, the total count rate should not exceed 1.1×10^5 imp.$\cdot s^{-1}$.

At the previous stage, spectral response matrices were independently generated in OpenMC and Geant4 models on the basis of the experimental data, and the fast-neutron and gamma-ray spectra at the collimator exit were reconstructed. In the present work, these reconstructed spectra were reprojected through the investigated media to the detector entrance surface and subsequently compared with the experimental spectra.

A spectral case is defined as a combination of one of the three investigated media—air, Al, or boron–paraffin—and one radiation type—fast neutrons or gamma rays. Thus, the analysis included six spectral cases. A comparison of the deviations of the OpenMC and Geant4 results from the experimental spectrum was done for a single spectral case according to one quantitative criterion. In each code, the independently reconstructed spectrum at the collimator exit was used as the source. During forward transport, the contributions of the neutron–neutron, gamma–gamma, and neutron–gamma channels were taken into account. The calculated and experimental differential flux densities were mapped onto a common energy grid. Since the integral normalization had been matched at the stage of solving the inverse problem, the main analysis focused on reproducing the spectral shape, peak amplitude, and redistribution of particles over energy.

The quantitative comparison was performed using four criteria: NRMSE–the ratio of the root-mean-square error over the active energy intervals to the experimental maximum; the mean absolute relative deviation; the logarithmic RMSE for positive spectral values; and the quantity |C/E-1|, where (C/E) is the ratio of the calculated peak to the experimental peak. In addition, the integral contributions of the energy regions 0–0.5, 0.5–2, 2–6, and >6 MeV for neutrons, and <0.3, 0.3–1, 1–3, and >3 MeV for gamma rays were analyzed. Consequently, for the six spectral cases evaluated according to four criteria, a total of 24 quantitative comparisons were performed.

In air, the OpenMC calculations reproduced the experimental fast-neutron and gamma-ray spectra most closely: the NRMSE values were 0.0004 and 0.0010, respectively, whereas for Geant4 they were 0.0457 and 0.0361. For fast neutrons behind aluminum, a lower NRMSE was obtained with Geant4–0.0556 compared with 0.0996 for OpenMC. At the same time, in the 2–6 MeV region, both calculations yield close to the experiment results (C/E = 1.0035 for OpenMC and 1.0022 for Geant4). For the gamma-ray spectrum behind aluminum, OpenMC provided a lower overall NRMSE (0.0244 versus 0.0321), whereas Geant4 more accurately reproduced the peak amplitude (C/E = 1.073 versus 0.817 for OpenMC) and the distribution in the 0.3–1, 1–3, and >3 MeV regions. For fast neutrons behind boron–paraffin, the NRMSE was 0.1105 for OpenMC and 0.1684 for Geant4. Both models underestimated the components below 2 MeV and overestimated them in the 2–6 MeV region. For gamma rays behind boron–paraffin, OpenMC also yielded a lower NRMSE (0.0284 versus 0.0360), whereas Geant4 result was closer to the experiment in three of the four selected energy regions.

Of the 24 quantitative comparisons, a smaller deviation from the experimental data was obtained with OpenMC in 15 cases and with Geant4 in 9 cases. Thus, neither code demonstrated an absolute advantage for all media and radiation types. However, according to the combined set of criteria used, OpenMC provided more consistent agreement with the experimental spectra. Therefore, the OpenMC results were adopted as the input spectral data for the subsequent stages of the calculations (Fig. 1).

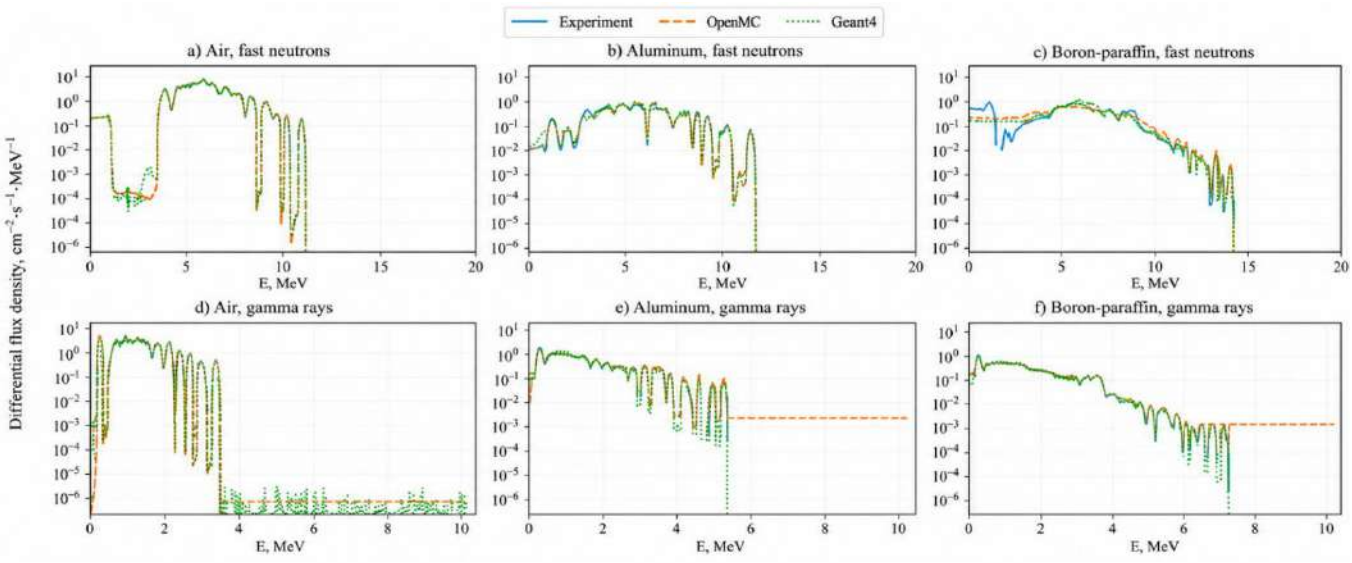

Figure 1. Experimental neutron–gamma spectra and those calculated using OpenMC and Geant4 in the investigated media. The energy scale is linear, and the flux-density scale is logarithmic.

The results showed that the degree of agreement between the calculated and experimental spectra depends on the type of medium, the energy region, and the selected evaluation criterion. OpenMC yielded a lower NRMSE in five of the six cases considered and reproduced the spectra in the air geometry most accurately, whereas Geant4 provided a better description of fast neutrons behind aluminum and of certain features of the energy redistribution of gamma rays in the aluminum and boron–paraffin media. The observed differences may be attributed to specific features of the particle-transport physics models and the nuclear-data libraries used. Based on the combined set of criteria, the OpenMC results were adopted as the input spectral data for subsequent calculations. Since the experimental spectra were used in the reconstruction of the source, the obtained agreement should be interpreted as a verification of spectral consistency by means of reprojection rather than as an independent absolute validation.

NUCLEAR STRUCTURE INVESTIGATION BY LASER SPECTROSCOPY METHODS AT FLNR JINR

Zemlyanoy S.G., Myshinsky G.V., Zhemenik V.I.

Joint Institute for Nuclear Research, Dubna, Russian Federation

The laser spectroscopy method is a powerful tool for investigation of nuclear structure. It allows us to determine such important nuclear characteristics as nuclear size and shape via root mean square charge radii, electromagnetic moments, parameters of deformation, and spins of nuclei. This contribution presents some interesting results, obtained using the laser spectroscopy during last years by our group in FLNR JINR, and in collaborations with our colleagues from CERN, Manchester, Juvaskyla and Leuven Universities at CERN (Switzerland) and Juvaskyla (Finland). For these investigations, we have used laser fluorescence spectroscopy in orthogonal beams, collinear laser spectroscopy with gas cell and resonance laser ionization with hot cavity.

The future plans are discussed.

DEVELOPMENT OF A LOW-COST MULTICHANNEL SPECTROMETER BASED ON THE DYNAMIC TIME-OVER-THRESHOLD METHOD

Temirzhanov A.[1,2], Zholdybayev T.[1], Sadykov B.[1,2], Ussabayeva G.[1,3], Duisebayev B.[1], Issatov A.[1,4]

[1]*Institute of Nuclear Physics, Almaty, Kazakhstan*
[2]*Satbayev University, Almaty, Kazakhstan*
[3]*KazNPU named after Abay, Almaty, Kazakhstan*
[4]*Joint Institute for Nuclear Research, Dubna, Russian Federation*

A low-cost digital spectrometer based on the Dynamic Time-over-Threshold (DTOT) method was developed for radiation detection and spectrometric applications [1,2]. The main objective of the work was to design a compact and scalable measurement architecture that could be extended to systems with a large number of detector channels, including multichannel gamma-ray detectors and ^{3}He neutron-counter arrays.

In conventional digital spectrometers, pulse amplitudes are measured using analog-to-digital converters, waveform buffers, and digital signal-processing algorithms. Although this approach provides high measurement accuracy, its implementation in multichannel systems can considerably increase hardware complexity, power consumption, data-transfer requirements, and total system cost. In the proposed DTOT approach, the amplitude of the detector pulse is converted into a time interval by comparing a shaped analog signal with a dynamically varying threshold. The resulting digital pulse duration is measured directly by a microcontroller hardware timer.

The experimental spectrometer consisted of a scintillation detector coupled to a silicon photomultiplier, a CR–RC shaping circuit with a time constant of 1.8 μs, a TLV3201 high-speed comparator, a dynamic-threshold circuit, and an STM32F411 microcontroller. The timer operated at 96 MHz, providing a temporal resolution of approximately 10.4 ns. The measured DTOT values were transmitted to an ESP32 module, which performed histogram accumulation, energy calibration, data storage, and real-time spectrum visualization through a web interface.

The system was experimentally evaluated using ^{137}Cs, ^{22}Na, and ^{226}Ra gamma-ray sources. The recorded spectra showed distinguishable photopeaks and characteristic spectral regions. For a 100 kBq ^{137}Cs source, the photopeak position remained stable within 2.273–2.294 μs at source-to-detector distances from 5 to 40 cm, confirming the stability of the amplitude-to-time conversion.

The proposed DTOT architecture eliminates the need for a separate high-speed ADC in each measurement channel. Therefore, it represents a promising low-cost solution for scalable multichannel radiation-monitoring systems, particularly detector arrays based on scintillation detectors or ^{3}He neutron counters.

Keywords: Dynamic Time-over-Threshold, DTOT, multichannel spectrometer, low-cost instrumentation, gamma-ray spectroscopy, neutron counter, STM32, radiation detection.

Acknowledgements. The work was carried out within the framework of program-targeted funding of scientific and technical programs of the Science Committee of the Ministry of Science and Higher Education of the Republic of Kazakhstan, grant No. BR34637238.

References:

1. Holík, M., Ahmadov, F., Sadigov, A., Pavlas, O., Urban, O., Ahmadov, G., ... & Filgas, R. (2024). Study of dynamic time over threshold (DTOT) method for application in spectroscopy

signal analysis toward a low-complexity front-end electronics with high spectroscopy resolution and wide energy range. *IEEE Transactions on Nuclear Science*, *72*(3), 749-756.
2. Orita, T., Shimazoe, K., & Takahashi, H. (2015). The dynamic time-over-threshold method for multi-channel APD based gamma-ray detectors. *Nuclear Instruments and Methods in Physics Research Section A: Accelerators, Spectrometers, Detectors and Associated Equipment*, *775*, 154-161.

STUDY OF FUSION OF Ca ISOTOPES with ^{208}Pb AT THE ENERGIES AROUND THE COULOMB BARRIER

Rachkov V.A.[1,2], Karpov A.V.[1,2] , Kozulin E.M.[1] , Knyazheva G.N.[1,2], Bogachev A.A.[1]
[1]*Joint Institute for Nuclear Research, Dubna, Russian Federation*
[2]*Dubna State University, Dubna, Russian Federation*

Recently, Yu. Ts. Oganesyan proposed to study the influence of structural effects in calcium isotopes on the reaction mechanism, fusion-fission and quasi-fission cross sections, as well as the characteristics of reaction fragments. For this purpose, the reactions ^{40,42,44,48}Ca + ^{208}Pb were chosen. Experiments ^{40,48}Ca + ^{208}Pb were carried out at the U-400 accelerator in FLNR JINR. The obtained data are currently being analyzed.

The present work is dedicated to theoretical studies of fusion mechanisms in ^{40,42,44,48}Ca+^{208}Pb at energies around the Coulomb barrier. The corresponding calculations of the fusion (capture) cross section have been performed within the standard quantum coupled-channels (QCC) approach (accounting for vibrational and rotational excitations) using the empirical model for additional channels of neutron rearrangement. The partial penetration probability though the multidimensional potential barrier is obtained in the QCC calculations. The probability of transfer up to four neutrons to states within a certain Q-window is estimated in semiclassical approximation [A.V.Karpov, V.A.Rachkov, and V.V.Samarin, Physical Review, C92 (2015) 064603]. The results are compared with the experimental data. The predictions of the fusion (capture) cross section for ^{42,44}Ca+^{208}Pb at energies around the Coulomb barrier have been also presented.

ALPHA-DECAY ENERGY NEW SUPERHEAVY NUCLEI

Nurmukhamedov A.M.
Tashkent State Medical University, Republic of Uzbekistan

In the present study, a new method is proposed for calculating the alpha-decay energies of new superheavy nuclei within the scheme of restored Wigner’s spin–isospin *SU*(4)-symmetry. The results of these calculations are compared with experimental data and with the results obtained by modern theoretical methods. The alpha-decay energies of a number of isotopes from alpha-chains are predicted for $Z = 120$ nuclei that are being searched currently.

The energy of alpha particles recorded by detectors enables to find the alpha-decay energy of nuclei. The alpha-decay energy Q_α is determined with allowance for the recoil effect in terms of the mass difference between nuclei. The respective expression has the form [1]

$$Q_\alpha(Z, N) = M_1(^{A}_{Z}X) - M_2(^{A-4}_{Z-2}Y) - M_\alpha + E_1 - E_2, \quad (1)$$

where $M_1(^{A}_{Z}X)$ and $M_2(^{A-4}_{Z-2}Y)$ are the ground-state masses of the parent and daughter nuclei, respectively; M_α is the alpha-particle mass; and E_1 and E_2 are the excited-state energies of the parent and daughter nuclei, respectively.

Table 1. Alpha-decay energies Q_α (in MeV units) of superheavy nuclei. The experimental values of Q_α, EDF, SHF, MMM, and SESM predictions were taken from Ref. [6].

Parent nucleus	Experiment [6]	According toWigner	EDF [7]	SHF [8]	MMM [9]	SESM [10]
^{294}118	11.81(0.06)	11.35	11.45	11.40	12.11	11.55
^{290}Lv	10.99(0.08)	10.95	10.81	10.70	11.08	11.42
^{286}Fl	10.37(0.06)	10.53	10.06	10.30	10.86	11.11
^{294}117	11.20(0.04)	10.79	10.98	11.10	11.43	10.90
^{290}115	10.45(0.04)	10.38	10.24	10.40	10.65	10.80
^{286}113	9.79(0.05)	9.96	9.31	9.40	9.98	10.50
^{282}Rg	9.18(0.03)	9.54	9.16	9.10	9.85	10.00
^{278}Mt	9.59(0.03)	9.12	9.76	9.45	9.55	9.49
^{274}Bh	8.97(0.03)	8.69	9.35	8.77	8.83	8.88
^{293}117	11.18(0.05)	10.97	11.07	11.00	11.53	11.23
^{289}115	10.52(0.05)	10.56	10.58	10.40	10.74	11.05
^{285}113	10.03(0.05)	10.14	9.33	9.50	10.21	10.69
^{291}Lv	10.89(0.07)	10.77	10.56	10.80	10.91	11.17
^{287}Fl	10.16(0.06)	10.35	9.81	9.80	10.56	10.89
^{283}Cn	9.67(0.06)	9.94	9.66	9.60	10.16	10.46
^{279}Ds	9.84(0.06)	9.51	10.35	10.08	10.24	9.93
^{275}Hs	9.44(0.06)	9.09	10.11	9.60	9.41	9.33
^{271}Sg	8.67(0.08)	8.66	8.57	8.20	8.71	8.70
^{288}115	10.61(0.06)	10.73	10.72	10.70	10.95	11.27
^{284}113	10.15(0.06)	10.32	9.35	9.50	10.68	10.87
^{280}Rg	9.87(0.06)	9.90	10.18	10.20	10.77	10.36
^{276}Mt	9.85(0.06)	9.48	10.19	9.85	10.09	9.77
^{272}Bh	9.02(0.06)	9.05	8.95	8.66	9.08	9.13
Root-mean-square deviation		0.26	0.44	0.35	0.44	0.58

Presently, it is used in the form [2]

$$M_{\text{nucl}}(A,Z) = a(A) + b(A)C_2 + E_{\text{Coul}}(A,Z) + E_{sl}(Z,N), \quad (2)$$

where $M_{\text{nucl}}(A,Z)$ is the mass of the nucleus (not of the atom) being considered, $a(A)$ and $b(A)$ are empirical Wigner's functions, $E_{\text{Coul}}(A,Z)$ is the Coulomb energy of the nucleus, $E_{sl}(Z,N)$ is the contribution of spin–orbit interaction to the ground-state mass of the nucleus; and C_2 is the Casimir operator of the $SU(4)$ algebra [3].

The explicit form of the empirical functions $a(A)$ and $b(A)$ in expression (4) is [4]

$$a(A)/A = a_1\exp(a_2A) + a_3\exp(a_4A) + a_5\exp(a_6A) + a_7\exp(a_8A), \quad (3)$$

$$b(A) = b_1\exp(b_2A) + b_3\exp(b_4A). \quad (4)$$

In the region of superheavy nuclei, the contribution of spin–orbit interaction to the nuclear mass is small (about 100 keV) because of the restoration of Wigner's symmetry. Therefore, we calculate the alpha-decay energy Q_α by formula (1) at $E_{sl}(Z,N) = 0$, which corresponds to restored Wigner's symmetry. Table 1 shows that our method based on the Wigner mass formula has the highest predictive power for calculating the alpha decay energy Q_α of superheavy nuclei.

Table 2 lists the alpha decay energies calculated as predictions for a series of superheavy nuclei from alpha chains for five elements starting from a $Z=120$ element with the mass number $A=300$ to $A=304$. At the present time searches for a hypothetical nucleus with charge number 120 are under way [11].

Table 2. Alpha-decay energy Q_α (in MeV units) of superheavy nuclei from the alpha chain starting from $Z=120$ according to the calculation by Wigner's mass formula.

Nuclide	Q_α	Nuclide	Q_α	Nuclide	Q_α	Nuclide	Q_α	Nuclide	Q_α
$^{300}120$	11.42	$^{301}120$	11.24	$^{302}120$	11.07	$^{303}120$	10.89	$^{304}120$	10.73
$^{296}118$	11.01	$^{297}118$	19.83	$^{298}118$	10.66	$^{299}118$	10.48	$^{300}118$	10.31
^{292}Lv	10.60	^{293}Lv	10.72	^{294}Lv	10.25	^{295}Lv	10.07	^{296}Lv	9.89
^{288}Fl	10.18	^{289}Fl	10.00	^{290}Fl	9.83	^{291}Fl	9.65	^{292}Fl	9.47
^{284}Cn	9.76	^{285}Cn	9.58	^{286}Cn	9.41	^{287}Cn	9.22	^{288}Cn	9.05

References:

1. S.G.Kadmenskii and V.I.Furman, *Alpha Decay and Related Nuclear Reactions* (Energoatomizdat, Moscow, 1985) [in Russian].
2. A.M.Nurmukhamedov, Phys. At. Nucl. **72**, 1489 (2009).
3. Yu.V. Gaponov, N.B. Shulgina, and D. M. Vladimirov, Nucl. Phys. A **391**, 93 (1982).
4. A.M.Nurmukhamedov, Phys. At. Nucl. **72**, 401 (2009).
5. A.M.Nurmukhamedov, Mod. Phys. Lett. **A31**, 1650145, (2016), DOI: 10.1142/S0217732316501455.
6. S.V.Tolokonnikov, Yu.S. Lyutostansky, and E.E. Saperstein, Phys. At, Nucl. **76**, 708, (2013).
7. S.V.Tolokonnikov *et al.*, Eur.Phys. J.A **53**, 33 (2017), DOI: 10.1140/epja/i2017-12220-y.
8. D.Vautherin and D.M. Brink, Phiz.Rev. C 5, 626 (1972).
9. P. Moeller, J.R.Nix, W.D.Myers, and W.J.Swiatecki, At. Data Nucl. Data Tables **59**, 185 (1995).
10. S.Liran, A.Marinov, and N.Zeldes, Phys. Rev. C **62**, 047301 (2000).
11. Yu.Ts.Oganessian *et al*., Phys.Rev. C **79**, 024603 (2009).

PRECISE MASS CALCULATIONS FOR ATOMIC NUCLEI OF ISOSPIN $T_z=51/2, 26, 53/2, 55/2, 28$, and $57/2$

Nurmukhamedov A.M.

Tashkent State Medical University, Republic of Uzbekistan

The present article gives an account of a method for calculating the masses of atomic nuclei including the contribution of the spin–orbit interaction to the nuclear mass. In the mass formula used, the contribution of spin–orbit interaction to the nuclide mass is a correction. The objective of the present study is to simulate this correction by means of existing mathematical methods with the aim of attaining the best agreement of the result of respective calculations with experimental data. These calculations are performed for nuclei with restored spin–isospin *SU*(4) symmetry that are characterized by isospin values in the range of $51/2 \le T_z \le 57/2$, and for which the contribution of spin–orbit interaction to the nuclide mass is determined on the basis of experimental data on nuclear masses [1]. The calculations of experimental values of the spin–orbit interaction contribution to

nuclear masses $E_{\text{sl, exp}}$, were described in detail in [1] and revised with allowance for the mass data from [2].

Figure 2 shows $E_{\text{sl}}(Z,N)$ as a function of the mass number A for nuclei with the isospin $T_z = 51/2, 26, 53/2, 55/2, 28$, and $57/2$ from the region under consideration.

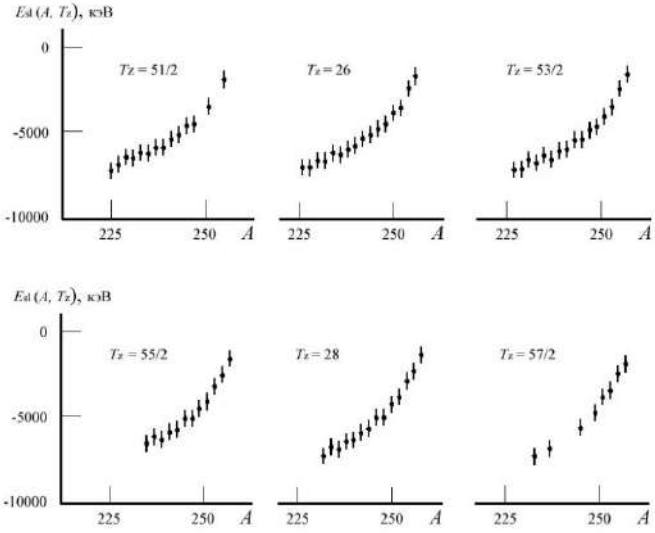

Figure 1. $E_{\text{sl}}(Z,N)$ as a function of the mass number A for nuclei with the isospin $T_z = 51/2, 26, 53/2, 55/2, 28$, and 57/2 from the region under consideration.

The dependence of $Esl(Z,N)$ on the mass number A can be represented as a polynomial of the form [3]

$$E_{\text{sl}}(Z,N) = q_0 P_0(A) + q_1 P_1(A) + q_2 P_2(A) + \ldots + q_n P_n(A) = \sum_{j=0}^{n} q_j P_j(A). \qquad (1)$$

Here, $P_0(A), P_1(A), P_2(A), \ldots, P_n(A)$ are Chebyshev orthogonal polynomials on the set of mass number points $A_1, A_2, A_3, \ldots, A_N$ with a statistical $w(A)$ ($w_k = w(A_k) = 1/dE^2_{\text{sl},k} > 0$), where $dE_{\text{sl},k}$ is the error in $E_{\text{sl},k}$. The parameters in expression (1) are calculated according to the formula

$$q_j = \sum_{k=1}^{N} E_{\text{sl},k} P_j(A_k) w_k \Big/ \sum_{k=1}^{N} P_j^2(A_k) w_k \qquad (j = 0, 1, 2, \ldots, n). \qquad (2)$$

The experimental values of the contribution of the spin–orbit interaction to nuclear masses $E_{\text{sl}}(Z,N)$, were processed in the present study according to the above procedure for describing data in terms of Chebyshev polynomials. Our analysis shows that it is sufficient to restrict oneself to the Chebyshev polynomial of the degree $j = 3$.

In Table 1, the experimental values of the parameters q_0, q_1, q_2, and q_3 are given along with their counterparts calculated according to the above method based on representing the spin–orbit interaction contribution to the mass of nuclei with isospins $T_z = 51/2, 26, 53/2, 55/2, 28$, and $T_z = 57/2$ in terms of Chebyshev orthogonal polynomials. The errors in the parameters are indicated parenthetically. An analysis of the data in Table 1 shows that the parameters q_0, q_1, q_2, and q_3 depend on the isospin T_z.

Table 1. Calculated and experimental values of the parameters $q_0, q_1, q_2,$ and q_3 (in keV units).

T_z	q_0		q_1		q_2		q_3	
	Exp.	Calcul.	Exp.	Calcul.	Exp.	Calcul.	Exp.	Calcul.
51/2	−5557(56)	−5559(92)	152(6)	153(6)	4.5(0.7)	4.6(0.6)	0.25(0.06)	0.26(0.04)
26	−5352(50)	−5349(58)	164(5)	162(4)	5.4(0.7)	5.1(0.4)	0.23(0.06)	0.23(0.03)
53/2	−5207(61)	−5211(65)	167(7)	171(4)	6.1(0.8)	6.5(0.4)	0.29(0.07)	0.29(0.04)
55/2	−4824(48)	−4824(62)	213(7)	211(4)	9.3(1.1)	9.1(0.5)	0.34(0.17)	0.34(0.07)
28	−4411(46)	−4409(55)	253(7)	255(5)	9.1(1.2)	9.1(0.6)	0.18(0.25)	0.12(0.13)
57/2	−3733(60)	−3734(95)	323(15)	222(10)	6.8(4.0)	7.3(1.4)	−1,21(1.48)	−0.39(0.28)

The dependence of the parameters $q_0, q_1, q_2,$ and q_3 on the isospin T_z. can be expressed in terms of Chebyshev polynomials as

$$q_j(T_z) = g_{0,j}P_0(T_z) + g_{1,j}P_1(T_z) + g_{2,j}P_2(T_z), \quad (3)$$

where $g_{0,j} \div g_{2,j}$ (j = 0, 1, 2, 3) are constants and $P_0(T_z)$, $P_1(T_z)$, $P_2(T_z)$ are Chebyshev orthogonal polynomials in the isospin T_z. The numerical values of the constants $g_{0,j} \div g_{2,j}$ are given in Table 2. The numbers in parentheses are the errors in the calculated parameters. The numerical values of the parameters q_j can be reconstructed by employing the values of the constants $g_{0,j} \div g_{2,j}$. The reconstructed values of q_j are listed in column "Calcul" of Table 1.

Table 2. Numerical values of the parameters $g_{0,j} \div g_{2,j}$ (the errors are given parenthetically)

j	$g_{0,j}$	$g_{1,j}$	$g_{2,j}$
0	−4843(55)	566(50)	186(54)
1	185(2)	42(3)	22(3)
2	6.0(0.4)	2.0(0.5)	−0.1(0.6)
3	0.27(0.03)	0.03(0.05)	−0.03(0.07)

In all, there are 74 experimental mass values. The root-mean square deviations of the calculated results from the experimental data is $\sigma = 140$ keV. The nuclear mass values calculated here agree with experimental data to a high degree of precision ($\sigma = 140$ keV). This gives grounds to state that the proposed method for calculating the mass excess for atomic nuclei on the basis of spin–isospin *SU*(4) symmetry of strong interaction is quite reliable. A simulation of the contribution of spin–orbit interaction to nuclear masses for nuclides with restored symmetry makes it possible to calculate nuclear masses with a record precision.

References:

1. A.M.Nurmukhamedov, Phys. Atom. Nucl. **72**, 401 (2009).
2. M.Wang, G.Audi, F.G.Kondev, W. J.Huang, S.Naimi, and X.Xu, Chin. Phys. C **41**, 030003 (2017).
3. L.Z. Rumshiskii, *Mathematical Processing of Experimental Results* (Nauka,Moscow, 1971) [in Russian].

MONTE CARLO SIMULATION OF INDUCED ACTIVATION OF ACCELERATOR COMPONENTS FOR THE U-400R AND DC-280 CYCLOTRONS

Kabytayeva R. K.[1, 2, 3], Teterev Yu.G.[1], Mitrofanov S.V.[1], Kalagin I.V.[1], Gulbekyan G.G.[1], Kuthudzhin D.V.[1]

[1]*Joint Institute for Nuclear Research, Dubna, Russian Federation*
[2]*Gumilyov Eurasian National University, Astana, Kazakhstan*
[3]*The Institute of Nuclear Physics, Almaty, Kazakhstan*

Beam losses in heavy-ion accelerators (≤30 MeV/nucleon) induce radioactivity in structural components, posing radiation hazards to personnel [1,2]. For the DC-280 and U-400R cyclotrons operating with a ^{48}Ca beam at 6 MeV/nucleon, quantitative assessment of activation is essential for maintenance planning and material selection. This work presents FLUKA [3] simulations for two key components: a tungsten electrostatic deflector (DC-280) and magnetic channel housings (U-400R) made of aluminium alloy D16 and copper M1. The methodology is supported by previous activation studies [4,5] and inter-code comparisons [6,7]. Beam parameters correspond to the operating conditions of the accelerators [8].

The FLUKA Monte Carlo code (versions 2025.1.0/2025.1.1) was used [3]. Deflector geometry: tungsten plate 0.5×10×380 mm. Magnetic channel: straight section 670 mm. Irradiation conditions: deflector – 1 pμA for 1 month; magnetic channel – 1000 W beam power, 10% losses (100 W) for 6000 h. Cooling times: 0, 1, 12, 36 h and 10 days.

Tungsten electrostatic deflector results. On the deflector surface, the ambient dose equivalent rate after 1 h is 77 mSv/h, dropping to 30.3 mSv/h at 36 h and 13.5 mSv/h at 10 days. At 0.5 m, the values are 39.8, 22.2 and 11 μSv/h, respectively. A 5 mm lead shield reduces the dose by 20-25% in the first hours but only by ~7% after 10 days. Major radionuclides (>10^7 Bq): ^{47}Sc (4.1×10^8), ^{105}Rh (1.8×10^8), ^{111}Ag (1.8×10^8), ^{109}Pd (1.4×10^8), ^{173}Ta (6.8×10^7), and ^{181}Re (2.0×10^7) Bq. Long-lived contributors: ^{46}Sc (83.8 d, 1.5×10^6 Bq), ^{179}Ta (1.82 yr), and $^{181-186}$Re. Notably, ^{54}Mn and ^{57}Co – typical for proton activation – are not produced significantly under ^{48}Ca irradiation. Cooling of at least 36 h and thicker shielding (10-15 mm) or remote handling are recommended.

Magnetic channel results. Total activities after 1 h cooling are close: 5.147×10^8 Bq (D16) vs. 4.948×10^8 Bq (Cu), but isotope distributions differ significantly (consistent with fragmentation mechanisms [3,5]). Cu peaks at A=100-110 (Rh, Pd, Ag, Cd); D16 at A=60-75 (Ga, Ge, Zn, As) and A=20-50 (Na, Sc, Ca, K). Key gamma emitters: D16 – ^{24}Na (15 h), ^{47}Sc (3.35 d), ^{46}Sc (83.8 d), ^{54}Mn (312 d), ^{22}Na (2.6 yr, minor); Cu – ^{64}Cu (12.7 h, early), ^{60}Co (5.27 yr, long-term), ^{58}Co (70.8 d) [3,6]. These findings are consistent with previous studies on Al and Cu activation [1,3,6,7]. The ambient dose equivalent rate at 50 cm decreases from 214.72 to 22.55 μSv/h (a factor of 9.5) for D16 and from 176.99 to 12.33 μSv/h (a factor of 14) for Cu. The absence of ^{60}Co in D16 makes it preferable for long-term disposal, while Cu gives lower dose for short-term maintenance (≤10 days).

Table 1. Photon flux and residual dose rate at 50 cm from the channel

Cooling time	Photon flux D16 (photon cm^{-2} s^{-1})	Photon flux (photon cm^{-2} s^{-1})	Ratio D16/Cu	Dose D16 (μSv/h)	Dose Cu (μSv/h)	Ratio D16/Cu
0 h	19525.35	16402.58	1.19	214.72	176.99	1.21
1 h	12671.77	6608.50	1.92	134.06	70.98	1.89
12 h	8196.98	3392.38	2.42	84.46	36.94	2.29
36 h	5793.62	2811.78	2.06	55.73	31.13	1.79
10 d	2285.72	1304.56	1.75	22.55	12.33	1.83

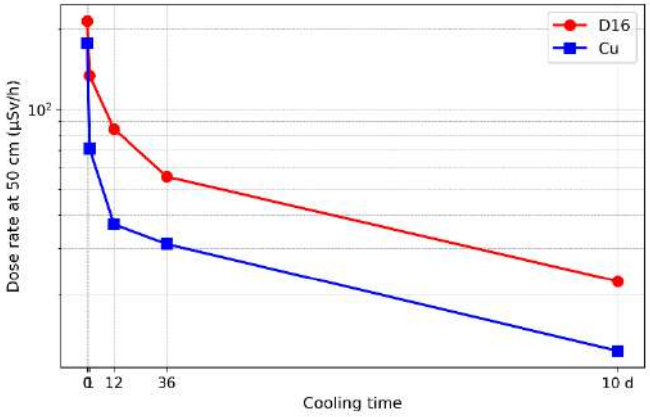

Figure 1. Dose rate at 50 cm from the magnetic channel as a function of cooling time for D16 and Cu. The plot shows that the dose from D16 is always higher, but the decay is slower for Cu due to the presence of ^{60}Co.

The dose from D16 exceeds that from Cu at all cooling times (ratio 1.21-2.29) because of lower self-absorption in aluminium and slightly higher total activity. However, Cu contains long-lived ^{60}Co, which makes disposal problematic; D16 lacks ^{60}Co and is therefore better for long-term waste management. The choice of material depends on the maintenance strategy: Cu is preferable for short-term access (≤10 days), while D16 is better for long-term storage and decommissioning [1,2]. The results confirm the applicability of FLUKA for activation modelling of structural materials and highlight the need for accurate elemental composition data [5,7].

The tungsten deflector requires a cooling time of at least 36 h and effective shielding. For the magnetic channel, D16 and Cu show similar total activities but very different isotope compositions and dose decay dynamics. These results provide practical guidance for radiation protection and material selection at the DC-280 and U-400R cyclotrons.

The authors thank the U-400R and DC-280 project teams for providing the technical specifications, and the HybriLIT heterogeneous computing platform (LIT, JINR) for computational resources.

References:

1. I. Strašík, E. Mustafin, M. Pavlovič, Phys. Rev. ST Accel. Beams 13, 071004 (2010).
2. I. Strašík, E. Mustafin, M. Pavlovič, Proc. HB2010, Morschach, Switzerland (2010).
3. A. Ferrari et al., FLUKA: a multi-particle transport code, CERN-2005-10 (2005).
4. V. Chetvertkova et al., Nucl. Instrum. Methods Phys. Res. B 269, 1336 (2011).
5. P. Katrík et al., Matter Radiat. Extremes 4, 055403 (2019).
6. D. Bozzato et al., Radiat. Phys. Chem. 236, 112879 (2025).
7. V. Chetvertkova, Verification of Monte Carlo transport codes by activation experiments, Dissertation, Frankfurt am Main (2012).
8. Yu.G. Teterev, R.K. Kabytayeva et al., Nucl. Instrum. Methods B 537, 133 (2023).

MAGNETIC PROPERTIES OF VIBRATIONAL STATES OF ^{182,184}W ISOTOPES

Usmanov P.N.[1], Izosimov I.N.[2]
[1]*Namangan State Technical University, Namangan, Uzbekistan*
[2]*Joint Institute for Nuclear Research, Dubna, Russian Federation*

In the works [1, 2], the energy and electrical characteristics of states with positive parity ^{182,184}W nuclei were studied within the framework of the phenomenological model [3-5]. At the same time, the Coriolis mixture of states from low-lying rotational bands with bands possessing certain quantum characteristics $K^{\pi}=1^{+}$ was taken into account.

In this work, we continued to study properties of the rotational states of ^{182,184}W nuclei. Using the wave functions obtained in Refs. [1, 2], we calculated the reduced probabilities of M1-transitions and other magnetic characteristics of excited states. Specifically, we investigated the influence of $K^{\pi}=1^{+}$ band levels on the magnetic characteristics of low-lying states.

The table presents the calculated values of the multipole mixture coefficients δ for transitions from the γ- and β-band states of the ^{182}W nucleus. These data are compared with the experimental results [6,7]. The table demonstrates that the model qualitatively describes M1-transitions from both γ- and β-bands.

Table. Multipole mixture coefficients δ for transitions from the γ- and β-band states of the ^{182}W nucleus.

I_iK_i	I_fK_f	E_i *MeV*	E^{γ} *MeV*	δ [6] *exp.*	δ [7] *exp.*	δ *theor.*
2^+2_1	2^+0_1	1,221	1,221	30^{+6}_{-4}	21^{+92}_{-9}	5,3
3^+2_1	2^+0_1	1,3311	1,231	-33^{+6}_{-9}	-72^{+28}_{-120}	6,7
3^+2_1	4^+0_1	1,3311	1,0017	-8.9^{+21}_{-18}	$>+22, <-35$	4,8
3^+2_1	2^+2_1	1,3311	0,1001	—	—	0,53
4^+2_1	4^+0_1	1,4428	1,1134	$+5.6^{+13}_{-10}$	4.7^{+6}_{-5}	2,4
5^+2_1	4^+0_1	1,6235	1,2941	>30	$>+30, <-60$	5,1
5^+2_1	6^+0_1	1,6235	0,9431	—	—	3,2
5^+2_1	4^+2_1	1,6235	0,1133	+0.36(1)	+0.36(3)	+0.35
6^+2_1	6^+0_1	1,769	1,0886	0.4(2)	—	1,6
8^+2_1	8^+0_1	2,180	1,0357	—	—	1,2
2^+0_2	2^+0_1	1,2574	1,1573	-9^{+3}_{-6}	—	−4,5
4^+0_2	4^+0_1	1,5102	1,1808	−2.08(10)	—	−9,9

References:

1. Усманов П.Н., Юсупов Э.К., Коржавов М.Ж. // Uzbek Journal Of Physics, Vol.27 No24 p.1. . https://doi.org/10.52304/.v27i4.609S1062873826700577
2. Усманов П.Н., Изосимов И.Н., Юсупов Э.К., Коржавов М.Ж. // Изв. РАН, т.90, № 6, с.1326. (Usmanov P.N., Vdovin A.I.,Yusupov E.K. Bull. Russs. Acad. Sci.:Phys. 2026. V.90. No 6.P. 890.
1. https://doi.org/10.3103/S1062873820080298.)

2. Usmanov P. N., Mikhailov I. N. // Phys. Part. Nucl. 1997. V. 28. No 4. P. 348. https://doi.org/10.1134/1.953044.
3. Usmanov P.N., Vdovin A.I., Yusupov E.K., Salikhbaev U. S., // Phys. Part. Nucl. Letters. 2019. V. 19. No 6. P. 706.
4. https://doi.org/10.1134/S1547477119060530.
5. Usmanov P. N., Vdovin A. I., Yusupov E. K. Bull. Russ. Acad. Sci.: Phys. 2020. V. 84. No 8. P. 968. https://doi.org/10.3103/S1062873820080298.
6. Coral M. Baglin // Nucl. Data Sheets, 2010. V. 111 P. 275. https://doi.org/10.1016/j.nds.2010.01.001.
7. Spanhoff R., Canty M.J., Postma H., Mennenga G. // Phys. Rev. C. 1980. V.21. P.361.

ENERGY CHARACTERISTICS OF LOW-LYING ROTATIONAL BANDS OF ISOTOPES ^{182,184}W

Usmanov P.N.[1], Korjavov M.J.[2], Yusupov E.K.[1]
[1]*Namangan State Technical University, Namangan, Uzbekistan*
[2]*Karshi State Technical University, Karshi, Uzbekistan*

The energies and probabilities of $E2-$transitions for positive-parity states of ^{182,184}W nuclei were investigated within the framework of the phenomenological model [1-3], which examines the Coriolis mixing of low-lying rotational band states. Within the framework of perturbation theory, taking into account the Coriolis interaction $(\Delta K=1)$ of $\gamma-$ and $K_\nu^\pi=1_\nu^+$ bands, an analytical formula was obtained, that allows for the numerical determination of parameter values ω_2 and $\langle 1_\nu|j_x|\gamma\rangle$ using experimental data for the energy of states with odd spins of $\gamma-$band.

The energy spectrum, state structure of the ground $\beta-$ and $\gamma-$ vibrational bands, probabilities of intraband and interband E2-transitions, and ratios of the probabilities of $E2-$ transitions from $\gamma-$ vibrational band levels are calculated. The possibility of studying mixing effects using the same inertial parameters for all mixing adiabatic bands is demonstrated which is impossible without taking into account the Coriolis interaction.

In both ^{182,184}W nuclei, a mixing of the states of the $\beta-$ and $\gamma-$ bands is more noticeable. However, in the ^{182}W isotope, even-odd splitting of the energy and structural characteristics of states in the $\gamma-$ band are more pronounced. This is due to the proximity of the $\beta-$ and $\gamma-$ bands in the given nucleus. This fact is manifested in the nonadiabaticity of the electromagnetic characteristics of states of $\beta-$ and $\gamma-$ bands.

The calculated values of energy, probabilities $E2-$transitions, and their ratios are in good agreement with experimental data. Experimental data on R ratios for transitions from both even and odd states of the $\gamma-$band can be described within the proposed model using a single set of parameters Q_0 and m_K. The analysis showed that the nonadiabaticity manifested in the energy spectrum and electromagnetic characteristics is associated with the strong mixing of the $\beta-$and $\gamma-$ band levels due to the proximity of their head levels. The results of our research are published in the following works [4, 5].

Tables 1 and 2 present the energy characteristics of the rotational states of the ground (gr), $\beta-$, and $\gamma-$bands of the ^{182,184}W isotopes in comparison with experimental data [6,7].

Energy characteristics of the rotational states of the ground (gr), β-, and γ-bands of the ^{182}W nucleus

I	$\omega_{rot}(I)$ MeV	$E_{rot}(I)$ MeV	$\varepsilon_{gr}(I)$ MeV	$E_{rot}(I)$, MeV		$\varepsilon_{\beta}(I)$ MeV	$E_{\beta}(I)$, MeV		$\varepsilon_{\gamma}(I)$ MeV	$E_{\gamma}(I)$, MeV	
				Exp.	Theor.		Exp.	Theor.		Exp.	Theor.
0	0,0	0,0	0,0	0,0	0,0	0,0	1,136	1,136	–	–	–
2	0,0813	0,100	- 0,001	0,100	0,099	1,157	1,257	1,257	1,139	1,221	1,239
3	0,1138	0,199	–	–	–	–	–	–	1,133	1,331	1,333
4	0,1451	0,330	- 0,003	0,329	0,327	1,155	1,510	1,485	1,116	1,443	1,446
5	0,1751	0,491	–	–	–	–	–	–	1,115	(1,624)	1,605
6	0,2038	0,681	- 0,006	0,682	0,675	1,155	–	1,837	1,083	(1,766)	1,764
7	0,2312	0,899	–	–	–	–	–	–	1,091	–	1,990
8	0,2573	1,144	- 0,010	1,145	1,134	1,155	–	2,298	1,045	2,180	2,189
9	0,2822	1,414	–	–	–	–	–	–	1,065	–	2,479
10	0,3060	1,709	- 0,014	1,712	1,695	1,155	–	2,863	1,005	–	2,714
11	0,3286	2,026	–	–	–	–	–	–	1,038	–	3,054
12	0,3503	2,366	- 0,011	2,373	2,345	1,155	–	3,521	–	–	–
14	0,3908	3,108	- 0,024	3,113	3,084	–	–	–	–	–	–
16	0,4280	3,928	- 0,030	3,910	3,898	–	–	–	–	–	–
18	0,4625	4,819	- 0,036	4,691	4,784	–	–	–	–	–	–
20	0,4945	5,777	- 0,042	5,429	5,735	–	–	–	–	–	–
22	0,5244	6,797	- 0,049	–	6,748	–	–	–	–	–	–
24	0,5526	7,874	- 0,055	–	7,819	–	–	–	–	–	–

Energy characteristics of the rotational states of the ground (gr), β-, and γ-bands of the ^{184}W nucleus

I	$\omega_{rot}(I)$ MeV	$E_{rot}(I)$ MeV	$\varepsilon_{gr}(I)$ MeV	$E_{rot}(I)$, MeV		$\varepsilon_{\beta}(I)$ MeV	$E_{\beta}(I)$, MeV		$\varepsilon_{\gamma}(I)$ MeV	$E_{\gamma}(I)$, MeV	
				Exp.	Theor.		Exp.	Theor.		Exp.	Theor.
0	0,0	0,0	0,0	0,0	0,0	0,0	1,002	1,002	–	–	–
2	0,0901	0,111	- 0,001	0,111	0,112	1,000	1,121	1,111	0,794	0,903	1,905
3	0,1257	0,221	–	–	–	–	–	–	0,780	1,006	1,001
4	0,1595	0,365	- 0,002	0,364	0,363	0,995	1,360	1,359	0,762	1,134	1,126
5	0,1917	0,541	–	–	–	–	–	–	0,747	1,294	1,285
6	0,2221	0,744	- 0,003	0,748	0,746	0,990	–	1,739	0,719	1,477	1,467
7	0,2508	0,986	–	–	–	–	–	–	0,701	–	1,687
8	0,2780	1,251	- 0,005	1,252	1,246	0,986	–	2,2375	0,670	1,925	1,921
9	0,3036	1,543	–	–	–	–	–	–	0,655	–	2,198
10	0,3279	1,859	- 0,008	1,861	1,851	0,984	–	2,844	0,621	2,472	2,479
11	0,3510	2,199	–	–	–	–	–	–	0,610	–	2,808
12	0,3728	2,561	- 0,010	2,557	2,551	0,982	–	3,543	0,572	3,109	3,133
13	0,3937	2,945	–	–	–	–	–	–	0,566	–	3,510
14	0,4136	3,349	- 0,014	3,319	3,335	0,980	–	4,329	0,525	–	3,874
15	0,4326	3,772	–	–	–	–	–	–	0,523	–	4,295
16	0,4508	4,214	- 0,017	4,117	4,196	0,979	–	5,193	0,481	–	4,695
17	0,4682	4,674	–	–	–	–	–	–	0,482	–	5,156
18	0,4850	5,151	- 0,022	–	5,129	0,979	–	6,129	0,440	–	5,590
19	0,5012	5,644	–	–	–	–	–	–	0,443	–	6,087
20	0,5167	6,153	- 0,026	–	6,127	0,978	–	7,131	0,441	–	6,554

References:

1. Усманов П.Н., Михайлов И.Н. // ЭЧАЯ. 1997. Т. 28. вып. 4. С. 887. (Usmanov P.N., Mikhailov I.N. // Phys. Part. Nucl. 1997. V. 28. No 4. P. 348. https://doi.org/ 10.1134/1.953044).

2. Усманов П.Н., Вдовин А.И., Юсупов Э.К. // Изв. РАН. Сер. физ. 2020. Т. 84. № 8. С. 1174. https://doi.org/10.31857/S0367676520080311 (Usmanov P. N., Vdovin A. I., Yusupov E. K. Bull. Russ. Acad. Sci.: Phys. 2020. V. 84. No 8. P. 968. https://doi.org/10.3103/S1062873820080298).
3. Усманов П.Н., Вдовин А.И., Нишоов А.Н. // Изв. РАН. Сер. физ. 2022. Т. 86. № 8. С. 1112. https://doi.org/10.31857/S0367676522080257 (Usmanov P. N., Vdovin A. I., Nishonov A.N. Bull. Russ. Acad. Sci.: Phys. 2022. V. 86. No 8. P. 918. https://doi.org/10.3103/S1062873822080251).
4. Усманов П.Н., Изосимов И.Н., Юсупов Э.К., Коржавов М.Ж. // Изв. РАН. Сер. физ. 2026. Т. 90. № 6. С. 1326. (Usmanov P. N., Izosimov I.N.,Yusupov E. K., Korjavov M.Zh Bull. Russ. Acad. Sci.: Phys. 2026. V. 90. No 6. P. 890. https://doi.org/10.1134/S1062873826700577).
5. Усманов П. Н., Юсупов Э.К., Коржавов М.Ж. // Uzbek Journal Of Physics, Vol.27 No24 p.1. https://doi.org/10.52304/.v27i4.609S1062873826700577
6. Balraj S. // Nucl. Data Sheets, 2015. V. 130 P. 21. https://doi.org/10.1016/j.nds.2015.11.002
7. Coral M.Baglin // Nucl. Data Sheets, 2010. V. 111 P. 275. https://doi.org/10.1016/j.nds.2010.01.001

FORMALISM OF NUCLEAR ROTATIONAL STRETCHING AND MOMENT OF INERTIA

Okhunov A.A.[1,2,3], Mohd’ Kh. M. Abu El Sheik[2]
[1]*International Islamic University Malaysia (IIUM), Kuala Lumpur, Malaysia*
[2]*Namangan Institute of Engineering and Technology, Namangan, Uzbekistan*
[3]*Department of Physics, Andijan State University, Andijan, Uzbekistan*

This study investigates the influence of the Coriolis effect on nuclear surface vibrations within the framework of a body-fixed coordinate system. We derive a formula demonstrating the direct dependence of the Coriolis interaction on the number of phonons in a given state. This dependency naturally explains why the Coriolis effect impacts the β and γ vibrational bands but has no effect on the ground-state band, which contains zero phonons. To validate this theoretical approach, it is applied to the ground-state, β, and γ bands of Erbium (Er) isotopes, showing good agreement with experimental data.

Formalism

1. **Angular Momentum Coupling**

In the body-fixed frame, the μ-component of the angular momentum for small surface vibrations is expressed in terms of the coupling of the spherical coordinates and their conjugate momenta as

$$L_{\mu}^{vib} = \sqrt{10}\sum_{\mu'\mu'} \langle 22\mu'\mu''|1\mu\rangle \alpha_{\mu'}\pi_{\mu}^{*} \tag{1}$$

In this framework, μ denotes the angular momentum components of a rank-1 tensor, whereas μ' and μ'' run over the components of quadrupole (rank-2) tensor. The coefficients $\langle 22\mu'\mu''|1\mu\rangle$ are Clebsch-Gordan coefficients.

2. **Decomposition of Nuclear Stretching**

Assuming the nucleus undergoes stretching due to its rotational motion, the $\alpha_{\mu'}$ can be linearly decomposed into two distinct components:

$$\alpha_{\mu'} = a_{\mu'}^{0} + \hat{a}_{\mu'} \tag{2}$$

where, $a^0_{\mu'}$ represents the stretching of the nucleus induced by rotation. It depends on the nuclear spin I. The terms $\hat{a}_{\mu'}$ is the small vibrations of the nuclear surface. The terms $\hat{a}_{\mu'}$ and their conjugate momenta $\pi^*_{\mu''}$ mentioned in Eq. 1 can be expressed in terms of creation and annihilation operators as:

$$\hat{a}_{\mu'} = \sqrt{\frac{\hbar}{2B\omega}}\left[b^+_{\mu'} + (-1)^{\mu'} b_{-\mu'}\right], \qquad \pi^*_{\mu''} = i\sqrt{\frac{\hbar B\omega}{2}}\left[(-1)^{\mu''} b^+_{-\mu''} + b_{-\mu''}\right]. \tag{3}$$

By substituting the decomposed stretching coordinates Eq. 2 back into the initial angular momentum expression Eq. 1, the system naturally separates into a static and a dynamic component:

$$\begin{aligned} L^{Static}_{\mu} &= -i\sqrt{10}\sum_{\mu',\mu''}\langle 22\mu'\mu''|1\mu\rangle a^0_{\mu'}\pi^*_{\mu''} \\ L^{Dynamic}_{\mu} &= -i\sqrt{10}\sum_{\mu',\mu''}\langle 22\mu'\mu''|1\mu\rangle \hat{a}_{\mu'}\pi^*_{\mu''} \end{aligned}. \tag{4}$$

3. Moment of Inertia via the Inglis Cranking Formula

To determine the moment of inertia we apply the standard Inglis cranking formula [1], which states as:

$$\Im = 2\sum_{K\neq K'}\frac{\left|\langle K|L_x|K'\rangle\right|^2}{E_K - E_{K'}}, \tag{5}$$

where, L_x is the Cartesian $x-$component of the angular momentum operator. It can be directly extracted from the spherical tensor basis components utilizing the standard transformation

$$L_x = -\frac{1}{2}(L_{+1} - L_{-1}). \tag{6}$$

Carrying out separately the static and the dynamic contributions of angular momentum defined earlier, we derive the respective moments of inertia [2–4]:

- Static Contribution: (7)
- Dynamic Contribution: $$\Im^{Dynamic} = 2\sum_{K'}\frac{\left|\langle 0|b_K L_x b^+_{K'}|0\rangle\right|^2}{E_{K'} - E_K} = \eta. \tag{8}$$

The total moment of inertia is simply the sum of these parts:

$$\Im_{total} = 3B\beta^2 + \eta. \tag{9}$$

4. Evaluation of the total moment of inertia

This formulated moment of inertia, coupled with the principle that the nucleus stretches to minimize its total energy (defined as the sum of rotational and stretching potential energies), yields the theoretical results for the beta and gamma vibrational bands.

The values of the energy levels of ground and β bands in keV

Nuclei	Bands	Results	Spin							
			0	2	4	6	8	10	12	14
$^{164}_{68}Er$	$gr-$	Exp. [5]	0.0	91.4	299.4	614.4	1024.6	1518.1	2082.8	2702.6
		Hu [6]	0.0	91.4	299.5	614.3	1023.2	1514.0	2075.7	2698.6
		Cal.	0.0	91.3	299.5	614.4	1022.9	1511.5	2068.4	2684.2
	$\beta-$	Exp. [5]	1246.1	1314.6	1469.7	1706.7	2068.9	2462.7	2733.3	3267.0
		Hu [6]	-	1332.7	1531.0	1832.2	2225.4	2699.5	3244.2	3850.6
		Cal.	1388.7	1459.9	1588.3	1758.6	1974.3	2239.4	2816.0	3290.8
$^{176}_{72}Hf$	$gr-$	Exp. [7]	0.0	88.3	290.2	596.8	997.7	1481.1	2034.7	2646.6
		Hu [6]	0.0	88.3	290.2	597.0	997.5	1480.8	2036.4	2655.3
		Cal.	0.0	88.3	290.2	596.8	996.4	1476.4	2025.8	2635

	$\beta-$	Exp. [7]	1149.9	1226.6	1390.2	1628.6	1932.7	2294.8	2646.6	-
		Hu [6]	-	1234.6	1428.6	1724.2	2111.7	2580.9	3122.1	3726.7
		Cal.	1149.1	1229.8	1386.6	1629.8	1960.8	2379.9	2887.0	3482.3

	The values of the energy levels of ground and $\gamma-$ bands in keV									
Nuclei	Bands	Results		Spin						
			2	3	4	5	6	7	8	9	10
$^{164}_{68}Er$	$\gamma-$	Exp. [5]	860.3	946.3	1058.5	1197.5	1358.7	1545.1	1744.9	1977.2	2184.3
		Hu [6]		948.2	1063.6	1205.2	1371.6	1561.2	1772.6	2004.3	2254.9
		Cal.	859.4	948.1	1059.3	1195.5	1357.7	1546.3	1761.4	2003.1	2271.6
$^{176}_{72}Hf$	$\gamma-$	Exp. [7]	1341.3	1445.8	1540.3	1727.8	1862	2106.5	2284.8	2318.7	-
		Hu [6]		1427.4	1540.7	1679.9	1843.8	2031.1	2240.2	-	-
		Cal.	1322.8	1436.6	1571.5	1723.7	1892.1	2077.0	2279.3	2499.9	2739.7

References:

1. Inglis, D. R. (1954). *Particle Motion in a Rotating Potential*. Physical Review, 96(4), 1059.
2. Mphd Kh.M. Abu El Sheikh, A.A. Okhunov, H. Abu Kassim, M.U. Khandaker *Chinese Physics* C 44(11), 114107 (2020).
3. Mohd Kh.M. Abu el Sheikh, Abdurahim, A. Okhyunov, Hasan Abu Kassim, Yoon Tiem Leong Science Malaysia (Sains Malaysiana) Vol. 51(4), pp. 1213–1227 (2022).
4. A.A. Okhunov, Mohd’ Kh.M. Abu El Skaikh, P.N. Usmanov Bulletin of the Russian Academy of Sciences: Physics **(2023)**.
5. E. N. Shurshikov, Nucl. Data Sheets 47, 433 (1986).
6. Jimin Hu, and Furong Xu, Physical Review C, Vol. 48(5) pp. 2270 – 2276 (1993)
7. D. J. Horen and B. Harmatz, Nucl. Data Sheets 19, 383 (1976)

DEPENDENCE OF THE α-PARTICLE MEAN FREE PATH ON RADIONUCLIDE SPECIFIC ACTIVITY IN THE URANIUM DECAY CHAIN

Toshev O.S.[1], Allaberganova G.M.[2], Muzafarov A.M.[2]

[1]Navoi State University, Navoi, Uzbekistan

[2]Navoi Mining and Technological University, Navoi, Uzbekistan

Alpha decay of heavy nuclei is accompanied by the emission of α-particles with energies of several MeV. In matter, their range is limited by intensive ionization and excitation losses and is therefore determined primarily by the initial α-particle energy and by the density and composition of the absorbing medium. Radionuclides of the uranium decay chain, however, differ strongly in half-life and consequently in specific activity. The purpose of the present analysis is to establish how these nuclear-decay characteristics are reflected in the calculated α-particle range and to clarify the physical meaning of the resulting dependence.

The calculations combine a semi-empirical expression for α-decay half-lives with the standard relation for radionuclide specific activity and an empirical range-energy relation for α-particles in air. The Royer-type half-life relation used in the model is

$$log\, T_{1/2} = a + b\, A^{1/6}\sqrt{Z} + cZ/\sqrt{Q\alpha}, \quad (1)$$

where A and Z are the mass and atomic numbers used in the adopted parameterization, Qα is the α-decay energy, and a, b, c are empirical coefficients. In the calculations, a = -25.31, b = -

1.1629, c = -1.5864. To avoid ambiguity, the specific activity is denoted only by A_{sp} throughout the text and is calculated as

$$A_{\mathrm{sp}} = \frac{ln\,2 \cdot N_A}{M \cdot T_{1/2}} \quad (2)$$

where N_A is Avogadro's constant and M is the molar mass of the radionuclide. The α-particle range in air is estimated from

$$R\alpha = 0.312\ E\alpha^{3/2} \quad (3)$$

where Rα is expressed in centimetres and Eα in MeV. Combining Eqs. (1)–(3) gives a semi-empirical analytical relation between the specific activity and the α-particle range:

$$\log A_{\mathrm{sp}} = log\left[\frac{ln\,2 \cdot N_A}{M}\right] - a - b\,A^{\frac{1}{6}}\sqrt{Z} - cZ/\left(\frac{R\alpha}{0.312}\right)^{1/3} \quad (4)$$

The derived expression demonstrates that a relationship between A_{sp} and Rα exists within the adopted semi-empirical description of the uranium-series radionuclides. It is therefore not appropriate to state that the two quantities are completely unrelated. At the same time, the mathematical dependence should not be interpreted as a direct physical action of specific activity on the stopping process. The α-particle range is governed immediately by particle energy and medium properties, whereas the specific activity is governed mainly by half-life and molar mass. Their connection arises because these quantities reflect different aspects of the same nuclear-decay system.

This interpretation removes the apparent contradiction between the analytical formula and the physical mechanism. When different α-emitting radionuclides are compared, changes in half-life and α-decay energy occur together, so variations in specific activity can be accompanied by systematic variations in particle range. In this sense, Eq. (4) represents a semi-empirical correlation useful for comparative analysis of radionuclides in the uranium decay chain. However, for a given radionuclide emitting α-particles of fixed energy into an unchanged medium, changing the amount of radioactive material or the total activity changes the number of emitted particles per unit time but not the individual range of each particle.

The result should therefore be formulated as follows: for the considered uranium-series radionuclides, the adopted semi-empirical equations yield a calculable dependence between specific activity and α-particle range, while the immediate transport characteristics of an individual α-particle remain controlled by its initial energy and the absorbing medium. The proposed relation is consequently applicable as a comparative semi-empirical model within the examined decay chain and should not be treated as a universal causal law independent of radionuclide identity or environmental conditions.

Such a formulation is relevant for radiation-physics and radiometric assessments because it separates two physically different quantities: activity characterizes the rate of radioactive transformations, whereas the particle range characterizes the spatial scale of energy deposition. Their joint analysis can be useful when comparing α-active radionuclides, provided that the limitations of the semi-empirical approximation and the properties of the medium are explicitly taken into account.

References:

1. Royer G., Zbiri K. Analytic expressions of alpha decay half-lives and potential barriers. Nuclear Physics A, 2021, Vol. 1008, 122077. DOI: https://doi.org/10.1016/j.nuclphysa.2021.122077
2. Ni D., Ren Z. New approach to alpha-decay calculations based on shell-model nuclear radii. Physical Review C, 2010, Vol. 82, 024311. DOI: https://doi.org/10.1103/PhysRevC.82.024311
3. Zhang H.F., Royer G. Preformation probability in alpha decay of heavy nuclei. Physical Review C, 2010, Vol. 82, 054318. DOI: https://doi.org/10.1103/PhysRevC.82.054318

4. Sun X.D., Guo P., Li X.H. Systematic study of α-decay half-lives for odd-A nuclei. Physical Review C, 2016, Vol. 93, 034316. DOI: https://doi.org/10.1103/PhysRevC.93.034316
5. Razavi R., Dixit A.K. Quantum tunneling and alpha-decay half-lives for favored decays. Nuclear Physics A, 2020, Vol. 1002, 121985. DOI: https://doi.org/10.1016/j.nuclphysa.2020.121985
6. Canto L.F., Leal B.V., Lotti P., Hussein M.S. Coulomb barrier penetration and quantum tunneling in nuclear reactions. Physical Review C, 2015, Vol. 92, 014626. DOI: https://doi.org/10.1103/PhysRevC.92.014626

QUANTUM-MECHANICAL ANALYSIS OF THE RELATIONSHIP BETWEEN NUCLEAR PROPERTIES OF URANIUM-SERIES NUCLIDES AND α-PARTICLE TUNNELING PROBABILITY

Toshev O.S.[1], Mustafoyev M.A.[1], Allaberganova G.M.[2], Muzafarov A.M.[2]
[1]Navoi State University, Navoi, Uzbekistan
[2]Navoi Mining and Technological University, Navoi, Uzbekistan

Alpha decay of heavy nuclei is one of the most direct manifestations of quantum-mechanical tunneling. According to classical mechanics, an α-particle with an energy below the Coulomb-barrier height cannot escape from the nucleus. In contrast, quantum mechanics predicts a finite probability of penetration through the classically forbidden region. In this work, the Wentzel-Kramers-Brillouin (WKB) approximation was used to compare eight α-emitting radionuclides of the uranium series: ^{238}U, ^{234}U, ^{230}Th, ^{226}Ra, ^{222}Rn, ^{218}Po, ^{214}Po, and ^{210}Po. The aim was to establish how α-decay energy and nuclear charge, together with the associated Coulomb-barrier parameters, affect the tunneling probability and the observed differences in half-lives.

The α-particle was treated as a cluster interacting with the daughter nucleus through the short-range nuclear potential and the long-range Coulomb potential. The classically forbidden region extends from the effective nuclear radius R to the external turning point R_C, defined by the condition $V_C(R_C) = Q_\alpha$. In the Coulomb term, the daughter-nucleus charge Z_d is used; since $Z_d = Z_p - 2$ for α decay, the influence of the parent-nucleus charge is incorporated consistently through this relation. The WKB action integral was then used to determine the barrier-penetration probability.

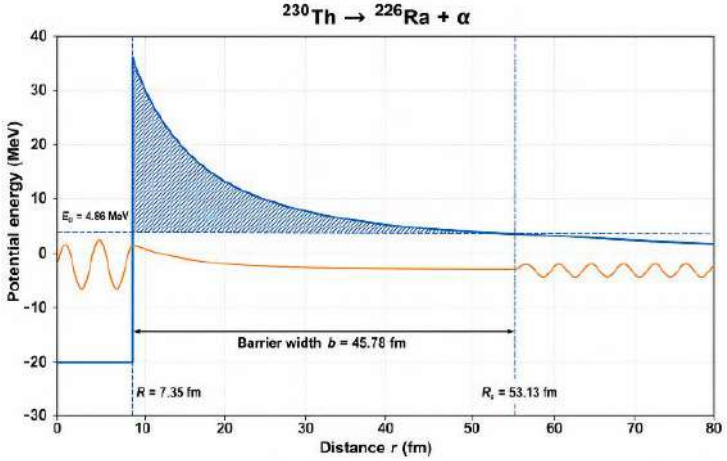

Figure 1. Potential-barrier representation of the ^{230}Th → ^{226}Ra + α decay and α-particle tunneling through the Coulomb barrier.

Within the WKB approximation, the action integral K and the corresponding barrier-penetration probability Pα are determined by Eq. (3).

$$K = \int_R^{R_C} \sqrt{\frac{2m}{\hbar^2}(V(r) - E)}\, dr, \qquad P_\alpha \approx exp(-2K) \tag{3}$$

Because Pα depends exponentially on K, relatively small changes in α-decay energy, nuclear charge, or barrier width can alter the tunneling probability by several orders of magnitude.

The calculations reveal a strong inverse relationship between α-decay energy and the effective width of the Coulomb barrier. As Qα increases, the external turning point moves inward, the classically forbidden region becomes narrower, the action integral decreases, and the tunneling probability rises exponentially.

For ^{238}U, an α-decay energy of approximately 4.27 MeV corresponds to an action integral K≈41.28 and $\log_{10}(P\alpha)$≈-35.86. In contrast, ^{214}Po, with an α-decay energy of approximately 7.88 MeV, has K≈19.04 and $\log_{10}(P\alpha)$≈-16.53. Thus, the increase in α-particle energy reduces the forbidden region and increases the tunneling probability by many orders of magnitude, providing a quantum-mechanical explanation for the very large differences in the half-lives of uranium-series radionuclides.

The comparison of ^{230}Th and ^{226}Ra shows that α-decay energy is not the only controlling parameter. Their α-decay energies are very close, approximately 4.86 and 4.87 MeV, respectively, whereas the calculated action integrals are K≈35.15 and K≈34.42 and the corresponding values are $\log_{10}(P\alpha)$≈-30.53 and -29.90. The remaining difference is associated with the daughter-nucleus charge, reduced mass, effective nuclear radius, and Coulomb-barrier geometry.

The exponential dependence of Pα on K confirms that even relatively small changes in nuclear parameters can produce large changes in decay probability. At the same time, deviations between a barrier-only estimate and experimental decay rates may reflect α-cluster preformation, nuclear deformation, and details of the nuclear potential; these effects define the natural limits of the simplified WKB comparison.

The obtained results show that the α-decay characteristics of uranium-series radionuclides can be interpreted consistently within the quantum-tunneling picture. The dominant trend is set by α-decay energy, while nuclear charge, reduced mass, nuclear radius, and barrier width provide additional isotope-dependent corrections. Increasing Qα lowers the action integral and exponentially increases the barrier-penetration probability.

The WKB approach is therefore suitable for comparative analysis of uranium-series α emitters and for explaining the systematic differences in their half-lives. Further refinement of the model can include nuclear deformation and α-cluster preformation probability.

References:

1. Royer G. Alpha emission and spontaneous fission through quasi-molecular shapes. Journal of Physics G: Nuclear and Particle Physics, 2000, Vol. 26, pp. 1149-1173.
2. Denisov V.Yu., Khudenko A.A. Alpha-decay half-lives, alpha-capture and alpha-nucleus potential. Atomic Data and Nuclear Data Tables, 2009, Vol. 95, pp. 815-835.
3. Delion D.S., Liotta R.J., Wyss R. Recent theoretical approaches to alpha decay in heavy nuclei. Physics Reports, 2006, Vol. 424, pp. 113-174.

Qi C., Xu F.R., Liotta R.J., Wyss R. Universal Decay Law in charged-particle emission and exotic cluster radioactivity. Physical Review Letters, 2009, Vol. 103, 072501.

ON THE VALIDITY OF APPLYING THE STUDENT'S t-CRITERION TO EXPERIMENTALLY PROVE THE RESTORATION OF WIGNER’S *SU*(4) - SYMMETRY IN NUCLEI

Mirbabaev Sh.R., Nurmukhamedov A.M.
Tashkent State Medical University, Tashkent, Uzbekistan

In Ref.[1], experimental values of the Franzini–Radicati factor *R* [1] were calculated over a broad range of mass number *A*. The theoretical expression obtained for this factor R_{teor}, and its experimental value, R_{exp}, make it possible to analyze data with the aim of testing the hypothesis of restoration of Wigner’s symmetry in the region of heavy nuclei.

In order to test this hypothesis, Student’s *t* criterion, which is a statistical method for testing hypotheses, was used in Ref. [1]. This method makes it possible to test agreement between the theory and experiment at a preset significance level α. In order to apply Student’s *t* criterion, as was done in Ref. [1], fulfillment of the following two conditions is necessary: (i) the expression for R_{teor} should be precise and (ii) a general set from which one takes a sample *R* should obey a normal distribution.

The first condition is satisfied since the expression for R_{teor} was obtained in [1] by means of simple transformations with the aid of Wigner’s mass formula and with allowance for the fact that a term that takes into account nucleon pairing in nuclei is present in this formula.

Student’s *t* criterion is optimal in the sense that only in those cases where the samples considered taken from a normally distributed general set, does it ensure the highest reliability of statistical conclusions. At large deviations from a normal distribution, the accuracy of the *t* criterion is substantially lower. In order to apply with confidence the optimum *t* criterion, it is therefore necessary to verify the assumption that the distribution of the sample R_{exp} is normal. Consistency criteria are used for this purpose.

There are several kinds of consistency criteria. The χ^2 consistency criterion or the Kolmogorov–Smirnov λ consistency criterion is applied in the cases of rather large samples ($n \geq 40$). If the sample being considered is such that $n < 40$, as in our case, the Shapiro–Wilk test [2], which permits revealing deviations from a normal distribution even at the sample size as small as $n \approx 10$, leads to more accurate conclusions. In view of this, we employed the Shapiro–Wilk (*W*) test to verify a normal character of the distribution of the sample $R_{\text{эксп}}$.

The *W* test is calculated by the formula [2]

$$W = \frac{s^2}{(n-1)D^2},$$

where *n* is the size of the sample being considered and

$$D^2 = \frac{1}{n-1}\sum_{i=1}^{n}(R_i - \bar{R})^2$$

is its variance.

Table gives values that we calculated for the Shapiro–Wilk test, *W*calc, for three groups of nuclei belonging to Wigner’s type. For the sake of convenience, we also present in the same table the critical values of the test, *W*crit, for the confidence level of $\alpha = 0.01$. Table shows that, for the overwhelming majority of values for the Shapiro–Wilk test, the inequality *W*calc > *W*crit holds,

which indicates that, at the confidence level of $\alpha = 0.01$, the sample R_{exp} obeys a normal distribution for those cases.

There are a number of cases where Wcalc < Wcrit is insignificant. For the majority of these cases, the calculated value of the Shapiro–Wilk test differs insignificantly from its critical value in the table; that is, Wcalc ≈ Wcrit. Therefore, there are modest deviations of the distribution from a normal distribution, but, for them, Student’s t criterion still has a sufficient power for ensuring a satisfactory accuracy.

Table. Calculated, *W*calc, and critical, *W*crit, values for the Shapiro–Wilk test for three groups of nuclei belonging to Wigner’s type

T_z	n	*W*calc<>*W*crit	T_z	n	*W*calc<>*W*crit	T_z	n	*W*calc<>*W*crit
odd-*A* nuclei			even–even nuclei			odd–odd nuclei		
3/2	28	0.795<0.896	1	14	0.863>0.825	1	10	0.921>0.781
5/2	37	0.929>0.914	2	16	0.970>0.844	2	17	0.964>0.851
7/2	41	0.917<0.920	3	19	0.955>0.863	3	18	0.966>0.858
9/2	43	0.969>0.923	4	21	0.944>0.873	4	23	0.955>0.881
11/2	43	0.954>0.923	5	22	0.959>0.878	5	22	0.375<0.878
13/2	34	0.844<0.908	6	18	0.897>0.858	6	18	0.928>0.858
15/2	29	0.975>0.898	7	16	0.917>0.844	7	17	0.931>0.851
17/2	34	0.962>0.908	8	15	0.992>0.835	8	13	0.937>0.814
19/2	42	0.206<0.922	9	22	0.892>0.878	9	14	0.971>0.825
21/2	40	0.966>0.919	10	23	0.956>0.881	10	21	0.899>0.873
23/2	37	0.981>0.914	11	22	0.950>0.878	11	22	0.955>0.878
25/2	31	0.929>0.902	12	19	0.917>0.863	12	20	0.942>0.868
27/2	28	0.962>0.896	13	20	0.889>0.868	13	16	0.876>0.844
29/2	25	0.868<0.888	14	19	0.852<0.863	14	17	0.932>0.851
31/2	30	0.882<0.900	15	19	0.857<0.863	15	18	0.788<0.858
33/2	35	0.831<0.910	16	20	0.821<0.868	16	19	0.896>0.863
35/2	25	0.917>0.888	17	19	0.940>0.863	17	17	0.842<0.851
37/2	24	0.941>0.884	18	11	0.923>0.792	18	13	0.914>0.814
39/2	19	0.967>0.863	19	10	0.862>0.781	19	12	0.961>0.805
41/2	16	0.863>0.844	20	9	0.960>0.764	20	9	0.959>0.764
43/2	16	0.915>0.844	21	8	0.980>0.749	21	7	0.940>0.730
45/2	16	0.679<0.844	22	8	0.982>0.749	22	5	0.915>0.686
47/2	12	0.785<0.805	23	7	0.871>0.730	23	6	0.851>0.713
49/2	8	0.868>0.749	24	6	0.923>0.713	24	6	0.931>0.713
51/2	7	0.960>0.730	25	9	0.960>0.764	25	3	0.750<0.753
53/2	9	0.826>0.764	26	8	0.952>0.749	26	6	0.935>0.713
55/2	9	0.891>0.764	27	7	0.950>0.730	27	8	0.979>0.749
57/2	6	0.944>0.713	28	5	0.916>0.686	28	4	0.753>0.687

References:

1. A. M. Nurmukhamedov, Phys. Atom. Nucl. **75**, 27 (2012).
2. S. S. Shapiro; M. B. Wilk, *Biometrika*, **52**, 591 (1965).

ELECTROMAGNETIC WAVES OF GENERAL APPEARANCE IN LEWIS SPACE-TIME IN VACUUME AND CONDUCTING MEDIA

Muminov A.T.
Institute of Nuclear Physics, Uzbekistan Academy of Sciences, Tashkent, Uzbekistan

The objective of this work is to study electromagnetic waves in the Lewis metric, maximally simplifying Maxwell data for their subsequent analytical or numerical solution. We attempt to extend previous approach to the case of the propagation of a "general" partial wave in a conducting medium. For example, neutron stars have a core conducting crust, making it relevant to search for analytical solutions of the Maxwell source for "general" electromagnetic waves in a conducting medium in an axisymmetric Lewis metric. Such studies may be a relevant task for correct interpretation of astrophysical observation data and thus for the study of nuclear physics of stars and etc.

The Lewis metric on a manifold, given in a set of coordinates $\{t, z, r, \varphi\}$, looks like

$$ds^2 = f(r)dt^2 - 2k(r)dtd\varphi - h(r)(dz^2 + dr^2) - l(r)d\varphi^2, \quad (1)$$

$$f(r) = ar^{1-n} - \frac{c_0^2}{n^2 a} r^{1+n}. \quad k(r) = -abr^{1-n} - \frac{c_0}{na}\left(1 - \frac{c_0 b}{n}\right) r^{1+n},$$

$$h(r) = r^{(n^2-1)/2}, \quad l(r) = -ab^2 r^{1-n} + \frac{1}{a}\left(1 - \frac{c_0 b}{n}\right)^2 r^{1+n}, \quad (2)$$

where a is the momentum along the gravitational strings, and the parameters b and c_0 describe angular momentum of the gravitational strings; $n = 1 - \varepsilon,\ 0 \le \varepsilon < 1,\ \ \varepsilon/2 -$ this creates the masses of the gravitating string. We use relativistic units ($c = 1$). According to the Newman-Penrose method, an isotropic tetrad is introduced:

$$\kappa = \sqrt{f}dt - \frac{k}{\sqrt{f}}d\varphi + \sqrt{h}dz, \quad \lambda = \sqrt{f}dt - \frac{k}{\sqrt{f}}d\varphi - \sqrt{h}dz,$$

$$\mu = \sqrt{h}dr + i\sqrt{\frac{J}{f}}d\varphi, \quad \nu = \sqrt{h}dr - i\sqrt{\frac{J}{f}}d\varphi. \quad (3)$$

Three independent 2-forms are constructed, each possessing the property of self-adjointness:

$${}^*\Phi_\alpha = i\,\Phi_\alpha, \quad \alpha = 1,2,3. \quad (4)$$

The complex combination of these 2-forms yields three other independent self-adjoint 2-forms $\bar{\Phi}_\alpha$ (${}^*\bar{\Phi}_\alpha = -i\,\bar{\Phi}_\alpha$).

Maxwell's equations in vacuum have the general form: $d\Psi = \tilde{0},\ d^*\Psi = \tilde{0}.$ (5)

Next, we expand the 2-form in terms of the 2-forms' frame:

$$\Psi = \Phi + X, \Phi = \widetilde{F_1}\Phi_1 + \widetilde{F_2}\Phi_2 + \tilde{G}\Phi_3, \quad X = \widetilde{I_1}\bar{\Phi}_1 + \widetilde{I_1}\bar{\Phi}_1 + \tilde{J}\bar{\Phi}_3. \quad (6)$$

By including Eq. (6) in Maxwell's equation (5), taking into account the self-adjoint property (4), we obtain: $d\Phi = \tilde{0}$, (7) $dX = \tilde{0}$. (8)

Thus, already at the initial stage, we decouple the equations for different basic polarizations. In the case of conducting media, the situation becomes more complicated:

$$d\Psi = 0, \qquad d^*\Psi = 4\pi^*\mathcal{J}, \mathcal{J} = \sigma\Psi(\bar{u}). \quad (9)$$

Maxwell's equations in our frame are written as follows:

$$d\Phi + d\mathrm{X} = \tilde{0}, \qquad i(d\Phi - d\mathrm{X}) = 4\pi\sigma^*[\Phi(\bar{u}) + \mathrm{X}(\bar{u})]. \quad (10)$$

We select the 4-velocity field of the medium as time-like normalized vectors resting in the coordinate system $\bar{u} = f^{-\frac{1}{2}}\partial_t = \bar{k} + \bar{l}$.

The form of metric (1) indicates that the partial derivatives of the coordinates ∂_t, ∂_z, ∂_φ will be Killing vectors. This means that we have partial electromagnetic waves characterized by certain conserved numbers ω, p_z, m, and their dependence on the corresponding coordinates is given by an exponential factor $e^{i(\omega t - p_z z - m\varphi)}$.

We have succeeded in decoupling Maxwell's equations for partial waves of general type $p_z \neq 0$ and of different polarizations in a vacuum and reducing them to a clearly consistent solution. In the particular case $p_z = 0$ [3], the equations are noticeably simpler and admit an analytical solution. A new feature compared to the case $p_z = 0$ [3] is the difference between the equations for G and J, which describe different polarizations.

When calculating Maxwell vacuum equations for partial electromagnetic wave basic polarizations, it is very convenient to use the obtained results for the calculations in a conducting medium, although the new equations are no longer have to be decoupled. Basic improvement functions $G^{\pm} = \frac{1}{2}(G \pm J)$ significantly simplify the equations:

$$(F_1 + I_2) = \frac{1}{\sqrt{h}\left(4\pi\sigma + \frac{i\omega}{\sqrt{f}}\right)}\left[\widehat{\mathcal{N}} + q\right](G - J); \qquad (F_1 - I_2) = -\frac{i\sqrt{f}}{\omega\sqrt{h}}\left[\widehat{\mathcal{N}} + q\right](G + J);$$

$$(F_2 + I_1) = -\frac{1}{\sqrt{h}\left(4\pi\sigma + \frac{i\omega}{\sqrt{f}}\right)}\left[\widehat{\mathcal{M}} + q\right](G - J); \qquad (F_2 - I_1) = \frac{i\sqrt{f}}{\omega\sqrt{h}}\left[\widehat{\mathcal{M}} + q\right](G + J).$$

Of the remaining four equations for $G^{\pm}$, two basic equations are proposed

$$\left[\widehat{\mathcal{M}} + \frac{1}{r} - 2p\right]\left\{-\frac{i\omega}{\sqrt{f}\sqrt{h}\tilde{\omega}^2}\left[\widehat{\mathcal{N}} + q\right]G^- + \frac{ip_z}{h\tilde{\omega}^2}\left[\widehat{\mathcal{N}} + q\right]G^+\right\} +$$

$$\left[\widehat{\mathcal{N}} + \frac{1}{r} - 2p\right]\left\{\frac{i\omega}{\sqrt{f}\sqrt{h}\tilde{\omega}^2}\left[\widehat{\mathcal{M}} + q\right]G^- + \frac{ip_z}{h\tilde{\omega}^2}\left[\widehat{\mathcal{M}} + q\right]G^+\right\} + 2ip_z G^+ + 2iRG^- = 0; \qquad (11)$$

$$\left[\widehat{\mathcal{M}} + \frac{1}{r}\right]\left\{\frac{ip_z}{h\tilde{\omega}^2}\left[\widehat{\mathcal{N}} + q\right]G^- - \frac{1}{\sqrt{h}\tilde{\omega}^2}\left(4\pi\sigma + \frac{i\omega}{\sqrt{f}}\right)\left[\widehat{\mathcal{N}} + q\right]G^+\right\} +$$

$$-\left[\widehat{\mathcal{N}} + \frac{1}{r}\right]\left\{\frac{ip_z}{h\tilde{\omega}^2}\left[\widehat{\mathcal{M}} + q\right]G^- + \frac{1}{\sqrt{h}\tilde{\omega}^2}\left(4\pi\sigma + \frac{i\omega}{\sqrt{f}}\right)\left[\widehat{\mathcal{M}} + q\right]G^+\right\} - \left(2i\omega\sqrt{\frac{h}{f}} + 8\sqrt{h}\pi\sigma\right)G^+ = 0,$$

where $\tilde{\omega}^2 = \frac{\omega^2}{f} - \frac{4i\pi\sigma\omega}{\sqrt{f}}$, $\widehat{\mathcal{M}} = \partial_r + \frac{\tilde{m}}{r}$, $\widehat{\mathcal{N}} = \partial_r - \frac{\tilde{m}}{r}$, $\tilde{m} = \sqrt{h}\left(\frac{k\omega}{\sqrt{f}} - m\sqrt{f}\right)$.

and: $p = \frac{1}{4}\left(\frac{f'}{f} - \frac{h'}{h}\right)$, $q = \frac{1}{2}\left(\frac{f'}{f} + \frac{h'}{h}\right)$, $R = \frac{k}{r}\left(\frac{f'}{f} - \frac{k'}{k}\right)$.

Note that in the case of $p_z = 0$ equations (11) for G^+, G^- are decoupled.

APPLICATION OF TALYS AND GEANT4 FOR THE STUDY OF PHOTONUCLEAR AND NEUTRON-INDUCED REACTION CROSS SECTIONS

Bozorboev Sh.G.[1], Khoshimjonov Kh.[1], Egamova F.R.[2], Beknazarova N.Y.[1]
[1]*Department of Physics, National University of Uzbekistan, Tashkent, Uzbekistan*
[2]*SI “Scientific and Technical Center for Radiation and Nuclear Safety”, Tashkent, Uzbekistan*

The study of photonuclear and neutron-induced reactions is of particular importance for obtaining reliable information on nuclear reaction mechanisms and energy-dependent reaction cross sections. In particular, the (γ,n), (γ,2n), and (n,2n) channels provide important information on neutron production and the competition between different reaction mechanisms [1,2]. Accurate determination of their cross sections is also essential for the interpretation of experimental measurements, since the number of registered reaction products depends not only on the reaction probability but also on particle transport and detector efficiency. In this context, the combined application of TALYS and Geant4 provides an opportunity to calculate reaction cross sections and to investigate the subsequent transport and registration of the produced particles [3,4].

The reaction rate can be expressed as $R(E) = \Phi(E)N_t\,\sigma(E)$, where $R(E)$ is the reaction rate, $\Phi(E)$ is the incident particle flux, N_t is the areal density of target nuclei, and $\sigma(E)$ is the energy-dependent reaction cross section. Accordingly, the reaction cross section can be estimated from the number of registered reaction events as $\boldsymbol{\sigma(E) = N_{rxn}(E)/[N_{in}c(E)N_t\varepsilon(E)]}$, where $N_{rxn}(E)$ is the number of registered reaction events, $N_{in}c(E)$ is the number of incident particles, and $\varepsilon(E)$ is the effective detection efficiency. For a target with density ρ, thickness x, and atomic mass A, the areal density of target nuclei is given by $\boldsymbol{N_t = (\rho N_a/A)x}$, where N_a is Avogadro’s constant. The corresponding energy-dependent cross sections considered in this work are $\sigma_{(\gamma,n)}(E_\gamma)$, $\sigma_{(\gamma,2n)}(E_\gamma)$, and $\sigma_{(n,2n)}(E_n)$ for the (γ,n), (γ,2n), and (n,2n) reaction channels.

TALYS provides a theoretical framework for calculating nuclear-reaction observables and energy-dependent partial cross sections. The code accounts for direct, pre-equilibrium and compound-nucleus reaction mechanisms and can be applied to photon- and neutron-induced reactions [3,4]. For photonuclear reactions, TALYS calculations allow the excitation functions of the (γ,n) and (γ,2n) channels to be considered separately. This channel-resolved treatment is important because the opening of additional neutron-emission channels changes the relationship between total photoabsorption and the experimentally observed neutron yield [1,2]. The same approach can be applied to the neutron-induced (n,2n) reaction, for which the energy dependence of the partial cross section is an important characteristic of secondary-neutron production.

Geant4 complements the nuclear-reaction calculations by describing the transport and interaction of particles in a defined target-detector geometry. Its photonuclear framework uses cross-section information to determine interactions and then generates the corresponding nuclear final state [5]. The emitted neutrons can subsequently be tracked through the target, surrounding materials and detector, allowing quantities such as neutron energy, multiplicity and deposited energy to be evaluated. Therefore, a detector count should not be identified directly with a reaction cross section: the registered signal also depends on particle flux, target areal density, geometry, secondary-particle transport and detection efficiency.

A combined TALYS-Geant4 approach consequently connects two stages of the same physical problem. TALYS is used to determine the energy dependence of the relevant reaction channels, while Geant4 is used to model the transport of the incident radiation and the reaction products under specified experimental conditions. The calculated cross sections can therefore serve as nuclear-

physics input for interpreting the simulated reaction yield and detector response. This framework is applicable to (γ,n), (γ,2n), and (n,2n) reactions and provides a consistent basis for studying how channel-specific nuclear probabilities are reflected in experimentally observable secondary-particle signals.

References:

1. IAEA, Handbook on Photonuclear Data for Applications: Cross Sections and Spectra, IAEA-TECDOC-1178, International Atomic Energy Agency, Vienna.
2. International Atomic Energy Agency, Photonuclear Data Library, IAEA Nuclear Data Services, Vienna.
3. A. J. Koning, S. Hilaire, S. Goriely, “TALYS: Modeling of Nuclear Reactions,” European Physical Journal A, 59, 131 (2023).
4. A. J. Koning, S. Hilaire, S. Goriely, TALYS-2.2: A Nuclear Reaction Program, IAEA Nuclear Data Section, 2025.
5. Geant4 Collaboration, Geant4 Physics Reference Manual: Gamma-Nuclear Interactions, CERN, Geant4 Documentation.

CALCULATION OF RELATIVE YIELDS AND FLUX-AVERAGED CROSS SECTIONS OF PHOTONUCLEAR REACTIONS IN THE ^{165}Ho NUCLEUS

Kuyliev F.Y.[1,2], Khushvaktov J. H.[3,4], Khoshimjonov Kh.[2]
[1]National Research Nuclear University "MEPhI", Moscow, Russian Federation
[2]National University of Uzbekistan, Tashkent, Uzbekistan
[3]Joint Institute for Nuclear Research, Dubna, Russian Federation
[4]Institute of Nuclear Physics, Uzbekistan Academy of Sciences, Tashkent, Uzbekistan

Photonuclear reactions are of great importance for studying the properties and reaction mechanisms of atomic nuclei. They provide valuable information on the formation mechanisms of isotopes near the stability region, the influence of the isospin effect on the decay of the giant dipole resonance, photonuclear reactions accompanied by multiple-nucleon emission, photofission of heavy nuclei, and isomeric ratios in photonuclear reactions [1–3]. Such reactions are commonly investigated using bremsstrahlung radiation produced by the deceleration of high-energy electrons in relatively heavy converter materials such as W, Ta, Pb, and Bi. The LINAC-200 accelerator at the Joint Institute for Nuclear Research provides an opportunity to study photonuclear reactions over a wide energy range [4,5]. Experimental studies of photonuclear reactions in ^{165}Ho nuclei were previously performed using this accelerator, and the corresponding reaction yields were determined [7]. Reaction cross sections were subsequently evaluated using a quasi-monoenergetic bremsstrahlung flux approach [6]. In the present work, the experimental yields from Ref. [7] were combined with newly calculated bremsstrahlung photon fluxes to determine relative reaction yields and photon-flux-averaged cross sections. The bremsstrahlung process was simulated using Geant4-11.4.1 [8] for electron energies of 50–110 MeV and Pb converter thicknesses of 3 and 5 mm. The experimental conditions corresponded to electron energies of 60, 80, and 100 MeV, with 3 and 5 mm Pb converters used for the 60 MeV and 80–100 MeV beams, respectively [11]. The TALYS-2.0 code [9] was used to calculate the photonuclear reaction cross sections of ^{165}Ho. The default level-

density model, ldmodel 1 (Constant Temperature + Fermi Gas Model), was applied. The relative reaction yields and photon-flux-averaged cross sections were calculated for the following photonuclear reactions:
^{165}Ho(γ,n)^{164}Ho, ^{165}Ho(γ,3n)^{162m}Ho, ^{165}Ho(γ,3n)^{162}Ho, ^{165}Ho(γ,4n)^{161}Ho, ^{165}Ho(γ,5n)^{160m}Ho, ^{165}Ho(γ,5n)^{160}Ho, ^{165}Ho(γ,6n)^{159}Ho, ^{165}Ho(γ,3p3n)^{159}Gd, ^{165}Ho(γ,7n)^{158}Ho, ^{165}Ho(γ,8n)^{157}Ho, ^{165}Ho(γ,7n2p)^{156}Tb, ^{165}Ho(γ,9n)^{156}Ho, and ^{165}Ho(γ,10n)^{155}Ho.

The yield of each reaction channel was normalized to the reference reaction ^{165}Ho(γ,n)^{164}Ho [10]:

$$Y_{rel,i}=\frac{\int_{E_{th}}^{E_{\gamma max}}\sigma_i(E)W(E,E_{\gamma max})dE}{\int_{E_{th}}^{E_{\gamma max}}\sigma_{(\gamma,n)}(E)W(E,E_{\gamma max})dE} \quad (1)$$

The photon-flux-averaged cross section was calculated by taking into account the energy distribution of the bremsstrahlung photons and the threshold energy of the corresponding reaction [11]:

$$\langle\sigma\rangle=\frac{\int_{E_{th}}^{E_{\gamma max}}\sigma_i(E)W(E,E_{\gamma max})dE}{\int_{E_{th}}^{E_{\gamma max}}W(E,E_{\gamma max})dE} \quad (2)$$

Here, $\sigma_i(E)$ is the reaction cross section of the *i*-th channel, E_{th} is the reaction threshold energy, and $E_{\gamma max}$ is the maximum photon energy corresponding to the initial electron energy. The flux-averaged cross section was determined by taking into account the bremsstrahlung photon spectrum above the corresponding reaction threshold.

The calculated bremsstrahlung flux was used to determine the relative reaction yields and photon-flux-averaged cross sections. The ^{165}Ho(γ,n)^{164}Ho reaction was selected as the reference channel because of its relatively low threshold energy, comparatively high intensity, and reliable experimental data. The calculated results were compared with the experimental yields reported in Ref. [7] for electron energies of 60, 80, and 100 MeV, as well as with the theoretical cross sections obtained using TALYS-2.0. Satisfactory agreement was observed for several multi-neutron reaction channels. More pronounced discrepancies were found for isomeric channels, which can be attributed to limitations of the TALYS model in describing isomeric-state production. Differences were also observed for the proton-emission channels leading to ^{159}Gd and ^{156}Tb, which may be related to their more complex reaction mechanisms. For the ^{165}Ho(γ,7n2p)^{156}Tb reaction, an additional comparison of Geant4 and TALYS-2.0 calculations was performed. The results demonstrate the applicability of Geant4 for modeling the bremsstrahlung flux and experimental geometry, while TALYS-2.0 provides a useful tool for estimating photonuclear reaction cross sections. In conclusion, relative yields and photon-flux-averaged cross sections of photonuclear reactions in ^{165}Ho were determined using Geant4-11.4.1 and TALYS-2.0. The calculated results were compared with experimental data. Satisfactory agreement was obtained for several multi-neutron channels, while discrepancies for isomeric and proton-emission channels indicate the need for further improvement of the corresponding nuclear reaction models and nuclear data.

References:

1. I.S. Timchenko, O.S. Deiev, S.M. Olejnik, S.M. Potin, V.A. Kushnir, V.V. Mytrochenko, S.A. Perezhogin. Study the isomeric ratios in photonuclear experiments on the LUE-40 Linac RDC “accelerator” NSC KIPT.
2. Tran Duc Thiep, Truong Thi An, Nguyen The Vinh, Phan Viet Cuong, A. G. Belov, O. D. Maslov, Trinh Thi Thu My. Study on the isomeric ratios of (γ,p) photonuclear reactions with

isotopes ^{92}Zr and ^{183}W in the giant dipole resonance region. Письма в ЭЧАЯ. 2007. Т.4, №5 (141). С. 668-675.
3. Tran Duc Thiep, Truong Thi An, Nguyen The Vinh, Phan Viet Cuong, A. G. Belov, O. D. Maslov, Trinh Thi Thu My. Experimental study and theoretical consideration of the isomeric ratio in photonuclear reaction ^{197}Au(γ,n)^{196m,g}Au in the giant dipole resonance region. Письма в ЭЧАЯ. 2006. Т.3, №4 (133). С. 7-16.
4. Yunenko K.E., Kobets V.V., Trifonov A.N., Barnyakov A.M. Research into the Accelerating Structure of the LINAC-200 Linear Electron Accelerator. Physics of Particles and Nuclei Letters, 21(3), 375–378 (2024).
5. M. A. Nozdrin, V. V. Kobets, R. V. Timonin et al., Physics of Particles and Nuclei Letters 17, 600 (2020).
6. Khushvaktov J.H., et al. Physics of Particles and Nuclei Letters, 19, 347 (2022).
7. Khushvaktov J.H., et al. *Physics of Particles and Nuclei Letters*, 17, 821–823 (2020).
8. J. Allison et al., Recent Developments in GEANT4. Nuclear Instruments and Methods in Physics Research A 835, 186 (2016).
9. Koning, A., Hilaire, S. & Goriely, S. TALYS: modeling of nuclear reactions. Eur. Phys. J. A 59, 131 (2023).
10. Rasulova F.A., Belyshev S.S., Demichev M.A., et al. *Chinese Physics*, 48, 114002 (2024).
11. F. A. Rasulova, R. A. Aliev, S. S. Belyshev et al. Nuclear Instruments and Methods in Physics Research Section A, 1054, 168428 (2023).

DEFORMED NUCLEAR SHELLS IN MASS AND ENERGY DISTRIBUTIONS OF FISSION FRAGMENTS OF ^{234}Np* COMPOUND NUCLEUS FORMED IN ^{233}U(p,f) REACTION AT Ep= 22 MeV

Alimov D.K.[1], Pan A.N.[1], Kovalchuk K.V.[1], Burtebayev N.[1], Janseitov D.M.[1,2], Boztosun I.[3], Kosherbayeva R.[1]

[1]Institute of Nuclear Physics, Almaty, Kazakhstan
[2]Al-Farabi Kazakh National University, Almaty, Kazakhstan
[3]Akdeniz Üniversitesi, Antalya, Turkey

Nuclear fission is a complex field of research that presents difficult challenges to solve, both theoretical and experimental ones. It is affected by a large number of macro- and microscopic quantum effects, including nuclear deformation. To study interplay of these effects we reanalyzed experimental data on mass and energy distributions of fission fragments of ^{234}Np* compound nucleus formed in ^{233}U(p,f) reaction at E_p=22 MeV. The proton beam energy is higher than a Coulomb barrier, resulting in excitation energy of compound nucleus of ~26.2 MeV leading to a blending of symmetric and asymmetric fission. We deconvoluted experimental data into yields of separate fission modes and nuclear shells using our method with increased sensitivity to smaller yields of deformed nuclear shells. Yields of spherical shells Z50, N82, N50 and deformed nuclear shells Z52, N84, N88 was shown.

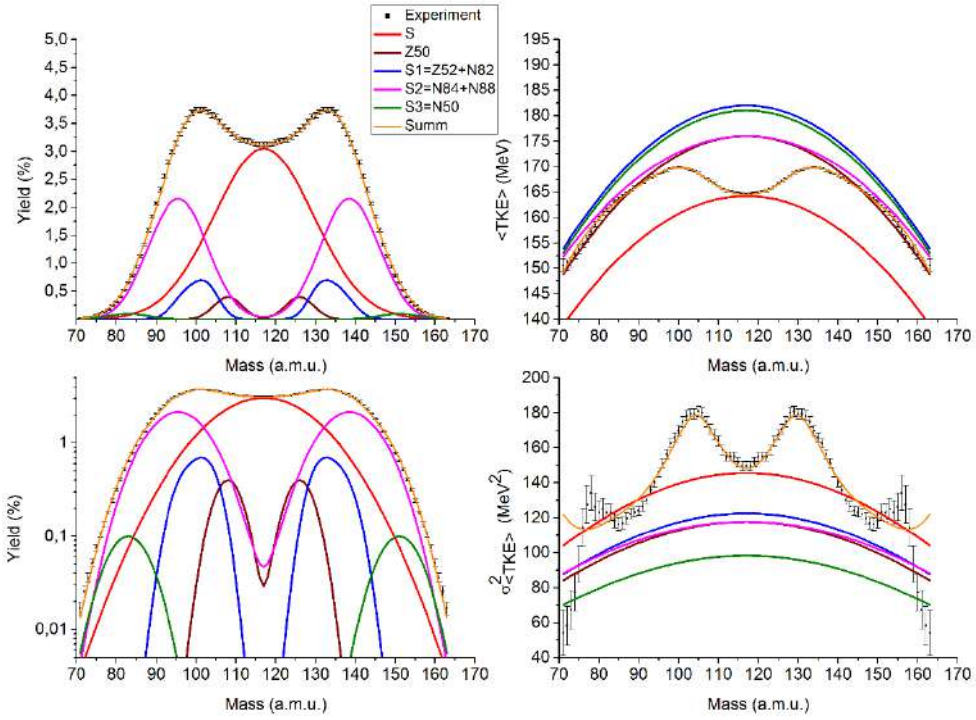

Figure 1. Mass and energy distributions of fission fragments of ^{234}Np* compound nucleus formed in ^{233}U(p,f) at Ep=22 MeV decomposed into yields of separate fission modes and nuclear shells.

MASS AND ANGULAR DISTRIBUTIONS OF REACTION PRODUCTS IN ^{40}Ca + ^{238}U AND ^{40}Ca + ^{197}Au USING A TOF SPECTROMETER

Aznabayev D.[1,2], Issatayev T.[1,2], Lukyanov S.M.[1], Maslov V.A.[1], Mendibayev K.[1,2]
[1]Joint Institute for Nuclear Research, Dubna, Russian Federation
[2]Institute of Nuclear Physics, Almaty, Kazakhstan

This work presents the results of measurements of fission-fragment characteristics in the reactions ^{40}Ca+^{238}U and ^{40}Ca+^{197}Au using a time-of-flight spectrometer at the MAVR facility. The spectrometer includes a start detector based on microchannel plates (MCP) and a stop silicon (Si) detector. A key feature of the applied method is the determination of the masses of nuclear reaction products from their time of flight and measured energy.

The spectrometer was modified by adding an ionization chamber (IC), which makes it possible to measure the energy losses of fission fragments and perform their charge identification. The proper operation of the spectrometer was verified through calibration using a ^{226}Ra source. The work presents the results of measurements of energy, time of flight, mass and angular distributions of reaction products, and discusses methodological aspects of applying this technique to the study of fission fragments from heavy nuclei.

The study is aimed at further optimization of the spectrometer and expansion of its capabilities for detailed analysis of heavy-nucleus fission products. The obtained results can be used to

investigate the mechanisms of heavy-nucleus fission and provide important data for theoretical studies in nuclear physics.

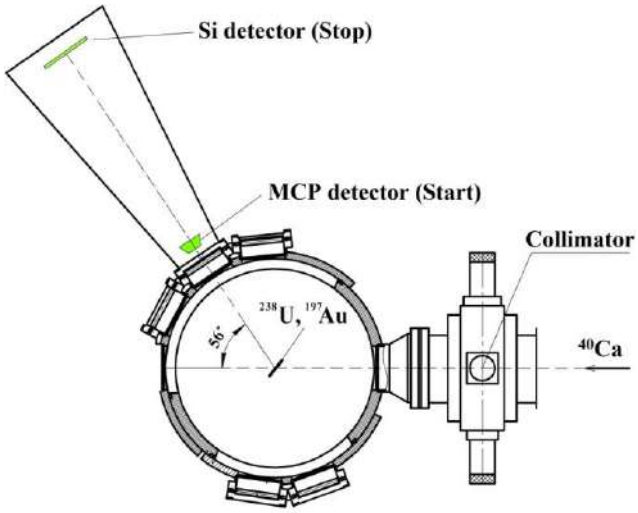

Figure 1. Schematic layout of the experimental setup.

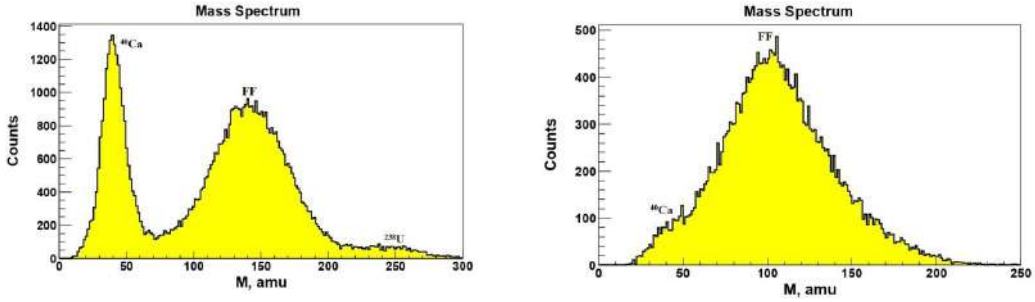

Figure 2. Mass distributions of reaction products in ^{40}Ca+^{238}U and ^{40}Ca+^{197}Au.

References:

1. E.M.Kozulin, A.A.Bogachev, M.G.Itkis et al., The CORSET time-of-flight spectrometer for measuring binary products of nuclear reactions, Instruments and Experimental Techniques 51, No. 1, 44–58 (2008).
2. K.D.Schilling, P. Gippner, W. Seidel et al., The Dubna double-arm time-of-flight spectrometer for heavy-ion reaction products, Nuclear Instruments and Methods in Physics Research Section A 257, No. 2, 197–208 (1987).
3. P.Auger et al., Mass and charge distributions of fission fragments in the reaction ^{40}Ar + ^{238}U at 926 MeV, Zeitschrift für Physik A 289, 255–259 (1979).
4. D.Aznabaev, V.I.Smirnov, A.Isatov et al., Measurement of the Time of Flight of Charged Particles by a Time Detector Based on the MCP for the MAVR Facility, Physics of Particles and Nuclei Letters 16, No. 6, 620–626 (2019).
5. L.Heffern, Ionization Chamber Design, Development, and Testing for the UNM Fission Fragment Spectrometer, June 26, 2015.

B MESON RARE DECAYS

Issadykov A.[1,2], **Ivanov M.A.**[2], **Sakhiyev S.K.**[1]
[1]*Institute of Nuclear Physics, Almaty, Kazakhstan*
[2]*Joint Institute for Nuclear Researches, Dubna, Russian Federation*

We study the B mesons decays within the Standard Model (SM) by using the relevant transition form factors obtained from the covariant confined quark model (CCQM) developed by us. The b → u(d), b → c, and b →s transitions form factors are obtained in the full kinematic q^2 range. The branching fractions are then calculated. Our results are in an agreement with those obtained in other theoretical approaches.

Table 1 presents the predictions for the rare decays of the B and B_0 mesons in comparison with other theoretical approaches, namely LCSR and RQM. The resonance branching result for $B^+ \to \pi^+\mu^+\mu^-$ is below the LHCb collaboration data. For other channels, only upper bounds are given in PDG. The Belle and BABAR collaborations studied the decays of $B^0 \to \pi^0 l^+ l^-$ with l= e and μ, and the results of the covariant quark confinement model are within their upper bound.

For the $B^+ \to \rho^+ l^+ l^-$ and $B^0 \to (\rho^0, \omega) l^+ l^-$ channels, experimental data have not yet been published. For the $B^{+(0)} \to (\rho^{+(0)}, \omega)\nu\bar{\nu}$ channels, the results of the covariant quark confinement model are within the upper limit of the PDG data.

Table 1. Branchings (10^8 B) of rare decays of B^+ and B^0 mesons

Mode	Nonresonant	Resonant	LCSR	Data
$B^+ \to \pi^+ e^+ e^-$	2.18 ± 0.30	1.82 ± 0.18	$1.89^{+0.23}_{-0.22}$	< 8.0
$B^+ \to \pi^+ \mu^+ \mu^-$	2.17 ± 0.30	1.81 ± 0.18	$1.88^{+0.24}_{-0.21}$	$1.83 \pm 0.24 \pm 0.05$
$B^+ \to \pi^+ \tau^+ \tau^-$	0.53 ± 0.15	0.41 ± 0.12	$0.90^{+0.13}_{-0.12}$	–
$B^+ \to \pi^+ \nu\bar{\nu}$	7.4 ± 1	–	–	< 1400
$B^0 \to \pi^0 e^+ e^-$	1.01 ± 0.14	0.84 ± 0.08	$0.87^{+0.11}_{-0.10}$	< 8.4
$B^0 \to \pi^0 \mu^+ \mu^-$	1.01 ± 0.14	0.84 ± 0.08	$0.87^{+0.11}_{-0.10}$	< 6.9
$B^0 \to \pi^0 \tau^+ \tau^-$	0.24 ± 0.07	0.19 ± 0.06	0.41 ± 0.06	–
$B^0 \to \pi^0 \nu\bar{\nu}$	3.4 ± 0.5	–	–	< 900
$B^+ \to \rho^+ e^+ e^-$	4.82 ± 2.39	3.70 ± 1.34	4.0 ± 0.4	–
$B^+ \to \rho^+ \mu^+ \mu^-$	4.05 ± 1.45	2.94 ± 0.94	3.9 ± 0.4	–
$B^+ \to \rho^+ \tau^+ \tau^-$	0.63 ± 0.14	0.43 ± 0.09	0.40 ± 0.04	–
$B^+ \to \rho^+ \nu\bar{\nu}$	14.5 ± 3.8	–	–	< 3000
$B^+ \to \rho^+ \gamma$	85.5 ± 13.8	–	138^{+16}_{-15}	98 ± 25
$B^0 \to \rho^0 e^+ e^-$	2.21 ± 1.09	1.70 ± 0.61	1.9 ± 0.2	–
$B^0 \to \rho^0 \mu^+ \mu^-$	1.86 ± 0.66	1.35 ± 0.43	1.8 ± 0.2	–
$B^0 \to \rho^0 \tau^+ \tau^-$	0.29 ± 0.06	0.20 ± 0.04	0.2 ± 0.02	–
$B^0 \to \rho^0 \nu\bar{\nu}$	6.7 ± 1.8	–	–	< 4000

$B^0 \to \rho^0\gamma$	39.6 ± 6.4	–	64 ± 7	–
$B^0 \to \omega e^+e^-$	1.85 ± 0.89	1.41 ± 0.59	1.3 ± 0.1	–
$B^0 \to \omega\mu^+\mu^-$	1.57 ± 0.55	1.14 ± 0.44	1.2 ± 0.1	–
$B^0 \to \omega\tau^+\tau^-$	0.25 ± 0.05	0.18 ± 0.03	0.13 ± 0.01	–
$B^0 \to \omega\nu\bar{\nu}$	5.6 ± 1.5	–	–	< 4000
$B^0 \to \omega\gamma$	31.1 ± 5	–	58^{+6}_{-7}	–

Table 2 shows that the predictions of the covariant confined quark model are within the range predicted in the LHCb data for the $B_s^0 \to \overline{K^*}(892)^0\mu^+\mu^-$ channel. While there are no experimental data for other rare B_s decays. The ratio of the muon channel to the electron channel for $B^+ \to \pi^+ \; and \; B^0 \to \pi^0$ approaches 1, whereas for $B^{+(0)} \to \left(\rho^{+(0)}, \omega\right)$ the ratio in the covariant quark model with confinement turns out to be equal to 0.85. However, taking into account the uncertainties in the form factors and transferring them to the corresponding branchings, the ratio approaches unity.

Table 2. Branchings (10^8 B) of rare decays of B_s^0 mesons

Mode	Nonresonant	Resonant	LCSR	Data
$B_s^0 \to \bar{K}^{*0}e^+e^-$	3.91 ± 1.47	2.95 ± 0.80	4.0 ± 0.4	–
$B_s^0 \to \bar{K}^{*0}\mu^+\mu^-$	3.32 ± 0.94	2.36 ± 0.57	3.8 ± 0.3	$2.9 \pm 1.0 \pm 0.2 \pm 0.3$
$B_s^0 \to \bar{K}^{*0}\tau^+\tau^-$	0.53 ± 0.10	0.37 ± 0.06	0.50 ± 0.04	–
$B_s^0 \to \bar{K}^{*0}\nu\bar{\nu}$	11.9 ± 2.5	–	–	–
$B_s^0 \to \bar{K}^{*0}\gamma$	66.6 ± 9.6	–	120^{+11}_{-12}	–
$B_s^0 \to \bar{K}^0e^+e^-$	1.65 ± 0.21	1.35 ± 0.12	$1.99^{+0.21}_{-0.20}$	–
$B_s^0 \to \bar{K}^0\mu^+\mu^-$	1.64 ± 0.21	1.35 ± 0.12	$1.99^{+0.21}_{-0.20}$	–
$B_s^0 \to \bar{K}^0\tau^+\tau^-$	0.39 ± 0.09	0.30 ± 0.08	0.74 ± 0.07	–
$B_s^0 \to \bar{K}^0\nu\bar{\nu}$	5.5 ± 0.7	–	–	–

OVERVIEW OF STUDIES OF THE ^{8}Be NUCLEUS AND THE HOYLE STATE IN THE DISSOCIATION OF RELATIVISTIC NUCLEI

Artemenkov D., Zaitsev A., Zarubin P.
Joint Institute for Nuclear Research, Dubna, Russian Federation

The report discusses the main results and general conclusions of the BECQUEREL experiment at JINR obtained in studies of unstable nuclear states formed in the relativistic dissociation of various nuclei [1]. The high efficiency of this approach is ensured by the exceptional spatial resolution of nuclear emulsion and by the possibility of detecting all fragments of nuclear interactions without exception. Using invariant masses reconstructed from precision measurements of fragment emission angles within a narrow fragmentation cone, contributions from the decays of

^{8}Be(0^{+}), ^{8}Be(2^{+}), ^{9}Be(1.7), ^{9}B, ^{6}Be, ^{12}C(0^{+}_{2}), corresponding to the Hoyle state, and ^{12}C(3^{-}) have been identified to date [2].

It has been shown that the contribution of ^{8}Be(0^{+}) increases with the multiplicity of accompanying α-particles; a similar trend is observed for ^{9}B and the Hoyle state ^{12}C(0^{+}_{2}) [3]. The structure of these states, together with the diversity of parent nuclei and the absence of a pronounced dependence on the initial energy, suggests the possible coalescence of α-particles and nucleons produced in the dissociation process. The initial density of such ensembles and the duration of their secondary interaction may be sufficient for the occurrence of the lowest-energy fusion reactions. This scenario calls for the concepts of low-energy nuclear physics to be incorporated into the interpretation of relativistic fragmentation.

The introduction of automated microscopy [4] for the analysis of exposures in beams of the JINR NICA accelerator complex provides a modern basis for further application of the nuclear emulsion method, which has played a fundamental role in the development of microscopic physics. The possibility of registering relativistic nuclear fragmentation events in nuclear emulsion, first demonstrated in the pioneering era of cosmic-ray physics, opens new prospects for studying extremely cold ensembles of H and He nuclei. This is important for the development of nuclear clustering physics and may also contribute to broadening the scenarios of nuclear astrophysics.

References:

1. Artemenkov D. A., Zaitsev A. A., Zarubin P. I., Natural Sci. Rev. **3** 200603 (2026).
2. P.I. Zarubin, Lecture Notes in Physics 875 Clusters in Nuclei **3** 51 (2013).
3. Zaitsev A. A. et al., Phys. Lett. B **820** 136460 (2021).
4. A.A. Zaitsev et al., Phys. Part. Nuclei **56** 881 (2025).

SURVIVAL PROBABILITY AND EVAPORATION-RESIDUE CROSS SECTIONS IN THE ^{48}Ca + ^{244}Pu → ^{292}Fl* REACTION

Amirov S.[1], Kayumov B.M.[1,2]
[1]*Department of Physics, New Uzbekistan University, Tashkent, Uzbekistan*
[2]*Institute of Nuclear Physics, Uzbekistan Academy of Sciences, Tashkent, Uzbekistan*

The synthesis of superheavy elements (SHEs) gives information on the stability of nuclei at the limits of the periodic table [1]. The evaporation residue (ER) cross section is a product of the capture cross section, the compound nucleus (CN) formation probability P_{CN} and the survival probability W_{sur} of the excited CN against fission during the emission of x neutrons. For $Z \geq 114$ it may be as small as 10^{-10} and therefore fixes the order of magnitude of the ER cross section. In the present work it has been calculated for ^{292}Fl produced in the ^{48}Ca + ^{244}Pu reaction, and the xn ER cross section has been obtained as

$$\sigma_{ER}(E_{\mathrm{c.m.}}) = \sum_{\ell=0}^{\ell_d}(2\ell+1)\,\sigma_{\mathrm{cap}}(E_{\mathrm{c.m.}},\ell) \times P_{\mathrm{CN}}(E_{\mathrm{c.m.}},\ell) \times W_{\mathrm{sur}}(E_{\mathrm{c.m.}},\ell), \quad (1)$$

where the CN excitation energy E^{*}_{CN} are taken from the dinuclear system (DNS) model calculations for each $E_{\mathrm{c.m.}}$ and each angular momentum ℓ. W_{sur} is the product of the probability emitting exactly x neutrons P_{xn} and of the branching ratios of the neutron emission over fission along the cascade,

$$W_{\text{sur}} = P_{xn}(E^*_{\text{CN}}) \prod_{i=1}^{x} \left(\frac{\Gamma_n}{\Gamma_n+\Gamma_f}\right)_{i,E^*} \quad (2)$$

where Γ_n and Γ_f are the neutron emission and fission widths of the x-th nucleus of the cascade. P_{xn} is calculated by the Jackson formula [2]

$$P_{xn}(E^*_{\text{CN}}) = I(\Delta_x,\, 2x-3) - I(\Delta_{x+1},\, 2x-1), \quad (3)$$

where $I(z,n)$ is Pearson's incomplete gamma function, $\Delta_x = \frac{E^*_{\text{CN}} - \sum_{i=1}^{x} B_{n,i}}{T}$, T is the temperature at the middle of the cascade and B_i is the neutron separation energy averaged over the x nuclei. In the second term the separation energy of the $(x+1)$-th neutron is replaced by the fission barrier B_f of the residue, which otherwise fissions [3]. The neutron–fission competition is treated by the Vandenbosch–Huizenga expression [4]

$$\frac{\Gamma_n}{\Gamma_f} = \frac{4A^{2/3}a_f\left(E^*_{\text{CN}} - B_n\right)}{K_0 a_n\left[2a_f^{1/2}\left(E^*_{\text{CN}} - B_f\right)^{1/2} - 1\right]} \exp\left[2a_n^{1/2}\left(E^*_{\text{CN}} - B_n\right)^{1/2} - 2a_f^{1/2}\left(E^*_{\text{CN}} - B_f\right)^{1/2}\right] \quad (4)$$

where $K_0 = 9$ MeV, and a_n and a_f are the level density parameters of the residual nucleus and of the saddle point. The asymptotic parameter $\tilde{a}$ is taken from the four-term expression of Nerlo-Pomorska *et al.* [5]. The neutron separation energies come from the same table and alternate between 7.05 and 5.64 MeV along the cascade owing to the pairing. The fission barrier follows the KEWPIE2 prescription [8],

$$B_f(A, Z, E^*_{\text{CN}}, \ell) = B_f^{(0)} + \delta W\left[1 - h(T)\, q(\ell)\right],$$

$$h(T) = \left[1 + \exp\left(\frac{T - T_0}{d}\right)\right]^{-1},$$

$$q(\ell) = \left[1 + \exp\left(\frac{\ell - \ell_{1/2}}{\Delta\ell_d}\right)\right]^{-1}$$

where $B_f^{(0)}$ is the ground-state barrier from the Möller table [7], T_0 = 1.40 MeV, d = 0.30 MeV, $\ell_{1/2}$ = 20 ħ and $\Delta\ell_d$ = 3 ħ. Since $\delta W < 0$ for the Fl isotopes, the second term of Eq. (6) removes the shell contribution to the barrier as T and ℓ increase: for ^{292}Fl it falls from 9.98 MeV at $E^*_{\text{CN}} = 0$ to 6.17 MeV at E^*_{CN} = 35 MeV, and at that energy to 0.72 MeV at ℓ = 30 ħ, so that the residues are formed mainly by the low partial waves.

Figure 1(a) presents W_{sur} of ^{292}Fl at ℓ = 0. It decreases by about ten orders of magnitude between E^*_{CN} = 20 and 60 MeV, and the dominant channel changes from 2*n* below E^*_{CN} = 25 MeV to 3*n* at 25–33 MeV and to 4*n* above 33 MeV.

The ER excitation functions obtained from Eq. (1) are compared in Fig. 1(b) and Table 1 with the ^{289}Fl (3*n*) and ^{288}Fl (4*n*) cross sections measured at FLNR [1] and LBNL [9]. Four of the five points are reproduced within a factor of 2.5, the geometric mean of the calculated-to-experimental ratio being 1.9. The 3*n* point at E^*_{CN} = 35.7 MeV is overestimated by a factor of six, which shows that the calculated 3*n* excitation function is shifted towards the lower energies and falls too steeply.

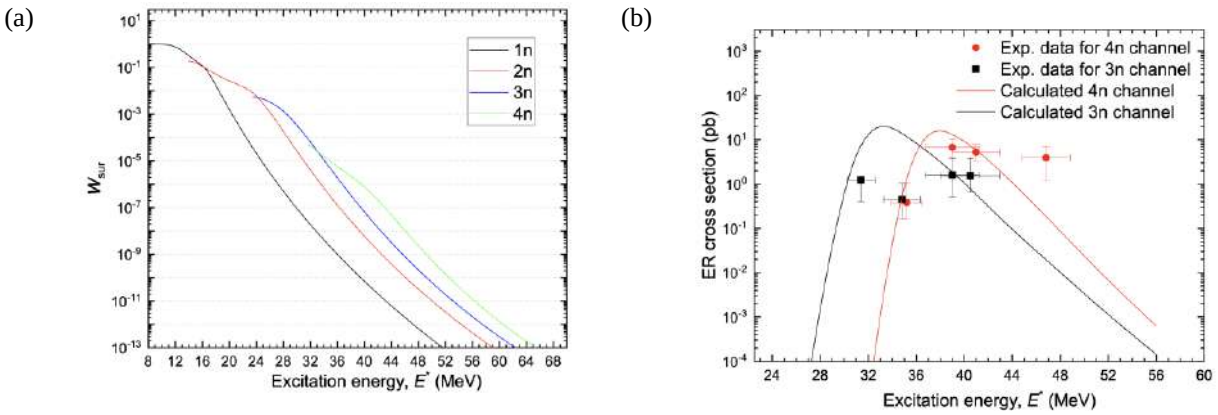

Figure 1. (a) Survival probability of ^{292}Fl for the 1*n*–4*n* channels at $\ell = 0$. (b) ER cross sections of the 3*n* and 4*n* channels in comparison with the data of FLNR [1] and LBNL [9]; the curves are B-splines through the calculated points, which are shown as dots.

Table 1. Calculated and measured ER cross sections of the ^{48}Ca + ^{244}Pu reaction.

Channel	E^*_{CN} (MeV)	σ_{exp} (pb)	σ_{calc} (pb)	calc/exp	Ref.
4*n*	35.2	0.4 (+0.6, –0.25)	0.45	1.13	[1]
4*n*	39.0	6.7 (+3.6, –2.5)	14.8	2.18	[9]
4*n*	41.0	5.3 (+2.2, –2.0)	5.2	0.98	[1]
4*n*	46.8	3.9 (+3.1, –2.7)	0.25	0.06	[1]
3*n*	31.3	1.2 (+0.8, –0.8)	1.1	0.92	[1]
3*n*	39.0	1.6 (+1.1, –1.1)	1.8	1.13	[9]
3*n*	40.6	1.6 (+0.9, –0.9)	0.95	0.59	[1]

The results show that W_{sur} of a superheavy CN is controlled mainly by the ratio B_f/B_n along the cascade and by the rate at which the shell contribution to the barrier is washed out with the temperature and the angular momentum. With the shell corrections and the barriers taken from the FRDM2012 tables, and without any renormalization of the level density parameters, the measured ER cross sections of ^{288,289}Fl are reproduced within a factor of about two.

References:

1. Yu.Ts.Oganessian *et al.*, Phys. Rev. C **69**, 054607 (2004); Phys. Rev. C **70**, 064609 (2004).
2. J. D. Jackson, Can. J. Phys. **34**, 767 (1956).
3. H. M. Rahmatinejad *et al.*, arXiv:2307.13437.
4. R. Vandenbosch, J. R. Huizenga, *Nuclear Fission* (Academic Press, 1973).
5. B. Nerlo-Pomorska, K. Pomorski, J. Bartel, Phys. Rev. C **74**, 034327 (2006).
6. A. V. Ignatyuk, G. N. Smirenkin, A. S. Tishin, Sov. J. Nucl. Phys. **21**, 255 (1975).
7. P.Möller *et al.*, At. Data Nucl. Data Tables **109–110**, 1 (2016); Phys. Rev. C **91**, 024310 (2015).
8. H. Lü, A. Marchix, Y. Abe, D. Boilley, Comput. Phys. Commun. **200**, 381 (2016).
9. J. M. Gates *et al.*, Phys. Rev. C **113**, 024611 (2026).

FIRST INVESTIGATION OF PROMPT NEUTRONS FROM SPONTANEOUSLY FISSIONING ISOMERS PRODUCED IN MULTINUCLEON TRANSFER REACTIONS

Sailaubekov B.[1,2,3], Svirikhin A.I.[1,4], Devaraja H.M.[1], Isaev A.V.[1,4], Mukhin R.S.[1], Bychkov M.A.[1], Chelnokov M.L.[1], Chepigin V.I.[1], Danilkin V.D.[4], Izosimov I.N.[1], Kalandarov Sh.A.[1], Katrasev D.E.[1], Kuznetsova A.A.[1], Malyshev O.N.[1,4], Popeko A.G.[1,4], Popov Yu.A.[1,4], Sokol E.A.[1], Teymurov E.[1,5], Tezekbayeva M.S.[1,3,4], Ulanova I.I.[4]

[1]*Joint Institute for Nuclear Research, Dubna, Russian Federation*
[2]*L.N.Gumilyov Eurasian National University, Astana, Kazakhstan*
[3]*Institute of Nuclear Physics, Almaty, Kazakhstan*
[4]*Dubna State University, Dubna, Russian Federation*
[5]*National Nuclear Research Centre, Qobu Settlement, Azerbaijan*

This work presents the first experimental results on prompt neutron multiplicities from short-lived spontaneously fissioning isomers produced in the multinucleon transfer (MNT) reaction of ^{26}Mg + ^{238}U. The observed prompt neutron multiplicity distribution yields an average neutron number of $\bar{\nu}$ = 2.65 ± 0.20 and a variance of σ_ν^2 = 1.4. The half-life of the spontaneously fissioning products was determined to be $T_{1/2} = (5.3^{+0.5}_{-0.4})$ μs. The shape of the multiplicity distribution of prompt fission neutrons was restored using the Tikhonov regularization technique and is characterized by a symmetrical distribution.

Among the known spontaneous fission (SF) isomers, ^{239m}Pu and ^{243m}Am exhibit half-lives and prompt neutron multiplicities that agree with the measured values within uncertainties. GEF model estimates yield $\bar{\nu}$ = 2.54 ± 0.20 for ^{239m}Pu and $\bar{\nu}$ = 2.91 ± 0.20 for ^{243m}Am, with the former showing slightly better agreement. Whether the activity arises from a single isomer or a mixture of both remains unresolved, as the current data do not allow for a clear separation of their contributions. Further high-statistics measurements, including fission fragment total kinetic energy and gamma-ray spectroscopy, are required for unambiguous identification of the fissioning nucleus.

POSSIBLE FORMATION OF FOUR-PROTON STATES IN ^{12}C–^{12}C COLLISIONS AT 3.37 A GeV

Olimov K., Gulamov K.G., Olimov Kh.K., Bakhodirov Sh.Sh., Olimov A.K.
Physical-Technical Institute, Uzbekistan Academy of Sciences, Tashkent, Uzbekistan

This work is devoted to the search for and analysis of the production of four-proton resonant states in carbon–carbon nucleus interactions at a primary energy of 3.37 A GeV.

The experimental material was obtained using the 2-meter propane bubble chamber of the Laboratory of High Energy of the Joint Institute for Nuclear Research (Dubna), exposed at the Dubna Synchrophasotron to a beam of carbon nuclei with a momentum of 4.2 A GeV/c. The dataset consists of 20527 ^{12}C^{12}C events. The procedure for selecting these collisions from interactions occurring on propane molecules is described in [1].

The search for and analysis of the formation of four-proton resonant states will be carried out in the laboratory reference frame for protons with momenta of $0.2 \le p \le 0.75$ GeV/c produced in the target carbon nucleus. In other words, we considered protons produced in the fragmentation region of the target carbon nucleus and excluded the so-called “evaporation” protons ($p < 0.2$ GeV/c).

Analysis of the four-proton invariant-mass spectrum, M(pppp), for events with four protons showed no statistically significant deviations from the overall shape of the distribution. For events with five, six, or more protons in the final state, however, peaks were observed at M(pppp) = 3.89 GeV and M(pppp) = 3.92 GeV. Therefore, the search for four-proton states was performed for events with five or more protons in the final state.

The figure shows the invariant-mass spectrum of four protons for events with five or more protons in the final state. The dashed histogram represents the background spectrum, constructed as the sum of three Gaussian functions:

$$y = y_0 + \frac{a_1}{\sqrt{\pi/2}}\frac{1}{\sigma_1} exp\frac{-2(x-x_{c1})^2}{{\sigma_1}^2} + \frac{a_2}{\sqrt{\pi/2}}\frac{1}{\sigma_2} exp\frac{-2(x-x_{c2})^2}{{\sigma_2}^2} + \frac{a_3}{\sqrt{\pi/2}}\frac{1}{\sigma_3} exp\frac{-2(x-x_{c3})^2}{{\sigma_3}^2} \qquad (1)$$

where y_0 is a free parameter; a_1, a_2, and a_3 are normalization coefficients; x_{c_1}, x_{c_2}, and x_{c_3} are the centers; and σ_1, σ_2, and σ_3 are the corresponding widths of the Gaussian functions. When fitting the experimental four-proton invariant-mass spectrum with the sum of three Gaussian functions (1), the data points at the maxima (M(pppp) = 3890 MeV and M(pppp) = 3920 MeV), as well as one point on either side of each maximum, were excluded from the experimental spectrum. In other words, the experimental points lying within the invariant-mass interval 3867.5 MeV ≤ M(pppp) ≤ 3942.5 MeV were excluded. The solid histogram was constructed as the sum of the background spectrum (1) and the relativistic Breit–Wigner function [2]:

$$BW(M) = \frac{\Gamma M M_0}{\left(M^2 - M_0^2\right)^2 - \Gamma^2 M_0^2}, \qquad (2)$$

where M_0 and Γ are the mass and width of the experimentally observed four-proton resonances, respectively.

As can be seen from the figure, function (1) provides an excellent description of the entire experimental invariant-mass spectrum, except for the points at M(pppp) = 3890 MeV and 3920 MeV. As a result of fitting the experimental four-proton invariant-mass spectrum with the sum of functions (1) and (2) (solid histogram, $\chi^2/ndf = 0.6$), the values of the parameters M_0 and Γ were determined. For the first peak, they were $M_0 = 3890 \pm 3$ MeV and $\Gamma = 1.3 \pm 0.4$ MeV, respectively, while for the second peak, $M_0 = 3920 \pm 3$ MeV and $\Gamma = 1.2 \pm 0.4$ MeV, respectively.

The excess number of events above the background spectrum for the first peak was found to be $N_1 = 89 \pm 22$, corresponding to 4.0 standard deviations; thus, this peak is statistically significant. The excess number of events above the background spectrum for the second peak was $N_2 = 106 \pm 24$, corresponding to 4.4 standard deviations; therefore, this peak is also statistically significant.

These two numbers (N_1 and N_2) practically coincide with the excess numbers of combinations obtained when considering the invariant-mass spectrum for events with four or more protons in the final state.

Using the values of N_1 and N_2, the total number of analyzed events (N_{total}), and the inelastic cross section for $^{12}C^{12}C$ interactions at an energy of 3.37 A GeV [3], the inclusive cross sections for the production of these possible four-proton resonant states can be estimated as follows: $\sigma_{incl1} = N_1 \cdot \sigma_{in}/N_{total} = 89 \times 830/20527 = 3.6 \pm 0.9$ mb, and $\sigma_{incl2} = N_2 \cdot \sigma_{in}/N_{total} = = 109 \times 830/20527 = 4.4 \pm 1.0$ mb.

These results indicate that, within the statistical uncertainties, the two states are produced with approximately equal probabilities.

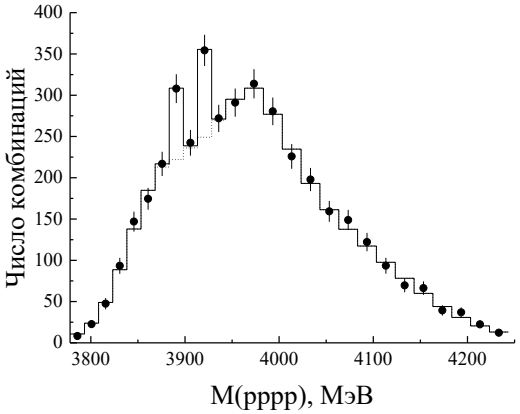

Figure. Experimental distribution of the invariant mass of four protons (●) in ^{12}C–^{12}C collisions at 3.37 A GeV for events with five or more protons in the final state. The dashed histogram represents the background spectrum constructed using the sum of three Gaussian functions (1). The solid histogram represents the result of fitting the experimental four-proton invariant-mass spectrum with the sum of functions (1) and (2).

Thus, it can be concluded that a statistically significant four-proton state is observed in events with five or more protons in the final state, whereas it is not observed in events with exactly four protons in the final state. Based on this observation and taking into account the Pauli exclusion principle, it can be assumed that the four-proton state is formed as follows. Since the carbon nucleus has an α-cluster structure, the breakup of two or three α clusters may produce two or three pairs of diproton states. Two such pairs may subsequently combine to form a four-proton (hadronic) molecule.

Reference:

1.E.N.Kladnitskaya, S.Yu.Sivoklokov, Some methodical problems concerning momentum measurement and event selection on Carbon from interactions in Propane bubble chamber, JINR Preprint P1-88-412, Dubna (1988).
2.Higgins D., Phys. Rev. D. – American Physical Society (USA),1979.− Vol.19.− p.731.
3.E.O.Abdrahmanov et al., *Z. Phys. C5*, 1 (1980); N. Angelov et al., *Yad. Fiz.* 33, 1046 (1981).

A CORRELATION METHOD FOR CENTRALITY ESTIMATION IN ASYMMETRIC NUCLEUS-NUCLEUS INTERACTIONS

Ibraimova S.A., Lebedev I.A.
Institute of Nuclear Physics, Institute of Physics and Technology, Almaty, Kazakhstan

Determining the collision centrality is one of the key tasks in the study of relativistic nucleus-nucleus collisions. It is the centrality that determines the number of participant nucleons, the energy deposition in the interaction zone, and the conditions for the formation of hot and dense nuclear matter. The correct classification of events by centrality is essential for searching for collective effects, studying the phase transition of hadronic matter into quark-gluon plasma, and investigating the critical point of the quantum chromodynamics phase diagram.This task is of particular relevance in connection with the commissioning of the NICA (Nuclotron-based Ion Collider fAcility) accelerator complex, which is designed to study heavy-ion collisions in the region of high baryon densities. Unlike the RHIC and LHC experiments, which primarily focus on the region of high temperatures and small baryon chemical potentials, the MPD and BM@N experiments at the NICA complex will allow for the exploration of the phase diagram region where a critical point and a first-

order phase transition are expected.This paper considers centrality determination criteria based on the experimental data of silicon nuclei interactions at 14.6 A GeV with NIKFI BR-2 nuclear emulsion nuclei. It is shown that for asymmetric collisions, the correlation dependence of the number of target fragments N_h on the shower particle multiplicity n_s serves as an effective criterion for estimating centrality. In the initial stage of this dependence, a decrease in multiplicity corresponds to an increase in collision peripherality, whereas after reaching the maximum value of N_h, a further increase in multiplicity characterizes an increase in the interaction centrality. This approach allows for a reliable separation of interactions with light and heavy target nuclei and minimizes the impact of initial-state fluctuations.The proposed criterion can be used in the analysis of experimental data from the NICA complex to select events of varying centrality, study collective effects, and improve the accuracy of interpreting the observed fluctuations associated with the search for new states of strongly interacting matter.

This research is funded by the Science Committee of the Ministry of Science and Higher Education of the Republic of Kazakhstan (Grant No. AP23487706).

STUDY OF THE FORMATION OF Δ^0 ISOBARS IN CENTRAL $p^{12}C$ AND $d^{12}C$ COLLISIONS AT 4.2 A GeV/c

Olimov K.[1], Bekmirzaev R.[2], Tugalov F.[2]

[1]*Institute of Physics and Technology, Uzbekistan Academy of Sciences, Tashkent, Uzbekistan*

[2]*Jizzakh State Pedagogical University, Jizzakh, Uzbekistan*

This work presents new experimental data on various characteristics of Δ^0 isobars produced in central $p^{12}C$ and $d^{12}C$ collisions at 4.2 A GeV/c.

Since the average number of protons was found to be close to 1 in both types of collisions (see Table 1), $p^{12}C$ and $d^{12}C$ collisions with a number of participant protons ≥3 were classified as central collisions. The mass spectra of Δ^0 isobars for the collisions under consideration are shown in Figs. 1 and 2, respectively.

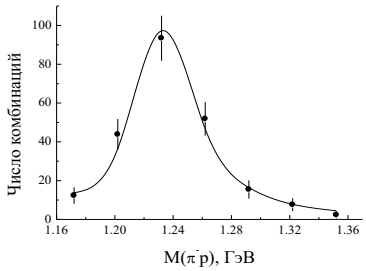

Figure 1. Distribution of the effective mass of π^-p pairs in central $p^{12}C$ collisions at 4.2 GeV/c

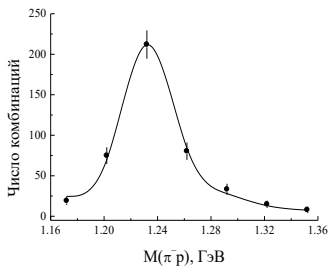

Figure 2. Distribution of the effective mass of π^-p pairs in central $d^{12}C$ collisions at 4.2 GeV/c

The curves in the figures represent fits to the experimental spectra of the effective masses of proton–π^- pairs, M(π^-p), using the relativistic Breit–Wigner formula [1]. The fitting results are presented in Table 1.

Table 1. Values of the mass MΔ and mass-spectrum width Γ of Δ^0 isobars

Collision type	Average number of participant protons	MΔ, MeV	Γ, MeV	χ^2 / degrees of freedom
p^{12}C	0.91±0.01	1235±3	51±6	0.69
d^{12}C	1.12±0.01	1234 ±2	44.9±3.8	0.54

As can be seen from Table 1, the widths of the mass spectra of Δ^0 isobars are close to each other for both types of collisions.

Reference:

1. D.Higgins, Phys. Rev. D 19, 731 (1979).

CENTRALITY DEPENDENCIES OF TRANSVERSE MOMENTUM SPECTRA OF PRIMARY CHARGED PARTICLES PRODUCED IN HIGH-ENERGY Pb+Pb COLLISIONS AT THE LHC

Olimov Kh.K.[1,2], Khudoyberdieva Sh.A.[1], Lebedev I.A.[3], Fedosimova A.I.[3,4], Liu Fu-Hu[5,b]

[1]*Physical-Technical Institute, Uzbekistan Academy of Sciences, Tashkent, Uzbekistan*
[2]*National University of Science and Technology MISIS, Almalyk, Uzbekistan*
[3]*Institute of Physics and Technology, Satbayev University, Almaty, Kazakhstan*
[4]*Institute of Nuclear Physics, Almaty, Kazakhstan*
[5]*Institute of Theoretical Physics, Shanxi University, Taiyuan, China*

Quark-gluon plasma (QGP), the plasma state of nearly free quarks and gluons, has been produced in high-energy heavy-ion collisions at the Large Hadron Collider (LHC, CERN, Switzerland) and Relativistic Heavy-ion Collider (RHIC, Brookhaven National Laboratory, USA). Having very short lifetime (~ 10^{-23} s) very dense and hot QGP matter has demonstrated almost perfect fluid properties with very small viscosity. During its very short lifetime, QGP goes through hadronization process, transforming into a great number of particles. Then, very hot and dense system of the generated hadrons goes through expansion and cooling down process, undergoing rapidly the chemical and kinetic freeze-out stages. The chemical freeze-out takes place when the hadrons stop interacting inelastically, which fixes the numbers of produced particles of different types. The chemical potential, μ, and the system's temperature, $T_{\rm ch}$, at the moment of chemical freeze-out are extracted, using statistical hadronization or thermal models, from analysis of the ratios of yields of various particle species. At the final kinetic freeze-out stage elastic interactions among particles of expanding fireball stop, which fixes the momenta and energies of the particles finally measured by detectors. Therefore, it is important to analyze the experimental transverse momentum (p_T) distributions of produced hadrons to estimate the thermodynamic and hydrodynamic properties of a collision system at the kinetic freeze-out.

Evolution of the experimental mid(pseudo)rapidity p_T distributions of primary charged particles with changing collision centrality, measured by the ALICE Collaboration in the long p_T range (up to 15 GeV/c) in Pb+Pb collisions at $\sqrt{s_{nn}}$=2.76 and 5.02 TeV, has been analyzed [1] using thermodynamically consistent Tsallis function with embedded transverse flow. The results [1] have been compared with the earlier results coming from simultaneous analysis of short p_T range (up to 5 GeV/c) of p_T spectra of the charged pions and kaons, protons and antiprotons in Pb+Pb collisions at $\sqrt{s_{nn}}$=2.76 and 5.02 TeV at the LHC. Transverse flow has been absent at low $\langle N_{part}\rangle$ values and it starts emerging between collision centralities (40-50)% and (30-40)% in Pb+Pb collisions at $\sqrt{s_{nn}}$ = 2.76 TeV and between collision centralities (50-60)% and (40-50)% in Pb+Pb collisions at $\sqrt{s_{nn}}$ = 5.02 TeV. Kinetic freeze-out temperature, T_0, has decreased greatly between collision centralities (40-50)% and (30-40)% in Pb+Pb collisions at $\sqrt{s_{nn}}$ = 2.76 TeV and between collision centralities (50-60)% and (40-50)% in Pb+Pb collisions at $\sqrt{s_{nn}}$ = 5.02 TeV. We have estimated border value of collision centrality for crossover phase transition from the dense hadronic state to that of QGP state (or mixed state of QGP and hadrons) to be $\langle N_{part}\rangle$ = 109 ± 8 and $\langle N_{part}\rangle$ = 71 ± 7 in Pb+Pb collisions at $\sqrt{s_{nn}}$ = 2.76 and 5.02 TeV, respectively. Non-extensivity parameter q has decreased systematically with increasing $\langle N_{part}\rangle$ and $\langle dN_{ch}/d\eta\rangle$ (with an increase in collision centrality) in both Pb+Pb collisions at $\sqrt{s_{nn}}$ = 2.76 and 5.02 TeV. This denotes systematic increase in degree of system thermalization with increasing centrality of Pb+Pb collisions at $\sqrt{s_{nn}}$ = 2.76 and 5.02 TeV at the LHC, in agreement with similar result of previous works. Strong negative correlation has been obtained between parameter q and $\langle N_{part}\rangle$ as well as between parameter q and $\langle dN_{ch}/d\eta\rangle$ with Pearson correlation coefficient $R(x,y) \sim -1$ in both Pb+Pb collisions at $\sqrt{s_{nn}}$=2.76 and 5.02 TeV. Kinetic freeze-out temperature parameter, T_0, has proved to be strongly anticorrelated with average transverse flow velocity, $\langle\beta_T\rangle$, with $R(T_0,\langle\beta_T\rangle) \sim -1$ in both Pb+Pb collisions at $\sqrt{s_{nn}}$=2.76 and 5.02 TeV, in agreement with analogous result of earlier works. The obtained results have been compared with those extracted in minimum bias p+p and p+Pb collisions at $\sqrt{s_{nn}}$=2.76 and 5.02 TeV.

References:

1. Khusniddin K. Olimov *et al., Centrality evolution of transverse momentum spectra of primary charged particles produced in high-energy Pb+Pb collisions at the LHC*, Mod. Phys. Lett. A 41, 2650120 (2026). https://doi.org/10.1142/S0217732326501208

A UNIFIED APPROACH TO TRANSVERSE MOMENTUM SPECTRA IN HIGH ENERGY HEAVY-ION COLLISIONS

Kakhorova A.N.[1,2], Olimov Kh.K.[2]

[1]*Samarkand State University, Samarkand, Uzbekistan*

[2]*Physical-Technical Institute, Uzbekistan Academy of Sciences, Tashkent, Uzbekistan*

Ultrarelativistic heavy-ion collisions at the Relativistic Heavy Ion Collider (RHIC) and the Large Hadron Collider (LHC) have provided a unique opportunity to investigate strongly interacting matter under extreme conditions of temperature and energy density, where a new state of matter, known as the quark-gluon plasma (QGP), is formed. The transverse momentum (p_T) spectra

constitute one of the most important experimental observables, as they carry essential information about both the dynamics of the system's evolution toward equilibrium and the anisotropic collective behavior developed in heavy-ion collisions [1].

The development of an adequate theoretical formalism for describing transverse momentum spectra remains an important challenge and continues to attract considerable interest within the high-energy nuclear physics community. In this context, numerous efforts have been devoted to constructing a generalized distribution function capable of describing the momentum distributions of produced particles. Due to the asymptotic freedom and the energy dependence of the quantum chromodynamics (QCD) coupling constant, interactions become exceedingly strong at low transverse momenta (p_T), rendering perturbative QCD techniques inapplicable in this kinematic regime. Consequently, statistical approaches become particularly important and have proven to be highly successful in describing transverse momentum spectra.

Most existing approaches are based on the assumption that the system under consideration has a thermal origin. Accordingly, by treating the system produced in heavy-ion collisions as a thermalized system of particles, the transverse momentum spectra of the produced particles can be successfully described within the framework of conventional Boltzmann–Gibbs statistics [2]. In this formalism, the transverse momentum (p_T) spectrum is expressed as follows:

$$\frac{1}{2\pi p_T}\frac{d^2N}{dydp_T} = \frac{gV}{(2\pi)^3} m_T \left[\exp\left(-\frac{m_T}{T}\right)\right] \qquad (1).$$

In the above equation, the parameter T represents the effective temperature, which incorporates contributions from both the random thermal motion of hadrons and the collective transverse flow of the expanding hadronic matter (when present). To disentangle these contributions to the effective temperature T, the transverse flow velocity is introduced into Eq. (1) through the Lorentz transformation $m_T \to \langle\gamma_T\rangle\cdot(m_T - p_T\langle\beta_T\rangle)$. As a result, Eq. (1) can be rewritten as follows:

$$\frac{1}{2\pi p_T}\frac{d^2N}{dydp_T} = \frac{gV}{(2\pi)^3}\cdot\langle\gamma_T\rangle\cdot(m_T - p_T\langle\beta_T\rangle)\cdot\left[\exp\left(-\frac{\langle\gamma_T\rangle\cdot(m_T - p_T\langle\beta_T\rangle)}{T_0}\right)\right] \qquad (2).$$

Equation (2) is referred to as the Maxwell-Boltzmann distribution with an embedded transverse flow. Here, T_0 denotes the kinetic freeze-out temperature of the system. Boltzman-Gibbs statistics provides an excellent approximation for systems whose constituent particles are either independent or only weakly correlated. In such systems, the entropy satisfies the properties of additivity and extensivity.

In Ref. [3], the proposed distribution was employed to fit the experimental transverse momentum spectra. The results showed that the Maxwell-Boltzmann distribution with an embedded transverse flow provides a satisfactory description of the experimental data. The quality of the simultaneous fits was characterized by χ^2/ndf values close to unity for fitting ranges extending up to p_T < 1.0 and 1.3 GeV/c.

However, this framework is not suitable for describing strongly correlated systems, where long-range interactions and correlations play a significant role [4].

Furthermore, in strongly correlated systems, the entropy may become non-extensive or non-additive, rendering Boltzmann-Gibbs statistics inapplicable. Experimentally, the transverse momentum spectra exhibit a clear deviation from the Boltzmann-Gibbs distribution in the high-p_T region. This deviation can be interpreted as a consequence of the presence of long-range interactions [5] within the produced fireball. As a result, the observed transverse momentum spectra exhibit a power-law behavior rather than the exponential behavior predicted by the Boltzmann-Gibbs distribution.

References:

1. S. Jena, R. Gupta, A unified formalism to study transverse momentum spectra in heavy-ion collision, Phys. Letters B 807 (2020) 135551.

2. L. Stodolsky, Temperature fluctuations in multiparticle production, Phys. Rev.Lett. 75 (1995) 1044–1045.
3. Kh. K. Olimov, A. Fedosimova, Fu-Hu Liu, I.A. Lebedev, A. Tokhirov, S. Ibraimova, E. Bondar, Centrality and energy dependencies of kinetic freeze-out parameters in high-energy p + Pb, Xe + Xe, and Pb + Pb collisions at the LHC, The Eur. Phys. Jour. Plus 140 (2025) 550.
4. M. Gell Mann, C. Tsallis, Nonextensive entropy - interdisciplinary applications, in: Murray Gell-Mann, C. Tsallis (Eds.), Nonextensive Entropy – Interdisciplinary Applications, Oxford University Press, Apr 2004, p. 440.
5. I. Bediaga, E.M.F. Curado, J.M. de Miranda, A nonextensive thermodynamical equilibrium approach in e+ e^- - hadrons, Physica A 286 (2000) 156–163.

MULTIPLICITY DEPENDENCIES OF MIDRAPIDITY P_T DISTRIBUTIONS OF IDENTIFIED CHARGED PARTICLES IN PROTON-PROTON COLLISIONS AT THE LHC WITHIN A TWO-COMPONENT MODEL

Olimov Kh.K.[1,2], Fedosimova A.[3,4], Liu Fu-Hu[5], Musaev K.A.[1], Lebedev I.A.[3], Tokhirov A.[1], Ibraimova S.[3], Bondar E.[3]

[1]*Physical-Technical Institute, Uzbekistan Academy of Sciences, Tashkent, Uzbekistan*
[2]*National University of Science and Technology MISIS, Almalyk, Uzbekistan*
[3]*Institute of Physics and Technology, Satbayev University, Almaty, Kazakhstan*
[4]*Institute of Nuclear Physics, Almaty, Kazakhstan*
[5]*Institute of Theoretical Physics, Shanxi University, Taiyuan, China*

In early works, analysis of high-energy proton-proton collisions was used as a baseline to extract the collective parameters of high-energy heavy-ion collisions, in which production of Quark-gluon plasma (QGP) was firmly established. Nevertheless, most of the known signatures of QGP creation were observed also in high-energy proton-proton collisions with large multiplicities at the LHC (Large Hadron Collider). One of the important signatures of QGP formation is significant enhancement of yield of multi-strange particles with respect to non-strange hadrons, which was observed in high-multiplicity proton-proton collisions at high energies. On the whole, the collective properties of high-multiplicity proton-proton collision events were found to be very similar to the corresponding properties observed in high-energy heavy-ion collisions. Hence, it is equally important to investigate high-energy heavy-ion as well as proton-proton collisions.

The recently proposed two-component Tsallis-Hagedorn Model with Transverse Flow (THMTF) function, which is the sum of thermodynamically consistent Tsallis function with embedded transverse flow and inverse power-law function (which is asymptotic of Hagedorn function at high p_T values), has described [1] quite well simultaneously the experimental midrapidity p_T spectra of the charged pions and kaons, protons and antiprotons in the whole measured p_T range up to 20 GeV/c at all ten multiplicity classes in proton-proton collisions at $\sqrt{s}$ =7 and 13 TeV at the LHC. Dependencies of non-extensivity parameter, q, kinetic freeze-out temperature parameter, T_0, momentum scale parameter, P_0, and power-index n of the two-component THMTF function on $\langle dN_{ch}/d\eta \rangle$ in proton-proton collisions at $\sqrt{s}$ =7 and 13 TeV have been analyzed and interpreted [1]. Analyzing $\langle dN_{ch}/d\eta \rangle$ dependencies of parameters T_0 and $\langle \beta_T \rangle$, the border $\langle dN_{ch}/d\eta \rangle$ values of transition towards plateau region of kinetic freeze-out temperature (T_0) (and simultaneous

emergence of transverse flow) and probable onset of deconfinement phase transition (towards QGP-like state) have been estimated [1] to be $\langle dN_{ch}/d\eta \rangle \approx 7.6\pm0.9$ and $\langle dN_{ch}/d\eta \rangle \approx 9.0\pm1.0$ in proton-proton collisions at $\sqrt{s}$ = 7 and 13 TeV, respectively. These estimates made using THMTF function in present work [1] have been above but close to the corresponding $\langle dN_{ch}/d\eta \rangle \approx 6.1\pm0.3$ and $\langle dN_{ch}/d\eta \rangle \approx 7.1\pm0.2$ estimates of possible onset of deconfinement phase transition in proton-proton collisions at $\sqrt{s}$ = 7 and 13 TeV, respectively, made in our earlier works using Hagedorn function with embedded transverse flow. Our estimates are consistent with and complement the corresponding early result ($(dN_{ch}/d\eta) \approx 6\pm1$) of Campanini and Ferri for probable onset of deconfinement phase transition, obtained from analyses of the experimental $\langle p_T \rangle$ versus $\langle dN_{ch}/d\eta \rangle$ curves and extracted experimental EOSs, and squared speed of sound in proton-proton and proton-antiproton collisions in wide energy, $\sqrt{s}$ = 31–7000 GeV, interval. The mean number of partons participating in a scattering, n_α=5, has been estimated [1] from extracted average value of power-index n in the analyzed proton-proton collisions. This suggests that $g + q \rightarrow meson + q$ and $g + g \rightarrow meson + g$ gluon fragmentation reactions are the main mechanisms for high p_T meson production in proton-proton collisions at the LHC. The obtained significant differences in $\langle dN_{ch}/d\eta \rangle$ dependencies of parameters q and n for pions and kaons, on the one hand, and for (anti)protons, on the other hand, can imply that pions and kaons demonstrate features of local thermalization in proton-proton collisions at the LHC with high enough multiplicity, whereas (anti)protons show significant deviations due to non-thermal production mechanisms [1]. The Pearson coefficients of linear correlation have been calculated between various parameters of the two-component THMTF function in proton-proton collisions at $\sqrt{s}$ = 7 and 13 TeV and compared with those obtained recently in Xe+Xe Pb+Pb collisions at the LHC [1].

References:

1. Khusniddin K. Olimov et al., Study of Multiplicity Dependencies of Midrapidity pT Spectra of Identified Charged Particles in Proton-Proton Collisions at the LHC Using a Two-Component Model, Preprints 2026071979 (2026). https://doi.org/10.20944/preprints202607.1979.v1

ADVANTAGES AND DISADVANTAGES OF THE ΓΓ CHANNEL IN HIGGS BOSON RESEARCH

Bakhromov J.O.[1,2]
[1]*Institute of High Energy Physics, Beijing, China*
[2]*University of Chinese Academy of Sciences, Beijing, China*

The diphoton decay channel H→γγ was crucial for the discovery of the Higgs boson at the LHC in 2012. This paper reviews its key advantages and disadvantages. The main advantages are clean experimental signature with excellent mass resolution, high signal-to-background ratio, and unique sensitivity to new physics through loop contributions. The main disadvantages are small branching ratio (~0.2%), loop-mediated nature requiring complex theoretical calculations, and experimental challenges from backgrounds and photon identification.

The discovery of a Higgs boson with mass ~125 GeV by ATLAS and CMS in 2012 marked a historic milestone [1, 2]. The H→γγ channel was one of the "golden channels" that provided the

clearest evidence. The decay is loop-mediated (primarily through WW bosons and top quarks) with a Standard Model branching ratio of approximately 0.2% [3].

The final state consists of two high-energy photons with excellent energy resolution. The diphoton mass resolution is ~1-2%, crucial for distinguishing signal from background and precisely measuring the Higgs mass [4].

Despite small branching ratio, the channel benefits from relatively low background compared to jet final states [5]. The primary irreducible background from QCD diphoton production can be suppressed through kinematic cuts.

The loop-mediated nature makes it sensitive to new charged particles (supersymmetric particles, charged Higgs, etc.) [6]. Any new particle in the loop can modify the diphoton branching ratio.

The angular distribution and polarization of photons allow determination of Higgs spin and CP properties [7].

BR(H→γγ) ≈ 0.23% means large datasets are required. This limits statistical precision and requires very large datasets. While it was sufficient for discovery, achieving percent-level precision measurements of its properties will require the full HL-LHC dataset and future colliders [8].

No tree-level coupling requires calculations to high orders in perturbative QCD and electroweak corrections, introducing theoretical uncertainties [9].

Dominant QCD diphoton background has much larger cross section. Photon identification requires sophisticated calorimeter techniques to distinguish from jets and $\pi^0\pi^0$ decays [10].

Not all new physics models modify the diphoton rate. Some scenarios affect other channels ($H \to b\bar{b}$, H→WW*) while leaving the diphoton rate unchanged.

The H→γγ channel offers unique advantages: clean signature, excellent resolution, and sensitivity to new physics. However, these come with costs: small branching ratio, theoretical complexity, and experimental challenges. Complementarity with other channels is essential for a complete understanding of the Higgs boson. As the LHC continues and future colliders emerge, this channel will remain central to the search for physics beyond the Standard Model.

References:

1. ATLAS Collaboration, Phys. Lett. B 716, 1 (2012).
2. CMS Collaboration, Phys. Lett. B 716, 30 (2012).
3. Probing 3-3-1 Models in Diphoton Higgs Boson Decay, Phys.Rev.D 84 (2011) 115004.
4. ATLAS Collaboration, "Search for the Standard Model Higgs boson in the two-photon final state in ATLAS," Phys. Rev. Lett. 108 (2012) 111803.
5. S.Frixione, Isolation of photons in perturbative QCD, Phys. Lett. B 429 (1998) 369.
6. A 125 GeV Higgs and Its Diphoton Signal in Different SUSY Models: A Mini Review, Adv. High Energy Phys. 2012 (2012) 312719.
7. ATLAS and CMS Collaborations, "Measurements of the Higgs boson production and decay rates and constraints on its couplings from a combined ATLAS and CMS analysis of the LHC pp collision data at √s = 7 and 8 TeV," JHEP 08 (2016) 045.
8. P.Englert, "New Physics Probes at Present/Future Hadron Colliders via Vh Production," Ph.D. thesis, Humboldt-Universität zu Berlin (2023).
9. Q.Yu and X.G.Wu, "Properties of the decay H → γγ using the approximate α_s^4 corrections and the principle of maximum conformality," arXiv:2403.12345 [hep-ph] (2024).
10. CMS Collaboration, "Indirect on-shell constraint on the Higgs boson width via signal–background interference in the diphoton channel at CMS," CMS-PAS-HIG-25-004.

EFFECTS OF DARK MATTER AND EINSTEIN–GAUSS–BONNET GRAVITY ON MASSIVE COMPACT STARS

Akhmedov S.E., Palvanov G.S.
National University of Uzbekistan, Tashkent, Uzbekistan

Compact stars are important laboratories for studying matter at supranuclear densities and testing gravity in the strong-field regime. Observations of massive neutron stars and the gravitational-wave event GW170817 provide important constraints on the equation of state and mass–radius relations of compact objects [1]. In this work, we investigate compact stars composed of deconfined quark matter admixed with self-interacting bosonic dark matter within regularized four-dimensional Einstein–Gauss–Bonnet (4DEGB) gravity [2].

The purpose of the present study is to investigate the combined effects of quark matter, self-interacting bosonic dark matter and Gauss–Bonnet corrections on massive compact stars. Particular attention is given to the maximum mass and the physical stability of the resulting configurations.

We investigate the structure and stability of massive compact stars composed of deconfined quark matter admixed with self-interacting bosonic dark matter in the framework of regularized four-dimensional Einstein–Gauss–Bonnet (4DEGB) gravity. The stellar interior is described as a two-fluid system in which the dark matter and quark matter components interact only through gravity. The quark matter equation of state is described by the MIT bag model, while the dark matter component is modeled using a self-interacting bosonic equation of state in the Thomas–Fermi regime. The equilibrium stellar configurations are obtained by numerically solving the modified Tolman–Oppenheimer–Volkoff (TOV) equations.

For quark matter, the adopted equation of state is

$$p_{qm} = \frac{1}{3}(\rho_{qm} - 4B)$$

where B=60 MeV/fm^3 is the bag constant. The total energy density and pressure of the two-fluid system are

$$\rho = \rho_{dm} + \rho_{qm}, \quad p = p_{dm} + p_{qm}.$$

The calculations focus on the influence of the Gauss–Bonnet coupling parameter α and the bosonic dark matter particle mass m_χ on the mass–radius relation, maximum gravitational mass, compactness, and stability of the configurations.

For m_χ=200 MeV, increasing the Gauss–Bonnet coupling from α=−10 km^2 to 10 km^2 increases the maximum mass from 1.413 $M_\odot$ to 2.417 $M_\odot$. This demonstrates that positive Gauss–Bonnet coupling can significantly enhance the maximum mass of compact stars.

At fixed α=10 km^2, increasing the dark matter particle mass from m_χ=150 to 250 MeV results in an increase of the maximum mass from 2.411 $M_\odot$ to 2.507 $M_\odot$, while the corresponding radius increases from 10.53 to 11.47 km. The obtained configurations are compatible with several astrophysical constraints, including those associated with GW170817, PSR J0348+0432, PSR J0952−0607, and HESS J1731−347.

The stability of the stellar configurations is examined using the Harrison–Zeldovich–Novikov criterion,

$$\frac{dM}{d\rho_c} > 0,$$

where M is the gravitational mass and ρ_c is the central energy density. Configurations satisfying this condition belong to the stable branch up to the maximum-mass turning point. Additional stability requirements are provided by the adiabatic index,

$$\Gamma > \frac{4}{3},$$

and the causality condition,

$$\vartheta_s^2 = \frac{dp}{d\rho} < 1.$$

where Γ is the adiabatic index and v_s is the sound speed. The investigated stable configurations satisfy these conditions, with subluminal sound speeds throughout the stellar interior.

The results indicate that the combined effects of self-interacting dark matter, quark matter, and higher-curvature corrections in regularized 4DEGB gravity can support compact stars with masses exceeding $2\,M_\odot$, reaching approximately $2.5\,M_\odot$. The model therefore provides a promising theoretical framework for studying ultra-massive compact stars and the interplay between dark matter, dense quark matter, and modified gravity.

References:

1. Abbott, B. P., et al. *Physical Review Letters*, **121**, 161101 (2018).
Das, K. P., Banerjee, A., Rayimbaev, J., et al. *The European Physical Journal C*, **86**, 824 (2026).

THEORETICAL PREDICTIONS FOR α-DECAY HALF-LIVES OF DEFORMED AND ORIENTED Z=119 ISOTOPES

Ganiev O.K., Bozarov O.A.
Institute of Nuclear Physics, Uzbekistan Academy of Sciences, Tashkent, Uzbekistan

The search for new superheavy elements beyond Oganesson (Z = 118) is one of the important directions of modern nuclear physics, which is partly associated with theoretical predictions of enhanced stability in the vicinity of Z ≈ 114–126 and N ≈ 184. Experimental attempts to synthesize element 119, considered as the first element of the eighth period of the periodic table, are still ongoing, while several fusion–evaporation reaction channels have been theoretically investigated to determine favorable production conditions [1,2]. Since superheavy nuclei, including element 119, are generally identified through correlated α-decay chains, reliable theoretical predictions of their decay characteristics are of great importance for future experiments [3].

In this work, the approach used to describe α-decay is based on the Proximity model, in which the interaction barrier consists of contributions from the nuclear, Coulomb, and centrifugal potentials. The Proximity concept was originally developed by Błocki, Randrup, Świątecki, and Tsang [4], while nuclear masses and deformation properties are described within the Myers–Świątecki formalism [5]. Proximity-model-based approaches have subsequently been applied to the α-decay and cluster radioactivity of heavy and superheavy nuclei [6–8]. In addition, empirical approaches such as the Royer relation have also been successfully used to estimate α-decay half-lives [9].

For deformed nuclei, the interaction potential depends not only on the separation distance *R*, but also on the orientation of the nuclear symmetry axis relative to the α-particle emission direction. Consequently, different orientations result in different potential-barrier shapes and tunneling probabilities. Previous studies have demonstrated that nuclear deformation and orientation can significantly affect α-decay half-lives when proximity interactions are taken into account [10,11]. The generalized orientation-dependent Proximity formalism makes it possible to investigate such effects for arbitrarily oriented deformed nuclear configurations [12].

In this work, we applied this approach specifically to the hypothetical decay of element 119, $^{295}119 \rightarrow {}^{291}117 + \alpha$, where the daughter nucleus is characterized by the deformation parameters $\beta_2 = 0.075$, $\beta_3 = 0$, $\beta_4 = -0.034$, and $\beta_6 = 0.008$. The α-decay half-life is calculated as a function of the orientation angle θ_1 (0°–180°) and the orbital angular momentum l (0–40). The aim of the work is to quantitatively evaluate the combined influence of nuclear deformation, nuclear orientation, and centrifugal forces on the α-decay probability of the still-unobserved Z = 119 system. These results are of particular importance for the prospects of identifying element 119 itself, which would open a new period of the periodic table. The Q_α value (12.94 MeV) was calculated from the nuclear binding energies obtained within the adopted Myers–Świątecki mass formalism [5]. Within the generalized orientation-dependent Proximity-potential formalism, the total interaction potential is calculated in the form $V_{tot}(R, \theta_1) = V_{prox}(R,\theta_1)+V_C(R, \theta_1; \beta_2, \beta_3, \beta_4, \beta_6) + V_{rot}(R,l)$. Based on the WKB approximation, the tunneling probability is determined from the following expression:

$$P = \exp\left\{-\frac{2}{\hbar}\int_{R_a}^{R_b}\sqrt{2\mu(V(R,\theta_1)-Q_\alpha)}\,dR\right\}$$

The α-decay half-life is then determined using $T_{1/2} = \ln(2)/(\nu \cdot P)$ relation.

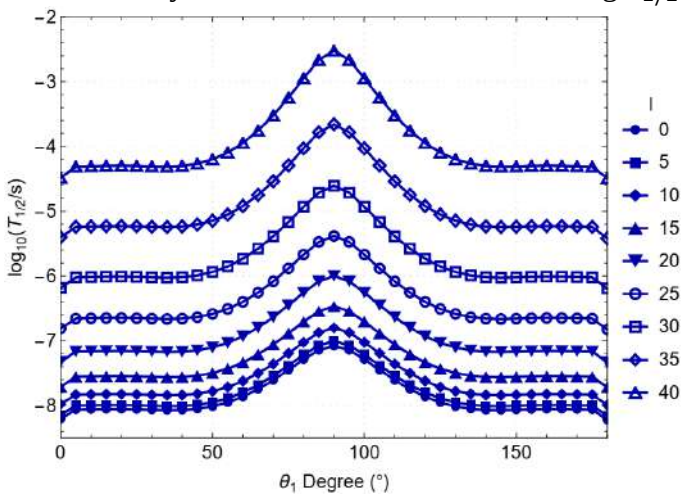

Figure 1. Dependence of $log_{10}(T_{1/2})$ on the orientation angle θ_1 for l = 0–40 in the α-decay $^{295}119 \rightarrow {}^{291}117 + \alpha$ of element 119.

The dependence obtained for l = 0–40, presented in Fig. 1, clearly demonstrates the expected orientation anisotropy for the daughter nucleus of element 119: the half-life reaches its minimum near the symmetry-axis directions ($\theta_1 \approx 0°$, 180°), whereas it reaches its maximum in the equatorial direction ($\theta_1 = 90°$), with $log_{10}(T_{1/2})$ changing approximately from −7.84 to −6.80, corresponding to a variation of about 1.1 orders of magnitude. This trend is also observed for other values of l and becomes more pronounced with increasing orbital angular momentum: for example, increasing l from 0 to 40 at $\theta_1 = 90°$ increases $log_{10}(T_{1/2})$ by approximately 4.6 orders of magnitude, which is explained by the strengthening of the centrifugal barrier and the resulting decrease in the tunneling probability.

The α-decay of the hypothetical superheavy system $^{295}119 \rightarrow {}^{291}117 + \alpha$ was investigated within a deformation- and orientation-dependent total potential and the WKB approximation. The

calculations demonstrate that nuclear deformation produces a pronounced angular dependence of the effective potential barrier and, consequently, of the α-decay half-life. The maximum values of $T_{1/2}$ are obtained around $\theta_1 = 90°$, whereas shorter half-lives are observed near the symmetry-axis directions. The orientation effect becomes significantly stronger with increasing orbital angular momentum: in particular, increasing l from 0 to 40 leads to an increase of approximately 4.6 orders of magnitude in $log_{10}(T_{1/2})$ at $\theta_1 = 90°$. These results demonstrate the necessity of explicitly taking deformation and emission orientation into account when predicting the α-decay characteristics of superheavy nuclei, particularly the still-undiscovered element 119, and may provide useful theoretical guidance for future experimental investigations of element 119 and its decay chains.

References:

1. F.-Y. Chen, J.-X. Li, H.-F.Zhang, Chin. Phys. C **49**, (6) 064107 (2025).
2. B.M.Kayumov, O.K.Ganiev, A.K. Nasirov, G.A. Yuldasheva, Phys. Rev. C **105**, 014618 (2022).
3. N. Sowmya, A.M. Nagaraja, H.C. Manjunatha, Can. J. Phys. **101**, (9) 453–459 (2023).
4. J. Błocki, J. Randrup, W.J. Świątecki, C.F. Tsang, Ann. Phys. **105**, 427–462 (1977).
5. W.D. Myers, W.J. Świątecki, Nucl. Phys. **81**, 1–60 (1966).
6. K.P. Santhosh, A. Augustine, C. Nithya, B. Priyanka, arXiv:1604.00296 (2016).
7. K.P. Santhosh, C. Nithya, arXiv:1609.05495 (2016).
8. K.P. Santhosh, C. Nithya, At. Data Nucl. Data Tables 119, (2018).
9. G. Royer, J. Phys. G: Nucl. Part. Phys. 26, 1149–1170 (2000).
10. E. Yazdankish, M. Nejatolahi, Phys. Scr. 98, 115309 (2023).
11. V.Yu. Denisov, A.A. Khudenko, At. Data Nucl. Data Tables 95, 815–835 (2009).

R.K. Gupta, N. Singh, M. Manhas, Phys. Rev. C 70, 034608 (2004).

ASYMPTOTIC NORMALIZATION COEFFICIENTS FOR ^{6}Li+n→^{7}Li AND CROSS SECTION FOR THE ^{6}Li(n,γ)^{7}Li REACTION

Igamov S.B.[1], Tursunmakhatov K.I.[2], Ikromkhonov E.Sh.[1]

[1]*Institute of Nuclear Physics, Uzbekistan Academy of Sciences, Tashkent, Uzbekistan*

[2]*Gulistan State University, Gulistan, Uzbekistan*

The total cross sections (CS) of the radiative netron capture reaction ^{6}Li(n,γ)^{7}Li were measured in Refs. [1,2]. In the present work, the analysis of the experimental total CS of the ^{6}Li(n,γ)^{7}Li reaction has been performed within the modified Two Body Potential Approach (MTBPA) [3] to obtain the "indirectly determined" values of the asymptotic normalization coefficients (ANCs) for the ^{6}Li+n→^{7}Li(0.0 MeV) and ^{6}Li+n→^{7}Li(0.48 MeV) configurations.

To verify the peripheral character of the ^{6}Li(n,γ)^{7}Li reaction, we have changed the geometric parameters r_0 and a of the Woods-Saxon potential in wide physically acceptable ranges ($r_0 = 1.10 \div 1.40$ fm and $a = 0.57 \div 0.73$ fm) with respect to their "standard" values ($r_0 = 1.25$ fm and $a = 0.65$ fm). Such variation of r_0 and a results in changing the single-particle ANCs in the ranges of $1.72 \le b_{1\ 1/2} \le 2.47$ fm$^{-1/2}$ and $1.81 \le b_{1\ 3/2} \le 2.56$ fm$^{-1/2}$ for the ground state of the ^{7}Li nucleus and of $1.62 \le b_{1\ 1/2} \le 2.31$ fm$^{-1/2}$ and $1.70 \le b_{1\ 3/2} \le 2.39$ fm$^{-1/2}$ for the first excited state of the ^{7}Li nucleus. Variations of the parameters r_0 and a cause $R_{3/2}$ functions to change in the range $8.34 \le R_{\frac{1}{2}} \le$

10.48 μb·fm, $8.50 \leq R_{\frac{3}{2}} \leq 10.71$ μb·fm for the ground state and $4.66 \leq R_{\frac{1}{2}} \leq 5.76$ μb·fm, $4.74 \leq R_{\frac{3}{2}} \leq 5.88$ μb·fm for the first excited state. These relatively small variations of the R functions with respect to the changes in the single-particle potential parameters r_0 and a indicate that the calculated cross sections are only weakly sensitive to the internal part of the nuclear interaction. The weak dependence indicates that the R functions remain nearly insensitive to reasonable variations of single-particle potential parameters. This stability confirms the peripheral nature of the transfer reaction and demonstrates that the ^{6}Li(n,γ)^{7}Li process is peripheral at low energies.

The calculations show that the E1 transition yields a dominant contribution in the entire energy range up to 1.0 MeV. The contributions of E2 and M1 transitions are much more suppressed. Our recommended average values of ANCs obtained from the experimental data from [1,2] are equal to $C^2_{n^6Li;1\frac{3}{2}} = 2.537 \pm 0.259$ fm^{-1} and $C^2_{n^6Li;1\frac{1}{2}} = 1.701 \pm 0.174$ for the ground state and $C^2_{n^6Li;\,1\frac{3}{2}} = 3.302 \pm 0.337$ fm^{-1} and $C^2_{n^7Li;1\frac{1}{2}} = 0.077 \pm 0.008$ for the first excited states of the ^{8}Li nucleus, respectively. A comparison of the calculated cross-section of the radiative direct-capture ^{6}Li(n,γ)^{7}Li reaction leading to the ground and first excited states of the ^{7}Li nucleus together with the calculated total cross-section and experimental data is presented in Fig. 1. The dashed and dotted lines, which are presented in Fig. 1, are the results of the calculations of the cross-section for the ^{6}Li(n,γ)^{7}Li reaction leading to the ground ($3/2^-$; E=0 MeV) and first excited ($1/2^-$; E=0.48 MeV) bound states of the ^{7}Li nucleus according to MTBPM, respectively, performed with the standard values of the parameters r_0 and a (r_0=1.25 fm and a= 0.65 fm) using the recommended weighted values of ANCs in this work. The solid line is the calculated total cross-section for the radiative capture reaction ^{6}Li(n,γ)^{7}Li. The widths of the bands in Fig. 1 correspond to the uncertainties of ANCs for ^{6}Li+n→^{7}Li(0 MeV) and ^{6}Li+n→^{7}Li(0.48 MeV) obtained in this work. As can be seen from Fig. 1, the cross section calculated within MTBPM is in good agreement with the experimental data from Ref. [1,2].

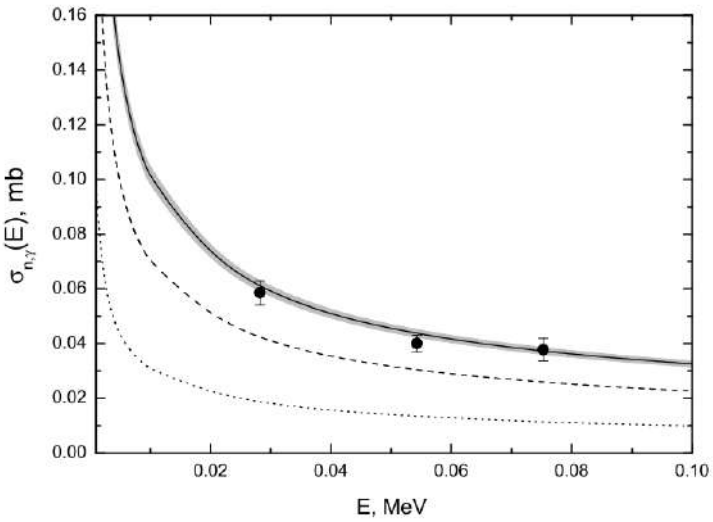

Figure 1. Experimental and calculated cross-sections of the ^{6}Li(n,γ)^{7}Li reaction. The solid line is the calculated total cross-section within MTBPM. The dashed and dotted lines are the calculated cross sections of the ^{6}Li(n,γ)^{7}Li reaction leading to the ground ($3/2^-$; E=0 MeV) and first excited ($1/2^-$; E=0.48 MeV) states of the ^{7}Li nucleus, respectively. The solid circles are the experimental cross-sections from Ref. [1,2]. The bandwidth corresponds to the uncertainties of ANCs for the ^{6}Li+n→ ^{7}Li configuration determined in this work.

The reaction rate $N_A\sigma v$ for the direct capture reaction ^{6}Li(n,γ)^{7}Li in the temperature range $0.01 \leq T_9 \leq 10$ has been calculated on the basis of the calculated cross section of the process.

References:

1. T. Ohsaki et al., AIP Conference Proceedings 529 (1), 678 (2001)
2. T. Ohsaki et al., AIP Conference Proceedings 529 (1), 458 (2001)
S. B. Igamov and R. Yarmukhamedov, Nucl. Phys. A 781 (2007) 247.

WIGNER'S SU(4) SPIN-ISOSPIN SYMMETRY AND MNT&FRAGMENTATION NUCLEAR REACTIONS

Izosimov I.N.
Joint Institute for Nuclear Research, Dubna, Russia

In the case of exact Wigner spin–isospin SU(4) symmetry, the energies of Isobar Analog Resonance (IAR) and Gamow-Teller Resonance (GTR) are degenerate, and we can expect that $E_{\mathrm{IAR}} \approx E_{\mathrm{GTR}}$. In experimental and theoretical analysis of GTR data, a tendency of convergence of GTR and IAR energies (Fig. 1) with increasing (N −Z)/A has been noticed [1,2]. This fact may be interpreted as an approximate realization of SU(4) symmetry in a certain nuclear region, namely for nuclei with large (N − Z)/A, where spin–isospin SU(4) symmetry determines nuclear properties (the SU(4) region). From a simple estimate (Fig.1), it follows that the value Z/N ≈ 0.6 corresponds to the SU(4) region [2].

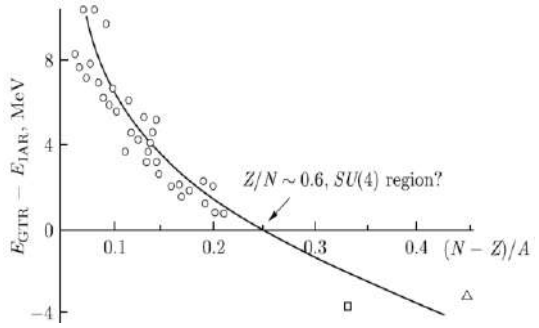

Figure 1. The difference $E_{\mathrm{GTR}} - E_{\mathrm{IAR}}$ as a function of the neutron excess [1]. Data for ^{11}Li (triangle) and ^{6}He (square) were added [2].

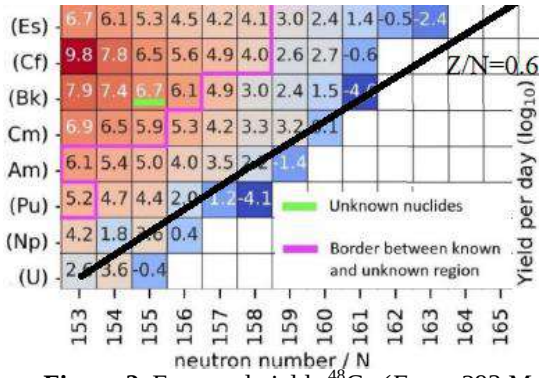

Figure 2. Expected yields ^{48}Ca (E_{lab} = 293 MeV, 1.2 p μA) + ^{251}Cf (500 μg/cm^2) at 1% transmission efficiency [3].

Based on theoretical predictions, multinucleon transfer (MNT) reactions offer an approach to these SU(4) region for heavy nuclei [3] and fragmentation reactions for light nuclei [4].

The pecularieties [5] in nuclear reactions with the excitation of GTR, its satellites and the β- and γ-decays of light (Fig.1) and heavy (Fig.2) nulei in the SU(4) region are discussed.

References:

1. Yu. V. Naumov, A. A. Bykov, I. N. Izosimov, Sov. J. Part. Nucl., **14(2)**, 175 (1983).
2. I. N. Izosimov, EPJ Web of Conferences **239**, 02003 (2020).
3. H.M. Devaraja, et al., Physics letters B, **862**, 139353 (2025).
4. T. Kubo, et al., IEEE Trans. Appl. Supercond. **17**, 1069 (2007).
5. I. N.Izosimov, Int. Journal of Modern Physics E, 35(6), 2641020 (2026).

DEFORMED NUCLEAR SHELLS IN MASS AND ENERGY DISTRIBUTIONS OF FISSION FRAGMENTS OF 240Pu* COMPOUND NUCLEUS FORMED IN 236U(α,f) REACTION AT $E_α$=24 MeV

Alimov D.K.[1], Pan A.N.[1], Kovalchuk K.V.[1], Burtebayev N.[1], Janseitov D.M.[1,2], Boztosun I.[3], Kosherbayeva R.[1]

[1]Institute of Nuclear Physics, Almaty, Kazakhstan
[2]Al-Farabi Kazakh National University, Almaty, Kazakhstan
[3]Akdeniz Üniversitesi, Antalya, Turkey

During the process of nuclear fission formed fragments are rarely spherical hence it is important to take into account not only the spherical, but also deformed nuclear shells into the analysis of the fission process. In experimental studies this could be complicated due to large number of various quantum effects exerting their influence on the process of fission. This requires a sensitive method of analyzing of experimental data to deconvolute all of these effects into tangible data. To achieve that we reanalyzed mass and energy distributions of fission fragments of ^{240}Pu* compound nucleus, experimentally measured with double energy (2E) method, formed in ^{236}U(α,f) reaction at $E_α$=24 MeV. The energy of alpha particle is below the coulomb barrier for that reaction, yielding ~18.3 MeV excitation energy of compound nucleus. Keeping the excitation energy to a minimum is important to preserve shell effect as they vanish with increasing excitation energy. The experimentally measured data were decomposed into yields of separate fission modes and nuclear shells using a method with enhanced sensitivity to smaller yields of deformed nuclear shells. Yields of spherical shells Z50, N82, N50 and deformed nuclear shells Z52, N84, N88 are shown.

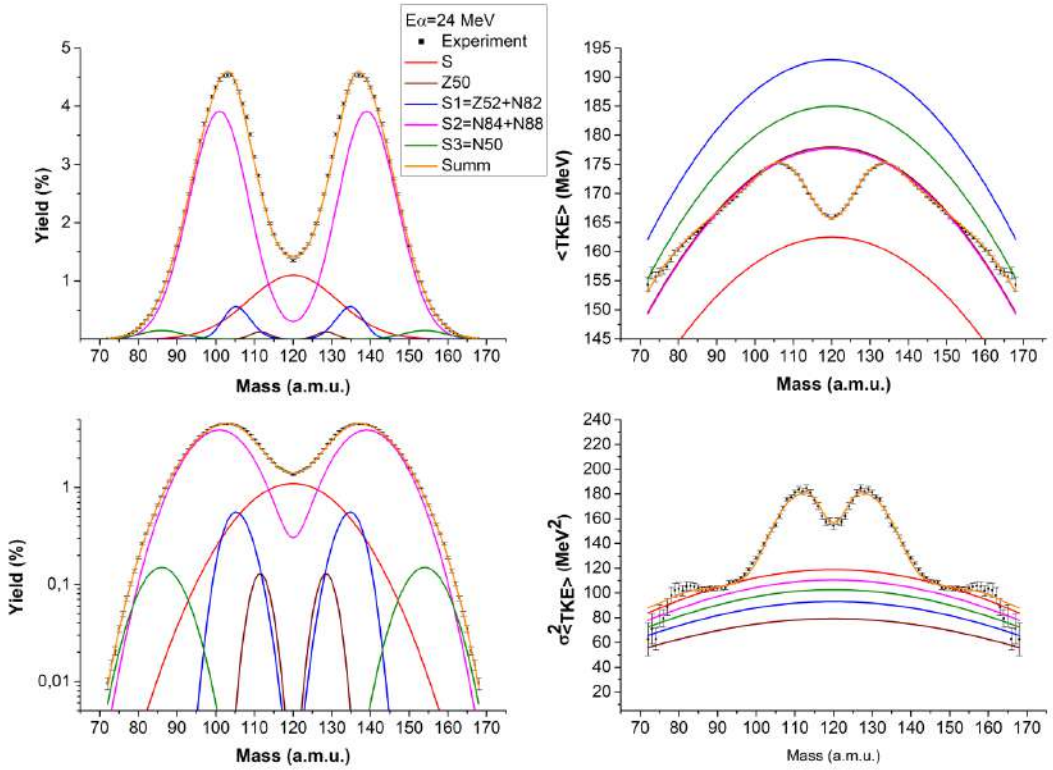

Figure 1. Mass and energy distributions of fission fragments of ^{240}Pu* compound nucleus formed in ^{236}U(α,f) at Eα=24 MeV decomposed into yields of separate fission modes and nuclear shells.

DEPENDENCIES OF MIDRAPIDITY P_T SPECTRA OF PRIMARY CHARGED PARTICLES ON CENTRALITY AND ENERGY OF Pb+Pb AND Xe+Xe COLLISIONS AT THE LHC WITHIN A TWO-COMPONENT MODEL

Olimov Kh.K.[1,2], Khudoyberdieva Sh.A.[1], Liu Fu-Hu[3], Musaev K.A.[1], Kanokova Sh.Z.[1]

[1]*Physical-Technical Institute, Uzbekistan Academy of Sciences, Tashkent, Uzbekistan*
[2]*National University of Science and Technology MISIS (NUST MISIS), Almalyk, Uzbekistan*
[3]*Institute of Theoretical Physics, Shanxi University, Taiyuan, China*

Quark-gluon plasma (QGP) is a plasma state of matter consisting of nearly free quarks and gluons, which is believed to be a matter of a newly born Universe a few microseconds after the so called Bing-Bang – starting point of Universe creation. QGP was generated in high-energy heavy-ion collisions at the Large Hadron Collider (LHC, Switzerland) and the Relativistic Heavy-ion Collider (RHIC, USA). With a very short lifetime of the order of ~ 10^{-23} seconds, this extremely dense and hot QGP matter has demonstrated almost perfect fluid behavior, characterized by very low viscosity. During its short existence, QGP undergoes a process called hadronization, converting colored quarks and gluons into many color-neutral particles, most of which are charged and neutral pions. Following this, the hot and dense cluster ("fireball") of newly produced hadrons expands (flows) longitudinally and radially, cooling down rapidly and passing through the chemical and kinetic freeze-out stages. Chemical freeze-out occurs when the hadrons cease inelastic interactions, which determines the final numbers of produced various particle species. The chemical potential and the temperature of the system at this moment are estimated by analyzing the yield ratios of different particle species with the help of statistical hadronization or thermal models. Finally, kinetic freeze-out stage is reached when elastic interactions among particles in the expanding fireball stop, which determines the particles' final momenta and energies as measured by detectors surrounding the interaction zone. Analysis of the experimental transverse momentum distributions of produced hadrons in the low ($p_T \leq 2–3$ GeV/c) and intermediate (2–3 GeV/$c \leq p_T \leq 5–6$ GeV/c) p_T range is needed for evaluating the thermodynamic and hydrodynamic properties of a collision system at the moment of kinetic freeze-out

A two-component model, which is the sum of thermodynamically consistent Tsallis function with embedded transverse flow and inverse power-law function (which is asymptotic of Hagedorn function at very high p_T), has been proposed to reproduce accurately the measured long p_T ranges of midrapidity transverse momentum spectra of primary charged particles at various centralities of high-energy heavy-ion collisions at the LHC. This two-component model function, called Tsallis-Hagedorn model with transverse flow (THMTF), has described [1] quite well the experimental midrapidity transverse momentum spectra of primary charged particles in the whole p_T range, measured by ALICE Collaboration in minimum bias p+p collisions at $\sqrt{s}$ =2.76 and 5.02 TeV, minimum bias p+Pb collisions at $\sqrt{s_{nn}}$= 5.02 TeV, and various collision centrality intervals of Xe+Xe collisions at $\sqrt{s_{nn}}$ =5.44 TeV and Pb+Pb collisions at $\sqrt{s_{nn}}$ =2.76 and 5.02 TeV. Dependencies of non-extensivity parameter q, kinetic freeze-out temperature parameter, T_0, momentum scale parameter, P_0, and power-index n of the two-component THMTF function on the average number of participant nucleons ($\langle N_{part} \rangle$) as well as mean charged-particle multiplicity density ($\langle dN_{ch}/d\eta \rangle$) in the analyzed Xe+Xe and Pb+Pb collisions at the LHC have been established. The probable border (threshold) values of collision centrality (values of $\langle N_{part} \rangle$) for

crossover phase transition from the dense hadronic state to that of QGP in Pb+Pb collisions at $\sqrt{s_{nn}}$ = 2.76 and 5.02 TeV, and in Xe+Xe collisions at $\sqrt{s_{nn}}$ =5.44 TeV have been estimated [1]. The average number of partons participating in a scattering, n_α=5, has been estimated from extracted average value of power-index *n* in the analyzed collisions. This has suggested that $g + q \rightarrow meson + q$ and $g + g \rightarrow meson + g$ gluon fragmentation reactions are the dominant mechanism for high p_T hadron production in the analyzed p+p, p+Pb, Xe+Xe, and Pb+Pb collisions at the LHC [1].

References:

1. Khusniddin K. Olimov *et al.*, Description of Midrapidity *p*T Spectra of Primary Charged Particles with Changing Centrality and Energy of Pb+Pb and Xe+Xe Collisions at the LHC with a Two-Component Model, Preprints 2026071892 (2026). https://doi.org/10.20944/preprints202607.1892.v1

CREATING AN INDEPENDENT AI AGENT FOR PHYSICAL RESEARCH AS A RESPONSE TO THE CHALLENGES OF TECHNOLOGICAL SOVEREIGNTY

Nishonov M.M.[1,2], Umaraliev A.T.[3]
[1]*Institute of Nuclear Physics, Uzbekistan Academy of Sciences,* ***Tashkent,*** *Uzbekistan*
[2]*Hydrometeorological Research Institute (at Green University),* ***Tashkent,*** *Uzbekistan*
[3]*Independent Researcher*

In an era of rapid artificial intelligence integration into all spheres of science and economics, a fundamental question arises regarding the sovereignty of research organizations. Many experts note that the dependence of critically important systems on the infrastructure of private companies (cloud platforms, API access to large language models, updatable software) threatens the independence of entire states and scientific schools. In the field of physics, this challenge becomes particularly acute, as modern AI agents are capable of radically accelerating hypothesis generation, data analysis, and computational experiments, but their creation and operation are often based on proprietary services.

Here, we propose the concept of a specialized laboratory aimed at developing a proprietary AI agent for physical research, fully independent of external commercial providers. Existing open-source developments (PhysicsIntern, GPD, Collider-Agent, URSA) that could serve as a foundation for such an agent are discussed. The minimum and target requirements for computer resources are analyzed: from workstations with 16 GB VRAM to clusters with hundreds of GPUs, as well as the role of high-performance data storage systems and network infrastructure. The necessary open-source software stack (Linux, Slurm, PyTorch, JAX, Docker) and the laboratory's staffing structure are presented—an interdisciplinary team comprising physicists, ML engineers, MLOps specialists, and system administrators.

Based on estimates of costs, complexity, and strategic benefits, we conclude that establishing such a laboratory is a justified and timely step, allowing not only to protect the research process from external interference but also to ensure the long-term development of its own technological competencies. A phased roadmap is proposed, starting with a pilot project to minimize risks and demonstrate the effectiveness of the approach. The existing issues related to the sanctions policies of foreign countries are also discussed.

THE ROLE OF EXTERNAL COULOMB FIELD IN LOWERING DECAY BARRIERS OF DINUCLEAR SYSTEMS

Otakhonov F.O., Kalandarov Sh.A.
Joint Institute for Nuclear Research, Dubna, Russian Federation

A series of experiments [1-3] on the spontaneous fission (SF) of ^{252}Cf revealed an intriguing phenomenon: primary fission fragments with masses in the range of ≈100-150, while traversing thin degrader foils (C, Al, Ni, Cu), exhibit a tendency for delayed secondary fission. The measured time delay exceeds 400 ns, indicating the existence of long-lived metastable states (shape isomers/cluster states) formed during the primary binary decay. Crucially, the fragments lose up to ≈20 mass units after passing through the foil [3]. This suggests that the Coulomb field of the foil nuclei plays a decisive role in catalyzing the decay of these isomeric states by lowering the fission barrier.

In this work, we propose a theoretical mechanism for this phenomenon based on the concept of a Dinuclear System (DNS) and a Trinuclear System (TNS) [4]. The process is considered as a sequential ternary decay. After the initial binary decay of the TNS formed in the SF of ^{252}Cf, one of the fragments can be in a weakly excited, metastable cluster state. We treat this state as an asymmetric DNS (e.g., ^{14}C + ^{108}Mo or ^{20}O + ^{102}Zr) formed alongside a magic ^{130}Sn nucleus. As this DNS flies towards the foil, it interacts with the Coulomb field of a foil nucleus (Cu, Z=29). This external field perturbs the intrinsic potential of the DNS, reducing the barrier that holds the two clusters together.

The total potential energy of the DNS is calculated as $U_{DNS}=V_{12}+Q_{DNS}$, where Q_{DNS} is the mass balance, and V_{12} is the interaction potential between the two fragments. V_{12} includes the Coulomb part, calculated with quadrupole deformations, and the nuclear part, obtained using the double-folding formalism with effective Skyrme-like forces. The driving potential for ^{252}Cf (Fig. 2 in [5]) shows clear minima corresponding to the formation of magic and near-magic nuclei like ^{130}Sn, which justifies the choice of our DNS configurations. The modification of the DNS barrier by the external Coulomb field of a Cu nucleus is demonstrated in Fig. 1. As the distance of closest approach *Rapp* decreases, the height of the decay barrier is significantly suppressed.

The half-life of the DNS is calculated using the Wentzel-Kramers-Brillouin (WKB) approximation for tunneling through the barrier. The tunneling probability is averaged over the excitation energy *Ex* (0-10 MeV) of the DNS, and the half-life is given by $T_{1/2}(Ex)=(\pi\ln 2)/(\omega_0 P_{av}(Ex))$, where ω_0 is the oscillation frequency in the potential well. The results for the two considered systems are presented in Table 1.

Table 1. Calculated half-lives of DNS with and without the influence of the Cu foil.

DNS System	$T_{1/2}$ without Cu (s)	$T_{1/2}$ with Cu (at *Rapp*) (s)	Reduction Factor
^{14}C + ^{108}Mo	~10^{11} – 10^{-10}	~10^{-4} – 10^{-3}	≈10^{15}–10^{3}
^{20}O + ^{102}Zr	~10^{7} - 10^{-10}	~10^{-3} - 10^{-12}	≈10^{10}–10^{2}

The calculations show that the half-life of the asymmetric DNS decreases dramatically under the influence of the Coulomb field of the Cu foil. For the ^{14}C + ^{108}Mo system, the reduction factor reaches 10^{15} at low excitation energies. For the ^{20}O + ^{102}Zr system, the effect is slightly weaker but still substantial (10^{10}). This dramatic decrease in half-life explains why these long-lived isomer states, which would normally survive the flight to the detector, undergo induced fission precisely when passing through the foil material. The more asymmetric the DNS (i.e., the lighter the cluster), the stronger the influence of the external field, which correlates with the observed mass loss of the heavy fragments.

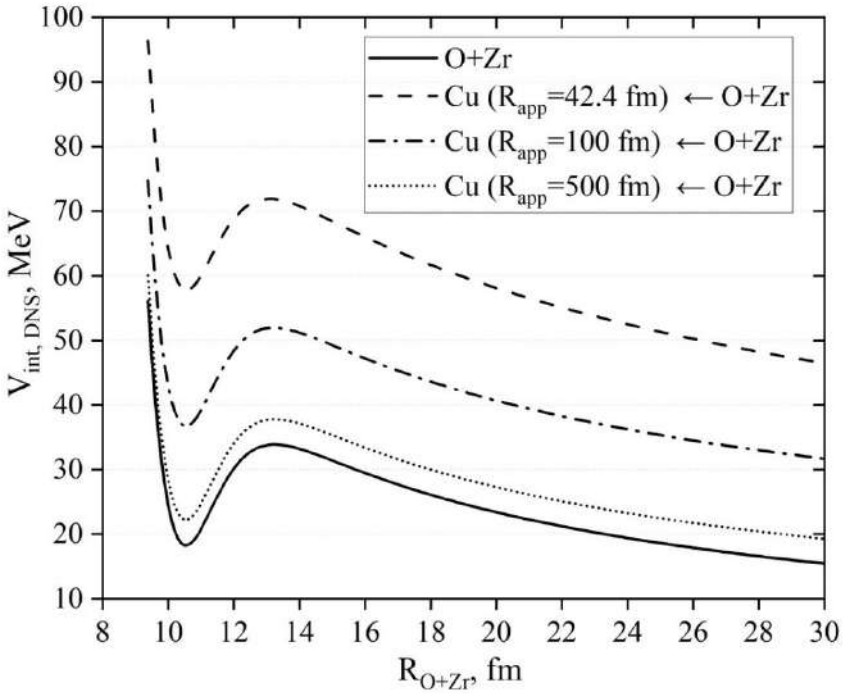

Figure 1. Modification of the interaction potential in the DNS $^{20}O + ^{102}Zr$ by the Coulomb field of a Cu foil nucleus at different distances of closest approach *Rapp*.

In conclusion, using the DNS and TNS models, we have demonstrated a physical mechanism for the foil-induced decay of cluster states in ^{252}Cf fission fragments. The external Coulomb field significantly lowers the intrinsic fission barrier, reducing the half-life by orders of magnitude and leading to the secondary decay observed in experiments. This work provides a theoretical foundation for understanding the collinear cluster tri-partition phenomenon and the role of external perturbations in nuclear decay.

References:

1. Y.V. Pyatkov, et al., Phys. At. Nucl. 87 (2024) 0419.
2. D.V. Kamanin, et al., Phys. Part. Nucl. Lett. 22 (2025) 0272.
3. Y.V. Pyatkov, et al., Phys. Part. Nucl. Lett. 22 (2025) 312.
4. A. Sh. Kalandarov, et al., Phys. Lett. B 850 (2024) 138522.
5. F.O. Otakhonov, et al., Phys. Lett. B 863 (2025) 140088.

INTER-BAND REDUCED E2-TRANSITION PROBABILITIES EXCITED COLLECTIVE STATES OF TRIAXIAL EVEN-EVEN NUCLEI

Nadirbekov M.S.[1], Sobirova Z.[1], Shadmanov K. K.[2]
[1]*Institute of Nuclear Physics, Uzbekistan Academy of Sciences, Tashkent, Uzbekistan*
[2]*Institute of Pharmaceutical Education and Research, Tashkent, Uzbekistan*

Reduced inter-band e2-transition probabilities are studied within Davydov-Chaban model with Davidson potential for β variable on the dependence of the effective triaxiality parameter γ_{eff}. The inter-band reduced e2-transition probabilities between the ground-state- and β-bands, the ground-state- and γ-bands, γ- and β-bands are presented and expressed in terms of three parameters: g, γ_{eff} and Q_0. Permitted and forbidden e2-transitions associated with γ-band are discussed. The sensitivity of the inter-band reduced e2-transition probabilities to the effective triaxiality parameter γ_{eff} are analyzed.

Reduced e2-transition probabilities between $i \equiv \{nI\tau\}$ and $f \equiv \{n'I'\tau'\}$ can be represented as

$$B(E2; i \to f) = B_a(E2; I\tau \to I'\tau')S_{if}^2, \tag{1}$$

where B_a(E2; $I\tau \to I'\tau'$) is reduced e2-transition probabilities in an asymmetric rotator approximation.

$$S_{if} = \int_0^\infty F_i(\beta)\frac{\beta}{\beta_0}F_f(\beta)\beta^4 d\beta, \tag{2}$$

which takes into account the β-deformability of an even-even nucleus. The general expression for matrix elements S_{if} is very difficult. We will consider specific cases.

The inter-band reduced e2-transition probabilities between the γ- and ground-state-bands are given by

$$S_{if} = \frac{1}{\sqrt[4]{2g}}\frac{\Gamma\left(s_i + s_f + \frac{5}{2}\right)}{\sqrt{\Gamma(2s_i+2)}\sqrt{\Gamma(2s_f+2)}} \tag{3}$$

where Γ(x) is the Gamma function.

The inter-band reduced e2-transitions probabilities between the β- and ground-state-/γ-bands reads

$$S_{if} = \frac{1}{\sqrt[4]{2g}}\frac{2s_i - 2s_f - 1}{4s_i + 4}\sqrt{\frac{2s_i+2}{\Gamma(2s_i+2)\Gamma(2s_f+2)}}\Gamma\left(s_i + s_f + \frac{5}{2}\right). \tag{4}$$

A comparison of the theoretical and experimental values of the reduced e2-transition probabilities (in W. u.) of the inter ground-state-, γ-, β-bands was done for the nuclei ^{154}Sm, ^{158}Gd, ^{162,166}Er, ^{168}Hf, ^{232}Th, ^{236}U, ^{238}U. Theoretical and experimental values of the reduced e2-transition probabilities are in a good agreement, including high spin states.

THE RIGID ROTOR APPROXIMATION TO ODD NUCLEI WITH EFFECTIVE TRIAXIALITY QUADRUPOLE AND OCTUPOLE DEFORMATIONS

Nadirbekov M.S., Sodiqova Z.Y.
Institute of Nuclear Physics, Uzbekistan Academy of Sciences, Tashkent, Uzbekistan

An approximation of a rigid asymmetric rotor for odd nuclei with effective triaxiality quadrupole and octupole deformations has been developed. For the analysis, the deformation parameters in the components of the moments of inertia of the even-even core were converted to polar coordinates for the reproduction of the general structure of low-energy sequences with the ground state and corresponding parity doublet rotational bands in the odd lanthanide and actinide nuclei. Interaction between an even-even nucleus and an unpaired nucleon is expressed in relative coordinates, which describes the particle’s motion in relation to the principal axes of the deformed even-even nucleus.

The following adjustable parameters are used in the triaxial rigid rotor approximation for odd nuclei: energy factor $\hbar\omega = \hbar^2/8B\sigma^2$ (in keV), ε_0 (in degree), γ_{eff} (in degree), η_{eff} (in degree), ξ (dimensionless), $\epsilon^{\pm}$ (in keV) and a (dimensionless). The proposed model is applied to describe energy levels of the parity doublet single-particle-rotational-band of the odd nuclei ^{155}Eu, ^{161,163}Dy, ^{223,225}Th, ^{237}U and ^{239}Pu by taking into account the K-mixing effect.

These comparisons show that the proposed rigid asymmetric rotor model provides a good description of the ground-states energy levels of the heavy odd nuclei in the lanthanide and actinide regions.

One can note that the proposed rigid asymmetric rotor approximation is an adiabatic approximation, which cannot explain the parity doublet splitting effect. This is because the parity doublet splitting effect is better explained in the case of dynamic deformation parameters. Therefore, it is necessary to develop a non-adiabatic approximation for odd nuclei with effective triaxial quadrupole and octupole deformations. Establishing the relationship between various approaches to the problem of the ground state and corresponding parity doublet rotational bands spectra in odd nuclei requires further, more detailed studies beyond the adiabatic approximation, including the corresponding vibrational modes.

INVESTIGATION OF REACTIONS WITH ^{50}Ti AND ^{54}Cr FOR THE SYNTHESIS OF NEW ELEMENTS

Oganessian Yu.Ts.[1], Utyonkov V.K.[1], Abdullin F.Sh.[1], Dmitriev S.N.[1], Ibadullayev D.[1,2], Itkis M.G.[1], Karpov A.V.[1], Kovrizhnykh N.D.[1], Kuznetsov D.A.[1], Petrushkin O.V.[1], Podshibiakin A.V.[1], Polyakov A.N.[1], Popeko A.G.[1], Sagaidak R.N.[1], Saiko V.V.[1], Schlattauer L.[1,3], Shubin V.D.[1], Shumeiko M.V.[1], Solovyev D.I.[1], Tsyganov Yu.S.[1], Voinov A.A.[1], Subbotin V.G.[1], Sabelnikov A.V.[1], Abdusamadzoda D.[1], Bodrov A.Yu.[1], Voronyuk M.G.[1], Bozhikov G.A.[1], Aksenov N.V.[1], Khalkin A.V.[1], Gan Z.G.[4], Zhang Z.Y.[4], Huang M.H.[4], Yang H.B.[4], Wang J.G.[4], Zhang M.M.[1,4], Huang X.Y.[1,4,5]

[1]*Joint Institute for Nuclear Research, Dubna, Russian Federation*

[2]*Institute of Nuclear Physics, Almaty, Kazakhstan*

[3]*Palacky University Olomouc, Department of Experimental Physics, Faculty of Science, Olomouc, Czech Republic*

[4]*Heavy Ion Science and Technology Key Laboratory, Institute of Modern Physics, Chinese Academy of Sciences, Lanzhou, China*

[5]*School of Nuclear Science and Technology, University of Chinese Academy of Sciences, Beijing, China*

The ^{238}U(^{54}Cr,4*n*)^{288}Lv and ^{242}Pu(^{50}Ti,3-4*n*)^{288,289}Lv reactions have been studied at the gas-filled separator DGFRS-2 at the SHE Factory at Flerov Laboratory of Nuclear Reactions, Joint Institute for Nuclear Research. Three new isotopes were discovered: two α-decaying nuclei ^{288}Lv with α-particle energy E_α = 11.08 MeV and half-life $T_{1/2}$ = 2.0 ms, ^{289}Lv with E_α = 10.90 MeV, $T_{1/2}$ = 2.4 ms, and granddaughter of ^{288}Lv, spontaneously fissioning ^{280}Cn with $T_{1/2}$ = 10 μs, which was observed after the first registration of α decay of ^{284}Fl with E_α = 10.57 MeV. Besides, for the first time we reliably registered the *pxn* channel of the ^{242}Pu + ^{50}Ti reaction which was not evidently observed in the ^{48}Ca-induced reactions in previous studies. The cross sections of the 3*n* and 4*n* channels of the ^{242}Pu + ^{50}Ti reaction of $0.32^{+0.34}_{-0.18}$ pb and $0.22^{+0.27}_{-0.15}$ pb, respectively, were measured at excitation energy of the ^{292}Lv compound nucleus E^* = 41 MeV. The cross section of the 4*n*-evaporation channel of the ^{238}U + ^{54}Cr reaction, leading to the same compound nucleus, at E^* = 42 MeV of 36^{+46}_{-24} fb turned out to be approximately 15 times lower than the total cross section of the ^{242}Pu + ^{50}Ti reaction at close excitation energy. Thus, for the first time, it was convincingly proved in an experiment that the reactions of isotopes of actinide elements with ^{50}Ti are an order of magnitude preferable to reactions with ^{54}Cr for the synthesis of new elements 119 and 120.

ASYMPTOTIC NORMALIZATION COEFFICIENTS FOR ^{7}Li+n→^{8}Li AND CROSS SECTION OF THE ^{7}Li(n,γ)^{8}Li REACTION

Tursunmakhatov K.I.[1], Igamov S.B.[2], Ikromkhonov E.Sh.[2]
[1]*Gulistan State University, Gulistan, Uzbekistan*
[2]*Institute of Nuclear Physics, Uzbekistan Academy of Sciences, Tashkent, Uzbekistan*

The differential cross sections (DCS) of the neutron transfer ^{7}Li(d,p)^{8}Li reaction leading to the ground and first excited states of the ^{8}Li nucleus were measured in Ref. [1] at the deuteron energy of 9.05 MeV and they have been used to extract spectroscopic factors for the ^{7}Li+p→^{8}Li vertices. In the present work, the analysis of the experimental DCS of the ^{7}Li(d,p)^{8}Li reaction has been performed within the modified Distorted Wave Born Approximation (MDWBA) [2] to obtain the "indirectly determined" values of the asymptotic normalization coefficients (ANCs) for the ^{7}Li+n→^{8}Li(0.0 MeV) and ^{7}Li+n→^{8}Li(0.981 MeV) virtual transitions. To determine the absolute values of the ANCs in ^{8}Li, the ANC value of 0.77 fm^{-1} was used for the d→p+n transition recommended in Ref. [3]. The calculations of the single-particle differential cross sections were performed using the DWUCK5 code of the Nuclear Reaction Video [4].

To test the peripheral character of the considered reaction, we have changed the geometric parameters r_0 and a of the Woods-Saxon potential in wide physically acceptable ranges ($r_0 = 1.13 \div 1.37$fm and $a = 0.59 \div 0.71$ fm) with respect to their "standard" values ($r_0 = 1.25$ fm and $a = 0.65$ fm). Such variation of r_0 and a results in changing the single-particle ANCs in the ranges of $0.670 \leq b_{1\,1/2} \leq 0.816$ fm$^{-1/2}$ and $0.690 \leq b_{1\,3/2} \leq 0.834$ fm$^{-1/2}$ for the ground state of the ^{8}Li nucleus and of $0.425 \leq b_{1\,1/2} \leq 0.503$ fm$^{-1/2}$ and $0.435 \leq b_{1\,3/2} \leq 0.512$ fm$^{-1/2}$ for the first excited state of the ^{8}Li nucleus. Variations of the parameters r_0 and a cause $R_{3/2}$ functions to change in the range $66.901 \leq R_{\frac{1}{2}} \leq 68.722$ mb/sr·fm, $70.954 \leq R_{\frac{3}{2}} \leq 71.787$ mb/sr·fm for the ground state and $90.088 \leq R_{\frac{1}{2}} \leq 90.835$ mb/sr·fm, $85.993 \leq R_{\frac{3}{2}} \leq 87.503$ mb/sr·fm for the first excited state. These relatively small variations of the R functions with respect to the changes in the single-particle potential parameters r_0 and a indicate that the calculated cross sections are only weakly sensitive to the internal part of the nuclear interaction. This weak dependence demonstrates that the transfer reaction is dominated by the asymptotic region of the nuclear overlap, where the R functions remain practically stable against reasonable variations of the single-particle potential parameters. Therefore, the observed stability of the R functions provides additional evidence for the peripheral character of the considered transfer reaction. Consequently, the extracted ANC values can be regarded as reliable and largely independent of the choice of the single-particle potential parameters.

The different parameters of the optical potentials also were used in the calculation for the estimation of the sensitivity of the optical potentials to the values of ANCs for the ^{7}Li+n→^{8}Li(0.0 MeV) and ^{7}Li+n→^{8}Li(0.981 MeV) vertices. Our recommended weighted average values of ANCs obtained from the optical potential sets are equal to $C^2_{n^7Li;\frac{1}{2}+\frac{3}{2}} = 0.418 \pm 0.021$ fm^{-1} and $C^2_{n^7Li;\frac{1}{2}+\frac{3}{2}} = 0.133 \pm 0.006$ for the ground and first excited states of the ^{8}Li nucleus, respectively. The results of the calculation of the differential cross-section of the ^{7}Li(d,p)^{8}Li reaction leading to the ground and first excited states of the ^{8}Li nucleus in comparison with the experimental data from Ref.[1] are shown in Fig.1 (*a*) and (b), respectively.

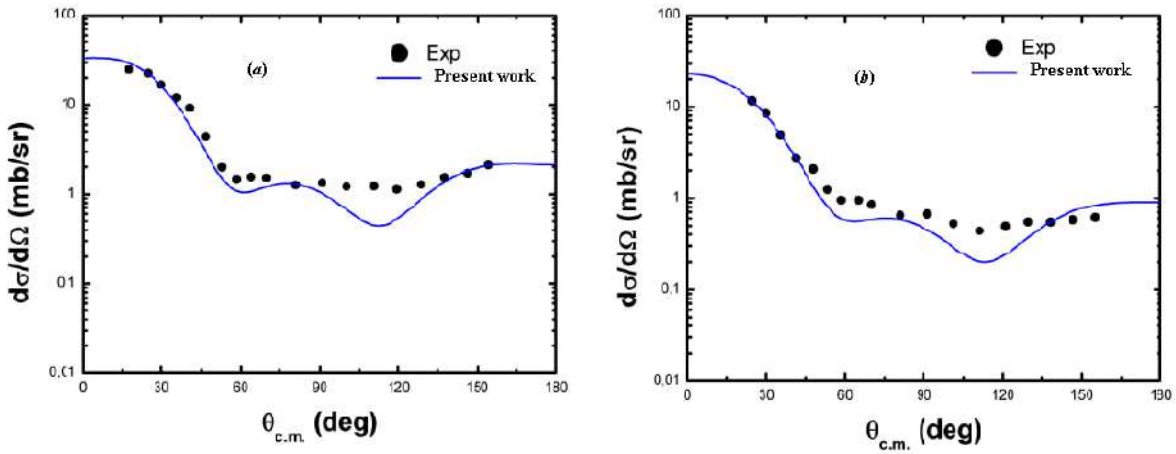

Figure 1. The DCS of the ^{7}Li(d,p)^{8}Li reaction leading to the ground (a) and first excited (b) states of ^{8}Li. The solid lines are the calculated DCS of the ^{7}Li(d,p)^{8}Li reaction for the ground (a) and first excited (b) states within the MDWBA. The experimental data are taken from Ref.[1].

The weighted mean values of the ANCs were used for the calculation of the astrophysical S-factors of the ^{7}Li(n,γ)^{8}Li reaction at low energies. The calculations of the astrophysical S factors of the ^{7}Li(n,γ)^{8}Li reaction were carried out within the framework of the modified R-matrix method [5]. Calculations were carried out for transitions to the ground and first excited states of the ^{8}Li nucleus. The χ^2 method was used for fitting to the experimental data from Refs. [5,6].

References:

1. Ye Binqi, Wen Keling, et al., Chin. J. Nucl. Phys. **2**, 147 (1980)
2. A.M. Mukhamedzhanov et al., Phys. Rev. C **56**, 3 (1997)
3. L.D. Blokhintsev, et al., Fiz. Elem. Chastits. t. Yadra. **8**, 1189 (1977)
4. Nuclear Reaction Video (NRV), https://nrv.jinr.ru//nrv/
5. W.L. Imhof et al., Phys. Rev. 114, 1037 (1959)
6. Y. Nagai et al., Astrophys. J. **381**, 444 (1991)

SECTION II: Radiation Physics of Condensed Matter and Nanophysics

INVESTIGATION OF THE STABILITY OF THE EQUILIBRIUM CONFIGURATION OF THE MAGNETIC MOMENT OF A MAGNETIC MATERIAL BASED ON THE BLOCH EQUATION

Jumaev M.R.[1], Mirjonova N.N.[1,2], Sanoev Kh.S.[1]
[1]Bukhara State Technical University, Bukhara, Uzbekistan
[2]Asian International University, Bukhara, Uzbekistan

The present work investigates the stability of the equilibrium (or steady-state) configuration of the magnetic moment, which is established as a result of the balance between the influence of an external magnetic field and relaxation processes. For this purpose, we used the Bloch equations, which take into account the longitudinal and transverse relaxation times.

From a physical point of view, the longitudinal relaxation time is determined by the spin–lattice relaxation process, whereas the transverse relaxation time is associated with spin–spin interactions. For the sake of specificity, we considered the case when two constant magnetic fields simultaneously act on the magnetic material: one field is directed along the z-axis, while the second field is directed along the x-axis.

Initially, we obtained a system of equations describing the changes in small deviations of the magnetic moment components from their equilibrium values, which can be written in the following form:

$$\left.\begin{aligned} \frac{dm_x}{dt} &= \gamma h_0 m_y - \frac{m_x}{T_2} \\ \frac{dm_y}{dt} &= -\gamma h_0 m_x + \gamma h m_z - \frac{m_y}{T_2} \\ \frac{dm_z}{dt} &= -\gamma h m_y - \frac{m_z}{T_1} \end{aligned}\right\} \qquad (1)$$

Here, γ represents the magnitude of the gyromagnetic ratio for an electron; T_1 and T_2 denote the longitudinal and transverse relaxation times, respectively; h_0 and h correspond to the main and additional magnetic fields, respectively.

Thus, the last system of equations represents a linear system of differential equations with respect to the required quantities m_x, m_y,m_z.

Next, we use the results of the theory of ordinary differential equations, according to which the solution of a system of linear ordinary differential equations can be sought in the following form:

$$m_x = ae^{\omega t}, \qquad m_y = be^{\omega t}, \qquad m_z = ce^{\omega t} \qquad (2)$$

Here, a, b, c and ω may generally be complex. Now, by calculating the derivatives of the corresponding components m_x, m_y and m_z, substituting them into the system of differential equations (1), and taking into account expressions (2), we obtain the following system of equations for determining a, b, and c.

$$\left.\begin{aligned} a\left(\omega+\frac{1}{T_2}\right)-b\gamma h_0+c\cdot 0=0\\ a\gamma h_0+b\left(\omega+\frac{1}{T_2}\right)-c\gamma h=0\\ a\cdot 0+b\gamma h+c\left(\omega+\frac{1}{T_1}\right)=0\end{aligned}\right\} \quad (3)$$

Thus, we obtained a system of homogeneous linear equations for determining a, b and c. However, as is well known, it has a non-zero solution if and only if the following determinant, formed by the coefficients of the unknowns a, b and c.

$$\Delta=\begin{vmatrix} \omega+\frac{1}{T_2} & -\gamma h_0 & 0\\ \gamma h_0 & \omega+\frac{1}{T_2} & -\gamma h\\ 0 & \gamma h & \omega+\frac{1}{T_1}\end{vmatrix} \quad (4)$$

is equal to zero. Next, by calculating this determinant and setting it equal to zero, we obtain the so-called characteristic equation.

$$a_3\lambda^3+a_2\lambda^2+a_1\lambda+a_0=0 \quad (5)$$

where a_3, a_2, a_1 and a_0 denote the coefficients of the characteristic equation for the dimensionless complex frequency

$$\left.\begin{aligned} a_3=1, a_2=\frac{2}{\tau_2}+\frac{1}{\tau_1}, a_1=1+\frac{1}{\tau_2}\left(\frac{2}{\tau_1}+\frac{1}{\tau_2}\right)\\ a_0=\frac{1}{\tau_2^2\tau_1}+\frac{1}{H^2}\left(\frac{h^2}{H^2}+\frac{h_0^2}{\tau_1}\right)\end{aligned}\right\} \quad (6)$$

As follows from the characteristic equation, its solutions depend on both the strengths of the applied magnetic fields (h, h_0) and the relaxation times (T_1, T_2).

It should be noted that the following notations have been introduced in the equation above for convenience.

$$\frac{\omega}{\gamma H}=\lambda, \qquad \gamma H T_1=\tau_1, \qquad \gamma H T_2=\tau_2 \quad (7)$$

Here, H represents the resultant magnetic field strength.

$$H=\sqrt{h_0^2+h^2}. \quad (8)$$

In conclusion, we have demonstrated that the solutions found for the magnetic moment components satisfying the system of equations (1) represent stable solutions, since all roots of the characteristic equation (5) have negative real parts. This also follows from the Routh-Hurwitz criterion.

MOLECULAR DYNAMICS SIMULATION OF RADIATION RESISTANCE IN LAYERED TUNGSTEN-GRAPHENE COMPOSITES

Sharipov Z.[1], Batgerel B.[2], Mirzayev M.[3], Popov E.[1], Sarkhadov I.[1], Tukhliev Z.[1], Hristov I.[4], Hristova R.[4]

[1]*Joint Institute for Nuclear Research, Dubna, Russian Federation*

[2]*Institute of Mathematics and Digital Technology, Ulaanbaatar, Mongolia*

[3]*Institute of Physics, Baku, Azerbaijan*

[4]*Sofia University "St. Kliment Ohridski", Sofia, Bulgaria*

The development of radiation-resistant materials for plasma-facing components remains one of the major challenges in the realization of next-generation fusion energy systems. Tungsten is widely regarded as the primary candidate material because of its high melting point, excellent thermal conductivity, low sputtering yield, and favorable compatibility with fusion plasmas. However, prolonged exposure to intense neutron and ion irradiation leads to the formation of displacement cascades, accumulation of radiation-induced defects, hardening, embrittlement, and degradation of the material's thermophysical properties. Layered tungsten-graphene (W/graphene) composites have recently attracted considerable attention owing to their outstanding mechanical properties, superior thermal conductivity, and the ability of graphene interfaces to act as efficient sinks for radiation-induced defects, thereby improving the radiation tolerance of the material.

In this work, the radiation response of a layered W/graphene composite was investigated using classical molecular dynamics simulations. Displacement cascades initiated by high-energy primary knock-on atoms (PKAs) were simulated employing a combination of Embedded Atom Method (EAM), Adaptive Intermolecular Reactive Empirical Bond Order (AIREBO), and Ziegler–Biersack–Littmark (ZBL) interatomic potentials. This combination enables an accurate description of equilibrium atomic interactions together with short-range ballistic collisions occurring during the early stages of irradiation. The simulations systematically examined the formation, migration, recombination, and evolution of vacancies, self-interstitial atoms, transient local melting, and small defect clusters generated during cascade development. A comparative analysis of radiation damage accumulation was performed for the layered W/graphene composite and single-crystalline tungsten under identical irradiation conditions.

The simulation results reveal that graphene interfaces significantly modify the evolution of displacement cascades by redistributing and localizing the deposited kinetic energy, thereby reducing cascade expansion and promoting efficient recombination of Frenkel pairs. Graphene layers serve as effective sinks for radiation-induced point defects, particularly self-interstitial atoms, resulting in a lower concentration of surviving defects and a reduced tendency for defect clustering compared with monolithic tungsten. In addition, the multilayer architecture suppresses the formation of large vacancy-rich regions that could evolve into extended radiation defects during prolonged irradiation.

The present study demonstrates that layered W/graphene composites are promising candidates for next-generation radiation-tolerant plasma-facing materials in fusion reactors operating under conditions extreme thermal loads and intense neutron irradiation. The obtained results provide valuable atomistic insight into radiation damage mitigation mechanisms, clarify the beneficial role of graphene interfaces in enhancing radiation tolerance, and contribute to the design and optimization of advanced nanostructured materials for future fusion energy applications.

PROPERTIES OF SILICON NANO-CLUSTERS CONTAINING OWN, BACKGROUND AND IMPURITY DEFECTS

Tashmetov M.Yu., Makhkamov Sh.M., Sulaymanov N.T.,
Nazarmamatov Sh.M., Rafikov A.K., Egamov S.R.
Institute of Nuclear Physics, Uzbekistan Academy of Sciences, Tashkent, Uzbekistan

It is known that monocrystalline silicon is currently the most in-demand material for micro- and nano-electronics. There are a number of methods for controlling silicon's properties, based on doping with atoms of various elements that form defects. Their interaction with intrinsic and background defects allows for effective control of silicon's properties. For example, by introducing impurity, radiation, and thermal defects into crystalline silicon, it is possible to control the structural parameters of low-dimensional states formed within the material and modify their fundamental properties.

This work is devoted to the determination of the structural and energy band parameters of clusters by studying the interaction of an impurity atom with intrinsic defects and background impurities in silicon clusters using computer modeling methods. To determine the structural parameters and the main energy characteristics of the $Si_{29}H_{36}$ nanocluster upon the introduction of an impurity atom and its interaction with an interstitial silicon atom and a vacancy, we used the ORCA software package [1]. The initial structures were created using the ChemBio3D 11.0 calculation program, when the coordinate center coincides with the central $\boldsymbol{T}_d$ node. Quantum-chemical models of the structure of nanosized $Si_{29}H_{36}$ and $Si_{28}VH_{36}$ silicon clusters with a reconstructed surface were previously investigated by us in [2] using the Khakimov semiempirical method and within the framework of the approximation to the density functional theory in the ORCA-3 software package in [4].

The simulation results show that upon reaching thermal equilibrium, the formation of $\boldsymbol{V_{Si}}$ in ultradispersed silicon nanoclusters does not lead to a sharp change in symmetry, but the densities of electron levels in the Urbach bands in the band gap change. Taking into account the influence of background impurities on the structural parameters when modeling these clusters leads to more correct conclusions regarding the nature of the formation of defect complexes with their participation: *a*) carbon in the bulk of the nanocluster can be either a substitutional or an interstitial defect, while the interaction of $\boldsymbol{V_{Si}}$ and $\boldsymbol{C_i}$ leads to the formation of an *E*-center (Fig. 1a); *b*) oxygen, regardless of the mechanism of introduction into the bulk of the nanocluster, upon reaching thermal equilibrium occupies an interstitial position and, interacting with $\boldsymbol{V_{Si}}$, forms an ***A***-center (Fig. 1b).

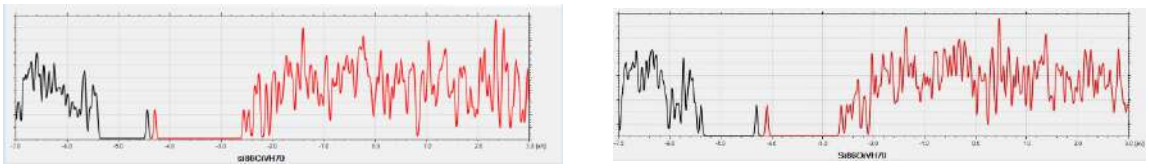

a *b*

Figure 1. Energy characteristics of silicon nanoclusters with an embedded atom of *a*) carbon and *b*) oxygen

The differences in the mechanisms of incorporation of atoms of elements that alter silicon's conductivity type (such as phosphorus and boron) between single-crystal silicon and nanostructures primarily manifest themselves in fundamental changes to the electron subsystem. According to our

modeling results, the incorporation of phosphorus (or boron) always leads to the destruction of Frenkel pairs and the formation of defects such as [V_{Si} – P_i] and [(V_{Si} – B_i) – 2Si] (Fig. 2). Moreover, the very high mobility of the boron atom in the silicon crystal lattice matrix also leads to a high probability of Frenkel pair restoration.

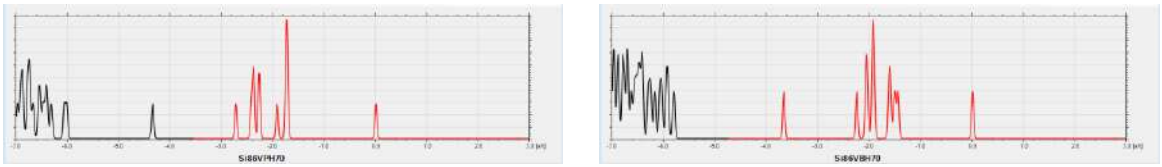

a *b*

Figure 2. Energy characteristics of silicon nanoclusters with an embedded atom of *a*) phosphorus and *b*) boron

A computational model of tellurium atom implantation allows us to determine the role of tellurium in the formation of an electron trap in the band gap of a silicon nanocluster. Our results showed that tellurium forms a stable defect center with V_{Si}, and the formation of the electron trap is caused by the defect complex [V_{Si} – Te_i] (Fig. 3). This indicates the possibility of controlling the photovoltaic properties of silicon nanoclusters by controlling the thermal diffusion process of tellurium.

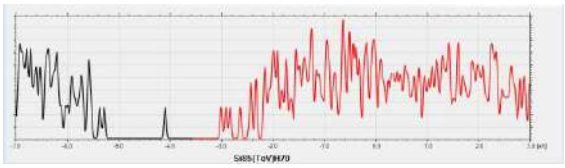

Figure 3. Energy characteristics of silicon nanoclusters with an embedded tellurium atom during the formation of a defective complex [V_{Si} – Te_i] in the volume of the nanocluster

An analysis of the energy characteristics shows that the presence of V_{Si} in the Te atom's implantation region influences the mechanism of electron trap formation and the position of the corresponding pairs of deep levels in the band gap. Simulation results, taking into account the interaction of the implanted tellurium atom with background impurities such as phosphorus and boron, indicate a high probability of a compensatory mechanism for the formation of such defective complexes. A comparison of the structural and electrical parameters shows that the implantation of a tellurium atom and its interaction with V_{Si} do not lead to a change in the conductivity type.

The work is financed from the state budget of the Republic of Uzbekistan.

References:

1. Frank Neese. Software update: the ORCA program system, version 4.0, 17 July 2017.
2. F. T. Umarova, A. P. Mukhtarov, P. L. Tereshchuk, N. T. Sulaimanov, M. T. Swihart. Quantum-chemical modeling of the structure of nano-sized silicon clusters with a reconstructed surface. // Uzb J. Physics. 2008. Vol. 10. B.1. Pp. 10-18.
3. //WIREs Computational Molecular sciences, Vol.8, Issue1, Jan./Febr. 2018, e1327.
4. Sh. Makhkamov, F. Umarova, A. Normurodov, N. Sulaymanov, O. Ismailova, M. Tashmetov. Ab initio investigation of ultra-small silicon nanocrystals doping by phosphorous //International Journal of Modern Physics B, 2020, 2050284, DOI: https://doi.org/10.1142/S0217979220502847

TOPOLOGICAL CONTROL OF THE VOLOVIK EFFECT IN CUPRATES: THE ROLE OF NONMONOTONIC d-WAVE SYMMETRY

Ganiev O.[1,2]
[1]*Institute of Nuclear Physics, Uzbekistan Academy of Sciences, Tashkent, Uzbekistan*
[2]*National University of Uzbekistan, Tashkent, Uzbekistan*

Despite decades of intense theoretical and experimental research, identifying the precise microscopic mechanisms governing the thermodynamic and magnetic responses of high-temperature cuprate superconductors remains a formidable challenge [1,2]. Standard weak-coupling Bardeen-Cooper-Schrieffer (BCS) paradigms systematically fail to capture the anomalous signatures observed across diverse cuprate families. Emerging experimental evidence suggests that cuprate superconductivity deviates from these standard models through an intricate angular structure of the pairing symmetry. High-resolution angle-resolved photoemission spectroscopy (ARPES) and Raman scattering reveal systematic deviations from a simple monotonic d-wave form [3,4]. In this work, we present a theoretical framework built upon a nonmonotonic d-wave gap symmetry, which successfully derives an explicit generalization of the Volovik effect [5], proving that the structural deformations of the gap nodes rigorously control the magnetic degradation of the condensate.

At the core of this framework is the replacement of the canonical monotonic d-wave gap with a highly anisotropic, nonmonotonic topology [6]. We define the gap function as $\Delta_{\mathbf{k}} = \Delta_d(T)g(\theta)$, where the angular modulation is parameterized by a symmetry coefficient B via the inclusion of a higher-order $\cos(6\theta)$ harmonic: $g(\theta) = B\cos(2\theta) + (1-B)\cos(6\theta)$. This precise gap topology directly dictates the material's magnetic response in the mixed state.

In an extreme type-II superconductor ($H_{c1} \ll H \ll H_{c2}$), circulating vortex supercurrents induce a semiclassical Doppler shift in the excitation energy of Bogoliubov quasiparticles. To quantify this magnetic pair-breaking, we explicitly derive a generalized Volovik effect [5]. The normalized field-dependent Sommerfeld coefficient, $\gamma(H)/\gamma_n$,is determined by spatially averaging the localized density of states over the vortex unit cell, represented by the self-consistent angular integral:

$$\frac{\gamma(H)}{\gamma_n} = \frac{1}{2\pi}\int_0^{2\pi} \frac{h}{h+g(\theta,B)^2}\,d\theta, \tag{1}$$

where $h = H/H_{c2}$ is the reduced magnetic field. To uncover the physical foundation in the low-field regime ($h \ll 1$), we evaluate this integral analytically near the four gap nodes, $\theta_i = (2i+1)\pi/4$. Expanding the gap function linearly near any given node as $g(\theta, B) \approx g'(\theta_i)(\theta - \theta_i)$, and extending the integration limits to infinity under the low-field approximation, the contribution of a single node evaluates to:

$$\frac{1}{2\pi}\int_{-\infty}^{\infty} \frac{h}{h+[g'(\theta_i)x]^2}\,dx = \frac{\sqrt{h}}{2|g'(\theta_i)|}. \tag{2}$$

Summing the contributions over all four identical nodes situated on the Fermi surface yields the generalized low-field Volovik relation:

$$\frac{\gamma(H)}{\gamma_n} \approx 4 \times \frac{\sqrt{h}}{2|g'(\theta_0)|} = \frac{2\sqrt{h}}{|g'(\theta_0)|}. \tag{3}$$

The absolute gap gradient at the primary node $\theta_0 = \pi/4$ is defined by the analytical derivative of our nonmonotonic gap symmetry:

$$\left|g'\left(\frac{\pi}{4}\right)\right| = \left|-2B\sin\left(\frac{2\pi}{4}\right) - 6(1-B)\sin\left(\frac{6\pi}{4}\right)\right| = |6-8B|. \tag{4}$$

Substituting this geometric gradient into the low-field limit yields the direct, explicit coupling between the topological parameter B and the field-induced specific heat:

$$\frac{\gamma(H)}{\gamma_n} \approx \frac{2}{|6-8B|}\sqrt{\frac{H}{H_{c2}}}. \quad (5)$$

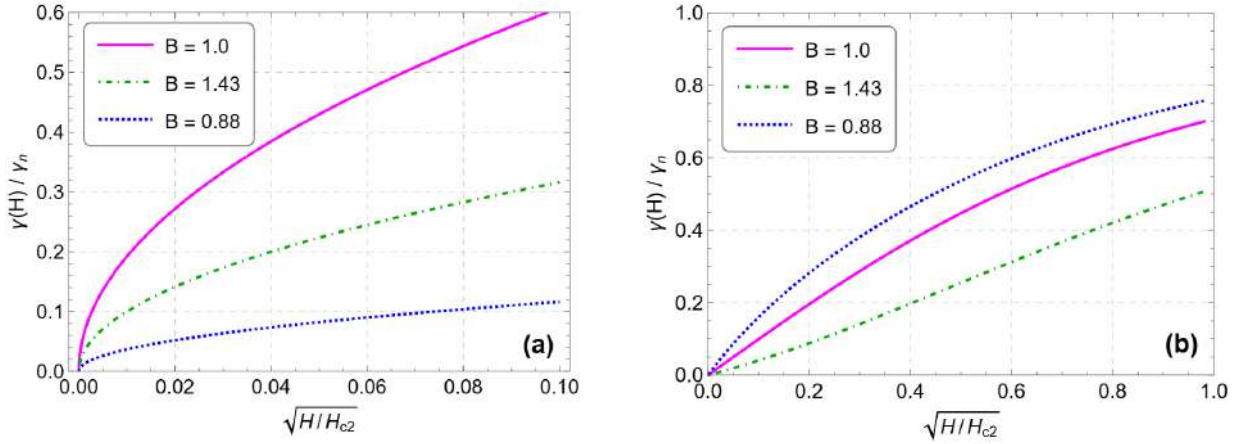

Figure 1. The generalized Volovik effect illustrating the normalized electronic specific heat capacity $\gamma(H)/\gamma_n$ versus $\sqrt{H/H_{c2}}$. **(a)** In the analytical low-field regime ($H \ll H_{c2}$, Eq. 5), flattened gap nodes ($B = 0.88$, dotted line) expose a vast momentum phase space to the Doppler shift, resulting in a fragile condensate with massively enhanced specific heat. Conversely, steepened nodes ($B = 1.43$, dot-dashed line) topologically protect the condensate, heavily suppressing the field-induced specific heat. **(b)** Semiclassical evaluation across the entire mixed state via the self-consistent numerical integral (Eq. 1) demonstrates that the topological vulnerability or protection established at low fields persists all the way to the upper critical field (H_{c2})

This rigorous derivation proves that magnetic pair-breaking is exquisitely sensitive to the topological structure of the gap nodes. As visualized in Fig. 1a, flattened nodes ($B < 1$) severely suppress the nodal gradient, exposing a vast momentum phase space to the Doppler shift. This results in a highly fragile condensate whose specific heat rises much faster than the standard $\sqrt{H}$ scaling, signaling rapid degradation. Conversely, steepened nodes ($B > 1$, representative of electron-doped cuprates [7]) drastically increase the nodal gradient, topologically protecting the condensate by heavily suppressing the field-induced specific heat and rendering the system remarkably robust against initial vortex penetration. Finally, extending beyond the analytical low-field approximation, Fig. 1b confirms that this microscopic topological control persists across the entire magnetic phase diagram. The full numerical evaluation of the self-consistent angular integral mirrors the hierarchy established by the nodal gradients, maintaining thermodynamic suppression up to the highest magnetic fields for steepened topologies.

In conclusion, by explicitly deriving the generalized Volovik effect, this theoretical framework conclusively demonstrates that the macroscopic magnetic vulnerabilities of cuprate superconductors are not universal, but are rigorously and mechanically dictated by the nonmonotonic topological deformations of the d-wave gap.

Acknowledgments

This work was supported by the Institute of Nuclear Physics of the Uzbekistan Academy of Sciences.

References:

1. J. Tallon, J. Loram, Physica C **349**, 53-68 (2001).

2. A. Shekhter, B. J. Ramshaw, R. Liang, *et al.*, Nature **498**, 75-77 (2013).
3. J. Mesot, M. R. Norman, H. Ding, *et al.*, Phys. Rev. Lett. **83**, 840-843 (1999).
4. T. Kondo, T. Takeuchi, A. Kaminski, *et al.*, Phys. Rev. Lett. **98**, 267004 (2007).
5. G. E. Volovik, JETP Letters **58**, 469-473 (1993).
6. O. Ganiev, B. Yavidov, Phys. Lett. A **543**, 130451 (2025).
G. Blumberg, A. Koitzsch, A. Gozar, *et al.*, Phys. Rev. Lett. **88**, 107002 (2002).

RABI DYNAMICS IN THE TAVIS-CUMMINGS MODEL

Rasulova M.Yu., Tishabaev I.A.
Institute of Nuclear Physics, Uzbekistan Academy of Sciences, Tashkent, Uzbekistan

Collective interaction between an ensemble of two-level atoms and a quantized radiation field represents one of the fundamental problems of quantum optics and many-body physics. The Tavis–Cummings (TC) model, which generalizes the Jaynes–Cummings model to many-atom systems, provides an important theoretical framework for the investigation of collective spontaneous emission, superradiance, cavity quantum electrodynamics, and coherent atom-field dynamics [1]. In recent years, collective light-matter interaction has attracted renewed interest due to its relevance to quantum information processing, cavity-QED systems, superconducting qubits, semiconductor nanostructures, and spin ensembles.

One of the most important dynamical manifestations of the TC interaction is the appearance of collective Rabi oscillations, corresponding to coherent excitation exchange between the cavity field and the collective atomic subsystem. In the resonant regime, the collective Rabi frequency, revealing the cooperative enhancement induced by the atomic ensemble. Conventionally, such oscillatory dynamics is derived through direct Hamiltonian diagonalization or via the Holstein–Primakoff (HP) representation of collective spin operators in the low-excitation regime.

Despite the success of the Hamiltonian-based description, the kinetic aspects of collective light-matter dynamics remain comparatively less explored. In particular, generalized kinetic approaches provide an alternative framework for describing temporal correlations, and memory effects in interacting quantum systems [2] and nonequilibrium evolution [3-5]. Such methods are especially useful for investigating memory effects, temporal correlations, and energy-transfer processes beyond purely unitary evolution.

Motivated by these developments, in the present work we employ the generalized kinetic equation (GKE) formalism to investigate the weak-coupling dynamics of the TC model. Considering an initially thermal cavity field, we derive analytical expressions for the collective atomic inversion, the excited and ground state populations, and the radiation intensity in the dispersive regime. We further identify the condition for complete Rabi oscillations and show that the obtained results can be straightforwardly generalized to an initial Fock-state cavity field.

The developed analytical approach provides additional insight into the interplay between collective emission, dephasing, and memory effects in interacting atom-field systems, and may be useful for the description of realistic quantum optical systems.

References:

1. M.Tavis and F.W.Cummings, Exact solution for an N-molecule-radiation-field Hamiltonian, Phys. Rev., **170** (2), 379 (1968)

2. N.N.Bogolyubov and N. N. Bogolyubov Jr., Aspects of Polaron Theory (Fizmatlit, Moscow, 2004).
3. N.N.Bogolubov Jr., M.Yu.Rasulova and I. A. Tishabaev, Proc. IEEE, 55 (2011).
4. M.Yu.Rasulova and I.A.Tishabaev, Mod. Phys. Lett. B, **25**, 1417 (2011).
5. N.N.Bogolubov Jr., M.Yu.Rasulova and I. A. Tishabaev, Theoretical and Mathematical Physics, **171**, 523 (2012).

CHANGES IN THE OPTICAL ABSORPTION SPECTRA OF Cr^{3+} IONS IN LiH_2PO_4 AND NaH_2PO_4 CRYSTALS UNDER THE INFLUENCE OF X-RAY IRRADIATION

Bayazova A.A.[1], Mamytbekov U.K.[2], Kidibaev M.M.[2], Joldoshov B.K.[3]
[1]*Kyrgyz National University named after J. Balasagyn, Bishkek, Kyrgyz Republic*
[2]*Academician J.Jeenbaev Institute of Physics, National Academy of Sciences, Bishkek, Kyrgyz Republic*
[3]*Issyk-Kul State University named after K.Tynystanov, Karakol, Kyrgyz Republic*

Introduction. With the active development of solid-state short-wavelength lasers, as well as nonlinear and integrated optics, there is a growing demand for nonlinear optical crystals possessing high radiation-optical stability for operation in the visible and ultraviolet spectral ranges. Interest in such materials stems from their widespread application in laser beam control devices, including modulators, deflectors, and frequency multipliers.

To date, wide-bandgap crystals of the potassium, ammonium, lithium, and sodium dihydrophosphate groups, as well as other similar compounds, have become the most widely used materials in industrial optical systems for laser beam control and frequency conversion. These same crystals play a key role in Q-switches for solid-state lasers, enabling the generation of high-power, ultrashort (nanosecond) pulses.

The study of radiation-stimulated processes in these crystals can yield valuable insights for assessing, controlling, and predicting radiation resistance, as well as understanding the specific effects of impurity ions. Despite extensive research into LiH_2PO_4 and NaH_2PO_4 group crystals, a number of fundamental questions remain unresolved. Specifically, there is insufficient understanding of the formation, accumulation, and decay of radiation defects under irradiation, the electronic structure of perfect crystals and point defects, the nature of radiation-optical stability, the dynamics of electronic excitations, and radiation-stimulated processes in these materials. Addressing these issues remains a pressing problem in condensed matter physics [1].

The state of ions within a crystal is a complex phenomenon, with different aspects described by complementary frameworks: crystal field theory, molecular orbital theory, valence bond theory, and band theory.

Experimental Technique. We measured the optical absorption spectra of the crystals using a Helios Omega UV-Vis spectrophotometer.

Results and Discussion.

A comparative study of the optical absorption spectra of unirradiated and X-ray irradiated LDP (LiH_2PO_4) and NDP (NaH_2PO_4) crystals showed that irradiation leads to a noticeable change in the spectra (figure 1).

In the spectra of the irradiated LiH_2PO_4:Cr^{3+} crystals, a decrease in the intensity of the Cr^{3+} absorption bands in the visible region was observed (curves 3 and 4 in Fig. 1). However, no new absorption bands could be recorded for these crystals, as their short-wavelength absorption increases very sharply. The absorption spectrum of the irradiated undoped LiH_2PO_4 crystal shown in the same figure (curve 2) indicates that this increase in short-wavelength absorption is associated with the generation of intrinsic radiation defects in lithium dihydrogen phosphate. Undoped and Cr^{3+} - doped NaH_2PO_4 crystals behave similarly under irradiation to LiH_2PO_4 crystals [2].

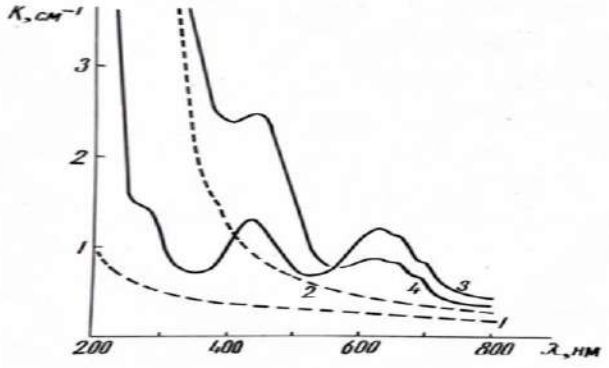

Figure 1. Absorption spectra of LiH_2PO_4 (1, 2) and LiH_2PO_4:Cr^{3+} (3, 4) crystals before and after irradiation, respectively, measured at 90 K. Irradiation duration: 12 hours.

The decrease in the intensity of the absorption bands assigned to Cr^{3+} ions indicates a reduction in the concentration of the impurity ions responsible for these bands. It can be assumed that the decrease in the concentration of Cr^{3+} ions occurs as a result of a change in their charge state under irradiation. The simultaneous decrease in the Cr^{3+} absorption bands and the growth of the band at 360 nm suggest that the 360 nm band is associated with centers formed due to radiation-stimulated charge state changes of the Cr^{3+} ions.

Since the absorption bands are attributed to transitions to antibonding orbitals, the molecular ion expands in size in the excited state, causing a shift in the Condon curve for the excited state relative to the ground-state configuration. As a result, the selection rule stating that transitions are only allowed between electronic levels with identical vibrational states is relaxed. This enables transitions from the ground state to various vibrational levels of the excited electronic state, which in turn can lead to the emergence of fine structure in the optical absorption spectrum. The average spacing between the components of this structure corresponds to the frequency of the fully symmetric stretching vibration [3].

Conclusion. We investigated how X-ray irradiation affects the optical absorption spectra of Cr^{3+} ions in the crystals. The alterations in the optical absorption spectra and the emergence of new lines in the spectra of the irradiated doped crystals are attributed to a change in the charge state of chromium. The attenuation of the absorption bands is associated with centers formed as a result of the radiation-induced charge transfer of chromium ions.

References:

1. Satibaldieva M.K. Radiasionno-stimulirovannie effekti v kristallax KH2PO4 i NH4H2PO4 // disser. kand. fiz.-mat. nauk: 01.04.07. – Karakol-Ekaterinburg, 2002.
2. Ogorodnikov I.N., Krujalov A.V. Radiasionno-stimulirovannie prosessi i elektronnie vozbujdeniya v nelineynix opticheskix materialax. //Izv. vuzov. Fizika. 2000. №3.
3. Bayazova A.A., Mamitbekov U.K., Kidibaev M.M., Denisov G.S. Izmenenie spektrov opticheskogo poglosheniya ionov Sr3+ v kristallax digidrofosfata kaliya (KH2PO4) i ammoniya (NH4H2PO4) pod deystviem rentgenovskogo oblucheniya. // Nauka, novie texnologii i innovasii Kirgizstana, 2024, №8, 3-8 s.

RADIATION RESISTANCE OF MoTiN AND NbTiN COATINGS IRRADIATED WITH INERT GAS IONS

Aldabergenova T.M.[1], Akaev S.O.[1], Kislitsyn S.B.[1], Klopotov A.A.[2]
Institute of Nuclear Physics, ARKAE, Almaty, Kazakhstan
[2]Tomsk State University of Architecture and Building, Tomsk, Russian Federation

Modern nuclear power engineering imposes stringent requirements on materials operating under the combined effects of high temperatures, mechanical stresses, and intense fluxes of ionizing radiation. One of the most effective approaches to extending the service life of materials exposed to radiation is the application of protective coatings that prevent direct interaction of the structural substrate with plasma, coolant, and nuclear transmutation products [1]. In this context, the aim of the present study is to identify the most promising systems for the development of protective coatings for structural reactor materials, as well as to experimentally investigate the effect of inert gas ion irradiation on the physical and mechanical properties of MoTiN and NbTiN nitride coatings.

This paper presents the synthesis methods of TiMoN and TiNbN coatings deposited on steel substrates, along with the results of testing the coated samples before and after irradiation with helium, krypton, and xenon ions. The characterization of the coatings included elemental composition analysis using energy-dispersive X-ray spectroscopy (EDS) and Rutherford backscattering spectrometry (RBS). The coating thickness was also determined by RBS. In addition, mechanical and corrosion tests were performed on both irradiated and non-irradiated coatings.

Based on the experimental results, the following conclusions can be drawn:

- TiMoN and TiNbN coatings are capable of maintaining high strength and excellent corrosion resistance under heavy-ion irradiation. In contrast, 12X18H10Tstainless steel is significantly more susceptible to degradation of these properties than TiMoN and TiNbN coatings.

- The investigation of the effect of inert gas ion irradiation on the mechanical properties of TiMoN and TiNbN coatings showed that irradiation leads to a reduction in their strength characteristics, manifested by a decrease in surface hardness. The degradation of mechanical properties was found to depend on both the mass and fluence of the irradiating ions. At the same time, the mechanical properties of TiMoN and TiNbN coatings irradiated with inert gas ions remain significantly superior to those of even unirradiated 12X18H10Tstainless steel.

- Corrosion tests of TiMoN and TiNbN coatings irradiated with inert gas ions in a 3 wt.% NaCl solution showed that corrosion resistance deteriorates with increasing ion fluence and also depends on the ion mass. An increase in ion mass and energy results in reduced corrosion resistance. Nevertheless, despite the irradiation-induced degradation in corrosion performance, the irradiated TiMoN and TiNbN coatings still exhibit substantially higher corrosion resistance than even unirradiated 12X18H10Tstainless steel.

This work was carried out within the framework of the Program-Targeted Funding of the Agency Republic Kazakhstan on Atomic Energy, Project No. BR23891530.

References:

1. Zinkle S.J., Was G.S. Acta Materialia. – 2013, Vol. 61, No.3, P. 735–758.

CALCULATION OF THE ENERGY YIELD OF NONEQUILIBRIUM ENERGY CARRIERS GENERATED IN NANO-SiO_2 UNDER ELECTRON IRRADIATION WITH ENERGIES OF T = 0.05-10 keV

Babayeva F.Sh.[1,2], Jafarov Y.D.[1,2], Abdullayev A.P.[2]

[1]*Institute of Physics, Ministry of Science and Education of the Republic of Azerbaijan, Baku, Azerbaijan*

[2]*University of Architecture and Construction, Baku, Azerbaijan*

Metal oxides possess unique electronic, optical, radiation-resistant, and structural properties, making them indispensable materials in various fields of science and technology, including radiation physics, radiation materials science, condensed matter physics, and micro- and nanoelectronics [1-3]. According to the mechanisms of radiation energy loss, ionizing radiation particles (γ-quanta, electrons, positrons, protons, neutrons, α-particles, high-energy ions, etc.) interact with atoms and molecules of a material during penetration, resulting primarily in the formation of electron-hole pairs through direct single ionization of molecular orbitals (MOs), various electronic excitation (exciton) states, structural displacements (radiation defects of the Frenkel-pair type), and heat release processes [4, 5]. Among these processes, the formation of electron-hole pairs and electronically excited states represents the most energy-intensive channels. Since electron-hole pairs and electronic excitation states generated in metal oxides under ionizing radiation play a crucial role in energy transport and transformation processes, these materials serve as important objects for both fundamental and applied research in radiation physics and materials engineering [1, 2]. Therefore, predicting radiation-induced modifications occurring within the bulk, on the surface, and in the surrounding environment of such materials remains an important scientific and technological challenge.

In the present work, a mathematical model was developed in the Mathcad environment using the Monte Carlo, single-collision, and stepwise-tracking methods. Based on this model, inelastic collision processes between primary electrons with kinetic energies of T = 0.05-10.0 keV and SiO_2 molecules were simulated. The calculations were continued until the kinetic energies of the primary electrons and each subsequently generated generation of δ-electrons decreased to the threshold energies for ionization and electronic excitation processes. At the physical stage of the interaction process, the energy yields of electron-hole pairs ($SiO_{2,j}^{+}/e^{-}$) produced through direct single ionization of the molecular orbitals (MOs) of Si ($1s^2$, $2s^2$, $2p^6$, $3s^2$, $3p^2$) and O ($1s^2$, $2s^2$, $2p^4$), as well as the energy yields of the electronic excitation states $SiO_{2,i}^{*}$ (2.21, 3.7, 4.7, 5.73, and 6.6 eV), were calculated using the proposed model. These processes can be represented schematically as follows:

$$e_0^- + SiO_2 \rightarrow \begin{cases} SiO_{2,i}^{*} + e_s^- & \Delta T = W_{0,i} \\ SiO_{2,j}^{+} + e_s^- + e_e^- & \Delta T = \varepsilon + B_j \end{cases}$$

where e_0^-, e_s^- and e_e^- denote the incident, scattered, and ejected electrons, respectively; ε is the kinetic energy of the ejected electron; $SiO_{2,j}^{+}$, $SiO_{2,i}^{*}$ represent the singly ionized j-th molecular orbital and the i-th electronic excitation state of the SiO_2 molecule, respectively.

The effective cross section for direct single ionization of the j-th molecular orbital in inelastic electron-SiO_2 collisions was determined using the modified form of the Mott equation proposed in Refs. [6,7]. For electronic excitation processes, the differential effective cross section corresponding

to the transition of an electron from the ground state (0) to the i-th excited state was calculated using the equation proposed by Kutcher and Green [8] and subsequently improved by Cobut [9].

The calculated values of the total energy yields of electron-hole pairs ($SiO_{2,j}^{+}/e^{-}$) generated through direct single ionization of the molecular orbitals of silicon and oxygen atoms in SiO_2, together with the total energy yields of the electronic excitation states (2.21, 3.7, 4.7, 5.73, and 6.6 eV), are presented in the table.

Table

States	Primary Electron Kinetic Energy, keV					
	0,05	**0,1**	**0,5**	**1**	**5**	**10**
Total Energy Yield of Molecular Orbital Ionization Events	5,069	6,576	6,62	6,257	5,434	5,137
Total Energy Yield of Electronic Excitation States	8,931	5,424	1,78	1,243	0,726	0,633
Total Energy Yield of Ionization and Electronic Excitation Processes	14	12	8,4	7,5	6,16	5,77

Model calculations showed that, within the physical stage of the interaction process (10^{-15}-10^{-12} s), the energy yields of products generated during inelastic collisions between electrons with energies of T = 0.05-10 keV and SiO_2 molecules depend on the kinetic energy of the incident electrons as follows:

• Electron-hole pairs: G($SiO_{2,j}^{+}$) = 5.069-6.62 electron-hole pairs per 100 eV;

• Electronic excitation states: G($SiO_{2,i}^{*}$) = 0.633-8.931 excitation events per 100 eV;

• Total yield of ionization and electronic excitation products: 5.77-14 particles per 100 eV.

References:

1. S.E. Alawaideh et al., Effect of different metal oxides on the radiation shielding features of borate glasses, Radiation Physics and Chemistry, 2024, vol.220, 111720.
2. H. Akhdar, Theoretical Investigation of the Influence of Different Heavy Metal Oxides Modifiers on ZnO-Bi_2O_3-B_2O_3-SiO_2's Photon- and Neutron-Shielding Capabilities Using the Monte Carlo Method, Applied Sciences, 2023, 13(16), 9332.
3. Diebold U. The surface science of titanium dioxide. *Surf. Sci. Rep.*, 2003, 48, 53–229.
4. D.M. Bagshaw et al., Radiation effects in oxide ceramics, J. Mater. Sci., 2022.
5. F. Singh et al., Secondary electron generation and energy transfer in oxide materials, Phys. Chem. Chem. Phys., 2023.
6. Kaplan I.G., Sukhonosov V.Y. Simulation of the passage of fast electrons and the ealy stage water radiolysis by the Monte Carlo method // Journal of Radiation Research, –1991. v.127, – p.1-10.
7. Lindsay, B.G., Mangan, M.A. In Photon and Electron Interactions with Atoms, Molecules and Ions // Landolt- Börnstein, New York, 2003, v.17, p.5001-5077.
8. Kutcher, G.J., Green, A. A model for energy deposition in liquid water / Radiation Research, 1976, 67, p.408-425.
9. Cobut, V. Monte-Carlo simulation of fast electron and proton tracks in liquid water / V. Cobut, Y. Frongillo, J.P. Patau, T. Goulet, M-J. Fraser, J-P. Jay-Gerin // Physical and physicochemical aspects Radiation Physics and Chemistry, 1998, 51, p.229-243.

FEATURES OF INTERSTITIAL ATOM ORDERING IN THE $Zr_{0.50}Ti_{0.50}N_{0.27}H_y$ SOLID SOLUTION

Tashmetov M.Yu., Parpiyev A.S., Makhmudov Sh.A.
Institute of Nuclear Physics, Uzbekistan Academy of Sciences, Tashkent, Uzbekistan

Systems based on transition metal nitrides and hydrides have attracted considerable attention due to their thermodynamic stability, corrosion resistance, and ability to interact with hydrogen [1-3]. Of particular interest are solid solutions in the Ti-Zr-N-H system, where the presence of titanium and zirconium atoms enables the formation of structures with tunable properties. The incorporation of hydrogen and nitrogen atoms into the metal sublattice alters the electron density, lattice parameters, and bonding energy, thereby influencing phase transformations and structural ordering. The study of the spatial distribution of interstitial atoms and their interaction with the metal sublattice is essential for understanding the formation of stable structures. In particular, the spatial arrangement and ordering of hydrogen and nitrogen atoms in the crystal lattice of the solid solution $Zr_{0.50}Ti_{0.50}N_{0.27}H_y$ remain insufficiently explored [3]. The aim of this work is to investigate the crystal structure and the ordering of interstitial atoms in the solid solution $Zr_{0.50}Ti_{0.50}N_{0.27}H_y$.

Neutron diffraction data combined with Rietveld refinement using FullProf reveal that the $Zr_{0.50}Ti_{0.50}N_{0.27}H_y$ sample, quenched from 1100 °C, crystallizes in a hexagonal structure (space group P-3m1) (Figure 1), with lattice parameters a = 3.287 ± 0.003 Å and c = 5.364 ± 0.007 Å. Within this structure, nitrogen atoms are fully ordered over the octahedral 1 (*a*) site, whereas hydrogen atoms are predominantly located in one of the two types of tetrahedral interstitial sites. A small fraction of hydrogen occupies the octahedral 1 (*b*) interstices that are not occupied by nitrogen atoms (Table 1).

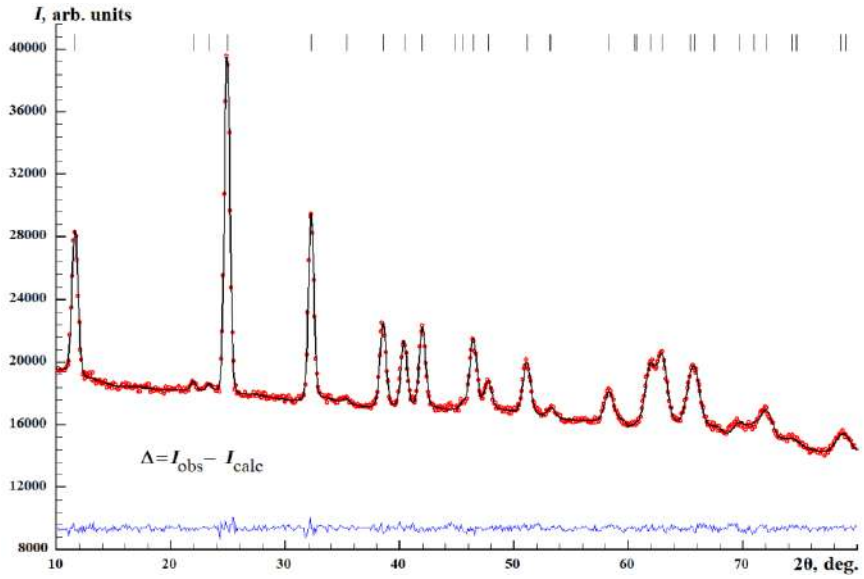

Figure 1. Neutron diffraction pattern of the $Zr_{0.50}Ti_{0.50}N_{0.27}H_y$ solid solution: dots represent the experimental data, the solid line corresponds to the calculated profile, and Δ denotes the difference between the experimental and calculated intensity values

Table 1 presents the structural characteristics of the hexagonal ordered solid solution $Zr_{0.50}Ti_{0.50}N_{0.27}H_y$, quenched from 1100 °C, within the P-3m1 space group.

Table 1. Structural characteristics of the $Zr_{0.50}Ti_{0.50}N_{0.27}H_y$ solid solution within the P-3m1 space group

1. Atom	*2.* Position	*3.* x	*4.* y	*5.* z	*6.* Δ z	*7.* n	*8.* Δ n
9. Zr	*10.* 2 d	*11.* 0.3333	*12.* 0.6666	*13.* 0.2470	*14.* 0.0008	*15.* 2.000	*16.* 0.00
17. Ti	*18.* 2 d	*19.* 0.3333	*20.* 0.6666	*21.* 0.2470	*22.* 0.0008	*23.* 2.000	*24.* 0.00
25. N	*26.* 1 a	*27.* 0.0000	*28.* 0.0000	*29.* 0.0000	*30.* 0.0000	*31.* 0.540	*32.* 0.009
33. H_1	*34.* 1 b	*35.* 0.0000	*36.* 0.0000	*37.* 0.5000	*38.* 0.0000	*39.* 0.090	*40.* 0.009
41. H_2	*42.* 2 d	*43.* 0.3333	*44.* 0.6666	*45.* 0.6172	*46.* 0.0020	*47.* 0.500	*48.* 0.010
49. B_{ef}= 0.77 Å^2; R_F=2.5 %; R_{Br}=1.9 %, χ^2 =1.40							

Neutron diffraction studies were also carried out on the $Zr_{0.50}Ti_{0.50}N_{0.27}H_y$ solid solution after quenching from 1100 °C in order to investigate its high-temperature state. The sample was annealed over the temperature range 600-1100 °C in 100 °C increments for 144 h in an evacuated and sealed quartz ampoule, followed by quenching from 1100 °C into water. However, within experimental error, no changes in lattice parameters or redistribution of interstitial atoms were observed. This indicates that the solid solution $Zr_{0.50}Ti_{0.50}N_{0.27}H_y$ is characterized by a higher ordering temperature (approximately 1100 °C). It should be noted that the type of ordering observed in $Zr_{0.50}Ti_{0.50}N_{0.27}H_y$ is similar to that found in $TiN_{0.26}H_{0.15}$ and $TiN_{0.26}D_{0.15}$ solid solutions [3], for which neutron diffraction studies also revealed stable arrangements of interstitial atoms after annealing at temperatures of approximately 900 °C and 750 °C, respectively. The higher onset temperature of ordering in highly defective solid solutions is attributed to the significant role of strain-induced interactions between interstitial atoms, which are long-range in nature. In the case of $Zr_{0.50}Ti_{0.50}N_{0.27}H_y$, the inhomogeneity within the interstitial sublattice further enhances these strain interactions, thereby leading to an increase in the ordering temperature.

Thus, the neutron diffraction study of the $Zr_{0.50}Ti_{0.50}N_{0.27}H_y$ solid solution enabled a comprehensive characterization of its crystal structure and the distribution of interstitial atoms after high-temperature treatment. Rietveld analysis of the diffraction data demonstrated that the $Zr_{0.50}Ti_{0.50}N_{0.27}H_y$ sample adopts a hexagonal structure within the P-3m1 space group, characterized by complete ordering of nitrogen atoms in the octahedral 1 (*a*) positions, while hydrogen atoms predominantly occupy tetrahedral interstitial sites, with partial occupancy of the octahedral 1 (*b*) positions. Comparison of different structural models showed that the proposed model provides the best agreement between the calculated and experimental diffraction intensities, thereby confirming its physical validity and accurately reflecting the actual distribution of atoms within the interstitial sublattice.

References:

1. F. Guo, J. Wang, Y. Du, J. Wang, S.L. Shang, S. Li, L. Chen (2018). First-principles study of adsorption and diffusion of oxygen on surfaces of TiN, ZrN and HfN. Applied Surface Science. 452, 457-462.

2. P. Hájková, J. Horník, E. Čižmárová, F. Kalianko (2022). Metallic materials for hydrogen storage-a brief overview. Coatings. 12, 1813, 1-24
3. I.Khidirov (2013). Neutron diffraction study of isotopic effect in arrangement of hydrogen atoms in solid solutions of the Ti-N-H, Ti-N-D and Ti-N-H-D systems. In: Neutron Diffraction: Instruments, Methodologies and Applications. Ed. X. Jin. Nova Science Publishers, New York.

CRYOGENIC HALL EFFECT ASYMMETRY AND STACKING FAULT SCATTERING IN 3C-SiC STRUCTURES FOR BETAVOLTAIC AND RADIATION-HARDENED APPLICATIONS

Atabaev B.G.[1], Malikov Sh.R.[2], Sulaimonov A.A.[2] Amanov O.O.[2] Dolgopolov M.V.[3]
[1]*Institute of Ion-Plasma and Laser Technologies, Uzbekistan Academy of Sciences, Tashkent Uzbekistan*
[2]*Institute of Nuclear Physics, Uzbekistan Academy of Sciences, Tashkent, Uzbekistan*
[3]*Samara State Technical University, Samara, Russian Federation*

The cryogenic magnetotransport properties of silicon carbide structures of the 3C-SiC polytype were studied in the temperature range of 77–320 K under opposite magnetic field directions. A pronounced asymmetry of the Hall effect and a splitting of the field dependences of the Hall resistance into two branches at temperatures below 140 K (Figure 1) were experimentally observed, indicating a significant influence of charge carrier scattering by stacking faults and the freeze-out effect of donor impurities.

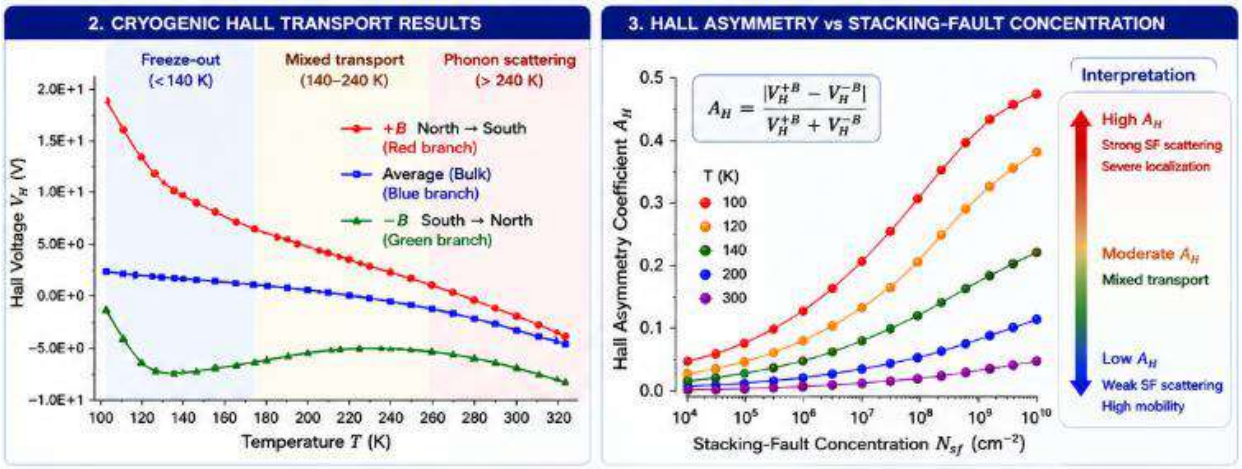

Figure 1.

Three characteristic transport branches are identified: two branches of the Hall resistance for opposite magnetic field directions and their averaged (symmetrized) characteristic, reflecting bulk transport. It is shown that with decreasing temperature, the asymmetry of the Hall effect increases significantly due to the suppression of phonon scattering and the increased role of localized transport due to structural defects.

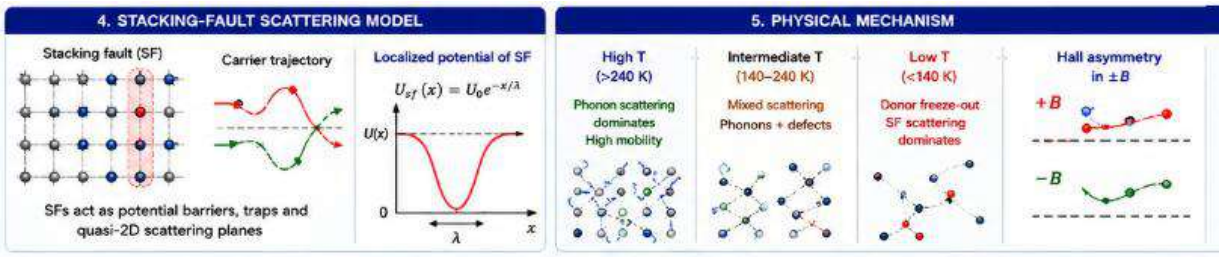

Figure 2.

A physical model (Figure 2) is proposed that takes into account the influence of potential barriers created by stacking faults, anisotropic magnetotransport, and cryogenic localization of charge carriers. It is shown that the Hall effect asymmetry value can be used as a highly sensitive, non-destructive diagnostic parameter for assessing the concentration of stacking faults in 3C-SiC structures. Experimental data were obtained using an HMS7000 photon Hall effect measurement system (Figure 3A). The sample used was 3C-SiC silicon carbide (Figure 3B), which was synthesized in the following steps:

1. Synthesis of a silicon carbide layer using atoms from the silicon substrate's crystal lattice and carbon atoms. Using a hydrogen flow rate of 0.3–0.5 l/min, molecular carbon was transferred to the reaction zone with the atoms from the silicon substrate's crystal lattice.
2. Formation of hydrocarbons on the silicon surface at a temperature of 1000–1200 °C through the reaction of carbon with hydrogen.
3. Formation of a p-n junction by doping the precursor silicon carbide layer with impurity atoms.



Figure 3. A B

To conduct measurements on the silicon carbide surface, ohmic contacts were formed on p-Si by soldering a Sn + In alloy (50%-50%) at 400 K.

These results are of interest for the development of SiC-based power electronics devices, radiation-hardened semiconductor systems, cryogenic electronics, space technology, and betavoltaic power sources [1], in which the structural perfection of the material determines the efficiency of charge carrier collection and the long-term stability of the devices.

References:

1. Atabaev B.G., Chepurnov V.I., Arutyunov N.Y., Dolgopolov M.V., Juraev K.N., Radzhapov S.A. Rapid 3D Defect Mapping in SiC Betavoltaics via Positron Annihilation Tomograph, Phys. Status Solidi (RRL) – Rapid Res. Lett., 2026, 20(1), e202500356. DOI: 10.1002/pssr.202500356.

RADIATION-INDUCED PHASE TRANSFORMATIONS AND MECHANICAL DEGRADATION OF Si_3N_4 CERAMICS UNDER HEAVY-ION IRRADIATION

Zhumazhanova A.T.[1,2]
[1]*Astana Branch of the Institute of Nuclear Physics, Astana, Kazakhstan*
[2]*L.N.Gumilyov Eurasian National University, Astana, Kazakhstan*

The radiation tolerance of silicon nitride (Si_3N_4) ceramics is of particular importance for their application in advanced nuclear, aerospace, and high-temperature engineering systems. In this work, the mechanisms of radiation-induced structural modification and degradation of mechanical properties of Si_3N_4 ceramics were investigated under irradiation with 130 MeV Kr^{15+} heavy ions. The samples were irradiated at 300 and 1000 K over a wide fluence range of 10^{11}-5×10^{14} ions/cm^2. Calculations showed that the penetration depth of Kr^{15+} ions does not exceed 14-15 μm, defining the characteristic thickness of the radiation-modified near-surface layer.

A key result of the study is the identification of a fluence threshold for pronounced radiation-induced structural transformation. At fluences below 10^{13} ions/cm^2, no significant β-Si_3N_4↔ α-Si_3N_4 transformation was detected. Above this threshold, a progressive increase in the α-Si_3N_4 fraction was observed, which is attributed to the accumulation and overlap of radiation-damaged regions along ion trajectories and the associated buildup of residual stresses. The transformation becomes more pronounced at 1000 K, demonstrating that irradiation temperature plays an important role in controlling defect evolution and phase stability.

Raman spectroscopy revealed a pronounced decrease in the intensity and broadening of characteristic vibrational bands above 5×10^{12} ions/cm^2, indicating increasing structural disorder and the onset of partial amorphization. At the maximum fluence of 5×10^{14} ions/cm^2, an amorphous-like layer with a thickness of up to 15 μm was formed, in close agreement with the calculated ion penetration depth. The simultaneous evolution of phase composition, Raman spectral characteristics, and mechanical properties demonstrates a direct correlation between radiation-induced disordering of the crystal lattice and softening of the irradiated near-surface region.

The scientific novelty of the work lies in establishing a dose-dependent sequence of radiation-induced processes in Si3N4 ceramics, from defect accumulation and residual stress formation to β-Si_3N_4 → α-Si_3N_4 polymorphic transformation, partial amorphization, and degradation of mechanical properties. The results demonstrate that high-dose irradiation-induced mechanical deterioration is governed by the combined contribution of lattice disorder, phase transformation, and amorphization rather than by crystallinity loss alone.

These findings provide a basis for assessing the radiation resistance of Si_3N_4-based ceramics and identifying irradiation conditions that determine the onset of critical structural and mechanical degradation. The established relationship between irradiation fluence, temperature, phase stability, and mechanical response is relevant to the development and lifetime prediction of ceramic materials intended for radiation-intensive and high-temperature environments.

Funding: This research was funded by the Committee of Science of the Ministry of Science and Higher Education of the Republic of Kazakhstan (No. AP22785867).

MACHINE LEARNING INTERATOMIC POTENTIAL FOR THE LOW-MODULUS Ti-Nb-Zr ALLOYS IN THE VICINITY OF DYNAMICAL INSTABILITY

Mukhamedov B.[1,2], Temirov D.[1], Karimbaev E.[1], Tasnádi F.[2], Abrikosov I.A.[2]
[1]*State Institution “Scientific and Technical Center for Radiation and Nuclear Safety”, The Committee for Industrial, Radiation and Nuclear Safety, Tashkent, Uzbekistan*
[2]*Theoretical Physics Division, Department of Physics, Chemistry and Biology (IFM), Linköping University, Linköping, Sweden*

Machine learning-augmented first-principles simulations facilitate the exploration of alloying and thermal treatments for tailoring material properties in industrial applications, yet extending these methods to compositions near dynamical instabilities remains a significant challenge. Reliable predictions in this regime require rigorous validation of machine-learned interatomic potentials (MLIP) to ensure their applicability where standard approaches often break down. In this study, we trained an MLIP using moment tensor potentials to simulate finite-temperature elastic properties of multicomponent β-$Ti_{94-x}Nb_xZr_6$ alloys across a broad range of compositions and temperatures [1]. Our simulations predict the presence of the elinvar effect over a wide range of temperatures. Importantly, we find that near the boundary of dynamical and mechanical instability, β-$Ti_{94-x}Nb_xZr_6$ alloys exhibit a strongly non-linear dependence of elastic moduli on Nb content, leading to values comparable to those of human bone. At room temperature, alloys with Nb content exceeding 12 at.% are predicted to be both dynamically and mechanically stable, with the Hill-averaged Young's modulus for compositions in the 12–17 at.% Nb range falling between 30 and 40 GPa; further increases in Nb content raise the modulus. Additionally, these alloys display pronounced anisotropy of directional Young's modulus, which becomes stronger upon approaching the instability boundary, offering a route to microstructure tailoring for materials with targeted elastic response. This work demonstrates that MLIPs can reliably capture elastic softening and instability-driven anisotropy, providing a practical and computationally efficient framework for the design of low-modulus, biocompatible Ti-Nb-Zr alloys through combined compositional and textural engineering strategies.

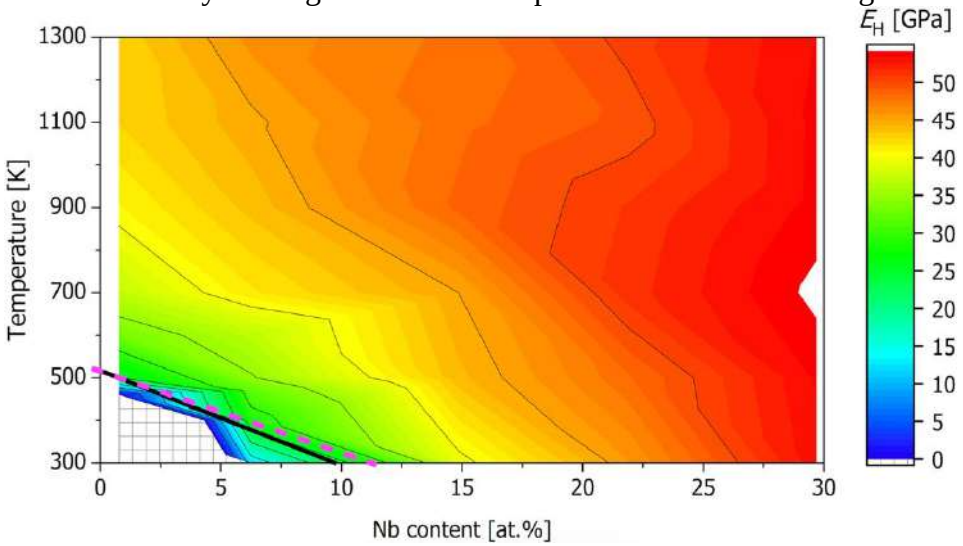

Color map of Young’s modulus E_{H} of $Ti_{94-x}Nb_xZr_6$ alloys plotted as a function of Nb-content and temperature, $E_H = f(T, x_{\mathrm{Nb}})$. The bottom left corner corresponds region of instability. Dashed and solid lines indicate to the borders of dynamical and mechanical instability, respectively.

References:

B.Mukhamedov, F.Tasnádi , I.A.Abrikosov. Machine learning interatomic potential for the low-modulus Ti-Nb-Zr alloys in the vicinity of dynamical instability. Materials & Design, 2025, 253 113865.

ANALYSIS OF ELECTRON DENSITY DISTRIBUTION AND SURFACE RMS PARAMETERS IN GaAs(O):Cr UNDER GAMMA IRRADIATION

Tashmetov M.Yu., Abdaminov A.B.
Institute of Nuclear Physics, Uzbekistan of the Academy, Tashkent, Uzbekistan

Gallium arsenide (GaAs) is a leading III-V compound semiconductor widely used in commercial applications, providing the foundation for high-speed and high-frequency electronic devices. Doping GaAs with chromium offers several advantages over other transition metals such as Mn, Fe, and Ni, including improvements in microstructural and electronic properties, as well as enhanced thermal and chemical stability [1-3]. The impact of ionizing radiation on III–V semiconductors involves energy transfer to both electrons and lattice atoms, leading to the formation of non-equilibrium defects and their subsequent evolution. It is important to investigate how different types of radiation (gamma rays, neutrons, and protons) influence atomic arrangement and defect formation in GaAs(O):Cr structures. These structural modifications, in turn, directly affect the functional properties of semiconductor materials.

In addition, gamma irradiation induces noticeable changes in electron density distribution and surface morphology. In particular, understanding the relationship between radiation dose, charge redistribution, defect formation, and their influence on surface structure remains a relevant scientific challenge. However, the physical mechanisms underlying the changes in electron density distribution and surface morphology under gamma irradiation are still insufficiently understood.

Therefore, the present study aims to perform a comprehensive analysis of the changes in electron density distribution and surface morphology in GaAs(O):Cr samples under gamma irradiation. GaAs(O):Cr single crystals investigated in this study were grown using the liquid-encapsulated Czochralski (LEC) method. The composition of the samples was determined to be Ga (47.7 at.%), As (44.37 at.%), Cr (0.1 at.%), and O (7.82 at.%) [4].

In this study, the structural model for electron density mapping (EDM) was determined from X-ray diffraction data using the Rietveld refinement method implemented in the FullProf software. Based on the refinement results, the electron density distribution was calculated via Fourier synthesis. The surface morphology of the samples was analyzed using an SPM 9700HT scanning probe microscope (Shimadzu). A 5×5 μm^2 area of the sample surface was selected for analysis, and the root mean square (RMS) roughness was calculated as [5]. Irradiation of GaAs(O):Cr crystals in the 0-500 kGy gamma dose range was carried out using a ^{60}Co gamma-ray source at the Institute of Nuclear Physics of the Academy of Sciences of the Republic of Uzbekistan.

The electron density of GaAs(O) samples was analyzed after gamma irradiation at different doses. For the unirradiated sample, the high electron density was determined to be 21.50 $Å^{-3}$. Following gamma irradiation, this value decreased to 18.72 $Å^{-3}$ at 100 kGy, increased slightly to 19.24 $Å^{-3}$ at 200 kGy, and reached its minimum value of 18.70 $Å^{-3}$ at 300 kGy. At higher doses, the high electron density slightly increased to 18.92 $Å^{-3}$ at 400 kGy and then decreased to 18.73 $Å^{-3}$ at 500 kGy. Overall, the high electron density decreased by approximately 13% after gamma irradiation, with the most pronounced reduction observed at 300 kGy. These dose-dependent variations indicate a redistribution of electron density within the crystal lattice induced by gamma irradiation.

When X-rays interact with a crystal, they are scattered by the electron clouds of atoms located within the lattice. In the antibonding region, the low electron density reflects the redistribution of valence electrons and a decreased electron probability within the bonding interaction region. In contrast, the high electron density observed in the interatomic region indicates an increased overlap of electron clouds between atoms, which is characteristic of the formation of a polar covalent bond [6].

The root mean square (RMS) roughness of the unirradiated sample was 16.5 nm, indicating a relatively degraded surface morphology, as shown in Table 1.

Table 1. Changes in the RMS surface roughness parameter of GaAs(O):Cr crystals under different gamma irradiation doses.

Gamma irradiation doses (kGy)	Unirradiated	100	200	300	400	500
RMS (nm)	16.5	9.5	5.3	7.5	7.2	6.5

At a dose of 100 kGy, the RMS roughness decreased to 9.5 nm, corresponding to a reduction of 42.4% compared to the initial state. This parameter further decreased to 6.5 nm at a dose of 500 kGy. At low irradiation doses, relaxation processes are predominant, which leads to the smoothing of micro-roughness features [7-8].

In conclusion, gamma irradiation induces correlated changes in electron density and surface morphology of GaAs(O):Cr crystals, reflecting dose-dependent defect formation and structural relaxation.

This research was conducted within the framework of the 2026 research program of the Institute of Nuclear Physics of the Academy of Sciences of the Republic of Uzbekistan on the following topic: “Optimization of the electrophysical and physicomechanical properties of $A^{III}B^{V}$ and $A^{II}B^{VI}$ semiconductor compounds using thermoradiation technology”. The authors would like to thank the scientific team of the Laboratory of Radiation Physics and Solid State Electronics Technology.

References:

1. Camilo Pulzara-Mora, José Doria-Andrade, Roberto Bernal-Correa, Andrés Rosales-Rivera, Álvaro Pulzara-Mora (2024). Characterization of GaAs and GaAs/Cr/GaAs interfacial layers fabricated via magnetron sputtering on silicon (100). Digest Journal of Nanomaterials and Biostructures. 19(2), 669-677.
2. P.V.Seredin, A. V. Fedyukin, V. N. Feklin, I. N. Arsentiev, Harald Leiste (2015). Condensed Matter and Interphases. 17(4), 518-525.
3. S.S.Khludkov, O. P. Tolbanov, M. D. Vilisova, I. A. Prudaev (2016). Semiconductor devices based on gallium arsenide with deep impurity centers.

4. M.Tashmetov, A.Abdaminov (2025). Influence of gamma doses on the optical and electrical properties of oxygen-impurity and chromium-doped GaAs. Journal of Physics: Condensed Matter. 37, 485702.
5. D.Whitehouse (2002). Surfaces and their Measurement. London: Hermes Penton Science, pp. 54-55.
6. U.Pietsch, V.G. Tsirelson, R.P. Ozerov (1986). X-ray electron density distribution of GaAs. Phys. Status Solidi B. 138, 47.
7. H.D.Dhaygude, S. K. Shinde, M. V. Takale, G. M. Lohar, M. C. Rath, V. J. Fulari (2016). Effect of electron irradiation on structural, morphological and photoluminescence properties of ZnS thin films. Ceramics International. 42(8), 10159-10164.
8. K.Priya, G.K. Rao, V.K. Ashith, G.Sanjeev, V.P. Verma, V.C. Petwal, J.Dwivedi (2019). The effect of 8 MeV electron beam irradiation on the structural, optical and photoluminescence properties of ZnS thin films. Ceramics International. 45(2, Part A), 2576-2583.

FTIR ANALYSIS OF ELECTRON-INDUCED MODIFICATIONS IN Si_3N_4 NANOPOWDER AT A FLUENCE OF 5×10^{15} e/cm^2 WITH AN ELECTRON ENERGY OF 2 MeV

Tashmetov M.Yu., Buriev M.M.
Institute of Nuclear Physics, Uzbekistan of the Academy, Tashkent, Uzbekistan

Silicon nitride (Si_3N_4) is a material known for its exceptional hardness, outstanding thermal stability, and strong resistance to chemical corrosion and oxidation. Due to these advantageous properties, Si_3N_4 has found extensive applications in diverse areas such as aerospace engineering, electronics, metallurgy, and energy technologies. In particular, Si_3N_4 in nanopowder form demonstrates a high level of surface reactivity, enabling precise tuning of its physical and chemical characteristics. As a result, it is considered an important and actively studied material in modern materials science [1,2].

The irradiation experiment was performed in Tashkent, Uzbekistan, using the Electron-U003 linear electron accelerator. The Si_3N_4 nanopowder was irradiated with accelerated electrons having an energy of 2 MeV. Following irradiation, the FTIR spectra of the sample were recorded using a Cary 600 Series FTIR spectrometer over the 400-1300 cm^{-1} spectral range. A helium-neon (He-Ne) laser with a wavelength of 632.8 nm and a maximum output power of less than 1 mW was used as the excitation source [1]. The obtained spectrum was compared with that of the unirradiated sample to evaluate the changes in chemical bonding and local structural characteristics induced by electron irradiation (Fig. 1*a*). To investigate the radiation-induced changes in the Si_3N_4 nanopowder, the sample was irradiated with 2 MeV electrons at a fluence of 5×10^{15} e/cm^2.

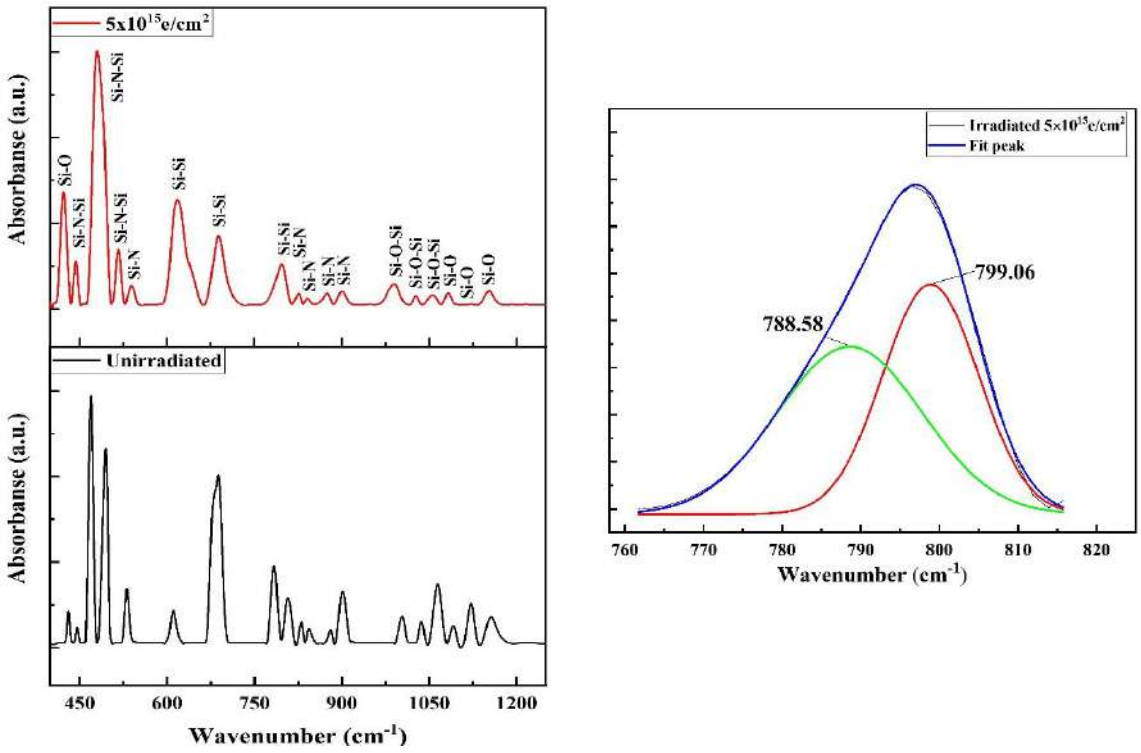

Figure 1. *a*) FTIR spectra of Silicon Nitride (Si_3N_4) nanopowder measured before irradiation and after electron irradiation at a fluence of 5×10^{15} e/cm^2 *b*) FTIR spectrum of the Si_3N_4 nanopowder irradiated at a fluence of 5×10^{15} e/cm^2. The deconvoluted peaks show that the previously merged Si-Si vibration modes shift to 788.58 cm^{-1} and 799.06 cm^{-1}, indicating irradiation-induced changes in the local bonding environment.

At a higher electron fluence of 5×10^{15} e/cm^2, partial separation of previously [1] merged spectral peaks was observed. This behavior can be attributed to radiation-induced local structural rearrangements, which lead to a clearer manifestation of certain vibrational modes.

At the previous fluence [1], these bands shifted from 783.6 to 778.94 cm^{-1} and from 807.78 to 795.93 cm^{-1}, respectively, but they remained partially merged and were not fully resolved. It is important to note that these bands are associated with Si-Si bonds [1,3,4], and their spectral changes may reflect modifications in the interactions between silicon atoms induced by electron irradiation. With a further increase in fluence, the bands remained partially merged, while a noticeable shift in their spectral positions was observed. Specifically, the bands at 778.94 and 795.93 cm^{-1} shifted to 788.58 and 799.06 cm^{-1}, respectively (Fig. 1*b*).

Such shifts may indicate modifications in the Si-Si bond environment, including possible bond shortening and an increase in the force constant, leading to a stronger bonding. At the same time, the incomplete separation of the peaks suggests that a certain degree of structural disorder still persists, implying a non-uniform local environment around silicon atoms. Overall, these results indicate that at higher electron fluence, processes such as bond rearrangement, defect formation, and partial amorphization occur simultaneously.

This research was conducted within the framework of the 2025 research program of the Institute of Nuclear Physics of the Academy of Sciences of the Republic of Uzbekistan on the following topic: “Optimization of the electrophysical and physicomechanical properties of $A^{III}B^{V}$ and $A^{II}B^{VI}$ semiconductor compounds using thermoradiation technology”.

References:
1. Tashmetov M.Yu. and Buriev M.M. Structural and vibrational characterization of Si_3N_4 nanopowders under electron beam irradiation. J. Phys.: Condens. Matter 38 (2026) 125702.
2. Riley F.L. Silicon Nitride and Related Materials. Am. Ceram. Soc. (2000) 83:245-265.
3. Paul F. Fewster. The Limits of X-ray Diffraction Theory Crystals (2023) 13:521
4. Sokovnin S.Yu., Il’ves V.G., Uimin M.A. Effect of annealing in different media and pulse electron beam irradiation on the properties of calcium fluoride nanopowder. Ceramics International (2024) Vol. 50 15790-15805.

TRANSPORT PROPERTIES OF GaAs(O):Cr UNDER HIGH-FLUENCE ELECTRON IRRADIATION

TashmetovM.Yu.[1], Djangabaev Kh.N.[2]
[1]*Institute of Nuclear Physics, Uzbekistan Academy of Sciences, Tashkent, Uzbekistan*
[2]*Berdakh Karakalpak State University, Nukus, Uzbekistan*

The electrical parameters of semiconductors, including resistivity, carrier concentration, and mobility, are sensitive to changes in the defect and structural subsystems under radiation exposure. With increasing electron fluence, further rearrangement of radiation-induced defect states can alter carrier generation, trapping, and scattering processes, thereby affecting the transport properties of the crystal [1,2].

For GaAs(O):Cr, particular interest lies in its electrical properties at high electron fluences, where further rearrangement of radiation-induced defect states can substantially affect carrier generation, trapping, and scattering processes. These changes are reflected in the carrier concentration, mobility, and resistivity, making Hall-effect measurements a useful approach for assessing the evolution of transport properties under irradiation. Accordingly, the carrier concentration, mobility, and resistivity of GaAs(O):Cr were determined after 2 MeV electron irradiation at fluences of 4, 5, and 6×10^{17} e/cm^2 using an HMS-7000 Photonic Hall Effect Measurement System.

Hall-effect measurements were performed over the 100–300 K temperature range before and after irradiation. The obtained temperature dependences are presented in Fig. 1.

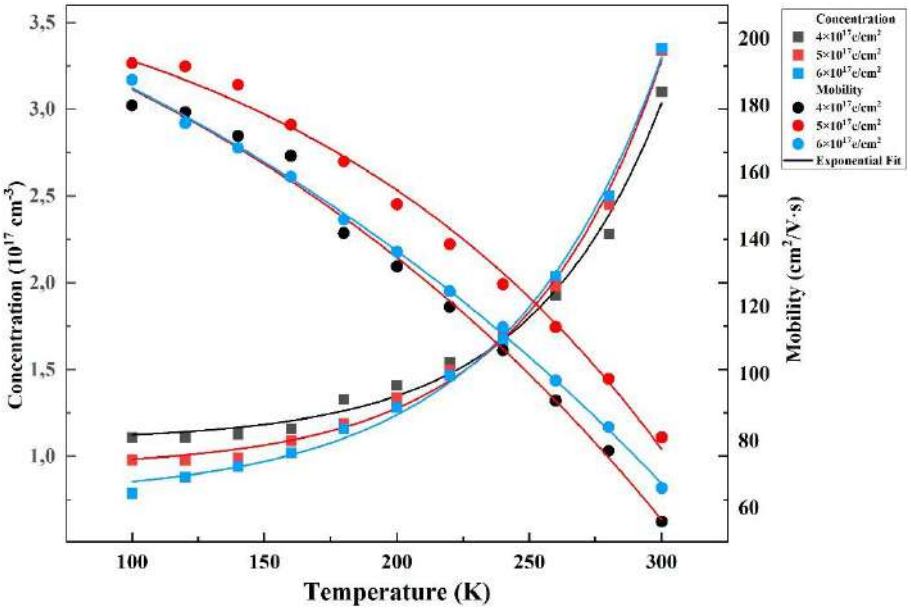

Figure 1. Temperature dependences of carrier concentration and mobility in GaAs(O):Cr at electron irradiation fluences of 4, 5, and 6×10^{17} e/cm^2.

At a fluence of 4×10^{17} e/cm^2, the carrier concentration increases from 1.11×10^{17} to 3.10×10^{17} cm^{-3}, while the mobility decreases from 180 to 56 cm^2/(V·s) and the resistivity increases from 3.13×10^{-1} to 3.58×10^{-1} Ω·cm. This behavior can be attributed to the thermal activation of carriers from radiation-induced defect and trap states, while the decrease in mobility reflects enhanced defect-related scattering.

At 5×10^{17} e/cm^2, the carrier concentration changes from 1.13×10^{17} to 3.04×10^{17} cm^{-3}, the mobility from 181 to 59 cm^2/(V·s), and the resistivity from 3.05×10^{-1} to 3.49×10^{-1} Ω·cm. The similarity of the temperature dependences to those at 4×10^{17} e/cm^2, together with the smaller variation in the transport parameters, may indicate partial rearrangement and redistribution of radiation-induced defects.

At the highest fluence of 6×10^{17} e/cm^2, the carrier concentration increases from 1.18×10^{17} to 2.84×10^{17} cm^{-3}, while the mobility decreases from 179 to 65 cm^2/(V·s) and the resistivity changes from 2.95×10^{-1} to 3.38×10^{-1} Ω·cm. The weaker temperature dependence of the parameters compared with that at 4×10^{17} e/cm^2 may indicate the formation of a relatively stable defect state, in which defect generation, recombination, and redistribution become more balanced.

Overall, the 4–6×10^{17} e/cm^2 range retains thermally activated transport, manifested by an increase in carrier concentration with temperature. With increasing fluence, the temperature dependence of the carrier concentration becomes weaker, the room-temperature mobility increases from 56 to 65 cm^2/(V·s), and the resistivity values become closer. These trends indicate stabilization of the transport characteristics at high fluences, associated with the formation of a relatively stable defect state in GaAs(O):Cr. This study was carried out within the 2026 research program of the Institute of Nuclear Physics, Academy of Sciences of the Republic of Uzbekistan, entitled “Optimization of the electrical and physicochemical properties of $A^{II}B^{VI}$ and $A^{III}B^{VI}$ compounds using thermo-radiation technology.”

References:

1. M.Yu.Tashmetov., Kh.Djangabaev (2025). Study of radiation-induced effects in GaAs(O):Cr under 2 Mev electron irradiation using Raman, FTIR and Hall effect measurements. Physica Scripta, **100**, No. 12.,125918 https://doi.org/10.1088/1402-4896/ae26ef
2. M.Tashmetov, A.Abdaminov (2025). Influence of gamma doses on the optical and electrical properties of oxygen-impurity and chromium-doped GaAs. Journal of Physics: Condensed Matter. **37**, 485702. https://doi.org/10.1016/j.physb.2025.417377
3. D.C.Look, 1977, The electrical characterization of semiinsulating GaAs: A correlation with mass spectrographic analysis. Journal of Applied Physics **48**, 5141 http://dx.doi.org/10.1063/1.323593
4. L.W.Aukerman, P.W.Davis, R.D. Graft, and T.S.Shilliday 1963, Radiation Effects in GaAs. J. Appl. Phys. 34, 3590 https://doi.org/10.1063/1.1729263

PHASE TRANSFORMATIONS IN THERMAL BARRIER CERAMICS BASED ON ZIRCONIUM DIOXIDE AND ALUMINUM OXIDE

Khametov Sh.

Eurasian National University named by L.N.Gumilyov, Astana, Kazakhstan

This paper examines in detail the role of structural, phase, and morphological changes in ZrO_2 – Al_2O_3-based ceramics caused by phase polymorphic transformations with varying concentrations of the stabilizing dopant Y_2O_3. It also establishes the relationship between these changes and the thermophysical properties and resistance of the materials to various types of external influences. Particular attention is paid to the influence of Y_2O_3 concentration on phase formation processes, changes in grain size and morphology during thermal sintering, and the formation of the thermal insulation and strength properties of the studied ceramics. The main factors of external influence are considered: abrupt cyclic changes in temperature, mechanical loads, and prolonged high-temperature exposure, which can lead to the accumulation of structural defects, the occurrence of localized stresses, and subsequent degradation of the performance characteristics of ceramic materials. An assessment of phase transformations caused by changes in the concentration of the stabilizing dopant Y_2O_3 revealed a pronounced dependence of the phase composition of the ceramics on the dopant content. It was established that at relatively low Y_2O_3 concentrations, polymorphic transformation processes of the m-ZrO_2 → t-Zr(Y)O_2 type play a dominant role in structural and phase changes. The introduction of yttrium ions into the zirconia crystal structure promotes the stabilization of the tetragonal modification of ZrO_2, which is accompanied by changes in the crystal lattice parameters and the formation of structural states that differ from the initial monoclinic phase. Moreover, the nature of the phase transformations directly affects the morphology of the grains and the characteristics of their growth during sintering, determining the formation of the final microstructure of the ceramic material.

With an increase in the concentration of the stabilizing dopant above 0.10 M, the nature of phase formation changes significantly. In this concentration range, the formation of the pyrochlore phase $Y_2Zr_2O_7$ begins to dominate. The formation of this phase is accompanied by structural changes in the ceramic material and changes in mass transfer mechanisms during high-temperature sintering. As a result, a pronounced coarsening of grains is observed, which may be due to the intensification of diffusion processes and changes in intergranular interactions under the conditions of pyrochlore structure formation.

ON THE STATE OF DOPED HOLE IN LSCO CUPRATE: DFT+U STUDY

Eraliev A.A.[1], Yavidov B.Ya.[1], Khajibaev D.G.[2]
[1]*Nukus State Pedagogical Institute named after Ajiniyaz, Nukus, Uzbekistan*
[2]*Institute of Fundamental and Applied Research, National Research University TIIAME, Tashkent, Uzbekistan*

The orbital character of the holes introduced by Sr substitution in $La_{2-x}Sr_xCuO_4$ (LSCO) remains a central open question in the physics of the cuprates. In the conventional picture the doped hole enters the planar Cu-3d(x^2-y^2)/O-2pσ band, consistent with the two-dimensional nature of superconductivity [1]. Perry *et al.* [2], using the hybrid B3LYP functional, proposed instead that doping forms a localized Cu-3d($3z^2-r^2$)/apical-O-$2p_z$ (z^2) hole on the CuO_6 octahedron adjacent to the Sr impurity. The two pictures imply different pairing scenarios. In our previous work the parent compound was studied under hydrostatic pressure within the same DFT+U framework [3]; here we extend that approach from mechanical to chemical tuning and test the z^2-hole hypothesis by explicit-Sr calculations.

Spin-polarized DFT+U calculations were carried out with the Quantum ESPRESSO package [4] using the PBE exchange–correlation functional [5] and ultrasoft pseudopotentials. On-site correlations in the Cu 3d shell were treated in the Dudarev formulation [6] of the DFT+U scheme [7] with U = 8 eV, chosen to reproduce the experimental antiferromagnetic (AF) moment and charge-transfer gap of the parent compound [1]. The orthorhombic *Cmce* structure [8] was adopted with checkerboard AF order and all internal coordinates fully relaxed. The parent compound was modeled in a 28-atom cell (Fig. 1a) and $La_{1.875}Sr_{0.125}CuO_4$ (x = 1/8) in a 56-atom supercell with one La replaced by Sr on the site apical to a Cu atom (Fig. 1b). The hole character was extracted from the site- and spin-resolved Cu 3d occupation matrices and the projected density of states.

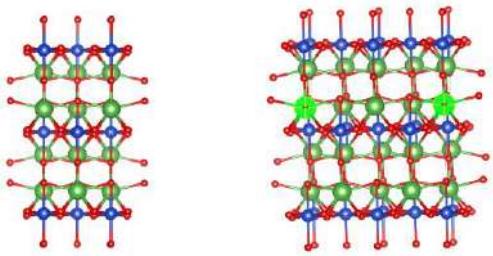

(a) *(b)*

Figure 1. Relaxed structures: (a) La_2CuO_4 (28 atoms); (b) $La_{1.875}Sr_{0.125}CuO_4$ (56 atoms), Sr apical to Cu.

The undoped calculation reproduces the AF charge-transfer insulator: a gap of 1.61 eV, a Cu moment of 0.57 μB and apical/planar Cu–O bond lengths of 2.468/1.936 Å, in good agreement with experiment [1, 8] (Table 1). The hole resides in the x^2-y^2 orbital with the z^2 shell full. Upon Sr substitution the doped hole remains in the planar Cu-x^2-y^2/O-2pσ band: the Cu atom directly below the Sr retains a nearly full z^2 shell (z^2 hole ≈ 0.06) and its full magnetic moment, in sharp contrast to the B3LYP value of 0.34 [2].

The apical Cu–O bond of the doped octahedron contracts, 2.468 → 2.294 Å. This contraction by itself does not discriminate between the two pictures, since B3LYP obtains a comparable shortening of 0.26 Å [2]; the discriminating quantity is the sign of the Sr–O displacement, which the z^2-hole scenario requires to be an elongation of 0.22 Å [2]. We obtain a shortening. The local pair-distribution-function refinement of Božin and Billinge yields the same sign, r(Sr–O) < r(La–O) [10],

and their bond-valence analysis assigns more than 85 % of the doped charge to the planar orbitals, the apical share at x = 1/8 being of the same order as the z^2 occupancy found here [10]. The contraction is therefore an electrostatic response to planar hole doping; the same response is obtained under hydrostatic compression, with no accompanying change in orbital character [3].

Table 1. Calculated properties compared with the B3LYP results of Perry et al. and experiment.

Quantity	This work	Perry (B3LYP)	Experiment	Refs.
Gap (eV)	1.61	2.0	1.8–2.0	[1]
Cu moment (μB)	0.57	0.61	~0.60	[1]
Planar Cu–O (Å)	1.936	—	~1.90	[8]
Apical Cu–O (Å)	2.468	2.40	~2.41	[8]
Doped Cu z^2 hole	0.06	0.34	weak	[9, 10]
Doped hole orbital	x^2-y^2	z^2/apical	x^2-y^2	[9, 10]

The density of states (Fig. 2) shows a doping-induced insulator-to-metal transition. The undoped system has a clean gap and no states at E_F; the doped system is metallic, with weight at E_F of predominantly planar Cu-3d(x^2-y^2)/O-2pσ character and no isolated in-gap z^2 impurity peak, contrary to the B3LYP prediction [2]. This agrees with polarization-dependent X-ray absorption [9], which finds the Cu-3d($3z^2-r^2$) character of the doped holes to be very weak, the out-of-plane weight residing instead on the apical O-$2p_z$ orbital.

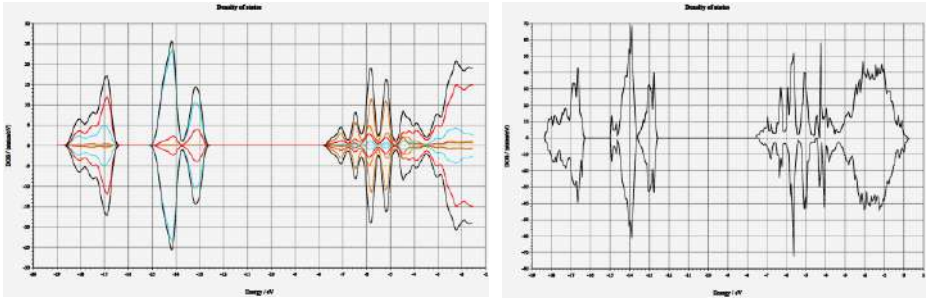

Figure 2. Density of states: La_2CuO_4 (left, insulating gap) and $La_{1.875}Sr_{0.125}CuO_4$ (right, metallic).

Explicit-Sr DFT+U calculations therefore place the doped hole of $La_{1.875}Sr_{0.125}CuO_4$ in the planar Cu-x^2-y^2/O-2pσ band; the localized Cu-z^2 hole predicted by B3LYP does not form. The new element is the separation of the structural from the orbital response: because the impurity occupies a definite crystallographic site, the contraction of the neighboring CuO_6 octahedron is identified as electrostatic and removed as evidence for z^2 doping. With the pressure results [3], neither chemical nor mechanical shortening of the apical Cu–O bond alters the x^2-y^2 character of the states at E_F, which constrains any model of high-T_c superconductivity in this family that relies on apical z^2 states. The conclusion is consistent with the only direct experimental test of the z^2-hole hypothesis reported so far [10].

References:

1. M.A.Kastner, R.J.Birgeneau, G.Shirane, Y.Endoh. Rev. Mod. Phys. 70, 897 (1998).
2. J.K.Perry, J.Tahir-Kheli, W.A.Goddard III. Phys. Rev. B 65, 144501 (2002); ibid. 63, 144510 (2001).
3. A.Eraliev et al. Scientific Bulletin of NamSU, No. 6, 40 (2026).
4. P.Giannozzi et al. J. Phys.: Condens. Matter 21, 395502 (2009).
5. J.P. Perdew, K. Burke, M. Ernzerhof. Phys. Rev. Lett. 77, 3865 (1996).

6. S.L. Dudarev et al. Phys. Rev. B 57, 1505 (1998).
7. V.I. Anisimov, J. Zaanen, O. K. Andersen. Phys. Rev. B 44, 943 (1991).
8. P.G. Radaelli et al. Phys. Rev. B 49, 4163 (1994).
9. C.T. Chen, L. H. Tjeng, J. Kwo et al. Phys. Rev. Lett. 68, 2543 (1992).
10. E.S. Božin, S. J. L. Billinge. Phys. Rev. B **72**, 174427 (2005).

RAMAN SPECTROSCOPIC FEATURES OF ELECTRON-IRRADIATED GaAs

Tashmetov M.Yu., Madiyarov D.N.
Institute of Nuclear Physics, Uzbekistan Academy of Sciences, Tashkent, Uzbekistan

Gallium arsenide (GaAs) is an important III–V semiconductor used in optoelectronic and high-frequency devices. Radiation-induced defects can modify its local lattice and phonon properties, which can be effectively studied by Raman spectroscopy **[1]**.

The aim of this work is to investigate the effect of 2 MeV electron irradiation at a fluence of 1×10^{17} e/cm^2 on the Raman characteristics of n-type GaAs single crystals. Particular attention is paid to the changes in the transverse optical (TO) and longitudinal optical (LO) phonon modes in comparison with an unirradiated reference sample.

Samples of Czochralski-grown n-type GaAs were irradiated at the “Elektronika U-003” linear electron accelerator at the Institute of Nuclear Physics, Academy of Sciences of the Republic of Uzbekistan. The nominal electron energy was 2 MeV and the beam current density was 0.085 μA/cm^2. The investigated samples included an unirradiated reference and a sample irradiated to a fluence of 1×10^{17} e/cm^2. After irradiation, the samples were prepared in powder form for Raman measurements.

Raman spectra were recorded at room temperature using a Renishaw inVia Raman spectrometer with 532 nm excitation in the range of 200-350 cm^{-1}. A 50× objective and 1800 lines/mm grating were used at a laser power of 0.05 mW. Gaussian fitting was applied to determine phonon peak positions, FWHM, and integral intensities.

The Raman spectra of both samples exhibit two dominant peaks located near 266 and 287 cm^{-1}, which are assigned to the first-order TO and LO phonon modes of GaAs, respectively. No additional Raman modes appear after irradiation, indicating that the characteristic phonon structure of GaAs is preserved **[2, 3]**. The representative Raman spectra of the unirradiated and 2 MeV electron-irradiated GaAs samples are shown in Figure 1. A clear change is observed in the TO phonon position after electron irradiation. For the unirradiated sample, the TO phonon occurs at 266.43 cm^{-1}, whereas after irradiation to 1×10^{17} e/cm^2 it shifts to 265.70 cm^{-1}. Thus, the TO phonon shift is $\Delta\omega_{TO} = -0.73$ cm^{-1}. In contrast, the LO phonon position changes only slightly, from 287.08 to 287.13 cm^{-1}. The observed shift of the TO mode toward lower wavenumbers indicates a modification of the local lattice environment caused by electron irradiation. Such a shift can be associated with local lattice deformation, changes in interatomic bonding conditions and radiation-induced defects **[3, 4]**. The irradiation-induced changes are also reflected in the phonon linewidths. The TO FWHM increases from 12.76 cm^{-1} for the unirradiated sample to 16.33 cm^{-1} after irradiation, while the LO FWHM increases from 12.32 to 13.08 cm^{-1}. The stronger broadening of the TO mode indicates an increase in phonon scattering and local structural disorder following electron irradiation **[3, 5]**.

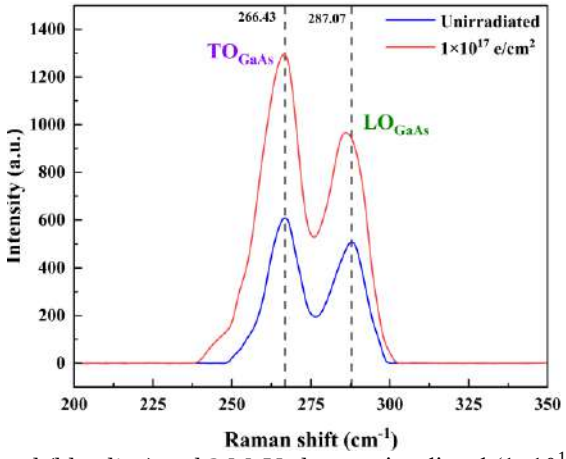

Figure 1. Raman spectra of unirradiated (blue line) and 2 MeV electron-irradiated (1×10^{17} e/cm^2, red line) n-type GaAs samples recorded at room temperature (λ_{exc} = 532 nm). The dashed lines indicate the TO and LO phonon positions of the unirradiated sample.

The TO phonon shift was additionally used to estimate the effective local deformation and stress parameters **[6]**. For the 1×10^{17} e/cm^2 irradiated sample, the obtained values are ε_{Raman} = 2.42×10^{-3} and σ_{Raman} = 0.30 GPa. Since the Raman measurements were performed on powder samples, these quantities should be considered effective local deformation and stress parameters rather than direct measurements of macroscopic uniaxial stress.

The relative contribution of the LO and TO phonon modes also changes after irradiation. The ratio of the integrated LO and TO phonon intensities (I_{LO}/I_{TO}) increases from 1.201 for the unirradiated sample to 1.562 after electron irradiation. This change may be related to modifications of phonon scattering conditions and the local structural environment produced by radiation-induced defects. The obtained Raman parameters are summarized in Table 1.

Table 1. Raman parameters of unirradiated and 2 MeV electron-irradiated GaAs.

Electron fluence (e/cm^2)	TO (cm^{-1})	LO (cm^{-1})	$\Delta\omega_{TO}$ (cm^{-1})	σ_{Raman} (GPa)	ε_{Raman} ($\times10^{-3}$)	$FWHM_{TO}$ (cm^{-1})	$FWHM_{LO}$ (cm^{-1})	I_{LO}/I_{TO}
Unirradiated	266.43	287.08	0.00	0.00	0.00	12.76	12.32	1.201
1×10^{17}	265.70	287.13	−0.73	0.30	2.42	16.33	13.08	1.562

The obtained results demonstrate that 2 MeV electron irradiation at 1×10^{17} e/cm^2 does not introduce new Raman-active modes, while it produces measurable changes in the local phonon environment of GaAs. The TO phonon softening, linewidth broadening and increase in the I_{LO}/I_{TO} ratio indicate that electron irradiation modifies local lattice deformation and phonon scattering conditions **[3, 5]**. Therefore, Raman spectroscopy can be effectively used to monitor radiation-induced local structural changes in GaAs even when the characteristic phonon modes of the crystal remain preserved.

Acknowledgements. This research was carried out within the framework of the 2026 research program of the Institute of Nuclear Physics of the Academy of Sciences of the Republic of Uzbekistan on the topic “Optimization of the Electrical and Physicochemical Properties of A^{II}–B^{VI} and A^{III}–B^{VI} Compounds Using Thermoradiation Technology.”

References:

1. R. Loudon, "The Raman Effect in Crystals," Adv. Phys., vol. 13, pp. 423–482, 1964, doi: 10.1080/00018736400101051.
2. R. Trommer and M. Cardona, "Resonant Raman scattering in GaAs," Phys. Rev. B, vol. 17, p. 1865, 1978, doi: 10.1103/PhysRevB.17.1865.
3. M. Yu. Tashmetov and K. N. Djangabaev, "Study of radiation-induced effects in GaAs(O):Cr under 2 MeV electron irradiation using Raman, FTIR and Hall effect measurements," Phys. Scr., vol. 100, 125918, 2025, doi: 10.1088/1402-4896/ae26ef.
4. G. Burns et al., "Phonon shifts in ion bombarded GaAs: Raman measurements," Solid State Commun., vol. 62, no. 7, pp. 449–454, 1987, doi: 10.1016/0038-1098(87)91096-9.
5. S. Dhamodaran et al., J. Phys.: Condens. Matter, vol. 18, pp. 4135–4142, 2006, doi: 10.1088/0953-8984/18/17/003.
6. De Wolf, "Micro-Raman spectroscopy to study local mechanical stress in silicon integrated circuits," Semicond. Sci. Technol., vol. 11, pp. 139–154, 1996, doi: 10.1088/0268-1242/11/2/001.

NATURE OF OPTICAL ABSORPTION BANDS IN CaF_2–YbF_3 SINGLE CRYSTALS AT DIFFERENT YTTERBIUM CONCENTRATIONS

Boyboboeva S.T., Utarov S.M.
Institute of Nuclear Physics, Uzbekistan Academy of Sciences, Tashkent, Uzbekistan

CaF_2:Yb single crystals are of considerable interest as active media for solid-state lasers due to their high thermal conductivity, low quantum defect, and ability to accommodate high ytterbium concentrations. In addition to Yb^{3+} ions, Yb^{2+} ions may be present in the crystals, forming characteristic absorption and luminescence bands whose is strongly dependent on the impurity concentration and the defect state of the crystal [1–3]. The absorption bands of Yb^{3+} ions in the IR region of the spectrum of CaF_2–YbF_3 single crystals has been extensively studied and are attributed to various types of local centers (O_h, C_{3v}, C_{4v}, and clusters) [2–4]. However, the nature of the absorption bands in the ultraviolet region of the spectrum, especially at high concentrations of ytterbium, is insufficiently studied. The aim of this work is to investigate of the nature of the optical absorption bands in CaF_2–YbF_3 single crystals with a YbF_3 content of 5 and 15 mol.%, and the comparison of the obtained results with literature data for crystals with lower concentrations of the activator (1–5 mol.%).

The optical absorption spectra of the initial CaF_2–YbF_3 crystals with a YbF_3 content of 1–5 mol.% are characterized by bands in the UV region with maxima at 214 (G), 228 (A_1), 263 (A_2), 274 (A_3), 320 (F), and 365 nm (A_4), as well as by lines in the IR region (860–1060 nm) [3,5]. As the YbF_3 concentration increases to 5 mol.%, the intensity of the absorption bands increases in both spectral regions. At 15 mol.% YbF_3, the absorption spectrum undergoes substantial restructuring: band A1 splits into components with maxima at approximately 214, 226, and 240 nm, whereas the intensities of bands A2–A4 decrease significantly, particularly that of band A4 (Fig. 1). The obtained results attest to a strengthening of the interaction between Yb ions, the formation of associated centers, and a change in the local crystal field.

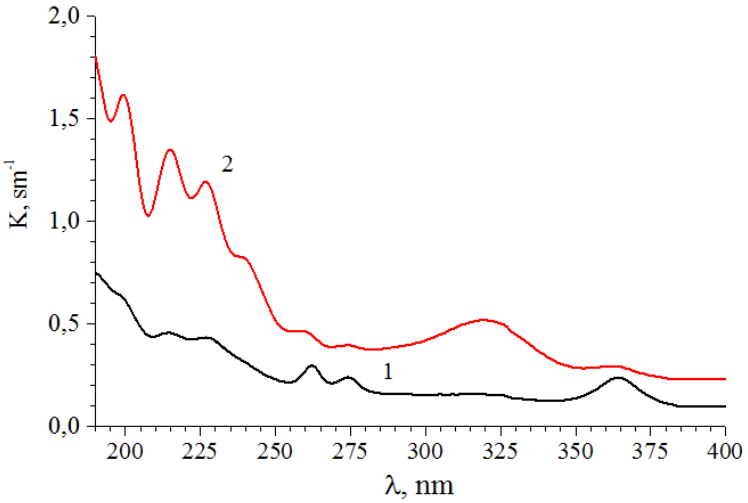

Figure 1. Optical absorption spectra of an unirradiated CaF_2–YbF_3 crystal in the UV region, 1) 5 mol % YbF_3, 2) 15 mol % YbF_3

2)

Of particular interest is the behavior of band F (~320 nm). At low Yb concentrations it appears only after γ-irradiation and is associated with radiation-induced lattice defects, then in the crystal with a content of 15 mol.% YbF_3 this band is already observed in the as-grown crystal. This indicates the stabilization of defect states owing to the high Yb concentration. It is assumed that band F is caused by Yb^{2+} ions associated with uncontrolled impurity centers or crystal lattice vacancies [4]. Moreover, an additional absorption band at around 199 nm, not previously described in the literature, was detected for the first time.

Thus, the results of the study show that an increase in the YbF_3 content to 15 mol.% leads to a substantial reorganization of the optical absorption spectra owing to the strengthening of inter-center interactions, the change in the local environment of Yb ions, and the formation of concentration-stabilized defect centers. In doing so, band F acquires a mixed nature, caused by both concentration-stabilized and radiation-induced defects.

The obtained results substantially expand the notions of the nature of the optical absorption bands in CaF_2–YbF_3 single crystals at high concentrations of ytterbium. For the first time, the features of the transformation of bands A_1 and F upon an increase in the YbF_3 content to 15 mol.% have been revealed, which makes it possible to more fully explain the influence of concentration-induced defects and the local environment of Yb ions on the shaping of the absorption spectra. The obtained data may serve as a basis for optimizing the composition of fluoride laser and luminescent materials.

References:

1. DeLoach L.D., Payne S.A., Chase L.L. *IEEE J. Quantum Electron.*, **29** (1993) 1179–1190.
2. Ito M., Goutaudier C., Lebbou K. et al. *J. Phys.: Condens. Matter*, **16** (2004) 1501–1521.
3. Nicoara I., Lighezan L., Enculescu M. et al. *Journal of Crystal Growth*, **310** (2008) 2026–2032.
4. Kaczmarek S.M., Tsuboi T., Ito M. et al. *J. Phys.: Condens. Matter*, **17** (2005) 3771–3786.
5. Ashurov M.Kh., Nuritdinov I., Boyboboeva S.T. *Physics of the Solid State*, **64** (2022) 1439–1443.

INFLUENCE OF LOW-ENERGY INERT GAS ION IMPLANTATION ON THE PROPERTIES OF $BaCe_{0.85}Nd_{0.15}O_{2.925}$

Khromushin I.V., Mirmanova D.S.
Institute of Nuclear Physics of the Atomic Energy Agency of the Republic of Kazakhstan, Almaty, Kazakhstan

Proton-conducting solid electrolytes with a perovskite structure are of significant interest as functional materials for solid oxide fuel cells, gas sensors, hydrogen pumps, and related applications. Most research in this field has been focused on the development of new compositions to enhance proton conductivity. Recently, studies have emerged indicating that ion implantation can influence the properties of such materials. Ion implantation enables modification of the material structure through defect formation without altering its chemical composition [1, 2].

In this work, the effect of implantation of inert gas ions (He, Ne, Ar, Kr) on the properties of the proton-conducting oxide $BaCe_{0.85}Nd_{0.15}O_{2.925}$, synthesized by the solid-state method (sintering at 1650 °C for 5 h), was investigated. The synthesized samples were annealed in air at 650 °C for 7 h and subsequently subjected to irradiation with inert gas ions. The ion energy was 20 keV/Z, and irradiation was performed to a fluence of 5×10^{16} см$^{-2}$. The studies were carried out using scanning electron microscopy (SEM) and thermal desorption spectroscopy.

According to SEM data, the nature of microstructural changes strongly depended on the mass of the implanted ions. After implantation with Ne and Ar ions, pronounced blistering was observed on the sample surfaces. In contrast, no such surface defects were detected in the case of Kr and He ion implantation. It should be noted that implantation with He ions led to an increase in the area of homogeneous regions and a densification of the surface structure.

Thermal desorption experiments showed that implantation of Ne, Ar, and Kr ions into doped barium cerate resulted in an increased O_2 yield and a noticeable decrease in H_2O yield. The latter can be explained by the influence of implantation-induced defects on the Nd^{3+}/Nd^{4+} ratio, since, as demonstrated in previous studies [2, 3], neodymium in barium cerate can exhibit mixed valence.

In contrast, implantation of He ions led to an increase in the yield of both O_2 and H_2O, which is attributed to the specific features of defect formation and the longer penetration range of He ions in the crystal lattice of barium cerate.

References:

1. Kim J.-H., Tsuchiya B., Nagata S., Shikama T. // *Solid State Ionics*. 2008. Vol. 179. P. 1182–1186.
2. Khromushin I.V., Yermolaev Yu.V., Kasmamytov N.K., Aksenova T.I., Tusseyev T., Stanbay L.A. // *Bulgarian Chemical Communications*. 2019. Vol. 51. P. 49–54.
3. Oishi M., Yashiro K., Mizusaki J., Kitamura N., Amezawa K., Kawada T., Uchimoto Y. // *Solid State Ionics*. 2008. Vol. 179. P. 529–535.

RADIATION-INDUCED REARRANGEMENT AND CRYOGENIC PRESERVATION OF HYDROXYL DEFECTS IN LiF:OH SINGLE CRYSTALS UNDER HIGH-ENERGY PULSED ELECTRON BEAM IRRADIATION

Mussaeva M.A., Nuritdinov I., Nurimbetov K.K.
Institute of Nuclear Physics, Uzbekistan Academy of Sciences, Tashkent, Uzbekistan

INTRODUCTION

Lithium fluoride (LiF) single crystals are widely used in photonics and radiation dosimetry due to their broad transparency window and effective accumulation of stable color centers at room temperature [1]. However, LiF crystals grown by directional crystallization contain unintentional hydroxyl impurities (OH^-) substituting for fluorine anions, which strongly influence the matrix radiation hardness and defect formation pathways.

Radiation-stimulated decomposition of impurity OH^- groups leads to the formation of U and U_1 centers [3], [5]. A U_1 center constitutes an interstitial hydrogen ion (H_i^-) localized at a regular interstitial site or stabilized near multivalent impurity cations like Mg^{2+}. The local high-frequency vibrations of such defects manifest in the IR absorption spectra within the 1900–2300 cm^{-1} domain. The accumulation kinetics of these centers under extreme fluences as a function of temperature remain poorly understood, especially in the intermediate cryogenic region (165–225 K) where the thermal diffusion of defects is partially frozen. This work establishes the correlation between the electron beam fluence and the defect locking temperature in LiF:OH single crystals.

MATERIALS AND METHODS

Plane-parallel polished LiF:OH plates (10×15 mm^2, thickness 1.0–1.4 mm, mean 1.2 mm) were prepared along the cleavage planes from bulk boules grown by the Kyropoulos method in air. Exposure was carried out using the "Electronica U-003" linear accelerator. The pulsed electron beam parameters were: mean energy E = 5 MeV, single pulse duration $\tau = 4 \times 10^{-6}$ s, repetition rate 250 Hz, and beam current density J = 400 nA/cm^2. The high energy ensured homogeneous through-volume dose absorption. The distance from the accelerator window to the sample was fixed at 48.5 cm. The crystals were irradiated up to cumulative fluences of φ = 10^{14}, 5×10^{14}, and 10^{15} cm^{-2}.

To analyze thermally activated kinetics, irradiation was executed at three fixed temperature regimes: room temperature (300 K), moderate cooling (225 K), and deep cryogenic cooling (165 K) maintained in a vacuum cryostat ($\pm$ 2 K). Low-temperature samples were warmed to 300 K at a heating rate of 2 K/min for spectral analysis of the stable, locked phases. IR transmittance spectra were registered at 300 K using an automated FSM-2201 FTIR spectrometer (370–7800 cm^{-1}, resolution 1 cm^{-1}). Mathematical data processing was performed using the OriginPro software suite.

RESULTS AND DISCUSSION

The pristine sample spectrum displays an absorption band near 2900 cm^{-1} (stretching vibrations of OH^- groups with hydrogen bonds) and a steep multi-phonon host lattice transmittance drop between 1800–1000 cm^{-1} [6]. Under electron irradiation up to 10^{14} cm^{-2} at 300 K, radiation-stimulated modification occurs: the 2900 cm^{-1} band drops from α = 0.87 to 0.05 cm^{-1}, while a broad U_1 band emerges at 1900–2200 cm^{-1} (α ≈ 0.28 cm^{-1}) [5]. At 5×10^{14} cm^{-2}, the U_1 band reaches its maximum intensity (α ≈ 0.56 cm^{-1}), whereas at a critical dose of 10^{15} cm^{-2}, ongoing electron impact destroys U_1 centers. The liberated hydrogen undergoes secondary recombination,

prompting a secondary strong absorption surge in the 2900 cm^{-1} region ($\alpha = 0.76\ cm^{-1}$ as a broadened profile of secondary defect aggregates).

Lowering the irradiation temperature to 225 K suppresses the direct modification path: at 10^{14} cm^{-2}, the 2900 cm^{-1} band preserves its high intensity ($\alpha = 0.71\ cm^{-1}$), and the U_1 band is absent. At 5×10^{14} cm^{-2}, the hydroxyl band collapses into a resonance peak at 2959.16 cm^{-1} ($\alpha = 1.93\ cm^{-1}$), while a discrete peak appears directly on the multi-phonon slope at 1750 cm^{-1} ($\alpha \approx 3.18\ cm^{-1}$). This indicates the formation of localized molecular-defect configurations with uniform hydrogen bonds. At 10^{15} cm^{-2}, this metastable phase breaks down. At deep cooling (165 K), a radiation preservation effect is discovered: up to 5×10^{14} cm^{-2}, the absorption spectrum remains identical to the pristine crystal due to the significant retardation of thermal diffusion. Only at 10^{15} cm^{-2} does vacancy accumulation cause the complexes to decompose into a featureless plateau.

Evaluations of energy transfer channels show that the Frenkel defect concentration from direct elastic collisions at 10^{15} cm^{-2} ($N_{disp} \sim 2.4 \times 10^{15}\ cm^{-3}$) is far below the OH^- concentration, ruling out the impact displacement mechanism. Thermal spike modeling showed a local temperature rise of only $\Delta T \approx 4$ K, refuting local melting. Thus, the primary mechanism is the non-radiative decay of self-trapped excitons (STEs) induced by intensive inelastic ionization losses [4, 7]. The relative change in the 2900 cm^{-1} band at $\varphi = 10^{14}\ cm^{-2}$ analyzed via an Arrhenius dependence yielded an effective activation energy of $E_a \approx 0.205$ eV, which aligns with the migration energy of H centers in LiF [2, 8]. At 300 K, thermal energy is sufficient to overcome this barrier and stabilize U_1 centers, whereas at 165 K, diffusion is frozen, causing immediate geminate recombination.

CONCLUSIONS

1) It has been verified that the fundamental multi-phonon IR absorption edge of the LiF matrix (1000–1800 cm^{-1}) is invariant to pulsed electron irradiation, pointing to the structural stability of the host framework.

2) Pulsed electron irradiation at 300 K triggers the decay of OH^- complexes at $\varphi = 10^{14}\ cm^{-2}$, generating stable interstitial U_1 centers ($\sim 2000\ cm^{-1}$), which decompose at $10^{15}\ cm^{-2}$ into complex hydroxyl-vacancy aggregates [2].

3) Cooling to 225 K slows down direct impurity modification, shifting the pathway toward a dose-resonant restructuring phase at 5×10^{14} cm^{-2} with a resonance peak at 2959.16 cm^{-1} and a discrete mode at 1750 cm^{-1}.

4) Deep cryogenic cooling to 165 K locks the impurity sublattice into a radiation-hard state by significantly retarding thermal diffusion, ensuring instantaneous geminate recombination of defects.

5) The estimated effective activation energy ($E_a \approx 0.205$ eV) aligns with the migration energy of H centers [8], confirming the controlling role of host lattice defect diffusion in the radiation stabilization of IR-active bonds.

Acknowledgments. The researchis supported by basic funding allocated to the Institute of Nuclear Physics of the Academy of Sciences of the Republic of Uzbekistan by the decree PP-4526.

References:

1. T.G. Stoebe, S. Watanabe, Phys. Status Solidi A 102 (1987) 11–42.
2. A.T. Akilbekov, E.A. Kotomin, S.A. Chernov, J. Appl. Phys. 78 (1995) 4501–4505.
3. F. Kerkhoff, Z. Physik 158 (1960) 595–606.
4. Ch.B. Lushchik, A.Ch. Lushchik, Decay of Electronic Excitations, Nauka, 1989.
5. S.P. Morato, L.C. Courrol, L.V.E. Caldas, Phys. Rev. B 44 (1991) 9211–9215.
6. J.R. Jasperse, A. Kahan, L.N. Plendl, S.S. Mitra, Phys. Rev. 146 (1966) 526–542.

7. R.T. Williams, K.S. Song, J. Phys. Chem. Solids 51 (1990) 679–716.
8. V.E. Puchin, E.A. Kotomin, A.L. Shluger, Phys. Status Solidi B 165 (1991) 115–123.

CHANGES IN THE ELECTROPHYSICAL PROPERTIES OF RHODIUM-DOPED SILICON UNDER γ-IRRADIATION

Rafikov A.K., Makhmudov Sh.A., Sulaymonov A.A.
Institute of Nuclear Physics, Uzbekistan Academy of Sciences, Tashkent, Uzbekistan

Under irradiation, particularly by γ-quanta, vacancies, interstitial atoms, and electrically active complexes involving these defects are formed in the silicon crystal lattice, resulting in changes in the charge-carrier concentration and recombination kinetics [1–3]. As a result, charge-carrier compensation in n-type silicon is enhanced, leading to an increase in electrical resistivity. The intensity of these processes depends on the nature of technological defects and impurity centers in the crystal.

One of the methods for enhancing the radiation resistance of silicon is doping it with metal impurities that form deep energy levels in the band gap. For this purpose, transition metals such as Ni, Cu, Au, Pt, Ir, and Rh can be used. However, these impurities differ significantly in their diffusion coefficients in silicon, electrical activity, solubility, and mechanisms of interaction with radiation-induced defects [4]. For example, Ni and Cu diffuse relatively rapidly in silicon and, at high concentrations, may form regions with a spatially nonuniform impurity distribution. Deep levels associated with Au and Pt, in turn, can act as efficient recombination centers and substantially reduce the lifetime of nonequilibrium charge carriers. Therefore, it would be inappropriate to regard any of these metal impurities as universally superior under all conditions; the choice of impurity also depends on the objective of the study and the technological regime employed.

The main reason for selecting Rh in this study is its ability to simultaneously form deep acceptor and donor centers in silicon. Rh-related levels at (E_C-0,32) eV and (E_C -0,53) eV have been reported in the literature [3, 4]. The presence of these levels makes it possible to control the charge-carrier concentration and the position of the Fermi level in Si through the compensation mechanism [4]. In addition, during diffusion doping, Rh atoms form [V–Rh] and [I–Rh] complexes with vacancies and interstitial silicon atoms, respectively. The rearrangement or dissociation of these complexes under irradiation may affect the electrical activity of radiation-induced defects and the kinetics of charge-carrier loss. The advantage of Rh for the present study lies not only in its ability to form deep levels, but also in the possibility of systematically investigating, within a single system, the processes of compensation, complex formation with defects, and the subsequent transformation of these complexes under irradiation.

The aim of this work is to determine the regularities of the relative change in electrical resistivity of Rh-doped n-Si samples cooled under different regimes as a function of γ-irradiation dose and to compare the obtained results with those for as-received and thermally treated n-Si samples.

Monocrystalline n-type silicon samples grown by the Czochralski method were used as the objects of investigation. The electrical resistivity of the samples was $\rho \approx 15$ Ω·cm, the oxygen concentration was $N_o \approx 2 \cdot 10^{17}$ cm^{-3}, and the dislocation density was $(0.2–2) \cdot 10^4$ cm^{-2}. Rhodium metal with a purity of 99.9% was deposited onto the silicon surface using a VUP-4 vacuum

deposition system, followed by thermal diffusion in a furnace at 1330 °C for 10 h. For comparative analysis, four sample conditions were prepared: as-received n-Si<P> (1); a thermal control sample without Rh subjected to the same high-temperature cycle (2); an Rh-doped sample subjected to slow cooling (3); and an Rh-doped sample subjected to rapid cooling (4). The thermal control sample was used to distinguish the effect of Rh from that of the high-temperature treatment. The samples were irradiated with ^{60}Co γ-rays at a dose rate of ~71 R/s. The diffusion coefficient of Rh in silicon (Eq. 1), the rhodium concentration (Eq. 2), and the impurity penetration depth (Eq. 3) were calculated using the following relationships [3, 4]:

$$D = D_0 \cdot \exp\left(-\frac{E_{diff.}}{kT}\right), \text{ cm}^2/\text{s (1)}, \quad N = N_0 \cdot \exp\left(-\frac{Q}{kT}\right), \text{ cm}^{-3} \text{ (2)}, \quad L = 2\sqrt{Dt} \cdot 10^{-6}, \text{ mkm (3)}$$

Where $D_0 = 1{,}6 \cdot 10^{-2}$ cm^2/s – is the pre-exponential factor, $E_{diff.} = 1{,}2 \pm 0{,}5$ eV – is the activation energy for rhodium diffusion, k – Boltzmann constant. At a diffusion temperature of T = 1330 °C the diffusion coefficient was $D = 3 \cdot 10^{-6}$ cm^2/s. The activation energy was $Q = 1{,}6 \pm 0{,}2$ eV, $N_0 = 2 \cdot 10^{21}$ c m^{-3} – is the initial rhodium concentration at the silicon surface. The calculated rhodium concentration was $N = 2{,}16 \cdot 10^{16}$ cm^{-3}. The calculated Rh penetration depth reached 6587 μm.

After the thermal cycle, the electrical resistivity increased from 17.6 to 52.9 Ω·cm. In the Rh-doped samples, the resistivity increased to 136 Ω·cm after slow cooling and to 165 Ω·cm after rapid cooling. Compared with the thermal control sample, Rh doping resulted in an additional increase in resistivity by factors of 1.57 and 2.12 for slow and rapid cooling, respectively. Thus, the increase in the initial electrical resistivity is attributed not to a pronounced decrease in charge-carrier mobility in the crystal lattice, but predominantly to carrier compensation associated with Rh and defects formed during thermal treatment. (To obtain more detailed information on the structural changes induced by Rh incorporation and thermal treatment, additional TEM and SEM investigations would be appropriate.) Rh incorporation and the cooling regime significantly modify the initial electrophysical parameters of silicon: under rapid cooling, the electron concentration n decreases, whereas the electrical resistivity ρ increases. However, the available calculated dose dependences do not provide sufficient evidence that Rh incorporation enhances the electrophysical stability of silicon against γ-irradiation or that a statistically significant difference exists between rapid and slow cooling regimes. As a scientific novelty, it may be demonstrated that the structural stabilizing effect of Rh and the radiation-induced degradation of electrical conductivity are not identical processes.

Under γ-irradiation, an increase in electrical resistivity and a decrease in charge-carrier concentration were observed in the samples (Fig. 1).

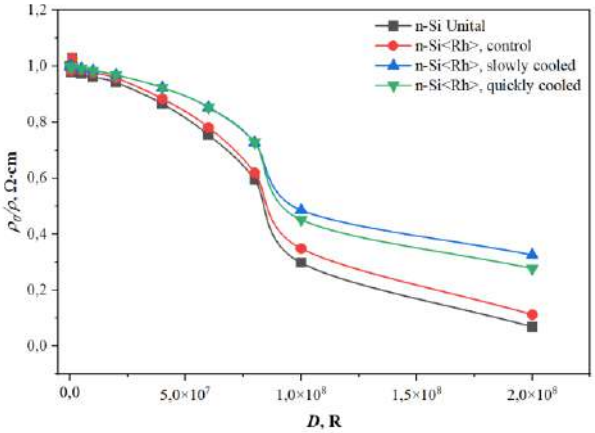

Figure 1. Dependence of the relative electrical resistivity on the γ-irradiation dose.

A comparative assessment of the effect of γ-irradiation on the electrophysical properties of as-received, thermally treated, and Rh-doped KEF-15 monocrystalline n-type silicon was performed. With increasing γ-irradiation dose, the ρ_0/ρ ratio decreased in all samples, corresponding to an increase in electrical resistivity and a decrease in charge-carrier concentration, while the carrier mobility changed relatively weakly. For the calculated extrapolation to a dose of $2\cdot10^8$ R, the ρ_0/ρ values for the rapidly and slowly cooled Rh-doped samples were 0.194 and 0.180 respectively. Thus, the ρ_0/ρ ratio in the rapidly cooled sample was 7.8% higher, indicating better retention of normalized electrical conductivity compared with the slowly cooled sample. At the same time, the obtained results do not yet provide sufficient evidence to conclude unambiguously that Rh doping improves the overall radiation resistance of silicon.

References:

1. Pintilie I., Fretwurst E., Lindström G., Stahl J. Results on defects induced by ^{60}Co gamma irradiation in standard and oxygen-enriched silicon // *Nuclear Instruments and Methods in Physics Research Section A*. 2003, 514, 18–24. DOI: 10.1016/j.nima.2003.08.079.
2. Liao C. et al. Investigation of high resistivity p-type FZ silicon diodes after 60Co γ-irradiation //Nuclear Instruments and Methods in Physics Research Section A: Accelerators, Spectrometers, Detectors and Associated Equipment. – 2024. – T. 1061. – C. 169103.
3. Yunusov, M.S., Karimov, M., & Zhalelov, M.A. (1997). The rate of current carrier removal under the action of gamma radiation in compensated n-type silicon. *Uzbek Physics Journal*, (1), 41-45. (in Russian)
4. Yunusov, M.S. (1981). The nature of deep impurity centers created by platinum group atoms in silicon. In V.I. Fistul (Ed.), *Deep levels in semiconductors* (pp. 45–51). Tashkent: TashSU. (in Russian)

CRYSTAL PHASE TRANSFORMATIONS IN As-Se-PET FILM HOLOGRAPHIC GRATING UNDER EXPOSURE TO 5 MeV ELECTRON BEAM

Ibragimova E.M., Temirbayeva I.N., Madaminov B.
Institute of Nuclear Physics, Uzbekistan Academy of Sciences, Tashkent, Uzbekistan

Holographic grating allows writing 3D image of static and dynamic object and is applied for nuclear particle track detection [1]. Electron lithography is widely used for making nano-relief on the photosensitive surface on glass substrate [2,3]. This work was aimed at studying structure-phase transformations in As-Se-PET films exposed to 5 MeV electrons. The holographic films were made by the techniques described in [4]. We recently observed tiny tracks of 5 MeV electrons on the As-Se film surface with scanning probe microscope and periodical structure in optical absorption spectra at nanoscale [5]. In this research we used the U-003 linear electron accelerator with the parameters: 5 MeV electron beam at current density 400 nA/cm^2, current pulse 4 μs, beam width 3 cm and scan 30 cm. Doses 2.5×10^{14} cm^{-2} (100 s) and 5×10^{14}cm^{-2} (200 s) at 290 K were chosen so as electron tracks are not overlapped.

IR-spectra were registered at 300 K at FTIR-spectrometer (Thermo Scientific Nicolet iS50) in transmittance mode (Fig.1 a, b). Periodic weak structure of IR transmittance occurs in the E_g window 4000-2000 cm^{-1} and attributes to As-Se film with a scribed holographic grating (A). While PET substrate is responsible for separate intensive peaks at 3370, 2700-3000, 1850 cm^{-1} and the valent band top at 1600 cm^{-1} (B).

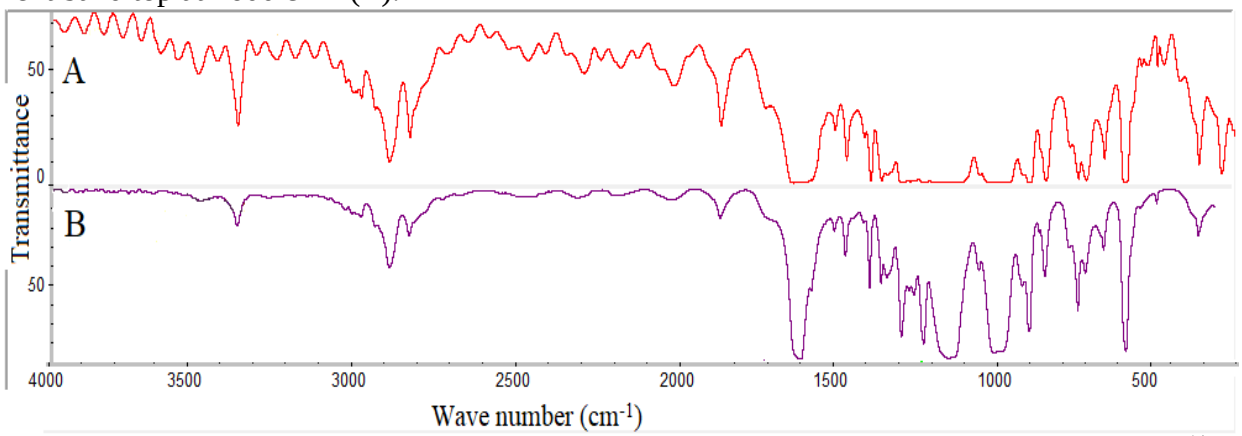

Figure 1. Infrared transmittance (%): (A)- As-Se-PET film after exposure to 5 MeV electrons during 200 s (5×10^{14} cm^{-2}) and (B)- PET substrate.

Crystal structure-phase analysis was done at diffractometer XRD (Goniometer: MiniFlex 600, X-Ray generator Cu Kα-tube λ= 0.154178 nm at applied voltage 40 kV, current 15-35 mA, absolute scan 5-120 grad, 2θ angular resolution is Kα1 line width 0.015 grad) in reflection mode. Figure 2 presents XRD spectra (registered at 300 K) of the film both pristine reference and irradiated at 290 K to the indicated fluencies. The analysis of crystal structure and phase composition was done with the use of FullProf code: As_2Se_3 monoclinic (C2/m) ID mp-1078443, As-Se monoclinic ($P2_1/c$) ID mp-542570 (**15°**), As trigonal (R3m) ID-mp-11, and PET-$C_{13}H_{24}O_3S$ triclinic (the most intensive peak **27°**) from data base PDF-2016.

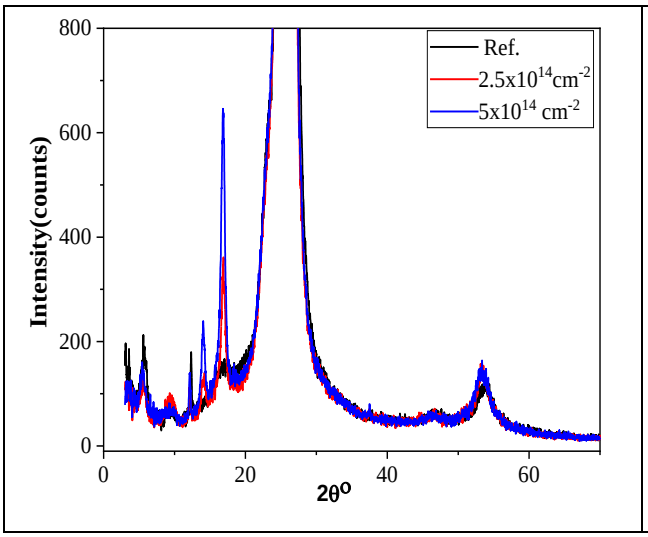

Crystal phase, Symmetry,	Lattice param meters	Reference Non-irra-diated	100 sec 2.5×10^{14} cm^{-2}	200 sec 5×10^{14} cm^{-2}
$C_{13}H_{24}O_3S$ PET substrate Triclinic (α=β=γ=90.000)	a	11.39513	12.01006	11.97192
	b	21.11163	21.51076	21.62190
	c	23.64087	22.28407	22.48246
Phase amount	%	96	55.9	69
As_2Se_3 Monoclinic(C2/m) (α=γ=90.000; β=109.1)	a	4.17551	4.28543	4.20331
	b	9.65223	9.90631	9.71648
	c	12.46828	12.79649	12.55126
Phase amount	%	3	44	30
AsSe Monoclinic ($P2_1/c$) (α=γ=90.000; β=95)	a	13.10906	13.53738	13.09683
	b	3.65720	3.77670	3.65379
	c	9.12830	9.42656	9.11978
Phase amount	%	0.6	0.1	1

Figure 2. X-ray diffraction spectra (left) and table of structure parameters and phase compositions (right) of the reference sample and those exposed to the indicated doses.

The table shows that the triclinic crystal phase of poly(ethylene terephthalate) amount is the largest due to 50 μm thickness, and a few μm thick As_2Se_3 film of monoclinic symmetry contributes only

3%. But after electron irradiation this film crystallizes up to 44%, while the amount of another AsSe phase decreases in 6 times. The next dose results in some decreasing of As_2Se_3. The lattice parameters *a,b,c* increase after the irradiation due to defects.

Reference:

1. Yu. N. Denisyuk's Ideas in the Development of Holographic Methods of Obtaining and Projection of Images. Technical Physics, 2017. Vol. 62(10), pp. 1449–1455
2. Ampere Tseng, Kuan Chen, C.D. Chen, Ma Kung Jeng. Electron beam lithography in nanoscale fabrication: recent development. IEEE Transcations on electronics packaging manufacturing. 2003. Vol. 26(2), pp.141-149. 10.1109/TEPM.2003.817714
3. M. Rommel, K.E. Hoffmann, T. Reindl, J. Weis. Benchmark test of Monte-Carlo simulation for high resolution electron beam lithography. Microelectronic Engineering. 2012. Vol. 98, pp. 202-205. 10.1016/j.mee.2012.07.032
4. M.F. Churbanov, V. Plotnichenko, all Influence of As2S3 stoichiometry on the opical transmission of glass in the spectral range 5-8 μm. Reports of the Russian Academy of Sciences on Chemistry and Materials Science. Report of the Russian Academy of Sciences. 2023. Vol 511, pp. 37-41.
5. I.N. Temirbayeva, E.M. Ibragimova. Effect of 5 MeV electrons on the periodic nanostructure of As-Se film on polymer. Interactions. 2026. Vol. 247, pp.165. 10.1007/s10751-026-02471-4

PROCESSES OCCURRING IN THE SUPERCONDUCTING LAYER OF HIGH-TEMPERATURE SUPERCONDUCTING YBCO TAPES IRRADIATED WITH 5 MEV ELECTRONS

Mussaeva M. A., Shodiev A. A.
Institute of Nuclear Physics, Uzbekistan of the Academy of Sciences, Tashkent, Uzbekistan.

Introduction. High-temperature superconducting (HTS) YBCO tapes are critical components in modern power engineering, fusion devices, and high-field magnetic systems. Radiation irradiation is widely recognized as an effective approach for introducing artificial pinning centers to enhance critical current density (J_c). While elastic collisions under low-fluence electron irradiation cannot fully account for the observed macroscopic properties [1], understanding the role of inelastic electronic energy loss is vital for optimizing HTS performance under radiation environments [2].

Objective. This work aims to identify and substantiate the underlying physical mechanisms responsible for radiation-induced defect formation in multilayer 2G YBCO tapes subjected to 5 MeV electron irradiation.

Methodology. Second-generation (2G) HTS YBCO coated conductors (SuperOx) were irradiated with 5 MeV electrons using a U-003 accelerator under a fluence of 10^{15} e/cm^2. Structural, phase, and morphological modifications were systematically characterized using X-ray diffraction (XRD) and atomic force microscopy (AFM). Magnetotransport and electrical properties were evaluated via Hall effect measurements. A theoretical interpretation of the localized energy dissipation was performed using the classical two-temperature model (TTM) to separate electron and lattice subsystem kinetics.

Results. Theoretical TTM calculations revealed that despite low primary ionization losses (dE/dx) for 5 MeV electrons, strong electron-phonon coupling combined with the low thermal conductivity of the oxide matrix leads to severe local energy accumulation. Local peak temperatures within the track area reach 1200–1800 K, exceeding the thermodynamic stability threshold of YBCO. This localized thermal spike triggers oxygen atom displacement and subsequent vacancy formation, reducing orthorhombic lattice stability. Consequently, XRD tracking confirmed local decomposition into simpler oxide phases Y_2O_3, CuO, $YCuO_2$ and $YBa_2Cu_3O_{6.94}$ along with metallic Cu nanophases. Electrical measurements revealed a unique phenomenon: a notable decrease in resistivity occurred in a narrow temperature window near T_c, while the critical temperature (T_c) itself remained stable. This effect is attributed to the radiation-induced "micro-excitation" of metallic Cu nanophases and modified grain boundaries, creating parallel, low-resistance pathways for current transport.

Conclusion. The study demonstrates that 5 MeV electron irradiation modifies YBCO tapes via inelastic thermal spike mechanisms rather than purely elastic displacement. The retention of critical temperature (T_c) alongside the reduction of near-transition resistance proves that radiation-induced nanophases and intergranular boundaries can be strategically optimized, offering a controlled pathway for material modification in radiation-resistant superconducting technologies.

The researches are supported by basic funding allocated to the Institute of Nuclear Physics of the Academy of Sciences of the Republic of Uzbekistan by the decree PP-4526.

References:

1. Oen O. S. Oak Ridge National Lab., Tenn. (USA), 1973, №. ORNL-4897
2. M. Toulemonde, et.al. Nuclear Instruments and Methods in Physics Research Section B: Beam Interactions with Materials and Atoms. 2000, Vol. 166, pp.903–912.

POLARON MASS IN THE MERCURY FAMILY OF HIGH TEMPERATURE SUPERCONDUCTORS

Otajonov S.M.[1], Saburova G.G.[1], Alibekova Sh.B.[1], Otajanov A.M.[1], Kurmantayev A.N.[2,3], Karimov Z.I.[4], Dzhumanov S.[5], Yavidov B.Ya.[1]

[1]Nukus State Pedagogical Institute, Nukus, Uzbekistan
Shymkent University, Shymkent, Kazakhstan
[3]Ahmed Yasawi Kazakh-Turkish International University, Turkestan, Kazakhstan
[4]Center of Nanotechnology Development of the NUU, Tashkent, Uzbekistan
Institute of Nuclear Physics, Uzbekistan of the Academy of Sciences, Tashkent, Uzbekistan

One of the important issues in cuprate high-T_c superconductivity is the effective mass of the charge carrier. It enters transport, optical, magnetic and superconducting properties. In strongly anisotropic layered materials, the carrier mass can be different for motion within the CuO_2 planes and along the *c*-axis. Experimental studies have shown that the effective mass may remain nearly constant in some doping intervals and become strongly enhanced in others [1-3].

The aim of the present paper is to study the doping dependence of the charge carrier mass simultaneously in Hg-1201, Hg-1212 and Hg-1223 within the same preformed-pair framework. We approximately associate the superconducting critical temperature with the BEC temperature of

intersite bipolarons and calculate the 3D and in-plane polaron masses using experimental information on T_c, carrier concentration, lattice parameters and anisotropy. In this way, the present study continues our previous studies of LSCO and YBCO [4,5].

Using the early reported methodology, the 3D and in-plane polaron masses were calculated over the superconducting region of each compound. Figure 1(a) shows the resulting m_p/m_e curves. The general behavior is similar for the three Hg compounds. The mass is large near the underdoped boundary, decreases inside the superconducting region and rises again toward the overdoped boundary. For clarity, Fig.1(a) is shown only in the range $0 \le m_p/m_e \le 50$. Therefore, when a curve reaches the upper edge of the figure close to a superconducting boundary, this does not indicate termination of the solution. The calculated masses continue to increase beyond the displayed range. Near optimal doping, the calculated 3D masses are approximately $m_p(Hg1201) \sim 10.2m_e$, $m_p(Hg1212) \sim 12.4m_e$ and $m_p(Hg1223) \sim 12.5m_e$. Thus, the 3D masses near optimum vary only moderately across the Hg family even though $T_{c,max}$ increases from 97K to 135K. Within the present model, this means that the increase of T_c cannot be understood simply as a reduction of the carrier mass. The bipolaron concentration also contributes through $m_p(\delta) = 3.31\hbar^2 n_b^{\frac{2}{3}}(\delta)/2k_B T_c(\delta)$.

In contrast to the 3D mass, the behavior of $m_{p,ab}$ is strongly affected by the mass anisotropy, Fig.1(b) . This is particularly important for Hg-1223 because its anisotropy is much larger than those used for Hg1201 and Hg-1212. Near optimal doping, the calculated values are approximately $m_{p,ab}(Hg1201) \sim 1.9m_e$, $m_{p,ab}(Hg1212) \sim 1.9m_e$ and $m_{p,ab}(Hg1223) \sim 0.89m_e$. As in the 3D case, the calculated in-plane masses also increase strongly near the superconducting boundaries. Since m_p formally diverges when $T_c \to 0$ and the anisotropy remains finite at the corresponding finite oxygen contents, $m_{p,ab}$ also becomes very large. The relatively low in-plane mass obtained for Hg-1223 is due to its large mass anisotropy. Therefore, a comparatively large 3D mass can coexist with a much smaller in-plane carrier mass. The calculations show both common and different features among the three compounds. The common feature is the strong increase of the calculated polaron masses when the superconducting boundaries are approached. This behavior originates mainly from the decrease of T_c. Near optimal doping, the 3D masses lie within a relatively narrow range of about $(10 \div 13)m_e$. The in-plane masses, however, show a stronger difference because of anisotropy. In particular, the larger anisotropy of Hg-1223 gives a smaller $m_{p,ab}$. It is important not to compare the three curves at the same numerical value of δ as if this represented the same planar hole concentration in all three systems.

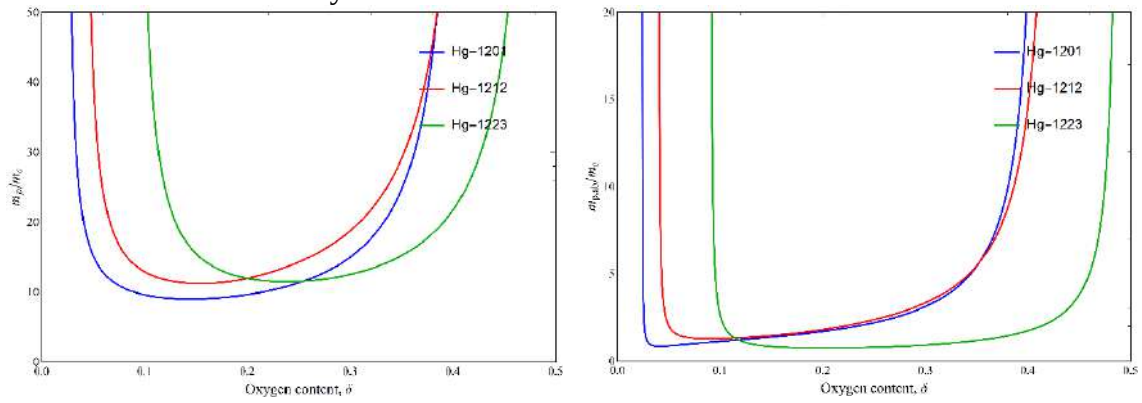

(a) *(b)*

Figure 1. Calculated polaron masses m_p/m_e (a) and $m_{p,ab}/m_e$ (b) as a function of oxygen content for Hg-1201, Hg-1212 and Hg-1223.

Hg-1201, Hg-1212 and Hg-1223 use different experimentally motivated oxygen-hole relations. The purpose of Fig.1 is therefore to show the doping evolution of each compound on its own oxygen scale and to compare the general tendencies within one figure. The results also continue the trends found in our previous LSCO and YBCO calculations. In LSCO, the inclusion of the crystal anisotropy was important for obtaining realistic in-plane mass values [4]. In YBCO, the doping-dependent anisotropy changed the behavior of the in-plane mass relative to the three-dimensional one [5]. The present Hg calculation shows again that the 3D carrier mass alone is not sufficient to characterize the charge dynamics of layered cuprates. The calculated in-plane masses are of the same order as the available experimental estimates for optimally doped Hg cuprates [6]. Together with our previous LSCO and YBCO results, the present calculations indicate that the preformed-pair approach provides a simple framework for studying the relation between superconducting transition temperature, carrier density, effective mass and crystal anisotropy in different cuprate families.

References:

1. W.J. Padilla et al., Phys. Rev. B 72 (2005) 060511
2. A. Legros et al., Phys. Rev. B 106 (2022) 195110
3. B.J. Ramshaw et al., Science 348 (2015) 317
4. S.M. Otajonov et al., Physica B 695 (2024) 416589
5. S.M. Otajonov et al., Physica B 727 (2026) 418383
6. R. Puźniak, Physica C 282--287 (1997) 1459.

FIRST-PRINCIPLES STUDY OF THE EFFECT OF HYDROSTATIC PRESSURE ON THE FERMI ENERGY AND SEEBECK COEFFICIENT OF La_2CuO_4

Kabulov I.Sh.[1], Karimbaev E.Kh.[1,2]

[1]*Institute of Fundamental and Applied Research, National Research University "TIIAME", Tashkent, Uzbekistan*

[2]*Institute of Nuclear Physics, Uzbekistan Academy of Sciences, Tashkent, Uzbekistan*

La_2CuO_4 (LCO) is the parent compound of the $La_{2-x}Sr_xCuO_4$ high-T_c superconducting family and represents a strongly correlated Mott insulator [1,2]. Owing to its layered crystal structure, the electronic properties of LCO are highly sensitive to external pressure, making hydrostatic pressure an effective tool for modifying its electronic structure and transport characteristics [2,3]. In this work, the influence of hydrostatic pressure on the Fermi energy and Seebeck coefficient of LCO was investigated using the DFT+U method implemented in the Quantum ESPRESSO package [4-6]. The calculations were performed within the PBE-GGA approximation using ultrasoft pseudopotentials. Convergence tests yielded optimal computational parameters of an energy cutoff of 80 Ry, an 8×8×4 Monkhorst–Pack k-point mesh, and a Hubbard parameter of U = 12 eV, which successfully reproduced the Mott insulating state with an energy band gap of approximately 1.8 eV. Hydrostatic pressure in the range of 1–10 GPa was then applied to evaluate pressure-induced modifications of the electronic structure and thermoelectric response.

The calculated results show that the Fermi energy increases monotonically with increasing hydrostatic pressure (Figure 1). The observed increase originates from lattice compression, which enhances the hybridization between Cu 3d and O 2p orbitals and shifts the electronic states toward higher energies. This behavior demonstrates that hydrostatic pressure effectively modifies the electronic structure and consequently influences the transport properties of LCO [2,3].

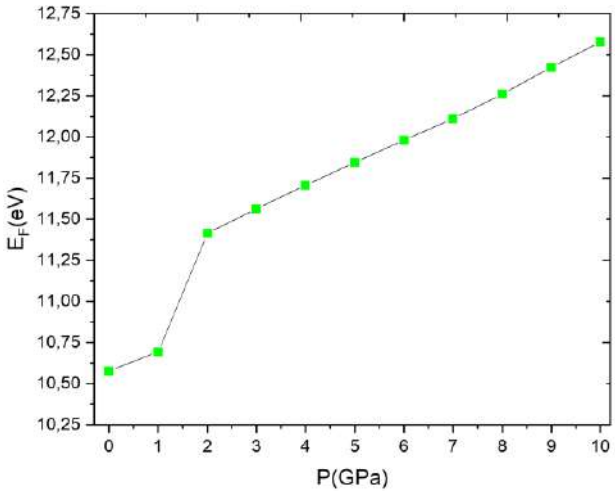

Figure 1. Pressure dependence of the Fermi energy of La_2CuO_4.

To evaluate the thermoelectric response, the pressure-dependent Fermi energy was introduced into the simplified Mott relation [7,8]

$$S(P,T)=\frac{\pi^2 k_B^2 T}{3eE_F(P)}.$$

where S is the Seebeck coefficient, T is the absolute temperature, and E_F is the pressure-dependent Fermi energy. According to this expression, an increase in the Fermi energy leads to a reduction in the Seebeck coefficient.

The calculated Seebeck coefficients at 290, 295, and 300 K are presented in Figure 2.

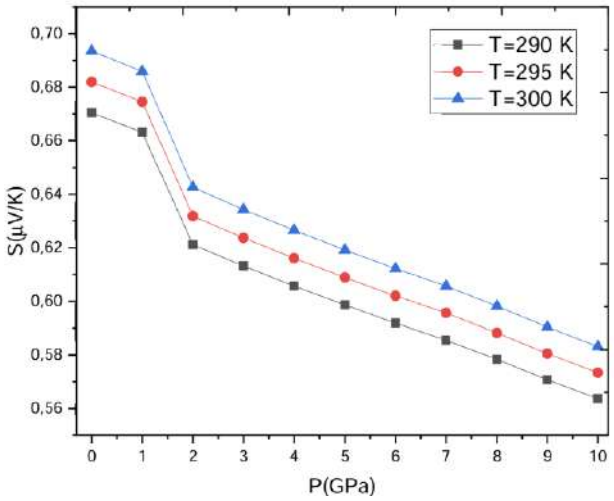

Figure 2. Pressure dependence of the Seebeck coefficient of La_2CuO_4.

For all investigated temperatures, the Seebeck coefficient decreases continuously with increasing hydrostatic pressure, while a slight increase is observed with increasing temperature. These results indicate that hydrostatic pressure modifies the thermoelectric response primarily

through pressure-induced changes in the electronic structure. The relationship obtained in this work can be summarized as

$$P \rightarrow E_F(P) \rightarrow S(P,T)$$

Thus, hydrostatic pressure first changes the electronic structure of LCO and subsequently determines its thermoelectric behavior.

The obtained results demonstrate that hydrostatic pressure is an efficient parameter for tuning the electronic and thermoelectric properties of LCO. The established correlation between pressure, Fermi energy, and Seebeck coefficient provides a theoretical basis for understanding transport phenomena in strongly correlated cuprates [2,7] and may be extended to other layered oxide materials.

References:

1. J.G. Bednorz, K.A. Müller. *Z. Phys. B Condens. Matter*, **64**, 189–193 (1986).
2. B. Keimer, S.A. Kivelson, M.R. Norman, S. Uchida, J. Zaanen. *Nature*, **518**, 179–186 (2015).
3. M.T. Czyzyk, G.A. Sawatzky. *Phys. Rev. B*, **49**, 14211–14228 (1994).
4. M. Calamiotou et al. *J. Phys. Chem. Solids*, **134**, 127–132 (2019).
5. P. Giannozzi et al. *J. Phys.: Condens. Matter*, **29**, 465901 (2017).
6. J.P. Perdew, K. Burke, M. Ernzerhof. *Phys. Rev. Lett.*, **77**, 3865–3868 (1996).
7. R.M. Martin. *Electronic Structure: Basic Theory and Practical Methods*, Cambridge University Press (2020).
8. H.J. Goldsmid. *Introduction to Thermoelectricity*, Springer (2010).

THE ROLE OF PHASE TRANSFORMATIONS IN ZIRCONIUM DIOXIDE CAUSED BY STABILIZING DOPANTS IN RESTRAINING DISORDER PROCESSES UNDER HEAVY-ION IRRADIATION

Kozlovskiy A.L.[1,2], Kenzhina I.E.[1,3]
[1]*Institute of Nuclear Physics, Almaty, Kazakhstan*
[2]*L.N.Gumilyov Eurasian National University, Astana, Kazakhstan*
[3]*Satbayev University, Almaty, Kazakhstan*

The use of zirconium dioxide-based ceramics as materials for nuclear power plants is one of the most promising areas, addressing the need to improve resistance to radiation-induced softening and high-temperature degradation during operation. Growing interest in this class of ceramics is driven by the need to develop ceramic materials capable of maintaining their physical, mechanical, thermal, and structural properties during operation under extreme conditions, including exposure to high temperatures, intense radiation, and mechanical loads. Moreover, one of the key challenges in the operation of ceramic materials is their gradual degradation caused by ion or neutron irradiation. This degradation is associated with the accumulation of radiation-induced defects and localized structural distortions, which is accompanied by a loss of mechanical strength, crack resistance, and destruction of damaged layers. High temperatures are an additional factor, as they can accelerate diffusion processes, promote grain growth, redistribution of defects, and the development of phase transformations. This paper presents the results of comprehensive studies, including determining the role of phase transformations associated with the structural polymorphism of zirconium dioxide,

which occurs as a result of intense mechanical stress or radiation exposure, as well as establishing the role of stabilizing dopants in inhibiting degradation processes in zirconium dioxide under high-dose heavy-ion irradiation. This research focuses on the radiation-induced structural and phase changes that occur during heavy-ion irradiation. The interaction of high-energy ions with the crystal lattice is accompanied by energy transfer to the electronic and nuclear subsystems of the material, leading to the formation of cascades of atomic displacements, point defects, vacancies, interstitial atoms, and their complexes. As the irradiation dose increases, the concentration of radiation-induced defects increases, which can be accompanied by localized structural disordering, increased internal stresses, changes in unit cell parameters, and the initiation of phase transformations. Particular attention is paid to high-dose irradiation, under which radiation defect accumulation processes can become nonlinear. Under such conditions, defect accumulation, migration, recombination, and partial annihilation compete. The relationship between these mechanisms largely determines the final degree of structural degradation and the preservation of the performance characteristics of zirconium ceramics.

These findings can be used to optimize the composition and structural-phase state of zirconium ceramics, as well as to develop new radiation-resistant materials designed for long-term operation under conditions of elevated temperatures, mechanical loads, and intense radiation exposure typical of modern and future nuclear power plants.

EFFECT OF γ-IRRADIATION ON THE ULTRAVIOLET PHOTOLUMINESCENCE OF CaF_2:SrF_2:YbF_3 SOLID-SOLUTION CRYSTALS AND NANOCERAMICS

Boyboboeva S.T., Nuritdinov I., Ashurov M.Kh.
Institute of Nuclear Physics, Uzbekistan Academy of Sciences, Tashkent, Uzbekistan

Fluoride materials based on CaF_2 doped with ytterbium ions have attracted considerable attention for applications in optoelectronics, laser technology, and scintillation detectors owing to their low phonon energy, high optical transparency, and high luminescence quantum efficiency [1,2]. Ultraviolet photoluminescence in these materials originates from the $4f^{14} \rightarrow 4f^{13}5d$ electronic transitions of Yb^{2+} ions, which are highly sensitive to the local crystal field and the defect structure of the host lattice [3,4]. Although CaF_2:YbF_3, crystals have been extensively investigated, the effect of γ-irradiation on the photoluminescence properties of CaF_2:SrF_2:YbF_3 solid solutions, particularly in a comparative study of single crystals and nanoceramics, has received limited attention. Therefore, the aim of the present work was to comparatively investigate the effect of γ-irradiation on the ultraviolet photoluminescence of single crystals and nanoceramics based on CaF_2:SrF_2:YbF_3 solid solutions.

The photoluminescence of CaF_2:SrF_2:YbF_3 solid-solution single crystals and nanoceramics was investigated at room temperature. Upon excitation in the 230–240 nm spectral region, a broad emission band extending from 200 to 450 nm was observed. This emission arises from the superposition of several components associated with different types of Yb-related luminescence centers. The dominant contribution to the emission spectrum originates from isolated Yb^{2+} centers (≈290–320 nm), Yb^{2+} centers with a distorted local coordination environment (≈320–380 nm), and Yb^{2+}–Yb^{3+} paired centers (≈400–430 nm) [4].

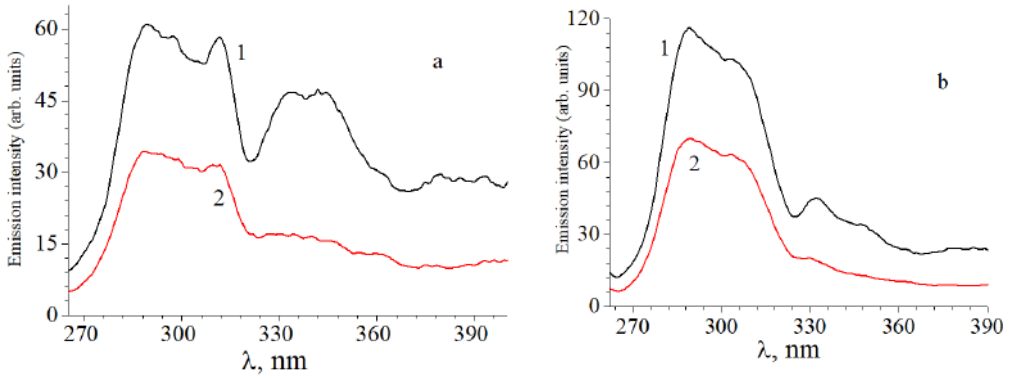

Figure 1. Photoluminescence spectra of the unirradiated CaF_2:SrF_2:YbF_3 crystal (1) and ceramic (2) measured at room temperature under excitation at 230 nm (a) and 242 nm (b).

Comparative analysis revealed that the spectral positions of the luminescence bands in the single crystals and nanoceramics are nearly identical, indicating a common origin of the emitting centers. However, the luminescence intensity of the nanoceramic samples is significantly lower, particularly in the 330–360 nm spectral range. This reduction is attributed to the extensive network of grain boundaries, the higher concentration of structural defects, and the enhanced probability of nonradiative relaxation processes [3]. Comparison with the CaF_2:YbF_3 system indicates that the incorporation of Sr^{2+} ions modifies the lattice parameter and the local crystal field, resulting in a shift of the excitation bands and a redistribution of the luminescence intensity [5]. In CaF_2–SrF_2:YbF_3 solid solutions, concentration quenching is reduced due to the more homogeneous distribution of Yb^{3+} ions and the lower probability of Yb-related cluster formation [3].

Following γ-irradiation at a dose of 10^5 rad (1 kGy), a decrease in the intensity of all photoluminescence bands was observed, while their spectral positions remained essentially unchanged (Fig. 2). The relative reduction in luminescence intensity was considerably more pronounced in the single crystals than in the nanoceramic samples. This behavior can be attributed to the initially more ordered crystal structure of the single crystals, which is more susceptible to the formation of radiation-induced defects. In contrast, the nanoceramics already possess a high concentration of intrinsic structural defects, resulting in substantial nonradiative relaxation even before irradiation. The observed decrease in photoluminescence intensity is associated with the formation of radiation-induced defects, including F-centers, fluorine vacancies, charge traps, and local lattice distortions. These defects introduce additional nonradiative recombination pathways, thereby reducing the luminescence quantum yield.

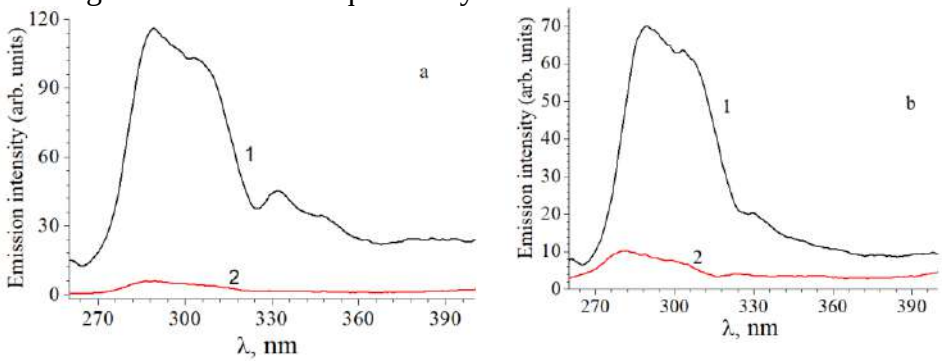

Figure 2. Photoluminescence spectra of crystalline (a) and ceramic (b) samples of CaF_2:SrF_2:YbF_3, measured at room temperature under excitation at 242 nm: (1) before γ-irradiation and (2) after γ-irradiation at a dose of 10^5 rad.

The obtained results demonstrate that the ultraviolet photoluminescence of CaF_2:SrF_2:YbF_3 solid solutions is governed by the contributions of different Yb^{2+} luminescence centers and is strongly influenced by the material's microstructure. The incorporation of SrF_2 was found to suppress concentration quenching of luminescence, whereas γ-irradiation promotes the formation of radiation-induced defects that introduce additional nonradiative relaxation pathways. Furthermore, the CaF_2:SrF_2:YbF_3 solid solutions exhibit greater resistance to radiation-induced luminescence quenching than CaF_2:YbF_3 crystals. These findings provide valuable insight into the radiation response of ytterbium-doped fluoride materials and may facilitate the development of radiation-resistant ultraviolet phosphors, laser materials, and scintillators.

References:

1. Henderson B., Imbusch G.F. Optical Spectroscopy of Inorganic Solids. Oxford, 2006.
2. Payne S. A., Smith L. K. *et al.* IEEE Journal of Quantum Electronics, 30 (1),1994.
3. Dorenbos P. 5d-level energies of lanthanides in inorganic compounds. J. Lumin..91. 2000.
4. B. Moine, B. Courtois, and C. Pedrini. Journal de Physique 50,1989.

Ashurov, M. Kh., et al. In: *Application of Nanoscale Systems in Modern Semiconductor Microelectronics and Photovoltaics*: Proceedings of the Scientific Conference, Andijan, Uzbekistan, 2025.

INFLUENCE OF ELECTRON IRRADIATION ON THE RECOVERY TIME OF REVERSE RESISTANCE OF DIODE STRUCTURES BASED ON n-Si DEPENDING ON THE PHOSPHORUS CONTENT IN THE SINGLE CRYSTAL

Erdonov M.N.[1], Makhkamov Sh.[1], Tashmetov M.Yu.[1], Ismatov N.B.[1], Kholmedov Kh.M.[2], Sobirov S.S.[3]

[1]*Institute of Nuclear Physics, Uzbekistan Academy of Sciences, Tashkent, Uzbekistan*
[2]*Tashkent Al-Khwarizmi University of Information Technologies, Tashkent, Uzbekistan*
[3]*Fergana State Technical University, Fergana, Uzbekistan*

It is known that the performance of silicon diodes can be changed by creating defect centers that form deep energy levels in the forbidden zone of the crystal. These levels, being recombination centers, significantly influence the electrophysical properties and allow one to control the performance of silicon products. The introduction of such centers can be achieved by doping the crystal with impurities or by irradiation with high-energy nuclear particles.

The aim of this work is to study the possibility of controlling the performance of p^+-n-n^+ diode structures made of n-type silicon with different phosphorus content in the base crystal by exposure to electron irradiation.

The study of the response time of silicon diodes was carried out by measuring the recovery time of the reverse resistance (τ_v) of diffusion p^+-n-n^+ structures irradiated with electrons with an energy of 2 MeV at the U-003 accelerator, in the fluence range from 10^{13} to 10^{15} cm^{-2}. The concentration of phosphorus in n-Si in the manufactured diodes varied from $8 \cdot 10^{13}$ to $3 \cdot 10^{15}$ cm^{-3}, the thickness of the p^+-layer in the diffusion diodes was $\simeq 60$ μm.

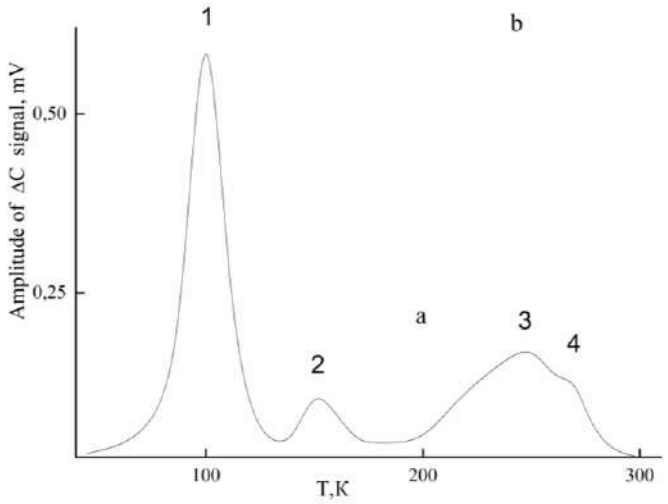

Figure 1. DLTS spectrum of n-Si diffused diodes irradiated with electrons with a fluence of 10^{16} cm^{-2} (a). The location of the RD levels in the band gap of n-Si (b); 1 – E_c-0.17 eV, 2 – E_c-0.23 eV, 3 – E_c-0.39 eV, 4 – E_c-0.44 eV

The location energy and concentration of deep radiation defect (RD) centers were determined by capacitance spectroscopy (DLTS). Analysis of the DLTS spectra of the samples showed that upon electron irradiation, four RD centers are formed in the forbidden band of n-Si, located in the upper half of the forbidden band of the base crystal, with ionization energies of E_c-0.17 eV, E_c-0.23 eV, E_c-0.39 eV and E_c-0.44 eV (Fig. 1).

From Figure 1 it can be seen that the highest concentration of the recombination RD center corresponds to a level with an energy of E_c-0.17 eV, the concentration of which increases with increasing electron irradiation fluence. All detected RD centers exhibit acceptor properties, which leads to partial compensation of current carriers and a decrease in the recovery time of the reverse resistance τ_v in diffusion p^+-n-n^+ structures. A comparison of the τ_v value of diodes with different phosphorus concentrations in n-Si, irradiated with electrons at the same fluence of ~10^{15} cm^{-2}, showed that an increase in the phosphorus concentration in the base crystal leads to a decrease in the efficiency of changing τ_v (Fig. 2, curves 1-3).

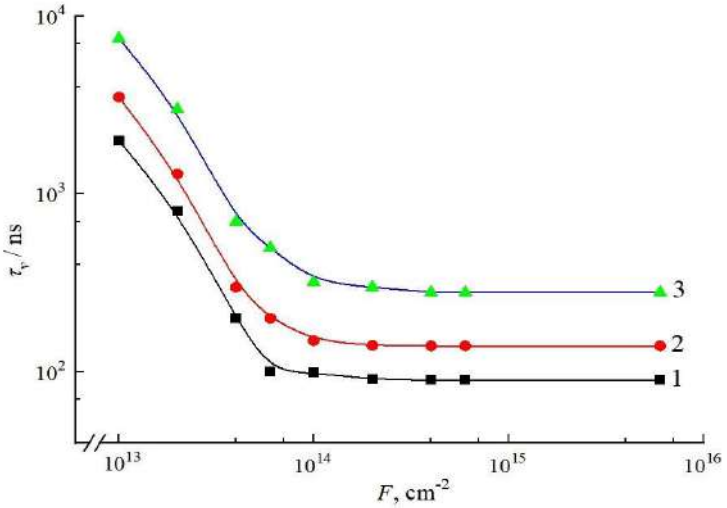

Figure 2. Dependence of τ_v on the electron irradiation fluence in n-Si with different phosphorus concentrations N_e cm^{-3}: 1 – $8 \cdot 10^{14}$, 2 – $1.5 \cdot 10^{15}$, 3 – $3 \cdot 10^{15}$

It was found that the change in τ_v is inversely proportional to the concentration of the introduced recombination RD center and is determined mainly by the RD center with a level of E_c-0.17 eV and a carrier capture cross-section $\sigma_p \approx 4 \cdot 10^{-14}$ cm^{-2}, which is two orders of magnitude greater than the value of σ_p of other RD centers. It was determined that the RD center with the E_c-0.17 eV level corresponds to the vacancy-oxygen complex and maintains thermal stability in the temperature range of 280 - 320 °C depending on the phosphorus concentration in the base crystal.

Thus, by adjusting the concentration of phosphorus (N_e) in the base crystal and the dose of electron irradiation, it is possible to achieve the optimal concentration of RD (N_p), which allows obtaining diodes with τ_v up to 75 ns. It was found that in order to increase the response time of diffusion diodes under electron irradiation with an energy of 2 MeV, the condition $N_e/N_p \approx 3$ must be met. It has been determined that in p^+-n-n^+ diffusion silicon structures, a decrease in the ratio $N_e/N_p < 3$ does not allow achieving an optimal reduction in τ_v, whereas an increase in the ratio $N_e/N_p > 3$ leads to a change in the values of the direct reverse current and forward voltage of the diodes.

Based on the obtained results on the change in τ_v depending on the phosphorus concentration in n-Si under electron irradiation, it was established that the response time of diffusion diodes can be increased by two orders of magnitude by selecting the ratio of the phosphorus impurity concentration and the concentration of introduced radiation defects in silicon p^+-n-n^+ structures.

STUDY OF RADIATION RESISTANCE OF ZIRCONIUM-CONTAINING CERAMICS UNDER IRRADIATION WITH HEAVY IONS

Tynyshbayeva K.M.[1], Kozlovskiy A.L.[1,2], Kenzhina I.E.[2,3]
[1]*L.N.Gumilyov Eurasian National University, Astana, Kazakhstan*
[2]*Institute of Nuclear Physics, Almaty, Kazakhstan*
[3]*Satbayev University, Almaty, Kazakhstan*

As part of the research, work was conducted to assess the influence of temperature factors on changes in the structural parameters of the studied ceramics depending on the composition of the modifying dopant and the phase composition during heavy-ion irradiation, simulating radiation damage to nuclear fuel fission fragments. It was determined that changes in phase composition due to phase transformations associated with cationic substitution during zirconium dioxide doping are one of the main factors inhibiting degradation processes caused by irradiation and the temperature effects of irradiation. It was established that polymorphic transformations arising from the addition of zirconium dioxide and yttrium oxide, associated with the dominance of the cubic phase in the ceramics, lead to inhibition of degradation processes caused by heavy-ion irradiation. The slowdown in structural degradation processes for stabilized ceramics, as opposed to monoclinic (unmodified) ceramics, is due to structural compaction resulting from polymorphic transformations associated with the rearrangement of the crystalline structure.

The main mechanisms of destruction of the near-surface layer of composite ceramics are determined, including the formation of defect clusters, local disordering of the crystalline structure, the development of microcracks, the formation of regions of increased residual stress, and the partial

amorphization of individual sections of the material. It is established that the intensity of these processes increases with increasing irradiation fluence; however, the nature of their development is largely determined by the phase composition and structural features of the studied ceramics. It is shown that phase transformations occurring during irradiation are one of the key factors in curbing the spread of radiation-induced damage.

EFFECT OF GAMMA-IRRADIATION TEMPERATURE ON THE FORMATION OF COLOR CENTERS IN LSO:Ce SCINTILLATION SINGLE CRYSTALS ADDITIONALLY DOPED WITH CALCIUM (Ca) IONS

Islamov A.Kh.[1], Ibragimova E.M.[1], Kudratov Kh.N.[2], Khayitov I.A.[3]
[1]*Institute of Nuclear Physics, Uzbekistan Academy of Sciences, Tashkent, Uzbekistan*
[2]*Scientific and Technical Centre for Radiation and Nuclear Safety, Tashkent, Uzbekistan*
[3]*International Agriculture University, Tashkent, Uzbekistan*

It is known [1] that adding a certain concentration of Ca^{2+} ions to LSO:Ce scintillation single crystals leads to a decrease in the scintillation decay time and an increase in the light yield, as well as to an improvement in energy resolution. Achieving high scintillation characteristics in LSO:Ce:Ca gives this material significant potential as a fast radiation detector for medical imaging, especially in PET, SPECT, and CT. It should be noted that the literature lacks sufficient data on the relationship between color centers and the activator luminescence yield. As we have shown previously in [2], with an increase in the irradiation temperature from 330 K to 500 K, the activator luminescence yield in the recombination process decreased significantly. In the present work, results are presented to reveal the effect of color centers on the activator luminescence yield in LSO:Ce single crystals additionally doped with Ca ions. In this connection, the optical absorption (OA) spectra of LSO:Ce (0.1 at.%) scintillation crystals additionally doped with Ca^{2+} at a concentration of 0.4 at.% were studied after irradiation with ^{60}Co gamma-quanta of energies 1.17 and 1.33 MeV at a dose rate of 0.7 Gy/s in the temperature range from 300 to 500 K.

After γ-irradiation at a temperature of 310 K, in contrast to the samples without Ca ions, LSO:Ce with increasing Ca ion concentration visually showed an enhancement of the violet coloration of the samples (see Photos 1 and 2). However, within ~1 hour at a temperature of 305 K, this coloration disappears completely, indicating its instability — 0.4 at.% Ca^{2+} forms only temporary color centers.



Photo 1. LSO:Ce (0.1 at.%) crystal after gamma-irradiation at 310 K



Photo 2. LSO:Ce (0.1 at.%), Ca (0.4 at.%) crystal after gamma-irradiation at 310 K

In contrast to the samples without Ca, in the sample with Ca (0.4 at.%), as the irradiation temperature increases, a yellow coloration is visually observed (see Photo 4), and the OA band in the (400 ÷ 440) nm region becomes more clearly pronounced in the spectrum (Fig. 1, curve 1). With increasing holding time at 305 K, a decrease in the intensity of the 425 nm OA band is observed: 2 hours (curve 2), 4 hours (curve 3), and 24 hours (curve 4); after 50 hours the spectrum is restored to its initial state (curve 5, Fig. 1) through a diffusion process.



Photo 3. LSO:Ce (0.1 at.%) crystal after irradiation with a dose of 675 Gy at 470 K



Photo 4. LSO:Ce (0.1 at.%), Ca (0.4 at.%) crystal after irradiation with a dose of 370 Gy at 400 K

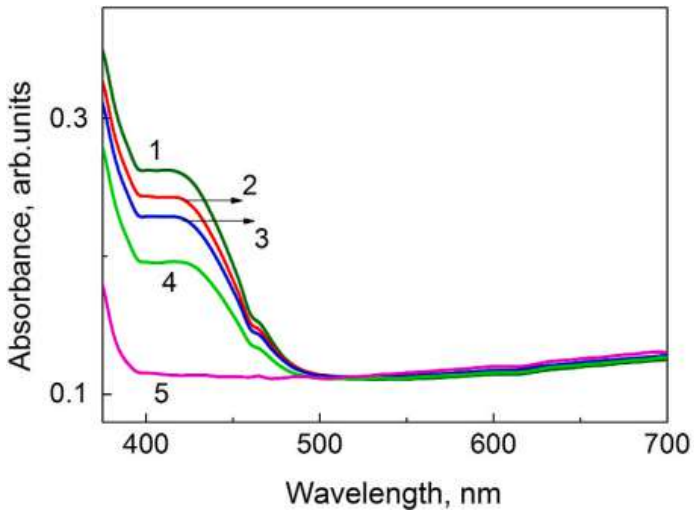

Figure 1. Absorption spectra in the visible region of an LSO:Ce (0.1 at.%) crystal with 0.4 at.% Ca, after irradiation with ^{60}Co gamma-quanta at a dose of 370 Gy at 423 K (1) and after holding outside the gamma field at 305 K for 2 hours (2), 4 h (3), 24 h (4), and 50 h (5)

Further, to isolate the effect of gamma-quanta or temperature on the appearance of the yellow coloration and the OA band at 425 nm in samples with Ca (0.4 at.%), the following experiments were carried out: LSO:Ce samples without Ca and with 0.1 at.% Ca, 0.2 at.% Ca, 0.3 at.% Ca, and 0.4 at.% Ca were *(a)* annealed at 500 K for 30 min in air; *(b)* pre-irradiated with a gamma dose of 10^3 Gy and then annealed at 400 K (30 min). In both cases *(a and b)*, neither the yellow coloration nor the OA band at 425 nm was observed. In this regard, it can be assumed that the appearance of the 425 nm OA band and the yellow coloration (see Photo 4) only in LSO:Ce,Ca (0.4 at.%) is associated with the combined effect of ^{60}Co γ-quanta and thermally activated processes. Thus, at temperatures ≥330 K, the quenching of the activator luminescence yield in the recombination process in LSO:Ce single crystals additionally doped with Ca ions is related to the predominance of the reabsorption process of the color center in the (400 ÷ 440) nm region, which overlaps the

scintillation luminescence in LSO:Ce crystals due to the thermal broadening of the absorption and luminescence bands.

References:

1. K. Yang, C.L. Melcher, M.A. Koschan, M. Zhuravleva, Effect of Ca Co-doping on the luminescence centers in LSO:Ce single crystals, IEEE Trans. Nucl. Sci. 58 (3), P. 1394 (2011).
2. A.Kh. Islamov, E.M. Ibragimova, Kh.N. Kudratov, *et al.*, Effect of Ca co-doping on gamma-stimulated luminescence of Lu_2SiO_5:Ce // Optical Materials. – V. 154. – id. 115699 (2024).

CHANGES IN THE STRUCTURAL-MORPHOLOGICAL CHARACTERISTICS AND VIBRATIONAL SPECTRA OF THERMOPLASTIC POLYMERS UNDER ELECTRON IRRADIATION

Tashmetov M.Yu., Ismatov N.B.
Institute of Nuclear Physics, Uzbekistan of the Academy of Sciences, Tashkent, Uzbekistan

At present, thermoplastic polymers are widely used as structural, packaging, and insulating materials [1]. One of the most effective methods for targeted modification of their properties is treatment with ionizing radiation, which causes cross-linking of macromolecules, chain scission, changes in the degree of crystallinity, and surface morphology [1]. Of particular interest for radiation materials science are low-density polyethylene (LDPE), a polyketone containing carbonyl groups, and the copolymer of ethylene with tetrafluoroethylene (ETFE) [2].

In this work, a comprehensive study of the influence of accelerated electrons with an energy of ~2 MeV in the fluence range from $1\cdot10^{15}$ to $3\cdot10^{16}$ cm^{-2} on the structural-morphological and spectral characteristics of three polymers was carried out using X-ray diffraction analysis, atomic force microscopy, and Raman spectroscopy. Low-density polyethylene, polyketone, and the copolymer of ethylene with tetrafluoroethylene were selected as the objects of study.

X-ray diffraction analysis showed that electron irradiation up to a fluence of $3\cdot10^{16}$ cm^{-2} does not change the crystal structure of the polymers, while LDPE and polyketone retain the orthorhombic lattice (space group Pnam), and ETFE retains the triclinic structure (space group P-1). The unit-cell parameters undergo only minor changes, indicating the stability of the crystal lattice under electron irradiation. The dependence of the degree of crystallinity on the electron fluence, presented in Fig. 1, is non-monotonic in nature and is determined by the chemical structure of the polymer chain.

At low electron irradiation fluences, an increase in the crystallinity of polyketone is observed (Fig. 1), which is followed by saturation and a subsequent gradual decrease as the fluence increases to $3\cdot10^{16}$ cm^{-2}. LDPE also exhibits an initial increase in crystallinity, however, with a further increase in electron fluence, its crystallinity decreases. The most pronounced decrease in crystallinity was established for ETFE, for which, after an initial increase from 20.8 to 25.9% at a fluence of $1\cdot10^{16}$ cm^{-2}, it decreases to 22.4% at $3\cdot10^{16}$ cm^{-2} which is due to the high sensitivity of its crystallites to degradation. Electron irradiation leads to smoothing of the surface of polyketone and LDPE. For polyketone, the arithmetic mean deviation of the profile (R_a) decreases from 54.7 to 23.8 nm, while the maximum height of profile irregularities (R_{max}) decreases from 285.3 to 210.9 nm at an electron fluence of $3\cdot10^{16}$ cm^{-2}. For LDPE, the R_a parameter decreases by 34.6%, while the R_{max}

parameter decreases by 42.2%. Unlike polyketone, the decrease in roughness of LDPE is more uniform in nature and is not accompanied by a threshold effect.

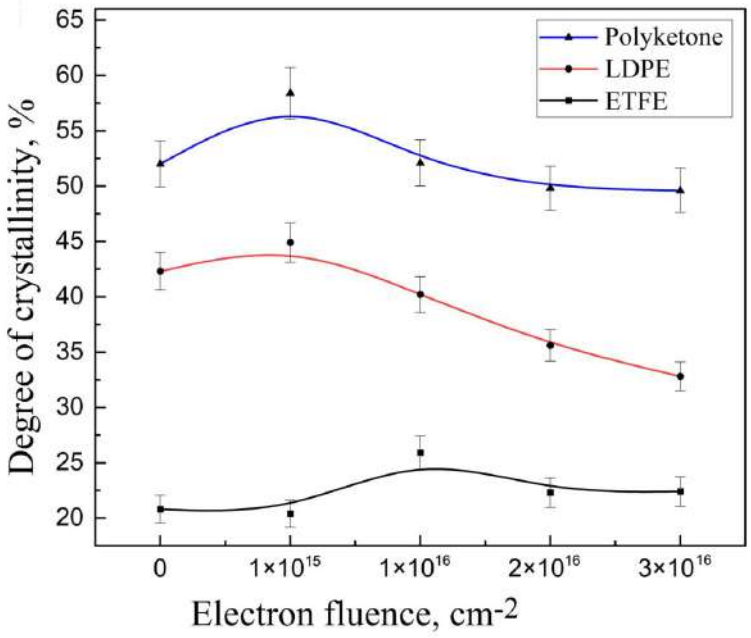

Figure 1. Dependence of the degree of crystallinity of thermoplastic polymers on electron fluence.

Raman spectroscopy data revealed structural changes at the molecular level, complementing the results of X-ray diffraction analysis. In the Raman spectrum of polyketone in the range of 1000-3200 cm^{-1}, characteristic bands are observed, caused by stretching and deformation vibrations of C-C, C=O bonds, as well as CH_2 and CH_3 groups. According to the literature data [3], the components in the region of 1380-1455 cm^{-1} have different phase assignments. Based on this, an analysis of the Gaussian components of the carbonyl band at 1708 cm^{-1}, which is sensitive to molecular disordering in polyketone, was carried out. The ratios of the integrated intensities of the crystalline components to the amorphous component and the ratio I_{1708}/I_{1711} reach a maximum at an electron fluence of $1 \cdot 10^{15}$ cm^{-2}, accompanied by narrowing of the bands, which indicates structuring. With further irradiation, the parameters return to their initial values, while the band widths increase, indicating an increase in structural inhomogeneity. In the spectra of irradiated LDPE at an electron fluence of $1 \cdot 10^{16}$ cm^{-2}, bands appear at ~1672 cm^{-1} (C=C) and ~1720 cm^{-1} (C=O), indicating the formation of unsaturated and carbonyl groups. In the ETFE spectra at an electron fluence of $2 \cdot 10^{16}$ cm^{-2}, additional bands appear at ~1688 cm^{-1} (C=C) and ~1766 cm^{-1} (C=O), indicating the onset of destructive processes.

Thus, the nature of radiation-induced changes is determined by the chemical structure of the polymer chain. The most pronounced two-stage evolution was revealed for LDPE, whereas ETFE exhibits the lowest sensitivity to irradiation up to an electron fluence of $1 \cdot 10^{16}$ cm^{-2}, while polyketone occupies an intermediate position. The established correlations between the data of X-ray diffraction analysis, atomic force microscopy, and Raman spectroscopy provide a basis for predicting the radiation resistance of thermoplastic polymers and optimizing their irradiation conditions.

References:

1. D. Manas, M. Ovsik, A. Mizera, M. Manas, L. Hylova, M. Bednarik, M. Stanek. The effect of irradiation on mechanical and thermal properties of selected types of polymers// Polymers, 10(2), (2018) 158.
2. M. Sabet, H. Soleimani. The impact of electron beam irradiation on Low-density polyethylene and Ethylene vinyl acetate// IOP Conference Series: Materials Science and Engineering, 204 (2017), 012005.
3. J.M. Lagaron, A.K. Powell, N.S. Davidson. Characterization of the structure and crystalline polymorphism present in aliphatic polyketones by raman spectroscopy//Macromolecules, Vol.33, 2000, pp.1030-1035.

STUDY OF THE MECHANISMS OF FORMATION OF RADIATION DAMAGE IN LITHIUM-CONTAINING CERAMICS Li_2TiO_3-Li_2ZrO_3 UNDER IRRADIATION WITH He^{2+} IONS AND PROTONS

Khametova A.[1,2]

[1]*Institute of Nuclear Physics, Agency of the Republic of Kazakhstan for Atomic Energy, Almaty, Kazakhstan*

[2]*L.N.Gumilyov Eurasian National University, Astana, Kazakhstan*

The mechanisms of radiation damage in lithium-based ceramics Li_2TiO_3-Li_2ZrO_3 were studied under high-temperature irradiation with helium ions and protons using SRIM Pro 2013 simulation software. The study focused on the correlation between defect distribution in the material and energy dissipation mechanisms. This work is relevant given the potential use of the studied materials for tritium breeding in fusion reactors.

The results of the study demonstrated the dependence of the penetration depth and defect distribution in the material structure on the energy and type of incident particles. For example, irradiation with He^{2+} ions at low energies leads to the formation of a highly localized damaged layer ~300–500 nm thick. He accumulates in the structure, leading to the formation of gas-filled bubbles, the accumulation of point defects, and defect clusters. With proton irradiation, increasing the initial energy significantly increases the penetration depth, and ionization losses sharply increase before the particle stops, forming a distinct Bragg peak. Nuclear losses, however, are an order of magnitude lower, indicating the dominance of ionization braking.

The results of the study provide an opportunity to improve the characteristics of lithium-containing ceramics that are resistant to external factors, such as radiation exposure and high temperatures encountered in fusion reactors.

Acknowledgments

This research was funded by the Science Committee of the Ministry of Science and Higher Education of the Republic of Kazakhstan (No. BR28712757).

SYNTHESIS OF CARBON NANOSTRUCTURED MATERIALS USING GAMMA RADIATION

Sadikov I.I.[1], Ibragimova E.M.[1], Malikov Sh.R.[1], Yuldashev M.B[1]. Amanov O.O.[1], Ashrapov U.T.[1], Dolgopolov M.V.[2]

[1]*Institute of Nuclear Physics, Uzbekistan Academy of Sciences, Tashkent, Uzbekistan*

[2]*Samara State Technical University, Samara, Russian Federation*

Currently, carbon nanostructured materials such as graphene and submicron carbon tubes have a wide range of applications in the fields of photonics, microelectronics and nanomotor systems due to their large specific surface area, high mechanical strength, chemical stability and unique electrical properties.

Like single-layer graphene, bilayer graphene, and graphene containing multiple layers, multilayer graphene (MLG), sometimes called ultrathin graphite, is also attracting considerable attention from research groups. Multilayer graphene is virtually equal in electrical and thermal properties to single-layer graphene, making it a promising material for future electronics. However, producing graphene nanosheets is a complex and expensive process.

In recent years, irradiation methods [1], which can be either non-ionizing or ionizing, have become a promising method for producing multilayer graphene. Non-ionizing irradiation methods include microwave, laser, infrared, and ultraviolet radiation. Ionizing radiation includes X-rays and gamma rays, of which gamma rays have the highest energy.

This paper presents information on a method for synthesizing multilayer graphene obtained by irradiating carbon-containing targets (obtained using magnetron sputtering) with gamma rays of the isotope Co60, with an average energy of 1 MeV. It is shown that irradiating the targets with an absorbed dose of 4 kGy produces multilayer graphene sheets larger than 100 μm on the target surface. Transmission electron microscopy studies revealed that the resulting multilayer graphene samples have 25 layers or more.

A comparison of the obtained radiation method for synthesizing multilayer graphene with other methods for producing graphene using gamma and X-ray radiation showed some advantages of the developed methods, the main advantage being the absence of the need to use graphene oxide to obtain graphene, which eliminates the need for concentrated acids and oxidizing agents. After synthesizing the multilayer graphene, the graphene-coated targets were ultrasonically treated to separate the synthesized multilayer graphene sheets from the substrate. The aqueous solution containing the multilayer graphenes was subsequently subjected to repeated gamma irradiation in the dry channel of the deactivated WWR-SM reactor.

Electron microscopy and Raman spectrometer measurements were used to study the synthesized nanostructured carbon materials.

Figures 1 and 2 show images of graphene structures obtained by gamma irradiation of a dielectric target with a 100 nm thick carbon coating. The images were obtained using a Carl Zeiss EVO® MA10 electron microscope at an accelerating voltage of 10 kV.

The images show that the multilayer graphene sheets are beginning to curl, leading to the hypothesis that further irradiation of the graphene sheets with gamma rays with energies exceeding 1 MeV may result in the formation of submicron carbon tubes. Studies of graphene samples irradiated with high-energy gamma rays showed that carbon microtubes do indeed form during irradiation (Figure 3).

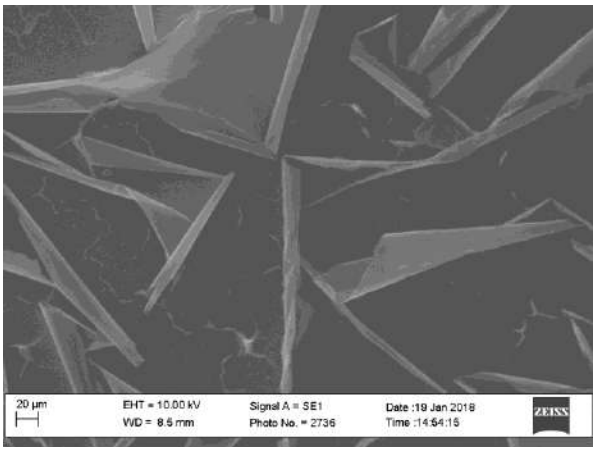

Figure 1.

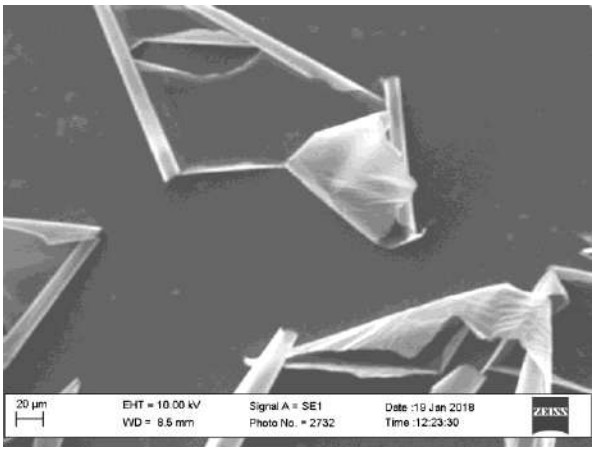

Figure 2.

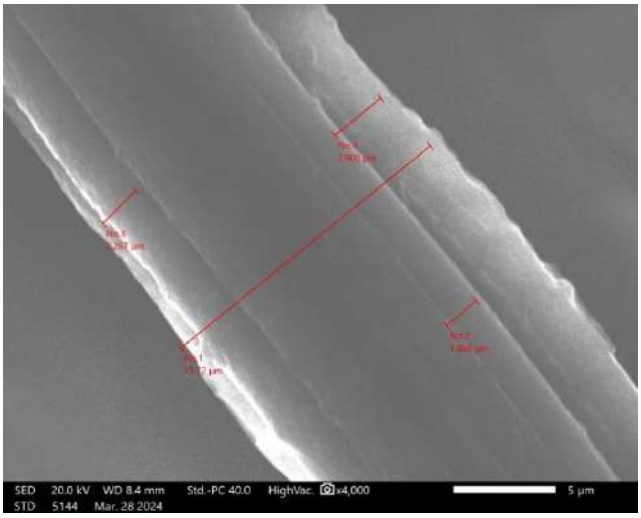

Figure 3.

The synthesized submicron carbon tubes have diameters ranging from 10 to 25 microns and lengths exceeding 300 microns.

Thus, the experiments confirmed the feasibility of synthesizing nanostructured carbon materials under gamma radiation.

References:

1. A.Ansón-Casaos a,∗, J.A.Puértolas b, F.J.Pascual b,c, J.Hernández-Ferrer a, P.Castell d, A.M.Benito a, W.K.Maser a, M.T.Martínez /The effect of gamma-irradiation on few-layered graphene materials //Applied Surface Science 301 (2014) 264–272.

POLYMORPHISM IN THE SiO2 IMPURITY PHASE OF A SILICON SINGLE CRYSTAL

Kalanov M.U., Sadikov I.I., Malikov Sh.R., Korakhodjaev A.A.
Institute of Nuclear Phtsics, Uzbekistan Academy of Sciencts, Tashkent, Uzbekistan

Oxygen atoms in silicon are the main background impurity that determines the thermal stability of the charge carrier lifetime and the formation of microdefects by impurities. These effects are directly related to the form of oxygen in a silicon single crystal. It has now been firmly established that oxygen in the bulk of silicon can be in a free and bound state: in the form of separate dissolved Si-O- Si quasi-molecules and in the form of particles of the second phase SiO2(c), crystalline silicon dioxide. In the near-surface layer of silicon, oxygen is also chemically bound with silicon atoms in the composition of the stoichiometric amorphous phase of silicon dioxide SiO2(a). However, during surface oxidation of silicon, which occurs with the volumetric oxygen content and the form of its presence, there is no reliable information in the literature. In this regard, the purpose of this work is to determine the stability of the volumetric oxygen content and its form of occurrence during surface oxidation of silicon.

To solve this problem, a high-temperature X-ray diffraction technique was chosen directly on the X-ray beam. As a sample, we used single-crystal n-Si silicon with a resistivity $\rho \approx 10$ Ω·cm, an oxygen concentration of No ≈ 4 × 1017 cm–3, and a dislocation density ND ≈ 102 cm–2, grown by the Czochralski method along the growth axis [111]. The sample size was 10 × 6 × 1 mm with a cut along the (111) plane. X-ray diffraction patterns were obtained on a DRON-UM1 diffractometer (Russia) using λCuKα = 1.54178 Å. The diffraction patterns of the samples were measured in the temperature range 293–1293 K according to the θ – 2θ scheme in the step scan mode. The error in the intensity measurements was about 1%. The required sample temperature was set using a UVD-2000 high-temperature attachment with an accuracy of ± 0.5° C.

A portion of the X-ray diffraction patterns of a silicon single crystal in the 2θ angle range from 8 to 43° at different temperatures is shown in Fig. 1, a – c, in particular, in Fig. 1a at T = 293K.

As the sample temperature was raised to 800 K, the character of the change in the intensity and angular positions of the diffraction reflections changed (Fig. 1b). The selective reflection of (111)Si from the matrix lattice and its β-component (111)β retained their initial parameters with experimental accuracy. However, a shift of the (110) structure line from the impurity phase – SiO2 at a temperature of 800 K towards small angles by about 10 arcmin was found. With a further increase in temperature to 1193 K, the displacement was 0.8°, and the new angular position of this reflection corresponded to 2θ = 35.6°, in place 2θ = 36.4° at T = 293 K. An increase in temperature to 1293 K did not lead to a significant change in the reflections of the diffraction spectrum (Fig. 1c). The shift of the (110) reflection by 0.8°cannot be explained by a random error of the experiment, since in this case the intensity would be lost primarily by the reference reflection of (111)Si from the silicon matrix lattice. However, as the experiment showed, the main reflection (111)Si does not change in intensity and angular position in accordance with the coefficient of linear thermal expansion of silicon (αSi = 2.54 × 10–6 K–1). The explanation of the observed shift of the (110) reflection by 0.8° became possible only under the assumption of the presence of a phase transition in the SiO2(c) impurity phase (similar to the phase transition in quartz under normal atmospheric conditions).

It is known from the literature that, under atmospheric conditions, the α - β phase transition in quartz (SiO2) occurs at a temperature of 846 K. The new angular position 2θ = 35.6° of the (110)

structural reflection of silicon dioxide SiO2(c) in the temperature range 1193--1293 K corresponded to the angular position of quartz in the β-phase (SiO2) with the lattice parameter a = 5.043 Å of the unit cell basis, which was in good agreement with literature data (a = 5.020 Å).

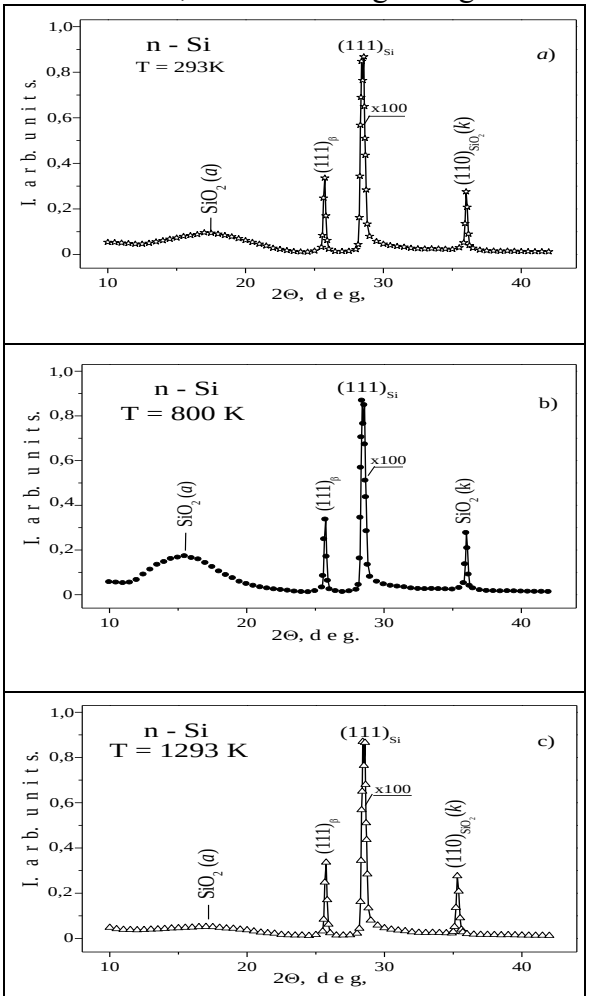

Figure 1. Portions of the XRD pattern of the n–Si single crystal at temperatures T = (*a*) 293, (b) 800 and (c) 1293 K.

Consequently, the phase transition occurs only in the lattice of the impurity crystalline phase of SiO2(c) silicon from the low-temperature α-phase to the high-temperature β-phase, and not in the matrix lattice of silicon.

The temperature dependence of the diffuse scattering intensity at 2θ ≈17° on SiO2(a) behaved anomalously. With an increase in the temperature of the sample, an increase in the intensity was observed, and at T = 800 K the intensity increased by more than 2.5 times compared to the intensity at T = 293 K (Figs. 1a and 1b). An increase in intensity indicates that, at this temperature, the volume of near-surface SiO2(a) grows due to an increase in the thickness of this layer with silicon oxidation. The growth kinetics of a SiO2(a) dioxide film is explained based on the Deal – Grove model. According to this model, the oxidation process occurs at the Si - SiO2 interface, the oxidizer (oxygen) molecules diffuse through the formed oxide layers and only then react with silicon at its interface: c-Si + O2 = SiO2.

An increase in the temperature of the sample from 800 to 1193 K did not lead to a further increase in the intensity of diffuse scattering, which indicates the suspension of the process of thermal oxidation of the single crystal surface, but a shift of the maximum towards small angles by 2θ ≈ 1.5° was observed. This indicates that, in this temperature range, the size of clusters of the amorphous layer grows. However, starting from a temperature of 1193 K, a decrease in the intensity of this reflection is observed, and upon reaching a temperature of 1293 K, the diffuse peak suddenly disappears (Fig. 1c). A possible explanation for this effect is the sublimation of amorphous dioxide – SiO2(a) in the form of silicon monoxide SiO at a given temperature. Some traces of diffuse scattering from the amorphous layer of silicon dioxide can still be seen in Fig.1c, which indicates that equilibrium between sorption of oxidant by silicon and sublimation of amorphous silicon dioxide from the single–crystal surface at a high temperature cannot be achieved during the experiment.

Thus, it was found that in a silicon medium in the temperature range 293–1293 K, phase transition α - β in the crystalline phase of SiO2 in the bulk of a silicon single crystal, similar to the α - β transition quartz in the atmosphere.

THERMAL STABILITY OF SPECTROMETRIC PROPERTIES OF γ-IRRADIATED GADOLINIUM SILICATE Gd_2SiO_5:Ce CRYSTALS

Ashurov M.X., Nuritdinov I., Saidakhmedov K.Kh.
Institute of Nuclear Physics, Uzbekistan Academy of Sciencts, Tashkent, Uzbekistan

Cerium-activated gadolinium silicate crystals Gd_2SiO_5:Ce or (GSO) are widely utilized as scintillation materials for detecting ionizing radiation. This paper investigates the characteristics of the primary spectrometric properties of GSO crystals with varying structural quality. For comparative analysis, GSO single-crystal samples from two different technological batches were used: defective (GSO-1) and dislocation-free (GSO-2). The primary spectrometric properties, namely relative light output (S) and energy resolution (R), were evaluated under γ-irradiation, along with the recovery kinetics of these parameters following radiation exposure.

The single crystals under study were grown by the Czochralski method from a stoichiometric melt of a (Gd_2O_3) and (SiO_2) oxide mixture using a modernized "Donetsk-1" growth system at the JSC "Institute for Single Crystals" of the NAS of Ukraine (Kharkiv). The concentration of the isovalent activator (Ce^{3+}), which substitutes the host matrix ions (Gd^{3+}) was 0.5 mol.%. No significant changes in spectrometric properties were observed in the GSO-2 samples after γ-irradiation, whereas the GSO-1 samples exhibited degradation of their spectrometric parameters.

Figure 1 illustrates the kinetics of thermal relaxation of the optical and spectrometric parameters of the GSO-1 crystal, pre-irradiated with a dose of $7 \cdot 10^6$ rad.

The graphical data (Fig. 1) indicate that upon heating to 200 °C, the energy resolution recovers by more than half, while the radiation-induced optical density (D) decreases by one-third. The relaxation kinetics of the light output (S) exhibit a different behavior: no changes are observed in the temperature range up to 200 °C, whereas a sharp increase in (S) and a corresponding improvement in resolution (R) are recorded in the temperature range of 300–350 °C.

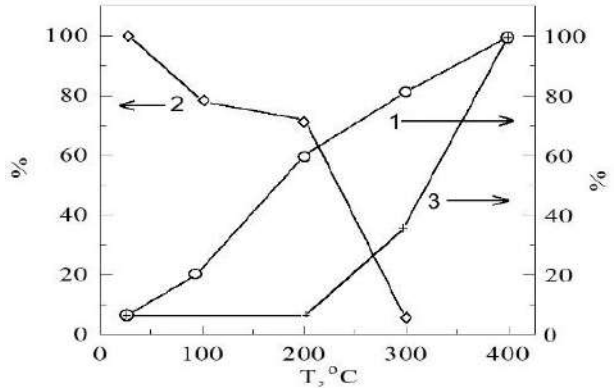

Figure 1. Property recovery of an irradiated crystal from the GSO-1 batch after γ-irradiation with a dose of $7 \cdot 10^6$ rad. The maximum relative change in parameters (R) (1), (D) (2), and (S) (3) after irradiation is taken as 100%.

Upon completion of the annealing cycle at 400 °C, the optical and spectrometric properties of the material are almost fully restored. This fact indicates the high thermal stability of the radiation-induced defects responsible for the degradation of the scintillator properties. Effective recovery of the spectrometric characteristics of GSO-1 crystals is achieved exclusively through high-temperature thermal annealing at 400 °C.

Consequently, the degradation of the spectrometric properties of GSO crystals under γ-irradiation is directly determined by the initial structural quality of the single crystal.

EFFECT OF THERMORADIATION TREATMENT ON THE STRUCTURAL PARAMETERS OF ZnS

Madaminov B.N., Tashmetov M.Yu., Makhkamov Sh., Ismatov N.B., Erdonov M.N.
Institute of Nuclear Physics, Uzbekistan of the Academy of Sciences, Tashkent, Uzbekistan

Zinc sulfide (ZnS) is a wide-band-gap II–VI semiconductor whose structural properties are sensitive to irradiation and thermal treatment. Previous studies have shown that annealing ZnS in air at temperatures above ~400–500 °C promotes progressive oxidation, resulting in the coexistence of ZnS and ZnO phases and corresponding changes in the XRD characteristics [1–3]. However, the effect of subsequent thermal annealing on the structural parameters of electron-pre-irradiated ZnS remains insufficiently studied. In the present work, thermally induced structural changes in unirradiated ZnS are compared with those in ZnS pre-irradiated with 2 MeV electrons to a fluence of 4×10^{17} electrons/cm^2.

The irradiated and initial unirradiated samples were isochronally annealed in air at 200, 400, 600, and 800 °C for 20 min. X-ray diffraction (XRD) measurements were performed using a PANalytical Empyrean diffractometer with Cu K_α radiation. The lattice parameter (a), crystallite size (D), and microstrain (ε) of ZnS were determined from the (111) reflection. The D and ε values were calculated using the Debye–Scherrer and Stokes–Wilson methods, respectively, with instrumental broadening determined using a Si standard taken into account. Figure 1 shows the XRD patterns of the unirradiated and electron-irradiated ZnS samples before and after annealing. The main reflections, indexed as (111), (220), (311), (400), and (331), confirm that the cubic sphalerite structure of ZnS is retained in both series of samples.

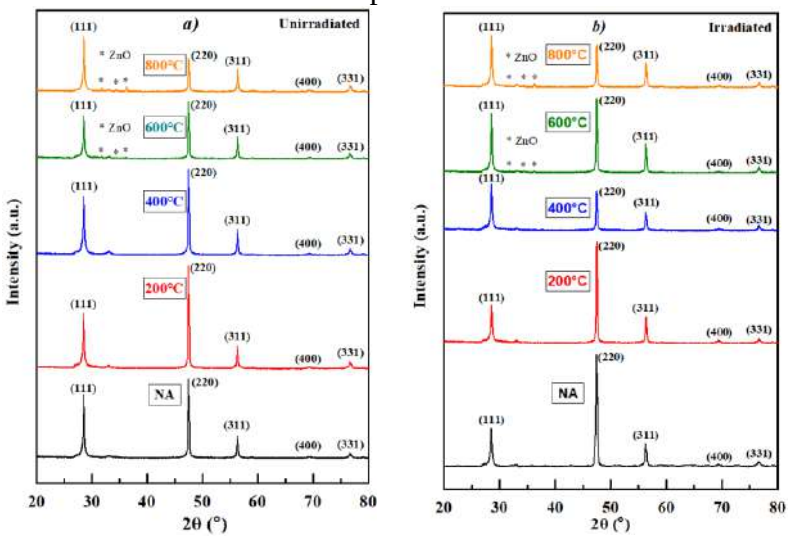

Figure 1. XRD patterns of (*a*) unirradiated and (*b*) electron-irradiated ZnS samples before and after annealing in air at 200, 400, 600, and 800 °C for 20 min.

No significant phase transformations are observed up to 400 °C. At 600 °C, weak reflections of the hexagonal wurtzite ZnO phase appear, and their intensity increases considerably at 800 °C, indicating progressive oxidation of ZnS. Nevertheless, the main ZnS reflections remain detectable even at 800 °C, indicating the coexistence of ZnS and ZnO phases.

The temperature dependences of the lattice parameter a and crystallite size D of the residual ZnS phase are presented in Fig. 2. For unirradiated ZnS, the lattice parameter a decreases

monotonically from 5.4413 Å in the initial state to 5.4047 Å at 800 °C. The most pronounced structural relaxation is observed already at 200 °C, where the crystallite size *D* increases from 21.0 to 34.8 nm, while the microstrain *ε* decreases from 6.89×10^{-3} to 4.13×10^{-3}.

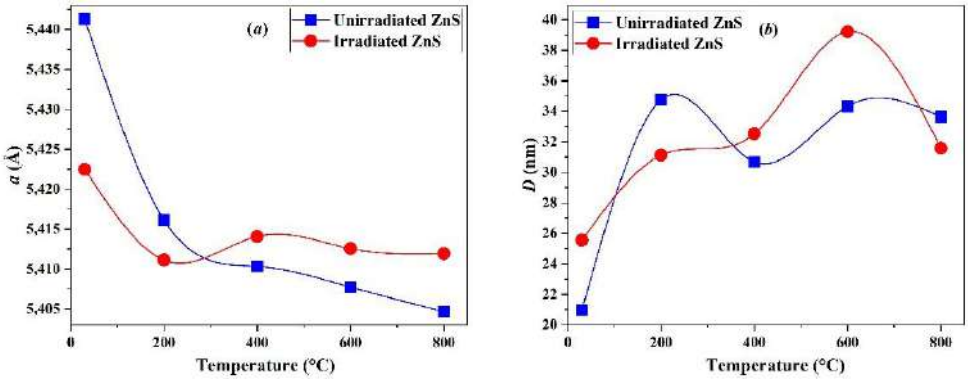

Figure 2. Temperature dependence of the (*a*) lattice parameter *a* and (*b*) crystallite size *D* of the ZnS phase in unirradiated and electron-irradiated samples.

A distinctly different structural response is observed for the electron-irradiated samples. Electron irradiation modifies the initial structural state of ZnS through the formation of radiation-induced defects and the associated lattice distortions and rearrangements. Accordingly, the irradiated sample in the initial unannealed state exhibits a larger crystallite size *D* (25.5 nm) and lower microstrain *ε* (5.63×10^{-3}) compared with the unirradiated material. The changes observed during subsequent annealing may be associated with thermally activated migration and recombination of radiation-induced defects. In this process, *D* gradually increases while *ε* decreases, reaching 39.2 nm and 3.66×10^{-3} at 600 °C, respectively. These changes indicate further relaxation of lattice distortions and an increase in the coherent-domain size. In contrast to unirradiated ZnS, for which the lattice parameter decreases monotonically with increasing annealing temperature, in irradiated ZnS it decreases up to 200 °C and remains nearly constant with a further increase in temperature, indicating a different thermal response of the pre-irradiated material.

At 800 °C, the irradiated sample shows a reversal of the structural relaxation trend: *D* decreases from 39.2 to 31.6 nm, whereas *ε* increases from 3.66×10^{-3} to 4.54×10^{-3}. Together with the pronounced increase in the intensity of the ZnO reflections in Fig. 1, this behavior indicates that high-temperature oxidation becomes a dominant factor in the structural changes. The formation of ZnO and the associated ZnS/ZnO interfaces may introduce additional lattice distortions and reduce the coherent-domain size of the residual ZnS phase. Overall, electron pre-irradiation produces a modified defect-structural state in ZnS. The structural relaxation observed during subsequent annealing may be associated with thermally activated migration and recombination of radiation-induced defects, accompanied by changes in the structural parameters of ZnS. In the temperature range of 600–800 °C, these processes are accompanied by the oxidation of ZnS, resulting in ZnO formation and the development of a two-phase ZnS/ZnO system.

References:

1. N. Dengo, A.F. De Fazio, M. Weiss, R. Marschall, P. Dolcet, M. Fanetti, S. Gross. Thermal evolution of ZnS nanostructures: Effect of oxidation phenomena on structural features and photocatalytical performances // Inorganic Chemistry, Vol.57, (2018), pp.13104–13114.
2. P. Devaraji, M. Mapa, H.M. Abdul Hakkeem, V. Sudhakar, K. Krishnamoorthy, C.S. Gopinath. ZnO–ZnS heterojunctions: A potential candidate for optoelectronics applications and mineralization of endocrine disruptors in direct sunlight // ACS Omega, Vol.2, No.10, (2017), pp.6768–6781.

TEMPERATURE KINETICS AND MECHANISMS OF RADIATION-INDUCED DEFECT FORMATION IN KCl CRYSTALS UNDER HIGH-ENERGY ELECTRON IRRADIATION

Mussaeva M.A.[1], Nuritdinov I.[1], Yuldashov D.P.[1], Atashov B.T.[2]
[1]*Institute of Nuclear Physics, Uzbekistan Academy of Sciences, Tashkent, Uzbekistan*
[2]*Nukus State Pedagogical Institute, Nukus, Uzbekistan*

This work is devoted to an experimental study of the influence of irradiation temperature (165 K and 300 K) and fast electron fluence on the energy efficiency of defect creation and the dynamics of their clustering in a model KCl crystal grown by the Kyropoulos method. Irradiation was performed using fluences of 10^{14}, 5×10^{14} and 10^{15} e/cm^2 under two temperature regimes: a low-temperature regime T = 165 K, which suppresses the thermal mobility of vacancies, and a room-temperature regime T = 300 K. The experiments were conducted on a “Electronica U-003” linear electron accelerator with a beam energy of E = 5 MeV. The choice of a high beam energy was dictated by the need to ensure a plane-penetrating regime to form a uniform (bulk) absorbed dose profile throughout the entire thickness of the sample. Optical absorption spectra were recorded immediately after irradiation using a spectrophotometer Perkin Elmer Lambda-35 UV/VIS Spectrometer in the energy range from 1.0 to 6.0 eV at a temperature of 300 K.

In all radiation-colored samples, the dominant spectral feature is an intense symmetric absorption band in the region of 2.3–2.4 eV, attributed to electronic transitions in isolated F-centers (Figs. 1 and 2).

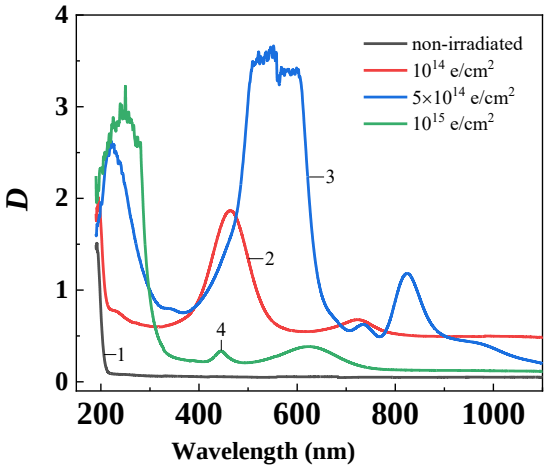

Figure 1. Absorption spectra of KCl irradiated with electrons at 10^{14}, 5×10^{14}, 10^{15} e/cm^2 at 165 K

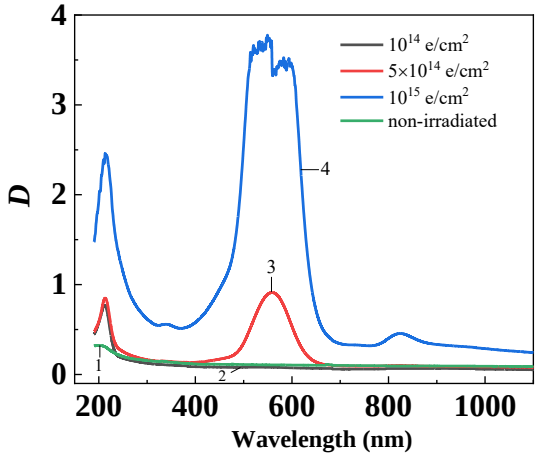

Figure 2. Absorption spectra of KCl irradiated with electrons at 10^{14}, 5×10^{14}, 10^{15} e/cm^2 at 300 K

To quantitatively evaluate the kinetics of radiation-induced defect formation, the bulk concentration of *F*-centers N_F was calculated from the experimental spectra using the classical Smakula formula for Gaussian band shapes. To quantify the efficiency of defect aggregation, an aggregation index K_{ag} was introduced, reflecting the ratio of the intensities of the divacancy (*M*-center, 825 nm) bands to those of simple vacancies.

A comparative analysis revealed an important physical paradox: at the maximum fluence, the peak amplitude at 165 K is nearly 1.7 times higher than that at 300 K, whereas their integral concentrations are close 5.24×10^{16} and 5.02×10^{16} cm^{-3} respectively. This phenomenon is caused by

strong homogeneous thermal broadening of the absorption band due to the intensification of electron-phonon interaction during the transition from 165 K $\Delta H \approx 0.22$ eV to 300 K $\Delta H \approx 0.36$ eV, while the area under the spectral curve remains conserved. The defect accumulation kinetics and the nature of the accompanying bands are fundamentally determined by the thermodynamic conditions:

- **At 165 K**, a strictly linear growth of the N_F concentration is observed. Vacancy diffusion is frozen. Primary defects are efficiently spatially separated. Complementary interstitial chlorine localizes at growth inhomogeneities, forming hole polyhalide complexes in the UV region of the spectrum (220 nm for V_3-centers, 345 nm for V_2-centers).
- **At 300 K**, defect mobility is activated, stimulating radiation annealing processes (mutual annihilation of vacancies and interstitials) and their coagulation. The aggregation index rises sharply to 0.28. This is confirmed by the cascade development of multi-vacancy complexes in the long-wavelength region: divacancies (825 nm — *M*-centers), trivacancies (625, 670 nm — *R*-centers), and tetravacancies (~970 nm — N_1-centers). The final stage of coagulation is phase separation with the formation of ultradispersed metallic potassium colloids (720–735 nm), which brings the accumulation curve of isolated *F*-centers to a saturation plateau.

To evaluate the energy efficiency of the processes based on the specific energy losses of fast electrons in KCl $dE/dx \approx 3.17\times10^6$ eV/cm, the radiation-chemical yield of defects at the initial linear stage 10^{14} e/cm^2 was calculated. The obtained values $G_{165K} \approx 3.97/100$ eV and $G_{300K} \approx 4.66$ centers/100 eV correspond to an average energy expenditure of ≈ 21-25 eV to create a single stable defect pair. Since this value is only about $3E_g$ ($E_g \approx 8.5$ eV), it serves as rigorous evidence for the dominance of the exciton mechanism of defect formation: the energy of the electron beam is spent on lattice ionization, followed by the non-radiative decay of self-trapped excitons into stable *F*- and *H*-centers.

Conclusion

1. The bulk concentration of *F*-centers in a KCl crystal irradiated with 5 MeV electrons was experimentally determined. At a fluence of 10^{15} e/cm^2, it reaches values of ~5.2×10^{16} cm^{-3}.
2. It is shown that the temperature-induced decrease in the *F*-band absorption amplitude during the transition from 165 K to 300 K is of a purely electron-phonon (instrumental) broadening nature and is not related to a decrease in the total defect concentration.
3. It is established that at 300 K, diffusion processes cause intensive vacancy clustering, with the aggregation index increasing up to 0.28. This leads to the sequential formation of *M*-, *R*-, and *N*-centers and the nucleation of a nanoscale metallic potassium phase (720–735 nm).
4. Based on the calculated values of the radiation-chemical yield (G ≈ 4 *defects*/100 eV), the exciton nature of the generation of primary Frenkel defects [1-4] under 5 MeV electron irradiation in the studied system is proven.

References:

1. Lushchik, Ch. B., & Lushchik, A. Ch. (1989). Decay of Electronic Excitations with Defect Formation in Solids. Moscow: Nauka. — 272 p.
2. Vitol, I. K. (1966). Mechanisms of radiation defect formation in alkali halide crystals. Bulletin of the Academy of Sciences of the USSR. Physical Series, 30(4), 564–570.
3. Smakula, A. (1930). Über lichtzerstreuung in gefärbten Kristallen. Zeitschrift für Physik, 59(9), 603–614.
4. Shvarts, K. K., & Ekmanis, Yu. A. (1989). Dielectric Materials: Radiation Processes and Radiation Stability. Riga: Zinatne. — 192 p.

FEATURES OF THE OPTICAL ABSORPTION SPECTRA OF Cr^{3+} IONS IN SINGLE CRYSTALS OF COMPLEX ALKALI-METAL SULFATES

Ganyeva A.S.[1], Sharsheev K.Sh.[2], Egamberdieva A.A.[1]
[1]Zhusup Balasagyn Kyrgyz National University, Bishkek, Kyrgyzstan,
[2]Academician Zh.Zheenbaev Institute of Physics, National Academy of Sciences of the Kyrgyz Republic, Bishkek, Kyrgyzstan

The optical absorption spectra of pure $Li_2SO_4 \cdot H_2O$ and $Li_2SO_4 \cdot H_2O$ doped with Cr^{3+}, measured at a temperature of 77 K, are presented in Fig. 1. The spectra of $LiKSO_4$ and $LiNaSO_4$ doped with Cr^{3+}, measured at the same temperature, are shown in Fig. 2.

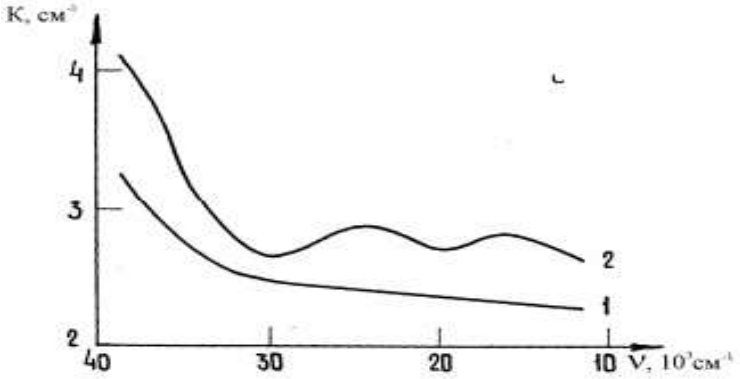

Figure 1. Optical absorption spectra of pure (1) and Cr^{3+}-doped (2) $Li_2SO_4 \cdot H_2O$ crystals at T = 77 K.

For the $Li_2SO_4 \cdot H_2O$ crystal at T = 77 K, the maxima of the absorption bands are located at ν_1 = 17,000 cm^{-1}, ν_2 = 23,800 cm^{-1}, and ν_3 = 37,280 cm^{-1}. As the temperature increases to 300 K, these maxima shift to 16,600 cm^{-1}, 23,300 cm^{-1}, and 36,300 cm^{-1}, respectively [1].

In $LiKSO_4$ and $LiNaSO_4$ crystals, in addition to the main absorption bands, weak bands were observed in the infrared region (14,500–15,300 cm^{-1}). These bands were identified as spin-allowed transitions $^4A_2g(F) \rightarrow {}^2T_1g(G)$ and $^4A_2g(F) \rightarrow {}^2E_g(G)$ (Fig. 3).

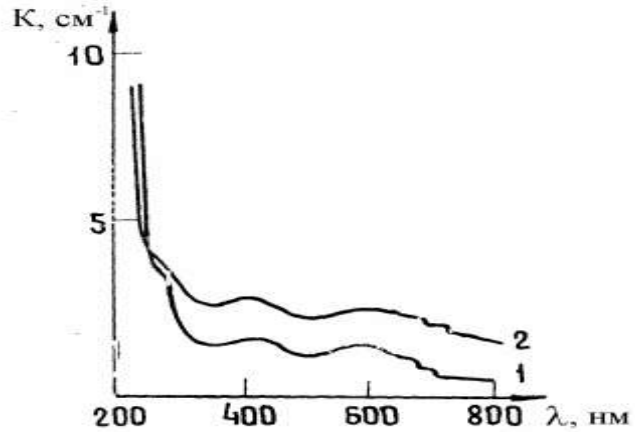

Figure 2. Optical absorption spectra of $LiNaSO_4$ (1) and $LiKSO_4$ (2) single crystals doped with Cr^{3+} at T = 77 K.

Undoped crystals are transparent in the visible spectral region. The introduction of Cr^{3+} ions into transparent undoped crystals leads to the formation of broad, intense absorption bands in the

ultraviolet and visible regions. These bands are attributed to spin-allowed transitions from the ground state $^4A_2g(F)$ to the $^4T_2g(F)$, ^2T_1g, and $^4T_2g(P)$ levels in an octahedral crystal field [2].
The significant size mismatch between Cr^{3+} ions and the Na^+ and K^+ cations (0.75 Å for K^+), as well as the formation of vacancies, causes a local reduction in symmetry and distortion of the octahedral sites. This may result in partial relaxation of the spin selection rule and the appearance of weak lines corresponding to the $^4A_2g(F) \rightarrow {}^2T_1g(G)$ and $^4A_2g(F) \rightarrow {}^2E_g(G)$ transitions [3].

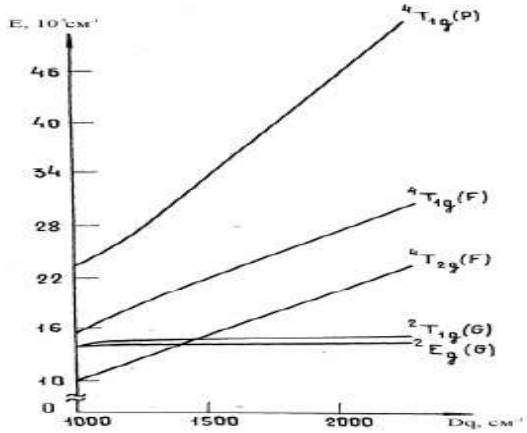

Figure 3. Energy-level diagrams of Cr^{3+} ions (3d configuration) in octahedral coordination for B/C = 4.5.

Upon cooling the crystals to 77 K, the decrease in the lattice parameters is accompanied by a reduction in the R(Cr–O) distances, which results in a shift of the spin-allowed absorption bands toward the higher-energy region due to an increase in the crystal-field strength Dq [6].

Conclusion. The optical absorption spectra of $Li_2SO_4 \cdot H_2O$, $LiKSO_4$, and $LiNaSO_4$ single crystals doped with Cr^{3+} ions were investigated. It was established that the spectra are formed by intraconfigurational transitions of Cr^{3+} ions in an octahedral crystal field. Additional weak bands attributed to spin-forbidden transitions were observed in $LiKSO_4$ and $LiNaSO_4$ crystals. It was shown that the temperature-induced changes in the spectra are associated with an increase in the crystal-field strength upon cooling. The obtained results confirm the localization of Cr^{3+} ions at sites with nearly octahedral symmetry and make it possible to characterize the features of their interaction with the crystal matrix of complex alkali-metal sulfates.

References:

1. Laksmana R., Purandar K. Optical absortion spectrum Cr^{3+} ion doped in Zinc cezium sulphate hexahydrate.// Sol. Stat. Comun. 1981.V.40, №5. P.567-569.
2. Sharsheev, K. *Radiation and Impurity Centers with Variable Valence in Crystals of Complex Alkali-Metal Sulfates.* Yekaterinburg–Karakol, 1999. 208 p.
3. Sviridov, D. T., Smirnov, Yu. F. *Theory of Optical Spectra of Transition-Metal Ions.* Moscow: Nauka, 1977. 328 p.
4. Ganyyeva, A. S., Raiymkul kyzy, N., Kidibaev, M. M., Sharsheev, K. “The Effect of Impurities on the Formation of Paramagnetic Centers.” *Science, New Technologies and Innovations in Kyrgyzstan*, 2024, Bishkek.
5. Ganyyeva, A. S. “Luminescence of $LiNaSO_4$ and $LiKSO_4$ Crystals Activated by Chromium Ions.” *Scientific Journal Physics*, 2025, No. 1, Bishkek.

6. Tanabe, Y., Sugano, S. “On the Absorption Spectra of Complex Ions.” *Journal of the Physical Society of Japan*, 1954, Vol. 9, No. 5, pp. 753–780. -1(68), P. 37–41. – EDN FLRWRO. https://www.elibrary.ru/item.asp?id=44273418.

INFLUENCE OF HEATING RATE ON GLOW CURVE CHARACTERISTICS AND DOSIMETRIC PERFORMANCE OF NANO A-AL_2O_3

Ahadov A., Mammadov S., Ahadova A.
Institute of Physics, Ministry of Science and Education of the Republic of Azerbaijan, Baku, Azerbaijan

The heating rate has a significant impact on the thermoluminescence (TL) properties of various materials. The effect of heating rate on the glow curve of MgB4O7:Tm,Dy has also been studied by , who found that the kinetics parameters can be accurately determined using the sequential quadratic programming glow curve deconvolution (SQPGCD) method. This is consistent with the findings of, who also observed changes in peak temperatures, peak intensities, and total area of glow peaks with increasing heating rates in other materials. Cruz-Zaragoza found that as the heating rate increases, the peak intensity at the maximum decreases and shifts to a higher temperature. This was also observed by Ogundare in the case of fluorite, where the glow-peak temperatures increased with heating rate. Piters highlighted the influence of a temperature lag on the TL analysis, which can lead to a decrease in activation energy and frequency factor. Kitis studied the effects of heating rate on the TL glow-peaks of different phosphors, providing a comprehensive comparison of experimental results and theoretical calculations. These studies collectively demonstrate the significant impact of heating rate on TL properties[1]. The thermoluminescence glow curve of alumina (Al2O3) is influenced by the heating rate, with the response of single-crystal detectors decaying exponentially and ceramic detectors decaying linearly. Thermoluminescence of α-Al2O3:C irradiated to low doses (0.04–7.20 mGy) similar to those measurable in the environment has been investigated. The glow curve consists of a dominant0 peak near 200 °C and two additional glow peaks of weaker intensity at around 74 and 342°C, respectively for measurements made at 5 °C/s. Analysis of the main peak using various methods shows that in this low dose range, the peak follows non-first order kinetics and also that the peak is unitary rather than being a composite of two overlapping peaks as is thought to be the case at comparatively higher dose. Its dose response was observed to be linear and the dependence of the luminescence intensity on heating rate showed that the thermoluminescence is subject to thermal quenching. However, further examination suggests that thermal quenching may be more of an effect with increase in luminescence excitation dose. However, Kumar cautions that the conservation of area under the glow curve is not always guaranteed, and that the glow peak height can increase with heating rate.

Considering the preceding discussions, the objective of this study was to explore the hermoluminescence (TL) characteristics of alpha-alumina (α-Al2O3) when subjected to varying radiation doses and heating rates[2]. The focus was on analyzing the dose-response relationship and conducting kinetic analysis of the primary glow peak.

In this study, nano-sized α-Al2O3 particles with sizes of 40 nm commercially available from Skyspring Nanomaterials, Inc. were used as samples. The samples were irradiated at ambient temperature with a 60Co gamma source with a dose rate of 1.76 Gy/s. The dose rate was determined

using a Magnette Miniscope MS400 EPR spectrometer with individually packed BioMax alanine dosimetry films with barcode markings developed by Eastman Kodak Company. The Harshaw TLD 3500 Manual Reader was utilized to assess the TL sample characteristics using a linear heating rate of 2°C/s from 323K to 673K in an N2 atmosphere with a Pilkington HA-3 heat-absorbing filter. Three aliquots of 5 mg each were used for each measurement, and the TL data points represented the average of the three aliquots. A thin layer of the sample powder was uniformly distributed on the planchet surface to ensure a uniform TL signal.

During our studies, TL luminescence curves were recorded, which revealed a distinct peak reaching a maximum at approximately 202°C. Notably, as the dose levels increased, the peak exhibited a consistent shift towards lower temperatures. This intriguing observation led us to conclude that the thermoluminescent peak adheres to non-first-order kinetics ($b \neq 1$).

The influence of heating rates emerged as a pivotal experimental variable in our study. Dosimetric materials, particularly nano α-Al2O3, demonstrated shifts in TL sensitivity and variations in dose curve trends in response to different heating rates. As the heating rate increased, the TL glow peak temperature shifted towards higher values, accompanied by a diminishing peak intensity. This aligns seamlessly with the expectations of TL theory. The decrease in TL glow peak intensity with escalating heating rates was elucidated as a consequence of thermal quenching, where the efficiency of quenching rises with higher temperatures.

A significant revelation emerged when we normalized the maximum TL intensities to the lowest heating rate (2°C/s), unveiling a substantial 22% decrease in peak intensity. Adding to the significance of our exploration, we observed a exponential increase in TL intensity of the exposed nanoparticles with the radiation dose. This points towards the potential use of alumina nanoparticle powder as a substrate material for ionizing radiation dosimetry, opening up promising avenues for practical applications in this field.

References:

1. Ahadova A. et al. Temperature Effect on Thermoluminescence kinetic parameters of Nano-Alumina // Adv. Phys. Res. 2024. Vol. 6, № 3. P. 239–246.
2. Ahadov A. et al. Isothermal Decay Analysis Of Intermediate Tl Peaks Of Nano-Alumina // V International Scientific Forum “Nuclear Science And Technologies.” Almaty, Kazakhstan, Kazakhstan, 2024. P. 128.

ANALYTICAL AND DIGITAL INSIGHTS OF ANCIENT CERAMIC TECHNOLOGIES USING XRD METHOD

Ahadova A., Ahadov A., Mammadov S.
Institute of Physics, Ministry of Science and Education of the Republic of Azerbaijan, Baku, Azerbaijan

This paper presents a comprehensive mineralogical analysis of Neolithic ceramic assemblages from Pashatepe and Khudutepe settlement in Jalilabad, Azerbaijan, contributing to the understanding of early ceramic production technologies. XRD results demonstrated a generally consistent mineralogical profile across the examined samples. The dominant phases identified included quartz and feldspar (specifically albite), along with various clay-related minerals. These secondary phases included calcite, muscovite, montmorillonite, diopside, maghemite, brucite, and zeolite, all of which contribute to our understanding of the raw materials and thermal conditions involved in the production process. To establish a baseline for comparison, a sample of raw ceramic paste — sourced from the same geographical region — was analyzed using the same XRD methodology. The exhaustive list of peak positions, spanning from approximately 28° to over 1200° 2θ, indicates a high-resolution, full-pattern XRD scan[1]. The identification of the crystalline phase as α-quartz (the most common polymorph at surface conditions) is foundational. The presence, relative intensity, and sharpness (crystallinity) of these quartz peaks allow for several inferences The quartz likely originates from the local lithic environment—potentially from the surrounding sandstone (Jalilabad region) or fluvial sands from nearby sources. Its grain size and distribution (inferred from peak broadening if full-width-half-maximum data were available) could inform on temper preparation techniques (crushing, sorting). Furthermore, quartz undergoes a well-documented inversion at 573°C (β-quartz). The presence of the characteristic α-quartz pattern suggests the ceramic was fired below this temperature or that it reverted to the alpha phase upon cooling. The absence of high-temperature silica polymorphs (cristobalite, tridymite) further constrains the maximum firing temperature to likely below 1000-1200°C, consistent with prehistoric open-firing or simple kiln technologies. If t analyze the fabric characterization, quartz serves as a primary aplastic inclusion. Its signature is key for defining petrographic fabric groups among samples. Comparative analysis of the quartz peak profiles across all four samples could reveal consistency (suggesting standardized paste recipes or a single clay source) or variability (suggesting multiple production episodes or clay sources). A complete mineralogical assemblage for each pottery sample would include other phases such as feldspars (e.g., microcline, plagioclase), micas (e.g., muscovite), clay minerals (e.g., illite, kaolinite—often indicated by broad, low-angle reflections), and calcite[2]. The presence or absence of calcite, which decomposes above ~750°C, is a crucial pyrotechnological indicator. For a robust interpretation, quantitative phase analysis (e.g., using the Rietveld method) is required to determine the weight percentages of quartz and other minerals. This would allow for precise comparisons of paste recipes.

Quartz is the dominant mineral phase in all analyzed samples, accounting for 53.9% and 55.6% of the ceramic bodies from Pashatepe and Khudutapa, respectively. The XRD patterns of both samples are dominated by intense diffraction peaks corresponding to quartz (SiO_2), indicating that quartz constitutes the principal mineral phase in the ceramic bodies. The sharpness and high intensity of these peaks suggest a well-crystallized phase, most likely originating either from naturally quartz-rich clays or from the intentional addition of quartz-rich temper. The consistently

high quartz content suggests either the intentional addition of quartz-rich temper or the use of naturally quartz-rich clays. In comparison, the raw ceramic paste contains a lower quartz proportion (42.6%), indicating that additional quartz may have been introduced during ceramic preparation to enhance mechanical strength and thermal stability during firing. Albite (feldspar) shows a marked increase in the fired ceramics relative to the raw paste. While the raw ceramic paste contains only 9.5% albite, the Pashatepe and Khudutapa samples exhibit substantially higher values (20.4% and 28.3%, respectively). This enrichment suggests selective use of feldspar-bearing raw materials or differential survival of feldspar phases following firing. The higher albite content in the Khudutapa ceramics may reflect either variations in clay sources or intentional technological choices aimed at improving vitrification properties. Calcite is present in low but significant amounts in both fired ceramic samples (4.1% at Pashatepe and 3.6% at Khudutapa), whereas it is entirely absent in the raw ceramic paste. This pattern supports the interpretation that carbonate components were either introduced during paste preparation or formed through secondary processes following firing. Importantly, the preservation of calcite in the ceramics indicates firing temperatures below the decomposition threshold of calcium carbonate, reinforcing the conclusion that low-temperature firing techniques were employed. Muscovite content shows a contrasting trend. The raw ceramic paste contains a high proportion of muscovite (40.5%), while its abundance decreases substantially in the fired ceramics (19.3% at Pashatepe and 11.3% at Khudutapa). This reduction reflects partial thermal degradation of mica minerals during firing, consistent with heating sufficient to alter but not fully decompose phyllosilicate structures. The lower muscovite content in the Khudutapa sample may suggest slightly higher firing temperatures or longer firing durations compared to Pashatepe. Other minerals include phases such as montmorillonite, diopside, maghemite, brucite, and zeolite, represents a minor proportion of the ceramic matrix. Their reduced abundance in the fired ceramics compared to the raw paste further indicates mineralogical transformations associated with firing and post-depositional processes. The quantitative XRD data corroborate the qualitative mineralogical observations derived from the diffractograms. The ceramics from Pashatepe and Khudutapa exhibit broadly similar compositions, implying shared raw material procurement strategies and ceramic production technologies. At the same time, subtle differences in feldspar and muscovite contents point to localized technological variability, particularly in firing regimes. These results contribute significantly to the reconstruction of Chalcolithic ceramic production practices in the Jalilabad region.

References:

1. Zhou X. et al. XRD-based quantitative analysis of clay minerals using reference intensity ratios, mineral intensity factors, Rietveld, and full pattern summation methods: A critical review // Solid Earth Sci. 2018. Vol. 3, № 1. P. 16–29.
2. Garcia-Guinea J. et al. Mineral inlays in natural stone slabs: techniques, materials and preservation // Constr. Build. Mater. 2000. Vol. 14, № 6–7. P. 365–373.

INFLUENCE OF GAMMA-IRRADIATION ON THE ELECTRIC RELAXATION IN $TlInSe_2$ SINGLE CRYSTAL

Mammadov M.A.[1], Asadova Z.I.[1], Asadov F.G.[1,2]
[1]*Institute of Physics, Ministry of Science and Education Republic of Azerbaijan, Baku, Azerbaijan*
[2]*Lenkaran State University, Lenkaran, Azerbaijan*

In this work, the current–voltage characteristics (CVC) and the electric current relaxation at different values of applied voltage (U = 0.1–5.0 V) and electric field intensity (E = 1.9–95.8 V/m) were investigated in $TlInSe_2$ single crystals irradiated with gamma-rays at absorbed doses of $\Phi\gamma$ = 100 krad, 500 krad, and 1 Mrad at room temperature. It was established that, depending on the absorbed dose, the electric current in irradiated crystals either increased by 1.5–2 times or decreased by 10–15 times compared to the initial crystals. Based on the CVC curves, the values of free charge carrier concentration (n_0), mobility (μ), and trap concentration (N_t) were calculated.

The observed changes in electrical conductivity are associated with modifications in the concentration of radiation defects and shallow traps formed as a result of irradiation. Ternary semiconductor compounds of the AIII BIII C_2VI type possess unique physical properties and are considered promising materials for optoelectronics, light-emitting diodes, lasers, and X-ray detectors. $TlInSe_2$ exhibits a chain-like, defect-containing structure and is a structural-coordination analogue of TlSe. The interest in these compounds is driven by their low-dimensional crystal structure, high defect concentration (10^{17}–10^{18} cm^{-3}), and strong anisotropy of physical properties. Localized energy levels within the band gap significantly affect device characteristics. Radiation-induced defects generated by ionizing radiation form localized levels, leading to electric current relaxation.

This study aims to investigate the kinetic parameters of charge-carrier traps and the influence of γ-irradiation on electric current relaxation in $TlInSe_2$ single crystals.

1. **Sample Preparation:** $TlInSe_2$ single crystals were grown using the directed crystallization method. The crystal has a tetragonal structure (a = 8.06 Å, c = 6.822 Å) with p-type conductivity and a band gap width of E_g = 1.23 eV.
2. **Measurements:** Parallelepiped-shaped samples (5.2 × 1.56 × 0.53 mm) with silver paste contacts were measured in a cryostat under vacuum (P = 10^{-2} Pa) using an E7-20 Immittance Meter.
3. **Irradiation Source:** ^{60}Co isotope (E = 1.25 MeV) was used. High-energy γ-quanta undergo Compton scattering, imparting recoil energy to electrons, which then collide with crystal atoms to create point defects (Frenkel defects).

Energy Calculations: The maximum kinetic energies transferred to lattice atoms during electron collisions were calculated as:

4. **Se atoms:** 53.2 eV
5. **In atoms:** 36.8 eV
6. **Tl atoms:** 20.6 eV

Table. Main Parameters Calculated from CVC Curves

Sample / Dose	Carrier Conc. n_0 (cm^{-3})	Mobility μ ($cm^2/V\cdot s$)	Trap Conc. N_t (cm^{-3})
Initial	5.45×10^{18}	3.03×10^{-3}	5.2×10^{10}

100 krad	8.24×10^{17}	2.91×10^{-3}	1.6×10^{11}
500 krad	9.86×10^{18}	3.11×10^{-3}	1.1×10^{10}
1 Mrad	8.49×10^{17}	2.93×10^{-3}	1.4×10^{11}

Analysis of Current Relaxation Behavior

1. **At 100 krad and 1 Mrad Doses:** Electrical conductivity decreases by 10–15 times compared to the initial sample. This decrease is attributed to a threefold increase in shallow trap concentration ($N_t \approx 1.4–1.6 \times 10^{11}$ cm^{-3}) and increased scattering of charge carriers by radiation defects.
2. **At 500 krad Dose:** Conductivity increases by 1.2–1.5 times at low fields (E < 20 V/m) due to a reduction in shallow trap concentration ($N_t = 1.1 \times 10^{10}$ cm^{-3}), leading to less charge trapping.
3. **Low Electric Field Regime (E<25 V/m):** Injected charge carriers are trapped, creating a space charge field that limits current transport, causing a decay of current over time (sublinear CVC region).
4. **High Electric Field Regime (E>25 V/m):** Thermal excitation and high electric fields release trapped electrons and lower the anode barrier, leading to a recovery and increase in current over time (by 1.2–1.4 times).

Gamma-irradiation alters electrical conductivity and current relaxation kinetics by modifying defect density and charge carrier traps. Depending on the absorbed dose, electrical conductivity either decreases (10–15×) due to an increase in shallow trap levels or increases (1.5–2×) due to defect annealing and trap reduction. These findings provide insights into controlling transport mechanisms in $TlInSe_2$ single crystals for radiation-resistant optoelectronic applications.

INVESTIGATION OF RADIATION DEFECTS AND THE LOCAL NEIGHBORHOOD OF ^{57}FE ATOMS IN THIN MO AND TA FILMS FOLLOWING HIGH-DOSE ION IMPLANTION

Bedelbekova K.A.[1], Andrianov V.A.[2], Izteleuova G.S.[3]

[1]*Institute of Nuclear Physics of the Atomic Energy Agency of the Republic of Kazakhstan, Almaty, Kazakhstan*

[2]*Lomonosov Moscow State University, Institute of Nuclear Physics, Moscow, Russian Federation*

[3]*Kazakh University of Innovative and Telecommunications Systems, Uralsk, Kazakhstan*

The study of the properties of structural materials for existing and future nuclear facilities remains one of the most important scientific and technical challenges. Under the influence of particles and radiation, complex structural and phase transformations occur in crystalline solids, leading to significant changes and degradation of their initial microstructure and properties. Radiation damage is initiated at the atomic level, but macroscopic degradation effects actually arise due to microstructural changes.

Tungsten, molybdenum, tantalum, and niobium—the so-called "big four" of refractory metals—constitute a distinct class of structural materials characterized by melting points above 2000 °C, chemical inertness over a wide temperature range, and high density. Along with these elements, titanium and nickel are among the six key metals that, in various forms, constitute the foundation of the material and raw material base for enterprises in the electronics, aviation, chemical, and nuclear industries.

The objective of this research was to evaluate the nuclear-physical and operational properties of structural reactor materials and to predict their behavior following irradiation up to damaging doses.

In this work, tantalum and molybdenum foils were studied using Mössbauer spectroscopy, X-ray diffraction high-dose irradiation with ^{57}Fe ions. Irradiation with ^{57}Fe ions allows for Mössbauer spectroscopy [1] studies of the atoms that directly cause radiation damage.

Mo and Ta foils with a thickness of 20 μm were selected as samples for the study. The foils were produced by repeated cold rolling of initial bulk samples with a purity of at least 99.9. Recrystallization annealing was performed in a vacuum of 5×10^{-6} mm Hg for 2 hours at temperatures ranging from 800 to 1000 °C. Irradiation with ^{57}Fe ions having an energy of 1 MeV was carried out on a heavy-ion accelerator at the Institute of Nuclear Physics (Almaty). The ion current density was maintained in the range of 50–100 nA. The ions flux density was 5×10^{16} ions/cm².

X-ray structural analysis was performed on a BRUKER D8 ADVANCE diffractometer. Diffractograms were measured from the irradiated surface side, as well as from the reverse side, in the angular range $2\theta = (200^{o}–900^{o})$, with an angular scan step of 0.020^{o} and a dwell time of 1.0 s.

Preliminary computer simulations of the radiation dose were performed using the SRIM-2008 [2] program, which allows for an assessment of the extent of the ion beam's impact on the crystal lattice of the irradiated material, typically expressed as the number of displacements per atom. The calculation results for Ta and Mo are shown in Figure 1. Note that the average number of displacements per atom (DPA) is approximately 200. This indicates an extremely strong irradiation effect on the surface.

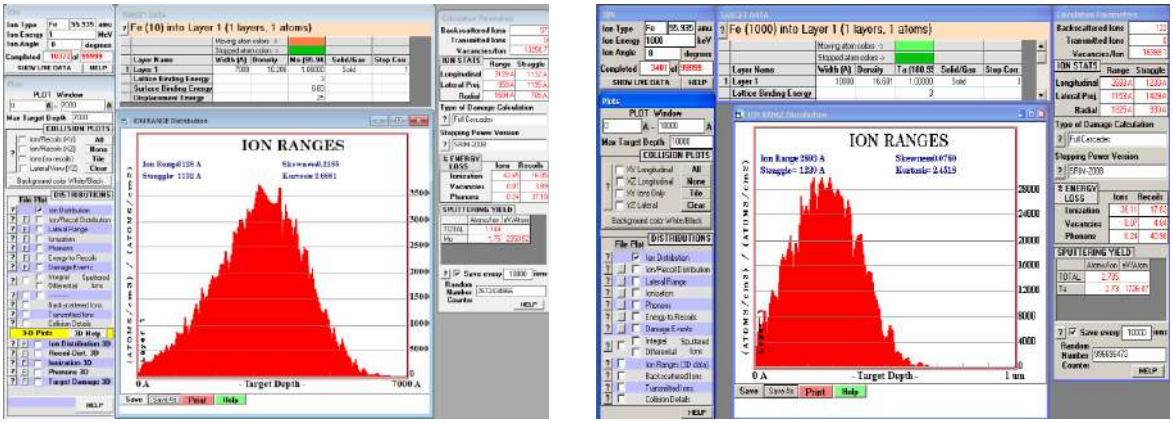

R_e (Mo)= 200 nm R_e (Ta)= 120nm

Figure 1. Results of the STRIM-2008 simulation of the ion range of ^{57}Fe in a Mo and Ta matrix

Mössbauer studies were conducted in two modes: 1) in the standard transmission geometry (MS) and 2) with the detection of conversion electrons from the irradiated material surface (CEMS).

As a result of this work, the effect of ^{57}Fe ion implantation with an energy of 1 MeV and a fluence of 5×10^{16} ions/cm² on the properties of structural materials used in the nuclear industry (Ta, Mo) was investigated. The implantation took place in a surface layer approximately 600 nm thick and corresponded to roughly 200 displacements of matrix atoms per ^{57}Fe ion. The diffraction patterns obtained from the irradiated and unirradiated sides were virtually identical. For the Ta matrix, a slight broadening of the lines was observed in the diffraction pattern of the irradiated side; for the Mo matrix, additional line broadening was practically absent. The broadening of the diffraction lines indicates disturbances in the crystal lattice of the surface layer. “Doublet” phases appear to be related to the formation of Fe + Ta/Mo + vacancy clusters in the regions of grain boundaries or are associated with regions of partial amorphization of the materials.

For metallic Ta and Mo, Mössbauer spectroscopy revealed the formation of two phases. The main “singlet” phase in molybdenum (84%) is a solid solution of Fe substituting for Mo. The “singlet” phase in tantalum (78%), given the zero solubility of Fe in Ta, apparently corresponds to the formation of (Fe + vacancy) clusters in the Ta matrix. The “doublet” phases presumably relate to the formation of Fe + Ta/Mo + vacancy clusters in intergranular boundary regions or are associated with regions of partial amorphization of the materials.

References:

1. G.N.Belozersky, “Mössbauer Spectroscopy as a Method for Studying Surfaces”. Moscow: Energoatomizdat, 1990. 205 pp.
2. Program SRIM. http://www.srim.org/

INVESTIGATION OF CHANGES IN THE PHONON PROPERTIES OF Si_3N_4 NANOPOWDER INDUCED BY ELECTRON IRRADIATION USING RAMAN SPECTROSCOPY

Tashmetov M.Yu., Buriev M.M.
Institute of Nuclear Physics ,Uzbekistan Academy of Sciences,Tashkent, Uzbekistan

To investigate the effect of electron irradiation on the phonon properties of Si_3N_4 nanopowder, the sample was irradiated with 2 MeV electrons at fluence of 5×10^{15} e/cm^2 using the “Electron-U003” linear electron accelerator at the Institute of Nuclear Physics of the Academy of Sciences of the Republic of Uzbekistan. Raman spectra were recorded using a Confotec MR350 Raman spectrometer to identify the phonon-related changes induced in the sample before and after irradiation. A solid-state laser with a wavelength of 532 nm was used as the excitation source for the Raman measurements. The signal integration time was set to 10 s for each measurement. To prevent possible local heating of the sample caused by laser irradiation, the average laser power was maintained below 10 mW.

The Raman spectrum of the unirradiated Si_3N_4 nanopowder exhibited a total of 10 characteristic Raman peaks in the wavenumber range of 150-1100 cm^{-1}, observed at 178.02, 200.20, 224.37, 435.85, 613.69, 724.37, 836.93, 914.28, 935.84, and 1071.33 cm^{-1}. Based on their spectral positions, these peaks were divided into three main regions [1,2,3]. In the low-frequency region, the peaks located at 178.02, 200.20, and 224.37 cm^{-1} were assigned to the E_{2g}, A_g, and E_{1g} vibrational modes, respectively. In the intermediate-frequency region, the Raman bands observed at 435.85 and 613.69 cm^{-1} were attributed to the E_{2g} mode. The high-frequency region was characterized by peaks located at 724.37, 836.93, 914.28, 935.84, and 1071.33 cm^{-1}, which were assigned to the A_g, E_{1g}, and E_{2g} vibrational modes, respectively (Fig. 1).

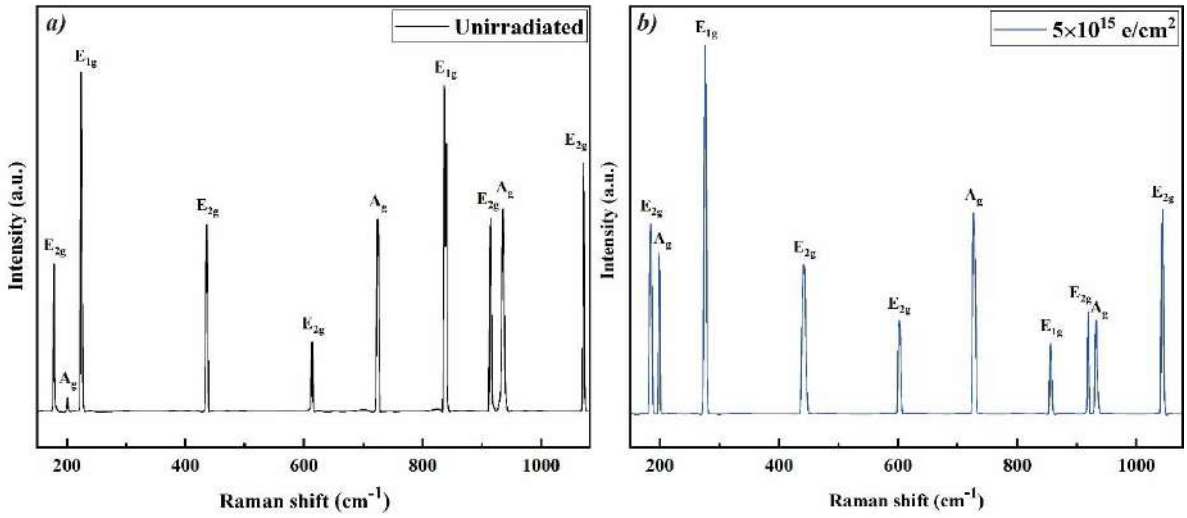

Figure 1. Raman spectra of Si_3N_4 nanopowder: *a)* unirradiated sample; *b)* sample irradiated with electrons at a fluence of 5×10^{15} e/cm^2.

The characteristic Raman peaks identified in the unirradiated sample and their corresponding vibrational mode assignments provided a basis for evaluating the phonon-related changes induced by electron irradiation. Changes in the spectral positions, intensities, and shapes of the peaks in the

Raman spectra after irradiation were analyzed to assess the effect of electron irradiation on the phonon properties of Si_3N_4 nanopowder. The Raman spectra of unirradiated Si_3N_4 nanopowder and samples irradiated with electrons at fluences of 5×10^{15} e/cm^2 were analyzed, and the spectral positions of the observed peaks and their corresponding vibrational modes were identified. The characteristic peaks in the Raman spectrum were divided into different spectral regions, and each peak was associated with the corresponding vibrational mode. The changes in the positions and shapes of these peaks induced by irradiation provide an opportunity to evaluate modifications in the phonon properties of Si_3N_4 nanopowder.

After irradiation at a fluence of 5×10^{15} e/cm^2, peak shifts, broadening, and an increase in the intensity of some modes were observed. These changes indicate an increase in local structural distortions and defect concentration in the Si_3N_4 nanopowder induced by electron irradiation [4].

References:

1. Tashmetov M.Yu. and Buriev M.M. Structural and vibrational characterization of Si_3N_4 nanopowders under electron beam irradiation. J. Phys.: Condens. Matter 38 (2026) 125702.
2. Wada N, Solin S.A, Wong J, and Prochazka S. Raman and IR absorption spectroscopic studies on α, β and amorphous Si_3N_4 Journal of Non-Crystalline Solids (1981) 43:7.
3. Cai, Y., Zhang, L., Zeng, Q., Cheng, L. & Xu, Y. First-principles study of vibrational and dielectric properties of β-Si_3N_4. Physical Review B - Condensed Matter and Materials Physics (2006) 74, 174301.
4. Zhumazhanova A. et al. Raman Study of Polycrystalline Si_3N_4 Irradiated with Swift Heavy Ions. Crystals (2021) 11:1313.

RADIATION-INDUCED REARRANGEMENT OF PHONON AND LOCAL VIBRATIONAL CHARACTERISTICS IN GaAs(O):Cr UNDER ELECTRON IRRADIATION

Tashmetov M.Yu.[1], Djangabaev Kh.N.[2]
[1]*Institute of Nuclear Physics, Uzbekistan Academy of Sciences, Tashkent, Uzbekistan*
[2]*Berdakh Karakalpak State University, Nukus, Uzbekistan*

Gallium arsenide (GaAs) is widely used in modern electronics owing to its unique electronic and optical properties. Its high sensitivity to radiation can lead to structural degradation, which is an important consideration for its potential use in radiation-resistant devices. High-energy electron irradiation induces point defects and their complexes, manifested by changes in the LO and TO modes in Raman spectra and local vibrational bands in infrared spectra [1].

Raman spectroscopy is a non-destructive method for characterizing the structural and defect states of semiconductors, providing information on phonon modes, local stresses, and lattice distortions. Combining Raman analysis with infrared spectroscopy enables assessment of changes in the local atomic environment and defect complexes. Phonon shifts, changes in FWHM and the intensity ratio (I_{LO}/I_{TO}), together with shifts of infrared bands, serve as sensitive indicators of structural disorder. Accordingly, this study aims to investigate the evolution of the phonon spectrum and defect state of GaAs(O):Cr after 2 MeV electron irradiation at fluences of 4×10^{17}–6×10^{17} e/cm^2 using Raman and infrared spectroscopy.

Polycrystalline GaAs(O):Cr samples were irradiated using the Elektronika U-003 electron accelerator (Institute of Nuclear Physics, Academy of Sciences of the Republic of Uzbekistan) at an electron energy of 2 MeV and a beam current density of 0.085 μA/cm^2 [2]. Raman measurements were performed using a Renishaw inVia spectrometer with a 785 nm laser at 0.5 mW, corresponding to a penetration depth of ~8.1 μm. FTIR absorption spectra were recorded in the 500–1000 cm^{-1} range using an Agilent Cary 600 Series FTIR spectrometer equipped with a Globar (SiC) source and a DTGS detector, with a spectral resolution of ≤4 cm^{-1}; each spectrum was averaged over 32 scans.

The irradiation-induced stress was evaluated from the shifts of the LO and TO phonon frequencies according to [3]: $\Delta\omega_{TO} = -2.45\delta = -302\varepsilon_p$. The intensity ratio $R = I_{LO}/I_{TO}$ was determined from the integrated intensities obtained by Gaussian fitting, with the TO mode used as a reference owing to the higher sensitivity of the LO mode to radiation-induced changes.

Representative Raman and infrared spectra of the samples before and after irradiation at different fluences are shown in Fig. 1. Gaussian fitting was applied to determine peak positions and linewidths and to resolve possible overlap between vibrational modes.

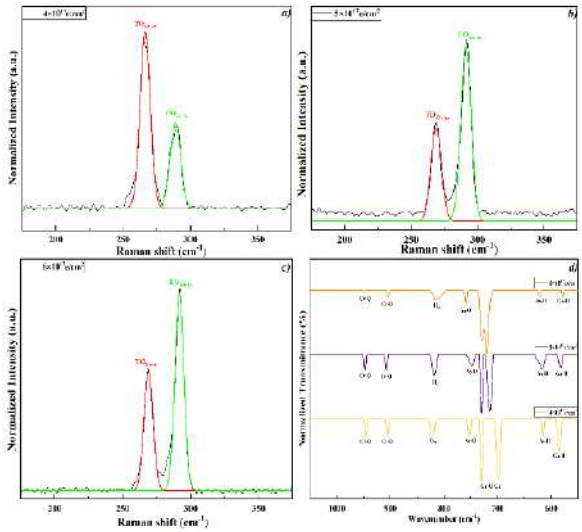

Figure 1. Raman (*a*–*c*) and FTIR (*d*) spectra of GaAs(O):Cr before and after electron irradiation at different fluences.

In the unirradiated GaAs(O):Cr, the TO and LO modes are located at 267.67 and 289.78 cm^{-1}, respectively [1]. At 4×10^{17} e/cm^2, their frequencies decrease to 266.44 and 288.89 cm^{-1}, with an induced stress of +0.50 GPa, TO/LO FWHM values of 9.44/9.63 cm^{-1}, and I_{LO}/I_{TO} = 0.338. At 5×10^{17} e/cm^2, the modes shift to 268.86 and 291.30 cm^{-1}, accompanied by a change in stress to −0.48 GPa, FWHM values of 9.37/9.16 cm^{-1}, and I_{LO}/I_{TO} = 1.919. At 6×10^{17} e/cm^2, the frequencies reach 269.03 and 291.83 cm^{-1}, with a stress of −0.55 GPa, FWHM values of 7.89/7.89 cm^{-1}, and I_{LO}/I_{TO} = 1.646. These changes indicate a rearrangement of the phonon subsystem and a transition in the strain state. FTIR spectra show a corresponding evolution of the local atomic environment: at 4×10^{17} e/cm^2, most bands shift toward lower wavenumbers, whereas the bands near ~584, ~819, and ~905 cm^{-1} shift to higher wavenumbers, indicating the coexistence of tensile and compressive strain regions. At 5×10^{17} e/cm^2, higher-wavenumber shifts dominate, while the bands near ~581, ~748, and ~817 cm^{-1} shift toward lower wavenumbers. At 6×10^{17} e/cm^2, most bands likewise shift toward higher wavenumbers, indicating dominant compressive strain, whereas the bands near ~578 and ~816 cm^{-1} retain their lower-wavenumber shifts, reflecting an inhomogeneous distribution of defects and local strain. Overall, the Raman and FTIR results reveal a complex radiation-induced

rearrangement of the phonon characteristics, local atomic environment, and strain state of GaAs(O):Cr. This study was carried out within the 2026 research program of the Institute of Nuclear Physics, Academy of Sciences of the Republic of Uzbekistan, entitled “Optimization of the electrical and physicochemical properties of $A^{II}B^{VI}$ and $A^{III}B^{VI}$ compounds using thermo-radiation technology.”

References:

1. M.Yu.Tashmetov., Kh. Djangabaev (2025). Study of radiation-induced effects in GaAs(O):Cr under 2 Mev electron irradiation using Raman, FTIR and Hall effect measurements. Physica Scripta, **100**, No. 12.,125918
2. M.Tashmetov, A. Abdaminov (2025). Influence of gamma doses on the optical and electrical properties of oxygen-impurity and chromium-doped GaAs. Journal of Physics: Condensed Matter. **37**, 485702.
3. Ye Shen, Xuan Fang, Xiang Ding, Haiyan Xiao, Xia Xiang, Guixia Yang, Ming Jiang, Xiaotao Zu and Liang Qiao (2020). Structural Features and Photoelectric Properties of Si-Doped GaAs under Gamma Irradiation. Nanomaterials, **10**, 340.

GAMMA-IRRADIATION RESISTANCE OF LAYERED $TlInTe_2$:Bi COMPOUND: RAMAN SPECTROSCOPY STUDY

Gadzhieva N.N., Khalilova K.G., Akhmedova G.B., Iskenderova G.M., Gafarova G.A.

Institute of Physics, Ministry of Science and Education of the Republic of Azerbaijan, Baku, Azerbaijan.

This paper presents the results of a Raman spectroscopy investigation of gamma-radiation-induced structural changes in the Bi-doped $TlInTe_2$ ($TlInTe_2$:Bi) compound. The samples were irradiated with E=1.25 MeV gamma rays energy over an absorbed dose range of D=0.5–5 MGy. The Raman scattering spectra reveal that the characteristic parameters of phonon modes remain unchanged after irradiation, indicating that the crystal structure exhibits high resistance to gamma radiation. The obtained results demonstrate the structural stability of $TlInTe_2$:Bi under high-dose gamma irradiation and suggest that this material is a promising candidate for radiation-shielding applications.

The layered semiconductor compound $TlInTe_2$ belongs to the $A_3B_3C_2^6$ family of chain-structured compounds. In the $TlInTe_2$ crystal structure, thallium ions are arranged in such a way that octahedral voids are formed between them. Occupation of these vacant octahedral sites by selected impurity atoms enables the formation of solid solutions with improved and tunable physical properties, making these materials attractive for various scientific and technological applications.

Bismuth (Bi) is one of the most suitable dopants for this purpose. Bi ions are expected to occupy the empty octahedral sites located between Tl atoms along the crystallographic [001] direction ($z = 0.5$) .

Numerous studies have demonstrated that bismuth metal and Bi-containing compounds exhibit excellent radiation protection performance against gamma rays and high-energy electron irradiation. Motivated by these findings, the present work investigates the influence of 1.25 MeV gamma irradiation on the structure of $TlInTe_2$:Bi compound. Radiation-induced structural changes were

monitored by Raman spectroscopy. The $TlInTe_2$:Bi compound was synthesized by the Bridgman crystal-growth method. It was previously established that the solubility limit of Bi in $TlInTe_2$ reaches approximately 5 at.%. Unpolarized Raman scattering spectra were recorded at room temperature (300 K) using a Nanofinder 3D confocal Raman microspectrometer (Tokyo Instruments, Japan) in the backscattering geometry with an excitation wavelength of λ=514 nm.

Gamma irradiation was carried out using a ^{60}Co MRX-γ-20 irradiation facility (Baku, Azerbaijan). The photon energy and the absorbed dose rate were 1.25 MeV and1.06 Gy s^{-1}, respectively. The samples were irradiated at room temperature (300 K) with absorbed doses ranging from 0.5 to 5 MGy.

Figure 1 presents the unpolarized Raman scattering spectra of the initial (curve 1) and gamma-irradiated to an absorbed dose of D=5 MGy $TlInTe_2$:Bi compound (curve 2).

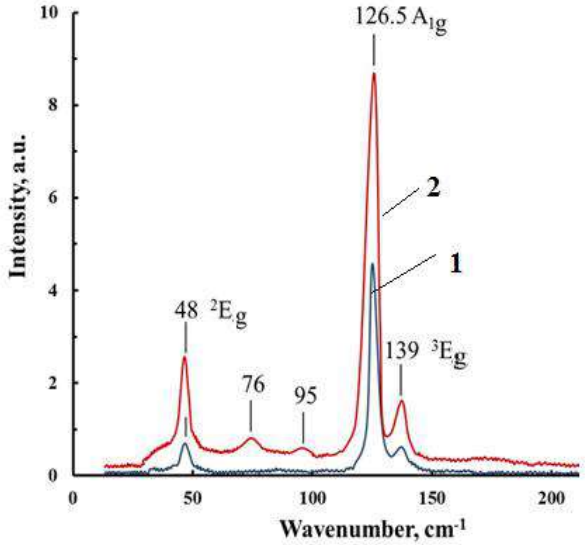

Figure 1. Unpolarized Raman scattering spectra of the initial (curve 1) and and gamma-irradiated to an absorbed dose of D=5 MGy $TlInTe_2$:Bi compound (curve 2).

As can be seen from the figure, three spectral Raman lines are experimentally observed at 48 cm^{-1} (^2E_g), 126.5 cm^{-1}(A_{1g}), and 139 cm^{-1} (^3E_g), which are also characteristic of the $TlInTe_2$ crystal, but differ in the redistribution of the intensity of the ^2E_g and ^3E_g modes. In particular, the intensity ratio I_{48}/I_{139} increases by ~2 times after Bi doping. The complete coincidence of the three Raman mode frequencies in $TlInTe_2$ and $TlInTe_2$: Bi indicates that the lattice distortion resulting from doping is very weak.

In the Bi-doped $TlInTe_2$ compound, the effect of gamma irradiation on the crystal structure is very weak, as no shifts are observed in the Raman band maxima or in the frequencies of the ^2E_g and A_{1g} modes. A slight increase in the full width at half maximum (FWHM) ($\nu_{1/2)}$ of the A_{1g} mode is observed only at an absorbed dose of D = 4.5 MGy, contained ~ $\nu_{1/2}\approx 2$ cm^{-1}. Thus, doping the $TlInTe_2$:Bi compound with bismuth atoms significantly enhances its radiation resistance. The radiation stability of the $TlInTe_2$:Bi structure under γ-irradiation is also confirmed by the results obtained using XRD analysis.

The effect of gamma irradiation on the structure of the $TlInTe_2$:Bi compound was investigated over the absorbed dose range of D = 0.1–5 MGy using Raman spectroscopy. The radiation stability of the spectral parameters, including the Raman peak positions and the FWHM of the characteristic vibrational modes, was analyzed. The results demonstrate that $TlInTe_2$:Bi is a promising material for applications in environments exposed to γ-radiation with an energy of E = 1.25 MeV.

MAGNETIC PROPERTIES OF TRANSITION METAL DOPED GaSe MONOLAYERS: FIRST-PRINCIPLES AND MACHINE-LEARNING APPROACHES

Huseynova S.
Institute of Physics, Ministry of Science and Education of the Republic of Azerbaijan, Baku, Azerbaijan

Two-dimensional (2D) GaSe has attracted considerable attention due to its tunable electronic and magnetic properties, making it a promising material for spintronic applications. In this work, first-principles density functional theory (DFT+U) calculations were performed to investigate the structural, electronic, and magnetic properties of transition-metal (TM)-doped GaSe monolayers, where TM = Co, Fe, Ni, Cu and Cr. Exchange-correlation effects were treated within the spin-polarized generalized gradient approximation (SGGA) using the Perdew–Burke–Ernzerhof (PBE) functional. A Hubbard correction of U = 4 eV was applied to the localized 3d orbitals of transition-metal dopants. The main thing is that with the exception of system doped with Cu element, which exhibit non-magnetic semiconductor properties, all other doped systems demonstrate magnetism.

Keywords: GaSe monolayer, DFT+U, transition-metal doping, ferromagnetism, spintronics, density of states.

Two-dimensional layered semiconductors have emerged as promising materials for next-generation electronic, optoelectronic, and spintronic devices. Among them, gallium selenide (GaSe) exhibits excellent optical response, high carrier mobility, and a tunable band gap.

Introducing magnetism into nonmagnetic 2D semiconductors through transition-metal doping is a promising strategy for realizing dilute magnetic semiconductors suitable for spin-based electronic applications. Recent studies have shown that substitutional doping of GaSe with transition metals such as Cr, Mn, Fe, Co, and Ni can significantly modify its electronic and magnetic properties through exchange interactions involving localized d orbitals. The results [1] confirm that monolayer GaSe is an indirect-band-gap semiconductor (Γ–M) with a quasiparticle band gap in good agreement with experimental measurements and a low exciton binding energy. The substitutional [2] incorporation of transition metal atoms into GaSe monolayer lattice can be recommended as efficient methods to open new functionality for this 2D material. The introduction of a single Ga vacancy [3] successfully induces a local magnetic moment of 1.00 μB in the GaSe system. This magnetism primarily originates from the spin polarization of Se atoms adjacent to the defect. V, Mn, and Fe doping leads to the emergence of the diluted magnetic semiconductor nature, while doping with Cr creates a new 2D half-metallic material from the GaS monolayer[4]. The study showed [5] that V-doped GaSe monolayer is a promising two-dimensional material for photocatalytic water-splitting and CO2 reduction under visible light, making it a potential material for clean fuel production.

First-principles calculations were performed using Density Functional Theory (DFT) within the spin-polarized generalized gradient approximation (SGGA). Exchange-correlation effects were described using the Perdew–Burke–Ernzerhof (PBE) functional. Supercells containing a substitutional Co, Fe, Ni, Cu or Cr atom at a Ga site were subsequently relaxed with a force convergence criterion of 0.05 eV Å−1. To correctly describe the localized d electrons of transition-metal atoms, an on-site Hubbard correction of U = 4 eV was applied to the 3d states. Magnetic properties were evaluated through spin-polarized calculations.

The calculated total magnetic moments of TM-doped GaSe monolayers are summarized in Table 1.

Table 1. Calculated magnetic moments of TM-doped GaSe monolayers.

GaSe-TM	$\mu/TM \quad (\mu_B)$	Teoretical value
GaSe-Co	2.011	---
GaSe-Fe	2.700	2.122 [14]
GaSe-Ni	2.514	---
GaSe-Cu	0	0 [6]
GaSe-Cr	2.703	---

The results show that the investigated dopants, with the exception of Cu, induce strong magnetic moments in the GaSe monolayer. The highest magnetic moments are observed for Fe, Ni, and Cr impurities. The magnetism primarily originates from the partially occupied 3d orbitals of the transition-metal dopants. Figure 1 presents the (a) atomic structure and (b) electronic band structure of a Ni-substituted GaSe supercell, denoted as Ni(Ga), where a Ni atom replaces a Ga atom in the lattice.

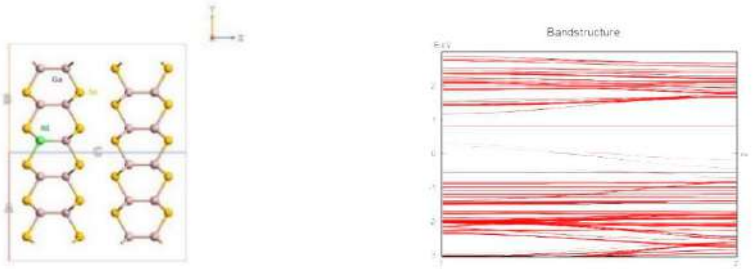

(a) (b)

Figure 1. Ni (Ga) substitution in the $Ga_{35}NiSe_{36}$ (a) structure and (b) band structure

In summary, the structural and magnetic properties of Co-, Fe-, Ni-, Cu-, and Cr-doped GaSe monolayers were systematically investigated using DFT+U calculations. The results reveal that the magnetic behavior originates primarily from the spin-polarized 3d orbitals of the transition-metal (TM) dopants, whereas the contributions from the *s* and *p* states are relatively minor. The calculated magnetic moments are 2.011 μB, 2.700 μB, 2.514 μB, 0 μB, and 2.703 μB for the Co-, Fe-, Ni-, Cu-, and Cr-doped systems, respectively. These findings demonstrate that TM-doped GaSe monolayers possess considerable potential for future spintronic and magnetic semiconductor applications.

References:

1. D.Wines, K.Saritas, Can A., A first-principles Quantum Monte Carlo study of two-dimensional (2D) GaSe, (2020) *J.Chem. Phys.* 153, 154704 https://doi.org/10.1063/5.0023223
2. Phuong Thuy Bui, Vo Van On, J.Guerrero-Sanchez , D.M.Hoat (2025), Journal of Magnetism and Magnetic Materials, 621, 172920, https://doi.org/10.1016/j.jmmm.2025.172920
3. Junyu Mou, Yongchao Liang, Li Ye, Wenqiang Li, Yijun Zhu, Haozheng Zhang, Yonghao Wang (2026) Theoretical prediction of half-metallic ferromagnetism in transition metal doping GaSe monolayers: 645, 173990, https://doi.org/10.1016/j.jmmm.2026.173990
4. D.M.Hoat, Nguyen Thanh Tien, Duy Khanh Nguyen, J.Guerrero-Sanchez, (2024) Antiferromagnetism in GaS monolayer doped with TM–TM atom pairs (TM = V, Cr, Mn, and Fe), Phys. Chem. Chem. Phys.,27, 18657-18666, https://doi.org/10.1039/D4CP01119H

5. Mohamed M. Fadlallah, Safwat Abdel-Azeim (2026) Study on substitutional doped GaSe monolayers using hybrid functional: Electronic, optoelectronic, and photocatalytic applications, Materials Science in Semiconductor Processing, 201, 110068 https://doi.org/10.1016/j.mssp.2025.110068
6. Wei Chen, Qi Chen, Jianming Zhang, Lin Zhou, Electronic and magnetic properties of transition-metal-doped monolayer B2S2 within GGA + U framework, RSC Advances, January 2024,14(5):3390-3399, DOI:10.1039/d3ra08472h

A STUDY OF RADIATION DEFECTS IN NANOSTRUCTURED NA-BENTONITE SILICATE LAYERS BY MEANS OF FT-IR SPECTROSCOPY AND NATURE OF RADIATION-INDUCED DEFECTS IN CLAY MINERALS

Ismayilova M.K., Mustafayev I.I., Akhundzada H.N., Khankishiyeva R.
Institute of Physics, Ministry of Science and Education of the Republic of Azerbaijan, Baku, Azerbaijan

The effect of high doses (up to 1000 kGy) of γ-radiation on the short-range structural organization in montmorillonite was studied using infrared spectroscopy. The results show that the montmorillonite structure can accumulate high doses of radiation with damage. The modifications most likely to be generated by the radiation were expected to be within the silicate layers. In this paper, the effects of ionizing radiation on the Na-bentonite clay investigated by FT-IR method. These spectra show the suitability of FT-IR study of mineral surfaces and the changes in the spectra brought about by the surface phenomena.

Various radiation-induced point defects have been observed in kaolinite, dickite, montmorillonite and illite. Extensive information has been collected on radiation effects on clay minerals over the last 35 years, providing a wealth of information on environmental and geological processes [1-3]. Radiation-induced defects were first observed in clay minerals using electron paramagnetic resonance (EPR) in the early 60s but their spectrum was erroneously assigned. Two main defects were identified in kaolinite (Al2Si2O5(OH)4). Their use for geological applications began in the late 1980s. However, understanding of radiation-induced defects had long been limited to kaolinite. Systematic studies of damages in other clay minerals are still scarce [1]. In addition, it is necessary to differentiate the effects of ionizing radiation (alpha, beta, gamma rays) and ballistic events (heavy ion beams) in a large range of doses consistent with natural (uncontaminated surface environments, U-deposits) or artificial (radioactive waste) systems. This research work presents the main radiation-induced defects in clay minerals, mostly investigated by FTIR measurements, and discusses applications in Earth, Environmental and Material sciences.

This study aims at examining a novel insight to characterize bentonites to find out the mineralogical and physicochemical properties of irradiated Na-bentonite clay samples.

Clay samples were packed in a closed Pyrex glass container. The bentonite clay samples were irradiated with gamma radiation from the ^{60}Co isotope under static conditions, within vacuum sealed quartz tubes at room temperature. The irradiated and unirradiated samples were characterized by FT-IR spectroscopy.

From the FTIR spectra, both of the samples show OH stretching vibrations in the Si-OH and Al-OH groups of the tetrahedral and octahedral sheets at 3693cm-1and 3622cm-1. Bands at 1115cm-1 and 1113 cm-1; 998 cm-1 and 1004 cm-1 were produced by the stretching mode of Si–O.

Many studies have been reported, trying to pin down the relations between acid strength and short-and long –range structural factors, such as Si-O-Al angles or Si-O, Al-O distances, flexibility of the frame-work and electrostatic potencial generated inside the cavities [2,4].

At present there are few researches done concerning the influence of radioactive irradiation on rock and soils, including clay deposits. Radiation stability of minerals usually reduces through quartz to aluminosilicates: quartz - microcline – kaolin – hydromica -montmorillonites.

According to the statements of the theory of radiation damages in a solid body, crystalline structure of minerals in changed owing to interaction among radiating particles and mineral constituent elements, which are disturbed from equilibrium condition at the points of the lattice and may cause the displacement of other elements. Such processes lead to crystalline structure disordering, vacancies making and forming defects on the micro-level, finally all these phenomena cause the change of mineral properties owing to their amorphization special investigations have shown that amorphization of quartz, which is one of the minerals existing in clay. When clay is exposed to radiation, it can either act as a highly effective radiation-shielding material or undergo structural alterations depending on the radiation type, dose, and duration.

The surface modification of clay minerals especially by gamma-rays, which occurs due to defects, could improve markedly their surface, physical and chemical properties so the modified bentonite clay could be applied as catalysts, adsorbents and so on [2,4,5].

The modification of bentonite clay from Alpoid deposit by gamma-rays creates future possible perspectives. In works [3,5] were shown that irradiated Na-bentonite clay plays key role for aromatization and isomerization reactions of hydrocarbons.

Nature of radiation-induced defects in clay minerals was discussed. During electronic excitations related to ionizing radiation, radiation-induced point defects form from neutral precursors. There is an upper limit in the concentration of the defects that can be produced, a saturation being attained because of the recombination of electron or hole centers [6].

The studies performed by reflection – absorption IR spectroscopy show the modification of Na-bentonite clay by γ-rays. The modified clays could be used as catalyst for aromatization and isomerization processes. This method is low-cost and environmental – friendly.

References:

1. Th.Allard, E.Balan, G.Calas, C.Fourdrin, E.Morichon, S.Sorieul. Radiation-induced defects in clay minerals: A review. Nuclear Instruments and Methods in Physics Research Section B: Beam Interactions with Materials and Atoms.Volume 277, 15 April 2012, P. 112-120
2. M. K. Ismayilova, Effects of gamma-irradiation on nanostructured Na-bentonite silicate layers at room temperature, Probl. At. Sci. Technol., 2021, 135, 51, DOI: 10.46813/2021-135- 051.
3. M.K.Ismayilova, I.I.Mustafayev, R.F.Khankishiyeva [et al.] Gamma radiation–induced molecular transformation of hydrocarbons in the presence of nanostructured sodium bentonite clay // RSC Advances. - London: -2025. Vol.15, p. 40299-40310. DOI: 10.1039/d5ra05244k rsc.li/rsc-advances https://doi.org/10.1039/D5RA05244K.
4. M.K.Ismayilova, I.I.Mustafayev, S.Z. Melikova, F.N.Nurmammadova and M.H.Aliyeva, The studies on dehydration reaction mechanism of irradiated solid acid – nanostructured sodium - bentonite clay, J. Phys. Chem. Sol., 2024, 25(2), 362–367, DOI: 10.15330/pcss.25.2.362-367.

5. M.K.Ismayilova, I.I.Mustafayev, S.Z.Melikova, F.N.Nurmammadova and M.H.Aliyeva, Radiation - induced isomerization reaction mechanism of hydrocarbons on the surface of solid acid, J. Phys. Chem.Sol., 2023, 24(3), 460–466, DOI: 10.15330/pcss.24.3.460- 466.
6. Th.Allard, G.Calas. Radiation effects on clay mineral properties. Applied Clay Science Volume 43, Issue 2, February 2009, Pages 143-149. https://doi.org/10.1016/j.clay.2008.07.032.

PROSPECTS FOR USING CARBON NANOTUBES FOR MODIFICATION OF TELLURIDE GLASS-LIKE CERAMICS

Kozlovskiy A.L.[1,2], Tleulessova I.K.[2], Kenzhina I.E.[1,3]
[1]*Institute of Nuclear Physics, Almaty, Kazakhstan*
[2]*L.N.Gumilyov Eurasian National University, Astana, Kazakhstan*
[3]*Satbayev University, Almaty, Kazakhstan*

Multicomponent glass-like ceramics or glasses combining various oxide compounds of heavy and light elements are considered one of the most promising classes of materials for replacing traditional shielding materials. The basic concept behind the creation of such materials is based on the ability to specifically control their structural and functional properties by selecting various components and varying their ratios. Among the various multicomponent ceramics, telluride glass-like ceramics or amorphous glasses based on tellurium dioxide have recently become prominent. However, despite the numerous advantages of multicomponent glass-like ceramics as shielding materials, their widespread practical application is limited by a number of factors. One of the key challenges of these types of materials is their low mechanical strength and susceptibility to cracking under mechanical stress, as well as exposure to high temperatures typical of operation in extreme conditions. These effects, combined with the degradation of structural features due to localized disorder, impose certain limitations on their applications and service life. In this regard, one of the promising areas for the development of shielding material manufacturing technologies based on multicomponent glass-like ceramics or amorphous glasses is the exploration of the potential for using reinforcing additives to increase resistance and mechanical strength.

Carbon nanostructures, particularly nanotubes or nanodiamonds, are considered among the most promising materials in this area. The addition of these nanostructures not only increases mechanical strength and crack resistance, but also enhances structural stability by redistributing internal structural stresses, forming interphase boundaries, and altering density by reducing porosity. The conducted studies revealed patterns in the influence of carbon nanotube concentration on the mechanical properties of multicomponent $TeO_2 – WO_3 – Bi_2O_3 – SiO_2 – MoO_3$ ceramics. These patterns include the existence of an optimal reinforcing additive concentration (0.05 wt. %), which provides the maximum reinforcing effect, ensuring maximum strengthening by redistributing mechanical stress, inhibiting the propagation of microcracks, and increasing resistance to localized failure under mechanical loads. It was shown that increasing the carbon nanotube content above the optimal value is accompanied by agglomeration of the reinforcing phase, a decrease in the efficiency of mechanical load transfer, the formation of stress concentrators, and a reduction in the strengthening effect.

COMPARATIVE RAMAN SPECTROSCOPIC INVESTIGATION OF $CuTlSe_2$ AND $CuTlS_2$ CRYSTALS UNDER γ-IRRADIATION

Mamishova R.M.
Institute of Radiation Problems, Ministry of Science and Education of the Republic of Azerbaijan, Baku, Azerbaijan

Raman spectroscopy was used to investigate the vibrational properties and radiation-induced structural modifications of ternary Cu–Tl–X (X = Se, S) chalcogenide single crystals. The Raman spectra of $CuTlSe_2$ and $CuTlS_2$ exhibit well-defined phonon modes associated with lattice vibrations and metal–chalcogen bonding. For $CuTlSe_2$, characteristic bands are observed near 134, 333, 415–436 and 643 cm^{-1}, while $CuTlS_2$ shows bands near 138, 261–322, 433–471 and 638 cm^{-1}. The systematic shift of Raman modes toward lower wavenumbers upon replacing sulfur with the heavier selenium atom is attributed to the increased reduced mass and softer, more polarizable Cu–Se bonds. γ-Irradiation at a dose of 10 kGy produces pronounced changes in the Raman response, including intensity attenuation and peak broadening, indicating enhanced phonon–defect scattering. The radiation effect is considerably stronger in $CuTlS_2$, whereas $CuTlSe_2$ preserves its characteristic Raman features more effectively. The results indicate a higher resistance of $CuTlSe_2$ to radiation-induced disorder and demonstrate the importance of atomic mass, bonding characteristics, lattice flexibility and defect-induced phonon scattering in determining the vibrational stability of these materials.

Keywords: $CuTlSe_2$; $CuTlS_2$; Raman spectroscopy; γ-irradiation; phonons; radiation-induced defects; chalcogenides.

Ternary chalcogenide crystals based on Cu, Tl and chalcogen elements are promising materials for investigations of structure–property relationships because their vibrational response is highly sensitive to chemical bonding, lattice symmetry and structural disorder. Raman scattering provides direct information on lattice dynamics through the interaction of incident photons with quantized phonon modes. The positions, intensities and linewidths of Raman bands are therefore useful indicators of local bonding environments, crystallinity and defect-induced changes in the lattice. In the present work, the Raman spectra of $CuTlSe_2$ and $CuTlS_2$ single crystals are comparatively analyzed before and after γ-irradiation.

The Raman spectrum of $CuTlSe_2$ contains prominent bands at approximately 134, 333, 415–436 and 643 cm^{-1}. The low-frequency feature near 134 cm^{-1} is associated with collective lattice vibrations involving Tl–Se and Cu–Se atoms. The band around 333 cm^{-1} is assigned to symmetric Cu–Se stretching, whereas the 415–436 cm^{-1} region originates from mixed Cu–Se/Tl–Se bending and stretching vibrations. The relatively intense band near 643 cm^{-1} corresponds to higher-energy metal–Se vibrations. Weak features at approximately 953–975 and 1332 cm^{-1} are attributed to second-order and multiphonon Raman processes.

$CuTlS_2$ exhibits characteristic Raman bands near 138, 261–322, 433–471 and 638 cm^{-1}. The low-frequency band is related to lattice vibrations involving Tl–S and Cu–S bonds. The bands in the 261–322 cm^{-1} region are associated with Cu–S stretching vibrations, while the 433–471 cm^{-1} features correspond to S–metal bending and symmetric stretching modes. The high-frequency band near 638 cm^{-1} is assigned to a strong Cu–S vibrational mode. A weak feature around 957 cm^{-1} is attributed to second-order Raman scattering.

A systematic red-shift of the vibrational bands is observed when sulfur is replaced by selenium. This behavior is consistent with mass-dependent lattice dynamics: the larger atomic mass of selenium increases the reduced mass of the vibrating system and consequently lowers phonon

frequencies. In addition, the greater polarizability and lower bond stiffness of Cu–Se bonds contribute to phonon softening. Thus, the Raman data demonstrate the strong influence of chalcogen substitution on lattice dynamics.

γ-Irradiation at 10 kGy modifies the Raman spectra of both crystals, indicating the formation of radiation-induced defects such as vacancies, interstitial atoms and locally distorted coordination environments. These defects break the translational symmetry of the lattice and create additional phonon-scattering centers. Consequently, Raman peak intensities decrease and linewidths increase, reflecting shorter phonon lifetimes and reduced vibrational coherence. Irradiation can also enhance lattice anharmonicity and phonon–phonon interactions, contributing to additional phonon damping.

The radiation response of the two crystals is distinctly different. In $CuTlSe_2$, γ-irradiation produces a moderate reduction in Raman intensity and slight peak broadening, while the principal vibrational features remain comparatively well preserved. This behavior indicates partial disruption of long-range order without severe degradation of the layered structure. In $CuTlS_2$, the irradiation-induced changes are substantially stronger: Raman intensities decrease markedly and broad spectral features are suppressed, suggesting a higher concentration of radiation-induced defects and a greater tendency toward local structural disorder. The comparative behavior indicates that $CuTlSe_2$ possesses higher radiation tolerance than $CuTlS_2$ under the investigated conditions.

Raman spectroscopy confirms the characteristic vibrational structures of $CuTlSe_2$ and $CuTlS_2$ and reveals a clear dependence of phonon frequencies on the chalcogen atomic mass and metal–chalcogen bonding. Replacement of S by Se shifts the Raman modes toward lower wavenumbers. γ-Irradiation at 10 kGy enhances phonon–defect scattering and phonon damping in both crystals, but the effect is substantially more pronounced in $CuTlS_2$. The better preservation of Raman features in $CuTlSe_2$ demonstrates its comparatively higher resistance to radiation-induced structural disorder. These results emphasize the potential of $CuTlSe_2$ as a more radiation-tolerant ternary chalcogenide for applications requiring stability in radiation-rich environments.

EFFECT OF GAMMA IRRADIATION ON THE SPECTRAL CHARACTERISTICS OF PAINT COATINGS

Melikova S., Dadashov I.
Academy of the Ministry of Emergency Situations of the Republic of Azerbaijan, Baku, Azerbaijan

The investigation of radiation resistance and structural-chemical transformations of polymeric paint coatings under ionizing radiation represents a highly relevant direction in modern materials science. In this study, Fourier-transform infrared spectroscopy (FTIR) was employed to analyze the spectral characteristics of interior and exterior (facade) paint samples subjected to gamma irradiation at doses of 300, 500, and 1000 kGy. Based on the obtained spectroscopic data, a comparative assessment was conducted regarding the crosslinking and degradation processes occurring within the polymer matrix.

In modern industries, including radiation materials science, nuclear power, and the aerospace sector, polymeric paint coatings are exposed to continuous extreme environmental factors. High-energy ionizing radiation occupies a critical position among these stressors. Evaluating the radiation resistance of protective and decorative coatings is a task of paramount importance, as radiation-

induced degradation of the polymer matrix compromises the physical, mechanical, adhesive, and protective properties of materials, thereby shortening the service life of facilities.

Under high doses of gamma radiation, two competing radiation-chemical processes occur simultaneously within the polymer structure: crosslinking (formation of a three-dimensional spatial network) and scission/degradation (cleavage of the main macromolecular chains resulting in low-molecular-weight fragments). The predominance of either mechanism depends not only on the absorbed radiation dose, but also on the chemical nature of the binder, as well as the presence of functional additives, pigments, and fillers.

A comparative analysis of the radiation stability of interior and exterior paints is of significant scientific and practical value. While interior coatings are primarily formulated for mild operating environments and feature a basic chemical composition, exterior paints are typically compounded with complex systems of light- and thermo-stabilizers, antioxidants, and durable inorganic pigments designed to withstand ultraviolet radiation and weathering. Determining the extent to which these modifying additives can inhibit radiation degradation under intense gamma radiation (spanning 300–1000 kGy) is an essential fundamental and applied challenge.

Fourier-transform infrared spectroscopy (FTIR) enables high-precision identification of subtle structural-chemical transformations occurring at the molecular level, including the accumulation dynamics of oxygen-containing functional groups (carbonyl C=O, hydroxyl -OH), transformations of multiple bonds, and alterations in intermolecular interactions. Consequently, spectroscopic monitoring of dose dependencies not only establishes the radiation stability threshold of functional paint systems, but also provides a scientific foundation for designing radiation-resistant polymer composites.

The objective of this research is to perform a comparative analysis of the spectral characteristics and radiation-chemical transformations occurring in interior and exterior paint matrices subjected to gamma irradiation doses of 300, 500, and 1000 kGy.

Fourier-transform infrared spectroscopy (FTIR) was utilized to monitor functional group transformations (carbonyl, hydroxyl, unsaturated bonds), absorption peak shifts, and variations in intensity.

Interior Coatings: At the initial irradiation stage, free radical generation takes place. Absorption bands corresponding to the main polymer chain retain their intensity, with primary radiation crosslinking being the predominant process. Broadening of absorption bands and an increase in their intensity are observed. Enhanced oxidation processes are detected, evidenced by increased absorption in regions characteristic of carbonyl (C=O) and hydroxyl (-OH) groups. At extreme doses, chain scission and degradation processes dominate the interior paint matrix. New low-intensity absorption peaks appear in the spectra, indicating the formation of low-molecular-weight oligomeric fractions or monomer evolution.

Exterior (Facade) Coatings: Owing to the inclusion of light- and thermo-stabilizers as well as specialized inorganic pigments, exterior paints exhibit high radiation resistance: This dose induces no substantial disruption of the spectral profile. The spectral pattern remains stable. Peak area analysis confirms the preservation of interfacial interactions between the filler and the polymer matrix. Minor indications of radiation-chemical degradation are observed; however, the polymer network retains its integrity to a significantly higher degree compared to interior counterparts.

Increasing the gamma radiation dose from 300 to 1000 kGy exerts a regular and deterministic influence on the spectral properties of the studied materials. Exterior paints, due to their effective stabilization systems, exhibit enhanced radiation resistance within the 500–1000 kGy range. Whereas a dose of 1000 kGy induces severe degradation of the polymer matrix in interior paints, exterior coatings retain their foundational structural network.

CHANGES IN THE SPECIFIC RESISTIVITY OF HDPE-BASED COMPOSITE MATERIALS WITH A CdS/ZnS PHOSPHOR FILLER UNDER GAMMA IRRADIATION

Melikova S.[1,2], Hajiyeva E.[3], Kerimova R.[4], Nasirova A.[4]
[1]*Academy of the Ministry of Emergency Situations of Azerbaijan, Baku, Azerbaijan*
[2]*Institute of Physics of Azerbaijan, Baku, Azerbaijan*
[3]*Institute of Geology of Azerbaijan, Baku, Azerbaijan*
[4]*Azerbaijan State Oil and Industry University, Baku, Azerbaijan*

Polymer compounds play a key role in the development of high-tech industries. Their functional capabilities are applied in mechanical engineering, microelectronics, and the aerospace industry. Furthermore, the physicochemical properties of polymers allow them to be used in the creation of devices ranging from pressure sensors and dosimeters to electret microphones and filtration systems, as well as in promising nanotechnological developments. The relevance of polymer composites is due to their ability to be modified. The introduction of dispersed fillers (20–25 μm) into the polymer matrix allows for targeted improvement of the strength, thermal, and electrical properties of the material, making such composites promising for modern industry. Modification of the supramolecular organization of polymer matrices and composite materials under the influence of ionizing radiation and the introduction of special additives is the main factor determining their final physicochemical and mechanical properties [1–5].

The physicomechanical and electret properties of a polymer are significantly affected by the ratio of its amorphous and crystalline phases. The structure of polymer composites is determined by both the intrinsic properties of the macromolecules and external factors. The addition of small doses of fillers, which act as crystallization centers, allows for targeted modification of the material. Depending on the nature of the filler, the rate of crystallization or curing, relaxation transition temperatures, and mechanical and electrical parameters of the composite vary. This study confirms the possibility of targeted control of the characteristics of polymer composites by selecting the type and dispersion of fillers, as well as optimizing crystallization conditions and radiation exposure. The introduction of fillers (including nanoparticles) promotes the formation of additional crystallization centers and localization of electrical charges. This effect allows for an increase in the surface density of electret charges to ~10^{-4} C/m² and an increase in their relaxation time (τ). Therefore, the creation of composites based on polyolefins with phosphor additives represents a promising area of radiation materials science.

The experiment established the dependence of the electrophysical properties of HDPE composites modified with CdS/ZnS on exposure to γ radiation. The results allow the following conclusions to be drawn.

1. It was found that the temperature minima of the specific volume resistance of HDPE and its composites with CdS/ZnS are caused by structural defects and the release of moisture adsorbed within them. Varying the filler concentration affects the density and type of these defects. In particular, at a filler concentration of 30–50 vol.%, the shift of the minima toward lower temperatures is explained by the formation of defects with reduced activation energy.

2. It was established that γ-irradiation stimulates chain degradation and cross-linking processes in the polymer matrix. At low doses, degradation predominates, causing a decrease in electrical resistance, whereas at high doses, cross-linking predominates, stabilizing this parameter. Composites with 30 vol.% CdS/ZnS are characterized by a highly homogeneous structure, which

ensures uniform energy absorption and stable electrical properties. At 50 vol.% filler, particle agglomeration occurs, which alters the electrical resistance of the composite and its behavior under radiation.

3. The study showed that the increase in the electrical conductivity of composite materials under γ-irradiation is caused by two main factors: the appearance of additional charge carriers and the restructuring of the trap system. The ability to flexibly tune material properties by varying the CdS/ZnS concentration and irradiation intensity opens up broad prospects for the use of these polyethylene composites in instrumentation, particularly in the development of radiation-resistant dosimetry systems and sensors.

References:

1. I.I. Mustafayev, S.Z. Melikova, E.G. Hajiyeva, R.J. Gasimov, M.A. Bayramov, N.I. Babayeva. Spectral Investigations of γ-Irradiated Polyethylene/CdS+ZnS Composite Films // Acta Physica Polonica A. 2023, v. 144, N 1, p. 35–37.
2. N.N. Gadzhieva, G.B. Ibragimov, G.B. Akhmedova, G.M. Ahmadov, M.V. Gojayeva, E.G. Hajiyeva. Effect of Gamma Irradiation on the Optical Properties of HDPE/GaAs Composite Films // Advanced Physical Research. 2026, v. 8, N 1, p. 102–110.
3. Mustafayev I.I., Melikova S.Z., Hajiyeva E.G. The effect of gamma irradiation on the dielectric properties of po lyethylene-based composites with the CdS-ZnS quasibinary system state. Journal “Physics and chemistry of solid state, 2024, vol.25, No. 4, p.700-703
4. M.M.Guliyev, M.N. Bayramov, N.Sh.Aliyev, R.S.Ismayilova, A.N. Nabiyeva-Mammadli. The frequency and dose dependence of the electrophysical properties of HDPE/ α-Fe3O4 nanocomposites modified by gamma irradiation. ISSN 1068-3755, Surf.Engen. and appl. Electrochem. 2026, v.62, No1, pp.95-103
5. M.K.Ismayilova, I.I.Mustafayev, S.Z.Melikova, F.N.Nurmammadova, M.H.Aliyeva. Radiation-Induced Isomerization Reaction Mechanism of Hydrocarbons on the Surface of Solid Acid // Physics and Chemistry of Solid State. 2023, v. 24, N 3, p. 460–466.

SPECTRALLY WEIGHTED ONE-PARTICLE COHERENCE IN THE ACTIVE FERMI-LEVEL SUBSPACE

Mukhtarov A.
Institute of Nuclear Physics, Uzbekistan Academy of Sciences, Tashkent, Uzbekistan

Near-Fermi states govern the low-energy response of a metal, but the density of states does not describe their orbital or spatial distribution. We construct an energy-filtered one-particle matrix in a Wannier subspace and derive descriptors of its intercell amplitude. Here *coherence* means nonlocal one-particle matrix amplitude, not pairing or a thermodynamic order parameter.

Let the Wannier Hamiltonian satisfy $H(\mathbf{k})U(\mathbf{k}) = U(\mathbf{k})\varepsilon(\mathbf{k})$. A Lorentzian filter of width Ω centered at E_F defines

$$w_{n\boldsymbol{k}} = \frac{\Omega^2}{(\varepsilon_{n\boldsymbol{k}} - E_F)^2 + \Omega^2}, \qquad P^F(k) = U(\boldsymbol{k}) diag\,(w_{n\boldsymbol{k}}) U^{\dagger}(\boldsymbol{k}) \qquad (1)$$

The matrix is Hermitian and positive semidefinite, but it is not generally idempotent. Its lattice blocks are

$$P^F(\boldsymbol{R}) = \frac{1}{N_k}\sum_{\boldsymbol{K}} e^{-i2\pi \boldsymbol{kR}}\, P^F(\boldsymbol{k}) \quad (2)$$

The construction combines energy resolution with density-matrix locality analysis [1,2]; Wannier interpolation supplies the localized representation and Fourier transform [3,4].

For each translation, $K_{\mathbf{R}} = \|P_{(F)}(\mathbf{R})\|_F$. Two direct descriptors are

$$C_F = \frac{\sum_{R\neq 0} K_R}{\sum_R K_R} \qquad \xi_F = \frac{\sum_{R\neq 0} |r_R| K_R}{\sum_{R\neq 0} K_R} \quad (3)$$

C_F is the fraction of block norm outside the home cell, whereas ξ_F is the first spatial moment of that off-cell distribution.

The block norms are invariant under a common unitary rotation of the retained orbitals, but not under an arbitrary k-dependent gauge change. Changing the disentangled subspace changes the matrix. Comparisons therefore require fixed orbital content, energy windows, Wannierization protocol, Ω, k mesh, and real-space cutoff. In an insulator, Lorentzian tails also make the residual weight sensitive to the position of E_F in the gap.

The first calculation used Quantum ESPRESSO and Wannier90 [4,6] for fcc Al with a = 4.05 Å, E_F = 7.8485 eV, Ω = 0.10 eV, and a uniform 24^3 k mesh. Hermiticity, positive semidefiniteness, Fourier symmetry, and the spectral sum rule were checked. Across the real-space cutoffs examined, ξ_F increased from 11.41 to 31.30 Å. Thus 31.30 Å is not an intrinsic Al value; it shows incomplete cutoff convergence. A result is reportable only after C_F and ξ_F stabilize under simultaneous enlargement of the real-space range and k mesh.

The descriptors separate the amount, mean range, and lattice distribution of near-Fermi intercell weight. The present Al result establishes the procedure and its dominant convergence requirement, not a material coherence length or many-body phase coherence.

References:

1. W. Kohn, Phys. Rev. Lett. 76, 3168 (1996).
2. S. Ismail-Beigi and T. A. Arias, Phys. Rev. Lett. 82, 2127 (1999).
3. N. Marzari et al., Rev. Mod. Phys. 84, 1419 (2012).
A. A. Mostofi et al., Comput. Phys. Commun. 185, 2309 (2014).
4. M. Fiedler, Czechoslovak Math. J. 23, 298 (1973).
5. P. Giannozzi et al., J. Phys.: Condens. Matter 29, 465901 (2017).

EFFECT OF GAMMA IRRADIATION ON THE OPTICAL PROPERTIES OF a-GaSe THIN FILMS

Madatov R.S.[1,2], Nurmammadova F.N.[3,1]

[1]Institute of Physics Ministry of Science and Education of the Republic of Azerbaijan, Baku, Azerbaijan

[2]National Aviation Academy, Baku, Azerbaijan

[3]Baku Engineering University, Baku, Azerbaijan

In recent years, the layered semiconductor GaSe has been extensively investigated as a functional material for optoelectronics, photodetection, nonlinear optics, radiation-sensitive sensors,

and computer technologies. Among such materials, gallium selenide (GaSe) is distinguished by its wide band gap, high optical transparency, and strong excitonic effects. Recent studies have shown that ionizing radiation can be used to deliberately modify the optical absorption and photosensitivity of GaSe thin films, thereby enabling the development of next-generation optical sensors and photonic devices [1,3].

For this purpose, the transmission spectra, optical absorption, and variation of the forbidden energy gap of gamma-irradiated amorphous GaSe thin films were investigated in this work. Recent studies have shown that the control of optical and electrical properties in GaSe and other chalcogenide compounds is closely related to the study of radiation effects on these materials. Such materials are considered promising for photodetectors, optical memory elements, memristive systems, and radiation-tolerant components. In this context, the investigation of the optical behavior of amorphous a-GaSe thin films under gamma irradiation is of particular importance. During irradiation, the formation of defects, the reorganization of broken bonds, and the emergence of local crystalline regions directly affect the transmission and absorption spectra of the material. Similar effects have also been observed in other chalcogenide systems. For example, gamma irradiation in amorphous Ge–Se and other Se-based thin films has been reported to cause narrowing of the forbidden gap, the growth of the Urbach tail, and changes in the optical response. Therefore, the study of the effect of gamma quanta on the optical properties of a-GaSe films is relevant from both fundamental and applied perspectives. Figure 1 shows the transmission spectra T∼f(λ)) of the a-GaSe thin film before and after irradiation.

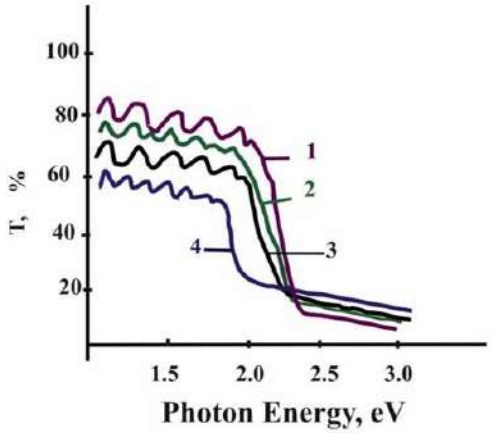

Figure 1. Transmission spectra of the a-GaSe film before and after irradiation:
1 - D=0; 2 - D=20 kGy; 3 - D=250 kGy; 4 - D=500 kGy

As can be seen from curve 1 in Figure 1, sharp interference fringes with a gradually decreasing amplitude are observed in the 1.0-2.0 eV energy range of the spectrum prior to irradiation, which indicates the uniformity of the film surface. With a further increase in photon energy (2.0-2.4 eV) a non-sharp fundamental absorption band is observed in the spectrum. In the photon energy range of 1.0-3.0 eV, the transmittance varies between 30 % and 80 %. The reflectance in the energy range of 1.0-3.0 eV was calculated using the method from [3] and was found to be R≈0,18. Upon γ-quantum irradiation (D=20 kQy, cur.2), although the transmittance in the transparency region (1,5-2,4eV) decreases partially, the character of the curve is preserved. Upon γ-irradiation (D = 20 kGy; curve 2), although the transmission coefficient partially decreases in the transparency region (1.5–2.4 eV), the overall character of the curve is preserved. At higher irradiation doses (D = 250–500 kGy, curves 3–4), the interference amplitude gradually decreases, and a sharply decreasing fundamental absorption band, shifted toward lower energy values, is

observed in the spectrum within the 1.8–2.1 eV energy range. A comparison of the spectra before and after irradiation shows that the sharp decrease in the transmission coefficient in the 1.5–2.0 eV spectral region, together with the shift of the fundamental absorption band toward lower energies at high irradiation doses, results from the formation of complex radiation-induced defects.

The spectral behavior observed in Fig. 1 indicates that gamma irradiation alters not only the structural state but also the optical stability of a-GaSe layers. In this respect, the dose-dependent change in the absorption edge and transmission spectrum of the material is an important indicator for evaluating its potential for radiation-sensitive optoelectronic and memory-oriented applications. At the same time, the obtained results demonstrate that it is possible to control the optical parameters of a-GaSe layers through defect engineering, which is important for developing new-generation functional materials intended for future photodetectors, optical sensors, and computer technologies [4].

Thus, the effect of gamma-quanta on the optical properties of amorphous a-GaSe thin films is clearly manifested through the spectral changes shown in Fig. 1. The decrease in interference amplitude, the shift of the absorption edge, and the changes associated with radiation defects indicate that the functional characteristics of the material can be controlled as a function of the irradiation dose. These results confirm that a-GaSe thin films are a promising material for radiation-resistant optoelectronic devices, optical sensors, and computer technologies.

References:

1. J.D. Maimon; K.K. Hunt; L.Burcin; J.Rodgers. Chalcogenide memory arrays: characterization and radiation effects. Published in: IEEE Transactions on Nuclear Science (Volume: 50, Issue: 6, December 2003).p-1878-1884, https://doi.org/10.1109/TNS.2003.821377
2. Shaveta Sharma, Rita Sharma, Praveen Kumar, R.Thangaraj, K.Asokan, M.Mian. Effect of gamma irradiation on structure and photoconductivity of amorphous Sb30Se70 chalcogenide films**.** journal of non-crystalline solids,volume 530, Article: 119807 https://doi.org/10.1016/j.jnoncrysol.2019.119807
3. Neumann H., Hörig W., Jones P.A., Lippold G., Sobotta H., Tomlinson R.D., Yakushev M.V. Comparative optical absorption and photoreflectance study of n-type CuInSe2 single crystals // Cryst. Res. Technol. – 1994. – Vol. 29. – P. 719. https://doi.org/10.1002/crat.2170290527
4. Sun, S., Wang, X., Jiang, Y. *et al.* High-throughput screening to identify two-dimensional layered phase-change chalcogenides for embedded memory applications. *npj Comput Mater* **10**, 189 (2024). https://doi.org/10.1038/s41524-024-01387-3

CURRENT–VOLTAGE CHARACTERISTICS OF GOLD-DOPED n-Si AT DIFFERENT TEMPERATURES AND EVALUATION FOR STRAIN-SENSITIVE ELEMENTS

Rafikov A.K.[1], Sulaymonov A.A.[1], Makhmudov Sh.A.[1], Abdukarimov A.A.[2], Suvanov A.Kh.[2], Yoqubjonov J.H.[2], Nematullayev J.R.[2]

[1]Institute of Nuclear Physics, Uzbekistan Academy of Sciences,Tashkent, Uzbekistan

[2]Namangan State Technical University, Namangan, Uzbekistan

The piezoresistive effect in silicon is determined by changes in its energy band structure, charge carrier concentration, and mobility under mechanical stress [1].

Gold is a metallic impurity that forms electrically active deep energy levels in silicon. In Au-doped Si, an acceptor level near (E_C-0.54) eV and a donor level near (E_V+0.35) eV have been reported [2]. In n-Si, acceptor-type Au centers can compensate phosphorus donors, thereby reducing the free-electron concentration and increasing the resistivity. The diffusion of gold in silicon is not fully described by a simple Fickian profile: Au atoms diffuse in a rapidly migrating interstitial state and, with the participation of intrinsic point defects in silicon, transform into an electrically active substitutional state. The aim of this work is to investigate the electrophysical parameters of BKEF-80 n-Si samples doped with gold at different temperatures and to study the possibility of using the obtained materials in strain-sensitive elements. The obtained results showed that the temperature range of 900–1000 °C can be considered an optimal technological range for introducing Au into BKEF-80 n-Si. At these temperatures, the necessary conditions are created for the diffusion of Au atoms throughout the sample volume and their transition to an electrically active substitutional state.

The negative sign of the Hall coefficient indicates that, even after thermal treatment, electrons remain the majority charge carriers in all samples, i.e., n-type conductivity is preserved (Table 1). When the diffusion temperature was increased from 900 °C to 1000 °C (average cooling rate of 300 °C/min), the electron concentration decreased from $4{,}54\cdot10^{13}$ to $3{,}79\cdot10^{11}$ cm^{-3}, while the resistivity increased from 109 to $6{,}85\cdot10^{4}$ Ω·cm.

Table 1. Electrophysical parameters of gold-doped silicon.

No	Diffusion temperature, °C	Heating time, min	ρ, Om·cm	N, cm^{-3}	μ, $cm^2/(V\cdot s)$
1	900	300	109	$-4{,}54\cdot10^{13}$	1604
2	950	300	2200	$-6{,}55\cdot10^{12}$	733
3	1000	300	68497	$-3{,}79\cdot10^{11}$	670

The observed changes in the electrophysical parameters were also clearly manifested in the current–voltage characteristics of the samples.

The I–V results showed that, in the control n-Si sample, the deviation of the current–voltage dependence from the quasi-linear region begins at approximately 2.4 V. In the gold-doped samples, the onset voltage of this deviation shifted from 6.5 to 9.9 V in accordance with the increase in resistivity (Fig. 1). This is explained by a decrease in the free-electron concentration from $4{,}54\cdot10^{13}$ to $3{,}79\cdot10^{11}$ cm^{-3} and an increase in resistivity from 109 to $6.85\cdot10^{4}$ Ω·cm as a result of compensation of phosphorus donors by deep acceptor-type Au centers in n-Si.

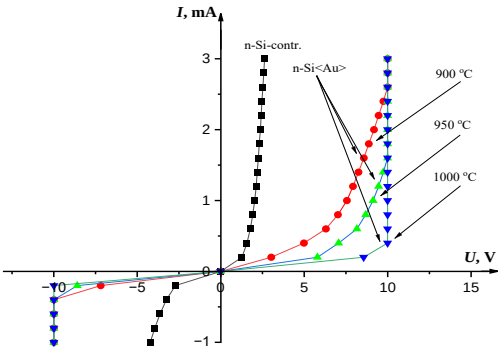

Figure 1. Current–voltage characteristics of n-Si<Au> samples.

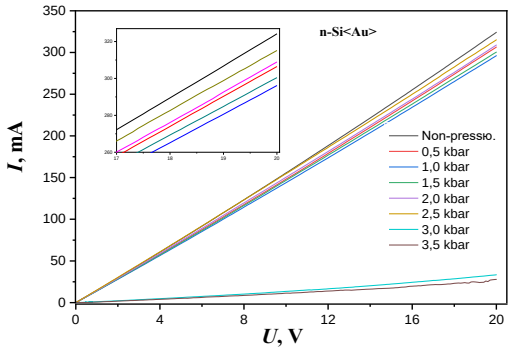

Figure 2. Variation of the current–voltage characteristic of n-Si<Au> under applied pressure.

In the BKEF-80 n-Si sample doped with gold by diffusion at 900 °C for 5 h and rapidly cooled, the effect of pressure on electrical resistance was recorded (Fig. 2). Each I–V characteristic was obtained after the pressure had stabilized. While the curves in the range of 0–2.5 kbar were located close to each other, a noticeably different electrical response was observed at 3 and 3.5 kbar. The nearly linear character of the I–V characteristics at the specified pressures makes it possible to compare the sample resistance using the *U/I* ratio. In this case, the linearity of the I–V characteristics and the pressure dependence of resistance are separate characteristics, while pressure calibration is performed on the basis of the R(P) relationship. In the BKEF-80 n-Si sample doped with gold by diffusion at 900 °C for 5 h and rapidly cooled, a change in electrical resistance under pressure was recorded, with a particularly noticeable electrical response observed at 3 and 3.5 kbar. In the analyzed dissertations, pressure-dependent I–V characteristics for BKEF-80 samples prepared under exactly this technological regime were not presented [2, 3]. The obtained results demonstrate the possibility of developing a resistive sensing element based on this material for detecting pressure through changes in resistance.

In BKEF-80 silicon samples doped with gold at 900–1000 °C for 5 h, n-type conductivity was preserved. In the sample prepared at 900°C, the I-V characteristics obtained after pressure stabilization showed a noticeable change in resistance at 3 and 3.5 kbar. This result supports the possibility of using n-Si<Au> as a pressure-sensitive resistive element.

References:

1. Smith C.S. Piezoresistance Effect in Germanium and Silicon // Physical Review. 1954. Vol. 94. P. 42–49. DOI: 10.1103/PhysRev.94.42.
2. Tursunov I.G. Strain-Induced Phenomena in Compensated Silicon and Surface-Barrier Diode Structures Based on It: Doctoral Dissertation in Physical and Mathematical Sciences. Tashkent, 2018.
3. Khamidov R.Kh. Strain-Thermal Effects in Silicon with Deep Levels and Structures Based on It: Doctoral Dissertation in Physical and Mathematical Sciences. Tashkent, 2023.

EFFECT OF γ-IRRADIATION ON THE ABSORPTION SPECTRA OF CU-INTERCALATED GaSe LAYERED CRYSTALS

Sadigli L.E.
[1]*Institute of Physics, Ministry of Science and Education of the Republic of Azerbaijan, Baku Azerbaijan*

2D layered semiconductors are among the most promising materials for nanoelectronics and optoelectronics due to their weak interlayer Van der Waals bonding, strong anisotropy, and tunable energy band structures. As a prominent member of the $A^{III}B^{VI}$ family, GaSe possesses a wide band gap, high photosensitivity, and stable exciton transitions observed at room temperature [1–3].

Intercalation serves as a universal engineering approach to modify the electronic structure of layered crystals without disrupting the integrity of the crystal lattice. Introducing atoms or molecules into the Van der Waals gaps enables intentional tuning of the Fermi level position, carrier concentration, and can even induce semiconductor–metal phase transitions. Specifically, the insertion of highly diffusive Cu atoms and the formation of gallium vacancies generate new donor-type local levels in GaSe, narrowing the band gap and modifying the character of optical transitions [4–7].

On the other hand, interaction with high-energy gamma rays leads to the creation of radiation defects (vacancies, interstitial atoms, and complex defect complexes) in the crystal lattice. These defects induce local energy levels in the band gap, alter carrier trapping and recombination processes, and modify the optical absorption edge [8, 9].

The primary objective of this study is to comparatively investigate the effect of various doses (1, 5, 10, 15 kGy) of γ-irradiation on the optical absorption spectra of p-GaSe single crystals electrochemically intercalated with Cu atoms, and to determine the mechanisms of exciton–defect interactions as well as the formed local energy levels.

Single crystals of GaSe were grown using the Bridgman–Stockbarger method. The obtained samples possess a β-modification hexagonal structure (space group $P6_3/mmc$) with lattice parameters a = 3.755 ± 0.01 A and c = 15.94 ± 0.01 A. Intercalation was performed electrochemically from an aqueous solution of $CuSO_4 \cdot 5\ H_2O$ at a cathodic position (T = 100 ± 0.1℃, applied voltage U = 1 V, duration t = 1 h, inter-electrode distance d = 2.5 cm). The intercalation degree was calculated as $x \approx 0.26$ ($Cu_{0.26}GaSe$), and EDS analysis confirmed the presence of 22.32 wt.% Cu in the intercalated samples [9]. Optical absorption spectra were recorded in the 300-800 nm wavelength range using a Varian Cary 50 UV–Visible spectrophotometer.

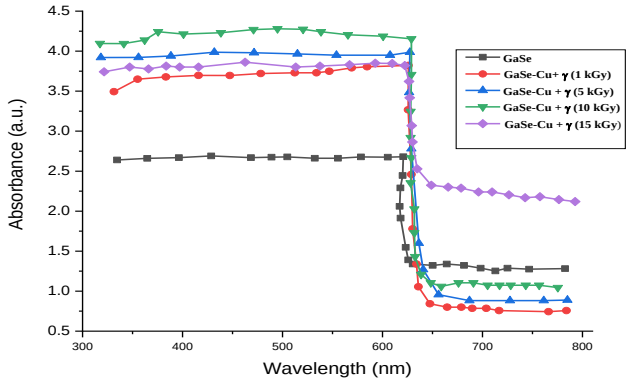

Figure. Wavelength dependence of optical absorption for GaSe crystal intercalated with Cu_x atoms (x = 0.26)

The figure illustrates the absorption spectra of GaSe-Cu and samples irradiated with gamma quanta at doses of 1, 5, 10 and 15 kGy. As seen from the absorption spectra, the intercalation of Cu atoms between the GaSe layers leads to an increase in optical absorption in the visible spectral region. This is attributed to the creation of additional local energy levels in the crystal as a result of Cu intercalation and the enhanced intensity of light-induced electronic transitions. Gamma irradiation at a dose of 1 kGy does not significantly alter this state, showing only a slight decrease in the absorption spectrum, which can be explained by the partial redistribution of existing defect centers at low radiation doses. However, when the irradiation dose is increased to 15 kGy, a further increase in absorption is observed. This behavior can be associated with an increased probability of light absorption due to the generation of additional structural defects and local energy states under high-dose radiation exposure. Thus, Cu intercalation followed by gamma irradiation modifies the optical absorption properties of GaSe crystals, causing them to exhibit higher absorption in the visible region.

References:

1. H. Du, Q.Chen, T. Liu, Y. He, Y. Jin. Research progress of nonlinear crystal and optoelectronic material GaSe // Materials Reports (2022). https://doi.org/10.11896/cldb.20080191
2. M. İşık, N. Gasanly. Spectroscopic ellipsometry-based linear and nonlinear optical characterization of GaSe crystals for optoelectronic applications // Journal of Electronic materials (2025). https://doi.org/10.1007/s11664-025-12278-8
3. N. Youbao, W. Haixin, H. Changbao, M. Mingsheng, W. Zhenyou, C. Xudong. Growth and quality of gallium selenide (GaSe) crystals // Journal of Crystal Growth, 381, 10-14 (2013). https://doi.org/10.1016/j.jcrysgro.2013.06.030
4. J. Zhou, Z. Lin, H. Ren, X. Duan, I. Shakir, Y.Huang, X. Duan. Layered intercalation materials // Advanced Materials, 33, 25 (2021). https://doi.org/10.1002/adma.202004557
5. R. Liu, C.Wang, Y. Li, Y. Xie, Q. Chen, Z. Chen, Q. Liu, Intercalating copper into layered TaS_2 Van der Waals gaps, RSC Adv., 7, 46699-46703 (2017). https://doi.org/10.1039/C7RA08630J
6. Z. Muhammad, K. Mu, H. Lv, C. Wu, Z. Rehman, M. Habib, Z. Sun, X. Wu, L. Song. Electron doping induced semiconductor to metal transitions in $ZrSe_2$ layers via copper atomic intercalation // Nano Research, 11, 4914–4922 (2018).
7. R.B. Ardakani. Theoretical insights into band gap tuning through Cu doping and Ga vacancy in GaSe monolayer: a first-principles perspective // Journal of Electronic materials, (2024). https://doi.org/10.1007/s11664-024-10977-2

8. R.S. Madatov, L.E. Sadigli, R.M. Mamishova, A.Sh. Khaligazadeh. Investigation of the optical properties of metal ion-intercalated GaSe semiconductor monocrystals // East European Journal of Physics (2025). https://doi.org/10.26565/2312-4334-2025-4-41
9. R.S. Madatov, R.M. Mamishova, L.E. Sadigli, G.I. Muradova. Structural, morphological and compositional modifications in Cu - intercalated GaSe crystals under gamma irradiation. Modern Physics B, (2026).

MODERN NUCLEAR TECHNOLOGIES IN THE DIAGNOSIS AND TREATMENT OF ONCOLOGICAL DISEASES

Ergeshbaev A.Zh., Sadyrova M.M., Kadenova B.A.
Osh State University, Osh, Kyrgyzstan

Relevance. Oncological diseases remain one of the most pressing problems in modern medicine. One of the key factors for successful treatment is the early detection of tumor processes and accurate assessment of their extent. In this regard, nuclear medicine is becoming increasingly important due to its ability to combine highly accurate diagnosis with targeted effects on pathological lesions.

Objective of the study. To examine the current possibilities of using nuclear technologies in the diagnosis and treatment of oncological diseases and to identify promising areas for their further development.

Materials and methods. An analysis of scientific literature and current studies devoted to the use of radionuclide methods in oncology was carried out. The main diagnostic methods were considered, including positron emission tomography (PET), PET/CT, and single-photon emission computed tomography (SPECT), as well as modern approaches to radionuclide therapy.

Results. Nuclear technologies make it possible to obtain functional information about tissues and detect pathological changes at early stages of disease. PET/CT is widely used to detect tumor lesions, assess the extent of the disease, monitor treatment effectiveness, and identify recurrences. An important area is radionuclide therapy, in which a radiopharmaceutical is selectively delivered to target cells and produces a localized therapeutic effect. Of particular interest is theranostics, an approach that combines diagnosis and treatment based on the same molecular target. Its application contributes to the personalization of therapy and the selection of the most appropriate treatment strategy for an individual patient.

Conclusion. Modern nuclear technologies expand the possibilities for the diagnosis and treatment of oncological diseases. The development of radiopharmaceuticals, molecular imaging, and theranostic methods creates prospects for improving diagnostic accuracy and the effectiveness of personalized treatment.

Keywords: nuclear medicine, oncology, radionuclides, PET/CT, radionuclide therapy, radiopharmaceuticals, theranostics.

References:

1. Yunosova A. A. Modern Technologies of Nuclear Medicine in the Diagnosis and Therapy of Oncological Diseases. *Young Researcher of Don*. No. 2(29), 2021, pp. 71–75.
2. Yunosova A. A. Radionuclide Treatment Methods at the Present Stage. *ONCOLOGY.RU Journal.* Available at: oncology.ru/specialist/journal_oncology/archive/0408/045/.

3. Stoffels I., Poppel T., Boy C., et al. Radiological Surgery: Advantages of the New Portable γ-Camera (Sentinella) for Real-Time Intraoperative Imaging and Detection of Sentinel Lymph Nodes in Cutaneous Malignancies. *JEADV*, 2011, 6 p.
4. The Only Integrated System for Radio-Guided Surgery with Real-Time Imaging. America Oncovision, Inc., 30 Newbury St., 3rd Floor, Boston. Available at: oncovision.com/mammi/ (accessed December 14, 2020).
5. Radioguided Surgery. Oncomed-solutions. Available at: oncomedsolutions.com/solutions_radioguided_surgery.html (accessed December 15, 2020).

RECOMBINATION EMISSION NEAR THE SURFACE OF SEMICONDUCTOR MICROCRYSTALS

Yuldashev N.Kh.[1], Mirzaev V.T.[1], Sabirov S.S.[1], Sulaymonov Kh.M.[1], Yulchiev I.I.[1], Shamirzaev T.S.[2]
[1]Fergana State Technical University, Fergana, Uzbekistan
[2]Institute of Semiconductor Physics, Russian Academy of Sciences,Novosibirsk, Russia

The mechanisms governing recombination emission in semiconductor micro- and nanocrystals are of both theoretical and practical interest, particularly for the development of new coherent light sources and photovoltaic applications [1–5]. The properties of these systems depend strongly on their geometrical dimensions. However, the role of the surface and the near-surface space-charge region in shaping the emission spectra of microcrystals remains insufficiently understood. In our previous study [3], we showed that, unlike single crystals, polycrystals, and individual microcrystals, thin polycrystalline films ($d_{cr} \leq 1\ \mu m$) exhibit neither excitonic nor donor–acceptor pair emission lines. Instead, new emission lines appear at photon energies $h\nu > E_g$, giving rise to the so-called “superhot luminescence” effect. This effect is attributed to size quantization in the near-surface region and arises from optical transitions of electrons from quantized levels in the potential well of the space-charge region (SCR) to quasi-continuous valence-band states. In this contribution, we discuss new mechanisms shaping the emission spectra of the near-surface layers of microcrystals, accounting for the quantum Franz–Keldysh effect and the possible formation of electron–hole or exciton gases or liquids in the SCR. We also consider the possibility of low-dimensional effects in microcrystals whose characteristic dimensions are comparable to the Debye screening length.

Figure 1 shows the near-surface band-edge photoluminescence (PL) spectra of CdTe films composed of microcrystals on a glass substrate. A distinct doublet is observed under laser excitation at 520 and 405 nm, whereas excitation at $\lambda = 637$ nm produces a characteristic triplet with overlapping spectral lines. As the excitation power increases, the intensity of the short-wavelength band increases monotonically, while that of the long-wavelength band initially increases and then decreases. At high excitation powers, the bands shift toward longer wavelengths (Fig. 2).

We further discuss how the near-surface band-edge PL spectra depend on film thickness. These effects include the appearance of new emission bands near the fundamental absorption edge ($E_g = 1.6$ eV) and at longer wavelengths. The long-wavelength bands are attributed to Coulomb interactions between photoexcited electrons and holes separated by the strong electrostatic field near

the microcrystal surface. The temperature dependence of the near-surface band-edge PL spectra of CdTe films will also be considered.

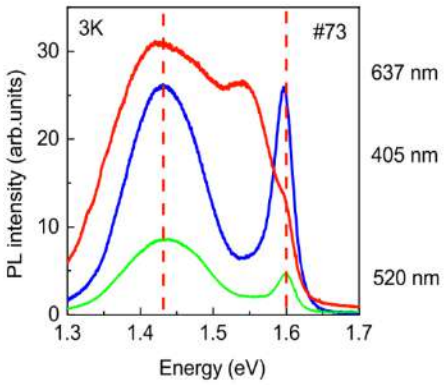

Figure 1. Near-surface band-edge photoluminescence spectra of 1.7-μm-thick polycrystalline CdTe films under excitation by lasers with wavelengths λ=637, 526, and 405 nm at T=3 K.

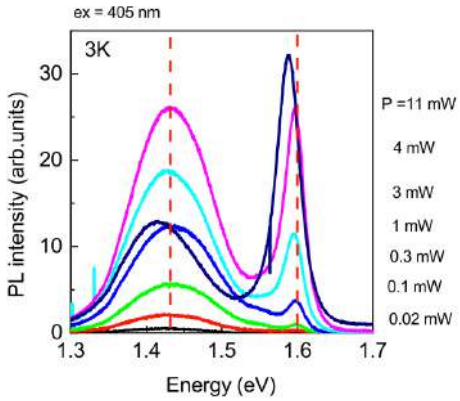

Figure 2. Photoluminescence (PL) spectra of CdTe films at T=3 K under excitation by a 405 nm laser at different excitation powers.

Conclusion. Previously unreported band-edge and “superhot” emission bands have been observed in the near-surface band-edge PL spectra, at frequencies both below and above the fundamental absorption edge of CdTe. These emission lines are attributed to optical transitions of electrons from size-quantized energy levels in a near-surface quantum well to valence-band states, or to the quantum Franz–Keldysh effect and the possible formation of an electron–hole or exciton liquid.

References:

1. Ekimov, I. A. Kudryavtsev, et al. Journal of Luminescence 46, 83 (1990).
2. J. Nozik et al. Chemical Reviews 110, 6873 (2010).
3. V. Selkin and N. Kh. Yuldashev. Bulletin of the Russian Academy of Sciences: Physics 87, 771–775 (2023).
4. J. Akhmadaliev, O. M. Mamatov, B. Z. Polvonov, and N. Kh. Yuldashev. Journal of Applied Mathematics and Physics 4, 391–397 (2016).
5. V. S. Bagaev, Yu. V. Klevkov, S. A. Kolosov, V. S. Krivobok, and A. A. Shepel. Optical and electrophysical properties of defects in high-purity CdTe. Fizika Tverdogo Tela 52(1), 37–42 (2010) [in Russian].

SECTION III: Application of Nuclear Technologies in Medicine, Ecology and Industry

APPLICATION OF EPITHERMAL NEUTRON BEAM IN NUCLEAR MEDICINE AND NUCLEAR PHYSICS.

Kulabdullaev G.A.[1], Abdullaeva G.A.[1], Kim A.A.[1], Yuldashev J.O.[2], Normatov E.Kh.[1]
[1]*Institute of Nuclear Physics, Uzbekistan Academy of Sciences, Tashkent, Uzbekistan*
[2]*Bukhara State Medical Institute, Ministry of Health, Bukhara, Uzbekistan*

As is well known, the nuclear physics basis for the development of the NCT (neutron capture therapy) technique is a neutron source with the required parameters for radiation therapy. According to the IAEA, neutron beams used for NCT must meet requirements for intensity and spectral composition; neutrons in the range of 1 eV–10 keV are considered epithermal. Both specially manufactured accelerator-based installations and existing research reactors are used as neutron sources. We used the 10 MW VVR-SM reactor at the Institute of Nuclear Physics of the Academy of Sciences of the Republic of Uzbekistan to develop the NCT technique. An epithermal neutron beam with the required characteristics was created [1].

	Φ_{ep}, n/sm^{2}s	D_f/Φ_{ep}, Gy sm^2	D_γ/Φ_{ep}, Gy sm^2	Φ_t/Φ_{ep}	J/Φ_{ep}
IAEA	$> 10^8$- 10^9	$<2\times10^{-13}$	$<2\times10^{-13}$	<0,05	>0,7
INP AS RUz	$6{,}54\times10^8$	$2{,}6\times10^{-13}$	$0{,}12\times10^{-13}$	0,008	0,77

Using this beam, we conducted research to develop the GdNCT method. The feasibility of using Magnevist for GdNCT research was demonstrated [2].

The study of highly excited states of nuclei is a pressing problem in nuclear physics. As excitation energy increases, the structure of nuclear states becomes more complex, their density increases, and the mixing of different states intensifies. Significant changes in the structure and density of levels are observed even at relatively low excitation energies, on the order of several MeV, comparable in magnitude to nucleon separation energies for a number of nuclei. Experimental study of highly excited states allows us to identify patterns in the changes in their characteristics and, based on this, obtain information on the structure and properties of atomic nuclei, necessary for the development of theoretical models [3].

In the energy range of the epithermal neutron beam used, radiative capture is a possible interaction channel; upon neutron capture, a compound nucleus is formed in a highly excited state, the relaxation of which is accompanied by a cascade of γ-transitions.

Therefore, this beam can be used for experimental studies of the characteristics of such states based on the γ-radiation spectra. As examples, the figure shows the energy dependences of the cross sections for radiative neutron capture by ^{40}Ca and ^{234}U nuclei. For the reaction $^{40}Ca(n,\gamma)^{41}Ca$, a pronounced resonance structure of the cross section is observed in the region of about 10^2–10^3 eV. For the reaction $^{234}U(n,\gamma)^{235}U$, the resonance structure begins already in the region of several eV and continues up to several keV. Thus, the resonance regions of both reactions are within the energy range of the formed epithermal beam 1 eV<En<10 keV. This creates the possibility of using this neutron beam for the resonant formation of highly excited compound nuclei and the subsequent study of their γ-relaxation for nuclei characterized by a resonant structure of the radiative capture cross-section in the epithermal energy range.

Financial support: The work is financed from the state budget of the Republic of Uzbekistan.

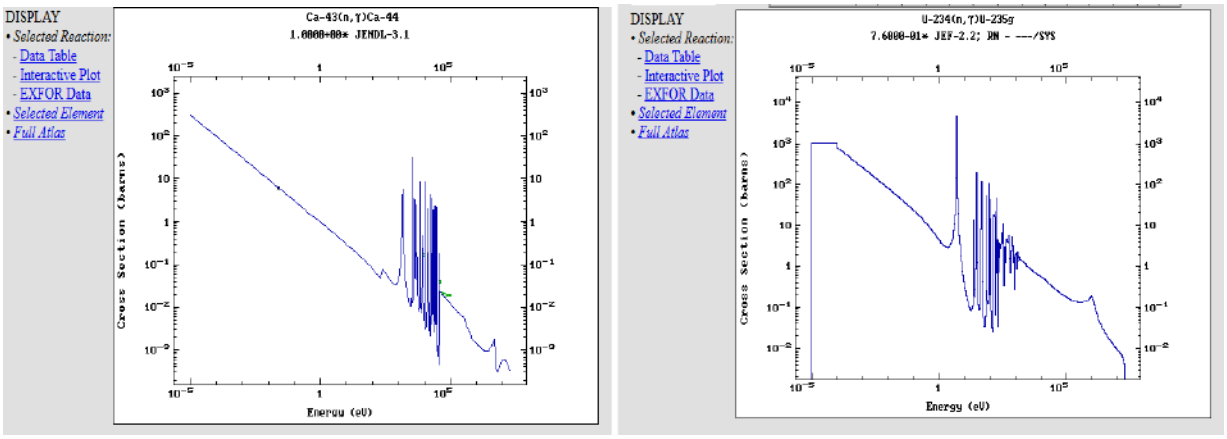

References:

1. Abdullaeva G.A., Koblik Yu.N., Kulabdullaev G.A. Use of the WWR-SMM Reactor for Developing Neutron-Capture Therapy in Uzbekistan // Bulletin of the Russian Academy of Sciences: Physics. – Pleiades Publishing, Ltd.: USA, 2009. – Vol. 73. – No. 4. – pp.512–516 (№3. Scopus; IF=1,1)
2. Kulabdullaev, G.A. Nuclear Physics Foundations of Gadolinium Neutron Capture Therapy Based on the WWR-SM Reactor. Abstract of a DSc thesis. Tashkent, 2026. 70 pages.
3. Kulabdullaev, G.A. Study of High-Lying Bound States of Nuclei by Exciting Them with Gamma Quanta from Radiative Neutron Capture. Abstract of a PhD. Tashkent, 1991. 21 pages.

INVESTIGATION OF VESICULAR STRUCTURE OF PhTNS AND PhTNS-BASED DRUGS USING THE SANS DATA ANALYSIS

Zemlyanaya E.V.[1], Kiselev M.A.[1], Chausova V.A.[1], Tereshkina Yu.A.[2], Tikhonova E.G.[2]

[1]Joint Institute for Nuclear Research, Dubna, Russian Federation

[2]Orekhovich Institute of Biomedical Chemistry, Moscow, Russian Federation

The structure of unilamellar vesicles of a phospholipid transport nanosystem (PhTNS) and PhTNS-based drugs is studied by analyzing small-angle neutron scattering (SANS) data obtained on the Yellow Submarine small-angle spectrometer (Budapest, 2020). The PhTNS system based on soy-bean phospholipids was developed at the Orekhovich Institute of Biomedical Chemistry (Moscow). Due to a small size and biodegradable composition of PhTNS particles, the medical drugs incorporation into the PhTNS particles sufficiently improves their therapeutic effectiveness, see [1] and references therein. The SANS measurements were performed on samples of polydispersed populations of unilamellar vesicles of PhTNS and PhTNS-based drugs prepared with various concentrations in heavy water and with varying purity of soy phospholipids. As example, Figure 1 demonstrates the theoretical and experimental spectra of “Indolip”, the PhTNS-based nano-form of the well-known drug Indometacin. Two concentrations of Indolip in heavy water (5% and 25%) and two variants of samples were analyzed: Lipoid S80 with a phosphatidylcholine

content of 77% and Lipoid S100 with a phosphatidylcholine content of 94%. The effect of soy phospholipid purity and concentration on vesicle size and bilayer structure is studied. The results are presented and compared with the characteristics of vesicular systems previously obtained by analyzing small-angle scattering data [2-4].

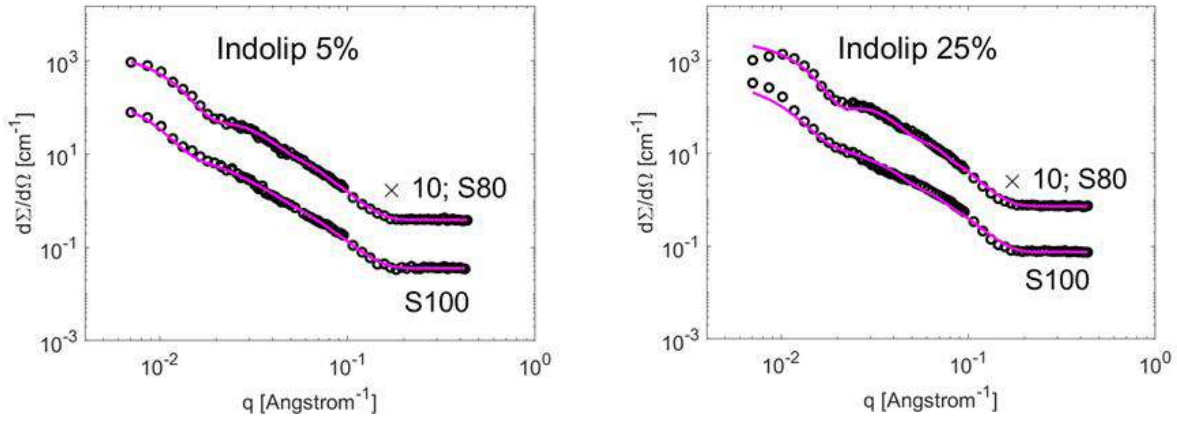

Figure 1. SANS experimental data and theoretical curves in case of S80 and S100 Indolip samples. Concentration of Indolip in the heavy water 5% and 25%.

References:

1. N.V. Medvedeva, et al. Biomedical Chemistry 61 (2015) 219
2. E.V. Zemlyanaya, et al. International Journal of Modern Physics E **35** (2026) 2641003
3. M.A. Kiselev, et al. Journal of Surface Investigation: X-ray, Synchrotron and Neutron Techniques **17** (2023) 1

V.A. Maslova, et al., Journal of Surface Investigation: X-ray, Synchrotron and Neutron Techniques **18** (2024) 929

STUDY OF RADIORESISTANCE AND INTRATUMORAL HETEROGENEITY OF HUMAN OLIGOASTROCYTOMA AND OLIGODENDROGLIOMA TUMORS IN EXPERIMENTAL CONDITIONS IN VITRO

Kim A.A.[1], Kulabdullaev G.A.[1], Abdullaeva G.A.[1], Yuldashev D.O.[1,3], Kadyrbekov N.R.[2], Beknazarov H.J.[2], Kadyrbekov R.T.[2]

[1] Institute of Nuclear Physics, Uzbekistan Academy of Sciences, Tashkent, Uzbekistan
[2] Republican Specialized Scientific and Practical Medical Center of Neurosurgery, Ministry of Health, Tashkent, Uzbekistan
[3]Bukhara State Medical Institute, Ministry of Health, Bukhara, Uzbekistan

Introduction. Currently, the issues of individual radioresistance and intratumoral heterogeneity of various tumor types are actively discussed in the scientific literature. Many authors believe these issues are key to determining the optimal tumor treatment strategy. We previously

developed a method for determining the individual radiosensitivity of live sections of human brain glial tumors in vitro [1]. Using this method, we conducted a series of studies to determine the individual radiosensitivity of anaplastic astrocytomas and meningiomas of the human brain. We demonstrated the presence of radioresistant forms of these tumors and determined the percentage of radioresistant forms for anaplastic astrocytomas and meningiomas. We also investigated the intratumor heterogeneity of radiosensitivity of astrocytomas, anaplastic astrocytomas, and glioblastomas and determined the percentage of heterogeneous forms of these tumors.

Objective. The aim of this study was to determine the radioresistance and intratumoral heterogeneity of radiosensitivity in human brain oligoastrocytoma and oligodendroglioma tumors.

Materials and Methods. In the study were enrolled 16 patients with confirmed diagnoses. Nine patients (7 men and 2 women) aged 8 to 60 years were included in the oligoastrocytoma group, while seven patients (6 men and 1 woman) aged 21 to 53 years were included in the oligodendroglioma group. Biopsy samples from human brain oligoastrocytoma and oligodendroglioma tumors were collected during planned surgeries. After extraction, tumor fragments were placed in saline with 5% glucose, cooled to 4°C, and all subsequent procedures were performed with cooling to 4°C using ice water. The extracted tissues were dissected into slices, and five standard-sized slices ranging in thickness from 3 to 5 mm were selected. From five prepared tumor slices, one slice was used as an initial control, and the second slice was used as a control after incubation without irradiation for 24 hours at 4°C. The remaining three slices were irradiated with gamma radiation using the gamma facility at the Institute of Nuclear Physics of the Academy of Sciences of the Republic of Uzbekistan with absorbed doses of 5, 10, and 15 Gray. After irradiation, the slices were transferred to fresh saline with 5% glucose, cooled to 4°C, and incubated at 4°C for 24 hours. After incubation, the irradiated slices were fixed in 10% formalin for histological analysis. Samples were analyzed using standard clinical histological methods.

Results and discussion. The oligoastrocytoma group included 9 patients diagnosed with oligoastrocytoma (6 patients) and anaplastic oligoastrocytoma (3 patients). The results of irradiation with absorbed doses of 5, 10, and 15 Gray showed that 2 patients (2/9, 22%) showed complete resistance to all three doses, and 2 patients (2/9, 22%) showed moderate resistance—necrosis appeared only at doses of 10 and 15 Gray. The remaining 5 patients showed radiosensitivity to all three absorbed doses, with 4 patients showing a linear increase in the degree of necrosis with increasing absorbed dose. Meanwhile, 1 patient (1/5, 20%) showed a nonlinear response to increasing absorbed dose—a decrease in the degree of necrosis in the irradiated samples with increasing absorbed dose.

The oligodendroglioma group included seven patients diagnosed with oligodendroglioma (four patients) and anaplastic oligodendroglioma (three patients). The results of irradiation with absorbed doses of 5, 10, and 15 Gray showed that two patients (2/7, 38%) demonstrated complete resistance to all three doses, while two patients (2/7, 38%) demonstrated moderate resistance, with necrosis occurring only at doses of 10 and 15 Gray. The remaining three patients demonstrated radiosensitivity to all three absorbed doses. All three patients demonstrated a nonlinear response to increasing absorbed dose, with a decrease in the degree of necrosis in the irradiated samples as the absorbed dose increased.

Thus, we found that in the oligoastrocytoma and oligodendroglioma groups, 40 to 60% of tumors were radioresistant. Moreover, intratumor heterogeneity in radiation response with increasing absorbed doses was observed in both groups.

Radioresistance and intratumoral heterogeneity are key factors in determining an unfavorable prognosis in the treatment of cancer patients. Therefore, the obtained data may be useful for clinical practice in radiation therapy of oligoastrocytoma and oligodendroglioma tumors, helping to predict

the effectiveness of gamma irradiation and improve the efficiency of radiation regimens. Furthermore, the obtained data should be taken into account when modeling radiation regimens for the development of new radiation therapy methods.

Acknowledgement (Financial support): The work is financed by the state budget of the Republic of Uzbekistan.

References:

1. Kim A.A., Kulabdullaev G.A., Djuraeva G.T., Kadyrbekov R.T., Kadyrbekov N.R. and Beknazarov H.J. Method of determining the radiosensitivity of anaplastic astrocytoma tissue under gamma irradiation in vitro. Patent of the Republic of Uzbekistan IAP 06855 (18 march 2020).

DEPENDENCE OF THRESHOLD-BASED PET SEGMENTATION ACCURACY ON ITERATIVE RECONSTRUCTION SETTINGS AND LESION SIZE: A PHANTOM STUDY

Emelyanenko E., Petkevich M., Yushkevich V.
N.N.Aleksandrov National Cancer Center, Lesnoy, Minsk region, Republic of Belarus

The integration of molecular imaging into the radiation therapy planning workflow is one of the key directions in modern radiation oncology. PET/CT enables the transition from purely anatomical visualization to biologically oriented target volume delineation, providing unique information on the metabolic activity of tumour foci [1]. This is particularly relevant for high-precision irradiation techniques – stereotactic body radiation therapy and radiosurgery – where the cost of an error in target boundary determination is exceptionally high. The incorporation of PET/CT into radiation oncology is accompanied by technical advances: support for 4D acquisition protocols with respiratory gating, compatibility with patient fixation systems, and continuous improvement of image reconstruction algorithms [2].

Despite progress in technical capabilities, the lack of standardized approaches to contouring pathological lesions on PET images remains a critical issue. Unlike CT, where density boundaries between tissues are well defined, PET image interpretation is hampered by several limitations: the partial-volume effect, reconstruction noise, dependence of quantitative parameters on scanner type and processing algorithm, and physiological organ motion [2, 3]. The most widely used clinical tool is the deterministic gradient-based threshold method, implemented in most commercial treatment planning systems (Eclipse, Monaco, Pinnacle) and requiring no dedicated software [3]. However, considerable variability in the results – driven by both subjective factors (threshold selection, seed-point placement) and objective technical parameters such as the reconstruction algorithm, iteration number, and subset count – limits its reliability, particularly for small lesions and targets of complex shape [3, 4].

Aim. To experimentally evaluate the effect of OSEM iteration and subset numbers on deterministic segmentation volumes of spherical inserts of various diameters and to justify an adaptive gradient-threshold selection strategy.

Materials and methods. The study was performed using an IEC NEMA Body Phantom containing spherical inserts of 37, 28, 22, 17, 13, and 10 mm diameter (nominal volumes 26.51, 11.49, 5.57, 2.57, 1.15, and 0.52 cm^3, respectively). The target-to-background activity ratio was 4:1. Images were reconstructed with the OSEM algorithm varying iterations (4–6 at 12 subsets) and subsets (16–24 at 3 iterations). Contouring was carried out in Eclipse (Varian Medical Systems) using the deterministic gradient method at threshold levels from 20 % to 60 % in 10 % increments.

Results. Raising the gradient threshold from 20 % to 60 % reduced the contoured volume by a factor of 2.5 for the 37-mm sphere and by 7.4 for the 22-mm sphere. For the 13- and 10-mm inserts, segmentation at thresholds ≤ 30 % was unfeasible due to partial-volume effects and signal loss in noise.

At a fixed subset number (12), increasing iterations from 4 to 6 led to volume growth for large models ($d \geq 28$ mm, ~2–3 % per iteration) and volume reduction for small ones ($d \leq 22$ mm). Varying subsets (16–24) at 3 iterations changed volumes within ±3–5 %, except for the 10-mm sphere at the 40 % threshold, where the range reached 1.4–3.0 cm^3.

Optimal gradient thresholds determined by partial interpolation were: 49.1 % (37 mm), 42.1 % (28 mm), 34.5 % (22 mm), 37.4 % (17 mm), 43.3 % (13 mm), and 57.3 % (10 mm).

Conclusions. The optimal segmentation threshold is not a universal constant but depends on lesion diameter. A single fixed threshold systematically overestimates the volume of large targets and underestimates that of small ones. An adaptive, size-dependent threshold combined with fixed reconstruction parameters in the clinical protocol is recommended to ensure delineation accuracy and reproducibility in radiation therapy planning.

References:

1. McKay M.J., Taubman K.L., Foroudi F., Lee S.T., Scott A.M. Molecular Imaging Using PET/CT for Radiation Therapy Planning for Adult Cancers: Current Status and Expanding Applications. Int. J. Radiat. Oncol. Biol. Phys., 2018, vol. 102, no. 4, pp. 783–791. doi: 10.1016/j.ijrobp.2018.03.013.
2. Nehmeh S.A., Erdi Y.E. Respiratory motion in positron emission tomography/computed tomography: a review. Semin. Nucl. Med., 2008, vol. 38, no. 3, pp. 167–176. doi: 10.1053/j.semnuclmed.2008.01.002.
3. Zaidi H., El Naqa I. PET-guided delineation of radiation therapy treatment volumes: a survey of image segmentation techniques. Eur. J. Nucl. Med. Mol. Imaging, 2010, vol. 37, no. 11, pp. 2165–2187. doi: 10.1007/s00259-010-1423-3.
4. Drever L., Roa W., McEwan A., Robinson D. Influence of reconstruction settings on the performance of adaptive thresholding algorithms for FDG-PET image segmentation in radiotherapy planning. Phys. Med. Biol., 2011, vol. 56, no. 8, pp. 2393–2413. doi: 10.1088/0031-9155/56/8/010.

POTENTIAL APPLICATION OF BIODEGRADABLE CHITOSAN MICROSPHERES CONTAINING ^{177}Lu FOR DOMESTIC BRACHYTHERAPY

Markelova E.A.[1], Vasidov A.[1], Sultanov M.[2], Asadullaev M.M.[3], Khujaev S.[1]
[1]*Institute of Nuclear Physics, Uzbekistan Academy of Sciences, Tashkent, Uzbekistan*
[2]*Peter the Great St. Petersburg Polytechnic University, St. Petersburg, Russian Federation*
[3]*Tashkent Medical Academy, Ministry of Health, Tashkent, Uzbekistan*

Brachytherapy is a type of radiation therapy in which the radiation source is placed directly inside or in close proximity to the affected organ or tissue. The principal advantage of this technique is the delivery of a high radiation dose directly to the tumor while minimizing exposure to surrounding healthy tissues and critical organs [1]. The use of advanced brachytherapy technologies, including ultrasound guidance and computerized treatment planning, provides several significant advantages, such as precise source placement, highly localized irradiation, improved treatment efficacy, shorter treatment duration, and a reduced incidence of adverse effects, including hematological changes, skin reactions, and general weakness.

The brachytherapy procedure involves the implantation of several dozen sealed radioactive capsules (seeds) into the target tissue. According to the requirements of nuclear medicine, radionuclides with half-lives of 4–17 days and photon energies of 30–40 keV are considered optimal for permanent brachytherapy. Currently, the most widely used radionuclides are ^{125}I, ^{103}Pd, and ^{131}Cs.

With the expanding application of nuclear medicine and the rapid development of theranostic approaches, there is an increasing demand for new therapeutic radionuclides. Theranostics is a personalized medical approach that combines diagnostic imaging and targeted radionuclide therapy using the same or a combination of radionuclides. Among the most promising neutron-activated radionuclides possessing both therapeutic and diagnostic properties are ^{166}Ho, ^{177}Lu, ^{186}Re, ^{188}Re, and ^{153}Sm. Several of these radionuclides are already in clinical use, while others are undergoing clinical evaluation.

The Republic of Uzbekistan has an established infrastructure in the field of radiopharmaceutical production. The State Enterprise “Radiopreparat” at the Institute of Nuclear Physics manufactures several radionuclides and radiopharmaceuticals, including carrier-free $^{177}LuCl_3$, pr In addition to radionuclide selection, brachytherapy seeds must satisfy stringent requirements regarding hermetic sealing, standardized dimensions and geometry, mechanical integrity, and adequate visibility under medical imaging modalities.

Biodegradable chitosan-based microspheres represent a promising alternative to conventional permanent titanium seeds. Chitosan offers several important advantages, including excellent biocompatibility, biodegradability, low toxicity, and the possibility of surface functionalization for targeted radionuclide delivery. Such biodegradable carriers may reduce long-term complications associated with permanent metallic implants.

Particularly promising applications of ^{177}Lu-labeled chitosan microspheres include the treatment of liver tumors, prostate cancer, breast cancer, soft tissue tumors, and locally recurrent malignancies following surgical treatment. In addition, the potential application of ^{177}Lu in coronary brachytherapy is currently under investigation.

Coronary brachytherapy is an intravascular radiation therapy technique used to prevent restenosis of coronary arteries following percutaneous coronary interventions, particularly after balloon angioplasty and stent implantation. Localized radiation suppresses excessive proliferation of vascular smooth muscle cells, thereby reducing the risk of recurrent arterial narrowing.

Uzbekistan possesses favorable conditions for the development of domestic ^{177}Lu-based brachytherapy sources. The country has an established production of ^{177}Lu, and a technology for preparing stable chitosan microspheres with high radionuclide retention has already been developed. The next stage of the project will involve comprehensive preclinical studies, including radiation dosimetry, biodistribution, radiochemical stability, and toxicological evaluation of the developed delivery system.

References:

1. Airmpilia C.I., Dale R.G., Coles I.P., Jones B., Antipas V. *The determination of radiobiologically optimized half-lives for radionuclides used in permanent brachytherapy implants.* International Journal of Radiation Oncology, Biology, Physics. 2003;55(2):378–385.
2. Usarov Z.O., Rustamov N.M., Nishanov Sh.Zh., Abdukayumov A.M., Rikhsiev A.Z., Abdukayumov M. Method for producing carrier-free lutetium-177 chloride. Patent of the Republic of Uzbekistan No. IAP 05930, Bulletin No. 8, 2019, p. 101.

EXPERIMENTAL INVESTIGATION OF PHOTON INTERACTION ENHANCEMENT IN A GADOLINIUM CHELATE CONTRAST AGENT UNDER ^{137}Cs AND ^{40}K GAMMA IRRADIATION

Abdullaeva G.A., Rasulova D.R.
Institute of Nuclear Physics, Uzbekistan Academy of Sciences, Tashkent, Uzbekistan

Radiotherapy remains one of the principal modalities for the treatment of malignant tumors; however, increasing energy deposition within a target while limiting the radiation burden to surrounding normal tissues remains an important challenge. One approach is the introduction of high-atomic-number (high-Z) materials into the irradiated medium, which can modify photon–matter interactions and thereby provide a physical basis for radiosensitization [1,2]. Gadolinium (Z = 64) is of particular interest because of its photon-interaction properties and its established medical use in the form of gadolinium-based contrast agents [2,3]. In clinical contrast agents, Gd^{3+} is incorporated into chelate complexes; Magnevist® (gadopentetate dimeglumine, Gd-DTPA) is a gadolinium complex of diethylenetriaminepentaacetic acid [3].

The aim of the present study was to experimentally investigate changes in the gamma-ray spectra and the number of registered events produced by the presence of a gadolinium-containing chelate under irradiation with photons of two different energies. Magnevist® and physiological saline (0.9% NaCl) were used as the investigated and reference media, respectively. The samples were exposed under identical experimental geometry to gamma radiation associated with ^{137}Cs (661.7 keV) and ^{40}K (1460 keV). The radiation spectra were registered using a RADEK scintillation spectrometer. The analysis was based on experimentally measurable quantities: the number of registered events and their energy distribution.

The measurements revealed a systematic difference between the spectra obtained with the gadolinium-containing medium and those obtained with physiological saline. In particular, an increase in the number of registered events was observed in the presence of Magnevist® under otherwise identical irradiation and detection conditions. Thus, the experiment demonstrates that introducing the gadolinium-containing chelate into the irradiated medium produces a measurable modification of the registered photon-interaction response. This experimentally observed spectral and counting-rate difference, rather than an assumed radiosensitizing potential, constitutes the principal result of the present study.

The physical interpretation of this effect requires consideration of the energy-dependent interaction cross sections. Photon interactions in matter include photoelectric absorption, incoherent (Compton) scattering, coherent scattering and, above the corresponding energy threshold, pair production; their relative contributions depend on both photon energy and elemental composition [4]. At photon energies of the order of 662 keV, Compton scattering becomes an important and, over a broad range of materials, dominant interaction mechanism, whereas the relative contribution of photoelectric absorption decreases substantially with increasing photon energy [4,5]. Therefore, the experimentally observed enhancement at 661.7 and 1460 keV should not be attributed exclusively to the photoelectric effect without a quantitative evaluation of the partial interaction coefficients. Instead, the results indicate a modification of the total photon-interaction response of the Gd-containing medium. Quantitative decomposition of the contributions from Compton scattering, photoelectric absorption and, at 1460 keV, pair-production processes using photon cross-section data and radiation-transport calculations represents the next stage of this investigation [4].

The novelty of the present work lies in the experimental comparison of a clinically used gadolinium chelate and a reference saline medium at two discrete gamma-ray energies through directly registered spectrometric parameters. The obtained results provide an experimental physical basis for further investigation of gadolinium-chelate-mediated radiosensitization, rather than claiming direct measurement of radiosensitization itself. The proposed approach can subsequently be extended by calculating energy-dependent interaction coefficients, absorbed-energy enhancement and dose-enhancement factors and by performing Monte Carlo simulations. Such quantitative analysis will establish whether the experimentally observed spectral changes translate into a physically significant increase in local energy deposition relevant to photon-based radiotherapy.

References:

1. Gong L., Zhang Y., Liu C., Zhang M., Han S. Application of Radiosensitizers in Cancer Radiotherapy. International Journal of Nanomedicine. 2021;16:1083–1102. doi:10.2147/IJN.S290438.
2. Robertson A.G., Rendina L.M. Gadolinium theranostics for the diagnosis and treatment of cancer. Chemical Society Reviews. 2021;50(7):4231–4244. doi:10.1039/D0CS01075H.
3. National Cancer Institute. Gadopentetate dimeglumine. NCI Drug Dictionary. Gd-DTPA (Magnevist®).
4. Berger M.J., Hubbell J.H., Seltzer S.M. et al. XCOM: Photon Cross Sections Database. National Institute of Standards and Technology (NIST).
5. Lerch S. et al. Breaking photoswitch activation depth limit using ionising radiation stimuli adapted to clinical application. Nature Communications. 2022;13.

MONTE CARLO CALCULATION OF RADIO-ENHANCED CONTRAST IN X-RAY IMAGING

Dushanov E.B.[1,2], Togtokhtur T.[1] Bugay A.N.[1,2]
[1]*Joint Institute for Nuclear Research, Dubna, Russian Federation*
[2]*State Budgetary Educational Institution of Higher Education "Dubna University", Dubna, Russian Federation*

In this work, we developed [1] the effect of radio enhancement for X-ray imaging using some contrast media on the imaging phantom with different attenuation sites by a Monte Carlo method. The optimal contrast effect has been performed on the target with iodine at the 8.0 mg/mL concentration. The X-ray image with the iodine shell was brighter than uniform distribution due to increased iodine volume density for shorter targets. Finally, this study indicates the possibility of obtaining improved X-ray images for soft tissue (ICRP) in potential concentrations below the toxic limit of iodine inside a mammal.

GEANT4 Monte-Carlo code was used to model the imaging phantom exposed by X-ray irradiation. The Livermore cross section was used in this simulation, which includes processes like the photoelectric effect, Compton, and Rayleigh scattering [2]. The model indicates the interaction of electrons and photons with matter down 30 to 10 eV (cut-off energy). The spectrum was generated by SpekPy software [3] based on physical model casim (PENELOPE data set) tube voltage 130 kVp [4] using inherent filtration of 0.8 mm beryllium and 3.9 mm of aluminum (HVL = 0.68 mm Cu) and used as an X-ray source in this simulation.

An imaging phantom is the optimal way to demonstrate the X-ray image when using the X-ray beam parallel with the front surface (XY) of the object. The following imaging phantom was designed using the experimental setup. The all geometries used in this simulation has built on the GEANT4. The incident beam was traveling through phantom parallel (XY) and plane size (60 × 60 mm) same as CsI detector [4].

The imaging phantom has been modified to have two rods for the purpose of identifying iodine contrast effects depending on their spread density and target thickness. We have chosen shell accumulation that way in the rod 5 due to iodine could not be absorbed by every cell inside the tissue trail in some experiments. Here, we are assumed in comparing the contrast effect that depends on the iodine distribution with uniformly (rod 5) and the 0.1 mm thick shell (rod 6).

We estimated the photon count recorded at the detector following procedure. Here, notice that we did not consider the scintillation process of the photon inside the CsI detector due to some barrier with the code. At first, the (x, y) coordinates of the photons reaching the detector surface area passing through the imaging phantom are recorded in GEANT4. It means that the coordinates (points) obtained in every single step are collected as the signal on the detector. The obtained points were counted after making pixels 0.04 mm^2 in size using two-dimensional frequency estimation (heatmap) in the OriginPRO software; the color contrast depends on the frequency count (the counted points) for each pixel, and when the frequency count is higher, the pixels are darker (see Fig. 1, top). The optimal value of primary photon intensity at the beam source was $N_0 = 10^7$.

When $N_0 < 10^7$, X-ray images with poor tolerance (blurry) are mainly obtained, which is associated with a low pixel density. At $N_0 > 10^7$, the pixel density increases, and, accordingly, it takes quite a long time to form the required picture. The color scale bar was interpolated between the color site at 0 mg/ml (imaging phantom) concentration and the color site at 8 mg/ml concentration (Fig. 1, bottom). In each case of N_0, the average frequency count ratio for the imaging

phantom and the brightest rod of the highest concentration is 1.525 ± 0.005; the color scale adjusted could not depend on the photon intensity.

The contrast effect between rod 1 with iodine and rod 2 with gadolinium contrast media at 8 mg/mL along the model is shown. The contrast effect was very similar to each other for contrast agents due to either their K-edge energy being below the characteristic peak of the X-ray spectrum. The projection image was calculated after uptake iodine at 2, 4, 6, and 8 mg/mL into the rods along clockwise. Particularly, the rod shape appeared applicable enough compared to soft tissue when 4 to 8 mg/mL iodine.

The result images from the second stage of the simulation. Here are the images we obtained according to the previous geometry. The contrast effect significantly increased by the thickness of the rod 5. Because the photon fluency into the iodinated area decreased rapidly when material depth increases. Nevertheless, the effect slightly increased in the rod 6 with iodinated shell. Also, surface sharpness was higher and optimal at the iodine accumulation on the surface area of the target than inside accumulation.

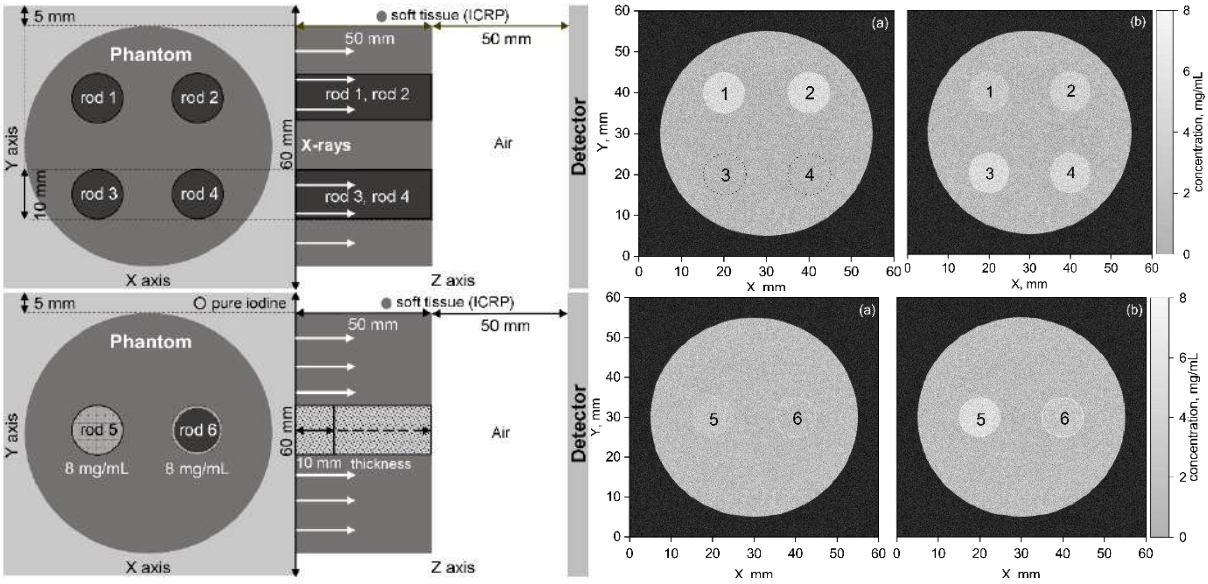

Figure 1. X-ray images obtained for different concentration (top): (a) rod 1 (8 mg/mL iodine), rod 2 (8 mg/mL gadolinium), black dotted rods 3, 4 (0 mg/mL); (b) rod 1 (2 mg/mL iodine), rod 2 (4 mg/mL iodine), rod 3 (8 mg/mL iodine), rod 4 (6 mg/mL iodine); for different thickness (bottom) of rod 5, 6 (a) 10 mm and (b) 50 mm with the same 8 mg/mL iodine concentration.

References:

1. Togtokhtur T., Dushanov E.B., Batmunkh M., Bugay A.N. Contrast enhancement calculation of X-Ray imaging // PEPAN Letters, 2025, v. 22, No 5 (262), p. 1066.
2. Allison, John et al. Recent developments in Geant4. // Nuclear instruments and methods in physics research section A: Accelerators, Spectrometers, Detectors and Associated Equipment – 2016. V. 835. P. 142 186-225.
3. Poludniowski, Gavin et al. SpekPy v2. 0 – a software toolkit for modeling 144 X-Ray tube spectra. // Medical Physics – 2021. V. 48(7). P. 3630-3637.
4. *Tilley, Steven et al.* Model-based material decomposition with a penalized nonlinear least-squares CT reconstruction algorithm. // Physics in Medicine & Biology – 2019. V. 64(3). P. 035005.

EXTRACTION-CHROMATOGRAPHIC SEPARATION OF ZINC AND GALLIUM FOR THE PRODUCTION OF RADIOACTIVE GALLIUM ISOTOPES

Mekhmonov G., Khujaev S., Markelova E.
Institute of Nuclear Physics, Uzbekistan Academy of Sciences, Tashkent, Uzbekistan

Efficient separation of gallium from zinc is a key step in producing carrier-free, high radiochemical purity radioactive gallium isotopes 66Ga, 67Ga, and 68Ga, which are needed for their use as radioactive tracers [1]. An extraction-chromatographic method for separating the Zn–Ga pair has been developed using petroleum-derived sulfoxides (PSO), dihexyl sulfoxide (DHSO), and tri-n-octylamine (TOA) as extractants from hydrochloric acid solutions.

The distribution coefficients of zinc and gallium were determined by a radiometric method as a function of hydrochloric acid concentration, extractant concentration, and metal content. For both elements, the distribution coefficients reach a maximum at a concentration of about 5 M HCl, and it is at this same concentration that the highest separation factor for the Zn–Ga pair is observed. The dependence of the distribution coefficients on extractant concentration is linear in logarithmic coordinates.

Extraction-chromatographic columns were prepared by depositing PSO or DHSO onto fluoroplastic powder. Such columns make it possible to quantitatively isolate microamounts of gallium from macroamounts of zinc, and conversely, microamounts of zinc from macroamounts of gallium, with a separation factor reaching 10^4–10^6. Zinc is not sorbed on the sulfoxide columns and is washed out with dilute HCl, whereas gallium is quantitatively retained and is then eluted with a more dilute acid solution. An additional system based on columns with TOA in o-xylene exhibits the opposite retention behavior for the elements, which broadens the applicability of the method for different Zn/Ga ratios.

The proposed method is simple, rapid, and convenient for remote operation in shielded radiochemical equipment. The method is of interest for nuclear medicine and the application of radioactive tracers, where high radionuclidic and radiochemical purity of the preparation is important [1,2].

References:

1. International Atomic Energy Agency, Gallium-68 Cyclotron Production, IAEA-TECDOC-1863, IAEA, Vienna, 2019.
2. Z. Ashhar, M.F. Ahmad Fadzil, M.F. Othman, N.A. Yusof, M.A. Abdul Onny, N. Mat Ail, S.F. Abd Rahman, Cyclotron Production of Gallium-68 Radiopharmaceuticals Using the 68Zn(p,n)68Ga Reaction and Their Regulatory Aspects, Pharmaceutics 15 (2023) 70.

METHOD FOR PRODUCING THE ^{131}I-MIBG RADIOPHARMACEUTICAL

Galdiev M.E.[1], Sadikov I.I.[2], Abdukayumov A.M.[1]
[1]State Institution "Radiopreparat", Tashkent, Uzbekistan
[2]Institute of Nuclear Physics, Uzbekistan Academy of Sciences, Tashkent, Uzbekistan

Introduction. Meta-iodobenzylguanidine (MIBG) is a structural analogue of norepinephrine that can be labeled with radioactive iodine isotopes (^{123}I, ^{125}I, and ^{131}I). ^{131}I-mIBG is an effective diagnostic tool for the detection of neuroblastoma, pheochromocytoma, carcinoid tumors (APUD system), sympathetic paraganglioma, and their metastases. The intensive uptake of the radiopharmaceutical by cells through sympathetic neurons enables tumor localization and assessment of their activity. At the same time, ^{131}I-mIBG is also used for therapeutic purposes, as the beta radiation emitted during radioactive decay exerts a direct cytotoxic effect on tumor cells, thereby minimizing damage to healthy tissues [1,2].

Aim of the study. This study aimed to develop a technology for producing a high-quality ^{131}I-mIBG radiopharmaceutical, optimize the synthesis process, improve the radiochemical purity of the preparation, and ensure the sterility and apyrogenicity of the final solution.

Materials and Methods. High-purity chemical reagents obtained from Sigma-Aldrich (USA) and conforming to the "A.C.S." high-purity grade were used for the synthesis of the ^{131}I-MIBG radiopharmaceutical. Radiometric measurements were performed using an SU-03P gamma spectrometer equipped with a Ge(Li) semiconductor detector. Qualitative and quantitative analyses of the ^{131}I-mIBG preparation were carried out using a Genesys 10S UV-Vis spectrophotometer (Thermo Scientific, USA). All experimental procedures were performed in accordance with radiation safety requirements and Good Manufacturing Practice (GMP) standards. The technological solutions required for the analyses, including buffers and eluents, as well as chromatographic sorbents (silica gel impregnated with Ag^+ ions), were prepared in the laboratory in accordance with specific procedures.

Results and Discussion. Based on the developed technology, optimization of the synthesis and purification processes enabled the production of a sterile and apyrogenic ^{131}I-mIBG radiopharmaceutical in solution form, with a radiochemical purity of 99.5–99.7%. The qualitative and quantitative analyses, radiochemical purity, and volumetric activity of the obtained preparation were evaluated using generally accepted analytical methods. In addition, for the isotope exchange reaction using Na^{131}I with a volumetric activity of 100 mCi/mL, the radiochemical yield exceeded 98% after 20 min at a reaction mixture pH of 6–7 and a temperature of 100 °C.

Conclusions. In this study, a technology based on the isotope exchange reaction followed by chromatographic purification was developed for the production of the ^{131}I-mIBG radiopharmaceutical. Based on the results of the study, **Utility Model Patent No. UZ FAP 02309** was obtained in the Republic of Uzbekistan. The developed radiopharmaceutical is currently manufactured on a batch-production basis at the State Institution "Radiopreparat".

References:

1. Huang Y., Kong X., Liu Y., Qing W., Tian J. *Preparation and quality control of [^{131}I]MIBG. IAEA Scientific Report*, IAEA-SR-209/17
2. Davarpanah M.R., Attar Nosrati S., Khoshhosn H.A., et al. (2013). *Establishment of a fast and high yield method for routine production of [^{131}I]MIBG and investigation of its radiochemical stability for diagnosis and treatment uses.* Journal of Labelled Compounds and Radiopharmaceuticals, 56(13), 686–688.
3. UZ FAP 02309.

METHOD FOR THE DETERMINATION OF THE MOLAR ACTIVITY OF CARRIER-FREE [^{32}P] ORTHOPHOSPHORIC ACID

Khajiyev L.O.[2], Sadikov I.I.[1], Abdukayumov A.M.[2], Rixsiev A.Z.[2]
[1]*Institute of Nuclear Physics, Academy of Sciences of the Republic of Uzbekistan*
[2]*State Institution “Radiopreparat”, Institute of Nuclear Physics, Uzbekistan Academy of Sciences, Tashkent, Uzbekistan*

This study is devoted to the development of a method for determining the molar activity of Carrier-Free Phosphorus-32-Labeled Orthophosphoric Acid ($H_3[^{32}P]PO_4$), produced at the State Enterprise "Radiopreparat", Institute of Nuclear Physics, Academy of Sciences of the Republic of Uzbekistan.

The molar activity of Carrier-Free Phosphorus-32-Labeled Orthophosphoric Acid was determined using ultraviolet (UV) spectrophotometry.

Among the quality attributes of radiopharmaceuticals used in nuclear medicine for diagnostic and therapeutic applications, molar activity is of particular importance. Molar activity is defined as the ratio of the radioactivity of a radionuclide to the amount of substance, expressed in moles. This parameter directly reflects the degree to which the radiopharmaceutical is free of carrier, influences its biological properties and efficacy, and contributes to accurate dose determination.

The aim of the present study is to develop a rapid, sensitive, and reliable method for determining the molar activity of ^{32}P-based radiopharmaceuticals, based on the spectrophotometric determination of phosphate ions using a vanadate–molybdate reagent, and to validate the method using real samples.

Determination of the Molar Activity of Carrier-Free Phosphorus-32-Labeled Orthophosphoric Acid by Spectrophotometry

The molar activity of Carrier-Free Phosphorus-32-Labeled Orthophosphoric Acid was measured using a Shimadzu UV-1900i spectrophotometer.

Analytical procedure. A series of calibration solutions was prepared to construct a calibration curve. Different volumes of a standard KH_2PO_4 solution (1.0×10^{-4} mol/L) were transferred into volumetric flasks. Subsequently, 5 mL of vanadate–molybdate reagent was added to each flask, and the solutions were diluted to volume with distilled water. The absorbance of the resulting colored complex was measured at 410 nm using a 1-cm path-length cuvette.

The absorbance of the sample solution of Carrier-Free Phosphorus-32-Labeled Orthophosphoric Acid was measured in parallel with the calibration solutions. Aliquots of the sample were transferred into two 25-mL volumetric flasks fitted with ground-glass stoppers, followed by the addition of the vanadate–molybdate reagent. The subsequent analytical procedure was identical to that used for the preparation of the calibration solutions. The amount of phosphorus-32 (^{32}P) in the sample aliquot was determined from the calibration curve.

The molar activity was calculated using the following equation (Ci/mmol):

$MA\ (Ci/mmol) = A_v \times V / (n \times 10^6)$

where:

- MA is the molar activity (Ci/mmol);
- A_v is the activity of the sample aliquot (Ci/mL);
- V is the volume of the sample aliquot (mL);

- n is the amount of phosphorus-32 in the aliquot (mol).

The results demonstrated that the proposed spectrophotometric method enables accurate determination of the molar activity of Carrier-Free Phosphorus-32-Labeled Orthophosphoric Acid. The relative determination error was 1.06%.

DETERMINATION OF RADIOCHEMICAL PURITY AND MOLAR ACTIVITY OF ^{33}P-LABELLED ORTHOPHOSPHORIC ACID

Khajiyev L.O.[2], Sadikov I.I.[1], Abdukayumov A.M.[2], Rixsiev A.Z.[2]
[1]*Institute of Nuclear Physics, Uzbekistan Academy of Sciences, Tashkent, Uzbekistan*
[2]*State Institution “Radiopreparat”, Institute of Nuclear Physics, Uzbekistan Academy of Science, Tashkent Uzbekistan*

This study is devoted to the methods for determining the radiochemical purity and molar activity of the substance Carrier-Free Phosphorus-33-Labeled Orthophosphoric Acid ($H_3[^{33}P]PO_4$), produced at the State Enterprise "Radiopreparat", Institute of Nuclear Physics, Academy of Sciences of the Republic of Uzbekistan.

Radiochemical purity of the Carrier-Free Phosphorus-33-Labeled Orthophosphoric Acid was determined using the paper chromatography method. Thin-layer chromatography was employed to evaluate its biological activity, while molar activity was determined by beta spectrometry.

Paper Chromatography (PC). Whatman 3MM chromatography paper was cut into strips measuring 15 × 150 mm. A start line was drawn 15 mm from one end of each strip. A 0.001 mL aliquot of the Carrier-Free Phosphorus-33-Labeled Orthophosphoric Acid sample (activity: 0.148–0.296 MBq) was applied to the start line.

A mixture of 12% nitric acid solution and *n*-butanol (1:3, v/v) was used as the mobile phase. Under these chromatographic conditions, orthophosphate ions ($^{33}PO_4^{3-}$) migrated with the solvent front, exhibiting an Rf value of 0.5–0.6, whereas metaphosphate ions ($^{33}PO_3^-$) and pyrophosphate ions ($^{33}P_2O_7^{4-}$) remained near the origin with Rf values of 0.0–0.1.

Under these conditions, the radiochemical purity of the substance, as determined by this method, was 99.6 ± 0.1%.

Determination of the Biological Activity of Carrier-Free Phosphorus-33-Labeled Orthophosphoric Acid by Thin-Layer Chromatography and Measurement of Molar Activity by Beta Spectrometry

Analytical procedure. A polyethylene «Eppendorf» tube containing 55 µL of an enzyme mixture used for the synthesis of γ-[^{33}P] ATP (adenosine triphosphate labeled with phosphorus-33) was supplemented with Carrier-Free Phosphorus-33-Labeled Orthophosphoric Acid (activity: 12.5 mCi). Subsequently, 5 µL of a 1×10^{-2} M ADP (adenosine diphosphate) solution was added. The reaction mixture was thoroughly mixed and incubated at 37 °C for 30 min.

After incubation, the reaction mixture was mixed again and diluted with 100 µL of 0.25 M potassium dihydrogen phosphate solution. An aliquot (0.001 mL) of the diluted reaction mixture was applied to PEI-cellulose chromatographic plates (Merck, 10 × 100 mm) at a point located 15 mm from one end of the plate. A 0.25 M potassium dihydrogen phosphate solution (pH 4.4–4.5) was

used as the mobile phase. Under these chromatographic conditions, orthophosphate ions ($^{33}PO_4^{3-}$) migrated with an Rf value of 0.5–0.6, whereas γ-[^{33}P] ATP exhibited an Rf value of 0.1–0.3.

The biological activity of the substance was calculated using the following equation:

$BA = (C\gamma\text{-}[^{33}P]\ ATP / C_0) \times 100\ (\%)$

where:

- BA is the biological activity (%);
- Cγ-[^{33}P] ATP is the count rate of the chromatographic zone containing γ-[^{33}P] ATP;
- C_0 is the total count rate of the entire chromatogram.

The molar activity was calculated using the following equation:

$MA = (4800 \times BA) / 100\ (Ci/mmol)$

where:

- MA is the molar activity of the aliquot (Ci/mmol);
- 4800 Ci/mmol is the theoretical molar activity of the carrier-free phosphorus-33-labeled orthophosphoric acid;
- BA is the biological activity (%).

The results demonstrated that the thin-layer chromatography method can be used to determine the molar activity of Carrier-Free Phosphorus-33-Labeled Orthophosphoric Acid with high accuracy. The determination error did not exceed ±0.6%.

DEVELOPMENT OF A TECHNOLOGY FOR PRODUCING THE SAMARIUM-153 RADIOISOTOPE AND A RADIOPHARMACEUTICAL BASED ON IT FOR LOCAL (IN HOUSE) USE IN SPECIALIZED MEDICAL CENTERS

Nishonov Sh.J.[1], Khujaev S.[2], Abdukayumov A.M.[1]

[1]*State Institution “Radiopreparat”, Institute of Nuclear Physics, Uzbekistan Academy of Science, Tashkent Uzbekistan*

[2]*Institute of Nuclear Physics, Uzbekistan Academy of Sciences, Tashkent, Uzbekistan*

This study is devoted to the development of a radiopharmaceutical composition based on oxa-bis(ethylenenitrilo)tetramethylenephosphonic acid [Oxabifor], intended for the production of a radiopharmaceutical with the radionuclide ^{153}Sm (samarium-153) – "Samarium-Oxabifor labeled with ^{153}Sm". The drug is used in oncology to sustainably reduce pain associated with bone metastases and slow tumor growth in bone lesions. It can also be used in rheumatology to reduce the severity of arthralgia in chronic musculoskeletal diseases, including rheumatoid arthritis and osteoarthrosis.

The research focuses on developing an improved technology for the production of a stable, non-radioactive form of the radiopharmaceutical composition—a lyophilisate [Oxabifor] suitable for subsequent (in-house) labeling with 153Sm radionuclide directly in a medical setting. This allows for expanded availability of the drug with increased stability during storage, transportation, and shelf life, as well as ensuring more effective and flexible use in the treatment of bone metastases in clinical nuclear medicine practice.

The proposed method for producing the radiopharmaceutical composition [Oxabifor] has been successfully tested in production for the preparation of high-quality radiopharmaceutical "Samarium-Oxabifor labeled with ^{153}Sm". Its characteristics fully comply with pharmacological requirements. The method has also been tested under production conditions, and the company is now moving to mass production of the radiopharmaceutical composition [Oxabifor] for the preparation of the radiopharmaceutical "Samarium-Oxabifor labeled with ^{153}Sm" directly in clinical settings for the treatment of bone metastases in specialized clinics in the Republic of Uzbekistan, with the potential for export to other countries.

References:

1. Krylov, V. V. Radionuclide Therapy with Samarium-153Sm for Metastatic Bone Lesions: Abstract of a Doctor of Medicine dissertation / V. V. Krylov. — Obninsk, 2007. — 40 p.
2. Houfu Deng. Radiopharmaceutical (Sm-153-EDTMP) therapy of skeletal metastases: clinical application in 350 patients / Houfu Deng, Tianzhi Tan, Shuenzhong Luo // The J. Radiol. — 2002. — Vol. 44. — P. 1637–1644.

DEVELOPMENT OF A RAPID METHOD FOR PRODUCING CARRIER-FREE IODINE-125 IN THE FORM OF SODIUM IODIDE

Nishonov Sh.J., Abdukayumov A.M.
State Institution “Radiopreparat”, Institute of Nuclear Physics, Uzbekistan Academy of Science, Tashkent Uzbekistan

This research project focuses on the development of a reliable and rapid method for producing iodine-125 radionuclide (^{125}I) in the form of sodium iodide without a carrier. ^{125}I is widely used to manufacture implantable microsources (Radioactive ^{125}I Seeds) used in prostate cancer brachytherapy, as well as for radiolabeling radiopharmaceuticals and biomedical research.

The starting material is xenon gas enriched to 99% in ^{124}Xe and irradiated with neutrons. After irradiation, the ^{125}I is separated from the xenon using an activated carbon sorption system. Residual ^{124}Xe is removed by subsequent distillation, after which the resulting ^{125}I is converted to sodium iodide by dissolution in sodium hydroxide.

The developed method minimizes the loss of expensive enriched ^{124}Xe, ensures a high technological yield of the target product, with a ^{126}I radionuclide impurity content of less than 10^{-6}% and a ^{125}I radiochemical purity of greater than 99.0%. The proposed technology is promising for the production of ^{125}I intended for the manufacture of microsources and for use in radiopharmaceutical and biomedical research.

References:

1. Rizvi S, Khan SA, Hallemeier CL, et al. Cholangiocarcinoma - evolving concepts and therapeutic strategies. *Nat Rev Clin Oncol*. 2018;15(2):95-111.
2. Wang Z, Zhao Z, Lu J, et al. A comparison of the biological effects of ^{125}I seeds continuous low-dose-rate radiation and 60Co high-dose-rate gamma radiation on non-small cell lung cancer cells. *PLoS One*. 2015;10(8):e0133728.

DEVELOPMENT OF THE LYOPHILIZED [LUTA-TATE] FORMULATION AND [^{177}Lu]Lu-DOTA-TATE RADIOPHARMACEUTICAL: STABILITY EVALUATION

Usarov Z.O.[1], Khujayev S.[2], Khajiev L.O.[1], Abdukayumov A.M.[1], Rikhsiev A.Z.[1]
[1]State Institution "Radiopreparat", Institute of Nuclear Physics, Uzbekistan Academy of Science, Tashkent Uzbekistan
[2]Institute of Nuclear Physics, Uzbekistan Academy of Sciences, Tashkent, Uzbekistan

Peptide receptor radionuclide therapy (PRRT) is an established molecularly targeted approach for treating unresectable or metastatic, well-differentiated and moderately differentiated gastroenteropancreatic neuroendocrine tumors (GEP-NETs) that overexpress somatostatin receptors. The therapeutic effect of PRRT is based on the selective delivery of ionizing radiation to receptor-positive tumor cells, thereby reducing irradiation of surrounding healthy tissues.

Among the radiopharmaceuticals used for PRRT, [^{177}Lu]Lu-DOTA-TATE has gained particular clinical importance. DOTA-TATE binds with high affinity predominantly to somatostatin receptor subtype 2 (SSTR2), which is commonly overexpressed on the surface of differentiated neuroendocrine tumor cells. Following receptor binding and internalization, lutetium-177 emits cytotoxic β^- particles within the tumor tissue. Its accompanying γ-emission also enables scintigraphic imaging, post-therapeutic dosimetry, and evaluation of radiopharmaceutical biodistribution.

Clinical investigations have shown that PRRT with [^{177}Lu]Lu-DOTA-TATE significantly improves progression-free survival, increases the duration of disease control, and helps maintain patients' quality of life compared with conventional high-dose somatostatin analogue therapy [1–5]. Long-term follow-up studies have also confirmed the acceptable safety profile of this treatment when hematological and renal functions are properly monitored [4–6]. The clinical value of [^{177}Lu]Lu-DOTA-TATE is further supported by its regulatory approval in the United States, European Union, and Japan for the treatment of SSTR-positive neuroendocrine tumors [2, 7–9].

The aim of the present study was to develop a lyophilized pharmaceutical composition, designated "[LUTA-TATE]," based on the peptide ligand DOTA-TATE and to determine the shelf lives of both the lyophilized kit and the resulting radiopharmaceutical "[^{177}Lu]Lu-DOTA-TATE, for injection."

DOTA-TATE consists of the somatostatin analogue octreotate, D-Phe-c(Cys-Tyr-D-Trp-Lys-Thr-Cys)-Thr, conjugated with the macrocyclic bifunctional chelator DOTA. The octreotate moiety provides high-affinity binding to SSTR2, whereas DOTA ensures the formation of a thermodynamically and kinetically stable complex with ^{177}Lu [10]. These properties contribute to selective tumor targeting and minimize the release of unbound lutetium ions under physiological conditions.

The developed lyophilized composition contained DOTA-TATE as the active peptide ligand, while ascorbic acid and L-cysteine were incorporated as radioprotective and stabilizing agents [11]. Formulation studies included optimization of the DOTA-TATE content, concentrations of the stabilizers, solution pH, component compatibility, filling conditions, and critical parameters of the freeze-drying cycle. Particular attention was paid to preventing oxidative and radiolytic degradation of the peptide during radiolabelling and subsequent storage.

Radiolabelling was performed using the precursor substance “Lutetium chloride [^{177}Lu]$LuCl_3$, no-carrier-added,” with a specific activity of 92–96 Ci/mg, produced by the State Institution “Radiopreparat.” The lyophilized kit was reconstituted with the required volume of the radionuclide solution, and the labelling reaction was conducted at 90 ^{0}C for 20 min under optimized mildly acidic conditions. The quality of the final radiopharmaceutical was assessed on the basis of its appearance, pH, radiochemical purity, and stability during storage.

The optimized procedure yielded “[^{177}Lu]Lu-DOTA-TATE, for injection” with a radiochemical purity exceeding 99.0% without the need for additional chromatographic purification. This simplifies the manufacturing process, reduces activity losses, shortens preparation time, and limits the radiation exposure of personnel.

Stability studies demonstrated that the lyophilized “[LUTA-TATE]” kit remained suitable for use for at least 6 months when stored at 2–8 ^{0}C. Throughout the investigated storage period, the kit retained its physicochemical properties and, following radiolabelling, yielded [^{177}Lu]Lu-DOTA-TATE with a radiochemical purity above 97%. The final radiopharmaceutical maintained a radiochemical purity exceeding 95% for up to 7 days after preparation under the established storage conditions.

The developed technology therefore provides a reproducible method for producing a ready-to-label DOTA-TATE kit and a high-specific-activity [^{177}Lu]Lu-DOTA-TATE radiopharmaceutical. Centralized manufacture and distribution of the lyophilized kit, followed by on-site radiolabelling in nuclear medicine departments, can simplify logistics, reduce the risk of peptide degradation, and increase the availability of PRRT. The obtained results support further pharmaceutical standardization and introduction of the “[LUTA-TATE]” kit into routine clinical practice.

Keywords: peptide receptor radionuclide therapy, PRRT, DOTA-TATE, lutetium-177, [^{177}Lu)Lu-DOTA-TATE] lyophilized kit, neuroendocrine tumors, SSTR2, radiopharmaceuticals, radiochemical purity, shelf life.

References:

1. J. Strosberg, G. El-Haddad, E. Wolin, A. Hendifar, J. Yao, B. Chasen, et al., “Phase 3 Trial of ^{177}Lu-Dotatate for Midgut Neuroendocrine Tumors,” *New England Journal of Medicine*, vol. 376, no. 2, pp. 125–135, (2017).
2. U.S. Food and Drug Administration (FDA), “FDA Approves Lutetium Lu 177 Dotatate for Gastroenteropancreatic Neuroendocrine Tumors,” FDA, Silver Spring, MD, USA, (2018).
3. L. Bodei, M. Kidd, I.M. Modlin, S. Severi, I. Drozdov, S. Nicolini, et al., “PRRT Genomic Signature in Blood for Prediction of ^{177}Lu-Octreotate Efficacy,” European Journal of Nuclear Medicine and Molecular Imaging. – 2018. Vol. 45. No. 7., pp. 1155–1169.
4. T. Brabander, W.A. van der Zwan, J.J.M. Teunissen, B.L.R. Kam, R.A. Feelders, W.W. de Herder, et al., “Long-Term Efficacy, Survival, and Safety of [^{177}Lu-DOTA0,Tyr3]Octreotate in Patients with Gastroenteropancreatic and Bronchial Neuroendocrine Tumors,” Clinical Cancer Research. – 2017.Vol. 23. No. 16. pp. 4617–4624..
5. D.J. Kwekkeboom, W.W. de Herder, B.L.R. Kam, C.H.J. van Eijck, M. van Essen, P.P.M. Kooij, et al., “Treatment with the Radiolabeled Somatostatin Analog [^{177}Lu-DOTA0,Tyr3]Octreotate: Toxicity, Efficacy, and Survival,” Journal of Clinical Oncology. – 2008. Vol. 26. No. 13., pp. 2124–2130.
6. A. Sabet, K. Ezziddin, U.F. Pape, H. Ahmadzadehfar, K. Mayer, T. Pöppel, et al., “Long-Term Hematotoxicity after Peptide Receptor Radionuclide Therapy with ^{177}Lu-Octreotate,” Journal of Nuclear Medicine. – 2013. Vol. 54. No. 11., pp. 1857–1861.

7. Pharmaceuticals and Medical Devices Agency (PMDA), "Approval of Lutathera® for the Treatment of Somatostatin Receptor-Positive Neuroendocrine Tumors in Japan," Tokyo, Japan, (2021).
8. U.S. Food and Drug Administration (FDA), "Lutathera® (Lutetium Lu-177 Dotatate) Prescribing Information," FDA, Silver Spring, MD, USA, (2024).
9. European Medicines Agency (EMA), "Lutathera®: European Medicines Agency Product Information," Amsterdam, Netherlands, (2024).
10. J.C. Reubi, J.C. Schär, B. Waser, S. Wenger, A. Heppeler, J.S. Schmitt and H.R. Mäcke, "Affinity Profiles for Human Somatostatin Receptor Subtypes SST1–SST5 of Somatostatin Radiotracers Selected for Scintigraphic and Radiotherapeutic Use". European Journal of Nuclear Medicine. – 2000. Vol. 27. No. 3. pp. 273–282.
11. Z.O. Usarov, S. Khujaev, L.O. Xajiyev. Preparation of a lyophilized kit based on the DOTA-TATE peptide ligand and the high-specific-activity radiopharmaceutical "[^{177}Lu]Lu-DOTA-TATE, for injection". – 2026. Interactions,– Springer Nature. Vol., 247. id. 132 p.12.

PREPARATION OF THE LYOPHILIZED HYNIC-IPSMA PHARMACEUTICAL COMPOSITION AND, BASED ON IT, THE [^{99m}Tc]Tc-HYNIC-iPSMA RADIOPHARMACEUTICAL

Usarov Z.O.[1], Khujayev S.[2], Sherov O.O.[1], Khajiev L.O.[1], Abdukayumov A.M.[1], Rikhsiev A.Z.[1]

[1]*State Institution "Radiopreparat", Institute of Nuclear Physics, Uzbekistan Academy of Science, Tashkent Uzbekistan*

[2]*Institute of Nuclear Physics, Uzbekistan Academy of Sciences, Tashkent, Uzbekistan*

Prostate cancer is one of the most frequently diagnosed malignancies and a major cause of cancer-related mortality among men. Accurate detection of primary tumours, lymph-node involvement, distant metastases, and recurrent disease is essential for selecting an appropriate treatment strategy. Prostate-specific membrane antigen (PSMA), also known as glutamate carboxypeptidase II, is a type II transmembrane glycoprotein expressed at high levels in most prostate cancer cells [1, 2]. Its extracellular catalytic domain and internalization following ligand binding make PSMA a suitable molecular target for diagnostic imaging and radionuclide therapy. Although PET/CT with ^{68}Ga- or ^{18}F-labelled PSMA ligands has high diagnostic value, its availability is limited by the cost of equipment and the need for specialized radionuclide-production infrastructure.

Technetium-99m is widely used in diagnostic nuclear medicine because of its favourable half-life of 6.01 h, 140.5-keV γ-emission, relatively low radiation burden, and availability from ^{99}Mo/^{99m}Tc generators. Consequently, ^{99m}Tc-labelled PSMA inhibitors provide an accessible option for PSMA-targeted imaging using conventional SPECT/CT systems. Comparative clinical investigations have demonstrated the diagnostic potential of ^{99m}Tc-labelled iPSMA in patients with prostate cancer [3–5].

Hydrazinonicotinamide (HYNIC) is a bifunctional chelating agent suitable for labelling peptides and small molecules with ^{99m}Tc. Since HYNIC does not completely occupy the technetium

coordination sphere, tricine and EDDA are employed as coligands to improve radiolabelling efficiency, hydrophilicity, and complex stability. HYNIC-iPSMA contains a Glu–urea–Lys-based pharmacophore that specifically binds to PSMA. Preclinical and clinical studies have demonstrated PSMA-specific tumour uptake, rapid blood clearance, predominantly renal elimination, and suitable image quality for detecting prostate cancer lesions [3, 4, 7, 8].

A multinational study reported that [^{99m}Tc]Tc-HYNIC-iPSMA SPECT detected PSMA-positive lesions in 77.5% of patients, changed patient management in 42.5% of cases, and caused no radiopharmaceutical-related adverse events [6]. Furthermore, recent studies on lyophilized HYNIC-PSMA formulations confirmed that kit-based preparation can provide high radiochemical purity and adequate in vitro stability [9].

Therefore, this study aimed to develop and optimize a lyophilized HYNIC-iPSMA pharmaceutical composition and establish the conditions for preparing [^{99m}Tc]Tc-HYNIC-iPSMA with high radiochemical purity and sufficient stability.

Materials and methods. The pharmaceutical composition contained HYNIC-iPSMA as a PSMA-targeting ligand, tricine and ethylenediamine-N,N′-diacetic acid (EDDA) as coligands, tin(II) chloride dihydrate as a reducing agent, and mannitol as a bulking and stabilizing excipient. The quantities of the ligand, coligands, and reducing agent, as well as the pH of the solution, were optimized experimentally. The selected composition per vial contained 30 μg of HYNIC-iPSMA, 20 mg of tricine, 10 mg of EDDA, 30 μg of $SnCl_2 \cdot 2H_2O$, and 50 mg of mannitol. The solution was aseptically filtered through a 0.22-μm membrane, filled into sterile vials, frozen, and lyophilized.

For radiolabelling, sodium pertechnetate [^{99m}Tc]TcO_4 solution obtained from a ^{99}Mo/^{99m}Tc generator was added to the vial. The reaction mixture was heated at 90–95 ^{0}C for 10–20 min. The influence of pH, ^{99m}Tc activity, reaction time, temperature, and ligand-to-radionuclide ratio on radiochemical purity was investigated. Radiochemical purity was evaluated by thin-layer chromatography using chromatographic systems capable of separating [^{99m}Tc]Tc-HYNIC-iPSMA from free pertechnetate and reduced hydrolysed technetium. The pH, appearance, sterility, bacterial endotoxins, and stability of the lyophilized composition and the final radiopharmaceutical were also assessed.

Results. The optimal radiolabelling conditions were achieved at a reaction-mixture pH of approximately 5.0–6.0 and a heating temperature of 90–95 ^{0}C. Under the selected conditions, the radiochemical purity of [^{99m}Tc]Tc-HYNIC-iPSMA was at least 95%. The contents of free [^{99m}Tc]TcO_4^- and reduced hydrolysed technetium were within the established acceptance limits. The resulting radiopharmaceutical was a clear, colourless solution without visible particles and retained acceptable radiochemical purity during the investigated period after preparation. The lyophilized product formed a uniform cake and was readily reconstituted after the addition of sodium pertechnetate solution.

Conclusion. A lyophilized HYNIC-iPSMA pharmaceutical composition suitable for kit-based preparation of [^{99m}Tc]Tc-HYNIC-iPSMA was developed. The optimized formulation and radiolabelling procedure provide a reproducible radiopharmaceutical with high radiochemical purity. The developed kit may represent an accessible option for the SPECT imaging of PSMA-positive prostate cancer lesions using widely available ^{99}Mo/^{99m}Tc generators.

Keywords: HYNIC-iPSMA, prostate-specific membrane antigen, technetium-99m, lyophilized kit, radiopharmaceutical, radiolabelling, SPECT, prostate cancer.

Keywords: DOTA-TATE, lutetium-177, [^{177}Lu)Lu-DOTA-TATE] peptide receptor radionuclide therapy, lyophilized kit, neuroendocrine tumors, radiopharmaceuticals, shelf life, PRRT.

References:

1. Israeli R.S., Powell C.T., Fair W.R., Heston W.D. Molecular cloning of a complementary DNA encoding a prostate-specific membrane antigen. // *Cancer Research*. – 1993. Vol.53(2). pp.227–230.
2. Silver D.A., Pellicer I., Fair W.R., Heston W.D., Cordon-Cardo C. Prostate-specific membrane antigen expression in normal and malignant human tissues. Clinical Cancer Research. – 1997. Vol.3(1). pp.81–85.
3. Ferro-Flores G., Luna-Gutiérrez M., Ocampo-García B.E., et al. Clinical translation of a PSMA inhibitor for ^{99m}Tc-based SPECT. Nuclear Medicine and Biology. – 2017. Vol.48. pp.36–44. doi:10.1016/j.nucmedbio.2017.01.012
4. Santos-Cuevas C., Davanzo J., Ferro-Flores G., et al. ^{99m}Tc-labeled PSMA inhibitor: biokinetics and radiation dosimetry in healthy subjects and imaging of prostate cancer tumors in patients. Nuclear Medicine and Biology. – 2017. Vol.52. pp.1–6. doi:10.1016/j.nucmedbio.2017.05.005
5. Vargas-Ahumada J.E., et al. Diagnostic performance of ^{99m}Tc-iPSMA SPECT/CT in comparison with ^{18}F-PSMA-1007 PET/CT in the primary diagnosis of prostate cancer. – 2023. PubMed
6. Tually P., García Quinto V., Omar Y., et al. Real world experience with [^{99m}Tc]Tc-HYNIC-iPSMA SPECT prostate cancer detection: interim results from the global NOBLE registry. EJNMMI Reports. – 2024. Vol. 8. P.43. doi:10.1186/s41824-024-00226-4
7. Xu X., Zhang J., Hu S., et al. ^{99m}Tc-labelling and evaluation of a HYNIC-modified small-molecular inhibitor of prostate-specific membrane antigen. Nuclear Medicine and Biology. – 2017. Vol.48. pp.69–75. doi:10.1016/j.nucmedbio.2017.01.010
8. Zhang J., Xu X., Lu L., et al. Evaluation of radiation dosimetry of ^{99m}Tc-HYNIC-PSMA and imaging in prostate cancer. Scientific Reports. – 2020. Vol.10. p.4179. doi:10.1038/s41598-020-61129-5
9. Bokhari T.H., et al. Development of freeze-dried kit for the preparation of [^{99m}Tc]Tc-HYNIC-ALUG: a potential agent for imaging of prostate-specific membrane antigen. Iranian Journal of Nuclear Medicine. – 2024. https://irjnm.tums.ac.ir/journal/article_40145.html.

ACCELERATED VOXEL-WISE 3D DOSIMETRY FOR ^{177}LU-PSMA THERAPY VIA PHYSICS-INFORMED NEURAL NETWORKS INCORPORATING TRANSPORT CONSTRAINTS

Bozorov E.Kh.[1], Baymuratova I.V.[2]
[1]*Institute of Nuclear Physics, Uzbekistan Academy of Sciences, Tashkent, Uzbekistan*
[2]*Tashkent State Technical University, Tashkent, Uzbekistan*

1. Introduction. Targeted radiopharmaceutical therapy with ^{177}Lu-PSMA-617 is a standard treatment for metastatic castration-resistant prostate cancer (mCRPC). However, fixed-activity protocols (7.4 GBq per cycle) neglect patient-specific pharmacokinetic and anatomical variations. The Medical Internal Radiation Dose (MIRD) scheme introduces systematic dosimetric errors of 25–40% in critical structures due to phantom homogeneity assumptions. While Monte Carlo (MC) simulations represent the dosimetric gold standard, their high computational cost prevents routine clinical deployment. Standard deep learning alternatives accelerate processing but introduce non-

physical artifacts, spatial over-smoothing, and conservation violations. This study presents a hybrid Physics-Informed Neural Network (PINN) that embeds radiation transport physics directly into model optimization.

2. Methods Patient Cohort & Pre-processing: Retrospective SPECT/CT scans from 112 patients undergoing ^{177}Lu-PSMA-617 therapy were evaluated at 4-, 24-, 48-, and 96-hours post-injection. CT images were converted into electron density and tissue composition maps using Hounsfield Unit (HU) bi-calibration. Data was partitioned into training (n=80), validation (n=12), and external testing (n=20) cohorts.

Monte Carlo Ground Truth: Reference dose distributions (DMC) were generated using GATE v9.2 / Geant4 11.0 with 5×10^8 primary decay histories per volume, ensuring statistical uncertainty below 1.5% in high-activity regions.

Network Architecture: A 3D Attention U-Net processes a three-channel tensor: cumulative activity ($\tilde{A}(r)$), tissue density ($\rho(r)$), and spatial density gradients ($\nabla\rho(r)$).

Optimization Objective: The model was trained using AdamW over 200 epochs. The loss function (Ltotal) combines empirical data loss (Ldata), strict volume-integrated energy conservation (L_{energy}), and tissue-boundary gradient regularization (L_{grad}): $L_{total}=W_{data}L_{data}+W_{energy}L_{energy}+W_{grad}L_{grad}$

3. Results Dosimetric Precision: The PINN model achieved a Structural Similarity Index (SSIM) of 0.984±0.007 and a mean absolute error (MAE) below 2.3% relative to reference GATE MC calculations. MAE in specific regions was 1.9±0.4% in renal parenchyma, 2.4±0.6% in bone lesions, 1.2±0.3% in liver, and 2.1±0.5% in enlarged lymph nodes ($p>0.05$ across all regions vs. MC) Fig. 1.

Clinical Parameters: Dose-volume histogram (DVH) parameters (D_{50}, D_{98}) for target lesions and organs-at-risk deviated by less than 1.8% from MC baselines, with Bland-Altman statistics showing a minimal mean bias of -0.02 Gy. Physical loss constraints successfully suppressed energy dispersion past the physical range of ^{177}Lu β-particles ($R_{max}\approx2$ mm).

Computational Speed: Generating a 128×128×128 voxel dose map required 1.12 seconds on an NVIDIA RTX 4090 GPU, accelerating computation over 40,000-fold compared to CPU-based Monte Carlo runs (14.2 hours) and outperforming GPU-accelerated MC runs (42 minutes).

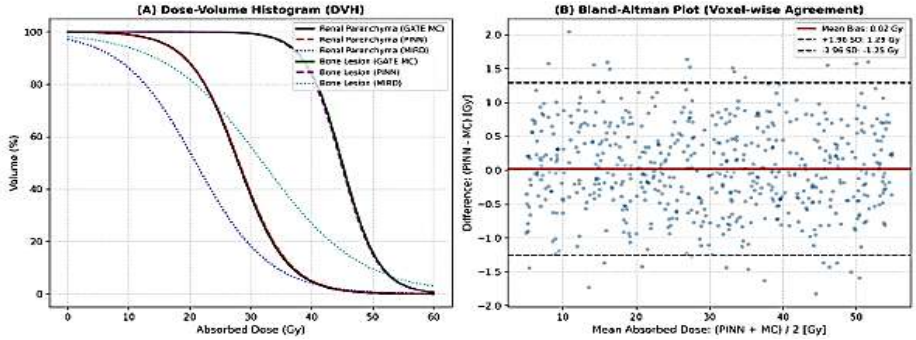

Figure 1. Qualitative 3D absorbed dose map evaluation for a representative patient undergoing ^{177}Lu PSMA-617 radioligand therapy.

4. Discussion & Conclusion. Integrating physical transport principles into neural network loss functions resolves the historical compromise between Monte Carlo precision and analytical execution speed. Physical constraints eliminate non-physical artifacts and preserve sharp gradients at soft tissue-bone interfaces. Current limitations include adaptation to high-LET alpha emitters

(225Ac) and partial volume effects in initial SPECT acquisitions. This framework provides a real-time foundation for personalized 3D voxel-level dosimetry in routine nuclear medicine clinical workflows.

References:

1. Alshehri Ali H. D. (2025). Advancing Internal Dosimetry in Personalized Nuclear Medicine: Toward Optimized Radiopharmaceutical Use 1741;https://doi.org/10.3390/ph18111741 in Clinical Practice. Pharmaceuticals, 18(11).
2. Brosch-Lenz, J. F., Delker, A., Schmidt, F., & Tran-Gia, J. (2023). On the use of artificial intelligence for dosimetry of radiopharmaceutical therapies. Nuklearmedizin, 62(6), 379–388. https://doi.org/10.1055/a 2179-6872.
3. Schneider, W., Bortfeld, T., & Schlegel, W. (2000). Correlation between CT numbers and tissue parameters needed for Monte Carlo simulations of clinical dose distributions. Physics in Medicine & Biology, 45(2), 459–478. https://doi.org/10.1088/0031-9155/45/2/314.
4. Pantelis, E., Logothetis, A., Zoros, E., Pappas, E. P., Papagiannis, P., Paddick, I., Nordström, H., Kollias, G., & Karaiskos, P. (2023). Dosimetric accuracy of the Convolution algorithm for Leksell Gamma Plan radiosurgery treatment planning: Evaluation in the presence of clinically relevant inhomogeneities. Journal of Applied Clinical Medical Physics, 24(5), e13903. https://doi.org/10.1002/acm2.13903 .
5. Petti, P. L., Rivard, M. J., Alvarez, P. E., Chen, Z., Followill, D. S., Halyard, M. Y., Klein, E. E., Moser, R. P., Sixel, K. E., & Wang, J. Z. (2021). Recommendations on the practice of calibration, dosimetry, and quality assurance for gamma stereotactic radiosurgery: Report of AAPM Task Group 178. Medical Physics, 48(7), e733–e770. https://doi.org/10.1002/mp.14831.
6. Hadjiiski, L., Cha, K., Chan, H. P., Drukker, K., Morra, L., Nappi, J. J., Sahiner, B., & Yoshida, H. (2023). AAPM task group report 273: Recommendations on best practices for AI and machine learning for computer-aided diagnosis in medical imaging. Medical Physics, 50(2), e1–e24. https://doi.org/10.1002/mp.16188.
7. Bas H.M. van der Velden, B. H. M., Kuijf, H. J., Gilhuijs, K. G. A., & Viergever, M. A. (2022). Explainable artificial intelligence (XAI) in deep learning-based medical image analysis. Medical Image Analysis, 79, 102470. https://doi.org/10.1016/j.media.2022.102470 .
8. Kim, K. M., Lee, M. S., Suh, M. S., Cheon, G. J., & Lee, J. S. (2023). Voxel-based internal dosimetry for 177Lu-labeled radiopharmaceutical therapy using deep residual learning. Nuclear Medicine and Molecular Imaging, 57(1), 18–27. https://doi.org/10.1007/s13139-022-00769-z.

REDUCING INDOOR RADON INGRESS: IMPREGNATING COMPOSITION BASED ON POLYALKYLHYDRIDE SILOXANE AND TETRAETHOXYSILANE HYDROLYSATE

Khaydarov R.R., Gapurova O.U.
Institute of Nuclear Physics, Uzbekistan Academy of Sciences, Tashkent, Uzbekistan

Radon (^{222}Rn) is a colourless, odourless radioactive gas with a half-life of 3.8 days that arises from the decay of uranium present in rocks. It enters buildings chiefly from the underlying soil, migrating through cracks and joints in foundations and basement walls, and is additionally released by the construction materials themselves, so that it accumulates in basements and on ground floors. The World Health Organization classifies radon as a Group 1 human carcinogen, and up to 15 % of lung cancer deaths worldwide are attributed to it. Conventional water-repellent impregnations reduce water uptake but have little effect on gas transport; what is required instead are formulations that plug the pore space throughout the bulk of the material. The aim of the present work was to increase the gas impermeability of concrete and other building materials, radon included.

The composition developed is the reaction product of a polyalkylhydride siloxane (polyethyl- or polymethylhydride siloxane) and tetraethoxysilane (TEOS) hydrolysate in an alcohol medium, prepared in the presence of an amine-containing catalyst; Sn-organic catalysts were examined as well. TEOS was selected because, among the esters of orthosilicic acid, it is the most readily available, the cheapest and the least toxic; unlike the alkyltriethoxysilane used in our earlier formulation [1], it is tetrafunctional and therefore gives a more highly branched network. The proposed mechanism comprises transesterification of TEOS by the alcohol to mixed esters of orthosilicic acid, hydrolysis of these esters by residual moisture in the alkaline environment of concrete (pH 11–12), and polycondensation in which ≡Si–O–Si≡ bonds grow in all directions. A spatially cross-linked gel, chemically bonded to the substrate, is thus formed within the pores and capillaries. The composition penetrates moist concrete to a depth of 9–10 mm, which increases to 15–20 mm when the specimens are pre-treated with $Ca(OH)_2$.

Concrete specimens (30 mm in diameter, 15 mm high) and gypsum specimens (30 mm in diameter, 10 mm high) were treated layer by layer, three to five coats being applied by brush or spray. Gas permeability was determined from the coefficient $\mathbf{K = V \cdot d/(S \cdot t \cdot p)}$, in which V is the volume of gas that passed through the specimen, d the specimen thickness, S its area, t the gas transit time and p the pressure drop (0.1–0.2 atm). The effect of the treatment was expressed as the ratio K_0/K_t, where K_0 and K_t are the permeability coefficients of the untreated and the treated specimen. Applied separately and without a catalyst, TEOS and the polyalkylhydride siloxane gave no more than $K_0/K_t = 1.0–1.4$. The optimum route proved to be hydrolysis of TEOS with the amine-containing catalyst in an open vessel for 40–45 h at 22–23 °C (mass loss 38–41 %), followed by dilution with isopropyl alcohol at 1:1 and addition of the polyalkylhydride siloxane, also at 1:1. For concrete, $K_0/K_t = 500$ was reached and retained for at least 60 days; for gypsum the value was 400, falling to 150 after 150 days.

The measurements were performed with air and argon, which were used as surrogate gases for radon. Four independent lines of evidence justify this approach. First, the kinetic diameter of argon (≈3.40 Å) is appreciably smaller than the atomic diameter of radon (≈4.17 Å), and according to the “square of the diameter” model [2] the logarithm of the permeation coefficient of polymer films varies linearly with the square of the molecular diameter, which allows the behaviour of the lighter noble gases to be extrapolated to radon; for barrier materials, an exponential dependence of noble-

gas permeability and diffusivity on the square of the atomic radius has been confirmed independently [3]. Second, free-volume theory predicts a steep fall in the diffusion coefficient as the size of the penetrant grows, so the steric hindrance imposed by the polymer network is necessarily greater for radon than for argon. Third, it has been shown [4] that once the Klinkenberg correction is applied the intrinsic permeabilities of helium and argon in concrete are practically identical; the reduction in argon permeability measured here therefore reflects a genuine rearrangement of the pore structure rather than gas-slippage effects. Finally, a positive exponential relationship between the gas permeability of a material and its radon exhalation rate has been established experimentally [5]. The K_0/K_t values obtained with argon may thus be regarded as a conservative lower bound on the barrier performance of the coating towards ^{222}Rn.

The composition is inexpensive and can be applied by brush or spray; its consumption amounts to 0.3–0.8 g per specimen 30 mm in diameter, which corresponds to approximately 0.4–1.0 L/m^2. It therefore appears promising as a radon barrier, particularly in regions where the soil is rich in uranium. Further work will be directed towards the direct measurement of the ^{222}Rn diffusion coefficient through treated specimens.

Acknowledgement. The present research work has been funded by the State budget of Uzbekistan within the fundamental research topic of the Laboratory of Interdisciplinary Technologies of the Institute of Nuclear Physics, Uzbekistan Academy of Sciences.

References:

1. Khaydarov R.R., Gapurova O.U. Composition for impregnating building materials to decrease their gas permeability // J. Environ. Sci. Health, Part A. 2026. DOI: 10.1080/10934529.2026.2684865.
2. Hammon H.G., Ernst K., Newton J.C. Noble gas permeability of polymer films and coatings // J. Appl. Polym. Sci. 1977. Vol. 21. P. 1989–1997.
3. Schowalter S.J., Connolly C.B., Doyle J.M. Permeability of noble gases through Kapton, butyl, nylon and “Silver Shield” // Nucl. Instrum. Methods Phys. Res. A. 2010. Vol. 615. P. 267–271.
4. Lamouchi T., Levasseur S., Potier L. et al. About gas permeability and diffusion through concrete // Mater. Proc. 2023. Vol. 13. P. 42.
5. Xiong G., Dai J., Wang H. et al. Experimental study on gas permeability and radon control performance of red clay covering layer on uranium mill tailings pond // Sci. Rep. 2025. Vol. 15. P. 8326.

MEASUREMENT OF THE SPECIFIC ACTIVITY OF ^{222}Rn AND ^{226}Ra IN DRINKING AND GROUNDWATERS IN TASHKENT

Vasidov A., Vasidova S.O.
Institute of Nuclear Physics, Uzbekistan Academy of Sciences, Tashkent, Uzbekistan

The paper presents the results of measuring the specific activities of ^{222}Rn and ^{226}Ra in drinking and groundwater in Tashkent, which changed in a 1.92÷5.70 Bq/l for ^{222}Rn and 0.22÷0.80 Bq/l for ^{226}Ra in drinking water and 4.40÷61.40 Bq/l for ^{222}Rn and 0.30÷0.56 Bq/l for ^{226}Ra in groundwater. The annual effective doses received from ^{222}Rn and ^{226}Ra as a result of water consumption during the year by adults and children were estimated. The values of specific activities of ^{222}Rn and ^{226}Ra in drinking and groundwater in Tashkent prove that the dose load from ^{222}Rn and ^{226}Ra does not pose a health hazard to the population, due to the lower concentration than the established radiation safety standards of the Republic of Uzbekistan.

ENVIRONMENTAL MONITORING OF RADIONUCLIDE SPECIFIC ACTIVITY IN MAN-MADE SITES IN THE NAVOI REGION

Jurakulov A.R.[1], Muzafarov A.M.[1], Kurbanov B.I.[2], Khaitov F.N.[2], Mingbayev Kh.S.[2], Elimov Kh.B.[1]

[1]Navoi State University of Mining and Technology, Navoi, Uzbekistan

[2]Institute of Nuclear Physics, Uzbekistan Academy of Sciences, Tashkent, Uzbekistan

This paper presents the results of radioecological monitoring of man-made objects in the Navoi region of the Republic of Uzbekistan. The study focuses on the specific activity of natural radionuclides uranium-238 (U-238) and radium-226 (Ra-226) in the liquid phase and drainage waters of the tailings pond of Hydrometallurgical Plant No. 1 (HMP-1). An assessment of the current state of the aquatic ecosystem in the affected area is provided, the risks of radionuclide migration into adjacent environments are analyzed, and recommendations for improving the environmental monitoring system are proposed.

Key words: radioecological monitoring, Navoi region, GMZ-1 tailings storage facility, uranium-238, radium-226, specific activity, radiation safety.

Introduction Navoi Region is the largest industrial region of the Republic of Uzbekistan, home to large-scale mining and processing facilities. Long-term mining and processing of uranium-containing ores has generated significant volumes of radioactive waste, which are stored in specialized tailings ponds. One of the key facilities requiring continuous radiation monitoring is the tailings pond of Hydrometallurgical Plant No. 1 (HMP-1). Tailings ponds are man-made anomalies that can act as potential sources of long-term radioecological impact on the environment. Therefore, systematic monitoring of the hydrosphere within the HMP-1 zone of influence is a priority for ensuring the region's environmental safety.

The purpose of the study A comprehensive radioecological assessment of the condition of water bodies in the area of the GMZ-1 tailings pond in the Navoi region was conducted based on the determination of the specific activity of uranium-238 and radium-226 radionuclides, as well as an analysis of their migration dynamics to prevent contamination of groundwater and surface water.

Research Materials and Methods The study focused on the liquid phase of the reclaimed beach of the GMZ-1 tailings dam, as well as a network of monitoring drainage wells located along the perimeter of the sanitary protection zone. Water sampling was conducted in accordance with current regulations (GOST R 51592-2000, SanPiN RUz). A total of over 1,000 water samples collected during the spring, summer, and fall were analyzed.

The specific activity of radionuclides was determined using laboratory radiation monitoring methods:

1. Uranium-238 (U-238) was determined photometrically using the "MVI C-136:2017 Methodology for Measuring the Mass Concentration of Uranium in Natural and Waste Waters..." .

2. Radium-226 (Ra-226) was analyzed using the KAMERA instrument using the emanation method (based on radon-222). The activity of the daughter decay product, Rn-222, which is in radioactive equilibrium with radium, was measured.

Results and Discussion During monitoring studies, numerical values of the specific activity of the radionuclides under study were determined at various sampling points within the GMZ-1 tailings pond. In process water samples (directly from the tailings pond basin), the specific activity of uranium-238 ranged from 3.2 to 8.4 Bq/L. These high concentrations are due to the specific nature of the sulfuric acid and soda leaching used in processing the raw materials. The specific

activity of radium-226 in these same samples ranged from 0.18 to 1.1 Bq/L. The relatively low radium content in the liquid phase compared to uranium is explained by its coprecipitation with calcium and barium sulfates in the solid fraction of the tailings (cake).

The following parameters were recorded in drainage and monitoring wells of the aquifer located immediately below the surface, adjacent to the tailings dam:

- U-238 specific activity ranged from 0.56 to 1.8 Bq/L, which in some places exceeds the regulatory levels for drinking water but complies with the limits for controlled access process zones.
- Ra-226 specific activity in groundwater within the monitoring loop ranged from 0.12 to 0.38 Bq/L, within hygienic safety standards.

Conclusions and Recommendations

1. Monitoring showed that the GMZ-1 tailings pond has a localized man-made impact on the hydrosphere. The main migrating component determining the radiation environment in the liquid phase is uranium-238.
2. The specific activity values of radium-226 in the observation wells are within the permissible regulatory limits, indicating the effectiveness of natural geochemical barriers in retaining this radionuclide.

DETERMINATION OF URANIUM ISOTOPE ACTIVITY IN PROCESS WATERS AND ADVANCED SORPTION MATERIALS FOR THEIR REMOVAL

Ydyrysheva S.K.[1,2], Lennik S.G.[1], Mirkhaji D.V.[1], Kunarbekova M.S.[2], Kaiyrbekova A.S.[1], Azat S.[2]

[1]Institute of Nuclear Physics of the Agency of the Republic of Kazakhstan for Atomic Energy, Almaty, Kazakhstan

[2]Satbayev University, Almaty, Kazakhstan

Uranium exhibits significant chemical toxicity and relatively low radiological hazard. Its mobility and solubility in aquatic environments facilitate migration and accumulation, posing risks to human health and water quality. Industrial processes utilizing uranium-containing materials frequently generate radionuclide-contaminated wastewater and sludge. Therefore, systematic monitoring of uranium in environmental and industrial waters is essential for assessing and mitigating ecological and health risks.

At the Institute of Nuclear Physics, uranium isotope activity concentrations in natural, industrial, and wastewater samples are measured using alpha spectrometry following radiochemical separation. The analytical procedure includes the addition of ^{232}U as an isotopic tracer, co-precipitation with iron hydroxide, extraction with tributyl phosphate, back-extraction, and electrochemical deposition onto a steel disk. Elevated uranium activity concentrations have been detected in mining and industrial wastewater. Specifically, settling pond waters from gold-processing facilities contained ^{234}U at 4.57 - 14.8 Bq/L and ^{238}U at 3.84 - 10.1 Bq/L, surpassing the intervention levels of 2.8 and 3.0 Bq/L, respectively. These findings highlight the need for effective technologies for uranium removal from contaminated waters.

Conventional treatment methods typically achieve limited uranium removal, emphasizing the necessity for more efficient purification technologies. Adsorption offers a promising solution because of its operational simplicity, cost-effectiveness, high efficiency, and potential for sorbent

regeneration. Among advanced sorbents, MXenes, which are two-dimensional transition-metal carbides and nitrides, are especially promising due to their high surface area, hydrophilicity, and abundance of surface functional groups that enhance uranium adsorption. Consequently, MXene-based materials constitute a promising platform for uranium removal from aqueous systems and merit further investigation regarding their selectivity, adsorption mechanisms, and performance in real wastewater conditions.

COMPREHENSIVE ASSESSMENT OF THE BASELINE RADIOLOGICAL STATE OF WATER RESOURCES IN THE ECOSYSTEM OF THE PLANNED NUCLEAR POWER PLANT CONSTRUCTION AREA

Sadikov I.I., Yarmatov B.Kh., Rozmetova F.Kh., Sharipova S.M., Akhmedov Ya.A., Solijonov S.N., Malikov A.A., Tashimova F.A.

Institute of Nuclear Physics, Uzbekistan Academy of Sciences, Tashkent, Uzbekistan

The primary objective of this study is a comprehensive assessment of the baseline radiation background of all types of water resources (drinking, surface, groundwater, and irrigation water) in the area of the planned nuclear power plant to ensure environmental safety and organize radiological monitoring.

Sampling was conducted in the 2nd quarter of 2026 at the NPP construction site. Given the high mineralization of all types of water samples (>1 g/kg), the radiochemical coprecipitation method was used to determine the gross alpha and beta activity. Measurements were performed using low-background UMF-2000 (alpha/beta), Canberra HPGe (gamma spectrometry), and MKGB-01 (radon and strontium) counting systems. To ensure the reliability of the measurements, alongside water sources, bottom sediments and aquatic vegetation from Lake Tuzkan were analyzed.

Comprehensive radiological analyses showed that in all water sources (drinking, groundwater, and surface), the gross beta activity is below the regulatory limit (2.0 Bq/kg). The specific activity of artificial radionuclides (^{137}Cs, ^{60}Co, ^{90}Sr) in all investigated objects (water, lake bottom sediments, and vegetation) was below the detection limit of the instruments used. It was confirmed that the specific activity of radon-222 in groundwater is significantly lower than the limit of 60 Bq/kg established by SanPiN No. 0193-06 requirements (the maximum value in well GW-7 was 11.62±1.9 Bq/kg). The contents of ^{40}K, ^{226}Ra, and ^{232}Th in the bottom sediments of Lake Tuzkan correspond to the background levels of the region's soils.

The main focus of the study was on the gross alpha activity exceeding the limit set by SanPiN No. 0193-06 for drinking water (0.2 Bq/kg) in several water samples from the given area. Specifically, this situation was observed in surface waters (1.15±0.20 Bq/kg in SW-01) and several groundwater wells (GW-6, GW-7, GW-8). Furthermore, a clear difference was identified in the alpha activity of drinking water (WP-1, <0.1 Bq/kg) and irrigation water (WO-1, 0.15±0.07 Bq/kg) within the same settlement—Uzunkuduk village. This difference is explained by the fact that drinking water is extracted from deep horizons (80-100 m), whereas irrigation water comes from shallow aquifers (20-30 m), as well as the susceptibility of shallow waters to the influence of surface geological formations and naturally occurring radioactive materials in the soil composition. Although the gross alpha activity in irrigation waters is high (up to 0.49 Bq/kg in WO-2), a direct comparison of this parameter with drinking water standards is radioecologically incorrect.

It was established that the radiation situation in the aquatic ecosystem at the NPP site is formed exclusively by natural factors, and there is no anthropogenic contamination in the area. The elevated gross alpha activity in shallow waters (including irrigation and lake waters) is driven by the lithological and geochemical characteristics of the territory. To assess the actual risk of the parameters in irrigation waters, it is recommended to conduct an isotopic analysis of agricultural products, taking into account the transfer factor of radionuclides along the "water-soil-plant" chain, rather than analyzing the water itself.

ASSESSMENT OF THE DISTRIBUTION AND INITIAL BACKGROUND LEVELS OF GAMMA-EMITTING RADIONUCLIDES (K-40, Cs-137, Co-60, Ra-226, and Th-232) IN SOILS AT THE SITE OF A NUCLEAR POWER PLANT UNDER CONSTRUCTION

Sadikov I.I., Yarmatov B.Kh., Rozmetova F.X., Akhmedov Ya.A., Solijonov S.N.
Institute of Nuclear Physics, Uzbekistan Academy of Sciences, Tashkent, Uzbekistan

Currently, in the design and construction of large energy facilities, particularly nuclear power plants (NPPs), ensuring the environmental radiation safety and thoroughly studying the initial (background) radiological situation are priority tasks. Determining the distribution patterns of natural and artificial radionuclides in the area, their migration through soil layers, and radioactive background indicators before the NPP is commissioned serves as the primary baseline data for future environmental monitoring.

The purpose of this study is to assess the total content, quantitative distribution, and depth-dependent variation characteristics of gamma-emitting radionuclides (^{40}K, ^{137}Cs, ^{60}Co, ^{226}Ra, and ^{232}Th) in soils from selected monitoring points at the NPP construction site.

During the study, a total of 10 monitoring points (from P-1 to P-10) were selected within the NPP construction area. Soil samples were taken layer-by-layer at 1 cm intervals down to a depth of 10 cm using a steel probe (a total of 100 layer-by-layer samples, plus 2 additional bottom sediment samples from the lake, P-11 and P-12).

According to the gamma-spectrometric analysis results, the specific activity of natural and technogenic radionuclides in the soils of the studied area demonstrated the following values:

Exhibiting the highest activity in the soil samples, the specific activity of 40K was determined to be in the range of 400–600 Bq/kg. The content of the natural radionuclide 232Th was noted to be stable, at around 20–30 Bq/kg. The specific activity of 226Ra fluctuated between 18 and 32 Bq/kg. The content of the technogenic radionuclide 137Cs was 4–15 Bq/kg, and in some layers, it was found to be below the detection limit (< 3 Bq/kg). In all analyzed samples, the 60Co content was below the minimum detectable activity (ranging from < 3 to < 7 Bq/kg), indicating the absence of technogenic contamination.

When analyzing the vertical distribution of radionuclides along the soil profile, it was found that the migration characteristics of natural (^{40}K, ^{226}Ra, ^{232}Th) and technogenic (^{137}Cs) radionuclides differ. The concentration of natural radionuclides was distributed relatively evenly within the 0-10 cm depth interval, and no sharp changes with depth were observed. However, the bulk of the ^{137}Cs was found to be accumulated in the upper soil layers. As the depth increased (7–10 cm), the amount of ^{137}Cs sharply decreased, showing values below the detection limit (< 3–4 Bq/kg) at most points.

This confirms that technogenic ^{137}Cs is retained in the topsoil, and its vertical migration into lower layers proceeds very slowly.

The assessment of the radiation-ecological state of the soils at the NPP construction site showed that the background levels of gamma-emitting radionuclides in the studied area are within the range characteristic of natural lithological rocks and do not exhibit signs of high-level technogenic contamination. The obtained baseline data will serve as a reliable foundation for conducting and controlling environmental radiation monitoring during the future operation of the NPP.

APPLICATION OF THE ASPIRATION METHOD FOR MEASURING THE VOLUMETRIC ACTIVITY OF RADON DECAY PRODUCTS IN THE ATMOSPHERE

Mukashova A.B.[1], Mamytbekov U.K.[1], Yusupov R.Kh.[2], Kidibaev M.M.[1], Jeenbaev N.J.[1]

[1]Academician J.Jeenbaev Institute of Physics, National Academy of Sciences, Bishkek, Kyrgyz Republic

[2]K.Tynystanov Issyk-Kul State University (IKSU), Karakol, Kyrgyz Republic

Radiation and environmental monitoring is an important component of the system for ensuring radiation safety of the population of Kyrgyzstan. Particular importance is given to the study of natural sources of ionizing radiation, including radon, in areas with elevated natural radiation exposure and in regions where facilities associated with radioactive materials are located.

The decay of ^{222}Rn produces short-lived decay products, including ^{218}Po, ^{214}Pb, and ^{214}Bi. These radionuclides can attach to airborne aerosol particles and, when inhaled, deposit in the human respiratory tract, thereby creating an additional radiation dose due to α- and β-radiation [1, 2].

Monitoring the concentration of radon decay products (RDPs) is important for assessing radiation safety in residential buildings. One of the methods used to determine their concentration is the aspiration method, which is based on passing air through a filter that retains radioactive aerosols, followed by measurement of their activity [3, 4, 5].

The concentration of radon decay products is characterized by their volumetric activity (VA), expressed in Bq/m³. To assess the radiation environment, the equilibrium equivalent radon concentration (EERC) is also used, which takes into account the degree of radioactive equilibrium between radon and its short-lived decay products. The degree of disequilibrium is characterized by the equilibrium factor F.

An active aspiration method was used in this study. The air under investigation was drawn through an AFA-RSP-20 aerosol filter at a specified flow rate. During sampling, aerosol particles containing radon and thoron decay products were deposited on the surface of the filter.

The measurements were performed using a RAMON-01M instrument. Alpha radiation was recorded after aerosol sampling. The measurement principle is based on detecting α-radiation from ^{218}Po and other decay products deposited on the filter.

The aerosol sample was collected for 4 minutes. After sampling was completed, the activity of the filter was measured for 30 minutes, with registration beginning no earlier than 5 hours after sampling. Measurements were performed during the 1st–4th and 7th–10th minutes of the counting period.

The volumetric activity of individual radon decay products was calculated taking into account the α-radiation detection efficiency, filtration efficiency, air flow rate, volume of the collected air sample, and the time elapsed between the end of sampling and the start of registration.

The study was conducted in a multi-story residential building located in the village of Kaji-Sai, Issyk-Kul Region. Measurements were performed in the basement and on the 1st–4th floors of the building. The results obtained showed that the volumetric activity of radon varies depending on the season and the air-exchange conditions inside the premises.

During the winter period, the volumetric activity of ^{222}Rn ranged from 22 to 87 Bq/m³, whereas during the summer period values of 30–65 Bq/m³ were observed. Thus, seasonal variations in radon concentration were identified in the building under study.

The increase in radon concentration during the cold season may be associated with reduced natural ventilation and decreased air exchange in the premises. As a result, radon entering the building from the soil and other sources accumulates indoors.

The volumetric activity of radon is also affected by the location of the premises within the building. The highest values were observed in the basement and on the first floor. This may be attributed to their direct proximity to the soil, which is one of the main sources of radon entering buildings. Additional sources may include construction materials, water, and outdoor air.

It was established that the volumetric activity of ^{222}Rn depends on seasonal conditions, the intensity of air exchange, and the location of the premises within the building. The highest values were observed in the basement and on the lower floors, while during the winter period, radon concentrations in some premises were higher than those observed in summer.

The results obtained confirm the need for systematic radiation monitoring of residential buildings, particularly in regions with potentially elevated levels of natural radiation. The aspiration method can be recommended for assessing the radiation environment and identifying premises that require additional measures to reduce radon exposure.

References:

1. Киселев С.М., Жуковский М.В., Стамат И.П., Ярмошенко И.В. Радон: от фундаментальных исследований к практике регулирования М.: ФГБУ ГНЦ ФМБЦ им. А.И. Бурназяна ФМБА России, 2016.- 432с.
2. Оценка облучения населения ионизирующим излучением. Доклад Научного комитета Организации Объединенных Наций (ООН) по действию атомной радиации. Нью-Йорк, 2023. https://news.un.org/ru/story/2026/02/1467364
3. Яковлева, В.С. Методы определения объемной активности изотопов радона и продуктов распада в воздухе. Национальный исследовательский Томский политехнический университет: Томск, 2019. –119с.
4. Асаналиева Т.М., Мамытбеков У.К., Кидибаев М.М., Мукашова А.А. О методах контроля облучения населения Иссык-Кульской области природными источниками, ионизирующего излучение: монография. – Б.: 2024. -262с.
5. Карпачев Б.М., Менг Б.М. Радиационно-экологические исследования в Кыргызстане: учеб. пособ. –Б.: 2000.- 100с.

THE USE OF CR-39 TRACK DETECTORS FOR AGE ASSESSMENT OF THE ANCIENT HUMAN AND ANIMAL BONES

Vasidov A.
Institute of Nuclear Physics, Uzbekistan Academy of Sciences, Tashkent, Uzbekistan

Among the methods of radiogenic dating of archaeological materials, radiometric methods for dating bone finds play an important role. Bone materials have always been of interest to archaeologists, paleontologists and historians, as they contain biological, archaeological and chronological information. Radiogenic dating methods include radiocarbon, potassium-argon, uranium-lead and thorium-lead methods. They are based on the constant rate of radioactive decay of natural radioisotopes in bone materials. A review of the literature on the measurement of ^{222}Rn and ^{226}Ra in bone samples was showed that radon measurements are mainly carried out using nuclear solid-state track detectors (NSSTDs), especially with type of track detector CR-39.

The aim of this work was to study of the correlation between specific activity of Ra-226 and age years of the ancient human and animal bones by using CR-39 track detector.

Being a radioactive metal, ^{226}Ra belongs to one of the subgroups of alkaline earth elements and is similar to calcium. The half-life of ^{226}Ra is 1602 year (y), it emits α- and γ-particles with energies of 4.5 MeV and 186.2 keV, respectively. As a α-decay of the ^{226}Ra is formation to inert radioactive gas radon-222 (^{222}Rn), with a half-life of 3.82 days. The radioactive equilibriums are reached between of ^{222}Rn and ^{226}Ra within 35-40 days at isolated system. However, a literature review reveals at the long-period bedding of skeletons affecting to the specific activity of Ra-226 in bone-soil system so far have remained scarce and are poorly understood.

The studied samples of bones and soils with a mass of 10 g were placed on the plastic cups and installed at the bottom of the plastic chamber, the CR-39 detector was fixed in the upper part of the plastic chamber. To protect against external atmospheric influences, the outer circle of the chamber was isolated with a thin layer of sealant. Fifteen chambers were exposed simultaneously for 35 days.

The author of this work have been developed very simple, accessible, highly sensitive and selective method, for assessment of the ages of the ancient bones of humans and animals by measuring specific activity of ^{226}Ra on the CR-39 track detector. There was suggested calibration curve and determined the existence of correlation between specific activity of ^{226}Ra and ages of skeletons. It is established the age of the Selungur archanthrop is ≤0.10 mln y. The old of bones Kashkadarya and Angren mammoths were 8.2 and 8.5 mln years. That claimed, some 10 mln years ago in territory Central Asia had been life.

As is well known, ancient bone remains have being the material cultural heritage of the country, where they are discovered. So, it is difficult to collect them in a center for study due to being of some barriers. This estimating method of the age of ancient bones is not complex to implement. I would like to see others results by using suggested method.

RADIONUCLIDE ANALYSIS OF ENVIRONMENTAL SAMPLES WITH DISTURBED RADIOACTIVE EQUILIBRIUM

Lennik S., Kabirova K., Silachyov I.
Institute of Nuclear Physics of the Agency of the Republic of Kazakhstan for Atomic Energy, Almaty, Kazakhstan

The behavior of radionuclides in the environment and their interaction with living organisms are of significant interest, particularly given the growth of the nuclear industry. Radioecological studies involve the determination of not only the parent radionuclides ^{238}U and ^{232}Th but also their daughter products, which pose an even greater hazard due to their high toxicity and mobility. The following gamma-lines of the natural radionuclides were observed in the spectra: ^{210}Pb (46.5 keV), ^{234}Th (63.3 keV), ^{212}Pb (238.6 keV), ^{224}Ra (241 keV), ^{214}Pb (242, 295.2, and 351.9 keV), ^{227}Th (236 keV), ^{208}Tl (583 keV), ^{214}Bi (609.3 keV), ^{212}Bi (727.3 keV), ^{228}Ac (338 and 911.2 keV), ^{234m}Pa (1001 keV), ^{40}K (1461 keV), as well as the low intensity lines of ^{235}U (163.3 and 205.3 keV), etc. Gamma-lines of artificial radionuclides can be recorded in the spectra as a result of contamination of environmental samples due to human activity. E.g., ^{137}Cs (661.7 keV) follows from global precipitation after the Chernobyl accident, ^{131}I (364.5 keV) is an emission of the operating nuclear power plants and nuclear reactors, ^{241}Am (59.5 keV) emerges in the ongoing nuclear tests, etc.

In this work the methods to determine activity of the natural radionuclides deprived of their own gamma-lines or having low-intensity ones, as well as of the radionuclides whose gamma-peaks interfere with that of the other radionuclides are discussed. They are ^{238}U, ^{226}Ra, ^{228}Ra, ^{232}Th, ^{228}Th, and some others.

Samples in the state of radioactive equilibrium are ideal for analysis. In this case, the activities of parent radionuclides are determined from the intensity of the gamma radiation emitted by their daughter decay products: ^{238}U by ^{234}Th and ^{234m}Pa; ^{226}Ra – by ^{214}Pb and ^{214}Bi; ^{234}U by ^{238}U and ^{226}Ra, ^{228}Ra and ^{232}Th by ^{228}Ac; ^{228}Th by ^{224}Ra, ^{212}Pb, ^{212}Bi, ^{208}Tl, etc. The activities of all decay products in the ^{235}U series will correspond to the activity of ^{235}U itself, which can be determined from the gamma spectrum using gamma peaks at energies of 163 keV and 205 keV that are free from spectral overlaps.

In fact, the above-mentioned approximation of radionuclide equilibrium is invalid when samples were dried, fired, crushed, or sieved. During these stages of sample treatment gaseous radionuclides of the natural series are usually released. ^{226}Ra decays into ^{222}Rn (radon gas) with the half-life $T_{1/2}$ = 3.8 days followed by ^{214}Pb and ^{214}Bi. In the course of sample preparations the gas escapes, and the radionuclide equilibrium between ^{226}Ra, ^{214}Pb and ^{214}Bi is disturbed. To establish the equilibrium samples are sealed hermetically and left to accumulate radon for 22 days (6 half-lives of ^{222}Rn). Unfortunately, this procedure does not solve the problem entirely due to radon emanation. ^{222}Rn comes to the day surface through fractures and cracks in the earth's crust, enters the air layers and causes fluctuations background of gamma-ray spectrometers with its decay products – ^{214}Pb and ^{214}Bi.

Therefore, a more reliable way is to determine the activity of ^{226}Ra by its own gamma-line 186.2 keV which is overlapped by a line of radionuclide ^{235}U (185.7 keV). Contribution of ^{235}U (defined as 1/21 of the activity of ^{238}U) is subtracted by a software used to calculate activities.

In such samples as water, atmospheric precipitation, or vegetation, due to the different solubility of the elements U, Th, and Ra, and to the physical and chemical processes which took

place, disturbance of RE between the radionuclides ^{238}U and ^{234}Th, ^{238}U and ^{234}U, and ^{232}Th and ^{228}Ra is observed.

Therefore, it is necessary to employ additional methods to determine the parent ^{238}U and ^{232}Th. In INP RK, inductively coupled plasma mass spectrometry (for liquid samples) and neutron activation analysis (for solid samples) are used to determine uranium and thorium content with high precision. Subsequently, using established relationships between concentrations and activities, the activity values for ^{238}U and ^{232}Th are obtained.

Alpha spectrometry with radiochemical sample preparation is used to determine ^{234}U.

When samples are contaminated with the long-lived radionuclides (^{226}Ra, ^{232}Th, etc.), possible spectral interferences with these radionuclides and their decay products for all energies of the gamma-ray spectra should be taken into account.

If the samples from the different stages of technological processes are analyzed, radionuclide disequilibrium should be generally assumed.

Thus, given the specific task of radionuclide analysis for samples with disrupted radioactive equilibrium (liquid samples, vegetation, process samples), it is useful to employ additional analytical methods and mathematical modeling alongside gamma spectrometry.

DISTRIBUTION OF THE SR-90 RADIONUCLIDE IN SOILS OF THE UNDER-CONSTRUCTION NPP TERRITORY AND ASSESSMENT OF BASELINE BACKGROUND INDICATORS

Yarmatov B.Kh., Sadikov I.I., Rozmetova F.Kh., Sharipova S.M. Solijonov S.N., Malikov A.A., Tashimova F.A.

Institute of Nuclear Physics, Uzbekistan Academy of Sciences, Tashkent, Uzbekistan

Assessing the radioecological state of soils in the pre-operational period within the territory of the nucear power plant under construction is of significant scientific and practical importance. Due to its chemical similarity to calcium and a long half-life ($T_{1/2}$≈28,8 years), the beta-emitting radionuclide ^{90}Sr poses a risk of entering biological chains; therefore, studying its depth distribution in the soil is necessary for baseline monitoring prior to the NPP startup. The main objective of the study is to determine the migration and current concentration of ^{90}Sr in the soil profile of the territory, as well as to create a basis for differentiating potential technogenic impacts in the future.

Soil samples selected from 10 control points within the under-construction NPP territory served as the research object. To accurately assess the vertical distribution of the radionuclide, a total of 100 layer-by-layer samples were taken from a depth of 0 to 10 cm with a 1 cm step. Initial radiochemical analyses (sample mass of 10 g) were carried out using liquid scintillation spectrometry on a "Tri-Carb 4810" device. However, since the radionuclide activity was below the minimum detectable activity (MDA) of the instrument, the sample mass was increased to 100 g to ensure the reliability of the analysis, and ^{90}Sr was separated from other beta-emitters via acid digestion.

According to the study results, the specific activity of ^{90}Sr in the tested soil samples was recorded in the range of 1.6–3.2 Bq/kg. The analysis of the vertical distribution in the soil profile showed that the maximum accumulation of ^{90}Sr occurs in the 2–4 cm layers, and its concentration

sharply decreases toward the 5–10 cm depth. It was found that the relatively low amount of precipitation in Uzbekistan restricts the migration of the ^{90}Sr radionuclide deeper into the soil profile, causing it to accumulate in the surface layers (2–4 cm). This result confirms the direct impact of regional climatic conditions on radionuclide migration.

It was confirmed that the baseline activity of the ^{90}Sr radionuclide within the under-construction NPP territory is within the range of global fallout and significantly below the regulatory permissible levels. The localization of ^{90}Sr primarily in the 2–4 cm layer is explained by the arid climate of the region, low leaching intensity due to scarce precipitation, and the physicochemical properties of the regional soils (cation exchange capacity level). The obtained results are recommended to be introduced into the information base of the NPP environmental monitoring as initial (baseline) data.

DEPENDENCE OF RADIATION INDICATORS ON TECHNOLOGICAL PROCESSES AT URANIUM PROCESSING PLANTS

Haydarov U.[1], Jurakulov A.[2], Muzafarov A.[2]

[1]Institute of Nuclear Technologies, Samarkand State University named after Sharof Rashidov, Samarkand, Uzbekistan

[2]Navoi State Mining and Technological University, Navoi, Uzbekistan

The sustainable development of nuclear power continues to drive demand for uranium as a raw material, making it urgent to ensure environmental and radiological safety at uranium mining and processing facilities. In-situ leaching (ISL) is the most widely used uranium mining technology [1]; as the pregnant solution is raised to the surface, the resulting pressure drop releases radon [2], after which the uranium is processed by ion exchange (sorption). ISL is standard practice in Central Asia and other major uranium-producing countries [3].

Radon and its decay products make the largest contribution to the dose received by humans from natural sources and are assessed through the equilibrium equivalent radon concentration (EERC) [4]. The decay products attach to aerosol particles, forming long-lived alpha-active aerosols (LLAA), which, through redeposition, affect surface contamination as well as the ambient dose equivalent rate H*(10).

Published data indicate that ISL facilities in the Navoi industrial region are a significant source of atmospheric contamination (H*(10) 0.16–0.67 μSv/h, annual dose 5–8 mSv) [5].

H*(10) was measured at a height of 1 m using the BDPG-96 gamma-detection unit (NaI(Tl), Ø 25 × 40 mm) of the DKS-96 dosimeter-radiometer. Surface alpha contamination was determined using the BDZA-96 unit of the same instrument (ZnS(Ag), 70 cm^2, calibrated against ^{239}Pu). EERC was measured by the aspiration method using the Alpharad Plus-AR complex, in accordance with ASTM D6327-10 [6]. LLAA activity was determined by sampling on an AFA-RSP filter and analysis with a “Progress-AR” alpha-radiometer (ZnS(Ag), Ø 60×60 mm, error ±10%) [7].

The results of the four indicators measured at 10 points on the uranium sorption site are presented in Table 1, arranged in order of proximity to the technological process source.

Table 1. Distribution of H*(10), surface alpha contamination (SAC), EERC and LLAA at the uranium sorption site, ordered by source proximity

№	Location	Abbrev.	H*(10), μSv/h	SAC, $min^{-1}·cm^{-2}$	EERC, Bq/m^3	LLAA, mBq/m^3
1	Sorption unit 1	SU-1	0.40–0.77	1.3–3.7	41	26.7
2	Sorption unit 2	SU-2	0.25–3.57	0.3–3.7	52	29.44
3	Operator room 1	OR-1	0.10–0.15	0.3–0.8	10	7.84
4	Operator room 2	OR-2	0.09–0.12	1.3–2.9	10	6.58
5	Electromechanical room	EMR	0.14–0.19	0.7–3.4	11	5.07
6	Oxygen station	OS	0.06–0.10	0.3–1.4	7	5.02
7	Changing room 1	CR-1	0.10–0.25	1.2–2.9	8	5.61
8	Changing room 2	CR-2	0.13–0.26	0.7–6.9	15	4.59
9	Dining room 1	DR-1	0.09–0.12	0.3–1.4	9	4.47
10	Dining room 2	DR-2	0.07–0.12	0.4–0.5	8	4.58

The highest values were recorded at SU-1 and SU-2. EERC reached 41 and 52 Bq/m^3, and LLAA 26.7 and 29.44 mBq/m^3, 3–7 times higher than elsewhere. H*(10) was also maximal at these points (0.40–0.77 and 0.25–3.57 μSv/h). In the auxiliary rooms, all indicators dropped sharply and remained stable (EERC 7–15 Bq/m^3, H*(10) 0.06–0.26 μSv/h). Surface alpha contamination did not fully follow this pattern; an elevated value (0.7–6.9 $min^{-1}·cm^{-2}$) was observed at CR-2, possibly due to secondary contamination from workers' clothing.

To illustrate the relationship between EERC and H*(10), Figure 1 compares the two quantities in order of proximity to the source.

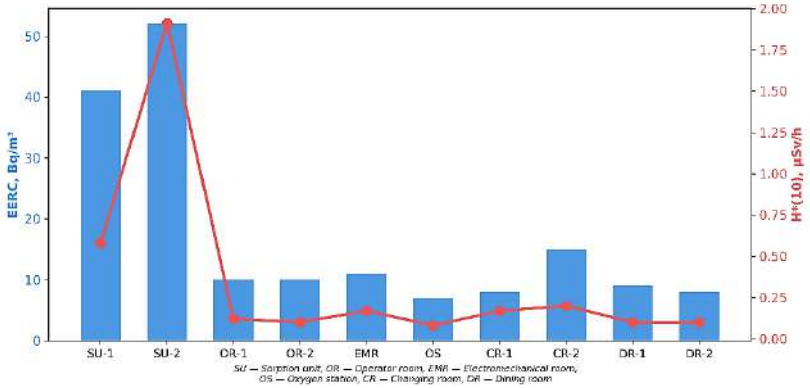

Figure 1. Relationship between EERC and H*(10) at the uranium sorption site, ordered by source proximity

As shown in Figure 1, the EERC and H*(10) curves move in an almost parallel manner, both peaking sharply at SU-1 and SU-2 and then remaining low and stable, reflecting the two indicators' dependence on a common source. However, because this relationship is driven mainly by two extreme points and the sample size (n=10) is small, the result should be regarded as preliminary.

The study showed that the distribution of radionuclides depends on the technological process source. All indicators are elevated in zones close to the source and decrease with distance, confirming that the sorption process is the main source of radon and its decay products for these indicators. The small sample size is a limitation, and increasing the number of points is planned for future work.

References:

1. Mussayeva, E., Bakhtin, M., & Kurbanova, A. (2026). Environmental Impacts of In Situ Leaching Uranium Mining: A Review. Environments, 13(7), 366. https://doi.org/10.3390/environments13070366
2. Xu, L., Zhang, H., Wang, Y., Niu, J., & Dai, X. (2023). Radon Release Features of Different Uranium Mines and the Relative Public Effective Doses. IntechOpen. https://doi.org/10.5772/intechopen.113123
3. World Nuclear Association. (n.d.). In-situ leach mining of uranium. https://world-nuclear.org/information-library/nuclear-fuel-cycle/mining-of-uranium/in-situ-leach-mining-of-uranium
4. Otahal, P. P., & Fialova, E. (2025). Determination of the radon progeny activity size distribution at different types of workplaces. Journal of Environmental Radioactivity, 289, 107781. *https://doi.org/10.1016/j.jenvrad.2025.107781*
5. Kholov D.M., Muzafarov A.M., Kholboev I., Hoshimov K.H. Methods of Determination of Radiation Factors and Radioecological Conditions in Navoi Industrial Region. Turkish J. Comput. Math. Educ., 2021, 12(7), 1112-1119.
6. ASTM International. (2016). Standard Test Method for Radon Decay Product Concentration in Indoor Atmospheres (No. D6327-10).
7. Alpha-radiometer "Progress-AR", State Register No. 15235-01. https://all-pribors.ru/opisanie/15235-01-progress

FAST NEUTRON PRIMING CONFERS CROSS-ADAPTATION TO SALINITY AND OSMOTIC STRESS IN TRITICALE – PHYSIOLOGICAL EVIDENCE AND FURTHER INTEGRATIVE STUDIES

Kruglyak A.I.[1,2], Aleksiayenak Yu.V.[1], Volkova P.Yu.[3], Doroshkevich A.S.[1], Zaharova E.V.[2]

[1]Joint Institute for Nuclear Research, Dubna, Russian Federation

[2]All-Russia Research Institute of Agricultural Biotechnology, Dubna, Russian Federation

[3]Independent Researcher, Geel, Belgium

Amid global climate change, crop varieties with enhanced tolerance to abiotic stressors are increasingly in demand. One promising approach is radiation priming – the exposure of seeds to low-dose ionizing radiation, which triggers protective mechanisms at both the cellular and organismal levels [1]. However, each genotype requires individual dose optimization, and the mechanisms underlying cross-tolerance to different stress types remain insufficiently understood. In this work, we determined the effective dose range of fast neutrons for priming seeds of spring triticale (*x Triticosecale*) cv. «Botanicheskaya 4» and evaluated the induced cross-tolerance to salinity (NaCl) and osmotic stress (PEG), while also outlining future molecular-genetic and cytogenetic studies.

Seeds of cv. «Botanicheskaya 4» were irradiated on the EG-5 accelerator (JINR, Dubna) with fast neutrons at doses ranging from 5 to 25 Gy; non-irradiated seeds served as controls. The

physiological state of seedlings was assessed under 150 mM NaCl and 25.8 mM PEG-8000 by measuring root and shoot length.

Preliminary experiments showed that for cv. «Botanicheskaya 4», doses of 3–5 Gy do not inhibit growth but create moderate stress sufficient to trigger an adaptive response. In stress tolerance tests, seedlings derived from treated seeds exhibited significantly higher growth parameters under both salt and osmotic stress compared to controls. Thus, the hypothesis of cross-tolerance to two types of stress after neutron priming was fully confirmed for the studied cultivar.

Future work will include qRT-PCR analysis of gene expression, focusing on the key salt-stress marker gene *LEA14*, whose rapid induction under salinity has been validated at transcriptomic and proteomic levels [2]; assessment of biochemical indicators and cytogenetic analysis (scoring of chromosomal aberrations in root meristems). The obtained data will contribute to understanding the mechanisms of radiation-induced stress tolerance in triticale.

References:

1. Wang J, Zhang Y, Zhou L, Yang F, Li J, Du Y, Liu R, Li W, Yu L (2022) Ionizing Radiation: Effective Physical Agents for Economic Crop Seed Priming and the Underlying Physiological Mechanisms. Int. J. Mol. Sci. 23:15212. doi:10.3390/ijms232315212
2. Wang D, Li J, Li S, Fu J, Liu B and Cao D (2025) Multi-omics analysis of hexaploid triticale that show molecular responses to salt stress during seed germination. Front. Plant Sci. 15:1529961. doi: 10.3389/fpls.2024.1529961

RAPID DETERMINATION OF INDIUM IN GEOLOGICAL SAMPLES USING WWR-K REACTOR

Bedelbekova K.A., Lennik S.G., Sokolenko E.K., Kaiyrbekova A.S., Zhiyenbayev I.M., Satpayev M.M.

Institute of Nuclear Physics of the Agency of the Republic of Kazakhstan for Atomic Energy, Almaty, Kazakhstan

Indium is one of the most abundant elements (its concentration in the Earth’s crust is estimated at approximately 0.1 parts per million). It is used in electronics, solar cells, displays, and semiconductors, and is included on the list of critical metals in many countries. Currently, the most commonly used methods for determining indium in ores involve preliminary chemical digestion: atomic emission spectroscopy, atomic absorption spectrometry, and inductively coupled plasma mass spectrometry.

In Institute of Nuclear Physics (Almaty, Republic of Kazakhstan*)* indium is determined using the instrumental method of neutron activation analysis (INAA) based on the short-lived radionuclide ^{116m}In (with a half-life of ~54 min). An automated pneumatic transport system (PTS) has been installed in the dry horizontal channel of WWR-K research nuclear reactor to conduct these studies. An analytical technique for INAA usings short-lived radionuclide (SLR) has recently been developed [1]. Metrological characteristics were determined for indium in accordance with the current regulatory documentation of Republic of Kazakhstan [2].

Ores and rocks were analyzed using 20 parallel subsamples, each weighing 100–200 mg. The samples were irradiated for 1 minute at a neutron flux density of 10^{12} n/s/cm². The “cooling-off” time was 10 minutes, and the recording time for the induced activity gamma spectra was 10 minutes using a Canberra horizontal gamma spectrometer. The spectra were processed using Genie-2000 software. Element concentrations were calculated using the relative method of INAA [3] with OREAS 995 and OREAS 996 certified reference materials which have indium content.

Based on the appendix to industry standard [4], the ranges of indium concentrations were determined to be from 0.05 ppm to 0.0049%. Table 1 presents the metrological characteristics of repeatability and laboratory precision for all ranges of concentrations.

Table 1 – Metrological characteristics of Indium by INAA SLR method

Range of Values, %	Repeatability, %	Laboratory Precision, %
from 0.0000050 to 0.0000099. incl.	1.29E-06	1.63E-06
from 0.000010 to 0.000019 incl.	1.93E-06	2.25E-06
from 0.000020 to 0.000049 incl.	4.35E-06	5.04E-06
from 0.000050 to 0.000099 incl	7.97E-06	9.70E-06
from 0.00010 to 0.00019 incl.	1.33E-05	1.63E-05
from 0.00020 to 0.00049 incl	9.70E-06	1.92E-05
from 0.00050 to 0.00099 incl.	1.02E-05	1.22E-05
from 0.0010 to 0.0019 incl	4.78E-05	6.28E-05
from 0.0020 to 0.0049 incl.	3.70E-05	4.95E-05

References:

1. Svetlana Lennik, Kamshat Bedelbekova, Yevgeniy Sokolenko, Igor Silachyov, Tatyana Suzdaltseva, Dilyara Mirkhaji and Saulet Ydyrysheva Development of an analytical technique for INAA using short-lived radionuclides // Interactions, 2026, 247:133 https://doi.org/10.1007/s10751-026-02459-0
2. RMG 76-2014 (2014) State system for ensuring uniformity of measurements. Internal quality control of quantitative chemical analysis results. Published by FSMC VIMS, Moscow.
3. Dmitriev, A.Y., Pavlov, S.S. Automation of the quantitative determination of elemental content in samples using neutron activation analysis on the IBR-2 reactor. Nucl. Lett.10, 33-36 (2013). https://doi.org/10.1134/S1547477113010056.
4. OST 41-08-212-04 (2004) Industrial Standard. Quality management of analytical work. Error guidelines for chemical analysis of mineral resources and precision classification of laboratory analytical techniques. Published by FSMC VIMS, Moscow.

THE ROLE OF STABILIZING REINFORCING ADDITIVES IN INCREASING RESISTANCE TO LONG-TERM THERMAL EFFECTS IN COMPOSITE CERAMICS

Zikirina A.M.[1], Kozlovskiy A.L.[2,3], Kenzhina I.E.[1,2]
[1]*Satbayev University, Almaty, Kazakhstan*
[2]*Institute of Nuclear Physics, Almaty, Kazakhstan*
[3]*L.N.Gumilyov Eurasian National University, Astana, Kazakhstan*

The paper presents the results of the influence of magnesium oxide addition to the composition of composite ceramics based on ZrO_2 – CeO_2 compounds on the change in the kinetics of phase transformations and resistance to external influences, including thermal effects simulating thermal operating conditions. As a result of the studies, the main mechanisms of phase formation of composite MgO – CeO_2 – ZrO_2 ceramics were determined by varying the ratio of the stabilizing MgO additive in the composition, the concentration of which varied from 0.01 to 0.15 M of the total mass of the composite. The main mechanisms of phase formation in the MgO–CeO_2–ZrO_2 system were determined, including solid-phase diffusion processes, solid solution formation, and the effect of defective structure on the thermodynamic stability of phases. It is shown that the optimal range of MgO content contributes to the formation of a more uniform and finely dispersed microstructure, which, in turn, improves mechanical properties, heat resistance, and thermal shock resistance. It has been established that the combined presence of cerium and magnesium oxides provides a synergistic stabilization effect associated with a change in the concentration of oxygen vacancies and a reduction in grain boundary mobility. This leads to a slowdown in the kinetics of degradation processes during high-temperature operation and increases the durability of the material.

A STUDY OF THE DISTRIBUTION OF MACRO- AND MICROELEMENTS IN HAIR SAMPLES OF STAFF WORKING IN UNFAVORABLE WORKING CONDITIONS

Kurbanov B.I.[1], Danilova E.A.[1], Khusniddinova S.Kh.[1], Khushvaktov N.Kh.[1], Khaitov F.N.[2]
[1]*Institute of Nuclear Physics, Uzbekistan Academy of Sciences, Tashkent, Uzbekistan*
[2]*Termez Branch of Tashkent State Medical University, Termez, Uzbekistan*

Assessing the impact of harmful occupational factors on the human body is one of the fundamental tasks of modern occupational medicine and radiation ecology. Traditional methods of analyzing biological media (blood, urine) reflect only short-term xenobiotic intake and are subject to rapid metabolic changes. In contrast, human hair is recognized by the World Health Organization (WHO) as an ideal bioindicator of chronic environmental and occupational exposure.

It possess a unique ability to accumulate macro- and microelements over a long period, recording the body's elemental status without invasive procedures. Monitoring the elemental

composition of hair from workers at industrial facilities with unfavorable working conditions allows for the early detection of risks of developing occupational pathologies associated with an imbalance of essential metals and the accumulation of toxic metals.

The objective of this study is to precisely determine the multielement profile and distribution patterns of macro-, micro-, and trace elements in hair samples from employees chronically exposed to harmful occupational factors using a highly sensitive instrumental neutron activation analysis (INAA) method.

The study involved hair samples from employees working at environmentally and industrially sensitive facilities (metallurgical, chemical, or mining industries) with long-term exposure to hazardous conditions. The control group consisted of healthy individuals of similar age and gender who had no occupational exposure to hazardous factors.

Hair sample preparation was performed in strict accordance with IAEA international recommendations. The samples were washed successively in acetone, deionized water, and again in acetone to completely remove external surface contaminants, after which they were dried at 60°C to constant weight. Homogenized samples weighing approximately 50–100 mg were packaged in high-purity polyethylene film bags.

Elemental composition analysis was performed using the INAA method at the WWR-SM research nuclear reactor of the Institute of Nuclear Physics of the Academy of Sciences of the Republic of Uzbekistan, with a thermal neutron flux density of 5×10^{13} neutrons/(cm² s).

To determine a wide range of elements, two irradiation schemes were used:

1. Short-term irradiation (30 seconds) in dedicated reactor irradiation channels, followed by measurement of induced gamma activity to determine short-lived radionuclides (Ca, Mg, Cl, Mn, Na, V, I).

2. Long-term irradiation (20 hours) in the reactor's central channel, followed by "cooling" of the samples for 5–30 days to detect long-lived isotopes (Fe, Zn, Se, Co, Cr, Sc, Rb, Cs, Sb, Ag, Hg). Gamma-ray spectra were measured using Canberra semiconductor spectrometers with high-purity germanium (HPGe) detectors with an energy resolution of at least 1.8 keV at the 1332 keV ^{60}Co line. Spectral data processing and elemental concentration calculations were performed using specialized software.

The developed integrated approach by INAA enabled the reliable identification and quantification of over 30 chemical elements in the hair samples without destroying the sample matrix. A comparative analysis of the data revealed distinct differences in the elemental profile of employees depending on their specific working conditions. Workers in the main workshops were found to have statistically significant ($p < 0.05$) elevated levels of toxic and conditionally toxic elements (such as Cr, Sb, Co, and As) compared to the control group. In particular, heavy metal accumulation in hair directly correlates with the employees' length of service.

At the same time, profound imbalances in the essential bioelement system were recorded. Decreased levels of zinc (Zn) and selenium (Se), which perform crucial antioxidant and immunomodulatory functions in the body, were found. Fluctuations in macronutrient levels (Ca, Mg, Na) were also detected, indicating disruption of overall electrolyte balance and cell membrane permeability under the influence of chronic man-made stress.

Conclusions. 1. The instrumental neutron activation analysis method at the WWR-SM reactor of the Institute of Nuclear Physics of the Republic of Uzbekistan demonstrated high accuracy, precision, and selectivity, enabling effective multi-element screening of human hair.

2. Marker technogenic elements accumulating in the bodies of workers in hazardous industries were identified, and a direct correlation between their concentrations and length of work experience was demonstrated.

3. The identified deficiency of vital elements (Zn, Se) justifies the need to implement targeted therapeutic and preventive measures and nutraceutical support programs (biofortification) for personnel at enterprises with unfavorable working conditions to minimize the risk of developing occupational diseases.

NEUTRON ACTIVATION ANALYSIS OF THE ELEMENTAL COMPOSITION OF WHEAT GROWN IN UZBEKISTAN

Kurbanov B.I.[1], Danilova E.A.[1], Khusniddinova S.Kh.[1], Kurbanova N.B.[2]
[1]Institute of Nuclear Physics, Uzbekistan Academy of Sciences, Tashkent, Uzbekistan
[2]Tashkent Institute of Chemical Technology, Tashkent, Uzbekistan

Wheat is the staple food crop determining food security and the nutritional status of the population of the Republic of Uzbekistan. Monitoring the elemental composition of agricultural crops is of paramount importance for assessing their nutritional value and environmental safety. Standard methods for determining elemental profiles often require complex and time-consuming chemical sample preparation, which can lead to sample contamination or the loss of volatile components. Instrumental Neutron Activation Analysis (INAA) is a rapid, highly sensitive, multi-element non-destructive method that allows for the simultaneous determination of a wide range of macro-, micro-, and trace elements in organic matrices without preliminary chemical decomposition. This work is dedicated to studying the elemental profile of various wheat varieties cultivated in different geographic and climatic zones of Uzbekistan.

Samples of wheat grain from various promising and locally adapted varieties were collected during the harvest period from key agricultural regions of the Republic of Uzbekistan, including the Tashkent, Samarkand, and Kashkadarya regions. Sample preparation included thorough washing with deionized water to remove surface dust contamination, drying at a constant temperature of 60–70°C to a stable weight, homogenization, and subsequent fine grinding in an agate mortar.

Analytical studies were carried out using the WWR-SM research nuclear reactor at the Institute of Nuclear Physics of the Academy of Sciences of the Republic of Uzbekistan. To ensure high reliability and coverage of the widest possible range of elements, two irradiation regimes were applied. Short-term irradiation (ranging from 15 seconds to several minutes) was used to determine short-lived radionuclides, including Al, V, Ca, Mg, Cl, and Mn. Long-term irradiation (up to several hours) followed by an optimal cooling period allowed for the reliable identification of long-lived isotopes, such as Fe, Zn, Se, Co, Cr, Sc, Rb, and Cs. Gamma spectrometry of the irradiated samples was performed using high-purity germanium (HPGe) detectors coupled with multi-channel pulse analyzers.

The application of the INAA method allowed for the highly precise determination of the concentration of more than 25 chemical elements in the studied wheat samples. Special attention was paid to essential micronutrients that directly affect the biological and nutritional value of the grain. Quantitative data obtained for Fe, Zn, Cu, Mn, and Se demonstrated noticeable variations depending on the wheat variety and the region of cultivation.

Toxicological monitoring showed that the concentrations of heavy metals and toxic elements, such as As, Sb, Hg, and Cd, in all analyzed samples did not exceed the maximum permissible

concentrations (MPC) established by international food safety standards and national SanPiN regulations. Analysis of regional specificity revealed a direct correlation between the mineral profile of the grain and the geochemical characteristics of the soils. In particular, wheat samples from the more arid and saline areas of the Kashkadarya region showed an increased accumulation of certain trace minerals compared to samples from the foothill areas of the Tashkent region.

Conclusions. 1. The results confirmed that Instrumental Neutron Activation Analysis is a highly efficient, accurate, and reproducible analytical tool for the comprehensive monitoring of the elemental composition of agricultural products.

2. The established database of elemental profiles forms a scientific foundation for compiling a digital map of the mineral composition of wheat grown in Uzbekistan.

3. These findings are highly practical for targeted selective breeding focused on developing biofortified crop varieties enriched with essential minerals (such as iron and zinc), as well as for regional environmental certification and food quality control systems.

USE OF PHOTONUCLEAR REACTIONS WITH THE FORMATION OF SHORT-LIVED ISOMERS IN ANALYTICAL PROBLEMS

Shovdirova S.L.[1,2], Kurbanov B.I.[1], Mingbaev Kh.S.[1,3]

[1]*Institute of Nuclear Physics, Uzbekistan Academy of Sciences, Tashkent, Uzbekistan*

[2]*Tashkent branch of the National Research Nuclear University "MEPhI", Tashkent, Uzbekistan*

[3]*JSC Navoi Mining and Metallurgical Plant, Navoi, Uzbekistan*

Efficient development of the Kyzylkum region's mineral resource base requires the implementation of highly sensitive, rapid, and non-destructive methods for analyzing the composition of rocks and ores. Traditional chemical analytical methods for determining precious and rare metals often require lengthy sample preparation, the use of aggressive reagents, and time-consuming analysis. Instrumental gamma activation analysis (IGAA) is an alternative. Using inelastic scattering of gamma quanta with the formation of short-lived isomeric nuclear states significantly reduces analysis time and improves selectivity, which is especially important for rapid process control and geological exploration.

A UELR-8-10A linear electron accelerator with a beam energy of 8.5 MeV was used as the activating radiation source in this study. Bremsstrahlung generated by bombarding a tungsten target was directed at the Kyzylkum rock samples under study. The choice of 8.5 MeV was dictated by the need to minimize interfering photonuclear reactions of the (γ, n) type, whose thresholds for most matrix elements lie above this value. This allows for the selective excitation of isomeric levels in inelastic scattering reactions (γ, γ').

The mass of the analyzed samples ranged from 0.4 to 0.6 kg. The induced gamma activity of short-lived isomers was recorded using a high-purity germanium (HPGe) semiconductor spectrometer with an energy resolution of at least 1.8 keV at the 1332 keV line of the 60Co radionuclide. An automated sample delivery system ensured sample transport time from the target to the detector within 1-2 seconds, which is critical for detecting isomers with half-lives of several seconds.

During the study, the time regimes (irradiation, cooling, and measurement times) were optimized for the reliable determination of silver (Ag), tungsten (W), iridium (Ir), and associated metals in samples with complex matrix compositions.

For silver determination, the gamma radiation of the 107mAg isomer (T 1/2 = 44.3 s; Egamma = 93.1 keV) and 109mAg (T 1/2 = 40.0 s; Egamma = 88.0 keV) served as the analytical signal. Use of the low-energy spectral region required a correction for gamma quanta self-absorption in the sample matrix. The detection limit for silver in the ore material was approximately 1 x 10 -4 wt %.

Tungsten content was analyzed using the 183mW isomer (T 1/2 = 5.3 s; Egamma = 107.9 keV and 157.5 keV). The short lifetime of this isomer allowed for the use of multiple irradiation-measurement cycles to collect the necessary statistics, reducing the analytical error to 5–7% at industrial-grade concentrations.

Iridium was determined using the 191Ir (γ, γ')191mIr nuclear reaction (T 1/2 = 4.9 s; Egamma = 129.4 keV). The high excitation cross section of this isomer by bremsstrahlung from a LUE enabled the reliable detection of trace amounts of iridium in the ultramafic and black shales of the Kyzylkum Desert without preliminary radiochemical preconcentration.

Additionally, the possibility of concomitant determination of other metals was studied, in particular, gold by the isomer 197mAu (T 1/2 = 7.7 s, Egamma = 279 keV), barium by 137mBa (T 1/2 = 153 s, Egamma = 661.7 keV), selenium by 77mSe (T 1/2 = 17.4 s; Egamma = 162.2 keV), etc. The influence of natural radioactivity of host rocks (uranium, thorium, potassium-40) was minimized due to the high flux density of activating radiation and the choice of the optimal measurement time window.

Conclusions. The developed gamma-activation analysis method based on the UELR-8-10A using short-lived isomers demonstrated high efficiency for the rapid determination of silver, tungsten, and iridium in Kyzylkum rocks. Eliminating the chemical decomposition step reduced the analysis time to just a few minutes. The absence of activation of matrix elements (silicon, aluminum, calcium) at the given electron energy ensures low background noise under the analytical peaks and guarantees high reproducibility of the results. The method can be recommended for the automation of ore sorting and the technological mapping of new deposits in the region.

POSSIBILITIES OF USING THE GEANT4 SOFTWARE PACKAGE IN PROTON AND ION THERAPY FOR MODELING AND CALCULATIONS

Palvanov S.R., Ramazonov A.X., Abdusalomova M.R.
National University of Uzbekistan, Physics Department

The development of radiation therapy methods is driven by the need to improve the effectiveness of tumor treatment while simultaneously reducing the radiation load on healthy organs and tissues. Proton therapy and heavy-ion therapy are of particular interest in this regard.

Unlike photon radiation, charged particles have a finite range in matter and are characterized by a pronounced energy release maximum at the end of their trajectory—the Bragg peak. This property allows for a significant portion of the dose to be concentrated in the tumor area and reduces the dose load beyond the target.

The use of carbon ions additionally exhibits high linear energy transfer and a pronounced biological effect. However, the interaction of heavy ions with matter is a significantly more complex process, involving electromagnetic interactions, nuclear reactions, fragmentation, and the formation of secondary particles.

Therefore, experimental methods do not always provide complete information on the spatiotemporal structure of processes. Monte Carlo methods, which allow detailed modeling of particle passage through matter, play an important role. One of the most powerful tools for such modeling is the Geant4 software package.

In proton therapy, a primary proton beam is directed at the patient's tumor site. As the protons pass through the tissue, they gradually lose energy. At the end of their path, there is a sharp increase in specific energy loss, corresponding to the Bragg peak.

This paper examines the capabilities of the Geant4 software package (GEometry ANd Tracking 4) for modeling the physical processes occurring during proton and ion therapy. This paper analyzes the capabilities of Geant4 for modeling proton and heavy ion transport, calculating energy losses, absorbed dose distribution, linear energy transfer (LET), secondary radiation, and nuclear fragments. The feasibility of constructing a virtual model of a therapeutic unit, patient, and beamforming system is discussed. The potential of Geant4 for use in scientific research, medical physics, and education is demonstrated. The study also simulated the dose distribution and linear energy transfer (LET) of radiation depending on depth during the treatment of ocular melanoma and other intraocular tumors with proton therapy. The braking properties of proton beams with energies of 55, 62.3, and 68 MeV were studied in water (soft tissue phantom) and dense bone (Compact Bone). The results showed that a distal LET shift (spatial shift) was observed between the Bragg peak and the maximum LET value. Specifically, at an energy of 62.3 mm, the Bragg peak formed at a depth of 29.0 mm in water, while the maximum LET value (46.55 keV/μm) was recorded at a depth of 30.5 mm (a distal shift of +1.5 mm). In dense bone, the Bragg peak was located at a depth of 16.8 mm, and the LET peak (39.81 keV/μm) was at a depth of 17.3 mm (a shift of +0.5 mm). The resulting dependences are shown in Fig. 1 and Fig. 2. These results are important for protecting healthy tissue around the tumor (the optic nerve and retina) from radiation damage.

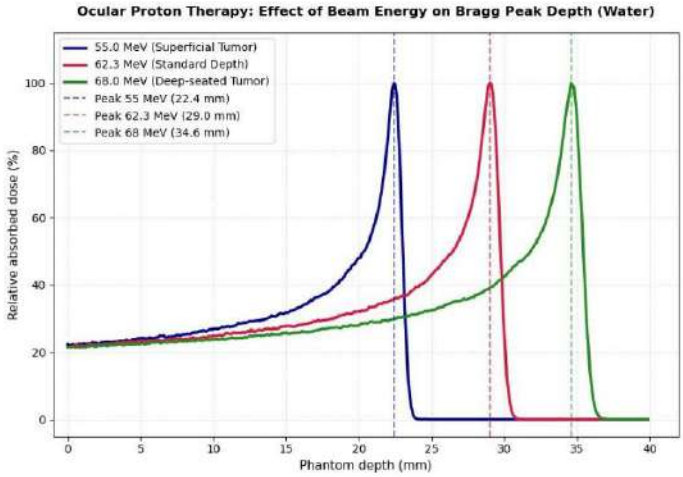

Figure 1.

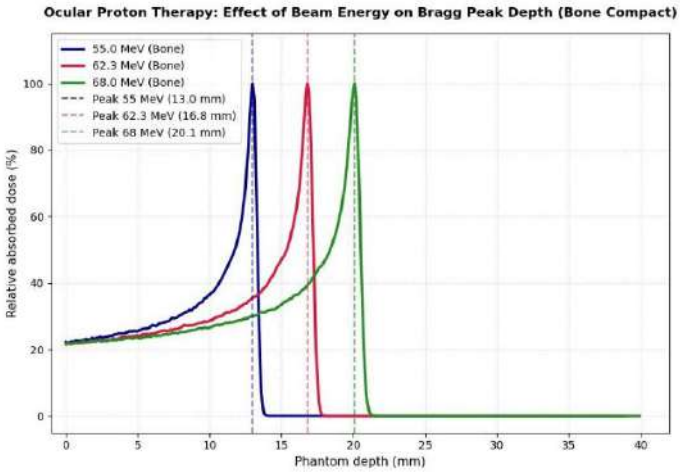

Figure 2.

Based on the obtained results, it can be said that the Geant4 program is a reliable tool for planning proton therapy of the eye, optimizing dose distribution and assessing radiobiological parameters.

References:

1. Agostinelli S., Allison J., Amako K. et al. Geant4—a simulation toolkit // Nuclear Instruments and Methods in Physics Research Section A: Accelerators, Spectrometers, Detectors and Associated Equipment. — 2003. — Vol. 506, No. 3. — P. 250–303.
2. Allison J., Amako K., Apostolakis J. et al. Geant4 developments and applications // IEEE Transactions on Nuclear Science. — 2006. — Vol. 53, No. 1. — P. 270–278.

DEVELOPMENT OF A HIGH-FREQUENCY INDUCTIVE METHOD FOR MEASURING MAGNETIC SUSCEPTIBILITY IN THE TEMPERATURE RANGE 80–300 K

Nebesniy A.F.
Institute of Nuclear Physics, Uzbekistan Academy of Sciences, Tashkent, Uzbekistan

An experimental setup for studying the temperature dependence of the magnetic susceptibility of materials using a high-frequency (HF) inductive method in the temperature range 80–300 K was developed previously [1]. The method is based on measuring changes in the frequency of an LC oscillator whose sensing coil contains the sample under investigation. The temperature dependence of magnetic susceptibility is determined by comparing the frequency–temperature characteristics of the empty measuring cell and the cell containing the sample.

Further development of the method has focused primarily on improving measurement stability and reproducibility. In the current configuration, the LC oscillator operates at approximately 5 MHz. It was found that the ability to resolve small changes in magnetic susceptibility depends on the stability of the entire measurement system rather than on the oscillator alone. The measurements

may be affected by the parasitic parameters of the HF transmission line, the mechanical stability of the measuring cell, the positioning of the temperature-sensing elements, and external electrical interference.

To identify the factors limiting measurement stability, individual components of the setup were tested systematically. The effects of the LC oscillator power supply, mechanical disturbances of the cryogenic measuring cell, the condition and mechanical fixation of the HF connecting cable, and the position and fixation of the sensing junction of the differential Chromel–Copel thermocouple were investigated. Particular attention was paid to the behavior of the measurement system during thermal cycling from liquid-nitrogen temperature to room temperature.

The experiments showed that the observed frequency instabilities can originate from both electrical and mechanical effects. Autonomous battery operation combined with a precision voltage supply for the LC oscillator eliminated interference coupled through the mains supply. Tests involving controlled mechanical disturbances revealed inadequate fixation of individual components of the measuring cell and of the thermocouple junction as additional sources of abrupt frequency changes. Eliminating these causes improved the frequency stability of the system. Further experiments demonstrated that the mechanical stability of the sensing coil itself is also significant, necessitating an improved coil design.

The results show that the sensing coil, HF transmission line, thermocouple, cryogenic measuring cell, LC oscillator, and its power supply must be treated as a single measurement system. The findings were used to further improve the setup and to develop a mechanically more stable sensing-coil design. These improvements provide a basis for subsequent application of the HF inductive method to measurements of the temperature dependence of magnetic susceptibility in various materials over the 80–300 K range.

References:

1. Nebesniy A.F. Inductive high-frequency method for determining magnetic susceptibility in the temperature range of 80–300 K. The XI International Conference “Modern Problems of Nuclear Energy and Nuclear Technologies”, Tashkent, October 14–16, 2025, pp. 210–211.

ARTIFICIAL INTELLIGENCE IN NEUTRON ACTIVATION ANALYSIS

Umaraliev A.T.[1], Nishonov M.M.[2]
[1]*Independent Researcher*
[2]*Institute of Nuclear Physics, Uzbekistan Academy of Sciences, Tashkent, Uzbekistan*

Modern neutron activation analysis (NAA) is a complex interdisciplinary methodology that combines nuclear physics, gamma-ray spectrometry, analytical chemistry, radiochemistry, and experimental data processing. Although a variety of specialized software solutions are available, most of them automate only individual stages of the analytical workflow, requiring researchers to use multiple software tools and possess extensive domain expertise.

An intelligent working environment for neutron activation analysis is currently being developed as a unified professional software platform integrating experiment planning and management, spectrometric data processing, specialized analytical tools, a domain knowledge base,

and intelligent decision support. The platform architecture is designed to support the entire research lifecycle, from experiment preparation to the generation of scientifically substantiated conclusions.

Intelligent support is achieved through the integrated use of modern large language models (LLMs) and specialized artificial intelligence models, international nuclear data libraries including **ENSDF** [1] (evaluated nuclear structure and radioactive decay data), **EXFOR** [2] (experimental nuclear reaction data), **JANIS** [3] (nuclear data information system), and **IAEA Nuclear Data Services** [4] (international evaluated and reference nuclear data), together with specialized gamma-spectrum processing libraries, scientific computing libraries, open scientific publications, and a proprietary knowledge base derived from the software package for modeling Instrumental Neutron Activation Analysis (INAA) methodologies developed at the Institute of Nuclear Physics of the Academy of Sciences of the Republic of Uzbekistan [5].

The platform is intended for practical deployment in research laboratories and can be used by specialists with different levels of experience, ranging from students and early-career researchers to engineers and research scientists. A unified working environment reduces the time required to master NAA methodologies, improves research efficiency, provides explainable recommendations, and assists in producing scientifically justified conclusions.

References:

1. **Evaluated Nuclear Structure Data File (ENSDF).** National Nuclear Data Center, Brookhaven National Laboratory, Upton, NY, USA.
2. **Experimental Nuclear Reaction Data Library (EXFOR).** International Atomic Energy Agency (IAEA), Nuclear Data Section, Vienna, Austria.
3. **JANIS (Java-based Nuclear Information System).** OECD Nuclear Energy Agency (NEA), Data Bank, Paris, France.
4. **IAEA Nuclear Data Services.** International Atomic Energy Agency (IAEA), Vienna, Austria.
5. Tillaev T., Umaraliev A.T., Urmanov Sh. *Software Package for Modeling Instrumental Neutron Activation Analysis (INAA) Methodologies, Version 1.0.* Software Registration Certificate No. DGU 20110106, June 10, 2011.

ADVENTIVE PLANTS IN THE SANITARY-PROTECTION ZONE OF THE INSTITUTE OF NUCLEAR PHYSICS, UZBEKISTAN ACADEMY OF SCIENCES

Tillayev T.S.[1], Tillayev Sh.B.[2]
[1]*Institute of Nuclear Physics, Uzbekistan Academy of Sciences, Tashkent, Uzbekistan*
[2]*International Agriculture University, Tashkent, Uzbekistan*

The sanitary-protection zone of the Institute of Nuclear Physics of the Academy of Sciences of the Republic of Uzbekistan (SPZ INP AS RUz) began to take shape immediately after the Institute's construction began in 1957. It is an artificial grove with historical natural elements (ravines, wastelands, waterways, etc.). Initially, the area was over 300 hectares, but over time, it gradually began to shrink due to the allocation of part of the zone for infrastructure construction. Its current area is approximately 190 hectares. According to the Decree of the President of the Republic of

Uzbekistan (PF-46 dated March 25, 2026), an arboretum will be created within the SPZ [1]. The SPZ is located in the Tashkent Botanical-Geographical Region.

Several studies have been published on the flora of the village of Ulugbek and the SPZ, identifying at least 390 native plant species and 262 cultivated species [2, 3, 4].

Most of the plants in the sanitary-protection zone include cultivated trees and shrubs, including adventitious species, among which are archaeophytes, neophytes, trees, shrubs and herbs There are also quarantine plants (category A2, part II – *Acroptilon repens* and *Ambrosia artemisiifolia*, but these plants are not invasive in sanitary-protection zone conditions) [5].

Adventitious species can be conventionally grouped into the following groups: archaeophytes: *Morus alba*, a food plant for the silkworm *Bombyx mori* (L., 1758), is running wild; *Ailanthus altissima*, a food plant for the ailanthus silkworm *Samia cynthia* (Drury, 1773), is running wild in China; *Hyoscyamus niger* L.; the rest are neophytes, among which soft invasive species predominate. Of the transforming species, only *Amorpha fruticosa* can be tentatively mentioned, where this species forms small thickets in the sanitary protection zone. Below is a list of 28 adventitious plants from 15 families found in the SPZ area.

Aceraceae: *Acer negundo* L. – a North American species, a cultivated plant, a soft invasive species in the sanitary protection zone;

Amaranthaceae: *Amaranthus retroflexus* L. – a North American species, an adventitious plant, an aggressive weed in oases;

Apiaceae: *Torilis nodosa* (L.) Gaertn. – Mediterranean species, an adventitious plant; *Foeniculum vulgare* Mill. – cultivated and running wild;

Asteraceae: *Acroptilon repens* (L.) DC. – a neophyte, on the list of quarantine plants of the Republic of Uzbekistan (category A2, II) [5], *Ambrosia artemisiifolia* L. – a North American species, a neophyte, on the list of quarantine plants of the Republic of Uzbekistan (category A2, II) [5], *Erigeron annuus* (L.) Pers. – a species from North America, sometimes forms thickets, *Erigeron canadensis* L. *(=Conyza canadensis* (L.) Cronquist) – native to North America, an aggressive weed, *Tragopogon graminifolius* DC. –species from Afghanistan, Iran, Turkmenistan, a soft invasive species, recently introduced to the flora of Uzbekistan, a superneophyte [6];

Caryophyllaceae: *Stellaria media* (L.) Vill. – an invasive, widespread weed, sometimes forming thickets; in the early 1950s, it was noted in scientific literature as "Possibly found in the Uzbek SSR" [7];

Convolvulaceae: *Ipomoea purpurea* (L.) Roth – a plant of the temperate tropics of North and South America, a cultivated and invasive plant, runs wild, an agriophyte;

Cuscutaceae: *Cuscuta campestris* Yunck. – a plant from North America, a parasitic plant, a xenophyte;

Euphorbiaceae: *Acalypha australis* L. – a plant from East Asia (Far East, China, Japan, etc.), a xenophyte;

Fabaceae: *Amorpha fruticosa* L. – an invasive plant from North America, *Robinia pseudoacacia* L. – an invasive plant from North America, naturalized in Europe and Asia;

Malvaceae: *Abutilon theophrasti* Medik. – is an aggressive weed, but rarely extends beyond the cultivated landscape, an agriophyte;

Moraceae: *Morus alba* L. – native to China and Korea, cultivated, runs wild, archaeophyte;

Portulacaceae: *Portulaca oleracea* L. – the species' native origin is unknown, an invasive and aggressive weed, but not widespread in sanitary-protection zones;

Scrophulariaceae: *Kickxia elatine* (L.) Dumort. – is an alien and naturalized plant, *Phelipanche aegyptiaca* (Pers.) Pomel – a parasite, parasitizes primarily on cultivated plants, less commonly on wild plants, *Veronica persica* Poir. ex Lam. – is an alien and naturalized plant, a

species from Southwest Asia, *Veronica polita* Fr. – an alien and naturalized plant. Plants of this family are not widely distributed in the sanitary-protection zone;

Simaroubaceae: *Ailanthus altissima* (Mill.) Swingle – a species from China, where the tree has long been cultivated for the breeding of the ailanthus silkworm, is widespread;

Solanaceae: *Solanum nigrum* L. is an alien and naturalized plant; *Physalis angulata* L. – is an alien plant that has not naturalized; *Hyoscyamus niger* L. – an alien plant that has long been naturalized; Datura *stramonium* L. – is an alien and long-naturalized plant; *Datura innoxia* Mill. – is an alien and naturalizing plant.

The list of adventitious plants in the sanitary-protection zone is not limited to this. It could include *Maclura pomifera* (Raf.) C.K. Schneid, *Juglans regia* L., *Juglans microcarpa* L., *Juglans nigra* L., and many other cultivated plants. However, the limited space of this thesis does not allow for this.

References:

1. Decree of the President of the Republic of Uzbekistan No. PF-46 dated March 25, 2026, paragraph 21a. (in Uzbek).
2. Tillaev, T.S., Gaziev, A.D. The role of the Sanitary-Protection Zone of the Institute of Nuclear Physics of the Academy of Sciences of the Republic of Uzbekistan in the Conservation of the Native Flora of the Tashkent Botanical-Geographical Region. Uzbek Biological Journal. No. 4, 2021. pp. 43–47. (in Russian).
3. Tillaev, T.S., Gaziev, A.D. Flora of Native Plants of the Village of Ulugbek and the Sanitary-Protection Zone of the Institute of Nuclear Physics of the Academy of Sciences of the Republic of Uzbekistan. Idem, No. 5, 2021. pp. 17–23. (in Russian).
4. Tillaev, T.S., Gaziev, A.D. Cultivated Plants of the Village of Ulugbek and the Sanitary Protection Zone of the Institute of Nuclear Physics of the Academy of Sciences of the Republic of Uzbekistan. Idem, No. 2, 2026. pp. 25–30. (in Russian).
5. On Approval of the List of Pests of Quarantine Significance for the Republic of Uzbekistan. Registered in the Ministry of Justice of the Republic of Uzbekistan, No. 3597 dated January 14, 2025. (in Uzbek).
6. Makhkamov T.Kh., Rakhmatov A.A., Khakimova D.A., Bakhodirova G.I. Invasive *Tragopogon graminifolius* DC. (Asteraceae) – muqobil oziq-ovqat va dorivor ўsimlik. Food safety: Global and national problems. Abstracts of IV International scientific-practical conference (October 14-15, 2022, Samarkand). pp. 176 – 177. (in Uzbek).
7. Flora of Uzbekistan. Editor-in-Chief Academician E.P. Korovin. Publishing House of the Academy of Sciences of the Uzbek SSR. Tashkent, 1953, 552 p. (in Russian).

DETERMINATION OF IRON CONTENT IN PLANT-BASED FOOD PRODUCTS USING NEUTRON ACTIVATION ANALYSIS

Kuldjanov B.[1], Danilova E.[2]

[1]*State Institution "Scientific and Technical Center for Radiation and Nuclear Safety" under the Committee for Industrial, Radiation, and Nuclear Safety, Tashkent, Uzbekistan,*

[2]*Institute of Nuclear Physics, Uzbekistan Academy of Sciences, Tashkent, Uzbekistan*

There are certain limits of the microelements concentrations in human body. Exceeding these limits disrupts the equilibrium of various functional systems of organism and it leads to different diseases. Addressing this negative phenomenon requires use of medications or adjustments of the diet to compensate elemental misbalance. Such an approach requires knowledge of the trace elements content of foods stuff and medications.

Iron is one of the most vital trace elements for the normal functioning of the human organism. Iron is essential for maintaining the immune and digestive systems and for human mental and physical activity due to its influence on metabolic processes. The most common cause of anemia is insufficient intake of iron into the organism. Anemia develops from iron deficiency through the intermediate stage of marginal iron deficiency, where hemoglobin levels in the blood remain normal, to the final stage of decreased hemoglobin concentration. Iron deficiency is corrected by appropriate nutrition to stop its development before the final stage. Thus, the relevance of the question of iron content in food products is evident.

There is a significant amount of literature regarding the elemental composition of food products. This article presents data on the iron contents in the main types of vegetables, melons, and fruits from Tashkent city markets. The data obtained using neutron activation analysis [1]. The iron contents in the samples determined by the long-lived radionuclide Fe^{59} from $Fe^{58}+n \rightarrow Fe^{59}$ nuclear reaction, $T_{1/2}$=44.5 days, Eγ=1099.2 keV.

Table 1 presents some values of iron content for the natural (non-dried) state, calculated from experimental data taking into account the corresponding drying coefficients. The table also provides data from the US Department of Agriculture [2], calculated (in ppm) from the original (in mg/100g).

Table 1. Iron content in vegetables, melons, and fruits, selected from the markets of the city of Tashkent (ppm)

Food product	Iron average content	
	recalculation to natural weight	**USDA data [2]**
Red chili pepper	44,5	10.3 (4.5-14)
Carrot	10,8	3 (1.2-11.5)
Apple	8,6	1.2
Pear	11,4	1.8 (1.1-4.3)
Peach	16,7	3.4
Apricot	10,1	3.9 (1.6-6.2)
Cherry	24,5	3.6
Walnut	11,1	29.1 (26-32)

The table 1 shows that local cherries, peaches, pears, apricots, apples, and carrots favorably differ from USDA data. The iron content in red bitter pepper can be particularly noted, which is four times higher than the USDA average values. At the same time, according to USDA data the iron content in walnuts is nearly three times higher than the data in this study.

The recommended average daily iron intake levels are provided [3], which represent the requirement levels for healthy individuals.

It should be noted that iron is absorbed differently. This depends, in particular, on the form in which iron enters the human body: heme (Fe^{2+}) and non-heme (Fe^{3+}) [4]. Both forms are found in meat, fish, and seafood, whereas plant-based foods contain only non-heme iron [5]. In this regard, this study is more relevant for compiling diets for predominantly vegetarian diets. Hemic iron is more easily absorbed than non-hemic one [6]. At the same time, there are rich in vitamin C products, which contributes to the more complete absorption of non-hemic iron [5]. Thus, certain combinations of plant-based products can approach the absorption level of non-hemic iron to the hemic one. At the same time, some substances and elements (for example, polyphenols and calcium) can hinder iron absorption [7]. The issue of iron bioavailability goes beyond the scope of this study.

The results obtained are recommended for use by dietitians when creating diets for preventive purposes.

References:

1. Бакиев С.А., Рахманов Ж., Кульджанов Б.К., и др. Применение инструментального нейтронно-активационного анализа для исследования элементного состава плодоовощной продукции и лекарственных растений // Узбекский физический журнал. Т. 12, №3, 2010, С.181-187.
2. FoodData Central. USDA’s comprehensive source of food composition data with multiple distinct data types. // U.S. DEPARTMENT OF AGRICULTURE. https://fdc.nal.usda.gov/
3. Institute of Medicine. Food and Nutrition Board. Dietary Reference Intakes for Vitamin A, Vitamin K, Arsenic, Boron, Chromium, Copper, Iodine, Iron, Manganese, Molybdenum, Nickel, Silicon, Vanadium, and Zinc: a Report of the Panel on Micronutrients // Washington, DC: National Academy Press; 2001.
4. M.Wessling-Resnick. Iron. In: Ross AC, Caballero B, Cousins RJ, Tucker KL, Ziegler RG, eds. Modern Nutrition in Health and Disease. // 11th ed. Baltimore, MD: Lippincott Williams & Wilkins; 2014:176-88.
5. P.J.Aggett. Iron. In: Erdman JW, Macdonald IA, Zeisel SH, eds. Present Knowledge in Nutrition. // 10th ed. Washington, DC: Wiley-Blackwell; 2012:506-20.
6. L.E.Murray-Kolbe, J.Beard. Iron. In: Coates PM, Betz JM, Blackman MR, et al., eds. Encyclopedia of Dietary Supplements. // 2nd ed. London and New York: Informa Healthcare; 2010:432-8.
7. R.Hurrell, I.Egli. Iron bioavailability and dietary reference values // Am.J.Clin.Nutr. 2010;91:1461S-7S.

PRODUCTION OF IRIDIUM-192 IONIZING RADIATION SOURCES FOR RADIOGRAPHIC TESTING OF METAL WELDED JOINTS

Ashrapov U.[1], Malikov Sh.[1], Amanov O.[1], Mogoch S.[2]
[1]*Institute of Nuclear Physics of Academy of Sciences, Tashkent, Uzbekistan*
[2]*Daesan NDE International Engineering, Tashkent, Uzbekistan*

For radiographic inspection of welded joints made of metals, made by welding, with a thickness of welded elements from 1 to 400 mm, X-ray or gamma radiation from closed ionizing radiation sources Ir-192 is used. ^{192}Ir radionuclide has decay $T_{1/2}$=73,826 days and the average energy of gamma radiation is 0.38 MeV, the maximum gamma energy is 1.06 MeV. The Iridium-192 ionizing radiation source (IRS) with an activity 120 Ci, in combination with gamma flaw detectors of the Gammarid-192/120M is used for radiographic non-destructive testing (NDT) of the quality of high-quality products (cast, welded, forged, pressed, etc.).

Based on the WWR-SM reactor and the Republican Central Isotope Laboratory a technology of production of Ir-192 IRS with an activity up 50 to 120 Ci was developed by irradiating disks of natural iridium-191 by thermal neutrons via the nuclear reaction ^{191}Ir(n, γ)^{192}Ir. The Ir-192 IRS was coupled with the Gammarid-192/120M gamma-ray flaw detector by placing the source in a holder with a roller and mounting it in the radiation head of the gamma-ray flaw detector. The technology for manufacturing the Ir-192 source and assembling it with the Gammarid-192/120M gamma detector includes the following stages: 1) 30 pieces of metal disks of natural iridium (∅=2.7 mm, h=0.2 mm, m=31.7 mg), packed in aluminum foil, were irradiated in a vertical reactor channel in an EK-20 block container in the internal cavity of the IRT-4M fuel assembly using thermal neutrons with a flux density of ~ 0.9·1014 neutrons/cm2s for 600 to 980 hours. 2) In the reactor's "hot cells," after irradiation, the iridium disks were placed in a special device where the radioactive iridium disks were placed in a special stainless steel capsule (Ø = 4.5 mm, h = 8.0 mm), closed with a lid, and spot welded. 3) The source capsule was checked for leaks using the immersion method [2]. 4) The source was rolled in the source holder using special equipment; 5) The source holder was connected to the Iridium-192 source with a flexible shaft and loaded into the radiation head of the Gammarida-192/120M gamma flaw detector [1]. To carry out NDT of the quality of the welded seam of a metal pipe sample with a diameter of 219.0 mm and a wall thickness of 8.0 mm, testing was carried out through two walls of the test pipe using Kodak Industrex AA-400 X-ray film, 0.1 mm thick lead screens, identification marks from sets No. 2 and 6, and groove sensitivity standards No. 2 according to gamma-graphic control according to GOST 7512-82.



Figure 1. X-ray image of a non-destructive electric welding test sample, which complies with GOST 7512-82 "Non-destructive testing. Welded joints. Radiographic method" [3].

Table 1 shows the main results of gamma radiography of the studied sample.

Table 1. Main results of gamma radiography of the test sample.

Serial number: Gammarid-192/120M (source number)	Radiation metal plate, mm	Exposure time, sec	Exposure dose rate on the surface of the radiation head with Ir-192 source , μSv/sec	X-ray sensitivity, by sensitivity class II (GOST 7512-82), mm	X-ray optical illumi-nator
1128 (01)	20.0	25	0.083	0.4	2.0

Several iridium-192 sources with Gamarid-192/120M gamma flaw detectors were delivered to the Syrdarya Thermal Power Plant, where NDT specialists performed non-destructive testing of welded seams of metal pipelines, resulting in the acquisition of over a thousand X-ray images.

Figure 2 shows a non-destructive X-ray image of a 219 x 8 mm diameter pipe, which is compliant with quirements of ASME Code [4]. Carestream (Kodak) Industrex AA400 NIF 30 x 40 X-ray film and lead-shielded cassettes were used to obtain this gamma-radiographic image. Non-destructive testing was performed through two pipe walls with a total thickness of 16 mm. The Ir-192 source activity was 60 Ci, the exposure time was 19 seconds, and the optical density of the X-ray image was 2.5.



Figure 2. X-ray image of a weld sample with a diameter of Ø=219x8 mm, obtained using the method of gamma radiography with an Ir-192 ionizing radiation source

As shown in the Fig.2, the defects in the image indicate insufficient weld root penetration and the presence of slag inclusions. The conclusion based on the non-destructive testing results: the weld quality is poor, requiring rewelding.

Sealed iridium-192 sources, complete with Gammarid-192/120M gamma-ray flaw detectors, were used for NDT at the Talimarzhan Thermal Power Plant (Kashkadarya, Nurafshon village), the Kandym Gas Processing Plant (Bukhara Region, Olot village) by VBM Engineering LLC, and the Syrdarya Thermal Power Plant (Shirin, Uzbekistan) by Desen NDT International Engineer LLC. All obtained gamma images met the sensitivity and quality requirements of GOST-7512-82 "Non-destructive testing. Welded joints" (Russia) [3] and ASME (USA) [4]. After the end of their service life, all Ir-192 RIS were disposed of and buried at the Republican Disposal Facility for Radioactive Waste.

References:

1. U.T. Ashrapov, S.S. Khujaev, I.I. Sadikov, M.Y. Tashmetov, and Y.A. Isaev. Manufacturing of an Iridium-192 Ionizing Radiation Source for Nondestructive Testing. Journal of Physics of Atomic Nuclei, 2021, Vol. 84, No. 9, pp. 1540–1549. https://doi.org/10.1134/S1063778821090052;
2. Kh.A. Ergashev, Sh.M. Makhkamov, U.T. Ashrapov. Method of Determination of Tightness of Radiation Ionization Source. Preliminary patent of the Republic of Uzbekistan. № 4943. 1997.
3. GOST 7512-82 "Non-destructive testing. Welded joints. Radiographic method". Publishing and Printing Complex of the State Standard of Russia "Publishing House of Standards". Moscow. 1982. 18. https://files.stroyinf.ru/Data2/1/4294852/4294852744.htm.
4. J.C. Spanner, Sr., 1992. "Nondestructive Testing Standards and the ASME Code," in Nondestructive Testing Standards: Present and Future, H. Berger, L. Mordfin. https://doi.org/10.1520/STP23815S.

IMPROVEMENT OF SPECTRAL AND PHYSICAL PARAMETERS OF THE NEUTRON RADIOGRAPHY AND TOMOGRAPHY FACILITY AT THE WWR-SM RESEARCH REACTOR

Tashmetov M.Yu.[1], Adizov S.M.[2], Ismatov N.B.[1]

[1]Institute of Nuclear Physics, Uzbekistan Academy of Sciences, Tashkent, Uzbekistan

[2]Navoi State University of Mining and Technologies, Navoi, Uzbekistan

The development of non-destructive testing methods using thermal and cold neutron beams requires the continuous enhancement of image quality, reduction of artifact levels, and improvement of spatial resolution. This work is dedicated to the experimental investigation and quantitative evaluation of the effectiveness of using a single-crystal sapphire filter in the horizontal channel of the WWR-SM research reactor to upgrade the neutron beam of the neutron radiography and tomography (NRT) facility. The implementation of filtering significantly reduces the accompanying gamma background and the hard component of the spectrum, which comprehensively improves the qualitative and quantitative characteristics of tomographic reconstructions.

For a comprehensive evaluation of the tomographic reconstruction quality and the degree of beam upgrade, four key analytical criteria were applied:

Beam Hardening/Cupping Effect Suppression: The cupping effect in the open beam was evaluated via the relative error $\delta = \frac{|\Delta I|}{I_{center}} \cdot 100\%$ where ΔI is the difference between the maximum intensity value at the edges and the minimum in the center (Fig. 1). The analysis of the radial flux density distribution profiles demonstrated that the installation of the sapphire filter reduces the relative error from critical values (up to 10.66 % on the right side) to stable values of 2.62 - 2.88 %, ensuring high uniformity of the radiation field [1, 2].

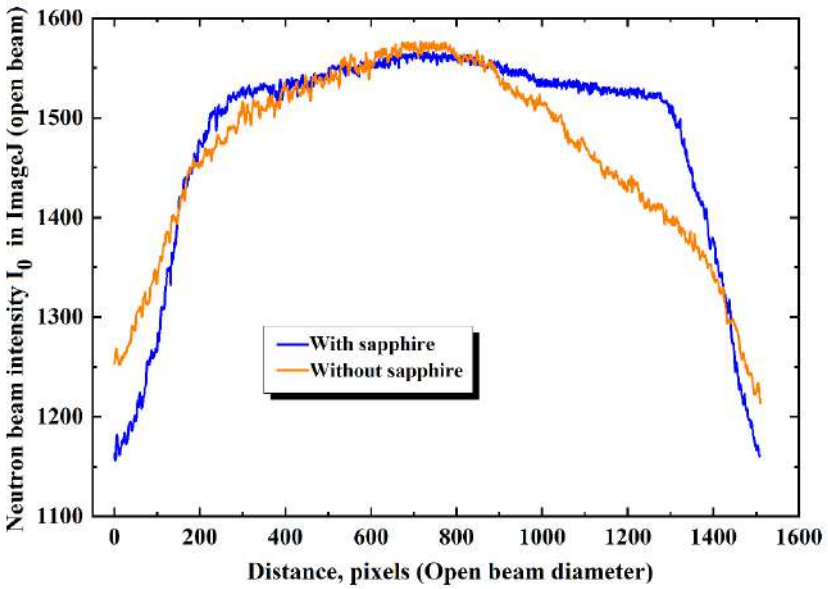

Figure 1. Radial profiles of the initial and upgraded neutron beam intensity I_0 along the open beam diameter before and after the installation of the single-crystal sapphire filter.

Edge Sharpness and Spatial Resolution (Edge Spread Function / MTF): The edge sharpness was evaluated using the signal intensity derivative (*dI/dx*) in gray levels. The modified beam demonstrated an increase in the coefficient of determination (R^2) from 0.638 to 0.952. Meanwhile, the transition edge width (*w*) decreased from 15,03±1,53 pixels to 10,83±0,33 pixels, and the full width at half maximum (FWHM) decreased from 17.7 to 12.7 pixels, indicating improved edge sharpness and a 28 % reduction in blurring (Fig. 2) [3, 4].

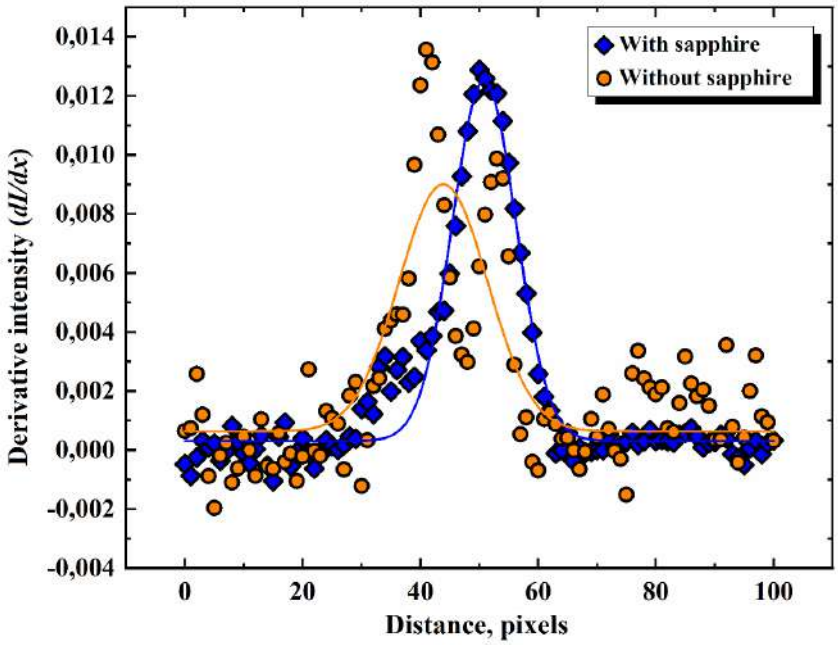

Figure 2. Signal intensity derivative (*dI/dx*) along the interface line profile for the initial and upgraded neutron beams.

Signal-to-Noise Ratio (SNR) and Contrast-to-Noise Ratio (CNR): For the quantitative analysis of fluctuations in homogeneous zones of reference objects (a mechanical stopwatch), integral parameters were calculated [5]: $SNR = \frac{Mean_{metal}}{\sigma_{noise}}$ and $CNR = \frac{Mean_{metal} - Mean_{background}}{\sigma_{noise}}$. The suppression of the gamma component using the sapphire filter led to a decrease in the standard deviation in the background zone (σ_{noise}) from $2{,}556 \cdot 10^{-4}$ to $1{,}787 \cdot 10^{-4}$. As a result, the SNR parameter increased by 43.47% (up to 17.49), and the CNR parameter increased by 54.72% (up to 15.36).

Phase Histogram Analysis and Peak-to-Peak Resolution: Phase separability (air/metal) was evaluated using a histogram analysis of the attenuation coefficient distribution according to the resolution formula:

$$\text{Resolution} = \frac{|\mu_1 - \mu_2|}{\sigma_1 + \sigma_2}$$

where μ_1, μ_2 are the mean values of the phase attenuation coefficients, and σ_1, σ_2 are their standard deviations. Beam optimization increased the separation coefficient from 5.42 to 7.82, which provided a 44.28 % increase in the separability parameter and enhanced the reliability of identifying the internal structure of archaeological artifacts.

Conclusion. The conducted studies confirm that the spectral optimization of the neutron beam from the fifth horizontal channel of the WWR-SM reactor using a single-crystal sapphire filter eliminates accompanying background noise, minimizes beam-hardening artifacts, and manifoldly enhances contrast-spatial resolution. The obtained results open up new opportunities for precision research in various fields of applied physics, materials science, and complex non-destructive testing of heterogeneous industrial and unique archaeological objects.

References:

1. Hachouf, N., Kharfi, F., Hachouf, M., & Boucenna, A. (2016). New analytical approach for neutron beam-hardening correction. *Applied Radiation and Isotopes*, 107, 353–358. DOI: 10.1016/j.apradiso.2015.11.024.
2. Kasperl, S., Schillinger, M., Münch, B., et al. (2005). Application of an iterative artefact reduction method to neutron tomography. *Nuclear Instruments and Methods in Physics Research Section A: Accelerators, Spectrometers, Detectors and Associated Equipment*, 542(1–3), 392–398. DOI: 10.1016/j.nima.2005.01.167.
3. Boukerdja, L., Guerrache, M., Dendene, O., & Ali, A. Spatial resolution study of a neutron imaging system using the slanted edge.
4. Konber, H. A. (2016). Development and characterization of a neutron tomography system. *Journal of Taibah University for Science*, 10(2), 195–204. DOI: 10.1016/j.jtusci.2015.03.002.
5. de Beer, F. C., Kaestner, A. P., Radebe, M., et al. (2013). Evaluation Procedures for Spatial Resolution and Contrast Standards for Neutron Tomography. *Physics Procedia*, 43, 138–148. DOI: 10.1016/j.phpro.2013.03.017.

RADIONUCLIDE FRACTIONATION DURING PHOSPHORITE PROCESSING AND SOURCE APPORTIONMENT OF ELEMENTAL ANOMALIES IN AN INDUSTRIAL AREA

Sadikov I.I., Akhmedov Ya.A., Yarmatov B.X., Danilova E.A., Malikov A.A.
Institute of Nuclear Physics, Uzbekistan Academy of Sciences, Tashkent, Uzbekistan

Phosphorite is a naturally occurring radioactive material (NORM) feedstock enriched in natural radionuclides. Acid processing disrupts the ^{238}U–^{226}Ra secular equilibrium and redistributes the radiological burden between the product and waste streams. In Almalyk, fertilizer and non-ferrous metallurgical plants are located side by side, so elemental anomalies cannot be attributed to a single source directly. This study quantifies ^{238}U–^{226}Ra fractionation and identifies the probable sources of these anomalies using geochemical indices and multivariate statistics.

Materials included Karatau and Toshqur phosphorites, intermediate products, ammophos, superphosphate, RS-AGRO and process wastes. Monitoring covered ZAV (plant site), ALM (Almalyk industrial area), GEN and PAX (more than 40 years of fertilizer application) and FON (background); at each site soil (0–30 cm) and leaf samples were taken from 20 locations (100 soil and 100 leaf samples). Elements were determined by INAA at the VVR-SM reactor; for phosphorus-rich matrices, RNAA with an AlOOH sorbent suppressed the ^{32}P bremsstrahlung background. Gamma emitters of the ^{238}U, ^{232}Th and ^{235}U decay series were measured by semiconductor gamma-ray spectrometry. Radium equivalent activity and the external hazard index (H_{ex}, used only as a comparative screening indicator of external gamma potential, not as a regulatory criterion), contamination and Fe-normalized enrichment factors (*CF*, *EF*; FON as reference), PCA of z-standardized data and Ward’s HCA were applied to the 100 individual samples.

The ^{238}U activity concentration increased from 470 Bq/kg in the feedstock to 840 Bq/kg in ammophos and 1,160 Bq/kg in superphosphate (1.8–2.5-fold), whereas ^{226}Ra decreased from 630 to 90–300 Bq/kg. The ^{226}Ra/^{238}U activity ratio therefore fell from ≈1.3 in the feedstock to ≈0.1–0.3 in the finished products, i.e. a 4–13-fold disruption of secular equilibrium. This fractionation is consistent with preferential partitioning of U into the phosphate phase and of Ra into the sulfate-rich phosphogypsum stream, but the inference is not yet closed by measurement: direct determination of ^{226}Ra in the phosphogypsum stream and a complete mass balance are required to quantify the transferred Ra fraction, and constitute the next stage of this work. H_{ex} was 1.76, 1.39, 0.84 and 0.26 for the feedstock, ground phosphate rock, superphosphate and ammophos, respectively. This decrease does not signify elimination of the hazard but the partitioning of ^{226}Ra into a separate stream; therefore ^{226}Ra and ^{222}Rn should be monitored directly at phosphogypsum storage facilities.

Cu showed the strongest enrichment at ZAV and ALM (*CF* ≈ 48/39; *EF* ≈ 30/29), followed by Sb (≈ 14/10), Zn (≈ 8/5) and As (≈ 4/3). The Cu–Sb–Zn–As association with *EF* > 2 indicates anthropogenic enrichment consistent with the aerosol signature of non-ferrous metallurgy, although no single facility can be identified conclusively. At GEN and PAX, *CF* ≈ 1 and *EF* < 1.5: within the present study design, no pronounced accumulation attributable to long-term fertilizer application was detected. PC1 explained 45.2% of the variance (loadings +0.89 to +0.94 for Sb, Au, As, Zn, Cu, Ag and Mo), with site scores ZAV (+6.2) > ALM (+2.6) > PAX (−1.4) ≈ GEN (−2.2) > FON (−5.2). In the HCA, ZAV formed a distinct cluster while GEN and PAX clustered near the background (cophenetic correlation 0.87 for soil and 0.97 for plants). *CF*/*EF*, PCA and HCA are mutually consistent descriptions of the same dataset rather than independent lines of evidence.

At ZAV, leaf-to-soil ratios for As, Sb and U ranged from 0.20 to 0.40 ($R^2 > 0.7$ for paired measurements). Because dust is retained on leaf surfaces, these ratios do not represent conventional root uptake and bioaccumulation; they underscore the role of atmospheric deposition. Disentangling the uptake pathways will require parallel analysis of washed and unwashed leaves of the same species together with atmospheric aerosols.

AI-ASSISTED SELECTION OF NEW RADIOLABELLED PHARMACEUTICALS BASED ON THE RADIOPREPARAT PRODUCTION PLATFORM

Usmanova S.A.
Institute of Nuclear Physics, Uzbekistan Academy of Sciences, Tashkent, Uzbekistan

Objective. This study identifies radiolabelled pharmaceuticals that can be developed by extending the radionuclide, formulation, and quality-control operations already established at the State Enterprise (SE) “Radiopreparat”. Artificial intelligence (AI) and mathematical models are used to rank candidates and optimise radiolabelling conditions, rather than to screen unrelated molecular structures.

Existing production platform. The published product catalogue includes carrier-free sodium iodide labelled with ^{125}I or ^{131}I; compounds of ^{32}P, ^{33}P, ^{35}S, ^{55}Fe, ^{59}Fe, and ^{203}Hg; and radiopharmaceuticals based on ^{32}P, ^{131}I, ^{198}Au, and ^{153}Sm [1]. A separate line comprises the ^{99}Mo/^{99m}Tc generator and nine lyophilised kits for skeletal, renal, hepatobiliary, hepatic, and myocardial imaging [1]. The relevant capabilities are therefore radioiodination, reactor production of radiometals, reductive ^{99m}Tc labelling, aseptic filling, lyophilisation, and radiochemical quality control. Published work from the enterprise describes analytical methods for Na^{125}I, Na^{131}I, and ^{153}Sm-oxabifor [2], as well as production of no-carrier-added ^{177}LuCl$_3$ and preparation of [^{177}Lu]Lu-PSMA-617 at approximately 99% radiolabelling yield [3]. The latter demonstrates technical feasibility of the ^{177}Lu-DOTA platform but is not listed as a routine commercial product.

Candidate-selection model. Each candidate is described by radionuclide availability, compatibility with existing labelling and lyophilisation procedures, additional equipment, analytical requirements, expected stability, clinical relevance, and dosimetric risk. The priority score is defined as $P_j = w_1T_j + w_2C_j + w_3M_j + w_4D_j - w_5E_j - w_6Q_j$, where T is technological readiness, C clinical relevance, M availability of starting materials, D dosimetric tractability, E additional experimental effort, and Q quality-control risk. Weights are assigned by an expert panel; Monte Carlo sampling tests whether the ranking is stable to weight uncertainty. Gaussian-process regression, random forests, and Bayesian optimisation are appropriate for the small, heterogeneous datasets expected during early radiopharmaceutical development [4].

Recommended products. The highest-priority candidate is a lyophilised kit for preparation of a ^{99m}Tc-labelled PSMA ligand for SPECT imaging of prostate cancer. It uses the existing generator, aseptic filling, Sn(II)-mediated reduction, and lyophilisation line. This selection also matches the current IAEA programme on next-generation ^{99m}Tc kits, which explicitly includes PSMA ligands [5]. The variables to be optimised are the chelating group, Sn(II) content, pH, buffer, temperature, reaction time, eluate activity, antioxidant concentration, and post-labelling stability.

The second priority is a therapeutic ^{177}Lu-DOTA product line. For [^{177}Lu]Lu-PSMA-617, the next step is not another measurement of labelling yield, but determination of the radiolysis profile, related impurities, shelf life, batch reproducibility, and dosimetric parameters required for a controlled production process. Once these procedures are established, [^{177}Lu]Lu-DOTATATE is the most direct additional product for peptide receptor radionuclide therapy of somatostatin-receptor-positive neuroendocrine tumours. It shares the radionuclide, DOTA coordination chemistry, and much of the analytical workflow with the PSMA compound. Development of ^{177}Lu-labelled peptides and other targeting vectors is a stated objective of IAEA CRP F22078 [6].

The third priority is ^{131}I-metaiodobenzylguanidine (^{131}I-mIBG) for targeted treatment of neuroendocrine tumours. It builds on routine Na^{131}I production and experience with several radioiodinated products; its clinical use and dosimetry are covered by dedicated guidelines [7]. Its development nevertheless requires a specific precursor, product purification, and quantification of free iodide, giving it lower technological readiness than the two leading candidates. ^{125}I-labelled compounds are more suitable as a reserve platform for radioimmunoassay and research reagents. Additional ^{153}Sm complexes would extend an existing bone-treatment class but add less product differentiation.

Computational workflow. Historical batch data are arranged as input-output records linking composition and process variables to radiolabelling yield, radiochemical purity, impurity profile, and stability. Bayesian optimisation selects the next experiment using expected improvement, precursor cost, and radiation exposure. Quantum-chemical calculations compare candidate chelators and metal-complex stability. A kinetic model describes complex formation and radiolysis, while a physiologically based pharmacokinetic model relates biodistribution to absorbed dose. Candidate conditions are selected from the Pareto front for purity, stability, target uptake, critical-organ dose, and cost. Model predictions do not replace pharmacopoeial testing, non-clinical evaluation, or good manufacturing practice [8].

Experimental validation. The initial design must span pH, temperature, reaction time, activity, ligand-to-radionuclide ratio, buffer, and antioxidant composition, including failed batches. For the ^{99m}Tc-PSMA kit, generator age, lyophilisate storage, and the usable lifetime of the reconstituted product are additional variables. For ^{177}Lu conjugates, the dependence of radiolysis on activity concentration and absorbed-dose rate must be resolved; for ^{131}I-mIBG, the relevant outputs include labelling yield, free iodide, and purification loss. Primary endpoints are radiolabelling yield, radio-HPLC purity, related impurities, molar activity, and stability. After the initial design, 5–10 active-learning cycles are performed. A reserved set of experiments provides independent validation and defines the admissible process window with uncertainty bounds.

Conclusion. The proposed sequence is: (i) a ^{99m}Tc-PSMA diagnostic kit; (ii) completion of a reproducible [^{177}Lu]Lu-PSMA-617 process followed by [^{177}Lu]Lu-DOTATATE; and (iii) development of ^{131}I-mIBG. This ranking maximises reuse of established production operations and restricts new investment to product-specific synthesis, analysis, and biological validation.

References:

1. SE “Radiopreparat”, Institute of Nuclear Physics, Academy of Sciences of Uzbekistan. Product catalogue: radionuclides, radiopharmaceuticals, the ^{99}Mo/^{99m}Tc generator, and ^{99m}Tc kits. https://radiopreparat.com/ (accessed 28 August 2026).
2. Khajiev L.O., Sadikov I.I., Abdukayumov A.M., Rikhsiev A.Z. Method for determining the radiochemical purity of radiopharmaceuticals based on iodine-125, iodine-131 and samarium-153-oxabifor. Int. J. Emerging Trends Eng. Res. 9(3), 217–220 (2021). https://doi.org/10.30534/ijeter/2021/11932021.

3. Usarov Z.O., Abdukayumov A.M., Rikhsiev A.Z., Hajiev L.O. Preparation of the radiopharmaceutical [^{177}Lu]Lu-PSMA-617 for targeted radionuclide therapy of prostate cancer. Universum: Chemistry and Biology 10(100) (2022). https://doi.org/10.32743/UniChem.2022.100.10.14241.
4. Shields B.J. et al. Bayesian reaction optimization as a tool for chemical synthesis. Nature 590, 89–96 (2021). https://doi.org/10.1038/s41586-021-03213-y.
5. IAEA. Development of new generation of Tc-99m kits. Coordinated Research Project F22077, 2024–2029. https://www.iaea.org/projects/crp/f22077.
6. IAEA. Development of potential ^{177}Lu radiopharmaceuticals: design, radiolabelling and nonclinical evaluation. Coordinated Research Project F22078, 2023–2028. https://www.iaea.org/projects/crp/f22078.
7. Giammarile F. et al. EANM procedure guidelines for ^{131}I-meta-iodobenzylguanidine therapy. Eur. J. Nucl. Med. Mol. Imaging 35, 1039–1047 (2008). https://doi.org/10.1007/s00259-008-0715-3.
8. WHO/IAEA. Good manufacturing practices for radiopharmaceutical products. WHO Technical Report Series 1025, Annex 2. WHO, Geneva (2020).

DEMAND FOR REACTOR- AND CYCLOTRON-PRODUCED ISOTOPES IN INSTRUMENTATION, METROLOGY, INDUSTRY, AND MEDICAL DIAGNOSTICS

Bespokoev A.A., Rogozev A.B., Buryanenko I.V.
RITVERC JSC, St. Petersburg, Russian Federation

Modern industry and science make active use of radioisotope methods and equipment. This constitutes a significant, technologically complex sector comprising metrology and measuring equipment for radiation safety, sanitary control and environmental monitoring; industrial process control and quality control systems; non-destructive testing; and measurement calibration anf quality control for medical applications.

Radioisotope methods rely on the activities of scientific centers engaged in multi-stage cooperation - ranging from the production of high-purity substances and stable isotopes, through radioisotope generation in accelerators or reactors and the preparation of pure radionuclide products, to the final manufacture of industrial items such as sealed radionuclide sources and radioisotope-based instruments. Methodological, metrological, and regulatory support for their use is also essential.

Current industrial demand is well-established: ^{60}Co, ^{192}Ir, ^{75}Se, ^{137}Cs, ^{241}Am, ^{252}Cf, ^{90}Sr are among the dozen or so nuclides widely used in industry. Application methodologies are mature, and production is supported and - broadly speaking - stable, although occasional disruptions do occur. Established leaders also exist in the fields of analytical instrumentation, quality control, and metrology: ^{3}H, ^{14}C, ^{63}Ni, ^{85}Kr, ^{57}Co, ^{68}Ge, ^{109}Cd, ^{133}Ba are the primary radionuclides used, with activity levels ranging from tens to thousands of curies. Periodic supply shortages arise, forcing entire industries to consider switching to alternative methods or questioning the viability of their continued operations. While the production of certain radionuclides is currently limited, there are signs of renewed interest in isotopes such as ^{147}Pm and ^{204}Tl.

There are also applications for which nuclide production is less systematic, resulting in low volumes or a complete lack of regular production. This category includes many nuclides used for metrological purposes and as tracers for environmental monitoring, such as ^{22}Na, ^{35}S, ^{36}Cl, ^{44}Ti, ^{54}Mn, ^{65}Zn, ^{88}Y, ^{110m}Ag, ^{134}Cs, ^{139}Ce,^{147}Pm, ^{152}Eu ^{153}Gd, ^{207}Bi, ^{228}Th, ^{232}Th, ^{234}U, ^{238}U. These materials are essential for national and international metrological comparisons and the manufacture of metrological reference sources; however, their production is challenging, even though their market value is relatively low.

Maintaining the production of the full range of isotopes used in industry and metrology is a task requiring constant attention and cooperation between research centers and manufacturers to ensure continued success and vision of nuclear industry as a reliable supplier and source of new industrial solutions.

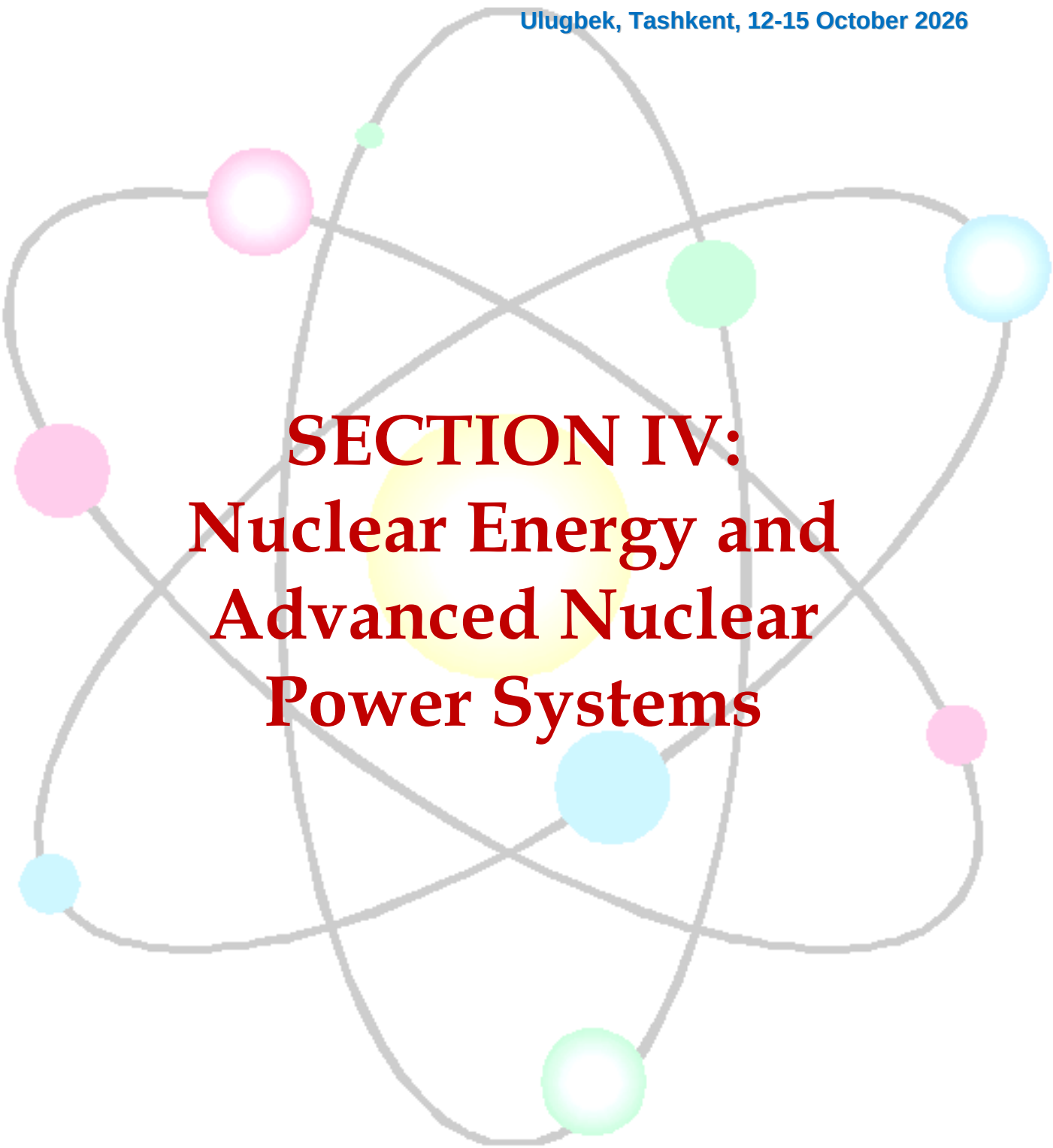

SECTION IV: Nuclear Energy and Advanced Nuclear Power Systems

SAFETY REGULATION AND LICENSING IN THE MANAGEMENT OF RADIOACTIVE WASTE AND THE OPERATION OF RADIATION SOURCES

Belkin D.Y., Sklifasovskaya Y.G.
Federal Environmental, Industrial and Nuclear Supervision Service (Rostechnadzor), Moscow, Russian Federation

The report provides an overview of the regulatory framework governing safety in the use of nuclear energy, with a focus on activities related to the management of radioactive waste and the operation of radiation sources, as well as the main principles of legal regulation.

The main functions and key areas of activity of Rostechnadzor in the field of regulating nuclear and radiation safety in the management of radioactive waste and the operation of radiation sources, as well as the specific features of federal state supervision in the field of nuclear energy use in relation to these facilities, are described.

The stages of licensing activities in the field of nuclear energy use, carried out by Rostechnadzor, are outlined.

PROSPECTS FOR THE USE OF REACTORS WITH HEAVY LIQUID METAL COOLANT IN UZBEKISTAN'S NUCLEAR PROGRAM

Yablochkina A.A., Elmurotova D.B.
State Institution “Scientific and Technical Center for Radiation and Nuclear Safety”, Tashkent, Uzbekistan

The development of nuclear energy is one of the priority directions of Uzbekistan's energy strategy. Currently, the country is implementing a large-scale project for the construction of a nuclear power plant in the Jizzakh region, comprising two power units with WWER-1000 reactors and two units with RITM-200 reactors. However, advanced nuclear energy technologies are not limited to thermal reactors – fast neutron reactors with heavy liquid metal coolant, particularly lead, are of considerable interest. This paper presents an assessment of the prospects for constructing such a reactor in Uzbekistan [3].

Reactors with heavy liquid metal coolant (HLMC) belong to Generation IV technologies. The most advanced project is the Russian Brest-OD-300 (300 MW), under construction in Seversk. Physical start-up is scheduled for 2028, with commercial operation planned for 2029. The facility possesses unique characteristics: lead coolant is chemically inert and does not react with water or air, eliminating the risk of severe accidents typical of sodium-cooled reactors; integral layout enhances reliability; dense nitride uranium-plutonium fuel and a closed fuel cycle enable the breeding of fissile materials and the multiplication of the fuel resource base. These features make Brest-OD-300 a reference design, which is expected to be scaled up to the commercial BR-1200 reactor [1,2].

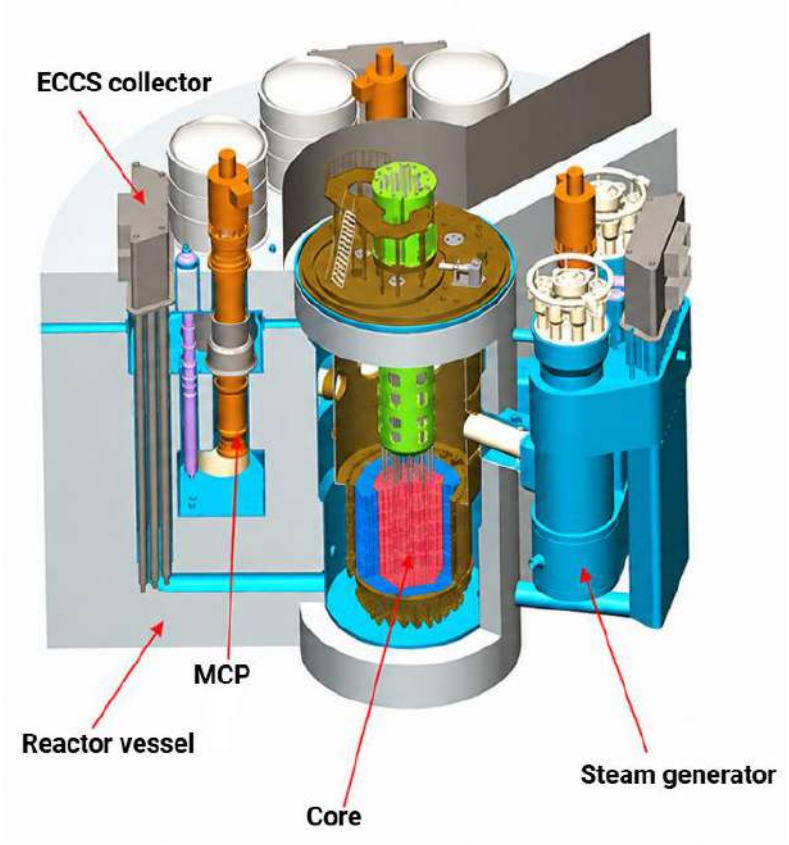

Figure. Arragement of the Brest-OD-300 reactor

Assessing the prospects for deploying HLMC reactors in Uzbekistan requires consideration of both enabling and constraining factors. The former includes the country's substantial raw material base: Uzbekistan ranks among the world leaders in uranium mining and export, providing a solid foundation for engagement in closed fuel cycles. The nation already possesses experience in operating research reactors and actively cooperates with the IAEA [4]. An important factor is the strategic partnership with Rosatom within the framework of the Jizzakh NPP project – this experience is building an institutional, regulatory, and human resource basis for the adoption of new technologies. Furthermore, Rosatom is considering the development of export versions of fast reactors by 2035, which opens a technological window for its partners.

At the same time, there are constraints that make the construction of an HLMC reactor in Uzbekistan unlikely in the near term. The Brest-OD-300 technology is currently at the pilot-demonstration stage, with commercial maturity not expected before 2035–2040. The project cost is comparable to the current investment program for the Jizzakh NPP ($9,5 billion). A lead-cooled reactor requires sophisticated solutions for corrosion control and maintaining a strictly controlled oxygen regime, increasing operational complexity and personnel qualification requirements. Moreover, most national financial and human resources in the coming decade will be focused on completing the VVER-1000 NPP, and a parallel large-scale project based on new technology appears premature.

Based on this analysis, a phased scenario is proposed. First phase (until 2030): completion of the first NPP construction, commissioning of VVER-1000 and RITM-200 units, and accumulation of operational competencies. Second phase (2030–2035): expansion of scientific and technical cooperation on fast reactors, joint research, staff exchanges, and feasibility studies. Third phase

(after 2035): subject to successful operation of Brest-OD-300 and the emergence of a commercial version – consideration and decision-making on a new project, likely as a small or medium-sized unit for capacity replacement.

Thus, HLMC technology holds considerable promise for energy security and resource efficiency, but its practical implementation is unlikely before 2035 – following the completion of the priority NPP project and the accumulation of necessary experience. A key condition will be the successful start-up and operation of the Brest-OD-300 in Russia, as well as Uzbekistan's readiness to adopt next-generation technologies. In the long term, the deployment of HLMC reactors could elevate the country's nuclear program to a qualitatively new level, aligned with global sustainable development trends.

References:

1. *Adamov, E.O. et al.* (2023). The "Proryv" (Breakthrough) Project: Creating a Technological Platform for a Closed Nuclear Fuel Cycle. Atomic Energy, Vol. 134, No. 5-6, pp. 243–250.
2. *Lebedev, I.V., Mikhailov, V.N.* (2024). Heavy Liquid Metal Coolant Reactors: Status and Prospects. Proceedings of Universities. Nuclear Energy, No. 3, pp. 89–101.
3. Decree of the President of the Republic of Uzbekistan "On Measures to Implement the Project for the Construction of a Nuclear Power Plant in the Jizzakh Region" No. PP-123 of 15.04.2025.
4. International Atomic Energy Agency (IAEA). (2026). Country Nuclear Power Profiles: Uzbekistan. Vienna.

PROBLEMS IN THE MANUFACTURE OF THE RITM-200 REACTOR PLANT

Elmurotova D.B., Yablochkina A.A.
State Institution “Scientific and Technical Center for Radiation and Nuclear Safety”, Tashkent, Uzbekistan

The RITM-200 reactor plant was developed by JSC “OKBM Afrikantov” and belongs to the modern generation of compact pressurized water reactor plants. One of its key design features is the integral layout: the core, steam-generating equipment and the main primary circuit components are housed within a single vessel. This design has made it possible to reduce the number of large primary circuit equipment items and enhance the compactness of the plant [1, 2].



Figure. General view of the RITM-200 reactor plant

Main Manufacturing Challenges

The high degree of equipment integration simultaneously constitutes an advantage and a technological challenge. The concentration of a large number of functional elements within the vessel increases the requirements for manufacturing accuracy, weld quality, the relative positioning of components, and the feasibility of subsequent inspection. One of the most critical operations is the fabrication of the reactor plant vessel. In practice, special technological stands, manipulators, roller supports and welding systems are employed to ensure the positioning of large cylindrical components and the execution of circumferential welded joints. Studies of the RITM-200 vessel manufacturing technology demonstrate that the use of special tooling enables improved welding quality, reduced auxiliary time, and the achievement of the required production accuracy [3].

A significant challenge is ensuring the quality of the base metal. The fabrication of large components requires the production of special alloy steels with specified mechanical and operational characteristics. A notable example is the production of the RITM-200N vessel flange for the ASMM under construction in Uzbekistan: for its manufacture in 2025, a special steel ingot weighing 205 t was produced. After metallurgical processing, the billet is transferred to subsequent stages of reactor vessel fabrication [4].

Another critical issue is welding. The vessel design requires high-quality welded joints, since possible defects can lead to reduced strength and leak-tightness of the equipment. Automated and manual welding techniques are used in production, along with specialized tooling for product positioning. Consequently, welding quality control must be carried out at all technological stages [3].

Geometric accuracy is of particular importance. For an integral design, even minor deviations in dimensions and the relative positioning of components can complicate assembly and inspection. In this regard, an expanding application of coordinate measuring systems, digital modelling and automated geometry control represents a promising direction.

Current Areas for Improvement

An important trend is the transition from single-unit production to serial manufacturing of the RITM-200. The repeatability of the technological process allows for the standardization of operations, the improvement of tooling and the enhancement of quality stability. Considerable production experience has already been accumulated in manufacturing plants of this type for the nuclear icebreaker fleet.

The introduction of additive technologies is also a promising avenue. In 2025, OKBM Afrikantov received authorisation to manufacture certain RITM-200 equipment components using a domestically produced 3D printer. The first such item was a terminal box for pump equipment [5].

It should be emphasised that the application of additive technologies in nuclear engineering requires confirmation of material property stability, qualification of the technological process, and assurance of the regulatory-mandated quality level.

Conclusion. Thus, the main manufacturing challenges of the RITM-200 are associated not so much with the fundamental impossibility of producing the plant, but rather with the need to ensure high accuracy, reproducibility and quality of the technological processes. The most critical stages are the fabrication of large vessel components, welding, inspection of geometric parameters and non-destructive testing.

For further improvements in production efficiency, it is advisable to advance the automation of welding processes, digital geometry control, end-to-end traceability of technological operations, enhance methods for metal and weld inspection, and expand the use of additive technologies for individual equipment components.

These issues acquire particular relevance in connection with the manufacture of the RITM-200N for the ASMM in Uzbekistan. The start of reactor equipment fabrication for the first ASMM unit was announced in May 2025, indicating that the project is moving from the design and process engineering preparation stage to the practical production of equipment.

References:

1. *Mishchenko, A.A.* Design solutions and advantages of the new-generation reactor plant "RITM-200" // Young Scientist. 2020. No. 27 (317). pp. 97–100.
2. OKBM Afrikantov. Reactor plants for nuclear icebreakers and other areas of the enterprise's activities.
3. *Grigoriev, I.S., Samoylenko, R.I., Shamaev, A.N.* Technological tooling for welding the RITM-200 reactor plant vessel // Young Scientist. 2017. No. 51 (185). pp. 35–37.
4. Ministry of Transport of the Russian Federation. Rosatom begins manufacturing reactor equipment for the first ASMM unit in Uzbekistan. 13.05.2025.
5. OKBM Afrikantov. Rosatom implements 3D printing technology for RITM-200 equipment components. 01.12.2025.

BERYLLIUM REFLECTOR POISONING EFFECT ANALYSES OF THE VVR-SM RESEARCH REACTOR

Umarov Sh.B.[1], Umarova M.O.[2], Nguyen Tran C.H.[3], Tikhomirov G.V.[1]

[1]*National Research Nuclear University MEPhI, Moscow, Russian Federation*

[2]*Tashkent Branch of National Research Nuclear University MEPhI, Tashkent, Uzbekistan*

[3]*University of Tennessee, Knoxville, USA*

The VVR-SM research reactor of the Institute of Nuclear Physics of the Academy of Sciences of the Republic of Uzbekistan reached first criticality on 10 September 1959 and, following the 1971–1978 core upgrade, operates at a nominal power of 10 MW. Its beryllium reflector shapes the high thermal neutron flux densities in the core and in the experimental channels. Under prolonged irradiation the ^{9}Be(n, α) reaction produces ^{6}Li, tritium and ^{3}He. Because ^{6}Li and ^{3}He have large thermal absorption cross sections, their build-up (beryllium poisoning) reduces the reactivity margin and distorts the spatial–energy distribution of the neutron flux. Unlike the reactivity loss due to fuel burnup, which is compensated by refuelling, poisoning losses accumulate monotonically and ultimately require replacement of the beryllium blocks.

The present work quantifies the accumulation of ^{6}Li, tritium and ^{3}He in the beryllium blocks of the VVR-SM reflector over the entire operating period and evaluates the resulting changes in the neutronic characteristics of the reactor.

The analysis was performed in three stages. First, a three-dimensional full-core model of the VVR-SM was developed with the Monte Carlo code OpenMC. The core comprises 24 IRT-4M fuel assemblies in a 4×6 lattice surrounded by square and corner beryllium blocks indexed A–H along X and 1–8 along Y. Each fuel assembly, beryllium block and control element was a separate tally region, which yielded the neutron flux and the ^{9}Be(n, α), ^{6}Li(n, t) and ^{3}He(n, p) reaction rates individually for every block. Second, the system of transmutation equations was solved with an in-

house Python code allowing an arbitrary number of time steps, each an operating interval followed by a shutdown interval; tritium decay and the associated ^{3}He build-up were accounted for during shutdowns. The calculation was driven by the documented operating history of the reactor for 1959–2024. Third, the resulting isotopic composition was assigned block by block to the neutronic model, and the “fresh” and “irradiated” reflector states were compared.

The reaction rates depend strongly on the block position, peaking in the first row adjacent to the core; for the ^{9}Be(n, α) and ^{3}He(n, p) reactions the spread between the extreme blocks reaches almost a factor of five, whereas the thermally driven ^{6}Li(n, t) rate varies far less. The ^{6}Li concentration reaches a quasi-stationary level by the late 1970s, when production and burn-out balance each other. Tritium accumulates throughout the whole period, most intensively after the power uprate to 10 MW, while ^{3}He follows tritium decay and grows appreciably only after 2000. By 2024 the atomic densities in the most irradiated cell A6 reached approximately 1.85×10^{-6} atom/(b·cm) for ^{6}Li, 4.8×10^{-5} atom/(b·cm) for tritium and 6.4×10^{-6} atom/(b·cm) for ^{3}He.

The change of the neutron field is markedly energy-dependent. In the thermal range the flux density in individual blocks decreases by 15–30 % relative to the fresh reflector, whereas for fast neutrons the reduction does not exceed 1–4 % in most blocks, with a maximum of about 4.5 %. Redistribution of the thermal flux near the core also alters the worth of the control elements: the shim rods KS-1, KS-2 and KS-4 gain 3.01 %, 2.25 % and 4.19 %, while the change for KS-3 stays below 1 %. For the safety rods the trend is not uniform — AZ1 gains 4.12 % whereas AZ2 and AZ3 lose 2.36 % and 0.40 % — which is attributed to their different positions relative to the regions of maximum flux perturbation and to mutual rod shadowing.

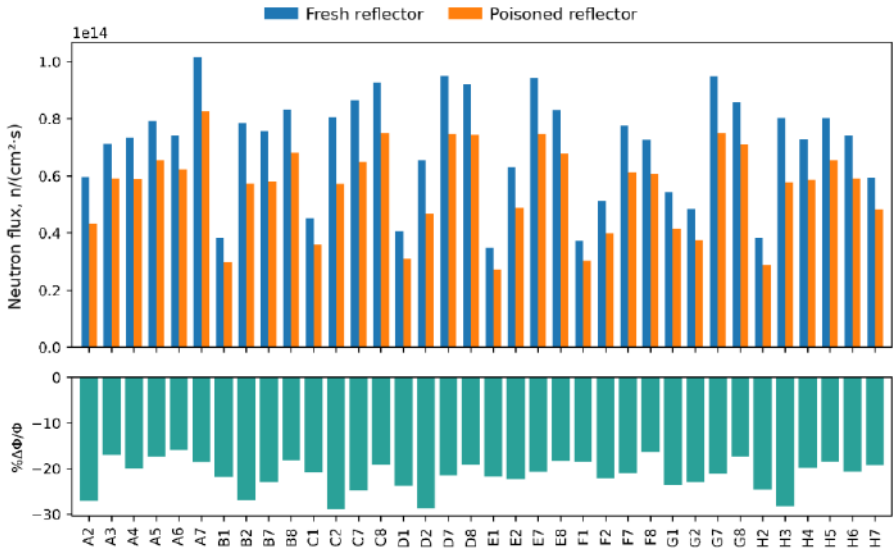

Figure 1. Thermal neutron flux in the beryllium blocks for the fresh and poisoned reflector

The integral effect on reactivity is summarised in Table 1 for four states of the reflector. Relative to the reference state with a fully fresh reflector (ρ = 5892.10 ± 33 pcm), the isotopes accumulated over 1959–2024 reduce the reactivity margin to 3635.82 pcm, i.e. by Δρ = 2256.28 pcm, or 38.3 %. The loss exceeds the statistical uncertainty of the calculation by a factor of sixty. Replacing only the first row of beryllium blocks with fresh ones restores about 92 % of the lost reactivity, the residual gap being 171 pcm (2.9 %). Permuting the blocks of the first and second rows, feasible for 12 peripheral blocks, restores about 66 % of the loss without introducing any fresh beryllium and therefore represents an acceptable intermediate measure.

Table 1. Effect of beryllium reflector poisoning on the reactivity margin of the VVR-SM

Reactor state	All blocks poisoned	First row replaced with fresh	First/second rows permuted	All blocks fresh
k_{eff}	1.03773 ± 0.00032	1.06068 ± 0.00032	1.05411 ± 0.00032	1.06261 ± 0.00033
ρ, pcm	3635.82 ± 33	5720.86 ± 33	5133.24 ± 33	5892.10 ± 33
Δρ, pcm	2256.28	171.24	758.86	—
$\Delta\rho/\rho_{fresh}$, %	38.29	2.91	12.88	—

Conclusions. Beryllium poisoning is a significant factor limiting the continued operation of the VVR-SM: it costs about 2256 pcm of reactivity, suppresses the thermal flux in the reflector by up to 30 % and shifts the worth of individual control and safety rods by up to about 4 %. Replacement of the first row of blocks is the most effective remedy, permutation of the first and second rows a low-cost alternative. The results can be used to justify the schedule and strategy of beryllium block replacement and to plan the modernisation and lifetime extension of the reactor; the approach is applicable to other research reactors with beryllium reflectors.

References:

1. Wróblewska M. et al. Beryllium poisoning in research reactors: a review. Ann. Nucl. Energy, 2021, vol. 163, 108540.
2. Sairanbayev D.S. et al. WWR-K performance during replacement of the water reflector by beryllium. Russ. Phys. J., 2021, vol. 63, pp. 2096–2104.
3. Romano P.K. et al. OpenMC: a state-of-the-art Monte Carlo code. Proc. SNA+MC 2013, Paris, 2014, art. 06016.

TESTS OF NEW IRT-4M FUEL ASSEMBLIES WITH UO_2–AL AND U_3Si_2–AL FUEL COMPOSITIONS

Baytelesov S.A., Kungurov F.R., Alikulov Sh.A., Tadjibaev D.P., Fayziev T.B.
Institute of Nuclear Physics, Uzbekistan Academy of Sciences, Tashkent, Uzbekistan

The VVR-SM research reactor was converted to low-enriched IRT-4M nuclear fuel in 2009. At present, the reactor core contains four new fuel assemblies (FAs): two IRT-4M FAs with UO_2–Al fuel composition (uranium density of 3.3 g/cm³ and fuel mass of 290 ± 14.5 g) and two IRT-4M FAs with U_3Si_2–Al fuel composition (uranium density of 3.6 g/cm³ and fuel mass of 316 ± 15.9 g).

Neutronic and thermal-hydraulic calculations were performed, followed by a comprehensive safety analysis and justification for the operation of the VVR-SM research reactor with two experimental six-tube IRT-4M fuel assemblies containing UO_2–Al dioxide fuel (uranium density of 3.3 g/cm³) and two experimental six-tube IRT-4M fuel assemblies containing U_3Si_2–Al uranium silicide fuel (uranium density of 3.6 g/cm³).

Based on the results of the calculations and safety analysis, two experimental IRT-4M fuel assemblies with UO_2–Al fuel and two experimental IRT-4M fuel assemblies with U_3Si_2–Al fuel were successfully loaded into the core of the VVR-SM research reactor.

During reactor operation, the readings of the radiation monitoring system remained below the established control limits, thereby confirming the safe operation of the new fuel assemblies.

DEVELOPMENT OF THERMOPHYSICAL MODEL OF FUEL ASSEMBLY OF THE IVG.1M REACTOR FOR ANALYSIS OF TEMPERATURE DISTRIBUTION UNDER DIFFERENT OPERATING MODES

Toleubekov K.[1], Martynenko Y.[1,2], Bekmuldin M.[1]
[1]*Institute of Atomic Energy of the RSE NNC RK, Kurchatov, Kazakhstan*
[2]*D.Serikbayev East Kazakhstan State Technical University, Ust-Kamenogorsk, Kazakhstan*

The IVG.1M reactor is a thermal neutron research reactor. Between 2020 and 2023, its core was converted from highly enriched uranium (HEU) to low-enriched uranium (LEU) fuel in accordance with international nuclear safety requirements. Following the modernization, the reactor retained its key operational characteristics, enabling the continuation of research activities [1-2].

The transition to LEU fuel has increased the importance of accurately assessing the thermal state of the fuel assemblies under various operating conditions. Since direct measurement of fuel temperature inside the reactor core is technically challenging, the thermal state is evaluated using computational methods based on experimentally monitored reactor parameters.

The development of a thermophysical model of the fuel assembly, as well as calculations of the temperature distribution in the coolant and structural materials were per-formed using the ANSYS Fluent software [3]. The three-dimensional computational model was developed the form of a fuel assembly sector representing a symmetric segment equal to 1/12 of the entire assembly geometry.

The initial and boundary conditions were defined for the simulations:

- During the modeling process, coolant flow was specified by inlet and outlet bound-ary conditions of the channel: at the inlet, the mass flow rate and water temperature are prescribed, while at the outlet a free outflow condition is applied;
- The k–ε model was used to describe the turbulent flow regime;
- The water flow rate is taken equal to 1/12 of the total flow rate. Inlet pressure is 1.1 MPa;
- The heat generation for each fuel element is specified taking into account the axial non-uniformity along the height of the reactor core.

The performed verification based on reactor power startup data demonstrated good agreement between calculated and experimental coolant temperature values, with a deviation of less than 1 °C, confirming the correctness of the selected modeling approach.

The obtained results confirm the applicability of the developed CFD model for analyzing the thermal state of the IVG.1M reactor fuel assemblies and may be used to justify reactor operating conditions during experiments, as well as to assess the prospects for im-proving its operational capabilities.

Funding. This research has been funded by the Science Committee of the Ministry of Science and Higher Education of the Republic of Kazakhstan (Grant No. AP32318589)

Reference

1. Sabitova, R.; Popov, Y.; Irkimbekov, R.; Prozorova, I.; Derbyshev, I.; Nurzhanov, E.; Surayev, A.; Gnyrya, V.; Azimkhanov, A. Results of experiments under the physical start-up program of the IVG.1M reactor. *Energies* **2023**, *16*, 6263. https://doi.org/10.3390/en16176263

2. Batyrbekov, E.; Vityuk, V.; Baklanov, V.; Gnyrya, V.; Azimkhanov, A.; Sabitova, R.; Prozorova, I.; Popov, Yu.; Irkimbekov, R.; Martynenko, Ye. Power start-up of the IVG.1M reactor with low-enriched uranium fuel: Main results. *Energies* **2025**, https://doi.org/10.3390/en18123187
3. ANSYS. ANSYS Fluent Workbench Tutorial Guide, Release 2021 R2; ANSYS Inc.: Canonsburg, PA, USA, 2021. Available online: https://dl.cfdexperts.net/cfd_resources/Ansys_Documentation/Fluent/Ansys_Fluent_Workbench_Tutorial_Guide_2021_R2.pdf (accessed on 24 April 2026).

COMPUTATIONAL ASSESSMENT OF THE FEASIBILITY OF TESTING ADVANCED NUCLEAR FUEL IN THE IGR REACTOR

Surayev A.S., Mukhamedov N.E., Irkimbekov R.A., Zhanbolatov O.M., Seken D.M.
Branch “Institute of Atomic Energy” National Nuclear Center of the Republic of Kazakhstan, Kurchatov, Kazakhstan

For many years, the IGR research reactor has served as an experimental facility for global power nuclear reactor projects. This reactor unit possesses a number of unique neutron-physical characteristics (thermal neutron fluence reaches 3.7×10^{16} n/cm^2, thermal neutron flux density is 7×10^{16} n/(cm^2 · s)). These technical specifications make it possible to simulate the behavior of fuel assemblies of power reactors inside irradiation devices (ID) both under normal operating conditions and in severe accident scenarios.

This study explores the feasibility of conducting such tests, given that power reactor fuel of the VVER-1000 (Figure 1), APR-1400, or HPR-1000 types has low enrichment (around 4%), is operated for long periods at stationary power (the fuel cycle lasts from 12 to 18 months), and fuel assemblies are typically profiled and contain various control elements (control rods, burnable absorbers, etc.), along with a loop containing circulating water coolant [1]. All these factors impose specific requirements on the ID design and the IGR reactor operating modes, which must be investigated.

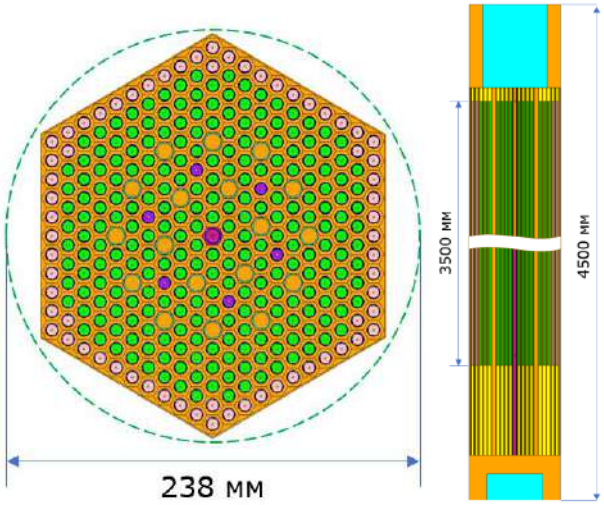

Figure 1. VVER-1000 fuel assembly neutron model

The relevance of this study lies in obtaining computational characteristics of previously unstudied advanced power reactor fuel, which can be tested in the IGR reactor to validate its performance under various power reactor operating modes, including emergency conditions. In the near future, the commissioning of the country's first nuclear power plant is expected, which will drive a new phase of nuclear industry development and increase scientific interest in research aimed at modernizing and optimizing power reactor fuel characteristics and searching for novel advanced options.

This work was supported by the Science Committee of the Ministry of Science and Higher Education of the Republic of Kazakhstan (Grant No. AP26199863).

References:

D. Seken, A. Surayev, R. Irkimbekov, et. al. «Calculation of fuel burnup in a VVER-1000 reactor installation». Recent Contributions to Physics, Vol. 94, No. 3, pp. 32–42, Sep. 2025, doi:10.26577/RCPh20259434.

COMPREHENSIVE STUDIES OF RADIATION RESISTANCE AND GASEOUS SWELLING PROCESSES IN BeO CERAMICS – PROMISING MATERIALS FOR NUCLEAR POWER ENGINEERING

Kenzhina I.E.[1,2], Kozlovskiy A.L.[1,2], Zhigalova A.[3]
[1]*Satbayev University, Almaty, Kazakhstan*
[2]*Institute of Nuclear Physics of the ARKAE, Almaty, Kazakhstan*
[3]*L.N.Gumilyov Eurasian National University, Astana, Kazakhstan*

Beryllium oxide (BeO)-based ceramics are considered promising for use in nuclear power applications due to their combination of high thermal conductivity, thermal and chemical stability, electrical insulation properties, and ability to maintain operational characteristics at elevated temperatures. However, long-term use of BeO-based ceramics under intense radiation exposure is accompanied by the accumulation of radiation-induced defects, changes in structural and strength properties, and the formation and accumulation of gas inclusions, which can initiate swelling processes and subsequent degradation of the material. Therefore, establishing the mechanisms of radiation damage and gas swelling is essential for assessing the service life and applicability limits of BeO-based ceramics in advanced nuclear power plants.

This paper presents the results of comprehensive studies of the radiation resistance of BeO-based ceramics, with particular attention to the mechanisms of structural damage accumulation and the development of gas swelling processes under exposure to ionizing radiation. The focus of this study is on establishing the relationship between irradiation conditions, changes in the crystal and defect structure, accumulation of gas impurities, formation of gas-filled defects, and changes in the mechanical properties of ceramic materials. The processes of formation of radiation-induced point defects, their migration and agglomeration, and subsequent formation of defect clusters are examined. The accumulation of gas atoms and their capture by structural defects can lead to the nucleation of gas-filled complexes and bubbles. The increase in size and concentration of these bubbles with increasing irradiation dose contributes to the development of localized deformation distortions and volumetric swelling of the ceramic. When critical concentrations of such defects are

reached, areas of increased internal stress, microcracks, and a decrease in the mechanical strength of the material can form.

These results provide insight into the sequence of structural transformations in BeO ceramics with increasing radiation exposure and establish the relationship between the accumulation of radiation defects, the formation of gas-filled cavities, volumetric swelling, and degradation of strength characteristics. Determining critical conditions for the development of gas swelling is of particular interest for predicting the long-term stability of a material and assessing permissible operating loads.

RELATIONSHIP BETWEEN ELECTRICAL RESISTIVITY AND THERMAL CONDUCTIVITY OF THE SAV-1 ALUMINUM ALLOY AT VARIOUS FAST NEUTRON FLUENCES

Baytelesov S.A., Kungurov F.R., Alikulov Sh.A., Tadjibaev D.P., Fayziev T.B.
Institute of Nuclear Physics, Uzbekistan Academy of Sciences, Tashkent, Uzbekistan

This study investigates the effect of fast neutron irradiation in the VVR-SM research reactor on the electrical resistivity and thermal conductivity of the SAV-1 aluminum alloy.

Experimental dependences of the electrical resistivity, ρ (Ω·m), and thermal conductivity, λ (W/(m·K)), of the SAV-1 aluminum alloy on fast neutron fluence were obtained over the fluence range from 10^{16} to 10^{20} n/cm². Based on the experimental data, an empirical correlation was derived for calculating the electrical resistivity and thermal conductivity, as well as for estimating the accumulated fast neutron fluence over the range from 10^{16} to 3.5×10^{22} n/cm².

A correlation between the thermal conductivity and the electrical resistivity of the SAV-1 aluminum alloy was established, enabling the thermal conductivity of the material to be determined from measurements of its electrical resistivity over the fast neutron fluence range from 10^{16} to 3.5×10^{22} n/cm².

ELECTROSTATIC INTERFACE ENGINEERING AS A DESIGN FRAMEWORK FOR RADIATION-HARDENED RESONANT-TUNNELING NANODOSIMETERS

Dosymova B.U.[1], Dolgopolov M.V.[2]
[1]Tashkent Branch of National Research Nuclear University MEPhI, Tashkent, Uzbekistan
[2]Samara State Technical University, Samara, Russia

The development of dosimetry in Uzbekistan has deep historical roots in the Institute of Nuclear Physics (INP) of the Academy of Sciences of Uzbekistan. One of the earliest works associated with this line of research was the 1960 publication by S.V. Starodubtsev, Sh.A. Ablyaev, and V.V. Generalova in *Atomnaya Energiya*, where γ-radiation dose was estimated from changes in the optical activity of aqueous carbohydrate solutions [1]. The method covered doses up to 200

Mrad, but it required delayed laboratory readout and was sensitive to storage conditions, which precluded real-time in situ dosimetry.

Over the intervening decades, the demands placed on dosimetry have evolved fundamentally. Contemporary nuclear energy, accelerator engineering, and space applications require real-time electronic readout, nanometer-scale spatial localization of the dose field, and calibration stability under repeated megagray exposure cycles. This work presents a design framework for a new generation of resonant-tunneling dosimeters (RTDs) based on the targeted electrostatic engineering of the contact–heterostructure interface. Resonant-tunneling diodes offer high sensitivity; however, degradation of the peak-to-valley current ratio (PVR) due to radiation-induced charge trapping at interface states remains a major limitation.

In this context, "radiation-hardened" refers to the stability of the electrostatic configuration, the peak-to-valley ratio, and the calibration curve under irradiation, while the device remains intrinsically radiation-sensitive as a dosimeter.

The central element of the framework is the dimensionless parameter $\boldsymbol{\eta} = C_Q / C_{geo}$, where C_Q is the quantum capacitance of the interfacial material [2] and C_{geo} is the geometric capacitance of the contact junction. The parameter η serves as a quantitative measure of electrostatic screening efficiency and defines the central design criterion of the proposed framework. This framework integrates a semi-analytical transport model based on the Landauer–Büttiker formalism [3], parameterized using self-consistent NEGF–Poisson simulations reported in Ref. [4], with an analytical charge-accumulation model [5].

Within this framework, higher values of η are associated with improved predicted stability of the peak-to-valley current ratio (PVR) under irradiation, owing to more effective suppression of trapped-charge-induced potential fluctuations. Conventional metallic contacts, which typically exhibit $\eta \ll 1$, do not provide the required level of electrostatic screening, whereas interfacial layers based on two-dimensional materials — in particular, graphene [5,6] — allow η to be increased substantially, thereby improving the predicted stability of the resonant-tunnelling characteristics under irradiation.

The principal contribution of this work is the formulation of an electrostatic design criterion that combines analytical electrostatics with a reduced quantum-transport model into a single framework, enabling rapid preliminary screening of candidate interface materials prior to detailed quantum-transport simulations. Knowledge of C_Q together with the device electrostatic parameters permits the expected degradation of RTD characteristics to be estimated at an early design stage, reducing the number of configurations requiring full-scale calculations and lowering the number of computationally expensive transport simulations needed for device development.

Practical Significance. The proposed methodology translates the materials-screening problem into a set of measurable or computable quantities — the quantum capacitance of candidate interfacial layers and the geometric capacitance of the target contact architecture — thereby enabling rapid, simulation-driven down-selection of radiation-tolerant material stacks before undertaking extensive experimental optimization. The η-criterion can be incorporated into existing TCAD workflows as a pre-screening module.

From an implementation perspective, the η-criterion provides a justified basis for: (i) selecting interfacial layers in MR–DWELL and TRD dosimeters intended for megagray-level monitoring in reactor instrumentation and space electronics, where stable PVR and peak-current retention are required; and (ii) pre-screening protective coatings and contact stacks for front-end readout ASICs exposed to mixed neutron–gamma fields, before committing to full device fabrication and irradiation campaigns.

The approach is of direct interest for the development of photovoltaic converters for space solar arrays, X-ray and gamma-ray detectors, and front-end electronics for nuclear facilities and high-energy physics experiments, thereby contributing to sustainable development through increased device lifetime and reduced material consumption. The criterion is general and extends to two-dimensional materials, functional nanocomposites, and protective coatings, connecting the pioneering dosimetry research initiated at the Institute of Nuclear Physics [1] with modern nanophysics-based radiation sensors. Thus, the proposed framework bridges the historical roots of dosimetry in Uzbekistan with a modern quantum-capacitance-based strategy for radiation-hard detector design.

Keywords: *resonant-tunneling dosimetry; radiation physics of condensed matter; electrostatic screening; quantum capacitance; nanophysics of interfaces; radiation-hardened electronics; NEGF modeling; graphene heterostructures; large-dose dosimetry*

References:

1. S.V.Starodubtsev, Sh.A. Ablyaev, and V.V. Generalova, "Izmerenie dozy γ-izlucheniya po izmeneniyu opticheskoy aktivnosti nekotorykh uglevodov" [Measurement of γ-radiation dose by the change in optical activity of certain carbohydrates], Atomnaya Energiya, vol. 8, no. 3, pp. 264–265, 1960. (In Russian)
2. J.Xia et al., "Measurement of the quantum capacitance of graphene," Nature Nanotechnology, vol. 4, pp. 505–509, 2009. DOI: 10.1038/nnano.2009.177
3. S.Datta, Quantum Transport: Atom to Transistor. Cambridge University Press, 2005. DOI: 10.1017/CBO9781139164313
4. B.U.Dosymova and M.V. Dolgopolov, "Radiation-Induced Spatial Reconstruction and Localization Crossover of Quasi-Bound Electron States in MR-DWELL Heterostructures: Results of Self-Consistent NEGF–Poisson Simulation," Vestnik TF NIYaU MIFI, vol. I, 2026 198-207. (In Russian)
5. B.U.Dosymova and M.V. Dolgopolov, "Graphene-Assisted Electrostatic Interface Engineering for Radiation-Hardened MR-DWELL Dosimeters," SSRN Electronic Journal, 2026. DOI: 10.2139/ssrn.6996579. https://papers.ssrn.com/sol3/papers.cfm?abstract_id=6996582
6. L.Britnell et al., "Field-effect tunneling transistor based on vertical graphene heterostructures," Science, vol. 335, pp. 947–950, 2012. DOI: 10.1126/science.1218461

NEUTRON IRRADIATION BEHAVIOR AND PHASE STABILITY OF BERYLLIDES

Aitkulov M.[1], Shaimerdenov A.[1], Sairanbayev D.[1], Askerbekov S.[1], Akhanov A.[1], Silnyagin P.[1], Averkova T.[1], Migunova A.[1], Udartsev S.[2]

[1]Institute of Nuclear Physics, Almaty, Kazakhstan

[2]JSC “Ulba Metallurgical Plant”, Ust-Kamenogorsk, Kazakhstan

Owing to its neutron-physical properties, metallic beryllium is widely used as a reflector in research reactors. Low neutron absorption and effective neutron scattering ensure its high performance as a reflector material. At the same time, prolonged neutron irradiation leads to the accumulation of radiation defects and nuclear transmutation products in beryllium. Neutron-induced reactions in the material produce helium isotopes and tritium. The accumulation of these products,

primarily helium, promotes gas bubble formation, swelling, loss of ductility and embrittlement of beryllium, which at high neutron fluences may lead to degradation of the structural integrity of reflector elements. Therefore, the search for beryllium-based materials combining favorable neutronic properties with improved resistance to prolonged neutron irradiation is of considerable interest. One promising direction is the use of beryllium intermetallic compounds, known as beryllides. Studies of individual beryllides show that in a number of characteristics, including radiation stability, high-temperature resistance and others, they can offer advantages over metallic beryllium. At present, such materials are considered primarily as functional materials for fusion systems, in particular as neutron multipliers. At the same time, the properties of beryllides make it possible to consider them as neutron reflector materials for nuclear installations as well. Accordingly, the authors are carrying out a comprehensive assessment of the applicability of beryllides manufactured by the Ulba Metallurgical Plant (Ust-Kamenogorsk, Republic of Kazakhstan) as a material capable of operating under irradiation.

This paper presents the results of post-irradiation examination, which included visual inspection, measurements of the equivalent dose rate and density, examination of the surface morphology by scanning electron microscopy, and X-ray diffraction analysis. The phase composition and lattice parameters were determined, and a comparative analysis of the irradiation-induced structural and microstructural changes was performed. The results obtained are compared with literature data on radiation-induced changes in beryllides.

Keywords: beryllium, reflector, beryllides, X-ray diffraction, nuclear reactor, radiation resistance

THERMOGRAVIMETRIC RESPONSE OF NEUTRON-IRRADIATED CHROMIUM BERYLLIDE IN A STEAM-ARGON ATMOSPHERE

Askerbekov S.[1,2], Shaimerdenov A.[1], Silnyagin P.[1], Bugybay Zh.[1], Akhanov A.[1], Chikhray Ye.[2], Kulsartov T.[2], Elishenkov A.[2], Kenzhina I.[1,2], Zaurbekova Zh.[2]

[1]Institute of Nuclear Physics, Almaty, Kazakhstan

[2]Institute of Experimental and Theoretical Physics, al-Farabi Kazakh National University, Almaty, Kazakhstan

The post-irradiation steam-corrosion behavior of chromium beryllide was evaluated using thermogravimetric analysis. The study focused on how neutron-induced damage accumulated under different irradiation conditions influences mass-change processes during subsequent high-temperature exposure to water vapor, which may represent possible operational and accidental conditions in fusion reactor blanket systems.

Specimens measuring 5×5×15 mm were irradiated in channel 2-6 of the WWR-K reactor core (Almaty, Kazakhstan) within a sealed helium-filled capsule. The specimens were positioned at different levels relative to the core midplane, producing varying neutron exposure conditions. The integral neutron flux reached approximately 8.17×10^{13} $cm^{-2}\cdot s^{-1}$. Damage calculations using the NRT and arc-dpa approaches indicated that after one irradiation cycle (21 EFPD), the damage level was approximately 0.012 dpa for Be and 0.016 dpa for Cr. After three irradiation cycles, the accumulated damage was about 0.034 dpa for Be and 0.045 dpa for Cr.

The irradiated specimens were examined using a TGA/DSC 3+ system under linear heating from room temperature to 900 °C at 10 °C·min^{-1} in a steam–argon atmosphere. This procedure enabled continuous monitoring of mass evolution and assessment of the material's response during interaction with water vapor.

The thermogravimetric curves revealed mass-change features associated with relaxation of the irradiation-induced defect structure, desorption of retained gases, and the onset of oxidation. Neutron irradiation produces vacancies, dislocations, and defect clusters that can modify diffusion pathways and increase the chemical activity of the material's surface, thereby influencing its subsequent high-temperature corrosion behavior.

Comparison of irradiated specimens with an unirradiated reference material showed that radiation-induced microstructural changes significantly affect the kinetics of steam-assisted, high-temperature corrosion. The results are relevant to evaluating chromium beryllide for use in functional components of blanket systems for DEMO-type fusion reactors.

METHODOLOGY FOR CORROSION TESTING OF TITANIUM BERYLLIDE $Be_{12}Ti$ AND CHROMIUM BERYLLIDE $Be_{12}Cr$ UNDER SUPERCRITICAL AND ULTRA-SUPERCRITICAL STEAM CONDITIONS

Yelishenkov A.[1], Chikhray Ye.[1], Kulsartov T.[1], Kenzhina I.[1], Zaurbekova Zh.[1], Askerbekov S.[1], Kenzhin Ye.[1], Udartsev S.[2]

[1]Satbayev University, Almaty, Kazakhstan

[2]JSC “Ulba Metallurgical Plant”, Ust-Kamenogorsk, Kazakhstan

Advances in nuclear and prospective fusion energy technologies, along with efforts to improve the efficiency of steam-turbine cycles, necessitate the development of materials capable of sustained operation at elevated temperatures and pressures in chemically aggressive environments. Using steam at supercritical and ultra-supercritical parameters can increase the thermal efficiency of power-generation systems; however, it also imposes substantially more stringent requirements on equipment materials. At temperatures of 500–700 °C and pressures of up to 30 MPa, steam acts as an aggressive corrosive medium, promoting high-temperature oxidation, the formation and degradation of surface oxide scales, and the mass transport of material constituents. Therefore, candidate materials for such applications must exhibit high thermal and chemical stability and low oxidation rates.

The materials selected for this study were binary beryllium-based intermetallic compounds, namely titanium beryllide Be12Ti and chromium beryllide Be12Cr. These materials are of particular interest because of their low density, high thermal stability, and potential chemical resistance at high temperatures. Their possible application in individual components of nuclear and fusion energy systems requires experimental validation of their corrosion resistance under conditions representative of service environments. For the Republic of Kazakhstan, research in this field is of both scientific and practical importance owing to the domestic production of beryllium and beryllium-based materials at JSC Ulba Metallurgical Plant.

The objective of this work was to develop an experimental setup and validate a methodology for corrosion testing of titanium beryllide ($Be_{12}Ti$) and chromium beryllide ($Be_{12}Cr$) in steam under

supercritical and ultra-supercritical conditions. An additional objective was to assess the feasibility of investigating the effects of temperature, pressure, exposure duration, and initial surface condition on the corrosion behavior of these materials. The proposed methodology was required to provide reproducible test conditions, stable control of temperature and pressure, and comparable data on the specimens' condition before and after exposure to the working medium.

The developed methodology and experimental setup enable corrosion testing of $Be_{12}Ti$ and $Be_{12}Cr$ beryllides in a controlled steam environment under supercritical and ultra-supercritical conditions. Continuous monitoring of temperature and pressure, combined with visual inspection and specimen mass-change measurements, provides comparable data on the materials' corrosion behavior and enables assessment of how the initial surface condition influences their corrosion resistance.

RADIATION-INDUCED SWELLING OF SAV-1 AND AMG-2 ALLOYS UNDER NEUTRON IRRADIATION

Akhmedzhanov F.R.[1], Boltabaev A.F.[2]

[1]*Institute of Ion-Plasma and Laser Technologies, Uzbekistan Academy of Sciences, Tashkent, Uzbekistan*

[2]*Republican Center for the Storage of Radioactive Waste, Tashkent, Uzbekistan*

Practical interest in radiation-induced deformation of structural materials stems from the danger of its consequences, associated with changes in the mechanical properties of these materials [1]. The degree of deformation depends on the energy and mean free path of the ionizing particles. Neutrons, compared to α particles and protons, create the greatest amount of structural damage due to their greater penetration depth. For example, the volume of austenitic steels increases linearly with increasing neutron flux and can increase by 20% or more [2].

From a fundamental perspective, deformation in irradiated materials is a pronounced manifestation of the competition between interaction forces within the defective structure of the crystal. Simultaneously, irradiation with high neutron fluxes causes the formation and growth of vacancy pores, leading to linear and volumetric deformation and, consequently, to radiation-induced swelling of the alloy.

We conducted a detailed study of the effects of neutron irradiation on the linear and volumetric deformation of SAV-1 and AMG-2 alloys, in which the main impurities are magnesium, manganese, and silicon. Uncontrolled impurities (Ni, Cu, Fe, Zn, etc.) totaled no more than 0.5%. The studies were conducted on specimens prepared from commercially available SAV-1 and AMG-2 alloys, having a regular cylindrical shape with approximate dimensions of 20 mm in height and 15 mm in diameter.

The density of the specimens was determined by hydrostatic weighing on an analytical balance with an accuracy of 0.2%. Linear dimensions were measured with a micrometer with an absolute accuracy of 1 μm. The specimens were irradiated with fast neutrons in the vertical channels of the VVR-SM reactor at the Institute of Nuclear Physics of the Academy of Sciences of the Republic of Uzbekistan.

Changes in the linear dimensions of the samples were determined under the influence of an integrated neutron flux (fluences F: $1{,}55\cdot10^{17}$, $1{,}1\cdot10^{18}$, $5{,}1\cdot10^{18}$ and $1{,}2\cdot10^{19}$ n/cm^2). The obtained results allow us to determine the relative change in sample volume $\Delta V/V_0$ under the influence of

neutron radiation. The calculation was performed using a relationship that is easily derived from mathematical formulas for the volume of cylindrical bodies:

$$\Delta V/V_0 = [(1+A)\cdot(1+B)^2 - 1] \quad (1)$$

where $A=\Delta L/L_0$ is the relative change in length L, and $B=\Delta d/d_0$ is the relative change in sample diameter. The calculation results are presented in Fig. 1.

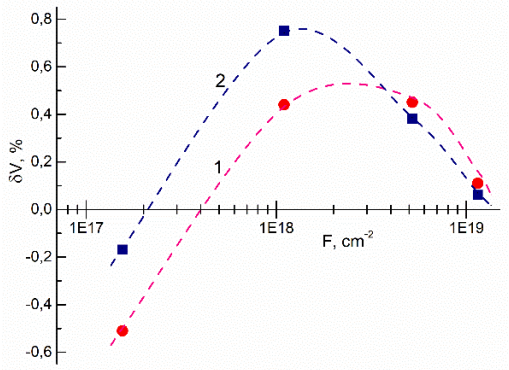

Figure 1. Relative change in volume of SAV-1 (1) and AMG-2 (2) alloys depending on neutron fluence

It can be seen that for SAV-1 and AMG-2 alloys, the swelling is observed at relatively low neutron irradiation doses (up to almost 1% with increasing fast neutron fluence). With further increases in irradiation dose, the volume of the samples decreases again, and upon reaching a dose of $1{,}2\cdot10^{19}$ N/cm^2, the volume returns almost to its original value.

The observed change in the volume of the alloys is apparently due to the dynamics of the change in the pore concentration in the crystal volume under the influence of neutron radiation. According to theory, the pore size distribution obeys the Gaussian distribution law and is associated with the simultaneous nucleation of pores due to the disruption of the stability of the system of excess vacancies in the irradiated material [2]. The reason for the further growth of the pore after the formation of a nucleus larger than the critical size is the vacancy flux caused by the vacancy concentration gradient under the influence of neutron radiation. The expression for the concentration of vacancies at the boundary of a pore, of radius R, due to which pore growth and a corresponding change in the volume of the material occur, is [3]:

$$C_v = C_i \exp\left[\frac{2\gamma\cdot\Omega}{k\cdot T}\left(\frac{1}{R} - \frac{1}{R_{cr}}\right)\right], \quad (2)$$

where C_i is the concentration of excess vacancies far from the pore, γ is the surface tension coefficient, Ω is the atomic volume, and R_{cr} is the critical pore radius.

As the pore radius increases, the vacancy flux per pore increases due to, firstly, a decrease in the vacancy concentration near the pore and a corresponding increase in the vacancy gradient, and, secondly, an increase in the pore surface area. Consequently, the increasing vacancy flux should lead to an increase in pore volume with increasing irradiation time and, consequently, to an increase in the volume of the irradiated sample. Initially, this results in an increase in pore radius and corresponding swelling of the alloy, which is observed at relatively low neutron fluences.

In an effort to minimize its free energy, the pore boundary layer creates a pressure difference on both sides and ensures dynamic equilibrium due to the additional pressure ΔP caused by surface tension, which counteracts the pressure generated by the site and interstitial atoms. This additional pressure is determined by the Laplace formula and depends on the average surface curvature at that point and the surface tension coefficient. For a cavity of radius R, the formula is written as [2]:

$$\Delta P = \frac{2\cdot\gamma}{R}. \quad (3)$$

According to formula (3), as pore size increases, the additional pressure ΔP decreases. Upon reaching a certain critical radius, large pores break apart into a series of smaller clusters, and the proportion of small-sized fractions (5-10 and 20-25 nm) increases. As a result, under the influence of neutron radiation, large vacancy pores fragment into smaller pores. According to this mechanism, with increasing irradiation dose, a reverse decrease in sample volume should occur, which is observed experimentally at neutron fluences of $5.1 \cdot 10^{18}$ and $1.2 \cdot 10^{19}$ n/cm2.

References:

1. Chakin P., Posevin A.O., Kupriyanov I.B. Swelling, mechanical properties and microstructure of beryllium irradiated at 200 °C up to extremely high neutron doses. Journal of Nuclear Materials, 2007. V. 367, part. 2. P. 1377-1381.
2. Vasilev A.A., Korolkov M.D., Melker A.I. The influence of elastic anisotropy on pore growth in irradiated cubic crystals. Solid State Physics, 1990. V. 32, No. 11. - P. 3345-3349.
3. Konoplev K.A., Fridman S.R., Orlov S.P., Ilatovskiy V.A. Study of radiation resistance of SAV-1 alloy irradiated to a fluence of $3.5 \cdot 10^{22}$ cm^{-2}. Atomic energy, 2015. V. 118, Issue 5, P. 274-278.

SYNTHESIS AND STUDY OF HIGH-ENTROPY RARE-EARTH ZIRCONATES

Zhumatayeva I.[1,2]

[1]*Institute of Nuclear Physics, Agency of the Republic of Kazakhstan for Atomic Energy, Almaty, Kazakhstan*

[2]*L.N.Gumilyov Eurasian National University, Astana, Kazakhstan*

High-entropy oxide ceramics have been actively studied in recent years due to their potential to produce materials with high thermal and phase stability resulting from their multicomponent composition. High-entropy rare-earth zirconates are one of the promising groups of these materials. They can be used at high temperatures and under high thermal loads, including as thermal barrier materials.

High-entropy zirconates based on ZrO_2 were synthesized by a mechanochemical method. ZrO_2, Nd_2O_3, Gd_2O_3, Sm_2O_3, Dy_2O_3, and Er_2O_3 were used as starting materials. Compositions containing from two to five rare-earth cations were prepared. For comparison, binary Ln_2O_3–ZrO_2 systems, where Ln = Nd, Gd, Sm, Dy, and Er, were also synthesized. After mechanochemical synthesis, the powders were heat-treated at 1000 °C, 1100 °C, 1200 °C, 1300 °C, 1400 °C, and 1500 °C for 5 h. In addition, pressed samples were prepared and annealed at 1500 °C for 5 h.

The obtained samples will be studied by X-ray diffraction, as well as by microstructural and elemental analysis. Comparison of samples with different numbers of components will make it possible to evaluate the effect of the multicomponent composition on phase formation and the thermal stability of the zirconate ceramics.

Acknowledgments. This research was funded by the Science Committee of the Ministry of Science and Higher Education of the Republic of Kazakhstan (No. BR 28713281).

NEUTRON METHODS AS REFERENCE TOOLS FOR NON-DESTRUCTIVE CHARACTERIZATION OF ENGINEERING MATERIALS

Altynbaev E.V., Gogolinsky K.V.
Saint Petersburg State University, St. Petersburg, Russian Federation

Neutron radiation combines deep penetration into metals, sensitivity to crystal-lattice strain and selected light elements, and the possibility of probing bulk objects non-destructively. In engineering applications its most useful role is often not to replace rapid industrial inspection, but to provide quantitative reference information that cannot be obtained reliably from the surface alone. Neutron diffraction therefore complements imaging and laboratory non-destructive testing by supplying bulk strain, residual-stress, and composition-sensitive information on technologically relevant components.

Recent developments in neutron stress diffractometry demonstrate that the method is moving toward technically relevant dimensions and spatial scales. At the STRESS diffractometer of the IR-8 reactor at the National Research Center “Kurchatov Institute”, Em et al. proposed a measurement configuration for ferritic-steel specimens thicker than 80 mm. The use of a 1.55 Å neutron wavelength and the (220) reflection at $2\theta = 99.4°$ reduced the neutron path in reflection geometry and provided strain uncertainties of about ±150 με, corresponding to a stress uncertainty of approximately ±30 MPa [1]. In another recent study, Karpov et al. used high-spatial-resolution neutron diffraction (~0.2 mm) to resolve residual-stress profiles in 5-mm 30KhGSA steel plates after shot peening. Compressive stress regions were detected near both surfaces, while tensile stresses were found in the central region of the plate [2]. These results are important for surface-strengthening technologies because the depth and magnitude of the induced stress field determine fatigue performance but are difficult to establish by purely surface-sensitive methods.

The reference role of neutron diffraction is also clearly illustrated by recent work at the KOWARI strain scanner of the Australian Nuclear Science and Technology Organisation. Mills et al. compared a phased-array ultrasonic approach for residual-stress assessment in robotically welded S275 steel plates with neutron diffraction and incremental hole drilling. Neutron measurements performed at depths of 2, 7, 10, and 13 mm provided a bulk benchmark; the methods showed qualitative agreement, while the remaining quantitative discrepancies indicated where the ultrasonic procedure requires further development [3]. This type of experiment is especially relevant for industrial metrology: neutron beam time is used to validate and calibrate a faster technique that can subsequently be applied outside a neutron facility.

A similar strategy is being developed in the United States for advanced manufacturing. At Oak Ridge National Laboratory, Lee et al. validated a finite-element model of wire-feed hybrid additive/subtractive manufacturing by neutron-diffraction measurements. Both experiment and simulation reproduced alternating tensile and compressive strains and stresses along the build direction, directly reflecting the sequence of deposition and machining operations [4]. The result demonstrates how neutron measurements can serve as an experimental constraint for process models, allowing residual-stress evolution and distortion to be predicted for manufacturing routes that are otherwise difficult to instrument during production.

Neutron imaging provides complementary information when the key problem is not lattice strain but the spatial distribution of internal phases, defects, or light-element-containing material. Nemati et al. applied neutron transmission imaging to Al6061 produced by solid-state friction stir additive manufacturing. Optimized regions of the components were found to be essentially void-

free, but the neutron contrast revealed segregation of hydrocarbon-based feedstock lubricant between deposited layers. Regions associated with this contamination exhibited about 14% lower strain to failure in mechanical tests [5]. This is a particularly instructive example of the applied advantage of neutron imaging: hydrogen-rich contamination can be detected inside a metallic component even when conventional attenuation-based X-ray contrast is insufficient.

Taken together, these studies show a practical direction for neutron methods in non-destructive testing and materials engineering. Neutron diffraction can quantify bulk strain fields, extend residual-stress measurements to thick engineering components, and provide reference data for ultrasonic methods and numerical models, while neutron imaging reveals composition-sensitive internal features that may be weakly visible by X-rays. An important institutional development is the NIST consortium model. The nSoft consortium, formed after an industry workshop in 2011 and launched in 2012, was designed around 'expertise transfer': industrial researchers work with the NIST Center for Neutron Research to define manufacturing-relevant problems and jointly develop sample environments, measurement methods, instrumentation, and data-analysis procedures rather than merely obtain isolated beam-time allocations [6]. Current NIST materials also identify an nMat consortium supporting industrial neutron programs across areas including residual-stress mapping, batteries, soft materials, and autonomous multimodal scattering. This evolution treats a neutron facility as shared metrology infrastructure in which industry, national laboratories, and academia co-develop reproducible reference measurements. A similar consortium-based approach could substantially broaden the practical impact of neutron methods for qualification of critical engineering materials and components.

The authors acknowledge Saint-Petersburg State University for a research project 161726507.

References:

1. Em V., Karpov I., Woo W., Mikula P. Neutron Diffraction Measurements of Residual Stresses for Ferritic Steel Specimens over 80 mm Thick. Metals. 2024;14:638. doi:10.3390/met14060638.
2. Karpov I.D., Em V.T., Nikolaeva E.P., Sergeichev I.V., Voloskov B.S., Mikula P. Investigation of residual stresses in steel plates after shot-impact treatment by high spatial resolution neutron diffraction. Physics of Metals and Metallography. 2024;125:1675–1684. doi:10.31857/S0015323024120208.
3. Mills B., Walker J., Javadi Y., MacLeod C.N., Alipooramirabad H., Reid M., Paradowska A. Residual stress analysis in robotically welded plates using phased array ultrasonics with validation through neutron diffraction and hole-drilling methods. International Journal of Pressure Vessels and Piping. 2025;216:105518. doi:10.1016/j.ijpvp.2025.105518.
4. Lee Y., Feldhausen T., Fancher C.M., Nandwana P., Babu S.S., Simunovic S., Love L.J. Prediction of residual strain/stress validated with neutron diffraction method for wire-feed hybrid additive/subtractive manufacturing. Additive Manufacturing. 2024;79:103920. doi:10.1016/j.addma.2023.103920.
5. Nemati S., Butler L.G., Ham K., Knapp G.L., Zeng C., Emanet S., Ghadimi H., Guo S., Zhang Y., Bilheux H. Neutron Imaging of Al6061 Prepared by Solid-State Friction Stir Additive Manufacturing. Metals. 2023;13:188. doi:10.3390/met13020188.
6. National Institute of Standards and Technology. nSoft/nMat consortium and NCNR industrial neutron programs. NIST, updated 2025-2026.

NUCLEOSYNTHESIS AT HIGH DUST PLASMA DENSITY.

Khasanov Kh.[1,2]
[1]*Sharof Rashidov Samarkand State University, Samarkand, Uzbekistan*
[2]*Lomonosov Moscow State University, Moscow, Russian Federation*

The results of an experimental study of the interaction of the oxidative combustion zone of natural energy carriers with supersonic, helically twisted dust-plasma jets [1], generated by a dynamic emitter, are presented. It is shown that under certain exposure conditions, a change in the nature of the combustion process is observed, accompanied by intense emission of light and thermal energy and a significant change in the composition of the products formed. The physical effect described above is observed due to nucleosynthesis.

Of particular interest is the spatiotemporal structure of the plasma-dust jet. The observed structure is characterized by helical geometry, self-organization, and collective dynamics of charged particles. Such properties are generally consistent with the known features of complex (dusty) plasma, which is characterized by collective effects, self-organization, and the formation of stable structures of various geometries [2, 3].

Due to the dynamic emitter, a high density of dust plasma is formed in the supersonic jet, which initiates nucleosynthesis; see Fig. 1. Coal (Fig. 1-a) is transformed into aluminosilicate rock (Fig. 1-b).

In the system under study, the action of the plasma jet on the combustion zone leads to the emergence of a regime that differs significantly from ordinary oxidative combustion of hydrocarbon fuel. The experiments showed intense light and thermal radiation accompanied by the transformation of the initial carbon-containing material into predominantly inorganic products.



Figure 1-a. The original coal before nucleosynthesis.



Figure 1-b. Nucleosynthesis of coal turned into rock aluminosilicate.

The results obtained can be considered promising for the development of new methods in nuclear technology. The advantage of the proposed approach lies in combining the generation of nucleosynthesis in dense dusty plasma. At the same time, the issue of the absence of harmful emissions and a complete balance of matter and energy requires further instrumental investigation, including quantitative analysis of the gaseous and condensed phases of the products of the nuclear reaction [5, 6, 7].

Thus, the experimentally observed effect of the interaction of a supersonic, helically twisted dusty plasma with the smoldering combustion zone is attributed to nucleosynthesis. These results are of scientific interest both for fundamental nuclear physics, complex plasma, and nonlinear

collective effects, and for the development of new technologies for the material transformation of natural energy carriers.

References:

1. Kh.Khasanov. Conversion of Oxidative combustion into powerful thermal and light energy. http://dx.doi.org/10.2139/ssrn.4820154
2. Khasanov, Kh. Visualization of Super-Compressibility in Supersonic Spiral-Twisted Jets. Physics Letters A. 376, 5, 748-752 (2012).
3. Khasanov, Kh. Super-Compressibility Phenomenon. Journal of Modern Physics. 4, 200-207. http://www.scirp.org/journal/jmp. (2013).
4. Khasanov, Kh. Spatial Super-Compression of the Continuous Media in High-Frequency Fields. American Journal of Modern Physics. 4(6):281. DOI:10.11648/j.ajmp.20150406.14 (2015).
5. Hyde T.W., Kong J., Matthews L.S. Helical structures in vertically aligned dust particle chains in a complex plasma // *Physical Review E*. 2013. Vol. 87. 053106. DOI: 10.1103/PhysRevE.87.053106.
6. Hsu S.C. et al. Laboratory plasma physics experiments using merging supersonic plasma jets // 2014.
7. Hsu S.C. et al. Experimental characterization of railgun-driven supersonic plasma jets motivated by high energy density physics applications. 2012.

DEVELOPMENT AND TESTING OF CATHODE STRIP CHAMBERS (CSC) WITH DIMENSIONS OF 1.5x2.2 M^2 FOR THE BM@N EXPERIMENT.

Kattabekov R.R.[1,2], Kapishin M.N.[1], Kiryushin Yu.T.[1], Kulish E.M.[1], Makankin A.M.[1], Piyadin S.M.[1], Spaskov V.N.[1]

[1]*Joint Institute for Nuclear Research, Dubna, Russian Federation*

[2]*Physical-Technical Institute, Uzbekistan Academy of Sciences, Tashkent, Uzbekistan*

The complete configuration of the BM@N outer tracking system consists of four CSCs with dimensions of 1.13×1.07 m² and two CSCs with dimensions of 1.5×2.2 m². The CSC detectors are located outside the magnetic field to ensure accurate matching with the tracks reconstructed in the GEM detectors inside the analyzing magnet. The tracks refined in the CSCs are used to improve particle momentum reconstruction and to search for corresponding hits in the ToF (Time-of-Flight) systems. In the full configuration, the six CSC detectors have 30 032 readout channels.

The first large 1.5×2.2 m² CSC was designed and assembled at VBLHEP JINR in 2021. It features 64 VA163 readout electronics cards (128 channels each) and 7 544 readout channels. The detector was tested during the BM@N technical run in January–February 2022. The entire CSC system was utilized in the physics run in 2026, Fig. 1. Charge distributions were obtained, and both the spatial resolution and detector efficiency were evaluated.

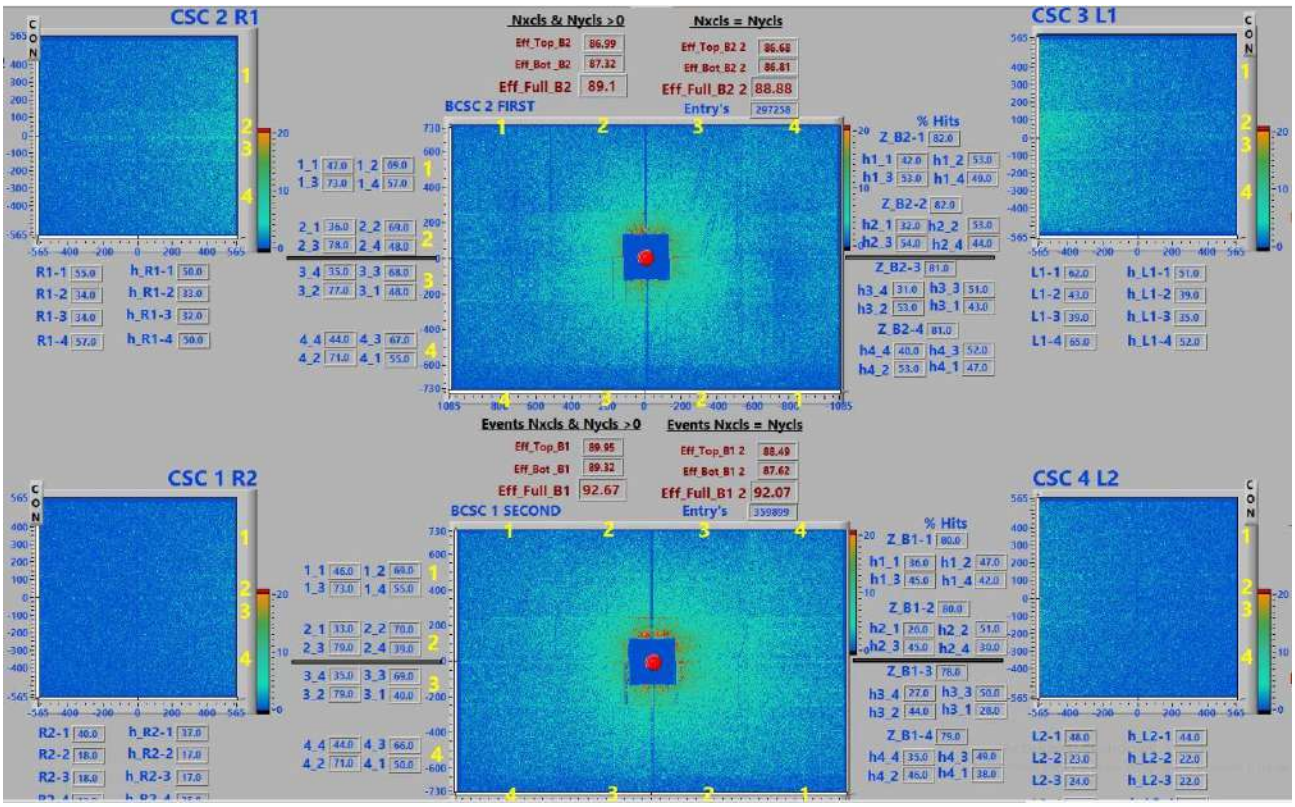

Figure 1. Monitoring of the CSC subsystem operation in the 2026 physics run.

References:

1. M. Kapishin, for the BM@N Collaboration, Studies of baryonic matter at the BM@N experiment (JINR), Eur. Phys. J. A52 (8) (2016) 213
2. The BM@N spectrometer at the NICA accelerator complex. Nucl.Instrum.Meth.A 1065 (2024) 169532
3. A. Galavanov et al., Performance of the BM@N GEM/CSC tracking system at the Nuclotron beam, EPJ Web Conf. 204 (2019) 07009
4. A. Galavanov, M. Kapishin, V. Karjavine, S. Khabarov, Y. Kirushin, E. Kulish, N. Kuzmin, V. Lenivenko, A. Makankin, A. Maksymchuk, S. Piyadin, V. Plotnikov, M. Rumyantcev, I.Rufanov, V. Sidorenko, S. Vasiliev, A. Vishnevskiy and A. Zinchenko, “Status of the GEM/CSC tracking system of the BM@N experiment”, 2020 JINST 15 C09038, https://doi.org/10.1088/1748-0221/15/09/C09038.

RESULTS OF THE FIRST TESTS OF ELECTROSLAG REMELTING OF METAL RADIOACTIVE WASTE AT THE ATOMIC ENERGY INSTITUTE OF THE RSE NNC RK

Mukhamedov N.E., Toleubekov K.O., Pakhnits A.V., Dolzhikov S.A.
Institute of Atomic Energy of the National Nuclear Center of the Republic of Kazakhstan, Kurchatov, Kazakhstan

One of the most promising methods of processing metal radioactive waste (MRW) is remelting. This method allows not only to reduce the volume of MRW due to the production of a compact metal ingot, but also to ensure the redistribution of radionuclides between the metal and slag phases. As a result, it is possible to obtain a metal suitable for further use or a conditioned product in the form of an ingot convenient for transportation, storage or disposal [1].

In this regard, to conduct experiments to study the possibility of reducing the level of radioactive contamination of MRW, an ESR experimental facility was developed at the branch of the IAE RSE NNC RK, located in the city of Kurchatov (Republic of Kazakhstan).

The facility is an electroslag furnace with a water-cooled crystallizer of a closed type. The crystallizer provides melting of the electrode metal and the working flux at a temperature of ~ 2000 °C and forms and ingot. Figure 1 shows the scheme of ESR facility [2].

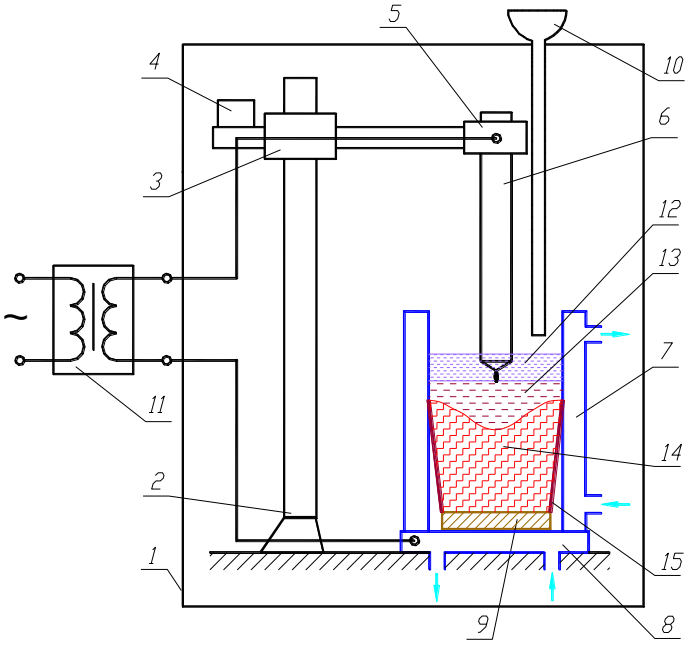

1 – box; 2 - bearing column; 3 – carriage; 4 – carriage movement drive; 5 – electrode holder; 6 – consumable electrode; 7 – crystallizer; 8 – pallet; 9 – seed; 10 – siphon attachment; 11 – transformer; 12 – slag bath; 13 – metal bath; 14 – ingot; 15 – slag garnissage

Figure 1. The scheme of ESR facility

To verify the operability of the facility, a pilot experiment was carried out using a MRW prototype in the form of a 12Cr18Ni10Ti (AISI 321) stainless steel pipe. The experiment confirmed the possibility of forming a stable slag bath and achieving a steady-state electroslag remelting

process. All major systems of the facility operated under normal conditions, ensuring stable process performance and continuous monitoring of the main operating parameters.

At the next stage, experiments were carried out using real radioactively contaminated metals. The material consisted of steel pipes made of the same grade of stainless steel as in the previous experiment. These pipes had previously been used in tests of fuel elements and fuel assemblies for a nuclear thermal rocket prior to the modernization of the cooling system of the IVG.1 reactor [3].

In total, two experiments were conducted on remelting steel pipes. Based on the results of the experiments, the following conclusions are summarized:

1. Cs-137 and U-235 are almost completely transferred to the slag phase during electroslag remelting;
2. Cs-137 is additionally accumulated in the filtering elements of the electroslag remelting facility;
3. Co-60 remains predominantly in the metallic phase after electroslag remelting;
4. The obtained steel ingots do not meet clearance criteria for unrestricted reuse;
5. Electroslag remelting leads to concentration of radionuclides in a reduced volume of slag;

The experimental results demonstrate the potential applicability of electroslag remelting for the decontamination of radioactive steel. At the same time, further detailed studies of radionuclide redistribution mechanisms are required to optimize the process and improve process efficiency.

Funding. This research has been funded by the Science Committee of the Ministry of Science and Higher Education of the Republic of Kazakhstan (Grant No. BR24993118)

Reference

1. Mukhamedov, N.; Surayev, A.; Dolzhikov, S.; Toleubekov, K.; Medetbekov, B. Radiological Characterization of Solid Radioactive Waste Generated During the Decommissioning of the BN-350 Reactor. *Appl. Sci.* **2026**, *16*, 4936. https://doi.org/10.3390/app16104936
2. Vurim A.D., Aleynikov Yu.V., Zhdanov V.S. and et.al. Decontamination of radioactive steel by the method of electroslag remelting. *NNC RK Bulletin*. 2002, 1, 34-40. (In Russian)
3. Smetannikov V.P., Cherepnin Yu.S., Romadova Ye.L. and et.al. Upgrade of the IVG.1M reactor for testing of NPP and BNTP components. In Proceedings of Space Nuclear Conference. 2007, 328-335.

METHODS FOR DETERMINING THE CONTENT OF BORON, CADMIUM, AND HAFNIUM IN FINISHED URANIUM PRODUCTS

Suyunov U.A., Allaberganova G.M., Muzaffarov A.M.
Navoi State University of Mining and Technologies, Navoi, Uzbekistan

This paper examines instrumental methods for determining boron, cadmium, and hafnium in finished uranium products. Monitoring these elements is important because of their high neutron-absorption capacity, which means that even trace concentrations can affect the neutron-physical characteristics of uranium materials. The applicability of inductively coupled plasma optical emission spectrometry (ICP-OES), inductively coupled plasma mass spectrometry (ICP-MS), and

atomic absorption spectrometry (AAS) is considered. The methods are compared in terms of sensitivity, selectivity, reproducibility, and multielement analysis capability.

Keywords: Uranium, boron, cadmium, hafnium, impurities, analytical control, ICP-OES, ICP-MS, atomic absorption spectrometry.

Introduction: The quality of uranium products depends not only on the content of the principal component but also on impurity concentrations. Boron, cadmium, and hafnium are of particular interest because of their ability to absorb neutrons. Therefore, their determination is necessary for controlling the chemical composition and assessing the neutron-physical characteristics of uranium materials.

Determining trace impurities in a matrix containing a high concentration of uranium is challenging due to spectral and matrix interferences, reduced sensitivity, and possible systematic errors. Consequently, appropriate analytical methods and sample preparation procedures are essential.

Objective of the Study: The objective is to comparatively evaluate instrumental methods for determining boron, cadmium, and hafnium in finished uranium products and to identify suitable approaches for monitoring trace concentrations of these elements.

Materials and Methods: Several instrumental methods can be applied to determine B, Cd, and Hf.

ICP-OES measures the characteristic radiation emitted by atoms and ions in high-temperature plasma. Its main advantage is the simultaneous determination of several elements in one sample, making it suitable for routine multielement analysis. However, analysis of uranium matrices requires consideration of spectral overlaps and matrix effects.

ICP-MS provides significantly higher sensitivity and enables the determination of trace and ultratrace concentrations by separating ions according to their mass-to-charge ratio. It is particularly promising for low concentrations of B, Cd, and Hf, although matrix effects, reagent purity, and possible isobaric and polyatomic interferences must be controlled.

Atomic absorption spectrometry (AAS) determines elements by measuring the absorption of light by free atoms. It provides good selectivity for individual elements but is less suitable for simultaneous multielement analysis than ICP-OES and ICP-MS.

Before instrumental analysis, uranium samples must be converted into a suitable soluble form. The sample preparation procedure should ensure quantitative transfer of the elements of interest into solution while minimizing contamination. Analytical reliability can be improved by using blank samples, certified reference materials, calibration solutions, and control samples. Repeatability, reproducibility, trueness, and detection limits should be considered when evaluating the results.

Results and Discussion: The choice of analytical method depends mainly on the required concentration range and uranium matrix composition. ICP-OES is effective for multielement analysis when concentrations are within its analytical range, whereas ICP-MS provides lower detection limits and is preferable when trace or ultratrace concentrations must be determined.

For boron, the selection of the analytical line, laboratory vessel material, and reagent purity can significantly influence the results. For cadmium, spectral and polyatomic interferences should be considered, particularly in ICP-MS measurements. For hafnium, appropriate isotope selection and control of matrix effects are important. A key factor affecting analytical reliability is the reduction of uranium matrix effects. This can be achieved by dilution, matrix matching of calibration standards, internal standards, standard addition, or preliminary separation of the major matrix component. The appropriate procedure depends on the composition of the product and the required sensitivity. Thus, ICP-based multielement methods are considered appropriate for

comprehensive control of B, Cd, and Hf. ICP-OES is a practical option for routine production control, while ICP-MS is more suitable when ultralow concentrations are required.

Conclusion: ICP-OES and ICP-MS are the most promising methods for multielement determination of boron, cadmium, and hafnium in finished uranium products. ICP-OES provides convenient simultaneous analysis, while ICP-MS offers higher sensitivity for trace concentrations. The reliability of the results depends strongly on sample preparation, uranium matrix control, proper selection of analytical lines or isotopes, certified reference materials, and validation of the analytical procedure. Comprehensive determination of B, Cd, and Hf improves the reliability of assessing the chemical composition of uranium products and supports compliance with established quality requirements.

References:

1. Allayarov R.M., Allaberganova G.M., Muzafarov A.M., Eshpulatov B.X. Osenka vozmojnosti analiticheskix metodov opredeleniya RZE v uranovix obrazsax Kizilkuma // Universum: texnicheskie nauki. -2024. -№ 11(128).
2. Nazarov J.T., Allaberganova G.M., Umarov F.Ya., Muzafarov A.M. Osenka radiasionnix pokazateley bednix uransoderjashix rud dlya privlecheniya ix k pererabotke metodom fiziko-ximicheskoy geotexnologii // Sifrovie texnologii v promishlennosti. -2024. -T. 2, № 4. -S. 57–64.
3. Junisbekov B.J. Texnologicheskie osobennosti peroksidnogo osajdeniya urana // Molodoy ucheniy. -2011. -№ 11(34). -T. 1. -S. 41–43.
4. Surikov V.T. Opredelenie primesey v gafnii metodom ICP-MS // Atomniy spektral'niy analiz: XVI Ural'skaya konferensiya po spektroskopii: tezisi dokladov. -Ekaterinburg: Institut ximii tverdogo tela UrO RAN. -S. 132–133.
5. Voda. Opredelenie soderjaniya 62 elementov metodom mass-spektrometrii s induktivno svyazannoy plazmoy. GOST R 56219-2014. -M.: Standartinform, 2015.
6. Kolichestvenniy ximicheskiy analiz pochv. Metodika vipolneniya izmereniy soderjaniya metallov v tverdix ob'ektax metodom spektrometrii s induktivno-svyazannoy plazmoy. PND F 16.1:2.3:3.11-98. -M., 1998.

METHODS FOR DETERMINING THE SPECIFIC ACTIVITIES OF ^{234}U, ^{235}U, AND ^{238}U ISOTOPES IN URANIUM OXIDE (U_3O_8)

Suyunov U.A., Urunov I.A., Allaberganova G.M., Muzafarov A.M.
Navoi State University of Mining and Technologies, Navoi, Uzbekistan

This paper considers methods for determining the specific activities of the main uranium isotopes, ^{234}U, ^{235}U, and ^{238}U, in uranium oxide (U_3O_8). Determination of radionuclide composition and specific activity is important for radiometric and chemical-analytical control of uranium materials. The applicability of alpha spectrometry, gamma spectrometry, and mass spectrometric methods, together with appropriate sample preparation procedures, is considered. The combined use of radiometric and isotopic methods provides a more comprehensive characterization of U_3O_8 and improves the reliability of analytical results.

Keywords: uranium, ^{234}U, ^{235}U, ^{238}U, U_3O_8, specific activity, alpha spectrometry, gamma spectrometry, mass spectrometry, isotopic composition.

Introduction: Uranium oxide (U_3O_8) is a common uranium compound used as an intermediate or starting material in nuclear fuel cycle processes. Important characteristics of this material include uranium content, isotopic composition, and the specific activity of individual radionuclides. Natural and processed uranium contains predominantly ^{234}U, ^{235}U, and ^{238}U. Although these isotopes have similar chemical properties, their radioactive characteristics differ significantly. Therefore, accurate assessment of U_3O_8 requires determination of both total activity and the contribution of individual isotopes.

Objective of the Study: The objective of this study is to comparatively evaluate methods for determining the specific activities of ^{234}U, ^{235}U and ^{238}U, in U_3O_8 and to identify effective approaches for radiometric and isotopic analysis.

Research Methods

Alpha spectrometry is an informative method for determining uranium isotopes because alpha-emitting radionuclides produce characteristic particle energies. Radionuclides can be identified from their energy spectra, while their activities are determined from the corresponding peak areas. Accurate measurements require consideration of detector efficiency, measurement geometry, background radiation, and radionuclide separation. Preparation of a thin and homogeneous source is particularly important because self-absorption of alpha particles can significantly affect the results.

Gamma spectrometry is based on detecting characteristic gamma radiation emitted by radionuclides. It enables rapid and, in many cases, nondestructive radiation monitoring. However, suitable gamma lines for some uranium isotopes have relatively low intensity, which can limit sensitivity and accuracy. Detector efficiency, sample geometry, self-attenuation, and spectral interferences must therefore be considered.

Mass spectrometric methods enable direct determination of isotope ratios such as $^{234}U/^{238}U$ and $^{235}U/^{238}U$. Depending on the analytical objectives, techniques such as inductively coupled plasma mass spectrometry (ICP-MS) and thermal ionization mass spectrometry (TIMS) can be applied. Their main advantage is high accuracy in determining isotopic composition. Since mass spectrometry measures isotope quantities rather than radioactive activity directly, the corresponding half-lives must be considered when calculating specific activity.

Results and Discussion

Comparison of the methods demonstrates that alpha spectrometry directly characterizes radioactive decay and is therefore effective for determining the activity of alpha-emitting uranium isotopes. Its accuracy, however, depends strongly on source preparation and detector efficiency.

Gamma spectrometry provides the advantages of nondestructive analysis and convenient radiation monitoring, although quantitative determination of individual uranium isotopes requires appropriate gamma lines and correction for detector and sample characteristics.

Mass spectrometry provides highly accurate isotopic composition data. The measured isotope ratios can be combined with nuclear constants and radionuclide half-lives to calculate the specific activity of each isotope.

Therefore, the combined application of radiometric and mass spectrometric methods is the most reliable approach. Radiometric techniques provide direct information on radioactive activity, while mass spectrometry independently determines isotopic composition. Comparison of results obtained by these approaches can help identify systematic errors and improve the reliability of analytical control.

Conclusion: The main methods for determining the specific activities of ^{234}U, ^{235}U and ^{238}U in U_3O_8 were considered. Alpha spectrometry is effective for direct determination of alpha activity,

gamma spectrometry is suitable for rapid and nondestructive radiometric control, and mass spectrometric methods provide accurate determination of isotopic composition.
Specific activity can be determined directly by radiometric methods or calculated from measured isotopic composition using the corresponding radionuclide half-lives. The integrated application of these methods provides comprehensive information on the radionuclide characteristics of U_3O_8 and improves the reliability of analytical control.

References:

1. Muzafarov A.M., Sattarov G.S., Petuxov O.F., Petrenko V.Z. Izuchenie izotopnogo sostava urana al'fa-spektrometricheskim metodom // Geotexnologiya: innovasionnie metodi nedropol'zovaniya v XXI veke: sbornik tezisov. – Moskva–Navoi, 2007. – S. 125.
2. Allaberganova G.M., Turobjonov S.M., Jurakulov A.R., Urunov I.A., Abdiraxmonov U.Sh. Metodika provedeniya izotopnogo analiza urana v razlichnix prirodnix vodax uranonosnix regionov Uzbekistana // International Journal of Academic Multidisciplinary Research. – 2019. – T. 3, № 10. – S. 52–55.
3. Allaberganova G.M., Urunov I.A., Boboev A.A., Suyunov U.A., Muzafarov A.M. Issledovanie radionuklidnogo sostava i koeffisientov radioaktivnogo ravnovesiya mejdu nimi v ximicheskix konsentratax urana. – 2025.
4. Nazarov J.T., Allaberganova G.M., Pulatov X.L., Muzafarov A.M. Analiz radionuklidnogo sostava gornix porod uchastkov dobichi urana metodom fiziko-ximicheskoy geotexnologii // Global'naya nauka i innovasiya 2023: Sentral'naya Aziya. – 2023. – № 2(20). – S. 48–50.
5. Nazarov J.T., Allaberganova G.M., Pulatov X.L., Muzafarov A.M. Analiz radionuklidnogo sostava prirodnix vod na uchastkax dobichi urana metodom fiziko-ximicheskoy geotexnologii // Global'naya nauka i innovasiya 2023: Sentral'naya Aziya. – 2023. – № 2(20). – S. 51–54.
6. Kalinin V.I., Larin A.N., Orlov V.V. Radiometricheskie metodi opredeleniya soderjaniya urana i produktov yego raspada v prirodnix i texnologicheskix ob'ektax // Atomnaya energiya. – M.
7. Surikov V.T. Mass-spektrometricheskoe opredelenie izotopnogo sostava urana // Atomniy spektral'niy analiz: materiali konferensii. – Yekaterinburg.

MODERN SPECTROMETRIC METHODS FOR THE ANALYSIS OF URANIUM CHEMICAL CONCENTRATES

Urunov I.A., Allaberganova G.M., Muzafarov A.M.
Navoi State University of Mining and Technologies, Navoi, Uzbekistan

Uranium chemical concentrates require reliable determination of uranium and impurity elements throughout production. This paper reviews the application of inductively coupled plasma optical emission spectrometry (ICP-OES), inductively coupled plasma mass spectrometry (ICP-MS), X-ray fluorescence spectrometry (XRF), atomic absorption spectrometry (AAS), and molecular spectroscopy to their analysis. The methods are compared in terms of sensitivity, multielement capability, sample preparation, matrix effects, and suitability for laboratory and process control. ICP-OES is effective for routine multielement measurements, ICP-MS for trace impurities and isotope ratios, and XRF for rapid direct analysis of solid samples. AAS and molecular spectroscopy provide complementary information. The most reliable analytical control is achieved by combining XRF screening with confirmatory ICP-OES or ICP-MS measurements.

Keywords: uranium concentrates, spectrometric analysis, ICP-OES, ICP-MS, XRF, atomic absorption spectrometry, impurity elements, quality control.

Introduction Uranium chemical concentrates are multicomponent materials whose composition depends on the initial ore and processing technology. Quality control requires determination of the principal component, uranium, together with accompanying and impurity elements that may influence subsequent refining and conversion processes.

Conventional chemical methods provide reliable results but often require lengthy sample preparation and considerable reagent consumption. Modern spectrometric methods reduce analysis time and allow several elements to be determined simultaneously. Nevertheless, the uranium-rich matrix may cause spectral interferences, signal suppression, and contamination of analytical equipment. Method selection must therefore consider sensitivity, matrix tolerance, calibration, sample preparation, and the purpose of the measurement.

Modern spectrometric methods. ICP-OES is widely used for routine multielement analysis of uranium concentrates. In this method, atoms and ions excited in argon plasma emit radiation at characteristic wavelengths. The intensities of the selected spectral lines are used to determine elemental concentrations. ICP-OES is suitable for monitoring iron, calcium, magnesium, aluminum, silicon, and other impurities. Its advantages include high productivity, a broad dynamic range, and automated analysis. The main limitations are spectral overlap and matrix effects in uranium-rich solutions. These effects can be reduced by dilution, appropriate wavelength selection, internal standards, matrix-matched calibration, or preliminary uranium separation.

ICP-MS provides substantially lower detection limits and enables trace-element and uranium-isotope analysis. Ions produced in the plasma are separated according to their mass-to-charge ratios. The method is particularly useful when impurity concentrations are below the detection capability of optical emission spectrometry. However, high uranium concentrations can produce polyatomic and isobaric interferences, signal drift, and memory effects. Controlled dilution, chemical separation, internal standards, and collision or reaction cell technologies are therefore required for reliable measurements.

XRF is suitable for rapid direct analysis of solid uranium concentrates. Characteristic secondary X-ray radiation emitted by the sample provides qualitative and quantitative information about its elemental composition. Powdered samples can be measured directly or prepared as pressed pellets or fused beads. The principal advantages of XRF are minimal sample preparation, short measurement time, and non-destructive analysis. These characteristics make it useful for operational process control. Its accuracy depends on sample homogeneity, particle-size distribution, matrix effects, and the availability of appropriate calibration standards.

AAS is applicable to the selective determination of individual elements. It offers good selectivity and relatively simple instrumentation but is less suitable for comprehensive multielement analysis because elements are usually measured sequentially. It is therefore mainly used for targeted or confirmatory measurements.

UV-Vi’s spectrophotometry, Fourier-transform infrared spectroscopy, and Raman spectroscopy provide complementary information about uranium compounds. UV-Vi’s methods can be used to study uranium-containing complexes and oxidation states, while FTIR and Raman spectroscopy assist in identifying molecular groups, chemical phases, and structural changes. These methods complement rather than replace elemental analysis.

Selection and combined application of methods. The analytical method should be selected according to the measurement objective. ICP-OES is appropriate for routine determination of major and minor components. ICP-MS is preferred for trace impurities and isotope ratios, whereas XRF provides rapid screening of solid samples. AAS is suitable for selected elements, and molecular spectroscopy supplies additional information about chemical form and structure.

A combined analytical scheme offers greater reliability than a single method. XRF can be used for preliminary screening and assessment of sample homogeneity. ICP-OES can then provide quantitative multielement confirmation after dissolution, while ICP-MS can be reserved for trace and isotopic measurements. This combination improves analytical efficiency and helps identify errors associated with matrix effects, incomplete dissolution, or sample heterogeneity.

Reliable quality control also requires certified reference materials, procedural blanks, duplicate measurements, calibration verification, and spike-recovery tests. Automated sample introduction, interference correction, and computerized data processing improve precision and reproducibility, but they cannot compensate for incorrect sampling or inadequate sample preparation.

Conclusion Modern spectrometric methods significantly increase the speed and information content of uranium-concentrate analysis. ICP-OES provides effective routine multielement control, ICP-MS offers trace-level and isotopic information, and XRF enables rapid examination of solid materials. AAS and molecular spectroscopy perform complementary analytical functions.

The integration of XRF, ICP-OES, and ICP-MS with validated sample preparation and interference correction provides comprehensive and reliable control of uranium and impurity composition. Further development should focus on automated analytical systems, reduced sample preparation, improved matrix correction, and rapid interpretation of results for industrial process control.

References:

1. Allayarov R.M., Allaberganova G.M., Muzaffarov A.M., Eshpulotov B.Kh. Analytical methods for determining rare-earth elements in uranium samples from the Kyzylkum region. Universum: Technical Sciences, 2024, No. 11(128).
2. Allaberganova G.M., Turobzhonov S.M., Muzaffarov A.M., Zhurakulov A.R. Uranium isotopic analysis in natural waters of uranium-bearing regions of Uzbekistan. International Journal of Academic Multidisciplinary Research, 2019, Vol. 3, No. 10, pp. 52-55.
3. Allaberganova G.M., Urunov I.A., Boboev A.A., Suyunov U.A., Muzaffarov A.M. Radionuclide composition and radioactive-equilibrium coefficients in uranium chemical concentrates. Proceedings: Collection of Scientific Papers, 2025.
4. Allaberganova G.M., Suyunov U.A., Kulmatov R.A. et al. Nuclear-physical characteristics and radiation indicators of low-grade uranium-bearing ores. Proceedings: Collection of Scientific Papers, 2025.
5. Pulatov Kh.L., Muzaffarov A.M., Nazarov Zh.T., Allaberganova G.M. Granulometric distribution of uranium in technogenic secondary uranium ores. Mechanics and Technology, 2024, No. 1(8), pp. 196-202.

OPERATIONAL ASPECTS OF THE IR-8 RESEARCH REACTOR

Andreev D.V.
National Research Centre "Kurchatov Institute", Moscow, Russia

The report "Operational Aspects of the IR-8 Research Reactor" presents:

1. Main characteristics of the IR-8 research reactor.
2. Basic information on the areas of research and development work carried out using the IR-8 and OR research reactors.
3. Basic information about the experimental devices of the IR-8 and OR research reactors, including information about their completed and planned upgrades.
4. Basic information regarding the results of extending the service life of the IR-8 reactor to 2036 (a process carried out in 2026), as well as work completed and planned under the IR-8 reactor life management program.

UNCERTAINTY ANALYSIS OF LEVEL-1 PSA FOR NPP USING MONTE CARLO METHOD WITH LATIN HYPERCUBE SAMPLING: A CASE STUDY OF THE EMERGENCY CORE COOLING SYSTEM

Mukhamedov B.O., Rakhimkulov M.M., Temirov D.T.,
Kuldjanov B.K., Salikhbaev U.S.
State Institution "Scientific and Technical Center for Radiation and Nuclear Safety", Committee for Industrial, Radiation, and Nuclear Safety, Tashkent, Uzbekistan

Ensuring nuclear power plant (NPP) safety is traditionally achieved through probabilistic safety assessment (PSA), which relies on point estimates of basic-event probabilities and therefore cannot indicate how conservative the resulting reliability figures are. This work quantifies the uncertainty of the conditional failure probability of the emergency core cooling system (ECCS) on demand = a simplified surrogate for the core damage frequency (CDF) used here to demonstrate the methodology = arising from the parametric uncertainty of the input data. A simplified three-train ECCS model (success criterion "2-out-of-3") was built, with basic-event probabilities assigned lognormal distributions per NUREG/CR-6823 database. Sampling was performed using Latin Hypercube Sampling (LHS, N = 50,000); sensitivity analysis was carried out by three complementary methods: Standardized Rank Regression Coefficients, Spearman rank correlation, and first-order Sobol indices.

The resulting CDF distribution is well approximated by a lognormal law ($\mu = -8.16$, $\sigma = 0.72$, coefficient of variation = 1.02). The classical point estimate obtained by substituting median parameter values (1.68×10^{-4}) corresponds to only the 23rd percentile of the Monte Carlo distribution — i.e., it is moderately optimistic rather than conservative: the Monte Carlo median (2.78×10^{-4}) is almost 1.7 times higher.

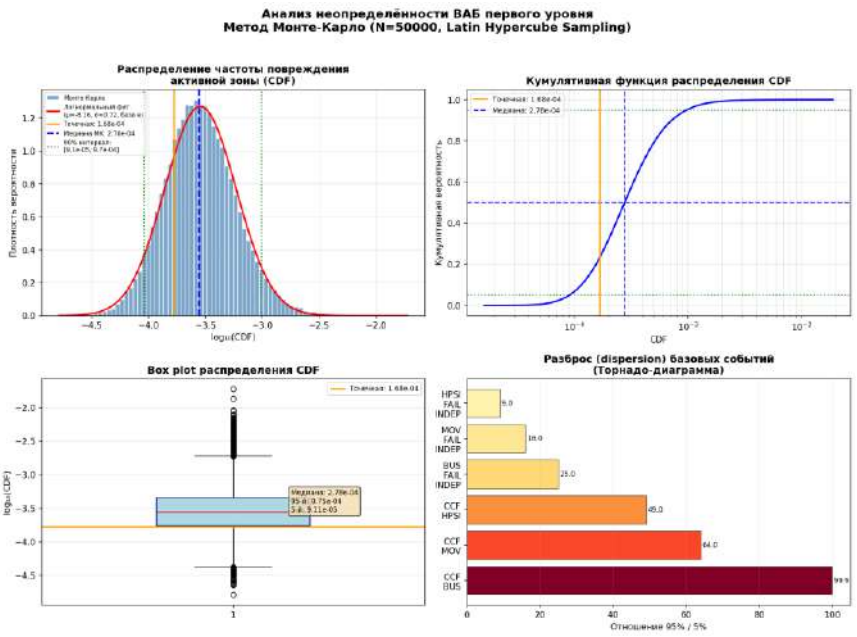

Figure 1. Statistical analysis of the CDF distribution obtained by the Monte Carlo method with LHS (N = 50,000): (a) histogram of $\log_{10}$(CDF) with the fitted lognormal curve; (b) empirical cumulative distribution function; (c) box plot of the distribution; (d) tornado diagram of the spread (95%/5% ratio) of the basic events.

The Monte Carlo method with LHS proved to be an effective tool for checking the conservatism of PSA results, and the discrepancy between sensitivity measures is shown to be practically significant for prioritizing the collection of additional operational data. This study is, to the authors’ knowledge, the first application of Monte Carlo uncertainty and sensitivity analysis to a PSA model in Uzbekistan, and it is particularly relevant given the country’s NPP project under construction = a non-reference configuration combining small modular reactors with a VVER-1000 unit, for which operational statistics remain limited and uncertainties are correspondingly large. The approach is fully transferable to full-scope Level-1 PSA models and marks the beginning of systematic development of uncertainty-analysis methodology within the national PSA practice.

Keywords: *probabilistic safety assessment, Level-1 PSA, ECCS, core damage frequency, Monte Carlo method, Latin Hypercube Sampling, sensitivity analysis, Sobol indices.*



ALPHABETICAL INDEX

A

Abdaminov A.B. 150
Abdukarimov A.A. 223
Abdukayumov A.M. 243,244,245,246,247,248,250
Abdullaeva G.A. 68,69,231,233,238
Abdullayev A.P. 142
Abdullin F.Sh. 127
Abdusalomova M.R. 275
Abdusamadzoda D. 127
Abrikosov I.A. 149
Adizov S.M. 286
Agayev T.N. 12
Ahadov A. 197,199
Ahadova A. 197,199
Aitkulov M. 307
Akaev S.O. 141
Akhanov A. 307,308
Akhmatova G.Y. 17
Akhmedov S.E. 66,114
Akhmedov Ya.A. 259,260,289
Akhmedova G.B. 208
Akhmedzhanov F.R. 310
Akhundzada H.N. 212
Aksenov N.V. 62, 127
Aldabergenova T.M. 141
Alekseev S.I. 62
Aleksiayenak Yu.V. 268
Alibekova Sh.B. 171
Alikulov Sh.A. 301,305
Alimov D.K. 96,120
Allaberganova G.M. 85,87,319,321,323
Altynbaev E.V. 313
Amanov O.O. 146,186,284
Amirov S. 101
Andreev D.V. 326
Andrianov V.A. 203
Artemenkov D. 100
Artemov S.V. 38,42,47
Asadov F.G. 201
Asadova Z.I. 201
Asadullaev M.M. 237
Ashrapov U.T. 186,284
Ashurov M.Kh. 17,176,190
Askerbekov S. 307,308,309
Atabaev B.G. 146
Atashov B.T. 193
Averkova T. 307
Azat S. 258
Aznabayev D. 97

B

Bakhromov J.O. 112
Bakhodirov Sh.Sh. 104
Batgerel B. 133
Baklanova Yu. 30
Baymuratova I.V. 252
Bayazova A.A. 139
Baytelesov S.A. 301,305
Babayeva F.Sh. 142
Bekmirzaev R. 107
Beknazarov H.J. 233
Belkin D.Y., 295
Beknazarova N.Y. 93
Bedelbekova K.A. 203,269
Belushkin A.V. 9
Berdibaev A.K 31
Bespokoev A.A. 292
Bekmuldin M. 302
Bodrov A.Yu. 127
Bogachev A.A. 73
Boltabaev A.F. 310
Bondar E. 26,111
Boyboboeva S.T. 161,176
Bozarov O.A. 115
Bozhikov G.A. 127
Bozorboev Sh.G. 93
Bozorov E.Kh. 252
Boztosun I. 96,120
Bryazgin A. 10
Bugay A.N. 240
Bugybay Zh. 308
Buriev M.M. 152,205
Burtebayev N. 47,96,120
Buryanenko I.V. 292
Bychkov M.A. 104

C

Chausova V.A. 232
Čebela M. 63
Chelnokov M.L. 104
Chepigin V.I. 104
Cherubini S. 35
Chikhray Ye. 308,309
Chuprakov I. 62
Churkin I. 29

D

Dadashov I. 216
Danilkin V.D. 104
Danilova E.A. 271,273,282,289
Dashkevich T. 33
Devaraja H.M. 104
Di Pietro A. 35
Djangabaev Kh.N. 154,206
Djumanov Sh.S. 23
Dmitriev S.N. 127
Dolzhikov S.A. 318
Dolgopolov M.V. 19,146,186,305
Dosymova B.U. 305
Doroshkevich A.S. 268
Dovbnenko M. 22
Duisebayev B. 36,65,72
Dushanov E.B. 240
Dzhumanov S. 23,171

E

Egamberdieva A.A. 195
Egamov S.R. 134
Egamova F.R. 93
Elimov Kh.B. 257
Elishenkov A. 308
Elmurotova D.B. 295,297
Emelyanenko E. 235
Ergashev F.Kh. 38,42,47
Eraliev A.A. 157
Ergeshbaev A.Zh. 227
Erdonov M.N. 178,191
Eshanqulov G.I. 66

F

Fateev S. 22
Fayziev T.B. 301,305
Fedosimova A.I. 26,108,111
Figuera P. 35
Fursova N.Yu. 62

G

Gadzhieva N.N. 208
Gafarova G.A. 208
Galdiev M.E. 243
Galiulin I.G. 14
Gan Z.G. 127
Ganiev O.K. 28,115,136
Ganyeva A.S. 195
Gapurova O.U. 14,255
Germenchk M. 33
Gogolinsky K.V. 313
Goldberg V.Z. 35,46,61
Gons Z. 48
Gulamov K.G. 104
Gulbekyan G.G. 78
Gulino M. 35
Gusakova O. 33

H

Hajiyeva E. 218
Hamada Sh. 43
Haydarov U. 266
Hristov I. 133
Hristova R. 133
Huang M.H. 127
Huang X.Y. 127
Huseynova S. 210

I

Ibadullayev D. 127
Ibragimova E.M. 168,181,186
Ibraimova S.A. 26,106,111
Ibrokhimov R.R. 17
Igamov S.B. 38,47,56,117,128
Ikromkhonov E.Sh. 47,117,128
Ilin K.P. 61
Inoyatov A.X. 63,66
Irgaziev B.F. 50
Irkimbekov R.A. 303
Isaev A.V. 104
Iskenderova G.M. 208
Islamov A.Kh. 181
Ismatov N.B. 178,183,191,286
Ismayilova M.K. 212
Issadykov A. 99
Issatayev T. 36,97
Issatov A. 72
Itkis M.G. 127
Ivanov M.A. 99
Izosimov I.N. 80,104,119
Izteleuova G.S. 203

J

Jafarov Y.D. 142
Janseitov D.M. 43,96,120
Jeenbaev N.J. 261
Joldoshov B.K. 139
Jordanov D. 63
Jumaev M.R. 131
Jurakulov A.R. 257,266

K

Kabirova K. 264
Kabulov I.Sh. 173
Kabytayeva R. K. 78
Kadenova B.A. 227
Kadyrbekov N.R. 233
Kadyrbekov R.T. 233
Kadyrov A.S. 24
Kaiyrbekova A.S. 258,269
Kakhorova A.N. 109
Kalagin I.V. 78
Kalandarov Sh.A. 104,123
Kalanov M.U. 188
Kalinnikov V.G. 48
Kanokova Sh.Z. 121
Kapishin M.N. 316
Karakhodzhaev A.A. 42,47,188
Karimbaev E.Kh. 149,173
Khromushin I.V. 163
Khudoyberdieva Sh.A. 108,121
Khugaev A. 56
Khujaev S. 237,242,246,248,250
Khurramova S.N. 54
Khusanov E.D. 27
Khushvaktov J.Kh. 48,62,63,64,94
Khushvaktov N.Kh. 271
Khusniddinova S.Kh. 271,273
Kidibaev M.M. 139,261
Kim A.A. 68,69,231,233
Kiryushin Yu.T. 316
Kiselev M.A. 232
Kislitsyn S.B. 141
Kiyavitskaya H. 33
Klopotov A.A. 141
Knyazheva G.N. 73

Karimov Z.I. 171
Karpov A.V. 73,127
Kartavenko V.G. 48
Katrasev D.E. 104
Kattabekov R.R. 316
Kayumov B.M. 27,101
Kayumova M.Sh. 58
Kenzhin Ye. 309
Kenzhina I.E. 30,175,180,214,271, 304,308,309
Kerimova R. 218
Khaitov F.N. 257,271
Khajibaev D.G. 157
Khajiyev L.O. 244,245,248,250
Khalilova K.G. 208
Khalkin A.V. 127
Khametov Sh. 156
Khametova A. 185
Khankishiyeva R. 212
Khasanov J.A. 50
Khasanov Kh. 315
Khaydarov R.R. 14,255
Khayitov I.A. 181
Kholmedov Kh.M. 178
Khoshimjonov Kh. 93,94
Kobets V.V. 48
Korjavov M.J. 81
Kosherbayeva R. 96,120
Kovalchuk K.V. 96,120
Kovrizhnykh N.D. 127
Kozlovskiy A.L. 175,180,214,271,304
Kozulin E.M. 73
Kruglyak A.I. 268
Kudratov Kh.N. 181
Kulabdullaev G.A. 68,69,231,233
Kuldjanov B.K. 282,326
Kulish E.M. 316
Kulsartov T. 30,308,309
Kunarbekova M.S. 258
Kungurov F.R. 301,305
Kurbanov B.I. 257,271,273,274
Kurbanov U.T. 23
Kurbanova N.B. 273
Kurmantayev A.N. 171
Kuthudzhin D.V. 78
Kuyliev F.Y. 94
Kuznetsov A.A. 22,62
Kuznetsov D.A. 127
Kuznetsova A.A. 104

L

LaCognata M. 11,35,38
Lamia L. 35
Lebedev I.A. 26,106,108,111
Lennik S.G. 258,264,269
Liu Fu-Hu 26,108,111,121
Lukyanov S.M. 97
Lychagin E.V. 16

M

Madaminov B.N. 168,191
Madatov R.S. 220
Madiyarov D.N. 159
Madumarov A.S. 62
Makankin A.M. 316
Makhkamov Sh. 134,178,191,223
Makhmudov Sh.A. 144,166
Malikov A.A. 259,265,289
Malikov Sh.R. 146,186,188,284
Malyshev O.N. 104
Mamishova R.M. 215
Mammadov M.A. 201
Mingbaev Kh.S. 257,274
Mirbabaev Sh.R. 89
Mirjonova N.N. 131
Mirkhaji D.V. 258
Mirmanova D.S. 163
Mirzaev V.T. 228
Mirzayev M. 133
Mitrofanov S.V. 78
Mogoch S. 284
Mohd’ Kh. M. Abu El Sheik 83
Mukashova A.B. 261
Mukhamedov B.O. 149,326

Mammadov S. 197,199
Mamytbekov U.K. 139,261
Markelova E.A. 237,242
Martynenko Y. 302
Maslov V.A. 97
Mekhmonov G. 242
Melezhik V. 43
Melikova S. 216,218
Mendibayev K.O. 36,97
Migunova A. 307
Mukhamedov N.E. 303,318
Mukhin R.S. 104
Mukhtarov A. 219
Muminov A.T. 91
Musaev K.A. 26,111,121
Mussaeva M.A. 164,170,193
Mustafayev I.I. 212
Mustafoyev M.A. 87
Muzafarov A.M. 85,87,257,266,319,321,323
Myshinsky G.V. 71

N

Nadirbekov M.S. 125,126
Nadjdjerdj L. 63
Nasirov A.K. 27
Nasirova A. 218
Nasurlla Maulen 47
Naumovskiy V.B. 14
Nauruzbayev D.K. 35,46,61
Nazarmamatov Sh.M. 134
Nebesniy A.F. 68,69,277
Nematullayev J.R. 223
Nesterenko V.O. 62
Nguyen Tran C.H. 299
Nishonov M.M. 52,122,278
Nishonov Sh.J. 246,247
Normatov E.Kh. 231
Nurimbetov K.K. 164
Nuritdinov I. 164,176,190,193
Nurmammadova F.N. 220
Nurmukhamedov A.M. 73,75,89
Nurmukhanbetova A.K. 35,46,61

O

Oganessian Yu.Ts. 127
Okhunov A.A. 83
Oksengendler B.L. 17
Olimov A.K. 104
Olimov K. 104,107
Olimov Kh.K. 26,104,108,109,111,121
Olkhovich N.M. 60,64
Oskonbaev M.Ch. 31
Otajanov A.M. 171
Otajonov S.M. 171
Otakhonov F.O. 123

P

Pakhnits A.V. 318
Palvanov S.R. 66,114,275
Pan A.N. 96,120
Parpiyev A.S. 144
Passiltay A. 43
Petkevich M. 235
Petrushkin O.V. 127
Piyadin S.M. 316
Pizzone R.G. 35
Podshibiakin A.V. 127
Polyakov A.N. 127
Popeko A.G. 104,127
Popov E. 133
Popov Yu.A. 104
Pyak P. 56

R

Rachkov V.A. 73
Rafikov A.K. 134,166,223
Rakhimkulov M.M. 326
Ramazonov A.X. 275
Rasulova D.R. 238
Rasulova F.A. 62
Rasulova M.Yu. 138
Rikhsiev A.Z. 244,245,248,250
Rogachev G.V. 61
Rogozev A.B. 292
Rosić M. 63
Rozmetova F.Kh. 259,260,265
Rozov S.V. 48
Rusek K. 38
Rustamova Kh.Z. 66

S

Sabelnikov A.V. 127
Sabirov S.S. 228
Saburova G.G. 171
Sadigli L.E. 225
Sadikov I.I. 186,188,243,244,245,259,260,265,289
Sadykov B.M. 36,65,72
Sadyrova M.M. 227
Sagaidak R.N. 127
Saidakhmedov K.X. 190
Saiko V.V. 127
Sailaubekov B. 104
Sairanbayev D. 307
Sakhiyev S.K. 99
Salikhbaev U.S. 326
Sanoev Kh.S. 131
Sarkhadov I. 133
Satpayev M.M. 269
Schlattauer L. 127
Seken D.M. 303
Sergi M.L. 35
Serikbayeva G.E. 46,61
Shadmanov K.K. 125
Shaimerdenov A. 307,308
Shakun N.G. 48
Shamirzaev T.S. 228
Sharipov Z. 133
Sharipova S.M. 259,265
Sharsheev K.Sh. 195
Sherov O.O. 250
Shirchenko M. 22
Shneidman T.M. 36
Shodiev A.A. 170
Shovdirova S.L. 274
Shubin V.D. 127
Shumeiko M.V. 127
Silachyov I. 264
Silnyagin P. 307,308
Sklifasovskaya Y.G. 295
Sobirov S.S. 178
Sobirova Z. 125
Sodiqova Z.Y. 126
Sokol E.A. 104
Sokolenko E.K. 269
Solijonov S.N. 259,260,265
Solnyshkin A.A. 48
Solovyev D.I. 127
Son I.Ya. 38,42
Spartà R. 35
Spaskov V.N. 316
Stegailov V.I. 48
Subbotin V.G. 127
Sulaymanov N.T. 134
Sulaymonov A.A. 144,166,223
Sulaymonov Kh.M. 228
Suleymanov S.Kh. 17
Sultanov M. 237
Surayev A.S. 303
Suvanov A.Kh. 223
Suyunov U.A. 319,321
Svirikhin A.I. 104

T

Tadjibaev D.P. 301,305
Taiirov M.M. 31
Tashimova F.A. 259,265
Tashmetov M.Yu. 134,144,150,152,154,159,178, 183,191,205,206,286
Tasnádi F. 149
Temirbaev M.M. 31
Temirbayeva I.N. 168
Temirov D. 149,326
Temirzhanov A. 36,65,72
Tenelbayev A.G. 61
Tereshkina Yu.A. 232
Teterev Yu.G. 78
Teymurov E. 104
Tezekbayeva M.S. 104
Tiagelskaia A.M. 60,64
Tikhomirov G.V. 299
Tikhonova E.G. 232
Tillayev Sh.B. 279
Tillayev T.S. 279
Tishabaev I.A. 138
Tleulessova I.K. 214
Togtokhtur T. 240
Tojiboev O.R. 38,42,47,66
Tokhirov A. 26,111
Toleubekov K.O. 302,318
Toshev O.S. 85,87
Toshova D.S. 40
Tsyganov Yu.S. 127
Tugalov F. 107
Tukhliev Z. 133
Tumino A. 35
Turaeva N.N. 17
Turakulov S.A. 40
Tursunmakhatov K.I. 45,117,128
Tursunov E.M. 40,54,58
Tuzov A.A. 10
Tynyshbayeva K.M. 180
Tyutyunnikov S.I. 48

U

Udartsev S. 307,309
Ulanova I. I. 104
Umaraliev A.T. 122,278
Umarov Sh.B. 299
Umarova M.O. 299
Urazbekov B.A. 36
Urunov I.A. 321,323
Usarov Z.O. 248,250
Usmanov P.N. 80,81
Usmanova S.A. 290
Ussabayeva G. 36,65,72
Utarov S.M. 161
Utyonkov V.K. 127

V – W

Valiolda D. 43
Vasidov A. 237,256,263
Vasidova S.O. 256
Voinov A.A. 127
Volkova P.Yu. 268
Vorobyev A.S. 60,64
Voronyuk M.G. 127
Wang J.G. 127

Y

Yablochkina A.A. 295,297
Yang H.B. 127
Yarmatov B.Kh. 259,260,265,289
Yavidov B.Ya. 157,171
Ydyrysheva S.K. 258
Yelishenkov A. 309
Yoqubjonov J.H. 223
Yulchiev I.I. 228
Yuldashev D.O. 68,69,233
Yuldashev J.O. 231
Yuldashev M.B. 186
Yuldashev N.Kh. 228
Yuldasheva G.A. 28
Yuldashov D.P. 193
Yushkevich V. 235
Yusupov E.K. 81
Yusupov R.Kh. 261

Z

Zaharova E.V. 268
Zaitsev A. 100
Zarubin P. 100
Zaurbekova Zh. 30,308,309
Zemlyanaya E.V. 232
Zemlyanoy S.G. 71
Zhanbolatov O.M. 303
Zhang M.M. 127
Zhang Z.Y. 127
Zhemenik V.I. 71
Zhigalova A. 304
Zhiyenbayev I.M. 269
Zholdybayev T.K. 36,47,65,72
Zhumatayeva I. 312
Zhumazhanova A.T. 148
Zikirina A.M. 271

CONTACTS OF CONFERENCE PARTICIPANTS

NAME	*ORGANIZATION, COUNTRY*	*E-MAIL ADDRESS*
ABDAMINOV Abror	Institute of Nuclear Physics, Academy of Sciences, Tashkent, **UZBEKISTAN**	abdaminov@inp.uz
ABDUSALOMOVA Mutabar	National University of Uzbekistan, Tashkent, **UZBEKISTAN**	palvanov1960@gmail.com
ADIZOV Sardor	Navoi State University of Mining and Technologies, Navoi **UZBEKISTAN**	sardoradizov447@gmail.com
AITKULOV Magjan	Institute of Nuclear Physics, ARKAE, Almaty, **KAZAKHSTAN**	magzhan.aitkulov@gmail.com, maitkulov@inp.kz
AKHMEDOV Yakub	Institute of Nuclear Physics, Academy of Sciences, Tashkent, **UZBEKISTAN**	yakub8788@gmail.com
AKHMEDZHANOV Farkhad	Institute of Ion-Plasma and Laser Technologies, Tashkent, **UZBEKISTAN**	akhmedzhanov.f@gmail.com
ALDABERGENOVA Tamara	Institute of Nuclear Physics, ARKAE, Almaty, **KAZAKHSTAN**	tamaraalga@mail.ru
ALIKULOV Sherali	Institute of Nuclear Physics, Academy of Sciences, Tashkent, **UZBEKISTAN**	alikulov@inp.uz
ALIMOV Dilshod	Institute of Nuclear Physics, ARKAE, Almaty, **KAZAKHSTAN**	D_alimov@inp.kz
ALTYNBAEV Evgeniy	Saint Petersburg State University, Saint Petersburg, **RUSSIA**	e.altynbaev@spbu.ru
AMIROV Sarvar	New Uzbekistan University, Tashkent, **UZBEKISTAN**	s.amirov@newuu.uz
ANDREEV Denis	NRC «Kurchatov Institute», Moscow, **RUSSIA**	andreev_dv@nrcki.ru
ANDREEV Alexey	DOZA SPC LLC, Zelenograd, Moscow, **RUSSIA**	aas@doza.ru
ASHIN Dmitrii	Federal State Unitary Enterprise "Electrochemical Plant", Lesnoy, Sverdlovsk Region, **RUSSIA**	ashin.d@ehp-atom.ru
ASHRAPOV Ulugbek	Institute of Nuclear Physics, Academy of Sciences, Tashkent, **UZBEKISTAN**	ashrapov-u@inp.uz
ASKERBEKOV Saulet	Institute of Nuclear Physics, ARKAE, Almaty, **KAZAKHSTAN**	askerbekov@physics.kz
ATABAEV Bakhtiyar	Institute of Ion-Plasma and Laser Technologies, Tashkent, **UZBEKISTAN**	atabaev@iplt.uz
AVERKOVA Tatyana	Institute of Nuclear Physics, ARKAE, Almaty, **KAZAKHSTAN**	taverkova@inp.kz
AZNABAYEV Dauren	Joint Institute for Nuclear Research, Dubna, **RUSSIA**	daur_is101@jinr.ru
BABAYEVA Fatima	Azerbaijan University of Architecture and Construction, Institute of Physics, Baku, **AZERBAIJAN**	fatima.babayeva@azmiu.edu.az bfatime126@gmail.com
BAKHROMOV Javlonbek	Institute of High Energy Physics (IHEP), **Beijing, CHINA**	javlonbek27032002@gmail.com
BAYAZOVA Aigul	Kyrgyz National University named after J. Balasagyn, Bishkek, **KYRGYZ REPUBLIC**	bayazova-a@mail.ru

NAME	*ORGANIZATION, COUNTRY*	*E-MAIL ADDRESS*
BELKIN Dmitry	Federal Environmental, Industrial and Nuclear Supervision Service (Rostechnadzor), Moscow, **RUSSIA**	D.Belkin@gosnadzor.gov.ru
BELUSHKIN Alexander	Joint Institute for Nuclear Research, Dubna, **RUSSIA**	belushk@nf.jinr.ru
BERDIBAEV Abdysalam	Kyzyl-Kiya Humanitarian-Pedagogical Institute, Kyzyl-Kiya, **KYRGYZ REPUBLIC**	aberdybaev@gmail.ru
BESPOKOEV Aleksandr	RITVERC JSC, Saint Petersburg, **RUSSIA**	abespokoev@ritverc.com
BOLTABAEV Azizbek	Republican Center for the Storage of Radioactive Waste, Tashkent, **UZBEKISTAN**	akhmedzhanov.f@gmail.com
BOYBOBOYEAVA Sohiba	Institute of Nuclear Physics, Academy of Sciences, Tashkent, **UZBEKISTAN**	sohibaboyboboeva@gmail.com
BOZORBOEV Shodlik	National University of Uzbekistan, Physics Department, Tashkent, **UZBEKISTAN**	shodnucphy@gmail.com
BRYAZGIN Aleksandr	Budker Institute of Nuclear Physics, Siberian Branch, Novosibirsk, **RUSSIA**	a.a.bryazgin@inp.nsk.su
BURIEV Maksud	Institute of Nuclear Physics, Tashkent, **UZBEKISTAN**	abdaminov@inp.uz
CHURKIN Igor	Budker Institute of Nuclear Physics, Siberian Branch of the Russian Academy of Sciences, Novosibirsk, **RUSSIA**	ichurkin@mail.ru
DJANGABAEV Khabibulla	Berdakh Karakalpak State University, Nukus, **UZBEKISTAN**	habibdjangabaev@mail.ru, habibdjangabaev@karsu.uz
DJUMANOV Safarali	Institute of Nuclear Physics, Academy of Sciences, Tashkent, **UZBEKISTAN**	dzhumanov@inp.uz
DOLGOPOLOV Mikhail	Samara State Technical University, Samara, **RUSSIA**	mikhaildolgopolov68@gmail.com
DOSIMOVA Bigul	National Research Nuclear University MEPhI, Moscow, Russian Federation, **UZBEKISTAN**	bbddggaa@gmail.com
DUB Alexey	Private Institution “Science and Innovation”, Moscow, **RUSSIA**	AlVDub@rosatom.ru
DUSHANOV Ermuhammad	Joint Institute for Nuclear Research, Dubna, **RUSSIA**	dushanov@jinr.ru
ELMUROTOVA Dilnoza	State Institution "Scientific and Technical Center for Radiation and Nuclear Safety", Tashkent, **UZBEKISTAN**	d.elmurotova@rnsc.uz
EMELYANENKO Evgeny	N.N. Aleksandrov National Cancer Center Engineer, Minsk, **BELARUS**	zheka-ava@mail.ru
ERALIEV Askar	Ajiniyoz Nukus State Pedagogical Institute, Nukus, **UZBEKISTAN**	asqar.eraliev@ndpi.uz
ERGESHBAEV Adilet	Osh State University, Osh, **KYRGYZ REPUBLIC**	ergeshbaevadilet98@gmail.com
ERDONOV Muzaffar	Institute of Nuclear Physics, Academy of Sciences, Tashkent,	erdonov@inp.uz

NAME	*ORGANIZATION, COUNTRY*	*E-MAIL ADDRESS*
	UZBEKISTAN	
GALDIEV Mirjalol	State Institution "RADIPREPARAT", Tashkent, **UZBEKISTAN**	gmerkinovich@gmail.com
GANIEV Orifjon	Institute of Nuclear Physics, Academy of Sciences, Tashkent, **UZBEKISTAN**	ganiev@inp.uz orif.ganiev@gmail.com
GANYEVA Aynagul	Zhusup Balasagyn Kyrgyz National University, Bishkek, **KYRGYZ REPUBLIC**	Gainagul1974@gmail.com
HAYDAROV Umidjon	Samarkand State University, Samarkand, **UZBEKISTAN**	xaydarovumid02@gmail.com
IBRAIMOVA Sayora	Institute of nuclear physics, Institute of physics and technology, Almaty, **KAZAKHSTAN**	Sayara_ibraimova@mail.ru
IGAMOV Sayrambay	Institute of Nuclear Physics, Academy of Sciences, Tashkent, **UZBEKISTAN**	Igamov63@gmail.com
INOYATOV Anvar	Joint Institute for Nuclear Research (JINR), Dubna, Moscow Region, **RUSSIA**	inoyatov@jinr.ru
ISLAMOV Ahatqul	Institute of Nuclear Physics, Academy of Sciences, Tashkent, **UZBEKISTAN**	Ahatqul@inp.uz
ISMATOV Normamat	Institute of Nuclear Physics, Academy of Sciences, Tashkent, **UZBEKISTAN**	normamat@inp.uz
ISSADYKOV Aydos	Institute of Nuclear Physics, ARKAE, Almaty, **KAZAKHSTAN**	a.issadykov@inp.kz
ITKIS Mikhail	Joint Institute for Nuclear Research (JINR), Dubna, Moscow Region, **RUSSIA**	itkis@jinr.ru
JORDANOV Dragana	Institute for Nuclear Science VINCA, Belgrade, **SERBIA**	djordano@vin.bg.ac.rs djordano@vinca.rs
JUMAEV Mustakim	Bukhara State Technical University, Bukhara, **UZBEKISTAN**	mrjumaev2011@mail.rru
JURAQULOV Alisher	Navoi State University of Mining and Technologies, Navoiy, **UZBEKISTAN**	ali_80_84@mail.ru
KABANOV Igor	Federal State Unitary Enterprise "Electrochemical Plant", Zelenogorsk, Krasnoyarsk Krai, **RUSSIA**	kabanov.i@ehp-atom.ru
KABULOV Ilyas	Tashkent Institute of Irrigation and Agricultural Mechanization Engineers National Research University, Tashkent, **UZBEKISTAN**	ilyoskabulov00@gmail.com
KABYTAYEVA Raushan	Joint Institute for Nuclear Research, Dubna, **RUSSIA**	kabytayeva@jinr.ru
KADENOVA Batmakan	Osh State University, Osh, **KYRGYZ REPUBLIC**	kadenova66@mail.ru
KADYROV Alisher	Department of Physics and Astronomy, Curtin University, Perth, **AUSTRALIA**	a.kadyrov@curtin.edu.au
KAIYRBEKOVA Altyn	Institute of Nuclear Physics, ARKAE, Almaty, **KAZAKHSTAN**	a.kaiyrbekova@inp.kz

NAME	*ORGANIZATION, COUNTRY*	*E-MAIL ADDRESS*
KAKHOROVA Aziza	Samarkand State University, Samarkand, **UZBEKISTAN**	azizakakhorova@gmail.com
KALANOV Makhmud	Institute of Nuclear Physics, Academy of Sciences, Tashkent, **UZBEKISTAN**	kalanov@inp.uz
KATTABEKOV Rasuljon	Joint Institute for Nuclear Research, Dubna, **RUSSIA**	kattabekov@jinr.ru
KAYUMOVA Mansuba	Institute of Nuclear Physics, Academy of Sciences, Tashkent, **UZBEKISTAN**	mansuba_qayumova@inp.uz
KENZHINA Inesh	Satbayev University, Almaty, **KAZAKHSTAN**	kenzhina@physics.kz
KHAJIEV Lazizbek	State Institution "RADIPREPARAT", Tashkent, **UZBEKISTAN**	hajiyev.lazizbek@mail.ru
KHAMETOV Shyngys	L.N. Gumilyov Eurasian National University, Astana, **KAZAKHSTAN**	kh.shyngys@gmail.com
KHAMETOVA Aynagul	Astana Branch of the Institute of Nuclear Physics, Astana, K**AZAKHSTAN**	khametovaaa@gmail.com
KHASANOV Javlonbek	National University of Uzbekistan, Tashkent, **UZBEKISTAN**	Khasanovjavlonbek20@gmail.com
KHASANOV Kholmurod	Samarkand State University, Samarkand, **UZBEKISTAN**	kholkh@bk.ru
KHAYDAROV Renat	Institute of Nuclear Physics, Academy of Sciences, Tashkent, **UZBEKISTAN**	renat@inp.uz renat2@gmail.com
KHUDOYBERDIEVA Shokhida	Physical-Technical Institute of Uzbekistan Academy of Sciences, Tashkent, **UZBEKISTAN**	xudoyberdiyevashohida676@gmail.com
KHURRAMOVA Sevara	Institute of Nuclear Physics, Academy of Sciences, Tashkent, **UZBEKISTAN**	xurramova@inp.u
KHUSHVAKTOV Jurabek	Joint Institute for Nuclear Research, Dubna, **RUSSIA**	khushvaktov@jinr.ru
KIM Andrey	Institute of Nuclear Physics, Academy of Sciences, Tashkent, **UZBEKISTAN**	aakim2012@mail.ru
KIYAVITSKAYA Hanna	International Environmental Sakharov Institute Belarussian State University, Minsk, **BELARUS**	hannakiev@gmail.com
KONSTANTINOV Vasily	LLC "Leader of the Consortium "International Research Center based on the MBIR Reactor" Moscow, **RUSSIA**	VasiLeoKonstantinov@rosatom.ru
KORJAVOV Mustafa	Karshi state technical university, Karshi, **UZBEKISTAN**	mkorj1965@gmail.com
KOSHERBAYEVA Raisa	Institute of Nuclear Physics, Almaty, **KAZAKHSTAN**	r.kosherbayeva@inp.kz
KOZLOVSKIY Artem	Institute of Nuclear Physics, Astana, **KAZAKHSTAN**	Artem88sddt@mail.ru
KRASSOVITSKIY Pavel	Institute of Nuclear Physics, Astana, **KAZAKHSTAN**	pavel.kras@inp.kz
KRUGLYAK Anastasiya	Joint Institute for Nuclear Research, Dubna, **RUSSIA**	kruglyakai@ya.ru

NAME	*ORGANIZATION, COUNTRY*	*E-MAIL ADDRESS*
KRUGLYAK Nikolai	Joint Institute for Nuclear Research, Dubna, **RUSSIA**	krugliak-nik-ak@mail.ru
KULABDULLAEV Gayratulla	Institute of Nuclear Physics, Academy of Sciences, Tashkent, **UZBEKISTAN**	gkulabdullaev@inp.uz, kulabdgairat@mail.ru
KULDJANOV Bakhrom	Scientific and Technical Center for Radiation and Nuclear Safety, Tashkent, **UZBEKISTAN**	kuldjanov@inp.uz
KULIKOV Sergey	Joint Institute for Nuclear Research (JINR), Dubna, Moscow Region, **RUSSIA**	ksa@nf.jinr.ru
KULSARTOV Timur	Institute of Applied Sciences and Information Technologies, Almaty, **KAZAKHSTAN**	tima@physics.kz
KURBANOV Bakhtiyar	Institute of Nuclear Physics, Academy of Sciences, Tashkent, **UZBEKISTAN**	bkurbanov@inp.uz
KUYLIEV Fayzullo	National Research Nuclear University "MEPhI", Moscow, **RUSSIA**	quyliyevfayzulla@gmail.com
LA COGNATA Marco	National Institute of Nuclear Physics Southern National Laboratories, Catania, **ITALY**	lacognata@lns.infn.it quarktop1979@gmail.com
LENNIK Svetlana	Institute of Nuclear Physics, ARKAE, Almaty, **KAZAKHSTAN**	lennik_s@inp.kz
LYCHAGIN Egor	Joint Institute for Nuclear Research, Dubna **RUSSIA**	lychag@nf.jinr.ru
MADAMINOV Bakhtiyar	Institute of Nuclear Physics, Academy of Sciences, Tashkent, **UZBEKISTAN**	madaminov.b@inp.uz
MADIYAROV Daniyar	Institute of Nuclear Physics, Academy of Sciences, Tashkent, **UZBEKISTAN**	madiyarov@inp.uz
MALIKOV Shavkat	Institute of Nuclear Physics, Academy of Sciences, Tashkent, **UZBEKISTAN**	malikov@inp.uz
MAMYTBEKOV Ulanbek	Institute of Physics named after Academician J. Zheenbaev, National Academy of Sciences of the Kyrgyz Republic, Bishkek, **KYRGYZ REPUBLIC**	Ulan-mk@bk.ru
MARKELOVA Elena	Institute of Nuclear Physics, Academy of Sciences, Tashkent, **UZBEKISTAN**	hopel1988@mail.ru
MARTYNENKO Yekaterina	Institute of Atomic Energy of the National Nuclear Center, Almaty, **KAZAKHSTAN**	Kirichek@nnc.kz
MEKHMONOV Golibjon	Institute of Nuclear Physics, Academy of Sciences, Tashkent, **UZBEKISTAN**	m.golibjon99@gmail.com
MIRBABAEV Shuhrat	Tashkent State Medical University, Republic of Uzbekistan, Tashkent, **UZBEKISTAN**	Shuhrat.mirboboyev@gmail.com
MIRMANOVA Diana	Institute of Nuclear Physics, ARKAE, Almaty, **KAZAKHSTAN**	d.meirmanova@inp.kz diana.uk.2014@gmail.com

NAME	*ORGANIZATION, COUNTRY*	*E-MAIL ADDRESS*
MUKASHOVA Aida	Institute of Physics named after Academician J. Zheenbaev, Bishkek, **KYRGYZ REPUBLIC**	aida_mukashova@mail.ru
MUKHAMEDOV Boburjon	Scientific and Technical Center for Radiation and Nuclear Safety, Tashkent, **UZBEKISTAN**	b.mukhamedov@rnsc.uz
MUMINOV Alisher	Institute of Nuclear Physics, Academy of Sciences, Tashkent, **UZBEKISTAN**	almuminov1969@yandex.com
MUSAEV Kobil	Physical-Technical Institute of Uzbekistan Academy of Sciences, Tashkent, **UZBEKISTAN**	qobilmusayev1986@gmail.com
MUZAFAROV Amrullo	Navoi State University of Mining and Technologies, Navoiy, **UZBEKISTAN**	a.muzafarov@ngmk.uz
NAURUZBAYEV Dosbol	Nazarbayev University Research Administration, Astana, **KAZAKHSTAN**	dosbol.nauruzbayev@nu.edu.kz
NEBESNIY Anatoliy	Institute of Nuclear Physics, Academy of Sciences, Tashkent, **UZBEKISTAN**	nanatoly@yandex.ru
NISHONOV Mukhtorali	National University of Uzbekistan, Tashkent, **UZBEKISTAN**	m.nishonov@nuu.uz
NISHONOV Sherzodjon	State Institution “RADIPREPARAT”, Tashkent, **UZBEKISTAN**	sherzod-n@rambler.ru
NURIMBETOV Kurbanbay	Institute of Nuclear Physics, Academy of Sciences, Tashkent, **UZBEKISTAN**	keunimjayuli@gmail.com
NURMUKHANBETOVA Aliya	Nazarbayev University Research Administration, Astana, **KAZAKHSTAN**	aknurmukhanbetova@gmail.com
NURMUXAMEDOV Abdufattax	Tashkent State Medical University, Tashkent, **UZBEKISTAN**	abdufattax@yahoo.com
OKHUNOV Abdurahim	Namangan State Technical University, Namangan, **UZBEKISTAN**	abdurahimokhun@iium.edu.my, mhsr70@gmail.com
OKSENGENDLER Boris	Institute of Materials Science, Academy of Sciences, Tashkent, **UZBEKISTAN**	oksengendlerbl@yandex.ru
OLIMOV Kosim	Physical-Technical Institute named after S.A. Azimov, Academy of Sciences, Tashkent, **UZBEKISTAN**	Kosolimov@gmail.com
OLIMOV Khusniddin	Physical-Technical Institute of Uzbekistan Academy of Sciences, Tashkent, **UZBEKISTAN**	khkolimov@gmail.com
OLKHOVICH Nikita	National Research Center “Kurchatov Institute”, Moscow, **RUSSIA**	olhovich_nm@pnpi.nrcki.ru
OSKONBAEV Maralbek	Batken State University (Batken SU), Batken, **KYRGYZ REPUBLIC**	o_manas@mail.ru
PARPIEV Adkhamjon	Institute of Nuclear Physics, Academy of Sciences, Tashkent, **UZBEKISTAN**	parpiev@inp.uz
PASSILTAY Ainur	Kazakh National University, Astana, **KAZAKHSTAN**	Pasyltay.aynur@mail.ru

NAME	*ORGANIZATION, COUNTRY*	*E-MAIL ADDRESS*
POLVONOV Satimboy	National University of Uzbekistan, Tashkent, **UZBEKISTAN**	palvanov1960@gmail.com
PYAK Pavel	Institute of Nuclear Physics, Academy of Sciences, Tashkent, **UZBEKISTAN**	pavelpyakuz@gmail.com
RACHKOV Vladimir	Flerov Laboratory of Nuclear Reactions, Joint Institute for Nuclear Research, Dubna, **RUSSIA**	rachkov@jinr.ru
RAFIKOV Avaz	Institute of Nuclear Physics, Academy of Sciences, Tashkent, **UZBEKISTAN**	rafikov@inp.uz
RASULOVA Dildora	Institute of Nuclear Physics, Academy of Sciences, Tashkent, **UZBEKISTAN**	rasulova.d@inp.uz; rasulovadildora0@gmail.com
RASULOVA Fazilat	Joint Institute for Nuclear Research, Dubna, Moscow, Russian Federation, **UZBEKISTAN**	rasulova@jinr.ru
ROGOZEV Alexey	RITVERC JSC, Saint Petersburg, **RUSSIA**	alexrogozev@ritverc.com
ROZMETOVA Feruza	Institute of Nuclear Physics, Academy of Sciences, Tashkent, **UZBEKISTAN**	frozmetova240489@gmail.com
SABUROVA Gulnoza	Ajiniyoz Nukus State Pedagogical Institute, Nukus, **UZBEKISTAN**	g.saburova@ndpi.uz
SADYROVA Mukhabat	Osh State University, Osh, **KYRGYZ REPUBLIC**	yasmin67@mail.ru
SADYKOV Bakhtiyar	Institute of Nuclear Physics, ARKAE, Astana, **KAZAKHSTAN**	sadykovbm@inp.kz
SAIDAKHMEDOV Kakhramon	Institute of Nuclear Physics, Academy of Sciences, Tashkent, **UZBEKISTAN**	skhahramon@yandex.ru
SERGI Maria Letizia	University of Catania & LNS-INFN, Catania, **ITALY**	marialetizia.sergi@gmail.com
SERIKBAYEVA Gulfairuz	Nazarbayev University Research Administration, Astana, **KAZAKHSTAN**	gulfairuz.serikbayeva@nu.edu.kz
SHADMANOV Kamoliddin	Institute of Pharmaceutical Education and Research, Tashkent, **UZBEKISTAN**	shodman@mail.ru
SHARIPOV Zarif	Joint Institute for Nuclear Research, Dubna, **RUSSIA**	zarif@jinr.ru
SHARIPOVA Sadokat	Institute of Nuclear Physics, Academy of Sciences, Tashkent, **UZBEKISTAN**	Sadoqatsharipova90@gmail.com
SHIRCHENKO Mark	Joint Institute for Nuclear Research, Dubna, **RUSSIA**	Mark.Shirchenko@jinr.ru
SHODIYEV Ahmad	Institute of Nuclear Physics, Academy of Sciences, Tashkent, **UZBEKISTAN**	akhmadshodiyev@gmail.com
SHOVDIROVA Saodat	Institute of Nuclear Physics, Academy of Sciences, Tashkent, **UZBEKISTAN**	shovdirovasaodat@gmail.com
SILNYAGIN Pavel	Institute of Nuclear Physics, ARKAE, Astana, **KAZAKHSTAN**	Silnyaginpp65@gmail.com

NAME	*ORGANIZATION, COUNTRY*	*E-MAIL ADDRESS*
SOBIROVA Zebo	Institute of Nuclear Physics, Academy of Sciences, Tashkent, **UZBEKISTAN**	zeboabduqahhorova4@gmail.com
SODIKOVA Zilola	Institute of Nuclear Physics, Academy of Sciences, Tashkent, **UZBEKISTAN**	zilolasodiqova28@gmail.com
SON Irina	Institute of Nuclear Physics, Academy of Sciences, Tashkent, **UZBEKISTAN**	tvist1378@mail.ru
STEGAILOV Vladimir	Joint Institute for Nuclear Research, Dubna, **RUSSIA**	Mark.Shirchenko@jinr.ru
SULAYMANOV Nodimjon	Institute of Nuclear Physics, Academy of Sciences, Tashkent, **UZBEKISTAN**	sulaymon@inp.uz
SURAYEV Artur	Institute of Atomic Energy of the National Nuclear Center, Kurchatov, **KAZAKHSTAN**	suraev@nnc.kz
SUYUNOV Uktam	Navoi State University of Mining and Technologies, Navoiy, **UZBEKISTAN**	Suyunovuktam040@gmail.com
TAIIROV Mutalip	Batken State University (Batken SU), Batken, **KYRGYZ REPUBLIC**	mtaiirov13@mail.ru
TEMIRBAEV Mederbek	Osh State University (Osh SU), Osh, **KYRGYZ REPUBLIC**	mtaiirov13@mail.ru
TEMIRBAYEVA Inabat	Institute of Nuclear Physics, Academy of Sciences, Tashkent, **UZBEKISTAN**	temirbayevainabat0101@gmail.com
TEMIRZHANOV Alisher	Institute of Nuclear Physics, ARKAE, Almaty, **KAZAKHSTAN**	alik-25.01.97@mail.ru
TENELBAYEV Assylzhan	Nazarbayev University Research Administration, Astana, **KAZAKHSTAN**	assylzhan.tenelbayev@nu.edu.kz
TIAGELSKAIA Aleksandra	National Research Center "Kurchatov Institute", Moscow, **RUSSIA**	tiagelskaia_am@pnpi.nrcki.ru
TILLAEV Tulkin	Institute of Nuclear Physics, Academy of Sciences, Tashkent, **UZBEKISTAN**	tillaev1946@mail.ru
TISHABAEV Ilkhom	Institute of Nuclear Physics, Academy of Sciences, Tashkent, **UZBEKISTAN**	itishaboev@yahoo.com
TOLEUBEKOV Kuanyshbek	Institute of Atomic Energy of the National Nuclear Center, Almaty, **KAZAKHSTAN**	toleubekov@nnc.kz
TOSHEV Oybek	Navoi State University, Navoiy **UZBEKISTAN**	sulaymonovichoybek@gmail.com
TOSHOVA Dilorom	Institute of Nuclear Physics, Academy of Sciences, Tashkent, **UZBEKISTAN**	toshova@inp.uz
TUGALOV Farkhod	Jizzakh State Pedagogical University, Jizzakh, **UZBEKISTAN**	farxodtugalov@mail.ru
TURSUNMAKHATOV Kakhramon	Gulistan State University, Guliston, **UZBEKISTAN**	tursunmahatovkahramon@gmail.com

NAME	*ORGANIZATION, COUNTRY*	*E-MAIL ADDRESS*
TUZOV Aleksandr	State Scientific Center – Research Institute of Atomic Reactors, Moscow, **RUSSIA**	niiar@niiar.ru
TYNYSHBAYEVA Kymbat	Satbayev University Almaty, **KAZAKHSTAN**	tinishbaeva.kimbat@mail.ru
UMARALIEV Akmal	Bondell Integrated Solutions MChJ, Tashkent, **UZBEKISTAN**	akmal.umaraliev@gmail.com
UMAROV Shohmirzo	Atomic Energy Agency under the Cabinet of Ministers of the Republic of Uzbekistan (Uzatom), Tashkent, **UZBEKISTAN**	shumarov@uzatom.uz
URUNOV Isakul	Navoi State University of Mining and Technologies, Navoiy, **UZBEKISTAN**	sulaymonovichoybek@gmail.com
USAROV Zafar	State Institution "RADIPREPARAT", Tashkent, **UZBEKISTAN**	zafar.usarov@yandex.ru
USMANOV Pazlitdin	Namangan State Technical University, Namangan, **UZBEKISTAN**	usmanov1956.56@mail.ru
USSABAYEVA Gulnaz	Institute of Nuclear Physics, ARKAE, Almaty, **KAZAKHSTAN**	gulnazim85@inbox.ru
UTAROV Serik	Institute of Nuclear Physics, Academy of Sciences, Tashkent, **UZBEKISTAN**	utarovserik7@gmail.com
VASIDOV Abdisamat	Institute of Nuclear Physics, Academy of Sciences, Tashkent, **UZBEKISTAN**	samad@inp.uz
VASIDOVA Sevara	Institute of Nuclear Physics, Academy of Sciences, Tashkent, **UZBEKISTAN**	vasidova91@mail.ru
WU Sang-Ik	KAERI, Korea Atomic Energy Research Institute, Daejeon, **SOUTH KOREA**	siwu@kaeri.re.kr
YABLOCHKINA Angelina	State Institution "Scientific and Technical Center for Radiation and Nuclear Safety", Tashkent, **UZBEKISTAN**	evelejn63@gmail.com
YARMATOV Bakhrom	Institute of Nuclear Physics, Academy of Sciences, Tashkent, **UZBEKISTAN**	yarmatov@inp.uz
YAVIDOV Bahram	Ajiniyoz Nukus State Pedagogical Institute, Nukus, **UZBEKISTAN**	bakhrom.yavidov@ndpi.uz
YDYRYSHEVA Saulet	Institute of Nuclear Physics, ARKAE, Almaty, **KAZAKHSTAN**	s.ydyrysheva@inp.kz
YELISHENKOV Alexandr	Satbayev University, Almaty, **KAZAKHSTAN**	aleksandrelisenkov282@gmail.com
YULDASHEV Djasur	Bukhara State Medical Institute, Bukhara, **UZBEKISTAN**	yuldashev.d@inp.uz
YULDASHOV Dauranbek	Institute of Nuclear Physics, Academy of Sciences, Tashkent, **UZBEKISTAN**	dawranfizika@gmail.com
YUSUPOV Elmurod	Namangan State Technical University, Namangan, **UZBEKISTAN**	yusupov.elmurod@mail.ru
ZAITSEV Andrei	Joint Institute for Nuclear Research, Dubna, **RUSSIA**	zaicev@jinr.ru
ZEMLYANAYA Elena	Joint Institute for Nuclear Research, Dubna, **RUSSIA**	elena@jinr.ru elena_zemlyanaya@uni-dubna.ru

NAME	*ORGANIZATION, COUNTRY*	*E-MAIL ADDRESS*
ZEMLYANOY Sergey	Joint Institute for Nuclear Research, Dubna, **RUSSIA**	zemlya@jinr.ru
ZHOLDYBAYEV Timur	Institute of Nuclear Physics, Almaty, **KAZAKHSTAN**	Zholdybayev@inp.kz
ZHUMATAYEVA Inesh	L.N. Gumilyov Eurasian National University, Astana, **KAZAKHSTAN**	Inesh.zhumatayeva@gmail.com
ZHUMAZHANOVA Ainash	Astana Branch of the Institute of Nuclear Physics, Astana, **KAZAKHSTAN**	a.zhumazhanova@inp.kz
ZIKIRINA Ainur	Satbayev University, Almaty, **KAZAKHSTAN**	agun_zikirina@mail.ru

CONTENTS

CONTENTS

PLENARY REPORTS

Neutron Research of Ferroelectrics, Ferroelastics and Superprotonic Materials. A Historical Overview and Current Developments
Belushkin A.V. 9

High-Energy Industrial Electron Accelerators ILU Type for Medical Device Sterilization and Food Irradiation
Bryazgin A. 10

Production of Radiochemicals for Medical Application at Rosatoms' Scientific Division
Tuzov A.A. 10

Measurement of $^{19}F(p, \alpha\gamma)^{16}O$ Reaction Reopens the Fluorine Conundrums in Stars
LaCognata M. 11

Radiation-Heterogeneous Processes of Water Decomposition on the Surface of Metallic and Nano-Aluminum
Agayev T.N. 12

Electrochemical Synthesis of Carbon Nanostructures and their Application for Heavy-Metal Removal from Water
Khaydarov R.R., Gapurova O.U., Naumovskiy V.B., Galiulin I.G. 14

The Experimental Infrastructure of the Laboratory of Neutron Physics for Research
Lychagin E.V. 16

Synergism of Ionization and Shock Wave Effects in Complex Media under Intense Radiation Exposure
Oksengendler B.L., Suleymanov S.Kh., Ashurov M.Kh., Turaeva N.N., Akhmatova G.Y., Ibrokhimov R.R. 17

Beyond the Headline Efficiency Number: A Metrology-Driven Benchmark of 2025–2026 Betavoltaic Converters from Perovskite to SiC
Dolgopolov M.V. 19

DSTAR: a Modular 4π Muon Detector Cosmic Ray Measurements
Dovbnenko M., Fateev S., Kuznetsov A., Shirchenko M. 22

Distinctive Doping- and Temperature-Dependent Metallic Conductivity in Moderately Doped Y-Based Cuprate Superconductors
Dzhumanov S., Kurbanov U.T., Djumanov Sh.S. 23

Collisional Breakup in a Coulomb Few-Body System with Two Attractive Centers
Kadyrov A.S. 24

Centrality Dependencies of Transverse Momentum Distributions of Identified Light-Flavor Hadrons in p+Pb Collisions at $\sqrt{s_{nn}}$ = 5.02 TeV at the LHC within a Two-Component Model
Olimov Kh.K., Fedosimova A., Liu Fu-Hu, Musaev K.A., Lebedev I.A., Tokhirov A., Ibraimova S., Bondar E. 26

The Effect of the Entrance Channels on the Dynamics of the Competition of Processes of in Heavy-Ion Collisions
Nasirov A.K., Kayumov B.M., Yuldasheva G.A., Ganiev O.K., Khusanov E.D. 27

Siberian Circle Source of Photons (SKIF): Physical Possibilities and Technical Requirements
Churkin I. 29

Assessment of the Possibility of Predicting the Average Integral CLTE of Reactor Materials up to 1800 °C Based on Dilatometry Data up to 1000°C
Kulsartov T., Baklanova Yu., Kenzhina I., Zaurbekova Zh. 30

Optical and Luminescent Development of Vacancy Defects in Alkali-halide crystals (KBr, KCl)
Taiirov M.M., Oskonbaev M.Ch., Berdibaev A.K.,Temirbaev M.M. 31

On Training of a Staff for Nuclear Power at the International Sakharov Environmental Institute of Belarusian State University
Kiyavitskaya H., Dashkevich T., Gusakova O., Germenchk M. 33

Section I. THEORETICAL AND EXPERIMENTAL NUCLEAR PHYSICS

^{21}Ne Structure in the ^{17}O (α,α) Resonance Reaction
Nauruzbayev D.K., Nurmukhanbetova A.K., Goldberg V.Z., La Cognata M., Di Pietro A., Figuera P., Cherubini S., Gulino M., Lamia L., Pizzone R.G., Spartà R., Tumino A. 35

Neutron Induced Reactions Explored Via the Trojan Horse Method
Sergi M.L. on behalf of ASFIN collaboration 35

Single-Proton Transfer in the Reaction ^{45}Sc(^{3}He,d)^{46}Ti at 29 MeV
Sadykov B.M., Zholdybayev T.K., Duisebayev B., Ussabayeva G., Temirzhanov A., Mendibayev K.O., Issatayev T., Urazbekov B.A., Shneidman T.M. 36

Calculation of the Astrophysical S-Factor and Reaction Rate for the ^{11}B(p,γ)^{12}C Reaction Using ANC Information for Bound States
Igamov S.B., Artemov S.V., LaCognata M., Rusek K., Son I.Ya., Tojiboev O.R., Ergashev F.Kh. 38

The Estimation of the Astrophysical $S_{17}(0)$-factor of the ^{7}Be(p,γ)^{8}B Direct Capture Process within a Three-Body Model
Tursunov E.M., Toshova D.S., Turakulov S.A. 40

New Spectroscopic Information for Nucleosynthesis Calculations: ANCs of ^{7}Li, ^{12}B, and ^{12}C
Son I.Ya., Artemov S.V., Karakhodzhaev A., Tojiboev O.R., Ergashev F.Kh. ... 42

Study of the ^{11}Be Halo Nucleus in Breakup Reactions Within a Quantum–Quasiclassical Approach
Passiltay A., Valiolda D., Janseitov D., Melezhik V., Hamada Sh. ……... 43

Influence of the Three-Body Coulomb Effects on the Values of Asymptotic Normalization Coefficients for ^{12}C+p→^{13}N and Astrophysical S-Factor of the ^{12}C(p,γ)^{13}N Reaction
Tursunmakhatov K.I. ……... 45

R-matrix Analysis of ^{22}Ne States Populated in ^{18}O(α,α) Resonant Elastic Scattering
Serikbayeva G. E., Nurmukhanbetova A.K., Goldberg V.Z., Nauruzbayev D.K. …… 46

Elastic and Inelastic Scattering of α Particles on ^{25}Mg AT E_α = 29 MeV
Artemov S.V., Tojiboev O.R., Burtebayev N., Nasurlla Maulen, Zholdybayev T.K., Ikromkhonov E.Sh., Ergashev F.Kh., Karakhodzhaev A.A., Igamov S.B. …….. 47

Study of the Decay of High-Spin Isomers of Holmium Nuclei with A=156,158,160
Kalinnikov V.G., Stegailov V.I., Rozov S.V., Gons Z., Khushvaktov J.Kh., Kobets V.V., Solnyshkin A.A., Kartavenko V.G., Tyutyunnikov S.I., Shakun N.G. ……..…… 48

Beta Decay Half-Life of ^{41}Sc
Irgaziev B.F., Khasanov J.A. ……... 50

From Orthogonalizing Pseudopotential to the Feshbach–Schur Projection
Nishonov M.M. ……..…… 52

Study of the ^{11}C and ^{11}B Nuclear Structures Within the Three - Cluster Models α+ α+^{3}He and α+ α+^{3}H
Tursunov E.M., Khurramova S.N. ……..……..…….. 54

Elastic Scattering and Breakup in the e^- + d Reaction Within the Three-Body Faddeev Formalism: a Verifiable Computational Scheme
Pyak P., Igamov S., Khugaev A. ……..…… 56

Comparative Assessment of Geant4 Cascade Models for the Production of ^{11}C in Proton-Induced Reactions on ^{16}O at 15–200 MeV
Kayumova M.Sh., Tursunov E.M. ……..……. 58

Calculation of the GNEIS Neutron Source Spectra Using Geant4 Software Package
Tiagelskaia A.M., Olkhovich N.M., Vorobyev A.S. ……...…… 60

Experimental Studies of Resonant Reactions at Low Energies
Nurmukhanbetova A.K., Goldberg V.Z., Nauruzbayev D.K., Serikbayeva G., Tenelbayev A.G., Ilin K.P., Rogachev G.V. …… 61

Isospin Splitting of Giant Dipole Resonance in Medium and Heavy Nuclei
Rasulova F.A., Kuznetsov A.A., Nesterenko V.O., Khushvaktov J.H., Alekseev S.I., Fursova N.Yu., Madumarov A.S., Chuprakov I., Aksenov N.V. .. 62

The metrology of HPGe Detectors: Application of a Novel Method to the Decay of Bi-07
Jordanov D., Nadjdjerdj L., Inoyatov A., Khushvaktov J.Kh., Čebela M., Rosić M. ……. 63

Simulation of the Process of Measuring the Fast Neutron Flux Using the Bicron Detector in the νGeN Experiment
Khushvaktov J.Kh. for the νGeN collaboration ……..……. 64

Calculation of the Efficiency of the FISCO Multi-Section Detector Using Geant4 Software Package
Olkhovich N.M., Tiagelskaia A.M., Vorobyev A.S. …….. 64

Mechanisms of Proton and Deuteron Emission from ^{59}Co and ^{103}Rh Induced by Deuterons at Medium Energies
Temirzhanov A., Zholdybayev T., Sadykov B., Ussabayeva G., Duisebayev B. .. 65

Excitation Cross Section of Isomeric States in Reactions (γ,n) and (n,2n) on ^{197}Au Nuclei
Palvanov S.R., Inoyatov A.X., Eshanqulov G.I., Rustamova Kh.Z., Axmedov S.E., Tojiboev O.R. ……..…… 66

Reconstruction and Comparison of Neutron-Gamma Spectra at the Collimator Exit of the VVR-SM Reactor Horizontal Channel Using OPENMC and GEANT4
Kulabdullaev G.A., Abdullaeva G.A., Kim A.A., Nebesniy A.F., Yuldashev D.O. ……..... 68

Comparison of Neutron–Gamma Spectra Calculated Using OPENMC and GEANT4 With Experimental Spectra in Different Media
Kulabdullaev G.A., Abdullaeva G.A., Kim A.A., Nebesniy A.F., Yuldashev D.O. ……..…….. 69

Nuclear Structure Investigation by Laser Spectroscopy Methods at FLNR JINR
Zemlyanoy S.G., Myshinsky G.V., Zhemenik V.I. …… 71

Development of a Low-Cost Multichannel Spectrometer Based on the Dynamic Time-Over-Threshold Method
Temirzhanov A., Zholdybayev T., Sadykov B., Ussabayeva G., Duisebayev B., Issatov A. …….……..…….. 72

Study of Fusion of Ca Isotopes with ^{208}Pb at the Energies Around the Coulomb Barrier
Rachkov V.A., Karpov A.V., Kozulin E.M., Knyazheva G.N., Bogachev A.A. .. 73

Alpha-Decay Energy of New Superheavy Nuclei
Nurmukhamedov A.M. ……..……..…… 73

Precise Mass Calculations for Atomic Nuclei of Isospin T_z = 51/2, 26, 53/2, 55/2, 28 and 57/2
Nurmukhamedov A.M. ……..……..…… 75

Monte Carlo Simulation of Induced Activation of Accelerator Components for the U-400R and DC-280 Cyclotrons
Kabytayeva R.K., Teterev Yu.G., Mitrofanov S.V., Kalagin I.V., Gulbekyan G.G., Kuthudzhin D.V. ……. 78

Magnetic Properties of Vibrational States of ^{182,184}W Isotopes
Usmanov P.N., Izosimov I.N. ……..……..…… 80

Energy Characteristics of States Low-Lying Rotational Bands Isotopes ^{182,184}W
Usmanov P.N., Korjavov M.J., Yusupov E.K. …… 81

Formalism of Nuclear Rotational Stretching and the Moment of Inertia
Okhunov A.A., Mohd' Kh. M. Abu El Sheik ……..……... 83

Dependence of the α-Particle Mean Free Path on Radionuclide Specific Activity in the Uranium Decay Chain
Toshev O.S., Allaberganova G.M., Muzafarov A.M. ……. 85

Quantum-Mechanical Analysis of the Relationship Between Nuclear Properties of Uranium-Series Nuclides and α -Particle Tunneling Probability
Toshev O.S., Mustafoyev M.A., Allaberganova G.M., Muzafarov A.M. ……. 87

On the Validity of Applying the Student's t-Criterion to Experimentally Prove the Restoration of Wigner's *SU*(4) - Symmetry in Nuclei
Mirbabaev Sh.R., Nurmukhamedov A.M. …….. 89

Electromagnetic Waves of General Appearance in Lewis Space-Time in Vacuume and Conducting Media
Muminov A.T. …… 91

Application of TALYS and Geant4 for the Study of Photonuclear and Neutron-Induced Reaction Cross Sections
Bozorboev Sh.G., Khoshimjonov Kh., Egamova F.R., Beknazarova N.Y. …….. 93

Calculation of Relative Yields and Flux-Averaged Cross Sections of Photonuclear Reactions in the ^{165}Ho Nucleus
Kuyliev F.Y., Khushvaktov J.H., Khoshimjonov Kh. ……... 94

Deformed Nuclear Shells in Mass and Energy Distributions of Fission Fragments of ^{234}Np* Compound Nucleus Formed in ^{233}U(p,f) Reaction at Ep= 22 MeV
Alimov D.K., Pan A.N., Kovalchuk K.V., Burtebayev N., Janseitov D.M., Boztosun I., Kosherbayeva R. …….. 96

Mass and Angular Distributions of Reaction Products in ^{40}Ca + ^{238}U and ^{40}Ca + ^{197}Au Using a TOF Spectrometer
Aznabayev D., Issatayev T., Lukyanov S.M., Maslov V.A., Mendibayev K. ….. 97

B-Meson Rare Decays
Issadykov A., Ivanov M.A., Sakhiyev S.K. ……. 99

Overview of Studies of the ^{8}Be Nucleus and the Hoyle State in the Dissociation of Relativistic Nuclei
Artemenkov D., Zaitsev A., Zarubin P. 100

Survival Probability and Evaporation-Residue Cross Sections in the $^{48}Ca + ^{244}Pu \rightarrow ^{292}Fl^*$ Reaction
Amirov S., Kayumov B.M. ……. 101

First Investigation of Prompt Neutrons from Spontaneously Fissioning Isomers Produced in Multinucleon Transfer Reactions
Sailaubekov B., Svirikhin A.I., Devaraja H.M., Isaev A.V., Mukhin R.S., Bychkov M.A., Chelnokov M.L., Chepigin V.I., Danilkin V.D., Izosimov I.N., Kalandarov Sh.A., Katrasev D.E., Kuznetsova A.A., Malyshev O.N., Popeko A.G., Popov Yu.A., Sokol E.A., Teymurov E., Tezekbayeva M.S., Ulanova I.I. ……. 104

Possible Formation of Four-Proton States in ^{12}C–^{12}C Collisions at 3.37 A GeV
Olimov K., Gulamov K.G., Olimov Kh.K., Bakhodirov Sh.Sh., Olimov A.K. … 104

A Correlation Method for Centrality Estimation in Asymmetric Nucleus-Nucleus Interactions
Ibraimova S.A., Lebedev I.A. ……... 106

Study of the Formation of Δ^0 Isobars in Central $p^{12}C$ and $d^{12}C$ Collisions at 4.2 A GeV/c
Olimov K., Bekmirzaev R., Tugalov F. ……... 107

Centrality Dependencies of Transverse Momentum Spectra of Primary Charged Particles Produced in High-Energy Pb+Pb Collisions at the LHC
Olimov Kh.K., Khudoyberdieva Sh.A., Lebedev I.A., Fedosimova A.I., Liu Fu-Hu …….. 108

A Unified Approach to Transverse Momentum Spectra in High Energy Heavy-Ion Collisions
Kakhorova A.N., Olimov Kh.K. …….. 109

Multiplicity Dependencies of Midrapidity Pt Distributions of Identified Charged Particles in Proton-Proton Collisions at the LHC within a Two-Component Model
Olimov Kh.K., Fedosimova A., Liu Fu-Hu, Musaev K.A., Lebedev I.A., Tokhirov A., Ibraimova S., Bondar E. …… 111

Advantages and Disadvantages of the $\gamma\gamma$ Channel In Higgs Boson Research
Bakhromov J.O. ……. 112

Effects of Dark Matter and Einstein–Gauss–Bonnet Gravity on Massive Compact Stars
Akhmedov S.E., Palvanov G.S. …….. 114

Theoretical Predictions for α-Decay Half-Lives of Deformed and Oriented Z=119 Isotopes
Ganiev O.K., Bozarov O.A. …….. 115

Asymptotic Normalization Coefficients for $^6Li+n \rightarrow ^7Li$ and Cross Section for the $^6Li(n,\gamma)^7Li$ Reaction
Igamov S.B., Tursunmakhatov K.I., Ikromkhonov E.Sh. ……. 117

Wigner's SU(4) Spin-Isospin Symmetry and MNT&FRAGMENTATION Nuclear Reactions 119
Izosimov I.N. ……

Deformed Nuclear Shells in Mass and Energy Distributions of Fission Fragments of 240Pu* Compound Nucleus Formed in ^{236}U(α,f) Reaction at E_α=24 MeV
Alimov D.K., Pan A.N., Kovalchuk K.V., Burtebayev N., Janseitov D.M., Boztosun I., Kosherbayeva R. …….. 120

Dependencies of Midrapidity P_T Spectra of Primary Charged Particles on Centrality and Energy Of Pb+Pb and Xe+Xe Collisions at the LHC Within A TWO-Component Model
Olimov Kh.K., Khudoyberdieva Sh.A., Liu Fu-Hu, Musaev K.A., Kanokova Sh.Z. ……. 121

Creating an Independent AI Agent for Physical Research as a Response to the Challenges of Technological Sovereignty
Nishonov M.M., Umaraliev A.T. ……. 122

The Role of External Coulomb Field in Lowering Decay Barriers of Dinuclear Systems
Otakhonov F.O., Kalandarov Sh.A. …… 123

Inter-Band Reduced E2-Transition Probabilities Excited Collective States of Triaxial Even-Even Nuclei
Nadirbekov M.S., Sobirova Z., Shadmanov K.K. ……. 125

The Rigid Rotor Approximation to ODD Nuclei With Effective Triaxiality Quadrupole and Octupole Deformations
Nadirbekov M.S., Sodiqova Z.Y. ……. 126

Investigation of Reactions With ^{50}Ti and 54Cr For the Synthesis of New Elements
Oganessian Yu.Ts., Utyonkov V.K., Abdullin F.Sh., Dmitriev S.N., Ibadullayev D., Itkis M.G., Karpov A.V., Kovrizhnykh N.D., Kuznetsov D.A., Petrushkin O.V., Podshibiakin A.V., Polyakov A.N., Popeko A.G., Sagaidak R.N., Saiko V.V., Schlattauer L., Shubin V.D., Shumeiko M.V., Solovyev D.I., Tsyganov Yu.S., Voinov A.A., Subbotin V.G., Sabelnikov A.V., Abdusamadzoda D., Bodrov A.Yu., Voronyuk M.G., Bozhikov G.A., Aksenov N.V., Khalkin A.V., Gan Z.G., Zhang Z.Y., Huang M.H., Yang H.B., Wang J.G., Zhang M.M., Huang X.Y. ……. 127

Asymptotic Normalization Coefficients for ^{7}Li+n→^{8}Li and Cross Section of the ^{7}Li(n,γ)^{8}Li Reaction
Tursunmakhatov K.I., Igamov S.B., Ikromkhonov E.Sh. ……..…….. 128

Section II. **RADIATION PHYSICS OF CONDENSED MATTER AND NANOPHYSICS**

Investigation of the Stability of the Equilibrium Configuration of the Magnetic Moment of a Magnetic Material Based on the Bloch Equation
Jumaev M.R., Mirjonova N.N., Sanoev Kh.S. 131

Molecular Dynamics Simulation of Radiation Resistance in Layered Tungsten-Graphene Composites
Sharipov Z., Batgerel B., Mirzayev M., Popov E., Sarkhadov I., Tukhliev Z., Hristov I., Hristova R. …… 133

Properties of Silicon Nano-Clusters Containing Intrinsic, Background and Impurity Defects
Tashmetov M.Yu., Makhkamov Sh.M., Sulaymanov N.T., Nazarmamatov Sh.M., Rafikov A.K., Egamov S.R. …….…….. 134

Topological Control of the Volovik Effect in Cuprates: the Role of Nonmonotonic D-Wave Symmetry
Ganiev O. ……..…….……. 136

Rabi Dynamics in the Tavis—Cummings Model
Rasulova M.Yu., Tishabaev I.A.…….…….……. 138

Changes in the Optical Absorption Spectra of Cr^{3+} Ions in LiH_2PO_4 and NaH_2PO_4 Crystals under the Influence of X-Ray Irradiation
Bayazova A.A., Mamytbekov U.K., Kidibaev M.M., Joldoshov B.K. ……..……. 139

Radiation Resistance of MoTiN and NbTiN Coatings Irradiated with Inert Gas Ions
Aldabergenova T.M., Akaev S.O., Kislitsyn S.B., Klopotov A.A. ……. 141

Calculation of the Energy Yield of Nonequilibrium Energy Carriers Generated in Nano-SiO_2 under Electron Irradiation with Energies of T = 0.05-10 keV
Babayeva F.Sh., Jafarov Y.D., Abdullayev A.P. ……. 142

Features of Interstitial Atom Ordering in the $Zr_{0.5}Ti_{0.5}N_{0.27}H_y$ Solid Solution
Tashmetov M.Yu., Parpiyev A.S., Makhmudov Sh.A. …….……..… 144

Cryogenic Hall Effect Asymmetry and Stacking Fault Scattering in 3c-SiC Structures for Betavoltaic and Radiation-Hardened Applications
Atabaev B.G., Malikov Sh.R., Sulaimonov A.A., Amanov O.O., Dolgopolov M.V. …….…….…….. 146

Radiation-Induced Phase Transformations and Mechanical Degradation of Si_3N_4 Ceramics under Heavy-Ion Irradiation
Zhumazhanova A.T. ……..……. 148

Machine Learning Interatomic Potential for the Low-Modulus Ti-Nb-Zr Alloys in the Vicinity of Dynamical Instability
Mukhamedov B., Temirov D., Karimbaev E., Tasnádi F., Abrikosov I.A. …..... 149

Analysis of Electron Density Distribution and Surface RMS Parameters in GaAs(O):Cr under Gamma Irradiation
Tashmetov M.Yu., Abdaminov A.B. ……..……... 150

FTIR and Raman Spectroscopy of Electron-Induced Modifications in Si_3N_4 Nanopowder at 2 MeV Electron Fluence of 5×10^{15} e/cm^2
Tashmetov M.Yu., Buriev M.M. ……..…… 152

Transport Properties of GaAs(O):Cr under High-Fluence Electron Irradiation
TashmetovM.Yu.[1], Djangabaev Kh.N.……. 154

Phase Transformations in Thermal Barrier Ceramics Based on Zirconium Dioxide and Aluminum Oxide
Khametov Sh. ……. 156

On the State of Doped Hole in LSCO Cuprate: DFT+U Study
Eraliev A.A., Yavidov B.Ya., Khajibaev D.G. ……..…….. 157

Raman Spectroscopic Features of Electron-Irradiated GaAs
Tashmetov M.Yu., Madiyarov D.N. …… 159

Nature of Optical Absorption Bands in CaF_2–YbF_3 Single Crystals at Different Ytterbium Concentrations
Boyboboeva S.T., Utarov S.M. …… 161

Influence of Low-Energy Inert Gas Ion Implantation on the Properties of $BaCe_{0.85}Nd_{0.15}O_{2.925}$
Khromushin I.V., Mirmanova D.S. ……..…… 163

Radiation-Induced Rearrangement and Cryogenic Preservation of Hydroxyl Defects In LiF:OH Single Crystals under High-Energy Pulsed Electron Beam Irradiation
Mussaeva M.A., Nuritdinov I., Nurimbetov K.K. ……..…… 164

Changes in the Electrophysical Properties of Rhodium-Doped Silicon under γ-Irradiation
Rafikov A.K., Makhmudov Sh.A., Sulaymonov A.A. …… 166

Crystal Phase Transformations in As-Se-PET Film Holographic Grating under Exposure to 5 MeV Electron Beam
Ibragimova E.M., Temirbayeva I.N., Madaminov B. …..……. 168

Processes Occurring in the Superconducting Layer of High-Temperature Superconducting YBCO Tapes Irradiated with 5 MeV Electrons
Mussaeva M. A., Shodiev A.A. ……..…….. 170

Polaron Mass in the Mercury Family of High Temperature Superconductors
Otajonov S.M., Saburova G.G., Alibekova Sh.B., Otajanov A.M., Kurmantayev A.N., Karimov Z.I., Dzhumanov S., Yavidov B.Ya. ……..…. 171

First-Principles Study of the Effect of Hydrostatic Pressure on the Fermi Energy and Seebeck Coefficient of La_2CuO_4
Kabulov I.Sh., Karimbaev E.X. …..……..…… 173

The Role of Phase Transformations in Zirconium Dioxide Caused by Stabilizing Dopants in Restraining Disorder Processes under Heavy-Ion Irradiation
Kozlovskiy A.L., Kenzhina I.E. …… 175

Effect of Gamma-Irradiation on the Ultraviolet Photoluminescence of CaF_2:SrF_2:YbF_3 Solid-Solution Crystals and Nanoceramics
Boyboboeva S.T., Nuritdinov I., Ashurov M.Kh. …… 176

Influence of Electron Irradiation on the Recovery Time of Reverse Resistance of Diode Structures Based on n-Si Depending on the Phosphorus Content in the Single Crystal
Erdonov M.N., Makhkamov Sh., Tashmetov M.Yu., Ismatov N.B., Kholmedov Kh.M., Sobirov S.S. ……. 178

Study of Radiation Resistance of Zirconium-Containing Ceramics under Irradiation with Heavy Ions
Tynyshbayeva K.M., Kozlovskiy A.L., Kenzhina I.E. ……..……. 180

Effect of Gamma-Irradiation Temperature on the Formation of Color Centers in $LuSiO_3$:Ce Scintillation Single Crystals Additionally Doped with Calcium (Ca) Ions
Islamov A.Kh., Ibragimova E.M., Kudratov Kh.N., Khayitov I.A. …….. 181

Changes in the Structural-Morphological Characteristics and Vibrational Spectra of Thermoplastic Polymers under Electron Irradiation
Tashmetov M.Yu., Ismatov N.B. …….……. 183

Study of the Mechanisms of Formation of Radiation Damage in Lithium-Containing Ceramics Li_2TiO_3-Li_2ZrO_3 Under Irradiation with $^{He2+}$ Ions and Protons
Khametova A. …….……... 185

Synthesis of Carbon Nanostructured Materials Using Gamma Radiation
Sadikov I.I., Ibragimova E.M., Malikov Sh.R., Yuldashev M.B. Amanov O.O., Ashrapov U.T., Dolgopolov M.V. ……..... 186

Polymorphism in the SiO_2 Impurity Phase of a Silicon Single Crystal
Kalanov M.U., Sadikov I.I., Malikov Sh.R., Karakhodjaev A.A. …….…… 188

Thermal Stability of Spectrometric Properties of γ-Irradiated Gadolinium Silicate Gd_2SiO_5:Ce Crystals
Ashurov M.X., Nuritdinov I., Saidakhmedov K.Kh. …….…….. 190

Effect of Thermoradiation Treatment on the Structural Parameters of ZnS
Madaminov B.N., Tashmetov M.Yu., Makhkamov Sh., Ismatov N.B., Erdonov M.N. ……..….. 191

Temperature Kinetics and Mechanisms of Radiation-Induced Defect Formation in KCL Crystals under High-Energy Electron Irradiation
Mussaeva M.A., Nuritdinov I., Yuldashov D.P., Atashov B.T. ……..…….. 193

Features of the Optical Absorption Spectra of Cr^{3+} Ions in Single Crystals of Complex Alkali-Metal Sulfates
Ganyeva A.S., Sharsheev K.Sh., Egamberdieva A.A. …..……. 195

Influence of Heating Rate on Glow Curve Characteristics and Dosimetric Performance of Nano A-AL_2O_3
Ahadov A., Mammadov S., Ahadova A. ……..…… 198

Analytical and Digital Insights of Ancient Ceramic Technologies Using XRD Method
Ahadova A., Ahadov A., Mammadov S. ...……... 199

Influence of Gamma-Irradiation on the Electric Relaxation in $TlInSe_2$ Single Crystal
Mammadov M.A., Asadova Z.I., Asadov F.G. ……..……. 201

Investigation of Radiation Defects and the Local Neighborhood of ^{57}Fe Atoms in Thin MO and TA Films Following High-Dose Ion Implantion
Bedelbekova K.A., Andrianov V.A., Izteleuova G.S. ……..… 203

Investigation of Changes in the Phonon Properties of Si_3N_4 Nanopowder Induced by Electron Irradiation Using Raman Spectroscopy
Tashmetov M.Yu., Buriev M.M. …….. 205

Radiation-Induced Rearrangement of Phonon and Local Vibrational Characteristics in GaAs(O):Cr Under Electron Irradiation
Tashmetov M.Yu., Djangabaev Kh.N. …… 206

Gamma-Irradiation Resistance Of Layered $TlInTe_2$:Bi Compound: Raman Spectroscopy Study
Gadzhieva N.N., Khalilova K.G., Akhmedova G.B., Iskenderova G.M., Gafarova G.A. …… 208

Magnetic Properties of Transition Metal Doped GaSe Monolayers: FIRST-Principles and Machine-Learning Approaches
Huseynova S. …….. 210

A Study of Radiation Defects in Nanostructured NA-Bentonite Silicate Layers by Means Of FT-IR Spectroscopy and Nature of Radiation-Induced Defects in C
Ismayilova M.K., Mustafayev I.I., Akhundzada H.N., Khankishiyeva R. …….. 212

Prospects for Using Carbon Nanotubes for Modification of Telluride Glass-Like Ceramics
Kozlovskiy A.L., Tleulessova I.K., Kenzhina I.E. …….. 214

Comparative Raman Spectroscopic Investigation of $CuTlSe_2$ and $CuTlS_2$ Crystals Under γ-Irradiation
Mamishova R.M. …….. 215

Effect of Gamma Irradiation on the Spectral Characteristics of Paint Coatings
Melikova S., Dadashov I. ……..... 216

Changes in the Specific Resistivity of Hdpe-Based Composite Materials With a CdS/ZnS Phosphor Filler Under Gamma Irradiation
Melikova S., Hajiyeva E., Kerimova R., Nasirova A. ……..……..... 218

Spectrally Weighted One-Particle Coherence in the Active Fermi-Level Subspace
Mukhtarov A. ……... 219

Effect of Gamma Irradiation on the Optical Properties of a-GaSe Thin Films
Madatov R.S., Nurmammadova F.N. ……..……..... 220

Current–Voltage Characteristics of Gold-Doped n-Si at Different Temperatures and Evaluation for Strain-Sensitive Elements
Rafikov A.K., Sulaymonov A.A., Makhmudov Sh.A., Abdukarimov A.A., Suvanov A.Kh., Yoqubjonov J.H., Nematullayev J.R. ……..……..... 223

Effect of γ-Irradıatıon on the Absorptıon Spectra of Cu-Intercalated GaSe Layered Crystals
Sadigli L.E. ……..……... 225

Modern Nuclear Technologies in the Diagnosis and Treatment of Oncological Diseases
Ergeshbaev A.Zh., Sadyrova M.M., **Kadenova B.A.** ……. 227

Recombination Emission Near the Surface of Semiconductor Microcrystals
Yuldashev N.Kh., Mirzaev V.T., Sabirov S.S., Sulaymonov Kh.M., Yulchiev I.I., Shamirzaev T.S. …… 228

Section III. **APPLICATION OF NUCLEAR TECHNOLOGIES IN MEDICINE, ECOLOGY AND INDUSTRY**

Application of Epithermal Neutron Beam in Nuclear Medicine and Nuclear Physics
Kulabdullaev G.A., Abdullaeva G.A., Kim A.A., Yuldashev J.O., Normatov E.Kh. …… 231

Investigation of Vesicular Structure of PhTNS and PhTNS-based Drugs Using the SANS Data Analysis
Zemlyanaya E.V., Kiselev M.A., Chausova V.A., Tereshkina Yu.A., Tikhonova E.G. ……..…… 232

Study of Radioresistance and Intratumoral Heterogeneity of Human Oligoastrocytoma and Oligodendroglioma Tumors in Experimental Conditions in Vitro
Kim A.A., Kulabdullaev G.A., Abdullaeva G.A., Yuldashev D.O., Kadyrbekov N.R., Beknazarov H.J., Kadyrbekov R.T. …… 233

Dependence of Threshold-Based PET Segmentation Accuracy on Iterative Reconstruction Settings and Lesion Size: A Phantom Study
Emelyanenko E., Petkevich M., Yushkevich V. …….. 235

Potential Application of Biodegradable Chitosan Microspheres Containing ^{177}Lu for Domestic Brachytherapy
Markelova E.A., Vasidov A., Sultanov M., Asadullaev M.M., Khujaev S. …….. 237

Experimental Investigation of Photon Interaction Enhancement in a Gadolinium Chelate Contrast Agent under ^{137}Cs and ^{40}K Gamma Irradiation
Abdullaeva G.A., Rasulova D.R. ……..……..... 238

Monte Carlo Calculation of Radio-Enhanced Contrast in X-Ray Imaging
Dushanov E.B., Togtokhtur T., Bugay A.N. ……...…… 240

Extraction-Chromatographic Separation of Zinc and Gallium for the Production of Radioactive Gallium Isotopes
Mekhmonov G., Khujaev S., Markelova E. ……..…….. 242

Method for Producing the ^{131}I-MIBG Radiopharmaceutical
Galdiev M.E., Sadikov I.I., Abdukayumov A.M. ……..…….... 243

Method for the Determination of the Molar Activity of Carrier-Free [^{32}P] Orthophosphoric Acid
Khajiyev L.O., Sadikov I.I., Abdukayumov A.M., Rixsiev A.Z.……..……. 244

Determination of Radiochemical Purity and Molar Activity of ^{33}P-Labelled Orthophosphoric Acid
Khajiyev L.O., Sadikov I.I., Abdukayumov A.M., Rixsiev A.Z. …….…….. 245

Development of a Technology for Producing the Samarium-153 Radioisotope and a Radiopharmaceutical Based on it for Local (in House) Use in Specialized Medical Centers
Nishonov Sh.J., Khujaev S., Abdukayumov A.M.……... 246

Development of a Rapid Method for Producing Carrier-Free Iodine-125 in the Form of Sodium Iodide
Nishonov Sh.J., Abdukayumov A.M. ……..…… 247

Development of the Lyophilized [LUTA-TATE] Formulation and [^{177}Lu]Lu-DOTA-TATE Radiopharmaceutical: Stability Evaluation
Usarov Z.O., Khujayev S., Khajiev L.O., Abdukayumov A.M., Rikhsiev A.Z. .. 248

Preparation of the Lyophilized HYNIC-iPSMA Pharmaceutical Composition and, Based on It, the [^{99m}Tc]Tc-HYNIC-iPSMA Radiopharmaceutical
Usarov Z.O., Khujayev S., Sherov O.O., Khajiev L.O., Abdukayumov A.M., Rikhsiev A.Z. ……...…….. 250

Accelerated Voxel-Wise 3D Dosimetry for ^{177}Lu-PSMA Therapy Via Physics-Informed Neural Networks Incorporating Transport Constraints
Bozorov E.Kh., Baymuratova I.V. ……...……... 252

Reducing Indoor Radon Ingress: Impregnating Composition Based on Polyalkylhydride Siloxane and Tetraethoxysilane Hydrolysate
Khaydarov R.R., Gapurova O.U. …… 255

Measurement of the Specific Activity of ^{222}Rn and ^{226}Ra in Drinking and Groundwaters in Tashkent
Vasidov A., Vasidova S.O. ……..……. 256

Environmental Monitoring of Radionuclide Specific Activity in Man-Made Sites in the Navoi Region
Jurakulov A.R., Muzafarov A.M., Kurbanov B.I., Khaitov F.N., Mingbayev Kh.S., Elimov Kh.B. …..…….. 257

Determination of Uranium Isotope Activity in Process Waters and Advanced Sorption Materials for Their Removal
Ydyrysheva S.K., Lennik S.G., Mirkhaji D.V., Kunarbekova M.S., Kaiyrbekova A.S., Azat S. ……..……. 258

Comprehensive Assessment of the Baseline Radiological State of Water Resources in the Ecosystem of the Planned Nuclear Power Plant Construction Area
Sadikov I.I., Yarmatov B.Kh., Rozmetova F.Kh., Sharipova S.M., Akhmedov Ya.A., Solijonov S.N., Malikov A.A., Tashimova F.A. ……..……... 259

Assessment Of The Distribution And Initial Background Levels Of Gamma-Emitting Radionuclides (K-40, Cs-137, Co-60, Ra-226, and Th-232) In Soils At The Site Of A Nuclear Power Plant Under Construction
Sadikov I.I., Yarmatov B.Kh., Rozmetova F.X., Akhmedov Ya.A., Solijonov S.N. …… 260

Application of the Aspiration Method for Measuring the Volumetric Activity of Radon Decay Products in the Atmosphere
Mukashova A.B., Mamytbekov U.K., Yusupov R.Kh., Kidibaev M.M., Jeenbaev N.J. ……. 261

The Use of CR-39 Track Detectors for Age Assessment of the Ancient Human and Animal Bones
Vasidov A. …….. 263

Radionuclide Analysis of Environmental Samples With Disturbed Radioactive Equilibrium
Lennik S., Kabirova K., Silachyov I.……... 264

Distribution of Sr-90 Radionuclide in Soils of the Under-Construction NPP Territory and Assessment of Baseline Background Indicators
Yarmatov B.Kh., Sadikov I.I., Rozmetova F.Kh., Sharipova S.M. Solijonov S.N., Malikov A.A., Tashimova F.A. ……..… 265

Dependence of Radiation Indicators on Technological Processes at Uranium Processing Plants
Haydarov U., Jurakulov A., Muzafarov A. …… 266

Fast Neutron Priming Confers Cross-Adaptation to Salinity and Osmotic Stress in Triticale – Physiological Evidence and Further Integrative Studies
Kruglyak A.I., Aleksiayenak Yu.V., Volkova P.Yu., Doroshkevich A.S., Zaharova E.V. ……..……. 268

Rapid Determination щf Indium ш n Geological Samples Using WWR-K Reactor
Bedelbekova K.A., Lennik S.G., Sokolenko E.K., Kaiyrbekova A.S., Zhiyenbayev I.M., Satpayev M.M. ……..…… 269

The Role of Stabilizing Reinforcing Additives in Increasing Resistance to Long-Term Thermal Effects in Composite Ceramics
Zikirina A.M., Kozlovskiy A.L., Kenzhina I.E. ……..…… 271

A Study of the Distribution of Macro- and Microelements in Hair Samples of Staff Working in Unfavorable Working Conditions
Kurbanov B.I., Danilova E.A., Khusniddinova S.Kh., Khushvaktov N.Kh., Khaitov F.N. ……...…… 271

Neutron Activation Analysis of the Elemental Composition of Wheat Grown in Uzbekistan
Kurbanov B.I., Danilova E.A., Khusniddinova S.Kh., Kurbanova N.B. …..…… 273

Use of Photonuclear Reactions with the Formation of Short-Lived Isomers in Analytical Problems
Shovdirova S.L., Kurbanov B.I., Mingbaev Kh.S. ……..……... 274

Possibilities of Using the Geant4 Software Package in Proton and Ion Therapy for Modeling and Calculations
Palvanov S.R., Ramazonov A.X., Abdusalomova M.R. ……. 275

Development of a High-Frequency Inductive Method for Measuring Magnetic Susceptibility in the Temperature Range 80–300 K
Nebesniy A.F. ……..……... 277

Artificial Intelligence in Neutron Activation Analysis
Umaraliev A.T., Nishonov M.M. ……. 278

Adventive Plants in the Sanitary-Protection Zone of the Institute of Nuclear Physics of the Uzbekistan Academy of Sciences
Tillayev T.S., Tillayev Sh.B. ……..…….. 279

Determination of Iron Content in Plant-Based Food Products Using Neutron Activation Analysis
Kuldjanov B., Danilova E. ……..……..……. 282

Production of Iridium-192 Ionizing Radiation Sources for Radiographic Testing of Metal Welded Joints
Ashrapov U., Malikov Sh., Amanov O., Mogoch S. ……..…… 284

Improvement of Spectral and Physical Parameters of the Neutron Radiography and Tomography Facility at the WWR-SM Research Reactor
Tashmetov M.Yu., Adizov S.M., Ismatov N.B. ……..….. 286

Radionuclide Fractionation During Phosphorite Processing and Source Apportionment of Elemental Anomalies in AN Industrial AREA
Sadikov I.I., Akhmedov Ya.A., Yarmatov B.X., Danilova E.A., Malikov A.A. .. 289

AI-Assisted Selection of New Radiolabelled Pharmaceuticals Based on the Radiopreparat Production Platform
Usmanova S.A. ……. 290

Demand For Reactor- And Cyclotron-Produced Isotopes In Instrumentation, Metrology, Industry, And Medical Diagnostics
Bespokoev A.A., Rogozev A.B., Buryanenko I.V. ……..… 292

***SECTION IV.* NUCLEAR ENERGY AND ADVANCED NUCLEAR POWER SYSTEMS**

Safety Regulation and Licensing in the Management of Radioactive Waste and the Operation of Radiation Sources
Belkin D.Y., Sklifasovskaya Y.G. …… 295

Prospects for the Use of Reactors with Heavy Liquid Metal Coolant in Uzbekistan's Nuclear Program
Yablochkina A.A., Elmurotova D.B. 295

Problems in the Manufacture of the Ritm-200 Reactor Plant
Elmurotova D.B., Yablochkina A.A. 297

Beryllium Reflector Poisoning Effect Analyses of the WWR-SM Research Reactor
Umarov Sh.B., Umarova M.O., Nguyen Tran C.H., Tikhomirov G.V. 299

Tests of New IRT-4M Fuel Assemblies with UO_2–AL and U_3SI_2–AL Fuel Compositions
Baytelesov S.A., Kungurov F.R., Alikulov Sh.A., Tadjibaev D.P., Fayziev T.B. . 301

Development of Thermophysical Model of Fuel Assembly of the IVG.1M Reactor for Analysis of Temperature Distribution under Different Operating Modes
Toleubekov K., Martynenko Y., Bekmuldin M. 302

Computational Assessment of the Feasibility of Testing Advanced Nuclear Fuel in the IGR Reactor
Surayev A.S., Mukhamedov N.E., Irkimbekov R.A., Zhanbolatov O.M., Seken D.M. 303

Comprehensive Studies of Radiation Resistance and Gaseous Swelling Processes in BeO Ceramics Promising Materials for Nuclear Power Engineering
Kenzhina I.E., Kozlovskiy A.L., Zhigalova A. 304

Relationship Between Electrical Resistivity and Thermal Conductivity of the SAV-1 Aluminum Alloy at Various Fast Neutron Fluences
Baytelesov S.A., Kungurov F.R., Alikulov Sh.A., Tadjibaev D.P., Fayziev T.B. . 305

Electrostatic Interface Engineering as a Design Framework for Radiation-Hardened Resonant-Tunneling Nanodosimeters
Dosymova B.U., Dolgopolov M.V. 305

Neutron Irradiation Behavior and Phase Stability of Beryllides
Aitkulov M., Shaimerdenov A., Sairanbayev D., Askerbekov S., Akhanov A., Silnyagin P., Averkova T., Migunova A., Udartsev S. 307

Thermogravimetric Response of Neutron-Irradiated Chromium Beryllide in a Steam-Argon Atmosphere
Askerbekov S., Shaimerdenov A., Silnyagin P., Bugybay Zh., Akhanov A., Chikhray Ye., Kulsartov T., Elishenkov A., Kenzhina I., Zaurbekova Zh. 308

Methodology for Corrosion Testing of Titanium Beryllide $Be_{12}Ti$ And Chromium Beryllide $Be_{12}Cr$ under Supercritical and Ultra-Supercritical Steam Conditions
Yelishenkov A., Chikhray Ye., Kulsartov T., Kenzhina I., Zaurbekova Zh., Askerbekov S., Kenzhin Ye., Udartsev S. 309

Radiation-Induced Swelling of SAV-1 and AMG-2 Alloys under Neutron Irradiation
Akhmedzhanov F.R., Boltabaev A.F. 310

Synthesis and Study of High-Entropy Rare-Earth Zirconates
Zhumatayeva I. 312

Neutron Methods as Reference Tools for Non-Destructive Characterization of Engineering Materials
Altynbaev E.V., Gogolinsky K.V. ……...……. 313

Nucleosynthesis at High Dust Plasma Density
Khasanov Kh. ……..…….. 315

Development and Testing of Cathode Strip Chambers (CSC) with Dimensions of 1.5x2.2 m^2 for the Bm@N Experiment
Kattabekov R.R., Kapishin M.N., Kiryushin Yu.T., Kulish E.M., Makankin A.M., Piyadin S.M., Spaskov V.N. ……..…. 316

Results of the First Tests of Electroslag Remelting of Metal Radioactive Waste at the Atomic Energy Institute of the RSE NNC RK
Mukhamedov N.E., Toleubekov K.O., Pakhnits A.V., Dolzhikov S.A. …….. 318

Methods for Determining the Content of Boron, Cadmium, and Hafnium in Finished Uranium Products
Suyunov U.A., Allaberganova G.M., Muzaffarov A.M. ……...……..... 319

Methods for Determining the Specific Activities of ^{234}U, ^{235}U, and ^{238}U Isotopes in Uranium Oxide (U_3O_8)
Suyunov U.A., Urunov I.A., Allaberganova G.M., Muzafarov A.M. …….. 321

Modern Spectrometric Methods for the Analysis of Uranium Chemical Concentrates
Urunov I.A., Allaberganova G.M., Muzafarov A.M. ……. 323

Operational Aspects of the IR-8 Research Reactor
Andreev D.V. ……..…… 326

Uncertainty Analysis of Level-1 PSA for NPP Using Monte Carlo Method with Latin Hypercube Sampling: a Case Study of the Emergency Core Cooling System
Mukhamedov B.O., Rakhimkulov M.M., Temirov D.T., Kuldjanov B.K., Salikhbaev U.S. …….. 326

ALPHABETICAL INDEX …….. 328

CONTACTS OF CONFERENCE PARTICIPANTS……. 337

THE XII INTERNATIONAL CONFERENCE

NUCLEAR SCIENCE AND ITS APPLICATION (ICNSA2026)

October 12-15, 2026, Ulugbek, Tashkent

BOOK OF ABSTRACTS

Institute of Nuclear Physics, Academy of
Sciences of Uzbekistan, 2026, 366 pages.

XII XALQARO KONFERENSIYA

"YADRO FANI VA UNING TATBIQI" (ICNSA2026):

2026-yil 12–15-oktabr, Ulug'bek, Toshkent

MA'RUZALAR TEZISLARI TO'PLAMI

O'zbekiston Respublikasi Fanlar Akademiyasi
Yadro Fizikasi Instituti, 2026, 366 bet.

The content of all abstracts is published in the author's edition

Содержание всех тезисов публикуется в авторской редакции

Barcha tezislarning mazmuni muallif nashrida chop etiladi

Mailing address: Institute of Nuclear Physics, Ulugbek
Tashkent, UZ-100214, Republic of Uzbekistan,
Telephone: (998-71) 289-31-41, (998-71) 289-35-57
E-mail: fazilovaz@mail.ru; leyla.valieva.00@bk.ru

https://inp.uz/research/conferences/2



Institute of Nuclear Physics of Uzbekistan Academy of Sciences

Ulugbek, Tashkent